AD-A079 115 NAVAL AIR DEVELOPMENT CENTER WARMINSTER PA F/G 1/3
PROCEEDINGS OF A WORKSHOP ON V/STOL AIRCRAFT AERODYNAMICS, VOLU--ETC(U)
MAY 79 C HENDERSON, M F PLATZER

UNCLASSIFIED NL

1 OF 7
AD
A079115

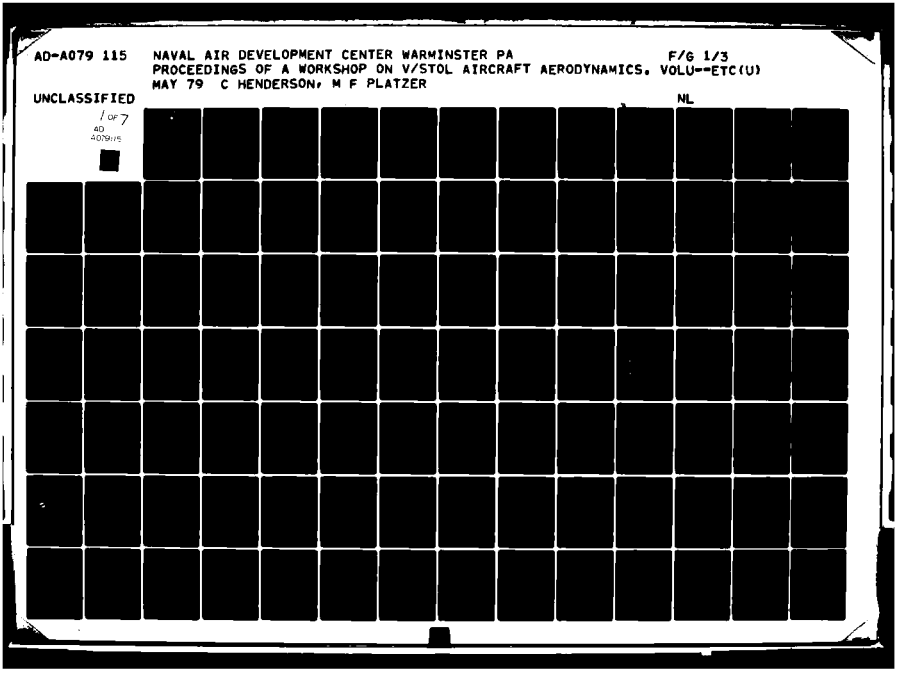

Proceedings

V/STOL AIRCRAFT AERODYNAMICS

Volume I

Sponsored by

NAVAL AIR DEVELOPMENT CENTER

---

16 to 18 MAY 1979

NAVAL POSTGRADUATE SCHOOL

MONTEREY, CALIFORNIA

PROCEEDINGS OF A WORKSHOP

ON

V/STOL AIRCRAFT AERODYNAMICS

VOLUME I

SPONSORED BY

NAVAL AIR DEVELOPMENT CENTER

HELD AT

NAVAL POSTGRADUATE SCHOOL

MONTEREY, CALIFORNIA

15 - 18 MAY [redacted], 1979

CHAIRMEN: C. HENDERSON, NADC

M. F. PLATZER, NPS

TABLE OF CONTENTS

OVERVIEW SESSION

x) This presentation was based on a movie and therefore is not included in the proceedings.

MAIN PRESENTATIONS

VOLUME I

PAGE

PAGE

PAGE

C. Session III:

Experimental Techniques in VSTOL Aircraft Development

Chairman: David Hickey, NASA-Ames Research Center

x) Not submitted for publication

VOLUME II

x) Not submitted for publication

FOREWORD AND ACKNOWLEDGMENT

A Workshop on V/STOL Aircraft Aerodynamics, sponsored by the Naval Air Development Center, was held at the Naval Postgraduate School during May 16-18, 1979 for the purpose of information exchange, status review and identification of critical problems by technical specialists working in the fields of V/STOL aircraft aerodynamics, propulsion and flight mechanics.

The proceedings of the workshop contain the papers presented in the five sessions and a transcript of the panel discussion. It is hoped that this information will prove useful not only to the relatively small group of specialists working in the field of V/STOL aircraft aerodynamics but will also provide helpful stimulus to others who wish to inform themselves about this challenging frontier in aeronautical engineering.

A number of people contributed to the success of this workshop whose contributions are gratefully acknowledged. Mr. C. J. Mazza, Naval Air Development Center, initiated and supported this meeting. RADM T. F. Dedman, Superintendent of the Naval Postgraduate School, gave the welcome address which was very much appreciated. Sincere thanks are extended to the many participants, including our friends from the United Kingdom and Canada, and to the session chairmen for their individual contributions. Finally, we are much indebted to Mmes. Evelyn Basham and Janice Cicconi for their help in organizing the workshop, transcribing the tapes and assembling the written material.

C. HENDERSON
Naval Air Development Center

M. F. PLATZER
Naval Postgraduate School

LIST OF PARTICIPANTS

D. Adler
Israel Institute of Technology
Technion City, Haifa 32000
Israel

K. Aoyagi
Research Engineer
NASA Ames Research Center
Moffett Field, California 94035

H. Arnaiz
NASA Dryden Flight Research Center
P.O. Box 273
Edwards, California 93523

R. O. Bailey
Aircraft Aerodynamics Branch
NASA Ames Research Center
Moffett Field, California 94035

A. J. Baker
Computational Mechanics Consultants, Inc.
3601-A Chapman Highway
Knoxville, Tennessee 37920

J. P. Barrack
NASA Ames Research Center
Moffett Field, California 94035

T. D. Beatty
Vought Corporation
P.O. Box 5907
Dallas, Texas 75222

D. P. Bencze
Aircraft Aerodynamics Branch
NASA Ames Research Center
Moffett Field, California 94035

M. D. Betzina
Aerospace Engineer
Aeromechanics Laboratory
U.S. Army Research & Technology Laboratories
NASA Ames Research Center
Moffett Field, California 94035

Paul M. Bevilaqua
Rockwell International
Columbus, Ohio 43218

W. W. Bower
McDonnell-Douglas Research Laboratories
P.O. Box 516
St. Louis, Missouri 63166

A. L. Byrnes
Lockheed-California Company
Burbank, California 91520

R. L. Carmichael
Aircraft Aerodynamics Branch
NASA Ames Research Center
Moffett Field, California 94035

Y. T. Chin
Lockheed-California Company
Department 75/41
Bldg 63G, Plant A-1
P.O. Box 551
Burbank, California 91520

S. J. Craig
Systems Tech., Inc.
Hawthorne, California 90250

R. G. Culpepper
NASA Langley Research Center
Hampton, Virginia 23665

J. V. Davis
Naval Air Systems Command
PMA 269
Washington, DC 20361

J. T. DeLany
D/71-6
Rockwell International
Columbus Aircraft Division
4300 E. Fifth Avenue
P.O. Box 1259
Columbus, Ohio 43218

J. H. Diedrich
NASA-Lewis Research Center
Cleveland, Ohio 44135

M. E. Dillenius
Research Engineer
Nielsen Engineering & Research, Inc.
Mountain View, California 94043

L. Duke
NASA Dryden Flight Research Center
P.O. Box 273
Edwards, California 93523

T. Duvvuri
Duvvuri Research Associates
651 Windsor Circle
Chula Vista, California 92010

J. C. Erickson, Jr.
Aerodynamic Research Department
Calspan Corporation
Advanced Technology Center
Buffalo, New York 14225

L. L. Erickson
Aircraft Aerodynamics Branch
U.S. Army Research & Technology Labs.
Moffett Field, California 94035

M. Falarski
Aerospace Engineer
NASA Ames Research Center
Moffett Field, California 94035

R. Fearn
Department of Engineering Sciences
University of Florida
Gainesville, Florida 32611

W. H. Foley
Aerodynamics Engineering Manager
General Dynamics Corporation
P.O. Box 748
Fort Worth, Texas 76101

R. J. Furey
David Taylor Naval Ship Research
and Development Center
Bethesda, Maryland 20084

D. B. Garland
Senior Engineer
The De Havilland Aircraft
of Canada, Ltd.
Downsview, Ontario M3K 1Y5

D. P. Gleiter
Naval Air Development Center
Warminster, Pennsylvania 18974

R. Greene
ASD/XRU
Wright-Patterson AFB, Ohio 45433

D. L. Hammond
AFFDL/FXB
Wright-Patterson AFB, Ohio 45433

J. D. Hawk
NASA Lewis Research Center
Cleveland, Ohio 44135

C. Henderson
Flight Dynamics, Code 6053
Naval Air Development Center
Warminster, Pennsylvania 18974

D. Hickey
NASA Ames Research Center
Moffett Field, California 94035

W. G. Hill, Jr.
Research Department, A-08-35
Grumman Aerospace Corporation
Bethpage, New York 11714

R. C. Jenkins
Research Department, A-08-35
Grumman Aerospace Corporation
Bethpage, New York 11714

J. Katz
Mail Stop 247-1
NASA Ames Research Center
Moffett Field, California 94035

G. Kidwell
NASA Ames Research Center
Moffett Field, California 94035

R. J. Kita
Grumman Aerospace Corporation
Bethpage, New York 11714

P. G. Knott
British Aerospace, Warton Division
Wind Tunnel Department
Warton Aerodome
Preston, Lancashire PRY1AX
England

D. Koenig
Mail Stop 247-1
NASA Ames Research Center
Moffett Field, California 94035

D. R. Kotansky
Section Chief, Aerodynamics
McDonnell Douglas Corporation
McDonnell Aircraft Company
P.O. Box 516
St. Louis, Missouri 63166

S. S. Kress
Vought Corporation
P.O. Box 5907
Dallas, Texas 75222

R. Kuhn
AMPAC Corporation
2640 Amy Drive
Norristown, Pennsylvania 19403

D. Lacey
David W. Taylor Naval Ship Research
and Development Center
Bethesda, Maryland 20014

R. J. Laib
Code 034Le
Naval Postgraduate School
Monterey, California 93940

B. A. Lampkin
Mail Stop 237-9
NASA Ames Research Center
Moffett Field, California 94035

J. A. Laughrey
Air Force Flight Dynamics Laboratory
AFFDL-FXM
Wright-Patterson AFB, Ohio 45433

D. Levine
Mailstop 247-1
NASA Ames Research Center
Moffett Field, California 94035

E. L. Lewis
Code 03APAJ
Naval Air Systems Command Headquarters
Washington, DC 20361

R. B. Lowry
AFFDL/FXB
Wright-Patterson AFB, Ohio 45433

J. R. Lummus
Senior Engineer
General Dynamics Corporation
Fort Worth Division
Fort Worth, Texas 76100

C. J. Martin
David W. Taylor Naval Ship Research
and Development Center
Bethesda, Maryland 20014

H. McMahon
Georgia Institute of Technology
School of Aerospace Engineering
Atlanta, Georgia 30332

M. R. Mendenhall
Nielsen Engineering & Research, Inc.
510 Clyde Avenue
Mountain View, California 94043

L. D. Miller
Lockheed-California Company
Burbank, California 91520

W. T. Miller
Naval Air Development Center
Warminster, Pennsylvania 18925

R. D. Murphy
Naval Air Systems Command
Washington, DC 20361

T. C. Nark
Boeing Aerospace Company
P.O. Box 3999
Seattle, Washington 98124

W. P. Nelms
Aircraft Aerodynamic Branch
NASA Ames Research Center
Moffett Field, California 94035

J. H. Nichols
David W. Taylor Naval Ship Research
and Development Center
Bethesda, Maryland 20014

M. E. Omar
Boeing Aerospace Company
P.O. Box 3999
Seattle, Washington 98124

W. Painter
NASA Dryden Flight Research Center
P.O. Box 273
Edwards, California 93523

R. E. Palmer
Naval Air Development Center
Warminster, Pennsylvania 18974

J. W. Paulson, Jr.
Mail Stop 286
NASA Langley Research Center
Hampton, Virginia 23665

S. Perkins
Nielsen Engineering & Research, Inc.
510 Clyde Avenue
Mountain View, California 94043

R. Perkins
Deputy Chief V/STOL Project Office
Naval Air Systems Command
Washington, DC 20361

M. F. Platzer
Code 67Pl
Department of Aeronautics
Naval Postgraduate School
Monterey, California 93940

H. C. Quigley
NASA Ames Research Center
Moffett Field, California 94035

D. Renselaer
Rockwell International
Los Angeles, California 90009

V. Rossow
Mail Stop 247-1
NASA Ames Research Center
Moffett Field, California 94035

A. Rubel
Research Department
Grumman Aerospace Corporation
Bethpage, New York 11714

R. L. Schaeffer
David W. Taylor Naval Ship Research
and Development Center
Bethesda, Maryland 20014

P. R. Scheurich, Jr.
David W. Taylor Naval Ship Research
and Development Center
Bethesda, Maryland 20014

D. B. Schoelerman
Vought Corporation
P.O. Box 5907
Dallas, Texas 75222

A. Sim
NASA Dryden Flight Research Center
Edwards, California 93523

C. W. Smith
Engineering Specialist
General Dynamics Corporation
Fort Worth Division
Fort Worth, Texas 76100

E. Snowden
General Dynamics
Fort Worth Division
Fort Worth, Texas 76100

E. D. Spong
Branch Chief, Propulsion
Dept. 343, Bldg. 32/2
McDonnell Aircraft Company
P.O. Box 516
St. Louis, Missouri 63166

V. R. Stewart
Member of Technical Staff
Rockwell International, Columbus
4300 E. Fifth Avenue
Columbus, Ohio 43218

N. O. Stockman
NASA Lewis Research Center
Cleveland, Ohio 44135

S. C. Stumpfl
U.S. Air Force Flight Dynamics Lab.
Wright-Patterson AFB, Ohio 45433

J. Syberg
Boeing Military Airplane Development
Boeing Aerospace Company
P.O. Box 3994
Seattle, Washington 98124

D. Tavella
Joint Institute of Aerodynamics
and Acoustics
Stanford, California 94305

T. H. Thompson
PMA 269T
Naval Air Systems Command
Washington, DC 20361

R. H. Traudt
Air Force Systems Command AFSC-XRL
Bolling Air Force Base
Washington,DC 20332

G. Vander Plaats
NASA Ames Research Center
Moffett Field, California 94035

R. F. Vomaske
Mail Stop 237-9
NASA Ames Research Center
Moffett Field, California 94035

S. A. Walker
U.S. Air Force Aeronautical Systems Division
Wright-Patterson AFB, Ohio 45433

R. Weinraub
AIR-5301
Naval Air Systems Command
Department of the Navy
Washington, DC 20361

R. Whitehead
Office of Naval Research
Department of the Navy
800 N. Quincy Street
Arlington, Virginia 22217

P. Whitten
General Dynamics Corporation
Fort Worth Division
Fort Worth, Texas 76100

F. W. Wilson
Code 1613
David W. Taylor Naval Ship Research
and Development Center
Bethesda, Maryland 20014

J. Wilson
Air Force Office of Scientific Research
AFOSR-NA, Building 410
Bolling Air Force Base
Washington, DC 20332

W. Woodrey
General Dynamics Corporation
Fort Worth Division
Fort Worth, Texas 76100

P. T. Wooler
Aerosciences Research
Department 3811, Zone 82
Northrop Corporation, Aircraft Group
3901 W. Broadway
Hawthorne, California 90250

K. T. Yen
Naval Air Development Center
Warminster, Pennsylvania 18974

A. Zalay
Lockheed MIssile and Space Company
Huntsville Research & Engineering Center
P.O. Box 1103
Huntsville Alabama 35800

H. Ziegler
Northrop Corporation
Aircraft Division
3901 W. Broadway
Hawthorne, California 90250

OVERVIEW SESSION

"NAVY V/STOL - A CONTINUING INITIATIVE"

by Russel G. Perkins, Jr.,
Deputy Project Manager
Naval Air Systems Command

ABSTRACT

A project overview of the Navy's V/STOL Project is presented. Discussion includes a brief review of V/STOL project history, current project philosophy, present and future V/STOL project activities and a simplified model for structuring comparisons between CTOL and V/STOL aircraft. The scope of the Sea Based Air Master Study (SBAMS) and the relationship of current V/STOL industry studies are reviewed. Some results of CTOL vs. V/STOL aircraft force level comparisons are contrasted against unit comparisons between V/STOL and CTOL aircraft to illustrate limitations of unit aircraft comparisons. Aircraft design studies supporting the SBAMS are summarized.

INTRODUCTION

The Navy V/STOL Project has been in existence for over two years without a definitive development program emerging. It is the objective of this paper to provide a project perspective on the technical challenge and operational issues related to NAVY V/STOL, and how the NAVY's project emphasis has shifted to address those issues. This paper will briefly review the V/STOL project history, current project philosophy, present and future V/STOL project activities, and provide some thoughts on V/STOL versus CTOL comparisons.

PROJECT HISTORY

The NAVY has had a serious, continuing interest in V/STOL aircraft since the early '70's beginning with the Sea Control Ship (SCS) exercises and initiation of the Thrust Augmented Wing (TAW) research aircraft project. A Naval Air Systems Command project office for V/STOL aircraft development was finally established in November 1976. Its objective was to develop a new subsonic, multi-mission V/STOL aircraft. This project received great emphasis within the NAVY in August 1977 when Admiral Holloway, then CNO, published his V/STOL concept paper. That paper established the objective to transition tactical naval aviation to an all V/STOL sea based aircraft force contingent upon proof of concept for V/STOL aircraft. Its rationale presented a need for expanding and dispersing sea based aviation over a large number of air capable platforms to provide increased flexibility of operations without a decrease in total fleet capability. The paper envisioned two classes of V/STOL aircraft -- a Type A subsonic, multi-mission aircraft and a Type B supersonic, fighter/attack aircraft. NAVY and Marine Corps aircraft acquisition programs at that time predicated that the V/STOL A aircraft would be developed first. A collateral objective of the V/STOL transition was to reduce the basic number of aircraft types within the Navy fleet. V/STOL A was to be a multi-mission family of related aircraft designs having a high degree of commonality between individual aircraft mission variants. Project office goals were to: (1) prove the technical feasibility of the V/STOL concept, and (2) establish a development and acquisition program for a subsonic, multi-mission V/STOL aircraft.

The V/STOL technological challenge was perceived to require significant technology advances across many technical disciplines leading to improvements in aircraft system characteristics in three distinct areas (performance, readiness and basing flexibility) which are illustrated in Figure 1. First, major weight reductions were required in structures, aircraft subsystems, fixed equipment, and mission loads to compensate for the large increase in propulsion system weight necessitated by the high thrust required for a V/STOL aircraft. Extrapolation of present operational aircraft technology exemplified by the S-3 to a V/STOL aircraft with the projected Type A mission load would yield an aircraft too large in size and weight to be affordable and practical to operate from smaller ships.

Substantial weight reductions were required to produce practical aircraft with sufficient mission performance. Second, achieving expanded basing flexibility required development of flight dynamics design criteria and terminal area operations compatible with V/STOL aircraft basing aboard smaller, air capable ships and integration of the aircraft flight control system and shipboard landing system. Third, major improvements in aircraft reliability and maintainability were necessary to achieve higher overall aircraft readiness to be consistent with dispersed operations of fewer numbers of aircraft aboard smaller ships as compared to a larger number of aircraft operating from a single aircraft carrier. Work efforts sponsored by the V/STOL project office were oriented toward achieving these technology goals.

Considerable energy was expended in development strategy planning during the first year of the V/STOL A project. The acquisition strategy which evolved was strongly influenced by OMB Circular A-109 and related Department of Defense acquisition directives which had been previously issued. The general description of the anticipated V/STOL A development program is depicted in Figure 2. The acquisition strategy set forth was designed to achieve the following objectives:

- stimulate sufficient innovation in airframe, propulsion and avionics technology areas to achieve advances needed to successfully execute the program,
- stimulate effective competition,
- establish prime contractors with a balanced approach in airframe, propulsion and avionics activity and in a position to promote total systems optimization.

It was structured into phases such that each phase was to be conducted as a logical extension of the previous phase:

- a concept formulation phase to provide funded contractor advanced design concepts and technology advancement efforts,
- an advanced development phase including aircraft and avionics prototype development,
- full scale development and ensuing production phases.

The complexity of the V/STOL technical challenge and the close interrelationship between the engine and aircraft development in conjunction with the level of competition deemed appropriate by A-109 philosophy lead to a level of competition unprecedented by any previous NAVY aircraft development program. Concept formulation was to be accomplished by multiple contractor teams leading to a selection of two contractor teams who would compete through a competitive prototype aircraft flyoff and substantial avionics systems technology validation. A single contractor team would be selected to proceed into full scale development of

an operational V/STOL aircraft weapon system. A single prime contractor approach was favored although complete agreement to this acquisition strategy had not been reached within the NAVY.

PROJECT TRANSITION AND CURRENT PHILOSOPHY

Reservations about progress and goals of the V/STOL A program developed in the spring of 1978 in three areas -- program affordability, apparent complexity of the V/STOL A design problem and justification of the V/STOL concept. At that time the V/STOL A program which was proceeding according to the basic acquisition plan outlined in Figure 2 demanded a commitment of resources for the ensuing FYDP (Five Year Defense Plan) years well in excess of amounts tolerable to the planned NAVY budget. The V/STOL acquisition strategy which was considered dynamic in its approach to stimulating significant technology advances in many areas and providing for a level of competition consistent with a strict interpretation of A-109 had essentially become an unaffordable program.

The design problem presented by the Type A aircraft multi-mission concept posed too many diverse and stringent design requirements to be satisfied by a single, practical aircraft configuration. Results of a Navy evaluation of Contractor responses to the Type A V/STOL RFQ/I indicated that a single basic aircraft configuration could not satisfy all of the specifications for ASW, AEW, COD and Marine Assault aircraft that were identified as design goals (although some aircraft concepts had shown greater potential than others). The resulting aircraft designs were too large and heavy to achieve the desired levels of performance. Ship compatibility with the DD963 class of destroyer was unacceptable for almost all proposed aircraft configurations. The R&M objectives established at that time appeared to be unrealistic goals considering complexity of the advanced V/STOL configurations and development constraints.

The affordability problem and, to a lesser extent, the apparent technical deficiencies of a single aircraft configuration to satisfy the range of Type A mission roles invisioned precipitated a Navy program decision to reorient the Navy V/STOL program. The lack of sufficient funding and an inadequate technology base precluded the planned execution of a V/STOL A development program. In addition, there was a growing concern within the Navy that a strong analytical case supporting extensive V/STOL aircraft development remained to be made, and that a decision to transition to an all V/STOL sea based aircraft force was premature. Attendant to this concern was a growing appreciation that the V/STOL question involved more than evaluating an alternative basing concept, but also a potential for more fundamental changes in sea based air warfare and missions.

Today, a greater emphasis is being placed on developing an understanding of operations of a V/STOL sea based air force, its potential role in tactical warfare, and to establish a justification (if warranted) for a V/STOL transition. The V/STOL program decision and subsequent Congressional action on the Fiscal Year 1979 Budget directed the current thrust of the

V/STOL project. The redirection emphasized a technology orientation to the project which would provide a foundation for undertaking either a supersonic or a subsonic prototype aircraft program but to emphasize planning for a supersonic fighter/attack prototype. The Congress, during their review of the FY-79 Navy Budget, directed the Navy to defer a commitment to major hardware development until completion of the Sea Based Air Master Study (the scope of the Sea Based Air Master Study will be discussed later). As a consequence of these actions, a greater amount of resources have been applied to addressing the operational issues and questions. Technology work is proceeding at a greatly reduced level compared to that initially established in the V/STOL A program plan. The critical path in current V/STOL project activities is to determine the need for V/STOL and reach a consensus on that determination. To provide some insight into the complexity of the problem, the next section discusses some difficulties in making comparisons between V/STOL (vertical or short take-off and landing) and CTOL (conventional take-off and landing using catapults and arresting gear for naval aircraft) aircraft and presents a simplified model for comparing them.

V/STOL VS. CTOL COMPARISONS

Previous comparisons between V/STOL and CTOL aircraft emphasize examination of one or more figures of merit which offer an intuitive engineering basis for drawing conclusions. Aircraft design take-off gross weight, aircraft weight empty, aircraft flyaway cost and/or aircraft life cycle costs for equivalent sized aircraft fleets are examples. Fundamental to these comparisons are assumptions of equal design mission performance and an aircraft unit evaluation of characteristics. Figure 3 presents some of these comparisons based upon Navy inhouse notional aircraft designs prepared for use in the Sea Based Air Master Study. Ratios of the V/STOL value over the CTOL value are plotted for both supersonic, fighter/attack aircraft and subsonic multi-mission aircraft. These aircraft were designed for equivalent payload and mission profile objectives with some slight variations dictated by the different basing flexibilities. Note that in every category of comparison the CTOL aircraft show a decided advantage over the V/STOL aircraft. They have smaller spotting factors, lower take-off weights, lower empty weights, and lower cost. The supersonic, fighter/attack aircraft exhibit smaller weight and cost differentials between CTOL and V/STOL aircraft but larger differences in spotting factors compared to the subsonic, multi-purpose aircraft trends. The cost comparison ratios are almost identical. These comparisons stand against usually very subjective arguments presented about the inherent advantages and attractive features of V/STOL aircraft. Historically, numbers tend to win most arguments.

These unit aircraft comparisons which are reasonable engineering comparisons of goodness may not accurately represent the relative values or utility of the respective aircraft. They may, in fact, be misleading. V/STOL aircraft present unique capabilities, but the utilization of that uniqueness tends to be difficult to project, quantify, and finally evaluate. There is a growing awareness that V/STOL advantages are inherently tied to effects on higher order comparisons between force

alternatives and that quantitative comparisons may be developed at that level. For example, a carrier's maximum combat potential as measured by the number of sorties completed during a given period is more of a basic unit of measure - not individual aircraft performance - for almost any naval engagement. A larger variety of tactics become possible by the integration of V/STOL and small air capable ships into a naval battle group making quantitative comparisons difficult to establish. The modern aircraft carrier is the most complicated unit of military force to be analyzed because of the flexibility of its airwing to adapt to different types of warfare under different circumstances. This flexibility produces confusion in understanding and quantifying its potential. V/STOL aircraft greatly expand the range of possible carrier platforms. Force level comparisons inevitably lead to questions about mission roles and scenarios. Reference (1) presents a good unclassified discussion of the potential types of war toward which defense planning should be oriented and suggested goals for U.S. tactical forces, air, sea and land. Selection between diverse sea based air force alternatives may reflect a strengthened role for the Navy in supporting vital U.S. interests in the future world.

Figure 4 presents results of a simplified evaluation of equal cost constrained, alternative sea based air force options for CTOL and V/STOL aircraft in a power projection role. For this particular case, the V/STOL force options show a significant advantage over their CTOL counterparts. This result is primarily determined by the increased number of sorties projected for V/STOL airwings operating from carriers compared to numerically equivalent CTOL airwings. Results are presented in terms of sortie ratios to eliminate disclosure of classified information. Alternative carrier force capabilities are normalized against the performance of a single aircraft carrier operating a ninety-seven (97) aircraft airwing. As the number of aircraft carriers increases, their individual sizes are decreasing. The appendix discusses a simple model for evaluating V/STOL and CTOL aircraft which was used to generate the results presented in Figure 4. The model considers unit aircraft carrier airwing performance, carrier deployment patterns, dynamics of carrier deployments, and relative ship and aircraft life cycle cost.

Actual conclusions cannot be drawn from Figure 4. It presents results only for a single mission role based upon cursory analysis. Figure 4 and the Appendix serve to illustrate the complexity of making meaningful comparisons between CTOL and V/STOL aircraft. The need for a V/STOL transition or the utility of V/STOL aircraft cannot be determined or estimated merely by making unit aircraft comparisons (as in Figure 3).

CURRENT NAVY V/STOL PROJECT ACTIVITIES

Current project activities address three different aspects of the V/STOL problem -- the technical challenge, the need for V/STOL versus the alternatives, and evolving an affordable development program with acceptable risks. Figure 5 presents an overall program schedule indicating time phasing between areas of project activity. Completion of the first round of the Sea Based Air Master Study is critical to achieving major

progress in the V/STOL program. That study will provide a comparative analysis of sea based aircraft alternatives which will establish the potential benefit or lack of it for V/STOL. Industry studies will contribute technical data and program planning information which combined with other inhouse studies are to provide the framework for structuring a request for quotation on a design definition phase. Technology based activities during calendar years 1979 and 1980 will investigate critical technical issues and provide substantiating data from hardware experiments where practical to reduce program risks and advance the state-of-the-art in key technology areas prior to or during the design definition phase.

The overall objective of the Sea Based Air Master Study (SBAMS) is to provide an assessment and comparisons between a number of future sea based air force alternatives for postulated missions of the U.S. Navy in the future. Figure 6 is a workflow diagram depicting the basic study logic. A fundamental assumption governing the study is that alternative forces are to be compared on an equal cost basis constrained by a projected budget ceiling for tactical sea based aviation forces. The threat projection and projection of mission roles for the Navy of the future are the principal guidance which governs these studies. Objective capabilities for weapons systems to meet the needs and the context in which they will be employed are derived from this guidance. It provides the basis for development of the operational concepts.

A number of technical studies are being conducted within the SBAMS which together investigate all major systems within the present and foreseeable future of naval tactical forces including aircraft, ships, weapons, communications, command and control, and logistics. These studies will output costs, system performance, physical characteristics, operating constraints, system interface descriptions and mission utilization data to be used in other elements of the Sea Based Air Master Study. The evolved operational concepts and the technical study outputs are the framework for constructing candidate ship and aircraft weapon fleets to be examined. The life cycle costs for these alternative forces are projected and the fleet composition adjusted to fall within an equal cost constraint derived from projections to the Navy budget. These constraints dictate the size of the total force. Each equal cost force is then analyzed to determine its mission capabilities or utility over a range of potential engagements and campaigns arising from possible geopolitical crises requiring U.S. naval action. The alternative forces' cost and effectiveness are then ranked to determine more promising force options. Later study exercises will then use the results of this first iteration to refine the specifications and design objectives for selected future force options and recycle a more detailed analysis.

Figure 7 is a summary of the planned schedule for various tasks within the Sea Based Air Master Study. Phase I reports for the various technical tasks were completed during November and December this past year somewhat behind schedule. Force analysis studies were initiated during that time period also. The schedule calls for the first round output in October of

this year, and an interim progress report was prepared during March. Execution of the study effort has required extensive aircraft conceptual design studies to provide a very large number of aircraft point designs. These aircraft point designs are used to construct the alternative aircraft forces for comparison. For each of the aircraft designs, basic physical characteristics, size, weight, and performance data are required to determine mission capabilities and ship compatability constraints. Fuel and weapons loadouts, basic reliability and maintainability parameters were estimated to determine logistics requirements and aircraft availability potential.

Figure 8 is a matrix of aircraft point designs prepared for initial evaluation. Mission areas of interest form the columns and aircraft categories form the rows of the matrix. Mission areas selected for study are those currently performed by a carrier task group and during a Marine amphibious assault. Heavy lift and airborne mine countermeasures missions are not examined. Sixteen different aircraft categories have been examined based upon representative aircraft concepts selected and designed to fulfill multi-mission applications. Within each aircraft category, one or two primary aircraft configurations (based upon a single aircraft concept) are the nucleus for dedicated mission variants which have a high degree of propulsion, airframe and core avionics commonality. A broad range of aircraft concepts was selected to provide a sufficient representation of probable future aircraft force options. All aircraft designs assumed advances in airframe, propulsion, avionics, weapon system technology consistent with a projected initial operational capability in the mid-1990's. Together these aircraft categories cover four different classes of basing capabilities:

(1) CTOL - aircraft designed for catapult assisted launch and arrested recovery,

(2) STOL - aircraft designed for unassisted short take-off and arrested or unassisted recovery,

(3) V/STOL - aircraft designed for a basic sizing mission from a vertical take-off; and a second, more demanding mission (at higher take-off gross weight) from a short take-off, and vertical landings,

(4) STOVL - V/STOL aircraft designed for a single basic design mission from a short take-off with vertical landings at normal landing weights.

Comparable aircraft designs within each class such as a CTOL ASW mission variant and a V/STOL ASW mission variant have equivalent objective mission performance for the sizing or design missions. This matrix of aircraft designs may be partitioned into four distinct groups: a high capability Type B aircraft subset: a low capability Type B aircraft subset; a Type A

aircraft subset; and a complementary helicopter aircraft family. The high capability Type B aircraft categories provide functional mission capabilities comparable to the F-14 and A-6 class of aircraft with some differences in maximum ordnance loads which may be carried. The low capability Type B aircraft provide mission capabilities more similar to the F/A-18 aircraft. The Type A aircraft subset provides candidate aircraft categories to fulfill a number of subsonic combat and combat support aircraft mission roles. The fourth aircraft subset consists of a single aircraft category with mission capabilities complementary to CTOL, STOL and STOVL aircraft categories.

Within the subset of high capability Type B aircraft designs, four (4) aircraft mission variants are developed for each of four (4) design basing philosophies: V/STOL, CTOL, STOL, and STOVL. Missions addressed are those of fighter, attack, reconnaissance and electronic warfare. Each basing category is addressed by a particular aircraft concept. A multi-mission aircraft configuration provides the capability to perform fighter or attack missions with only immediate reconfiguration of the aircraft by loading ordnance peculiar to the mission to be conducted. The aircraft incorporates multi-mission avionics capable of handling a number of fighter and attack operations by simple onboard redirection of function. In addition, this multi-mission basic aircraft configuration is able either by reconfiguration or by a variant design to perform reconnaissance and electronic warfare missions by incorporating equipment dedicated to those missions. This design philosophy was also used for the low option subset of Type B aircraft designs.

For the Type A subset a total of seven aircraft categories were examined covering up to a maximum of eight (8) possible mission roles including ASW/ASUW, AEW, COD, VOD, Marine Assault, Tanker, SAR and AAW. The term "COD" refers to the long range resupply of a carrier task group by airborne means with basing capability/flexibility corresponding to the basic design basing philosophy used for a particular aircraft class (e.g. V/STOL, STOVL, STOL, or CTOL). The term "VOD" covers the vertical onboard delivery mission where supplies are transferred from an underway replenishment group to an aircraft carrier by airborne means. This is a short range, nearly all hover mission. The "SAR" mission corresponds to the attack search and rescue concept calling for the capability to provide a long range, real time rescue capability. The "anti-air warfare" mission for a Type A V/STOL aircraft is similar to the "missileer" concept whereby a subsonic, reasonably long endurance aircraft performs a combat air patrol function utilizing high performance, long range, air-to-air missiles. No air-to-air combat role is envisioned for this aircraft involving any type of maneuvering combat. ASW/ASUW and AEW are the anti-submarine warfare, anti-surface ship warfare and airborne early warning missions.

The Type A V/STOL High Speed category is based upon two different aircraft concepts -- a lift/cruise fan and a folding tilt-rotor aircraft concepts. For those missions that do not involve extended periods of hover (or near hover) flight and/or operations from unimproved terrain, aircraft designs

are based upon the lift/cruise fan concept. For missions involving extensive hover flight and/or operations from unimproved terrain, aircraft designs are based upon the folding tilt-rotor aircraft concept. For the lift/cruise fan aircraft concept, two primary aircraft configurations (large and small fuselages) and three derivative mission variants were designed around the folding tilt-rotor concept. The Type A V/STOL Medium Speed category is based upon the tilt rotor concept. Two primary aircraft configurations and six derivative mission variants were prepared. The Type A V/STOL Low Speed category is represented by a compound helicopter concept. The Tanker mission was not addressed because of a requirement for refueling high performance aircraft at speeds up to 250 knots at altitude. The AAW mission role was not investigated because of inadequate speed for timely repositioning of the missile launching platform. The fourth Type A aircraft category is titled CTOL High Speed. It is based upon a high by-pass ratio turbofan propulsion system similar to the S-3. By definition this aircraft category is incompatible with the VOD, Marine Assault, and SAR Missions. The Type A STOL High Speed category is represented by a turbofan powered aircraft concept with blown flaps, upper surface blowing or other STOL high lift devices. The Type A STOL Medium Speed category is represented by a propeller driven, slip stream lift aircraft concept. The STOL aircraft categories are incompatible with the VOD, Marine Assault and SAR missions. A seventh Type A aircraft category is STOVL High Speed category. It also is based upon a lift/cruise fan aircraft concept. Since this aircraft category cannot provide a significant useful load in hover, it is basically incompatible with the VOD, Marine Assault, and VOD missions.

The fourth subset in the matrix of aircraft design cases to be studied initially is a conventional helicopter category. It includes two (2) primary aircraft configurations with two (2) additional mission variants all based on a conventional helicopter design. The helicopter category is assumed incompatible with the AEW mission because of inadequate high altitude loiter capability required for long range AEW, the COD mission because of its long range requirements and the Tanker and AAW missions because of limited speed capability.

These aircraft design studies have been conducted with the intent of providing aircraft families that are believed to represent practical alternative acquisition approaches for the U.S. Navy and Marine Corps to investigate in order to meet their collective mission objectives. Penalties in levels of performance for one mission with respect to another had to be made. These penalties were not entirely consistent across the various aircraft categories, but in the judgement of the designers represented the most attractive design approach — cost and performance impacts considered. The Sea Based Air Master Study is a broad cost/benefit study designed to provide insight with respect to goals and perhaps direction for future sea based naval aviation. The scope of studies to be completed is very broad necessitating a number of compromises with respect to the level of detail to allow a tractable problem. During succeeding

phases of the Sea Based Air Master Study additional design cases will be prepared and the present design cases adjusted to reflect additional information.

INITIAL INDUSTRY STUDIES

Complementary to the Sea Based Air Master Study, a series of initial industry studies are ongoing whose output will focus on examining other V/STOL project issues raised previously which led to a restructuring of the V/STOL A program. They are substantiating a definitive V/STOL operational concept and related weapons system design objectives, identifying an affordable development approach with acceptable risk and reaching a consensus on the technical feasibility. The initial industry studies are divided into five task areas; the outputs of which are listed in Figure 9. These efforts support the Sea Based Air Master Study and will assist in establishing the basis for a V/STOL concept formulation phase. Previous recognized divisions of mission responsibility between the Type A and B V/STOL are no longer valid. Contractors are now defining new mission mixes for each of their originated V/STOL aircraft weapon system concepts. It is the expressed purpose of these studies to allow industry to evolve and justify basic V/STOL weapon systems design goals with a minimum of interference or guidance from the government.

Task I requires an operational analysis of an all V/STOL force to be conducted based upon the V/STOL operational concept approved by the Chief of Naval Operations in April 1978. Modifications to or reformulation of the operational concept and justification thereof are outputs of this first task. In Task II the contractors are asked to define recommended missions and mission mixes consistent with their evolved operational concept; also to identify preliminary concepts for V/STOL weapon system designs. Task III requires the contractor to identify critical technologies associated with the development of the V/STOL weapons systems to be measured against the applicable state-of-the-art for the purpose of establishing a prioritized technology development plan. Operational constraints including basing and logistics were to be considered in this examination. Task IV is an attempt to deal with the selection of a recommended acquisition approach based on quantitative and subjective criteria. It involves the development of alternative program options for each of the V/STOL efforts and systems. Relative program costs and risks, milestone phasing, technology advances, and risk reduction at major decision points are to be assessed. In Task V a selection of a recommended approach from those examined in Task IV and a rationale for the recommended approach are required. Development cost estimates and an analysis of the new approach relative to past, related, major weapon system development projects will be completed. These studies are organized to substantiate a basic V/STOL operational concept, to help establish mission goals for the V/STOL weapon system and to provide project planning and technology advancement recommendations suitable for reaching a decision on a new acquisition strategy for V/STOL at the end of this year.

TECHNOLOGY ADVANCEMENT

Navy V/STOL and advanced aircraft technology funding include areas of research applicable to both supersonic and subsonic V/STOL aircraft. These research and technology efforts remain generally oriented to the goals of Figure 1. Additionally, a greater emphasis is being placed on identifying and bringing a number of attractive configurations to a higher level of understanding and concept validation by exploring their unique risk areas. Massive weight reduction efforts remain a necessity for practical V/STOL aircraft to evolve. The technology base must be established to allow substantial reduction in aircraft structural weight fraction, reduced aircraft subsystem weight and improved propulsion system thrust to weight ratios. Despite the risks and costs associated with composite materials, they represent one of the least speculative and most economic approaches to achieving major weight reduction in future aircraft. Overall structural weight reductions of 15% or more relative to conventional materials are an established goal for the Navy V/STOL program. Support continues for an aggressive exploratory composites application program. Efforts are oriented to establishing the practicality of composites utilization in primary structures, principally fuselage and major subsystems such as the landing gear. Avionics systems architecture studies are planned to define from a "bottoms up approach" highly integrated core avionics systems suitable for high performance fighter/attack or subsonic ASW/AEW tactical V/STOL aircraft. Objectives are to identify design architectures which will allow maximum weight reduction in avionics while increasing functional capabilities and basic reliability.

Substantial effort is directed toward the general design problem of insuring adequate hover and transition flight dynamics for future V/STOL aircraft and determining requirements and design criteria necessary to allow V/STOL operations from smaller air capable ships. Under a cooperative effort with NASA, an expanded field-of-view visual display, an enlarged computer and realistic ship motion generation capabilities are being developed for the Flight Simulator for Advanced Aircraft and Vertical Motion Simulator at NASA Ames. These modifications will allow realistic simulation of V/STOL terminal area operations aboard ship under variable sea state conditions. When completed this facility will be an impressive new research tool that will be used extensively in upcoming studies to define the logic and control interfaces for a highly integrated, digital, propulsion, flight control system for future V/STOL aircraft, to conduct experiments to evaluate candidate all weather landing system schemes to provide basing and/or staging capability from ships down to a DD963 class destroyer under varying climatic conditions, and to conduct trade-offs between level of design complexity, cockpit controls, cockpit displays and pilot workload. Much of this work within the Navy is under the umbrella of the NAVTOLAND project. Of particular importance is the need to establish the impact of small ship V/STOL operations on:

1. Flying qualities requirements such as control power margins, minimum design thrust to weight ratios, required system time constants, and control display complexity.

2. Level of integration needed between the aircraft flight control systems, propulsion control and the all weather landing system.

Most of the remaining technology is directed at advancing particular V/STOL aircraft and propulsion system configurations. The characteristics of a good design are easily identified but the process for evolving that design must blend art with engineering. In addition to displaying all of the capabilities required for V/STOL flight operations, these good designs must achieve a more fuel efficient system despite demands of a high installed thrust to weight ratio, nullify the possible detrimental ground effects including hot gas reinjestion and suck down and represent refined aerodynamic designs to minimize high speed drag penalties predicated by other V/STOL design constraints relative to conventional aircraft. Yet the configuration of the aircraft and its propulsion system must be as simple as possible; not merely adding to level of design complexity to resolve the additional design problems and constraints associated with V/STOL. These configurations must be elegant design solutions not overpowering design solutions.

The NAVY with NASA support is continuing a broad based effort to mature V/STOL nozzle and inlet technology through studies and small scale wind tunnel testing for a number of configuration dependent design concepts. Propulsion systems studies addressing mechanical feasibility of design performance and thermal cycle analysis are planned for configurations of interest identified in the current initial industry studies. Additional small scale wind tunnel test projects and investigation of ship environmental constraints on high disk loading V/STOL aircraft are also planned. Other NAVY projects are continuing support of flight research with the Advancing Blade Concept (ABC) and the tilt rotor research aircraft. These efforts won't guarantee the emergence of the needed elegant design solutions to the NAVY V/STOL problem, but they are expanding a basic technology base and understanding of the V/STOL ship basing problem and attendant design criteria necessary to proceed into a design definition phase.

FUTURE ACTIVITY

Efforts proceeding this year and planned for next year are establishing a foundation to go forward with the design definition phase which should ultimately lead to prototype aircraft development. Results of the initial industry studies will be used to prepare the RFQ for this design definition phase. Outputs from the Sea Based Air Master Study and initial industry studies will establish mission design goals for the aircraft weapon systems to be examined. Technology advancement efforts will better define V/STOL unique design criteria, and further investigations of risk areas for a number of attractive V/STOL supersonic, fighter/attack and subsonic, multi-mission aircraft configurations.

Presuming that results from the Sea Based Air Master Study support development of V/STOL aircraft and identify a development sequence, an RFQ

for design definition of a V/STOL weapons systems will be released in the spring of 1980. This effort will address design studies and development proposals for either a supersonic, fighter/attack or a subsonic, multi-mission aircraft. Design definition contracts will be awarded to at least two contractors. Contract efforts envisioned at this time are:

1. Conduct weapons systems preliminary design studies including trade-off and sensitivities,

2. Perform wind tunnel and simulation efforts using powered and unpowered wind tunnel models and provide a complete flight dynamics model for simulation of the evolved aircraft configuration,

3. Conduct subsystem hardware development and tests to validate key risk areas peculiar to individual configurations, and

4. Prepare proposals for conducting an appropriate validation phase leading to follow-on development of an operational V/STOL aircraft system.

Precise definition of the scope of studies is premature at this time since planning for the design definition phase will reflect knowledge gained from evaluation of the initial industry studies, the level of emphasis placed on V/STOL development arising out of the Sea Based Air Master Study, and subsequent prioritization of Navy development goals.

Current planning envisions that the RFQ will solicit industry responses which address a complete V/STOL weapons system, describe the contractor's single preferred basic concept, contain a plan for the conduct of all relevant studies, and contain a plan for technology advances during the term of contract to reduce critical risk areas peculiar to the contractor's perferred concept. The nature of development efforts past the design definition phase remains to be determined.

CONCLUSIONS

The V/STOL project is a deliberately paced progression of activity in several distinct but related areas. The slow development of a consensus regarding V/STOL development reflects the difficulty of establishing a V/STOL need because of the basic issues raised and the large commitment of resources required to surmount the formidable technological challenge. Current project plans are believed to present a balanced approach on a very constrained budget to develop a comprehensive program rationale and continue to expand the technology base in selected critical risk areas. At the present time, a major aircraft development decision is not anticipated before calendar year 1982.

REFERENCES

1. Taft, Robert Jr., "A Modern Military Strategy for the United States", Congressional White Paper on Defense (1978 Edition), May 1978.

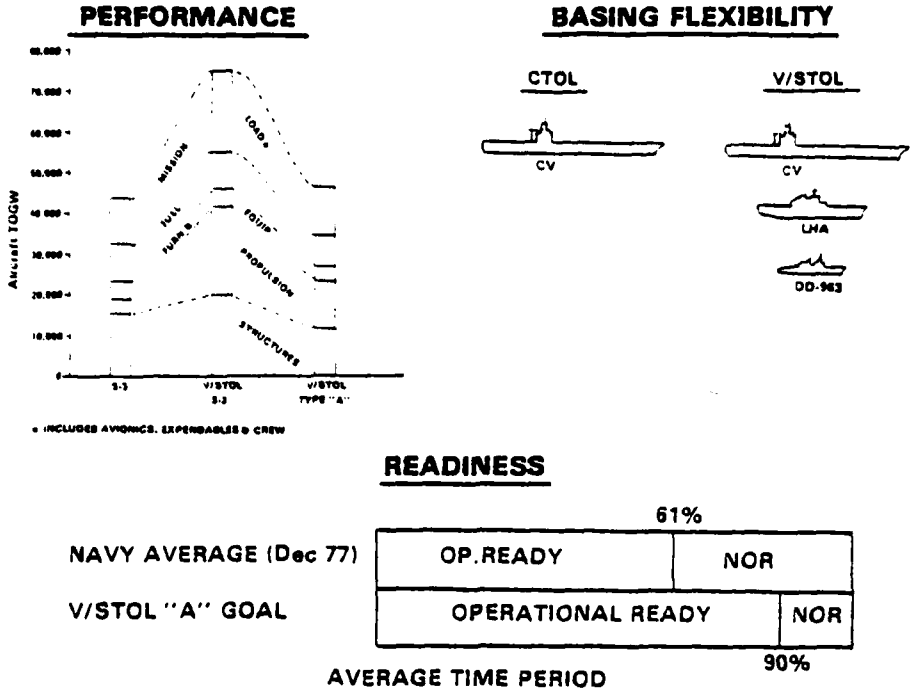

Figure 1. V/STOL A Technology Needs

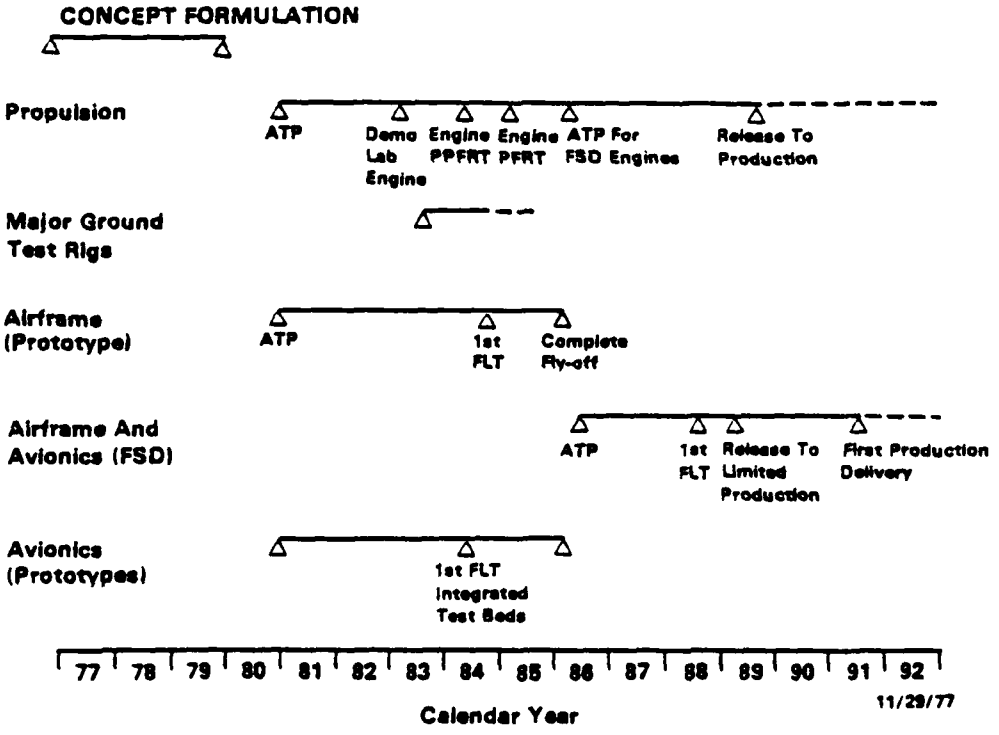

Figure 2. V/STOL A Program

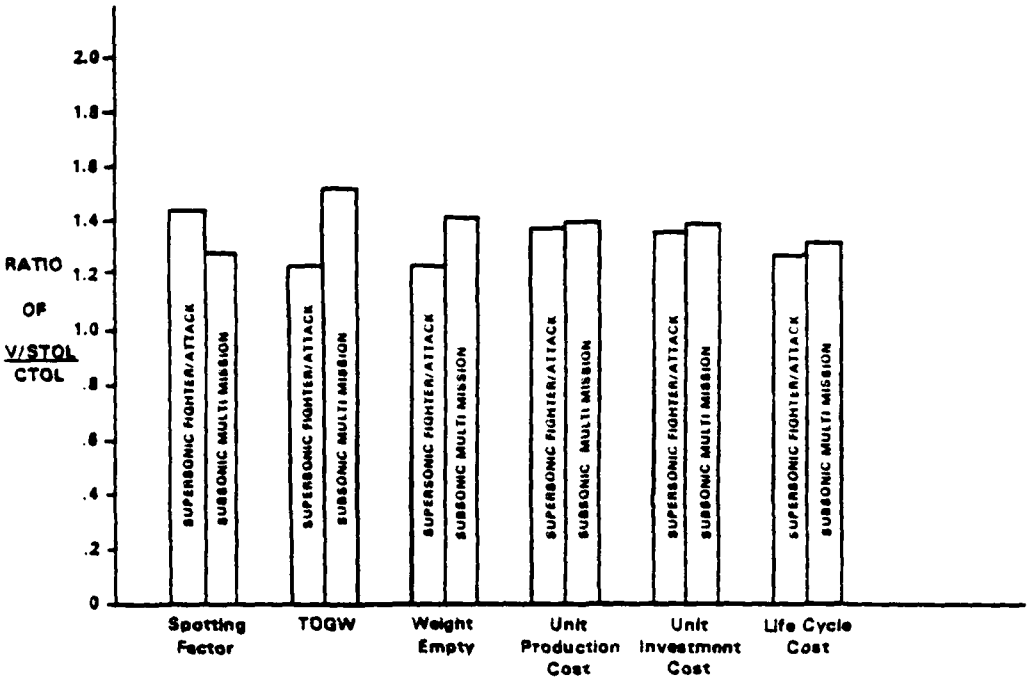

Figure 3. Unit Comparisons Between V/STOL and CTOL Aircraft

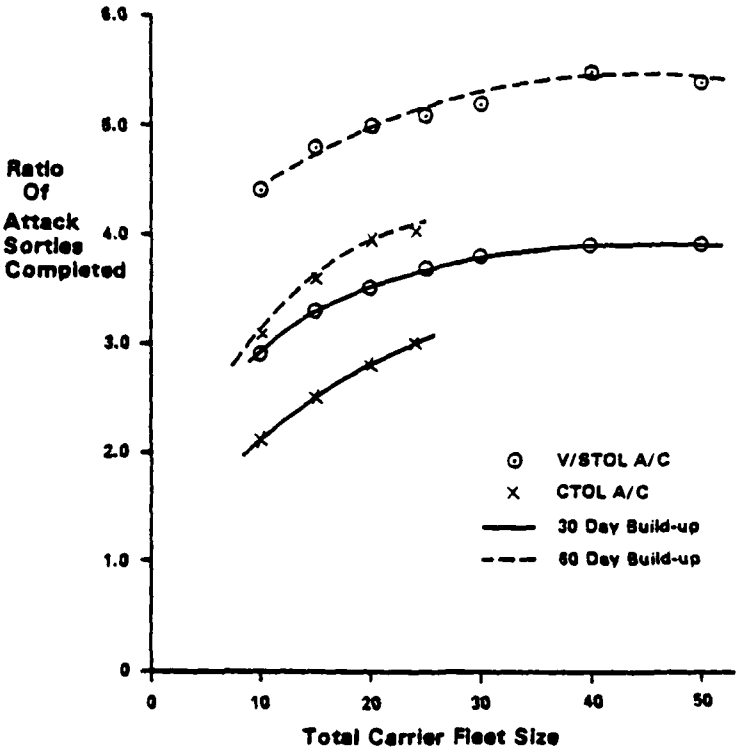

Figure 4. Relative Carrier Force Effectiveness - Power Projection Role

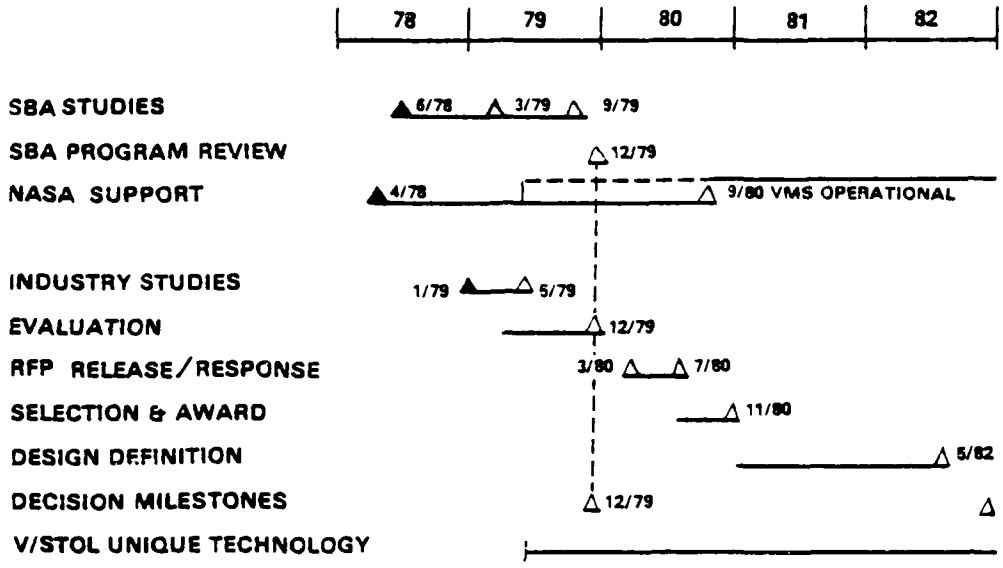

Figure 5. V/STOL Project Milestones

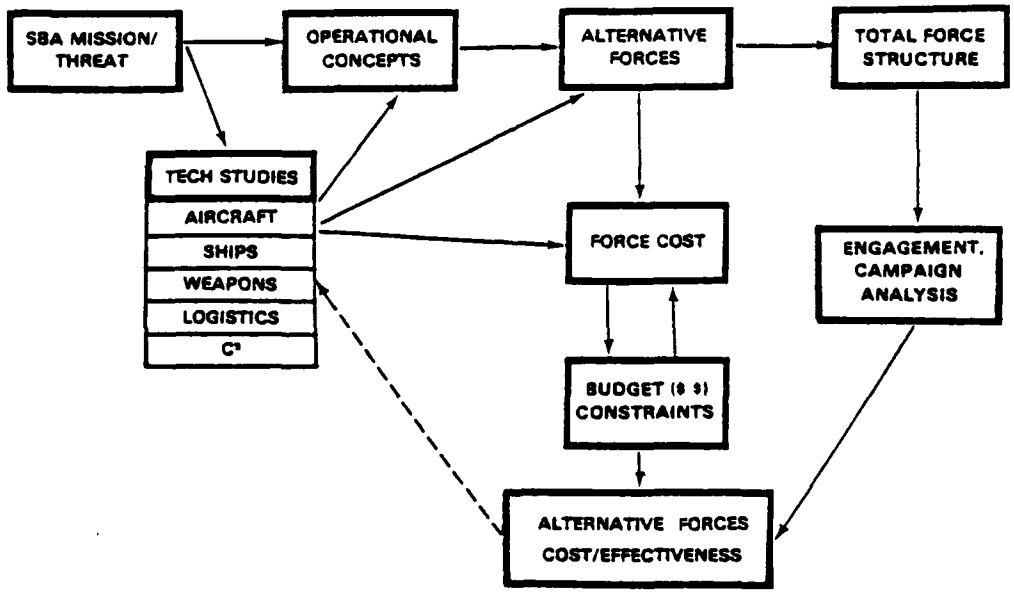

Figure 6. Schematic of Sea Based Air Master Study

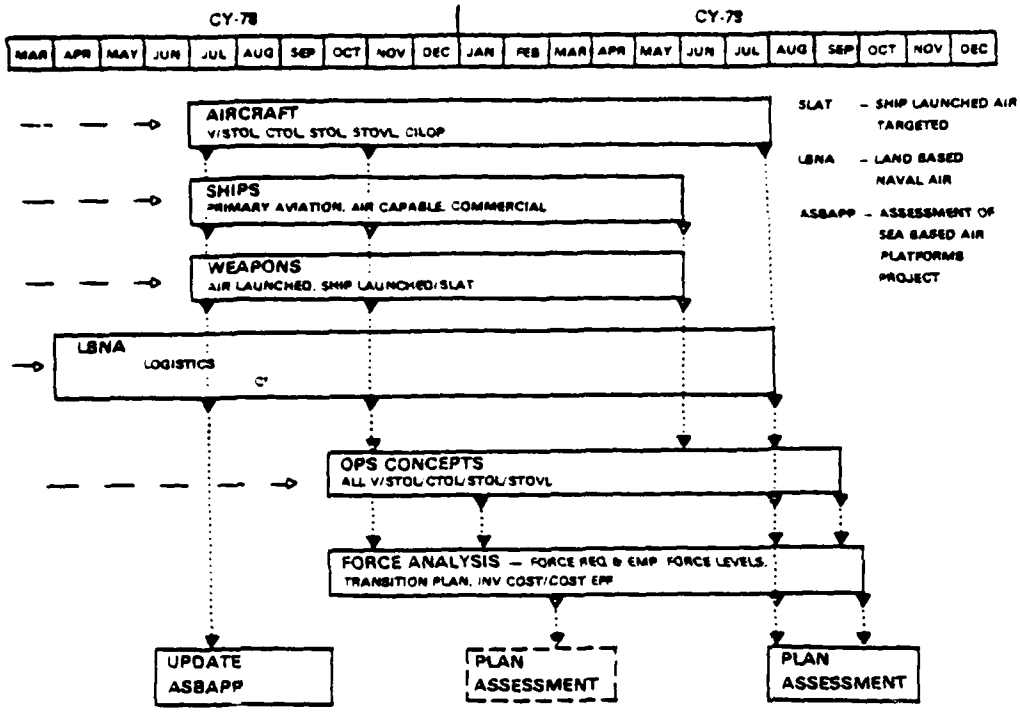

Figure 7. Sea Based Air Master Study Plan

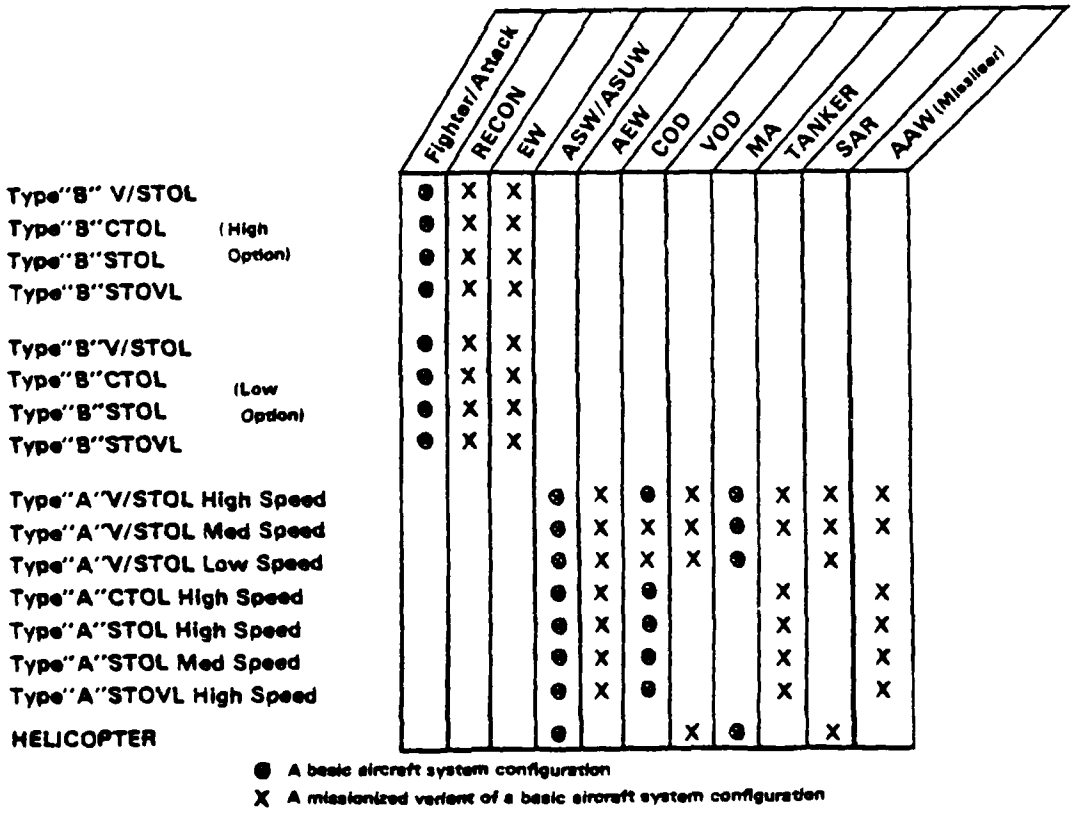

Figure 8. Matrix of Aircraft Designs For Study

TASK I

- Engagement Analysis
- New/Revised " All V/STOL Force " Operational Concept

TASK II

- Mission Mixes By Vehicles Proposed
- Weapon System Performance Goals
- Summary Size " Concept " Aircraft
  - Supersonic/Subsonic
- Core Engine Size Estimates
- Operational Constraints

TASK III

- Technology Developments Required
- Prioritized Development Plan
- State-Of-The-Art Assessment

TASK IV

- Cost/Risk Analysis Of Three Alternative Acquisition Strategies For Each Aircraft Proposed

TASK V

- Recommended Acquisition Strategy For Aircraft Proposed
- Cost/Risk Reduction Methods/Tradeoffs

Figure 9. Summary of Initial Industry Studies Output

APPENDIX

To provide an understanding of the basic analysis problem to be completed, a simplified model for the evaluation of V/STOL and CTOL aircraft has been structured for illustrative purposes. Because of the inherent limitations of an unclassified discussion, data interrelationships within the model are normalized to eliminate disclosure of classified information. The objective is to construct a straight forward rationale for comparison between equal cost CTOL and V/STOL forces which will illustrate quantitatively the interplay of considerations discussed in the basic paper. Data points used to construct appropriate ratios in succeeding figures are drawn from actual data developed in recent preliminary force level cost/benefit studies undertaken by the Department of the Navy.

Figure A-1 presents a range of alternative aircraft and ship forces which fall within a projection of available funding for a sea based aviation force extrapolated from current budget trends. Several observations are appropriate. Each point along the graph represents a unique number of operating aircraft in the fleet based upon a fixed number of aircraft carriers of a given size. As the number of ships increases, their individual sizes decrease. A cost advantage for the CTOL aircraft is clearly distinguishable. Both the CTOL and V/STOL operating aircraft forces show increasing unit cost efficiency with fewer, larger aircraft carriers. Also note that the V/STOL aircraft ship fleets extend down to much smaller, more numerous carrier fleet options.

Having identified a range of carrier/aircraft force options within the equal cost constraints, the second step is to establish a unit output performance or figure of merit for the various carrier and airwing alternatives. In actuality, this is a very complex task which is highly dependent upon assumptions about force tactics, the general composition of the total naval battle group and specific scenario parameters. Actual comparisons should be made on the basis of engagement or campaign simulations which determine results for the two opposing forces. For simplicity this model compares trends of CTOL aircraft operating from various size ships versus V/STOL aircraft operating from similiar size ships. The figure of merit is the ratio of strike sorties per ship over a 5 day battle period in a power projection role. Relative performance of alternative carriers and their associated airwings are normalized against the performance of a ninety-seven (97) CTOL aircraft, carrier airwing. Ratios are derived for other aircraft carrier platforms and their associated aircraft from data developed by the Center for Naval Analysis (CNA) during their "Sea Based Air Platform Cost/Benefit Study" and are shown in Figure A-2. V/STOL airwings are able to generate more sorties than numerically equivalent CTOL airwings. As the carrier airwing sizes increase, differences in maximum strike sorties for the V/STOL force over the CTOL force of equivalent numbers increase. This reflects the increasing traffic pattern constraints on catapult take-off and arrested landing aircraft operating from a large aircraft carrier. These curves were derived from data which assumed significant increases in aircraft availability over present day aircraft. Under those circumstances, a

number of operating constraints related to the deck cycle of conventional take-off and landing aircraft more severely impacted the airwing sortie generation potential than for the V/STOL aircraft which were less directly influenced by these same deck operating constraints. The basic scenario from which Figure A-2 was prepared was developed in some detail by CNA identifying not only the net useful sortie output of the carrier but also determining associated reconnaissance and other necessary aircraft mission sorties which had to be completed.

The third step in this simplified illustrative model is to determine the number of ship and aircraft assets which may become involved in the conflict being examined. To accomplish this it is first necessary to examine how an aircraft carrier and its operating airwing function during an operational duty cycle to determine an active combat ready period and a support period with varying states of operational readiness. Figure A-3 depicts a representative carrier duty cycle showing the various states a carrier transitions through in completing a single operational cycle. These states include loading and unloading of ammunition and supplies before and directly after a major deployment, the transit time to the duty station, overhaul periods (both major and minor), and training periods among others. The training periods have the principal function of bringing the carrier airwing including new flight crews and support crews to a full state of readiness and knowledge of tactics prior to an operational deployment. Figure A-3 supports the accepted rule of thumb that an aircraft carrier maintains on station coverage approximately one-third of the time. Therefore, in a given total carrier force approximately one-third of the carrier fleet is fully deployed and combat ready. Other parts of the fleet may be pressed into service after varying periods required for preparation and outfitting. Substantially increasing the carriers forward deployed at a given time, fully prepared for combat operations will require major adjustments to manning, training and support schedules for the entire carrier force.

To determine the number of force units available in a particular conflict, hypothetical carrier force build-ups and deployments were estimated. Primary assumptions were:

1. Forward deployment of two-thirds of the total force is assumed to be the maximum practical mobilization which may be accomplished within a 60 day period.

2. A dedicated national mobilization is precluded because of the uncertainties in international relations between different nations having conflicting goals, and limited understanding of each others' interests.

3. Limited intelligence prevents significant a priori action, but partial knowledge of an impending conflict will allow tailoring of deployed forces to the probable theater of conflict.

Deployment patterns were postulated for ten, fifteen, twenty, and forty carrier force options to provide a U.S. presence in five ocean regions involving vital U.S. interests. Normal peacetime deployment, thirty and sixty day warning periods prior to a probable conflict were examined. The fraction of the carrier force available for action in each theatre was determined. Figure A-4 results from averaging the postulated carrier deployments over the regions of interest, and may be used to approximate the number of carriers out of the total force being examined which can be involved in the conflict. A numerically larger ship force may have an advantage in bringing a greater fraction of its assets to bear in the theater of conflict (This is true only for a non-global conflict).

Using Figures A-1 through A-4, the potential of various aircraft carrier fleet options to perform a power projection role may be determined. Results are plotted in Figure 4 of the basic paper. V/STOL aircraft force options indicate increased effectiveness over CTOL aircraft force options. This single case incorporates data derived from the Center for Naval Analysis' "Sea Based Air Platform Cost/Benefit Study". The result is not the conclusion of the CNA study. Actual conclusions cannot be made from this model. It only serves to illustrate the complexity of making meaningful comparisons between CTOL and V/STOL aircraft.

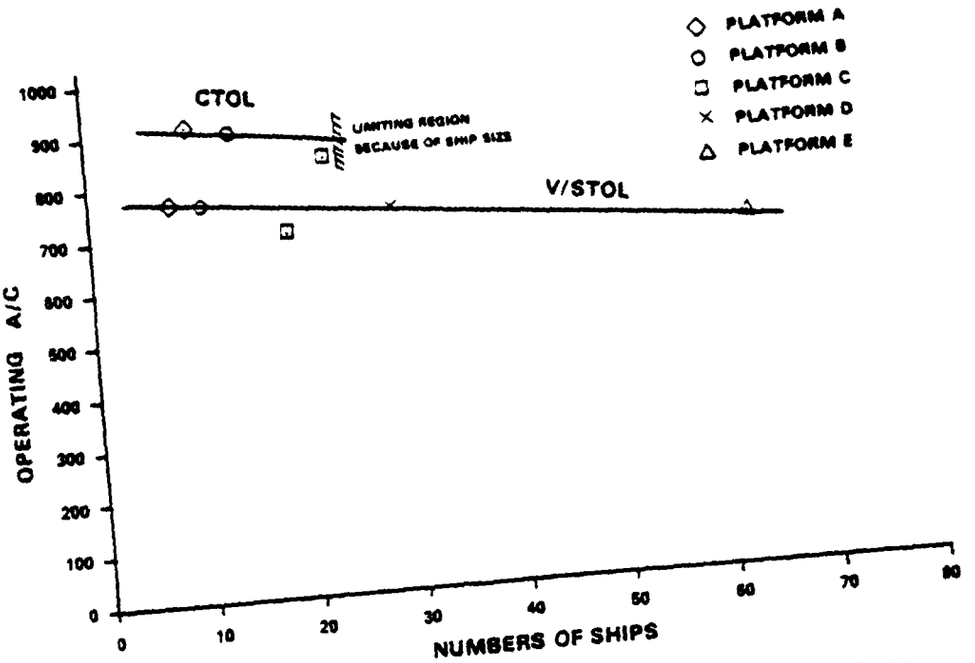

Figure A-1. Equal Cost Sea Based Air Force Alternatives

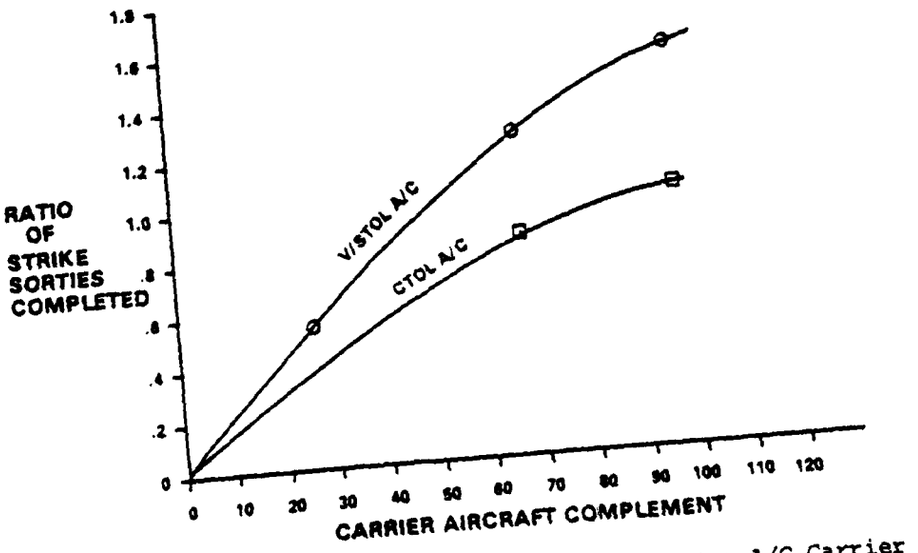

Figure A-2. Ratio of Strike Sorties Completed Per A/C Carrier

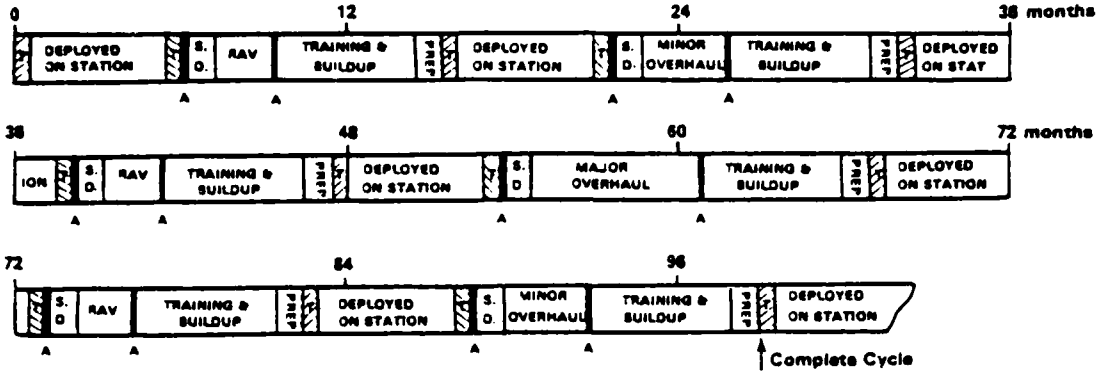

- Deployed on-station tours defined to be five months with an additional month transit time allowance
- Major overhauls last six months and minor overhauls last three months
- RAV — Restricted availability periods last two months
- Training & buildup periods last five months
- PREP — Thirty days allowed for outfitting and loading prior to deployment
- S.D. — Thirty days allowed for stand-down after completion of deployment
- T — Fifteen days transit time
- A — Ammunition loadings & unloadings average one week

Figure A-3. A Typical Carrier Duty Cycle

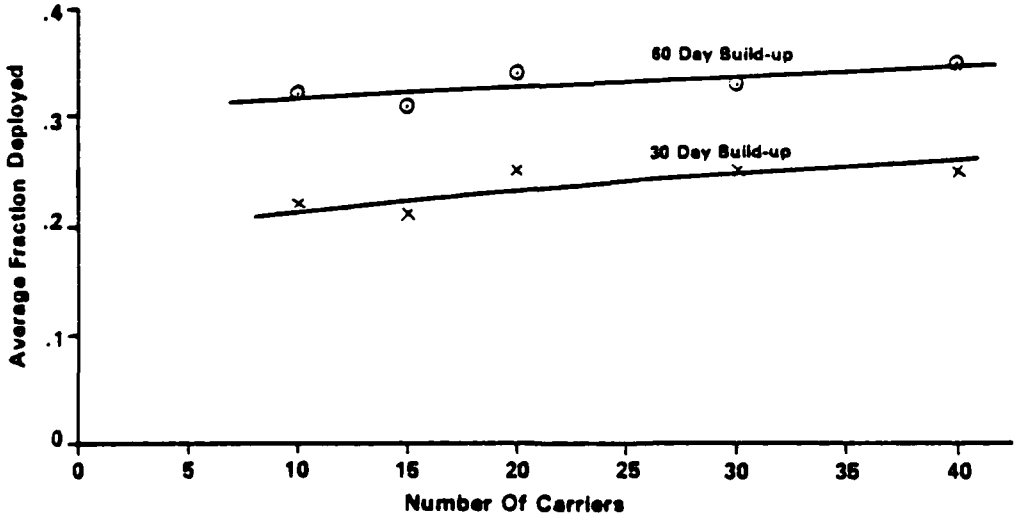

Figure A-4. Average Fraction of Carrier Force Deployed To Theater of Conflict

A WORKSHOP OVERVIEW

by C. Henderson
Flight Dynamics Branch
Naval Air Development Center

Developments in V/STOL aircraft technology encompass a time span of 20 years or more, starting with such aircraft as the early X-13 tailsitter and the first horizontal attitude X-14, progressing up to today's operational AV8-A and AV8-B fighter aircraft. There has been a great deal of interest during this time in the capability offered by V/STOL, but there has not been such urgent need as to warrant all-out efforts. Of course, early experimental craft had not only performance problems (lack of payload) but also many aircraft had stability and control problems stemming from a lack of knowledge regarding the complex aerodynamic/propulsive flow fields in the powered lift flight modes. Planes and pilots were lost because of a lack of appreciation for these aerodynamic and stability and control problems.

Steady research over the years have developed a better understanding of the basic phenomena of the flows involved, and a better understanding of directions to take to minimize the problems and improve aircraft performance. Similar studies in the area of structures, propulsion, avionics, etc. have also led to greatly improved performance potential for V/STOL. However, difficulties still remain in the ability to quantify the aerodynamics of V/STOL, causing a need for further analytical and experimental work in many areas to support V/STOL aircraft developments. The interest in V/STOL for application to Navy missions has been well expressed by the remarks of Captain McHugh, and leads us to an increased emphasis in areas of V/STOL technology.

The NADC has undertaken several efforts to upgrade V/STOL aerodynamics and stability and control technology and with it the concurrent ability to predict flight characteristics in the critical V/STOL flight modes.

In-house and contracted efforts are in progress on problem areas including the hovering jet induced problem and the aerodynamics of transition/STO. Figure (1) is an early caricature familiar to many of the hovering problem areas still remaining, caused by the flow field of a V/STOL in the hovering flight mode. This is: 1) induced pressure effects (suckdown) on aircraft surfaces caused by jet entrainment, and 2) hot gas re-circulation into engine inlets causing substantial thrust penalties and even engine surge or stall.

Efforts in progress in this area include the development of empirical prediction techniques for the jet induced effects in both static hovering flight conditions and in conditions of a moving deck environment. The upper part of Figure (2) shows a schematic of the several elements contributing to the jet induced lift of V/STOL for which empirical predictions are needed. These elements are: 1) the out-of-ground effect base loss caused by entrainment of the free jets, 2) the additional lift loss caused by entrainment of the ground flow jets which become pronounced at lower ground heights, and 3) the positive upload effect which occurs at lower heights caused by the fountain between multiple jets. Both theoretical/empirical and pure empirical approaches to predicting the build-up of these effects are being pursued. The lower part of Figure (2) is representative of test results obtained in a dynamic deck environment. Results have shown that both amplification and time lag effects can be significant in accounting for hover jet induced effects. A number of workshop papers will address this whole area of hover jet induced effects.

In the area of transition aerodynamics, improvement in prediction techniques are also being sought. An effort underway by Bob Palmer of NADC is the development of a purely empirical prediction technique to estimate jet induced lift and moments of jet V/STOL's in transition flight. The body of data used in the correlation was obtained on flat plate models with jets issuing into a crossflow as well as on models of specific configurations. Figure (3)

illustrates the type of tests conducted on the flat plate models. The tests determined not only the characteristic Velocity profiles and Vortex development in the downstream jet, but also the pressure distributions induced on the issuing surface. Polynomial expressions for the induced pressure coefficients on the surface have been developed as functions of velocity ratio, Voo/Vj, and longitudinal and lateral distance from the issuing jet. Application of the pressure relationships to a variety of simple planform models has shown good comparison with test results. An example of the data comparisons is shown in Figure (4), which gives results for a delta wing configuration with a single issuing jet. Both the lift loss and pitching moment predictions compare well with measured results. Similar comparisons for jets issuing from various body shapes have also compared well with test results. However, for jets located in a more aft wing position, a positive lift develops at higher velocity ratios which is attributable to a "jet flap" lift effect which is yet to be accounted for. Further development of this type of empirical correlation must account for other configuration variables, including multiple jets, jet height and deflection angle.

Developments in computerized aerodynamics being sponsored, shown in Figure (5), include a potential flow program under development by Vought Corporation, and a program employing finite element solutions of Navier-Stokes equations for jets in a crossflow being conducted by the Computational Mechanics Corp. The Vought VAPE program will incorporate - in addition to the Wooler-Ziegler jet model - a vortex jet flow model of Fearn and Weston, with some refinements to account for the wake region, as well as a flow model applicable to rectangular jets. A routine to permit calculations for in-ground effect STOL flight conditions is also being incorporated. Papers on these developments are included in the variety of papers being presented in the area of flow modeling techniques at the workshop.

A further undertaking involves the semi-empirical development of design type charts to estimate engine inlet momentum effects. These are known to produce large forces and moments in the transition flight mode particularly for the high flow rate fan engines being considered for V/STOL. Design type charts are also being sought to permit determination of conditions for inlet separation as functions of inlet geometry and flight condition. Figure (6) provided some early information on the effect of inlet radius on the inner lip stall of ducted propellor units used in V/STOL. As shown, the duct angle for inner lip stall decreases substantially with decreasing lip radius and with decreasing thrust coefficient (higher transition speeds). Although these are only rough trends, they imply a marked effect of inlet geometry on the useable transition flight corridor of a duct unit in order to remain in a stall free condition. More generalized forms of these stall boundaries need to be developed for rotating nacelle inlets as well as for flush mounted inlets - as applicable to lift fans or lift jets. The session chaired by N. O. Stockman will address this important area.

Another overall aerodynamic effort presently being conducted at NADC is the preparation of a V/STOL aerodynamics and stability and control manual having similarities to the USAF DATCOM. It has two main purposes: 1) to provide a concise compendium of semi-empirical methods to predict aerodynamics and stability and control characteristics of a wide variety of V/STOL concepts throughout the V/STOL flight modes, and 2) to identify technology gaps for needed research undertakings. The problem being addressed and the objective of the manual development is indicated in Figure (7). The problem is that the V/STOL designer (in the broad sense) and V/STOL analyst needs a means to rapidly assess V/STOL mode flight characteristics and trade-offs of various configuration alternatives at the early design stage. The objective is to prepare a

compendium of methods to predict these powered mode flight characteristics, to identify technology gaps, and to carry out the needed research. The manual thus provides a means to focus and coordinate efforts in V/STOL aerodynamics development. Figure (8) presents a work flow diagram of this effort. The manual format has been reviewed widely and the significant suggestions for revision have been included. A data bank of methods and test data has served as a starting point. A feedback from this work flow will be a continuing awareness of the limitations and gaps in the technology for which research efforts must be expended. The manual methods will be used to provide estimates of aero/propulsive effects of the various V/STOL categories listed in the Figure (8) for the different modes of V/STOL flight: hover, transition and STOL. This will include methods to estimate control characteristics which may be pertinent to a given class or which may be applicable across the V/STOL categories. Stability and control analysis techniques generally common to all classes will also be incorporated. Baseline unpowered aerodynamics, which to a large extent are derived from the existing USAF DATCOM, will be included. Many areas in the manual development will require additional analysis, tests, and data correlations to provide semi-empirical means to predict aerodynamics of V/STOL. A first issue of the manual is planned for late 1979, covering major results for the jet/fan V/STOL category. Its complete development will, of course, benefit from the many research undertakings and results being presented at this workshop.

It seems appropriate at various times to have an overall look at where we stand in order to better judge where we should be going. The workshop will be of great benefit in that endeavor. A summary session will be held on Friday giving an assessment of the overall state-of-the-art, describing the areas that are progressing satisfactorily, and discussing those areas that need increased attention.

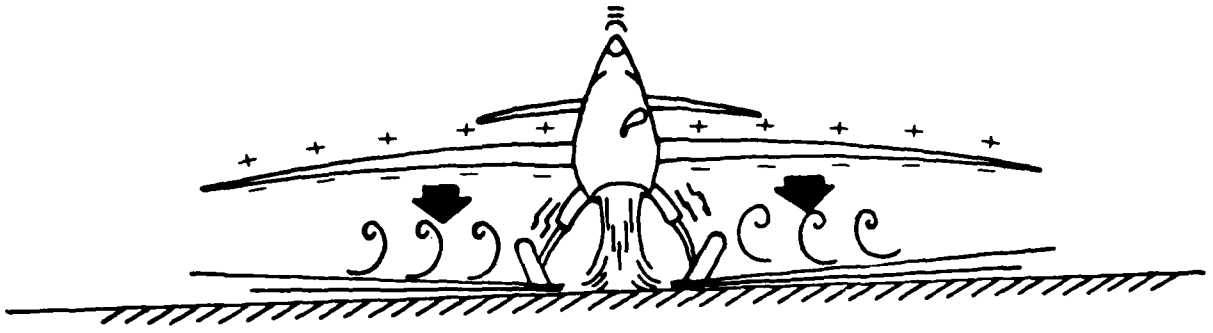

INDUCED PRESSURES

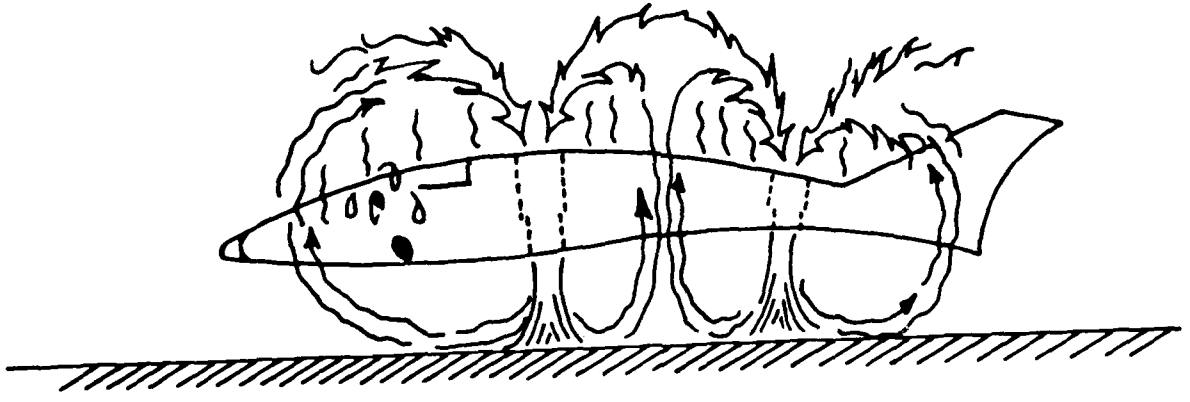

HOT GAS RECIRCULATION

FIGURE 1. JET V/STOL OPERATION IN GROUND PROXIMITY

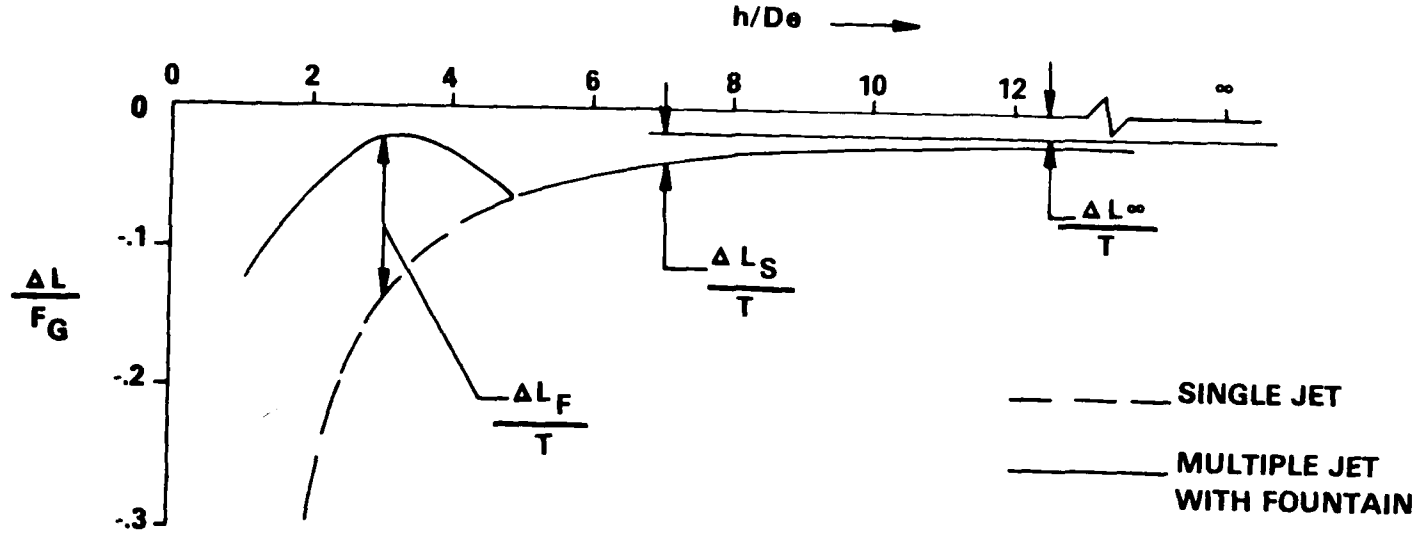

SCHEMATIC OF STATIC HOVERING INDUCED LIFT

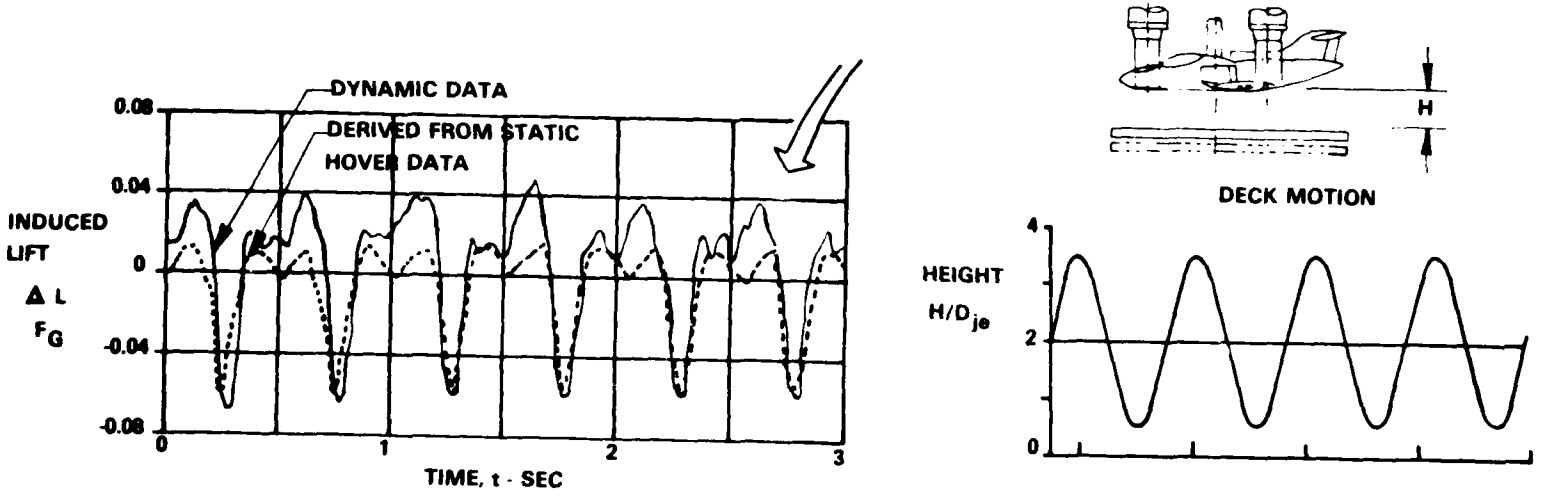

FIGURE 2. DYNAMIC DECK MOTION INDUCED LIFT

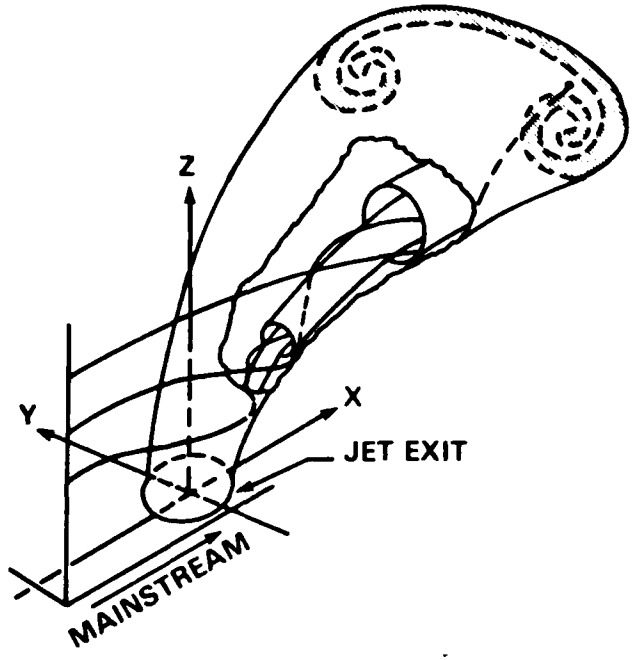

JET IN A CROSS FLOW

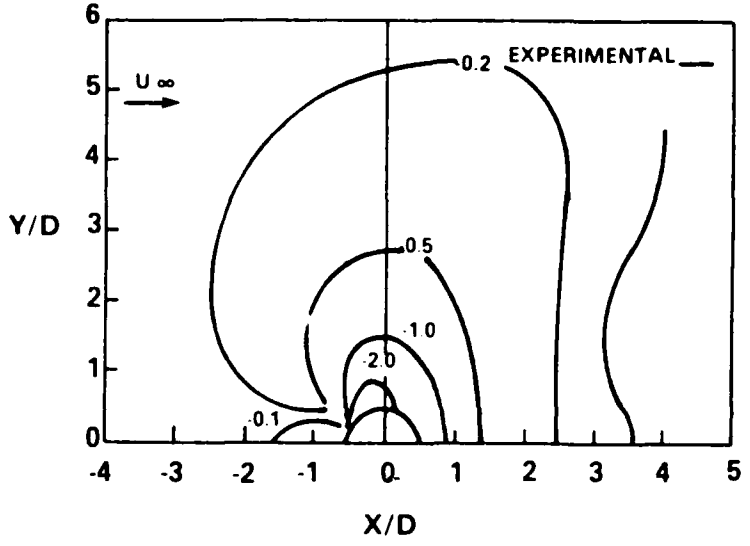

PRESSURE PROFILES

FIGURE 3

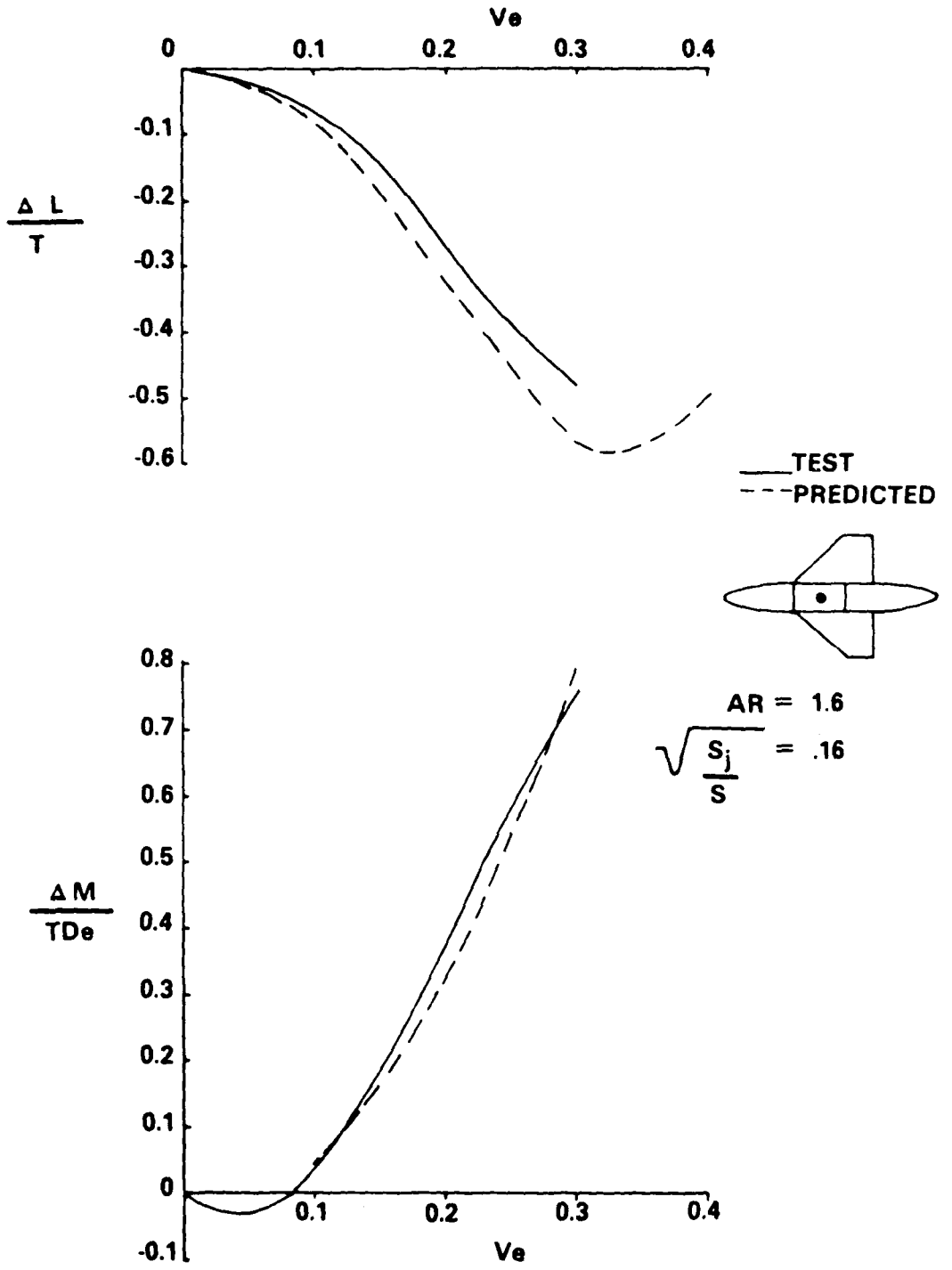

FIGURE 4. INDUCED EFFECTS FOR DELTA WING - SINGLE JET

PROGRAM	AIRCRAFT MODEL	JET REPRESENTATIONS		GROUND EFFECT
		MODEL	GEOM.	
VOUGHT CORP. - VAPE	DOUGLAS-NEUMANN PANEL METHOD	WOOLER-ZIEGLER OR FEARN & WESTON OR F. THAMES	CIRC.	OGE
			CIRC.	OGE, IGE
			RECT.	OGE
COMPUTATIONAL MECHANICS	FLAT SURFACE	PARABOLIC NAVIER STOKES-FINITE ELEMENT	ARBITRARY	OGE

FIGURE 5. TRANSITION AERO. COMPUTERIZED FLOW ANALYSES

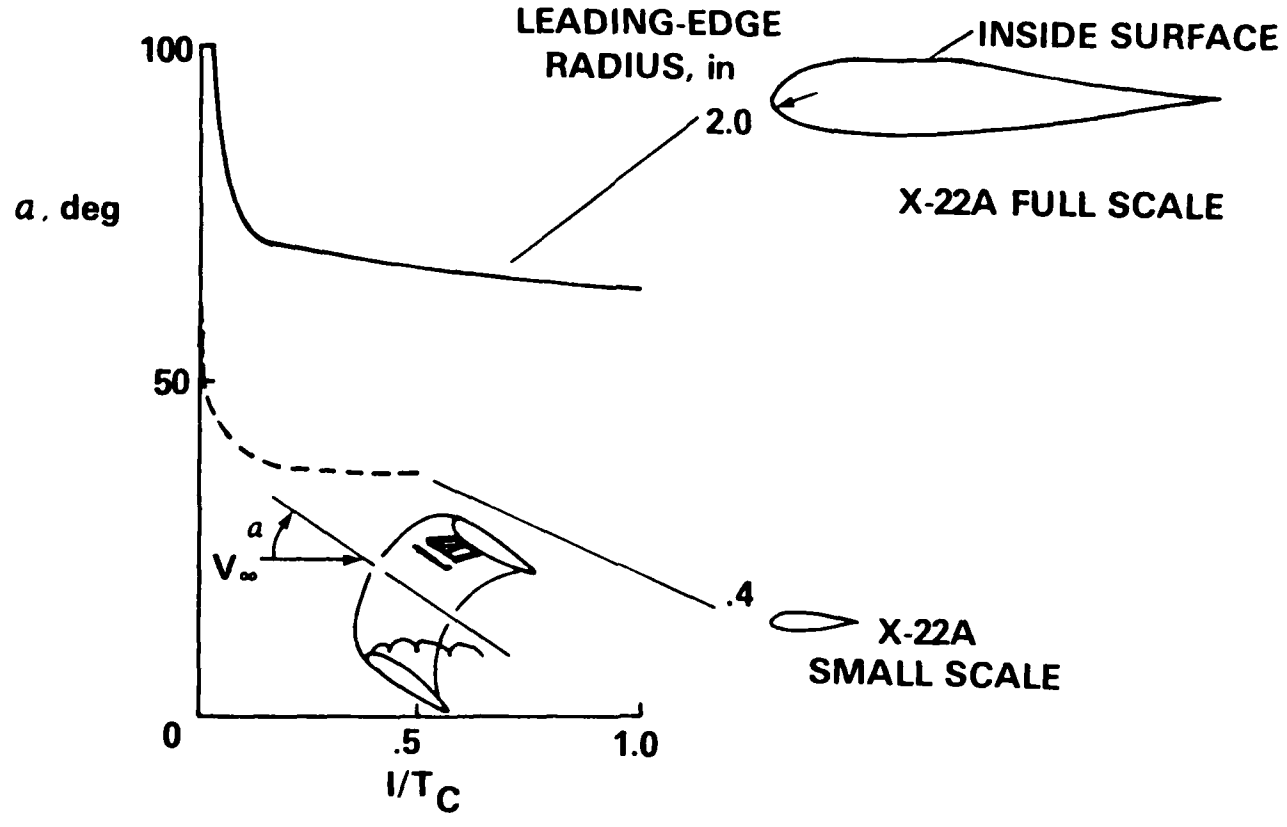

FIGURE 6. DUCT ANGLE OF ATTACK AT WHICH INNER LIP STALL OCCURS

PROBLEM: THE V/STOL DESIGNER/ANALYST NEEDS A MEANS TO RAPIDLY ASSESS V/STOL MODE FLIGHT CHARACTERISTICS OF CONFIGURATION ALTERNATIVES AT THE EARLY DESIGN STAGE

OBJECTIVE: TO PROVIDE A CONCISE COMPENDIUM OF AERODYNAMIC AND STABILITY & CONTROL METHODS TO PREDICT FLIGHT DYNAMICS OF A WIDE VARIETY OF V/STOL CONCEPTS THROUGHOUT THE V/STOL FLIGHT MODES.
TO IDENTIFY TECHNOLOGY GAPS AND CONDUCT NEEDED RESEARCH

FIGURE 7. V/STOL STABILITY & CONTROL MANUAL

VSTOL STABILITY & CONTROL MANUAL
PLANNED DEVELOPMENT WORK FLOW

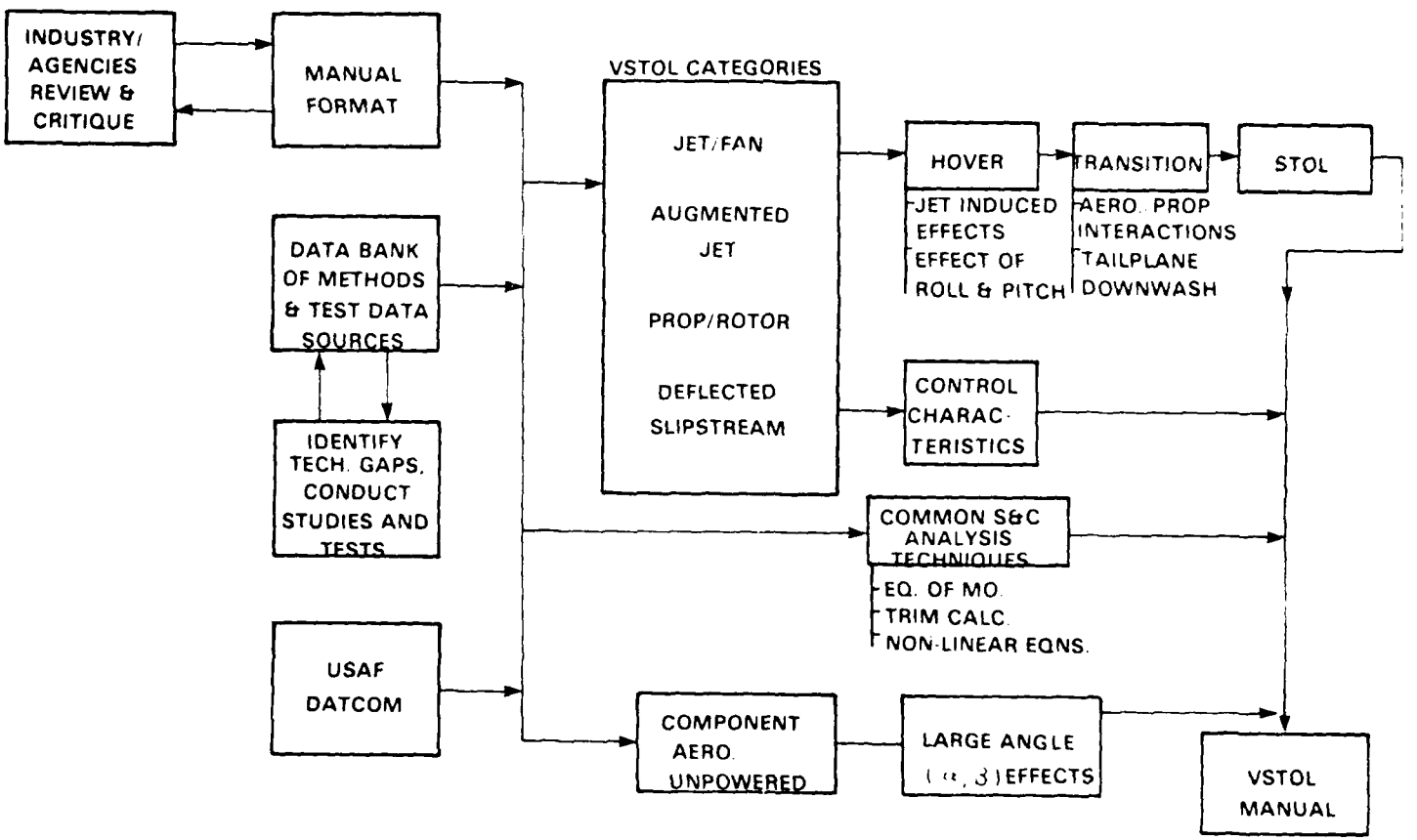

SESSION I

FLOW MODELLING TECHNIQUES

AND

PREDICTION METHODS FOR TRANSITION AERODYNAMICS

Chairman:

Dr. K. T. Yen
Naval Air Development Center

A JET/AERODYNAMIC SURFACE INTERFERENCE MODEL

BY RICHARD FEARN*, CARL KALOTA† AND W. E. DIETZ, JR.‡
UNIVERSITY OF FLORIDA

A model is presented that relates the pressure distribution on an aerodynamic surface to properties of the jet plume. The primary characteristics of a jet in a crossflow that determine the pressure distribution on the aerodynamic surface are assumed to be:

(1) the pair of contrarotating vortices associated with the jet.
(2) entrainment of fluid by the jet.
(3) a wake region near the aerodynamic surface immediately downstream of the jet.

The model is applied to the configuration of a round jet exhausting through a flat plate into a crossflow. Experimentally determined properties of the vortex pair are utilized in the model for perpendicular jet injection and a range of jet to crossflow velocity ratios. Reasonable values of entrainment and a simple wake assumption are used. Comparisons of the calculated pressure distributions and aerodynamic loading with experimental results are included.

* Associate Professor, University of Florida
† Graduate Student, University of Florida
‡ Engineer, ARO, Inc.

This work was supported by NASA through Grants NSG-2288 and NGL 10-005-127.

INTRODUCTION

In the transition from hover to conventional flight, vertical take-off and landing (VTOL) aircraft supplement wing-generated lift with direct thrust from lift jets, lift fans or tilt-proproters. The proposed configurations involve the injection of relatively high-velocity jets of air and/or exhaust gases into the crosswind caused by the forward motion of the aircraft. The interaction between these jets in a crossflow and the aerodynamic surface of the aircraft can be described in terms of an interference effect. Qualitatively, this interference effect results in a loss of lift and an increment of nose-up pitching moment, both of which tend to increase with increasing forward velocity of the aircraft. This jet/aerodynamic-surface interference effect is one of the significent problems in V/STOL aerodynamics.

The goal of the research conducted by the group working with me at the University of Florida, is to contribute to the development of a mathematical model to predict the jet/aerodynamic-surface interference effect for V/STOL aircraft. To be most useful, this model should be versatile in application and compatable for use in conjunction with existing lifting surface computer codes. Our approach has been to simplify the problem as much as possible without destroying its essential features which leads to the study of a single jet exhausting through a flat plate into a crossflow. The success of this approach depends on our ability to solve the simplified problem of a jet in a crossflow in a manner that can be utilized in solving the actual problem of predicting the aerodynamic loading on a V/STOL aircraft in transition.

Our research has proceeded with the assumption that the key to a successful and versatile scheme for predicting the pressure distribution and aerodynamic coefficients on a flat plate (or any other aerodynamic surface)is an adequate understanding and description of the flow in the jet plume itself. Development of a jet/aerodynamic-surface interference model has proceeded in parallel with a series of experiments in the NASA Langley V/STOL and Ames 7' x 10' wind tunnels and with the identification and description of the dominant flow properties of the jet plume based on these experiments.

The series of experiments conducted in the Langley V/STOL wind tunnel studied a single round jet exhausting through a flat plate into a crossflow. Jet to crossflow velocity ratios in the range of 3 to 10 and jet injection angles with the crossflow from 45° to 105° were studied. The pressure distribution on the flat plate was measured for perpendicular jet injection and for a range of velocity ratios (ref. 1), and the velocity and pressure in the jet plume were measured for a range of velocity ratios and jet injection angles (refs. 2 & 3). The pressure distribution on the flat plate for the test conditions reported in reference 3 are currently being measured in the Ames 7' x 10' wind tunnel by D. Koenig and K. Aoyagi.

Based on the results of the first wind-tunnel experiment, a contrarotating pair of diffuse vortices was identified as a significant and persistent feature of the flow field. These vortices were modeled in such a way that the vortex properties could be inferred from selected velocity measurements

in the jet plume (refs. 4 & 5). It has also been demonstrated that the properties of this vortex pair associated with a jet in a crossflow can be utilized to calculate the pressure distribution on the flat plate for perpendicular jet injection of a round jet for a jet to crossflow velocity ratio of 8 (ref. 6).

Similar experiments and modeling of the vortex pair have been accomplished by Frank Thames and R. P. Weston (ref. 7) for a single rectangular jet exhausting through a flat plate and from a faired aerodynamic body.

The purpose of the present paper is to describe our efforts to utilize the most recent experimental and theoretical results for a jet in a crossflow to develop a state-of-the-art jet/flat plate interference model that can hopefully be extended to more general aerodynamic surfaces. The resulting model could also be utilized to calculate wind-tunnel wall effects for the testing of V/STOL models.

PHYSICAL DESCRIPTION OF A JET IN A CROSSFLOW

From the numerous investigations of a round subsonic jet injected through a flat plate into a subsonic crossflow, there emerges a realistic qualitative description of the flow field. Most of the experiments upon which this qualitative description is based are for perpendicular jet injection into the crossflow, but the description should be applicable for a range of jet injection angles.

At the jet nozzle exit plane, the velocity profile and turbulent intensity in the jet are characteristic of the jet nozzle. A shear layer exists at the boundary between the jet and crossflow fluids, and this layer diffuses into a highly turbulent mixing region. A core of jet fluid, approximately conical in shape and maintaining the properties of the jet nozzle, extends a short distance from the nozzle exit plane. For a free jet (no crossflow), this core extends approximately six jet diameters before it is eroded and the flow becomes highly turbulent throughout the entire cross section of the jet (ref. 8). If a crossflow is introduced and the jet speed held constant, the length of the jet core decreases with increasing crossflow speed. The flow in this initial region is further complicated by a separation of the crossflow around the jet near the flat plate. This separation and the resulting wake region are clearly visible from oil smear studies on the flat plate (ref. 9).

The jet plume itself is readily observable by flow visualization (ref. 10). The deflection and decay of the initial jet of fluid can be detected by total pressure or velocity measurements in the jet plume. The curve tracing the locations of maximum jet speed from the terminus of the jet core through subsequent cross sections of the jet plume is called the jet centerline (refs. 11 & 12). This curve can be determined to a location where the local maximum of the jet velocity is experimentally indistinguishable from the crossflow velocity. This occurs 15 to 20 jet diameters downstream of the jet orifice for the instrumentation currently in use (ref. 4).

Another feature of the flow field is a pair of diffuse contrarotating vortices which forms near the jet orifice and is deflected and swept

downstream along curved paths which lie to either side of the plane of flow symmetry (see Figure 1) and on the concave side of the jet centerline (refs. 2, 12 and 13). These vortices are more persistent than the other distinguishing characteristics of a jet in a crossflow and they dominate the flow field for distances greater than about 10 jet diameters downstream of the jet orifice. As these contrarotating vortices are deflected and swept downstream they diffuse rapidly to the extent that their core radius is comparable to the half-spacing between vortex centers. As these vortices are swept downstream, diffusion of vorticity of opposite signs across the plane of flow symmetry causes a decrease in the effective strength of each vortex. The vortex structure plays a primary role in determining the pressure distribution on the flat plate (ref. 6).

Some of the pertinent features of the jet plume are sketched in Figure 1 for a jet to crossflow velocity ratio of about 8. The stippled area represents the plume of the jet as observed by flow visualization (ref. 10). The flow exhibits mirror symmetry about the plane y=0. Positions of the jet centerline and the pair of vortices relative to the smoke plume are also indicated. The projection of the centers of the vortices onto the symmetry plane defines the vortex curve. No attempt has been made in Figure 1 to display the jet core or the region of separated flow near the flat plate.

JET/AERODYNAMIC-SURFACE INTERFERENCE MODEL

Based on the identification and quantitative description of the dominant features of the flow field in the jet plume, a model can be constructed to calculate the velocity and pressure on the aerodynamic surface from which the jet exhausts or at locations of wind-tunnel walls. Based on the experimental studies (refs. 2 & 3) the significant features of the flow field of a jet in a crossflow are assumed to be:

(1) A pair of diffuse contrarotating vortices. This is the dominant and most persistant feature of the flow.
(2) Entrainment of crossflow fluid into the jet plume. This effect is secondary to that caused by the vortex pair.
(3) A wake region immediately downstream of the jet and restricted to the region near the aerodynamic surface. This is a significant effect but localized in extent.

The diffuse vortex pair.- Currently, the properties of the diffuse vortex pair at a given cross section to the jet plume are inferred by a model (ref. 4) whose parameters are determined from selected velocity measurements in that cross section. This means that for a given set of conditions (for example; single round jet through a flat plate, perpendicular jet injection into the crossflow and effective jet to crossflow velocity ration of 8), velocity measurements must be made at several cross sections to the jet plume to determine the vortex properties for that set of conditions.

Figures 2, 3 and 4 indicate the measured velocity in a cross section and the ability of the diffuse vortex model to describe the projection of the measured velocity onto the cross section. Figure 2 represents

velocity measurements at 294 locations in a cross section to the jet plume. The projection of the measured velocity at a given location is represented by an arrow and the velocity component perpendicular to the cross section is represented by a contour plot. Figure 3 shows only the projection of the velocity onto the cross section, which the diffuse vortex model attempts to describe, and Figure 4 shows the velocity field calculated from the diffuse vortex model. An overlay of Figures 3 and 4 indicates that the diffuse vortex model provides a reasonably good description of these velocities. It should be noted that the diffuse vortex model can accurately infer the vortex properties (location of a vortex center, diffuseness and strength of a vortex) from a sample of approximately 30 velocity measurements in the vicinity of the vortex system.

For utilization in the jet/aerodynamic-surface interference model, the pertinent features of the diffuse vortex pair can be summarized for a given set of test conditions by providing quantitative descriptions of:

(a) the location of the center of vorticity for each diffuse vortex; $(x, \pm y(x), z(x))$, where $y(x)$ is called the vortex half-spacing and $z(x)$ is called the vortex curve.
(b) the diffuseness, or equivalently, core radius for each vortex, $r_c(x)$.
(c) the effect strength (circulation) of each vortex, $\mp \Gamma(x)$.

Entrainment.- Entrainment is represented by a line sink placed along the jet centerline. The equation for the jet centerline and the variation of strength of the line sink must be specified. There have been upper bounds established for the value of entrainment (ref. 14).

Wake region.- For the region external to the jet plume, both the diffuse vortex pair and entrainment can be represented by potential flow calculations. The effect of the viscous phenomenon of flow separation around the jet is represented by defining the boundary of the wake region and making a quantitative statement about the change of the pressure distribution in the wake from that calculated by potential flow theory.

Surface. - The aerodynamic surface would be represented by a lifting surface code such as a vortex lattice method and the solution carried out with the jet-induced velocities superimposed with the velocities induced by the lifting surface elements. The lifting surface code would thus account for the jet induced velocities in calculating the velocity at each control point. The resulting pressure distribution and calculation of aerodynamic coefficients by the lifting surface code would include the interference effects caused by the jet.

Application To A Single Round Jet Exhausting From A Flat Plate

Some of the advantages and disadvantages of this jet/aerodynamic-surface interference model at its current stage of development are illustrated by attempting to apply it to a specific set of test conditions. The most extensive velocity measurements in the jet plume have been made for perpendicular jet injection into the crossflow for an effective jet to crossflow velocity ratio of eight (refs. 2 and 3), so this will be chosen as a test case. An experimentally determined pressure distribution is also available for this case (ref. 1) for comparison of results.

The diffuse vortex pair.- Figures 5 thru 8 display the pertinent properties of the diffuse contrarotating vortex pair as inferred by the diffuse vortex model from selected velocity measurements in several cross sections to the jet plume. The lines on each graph represent functions that have been chosen to describe the property in the interference model. There is a well established empirical equation to describe the vortex curve for all velocity ratios studied for perpendicular jet injection. The equation is

$$z(x)/D = aR^b(x/D)^c \qquad (1)$$

where R is the jet to crossflow velocity ratio, D is the jet diameter, a, b and c are parameters determined to provide a least squares best fit to the experimentally determined points defining the vortex curve. Figure 5 shows the ability of this equation to describe the vortex curve for several jet to crossflow velocity ratios. Figures 6, 7 and 8 provide the vortex half-spacing, core radius and vortex strength as a function of arc-length along the vortex curve.

It should be noted that in the region very near the jet orifice there is a lack of information about the vortex properties. This is due to two reasons. First the probe system utilized in the wind-tunnel experiments was not suitable for measurements in this region of very large velocity gradients. Second, the diffuse vortex model utilized to infer the vortex properties from measured velocities involves assumption that are not valid in the region near the jet orifice. Thus, we have a "region of ignorance" which has a significant influence on the pressure distribution induced on the flat plate. Figures 6 and 8 illustrate several possibilities for extrapolating the vortex spacing and effective vortex strength to the jet orifice.

For the purpose of calculating the pressure distribution on the flat plate each vortex is represented by a vortex filament composed of many short straight line segments, the strength (circulation) being constant over the length of each segment.

Entrainment.- Figures 9 and 10 display the pertinent properties for calculating the effect of entrainment of the crossflow fluid into the jet plume. Figure 9 provides a description for the jet centerline for a range of jet to crossflow velocity ratios. The jet centerline

can also be described by equation (1) but with different values of the parameters a, b and c from those describing the vortex curve. The entrainment coefficient shown in Figure 10 is a dimensionless measure of the entrainment volume flux per unit length of the jet plume. It is assumed for this case that entrainment is numerically equal to that of a free jet after the jet core has been eroded (ref. 8). Entrainment effects are represented by a line sink coincident with the jet centerline. For the purpose of calculating the pressure distribution on the flat plate, the line sink is approximated by many short straight line segments, the sink strength being constant over the length of each segment.

Wake effect.- The wake boundary is currently being defined simply as the region where the potential flow model results differ significantly from the experimentally determined pressure distribution. In the wake region, the pressure is assumed to be determined from the potential flow values at the wake boundary.

Flat plate.- For the sake of simplicity, the flow over the flat plate is currently being represented by the method of images.

Results.- It is apparent from the above description that the high-confidence part of the interference model at the current stage of development is the description of the contrarotating vortex pair in a region sufficiently far from the jet orifice. Additional study of the other jet properties affecting the pressure distribution should lead to a more accurate description of these properties and thus to a more accurate model for calculating the pressure distribution.

It is interesting to note the effect of the various parts of the interference model on the calculated pressure distribution. This is shown as contour plots of the pressure distribution on the flat plate in Figures 11, 12 and 13. In each figure, the experimental pressure distribution (ref. 1) is shown for the purpose of comparison. Figure 11 shows the pressure distribution induced by the vortex system alone. Figure 12 shows the effect of adding entrainment and Figure 13, the effect of adding the wake assumption.

The jet/aerodynamic surface interference model based on a contraroting vortex pair, entrainment and a wake effect provides an adequate description of the pressure distribution on a flat plate for perpendicular jet injection and a jet to crossflow velocity ratio of 8.

Work is currently underway on applying this model to the cases of perpendicular jet injection and jet to crossflow velocity ratios of 3, 4, 5, 6, 7, 8 and 10. Figure 14 shows the integrated effects displayed as lift and pitching moment. The lines representing experimental values are obtained by fairing a curve through the results obtained from integrating the experimental pressure distribution presented in reference 1. Preliminary model results for jet to crossflow velocity ratios and 4 and 6 are included on the figure.

Improvement of the Model

The prototype jet/aerodynamic-surface interference model described in this paper appears to have promise as a useful tool in calculating the aerodynamic coeficients of V/STOL aircraft in the transition flight regime. Subsequent development of the model should include the following:

(1) The region near the jet orifice should be studied experimentally to provide the data base for modeling the flow in this region.

(2) There is a well-defined distribution of vorticity at the jet exit plane. There should be a theoretical study of the process by which the vortex sheet at the jet exit distorts and rolls up into the contrarotating vortex pair. Such a study could lead to results that would greatly reduce the amount of experimental data required to infer the vortex properties.

(3) The wake area should be studied with the goal of providing a realistic treatment of this region in the model.

(4) A continuing effort should be made to simplify the system of equations describing the vortex properties and to search for representations that can be conveniently generalized to new test conditions.

(5) Studies should be made of more complex configurations, such as multiple jets through a flat plate or replacing the flat plate with a wing to see if it is feasible to generalize the model to more complicated configurations.

Summary of Results

A prototype model is presented for calculating the jet/aerodynamic surface interference effect of a jet exhausting from a surface into a crossflow. This model is based on the identification and quantitative description of the dominant features of the jet plume. The model is applied to the case of a single round jet exhausting perpendicularly through a flat plate into a crossflow and the results are compared with experiment. Suggestions are made for future development of the model.

References

1. Fearn, R. L.; and Weston, R. P.: Induced Pressure Distribution of a Jet in a Crossflow, NASA TND-7916, 1975.
2. Fearn, R. L.; and Weston, R. P.: Induced Velocity Field of a Jet in a Crossflow, NASA TP-1087, 1978.
3. Fearn, R. L.; and Weston, R. P.: Velocity Field of a Round Jet in a Crossflow for Various Jet Injection Angles and Velocity Ratios, NASA TP-XXXX (To be Published).
4. Fearn, R. L.; and Weston, R. P.: Vorticity Associated with a Jet in a Crossflow, AIAA Vol. 12, No. 12, Dec. 1974, pp. 1666-1671.
5. Krausche, D.; Fearn, R. L.; and Weston, R. P.: Round Jet in a Crossflow: Influence of Jet Injection Angle on Vortex Properties, AIAA J., Vol. 16, No. 6, June 1978, pp. 636-637.
6. Dietz, W.; A Method for Calculating the Induced Pressure Distribution Associated with a Jet in a Crossflow, M. S. Thesis, University of Florida, or NASA CR 146434, 1975.
7. Thames, F. C.; and Weston, R. P.: Properties of Aspect-Ratio 4.0 Retangular Jets in a Subsonic Crossflow. AIAA Conference Paper 78-1508.
8. Albertson, L. M.; Dai, Y. B.; Jenson, R. A.; and Rouse, H.: Diffusion of Submerged Jets., Trans. ASCE, Vol. 115, 1950, pp. 639-664.
9. Wu, J. C.; McMahon, H. M.; Mosher, D. K.; and Wright, M. A.: Experimental and Analytical Investigations of Jets Exhausting Into a Deflecting Stream. J. Aircraft, Vol. 7, No. 1, Jan.-Feb. 1970, pp. 44-51.
10. Margason, Richard J.: The Path of a Jet Directed at Large Angles to a Subsonic Free Stream. NASA TN D-4919, 1968.
11. Jordinson, R.: Flow in a Jet Directed Normal to the Wind. R. & M. No. 3074. Brit, A. R. C., 1958.
12. Kamotani, Yasuhiro; and Greber, Isaac: Experiments on a Turbulent Jet in a Cross Flow. AIAA J., Vol. 10, No. 11, Nov. 1972, pp. 1425-1429.
13. Thompson, A. M.: The Flow Induced by Jets Exhausting Normally From a Plane Wall Into an Airstream. Ph.D. Thesis, University of London, 1971.
14. Fearn, R. L.: Mass Entrainment of a Circular Jet in a Crossflow, NASA SP-218, September 1969.

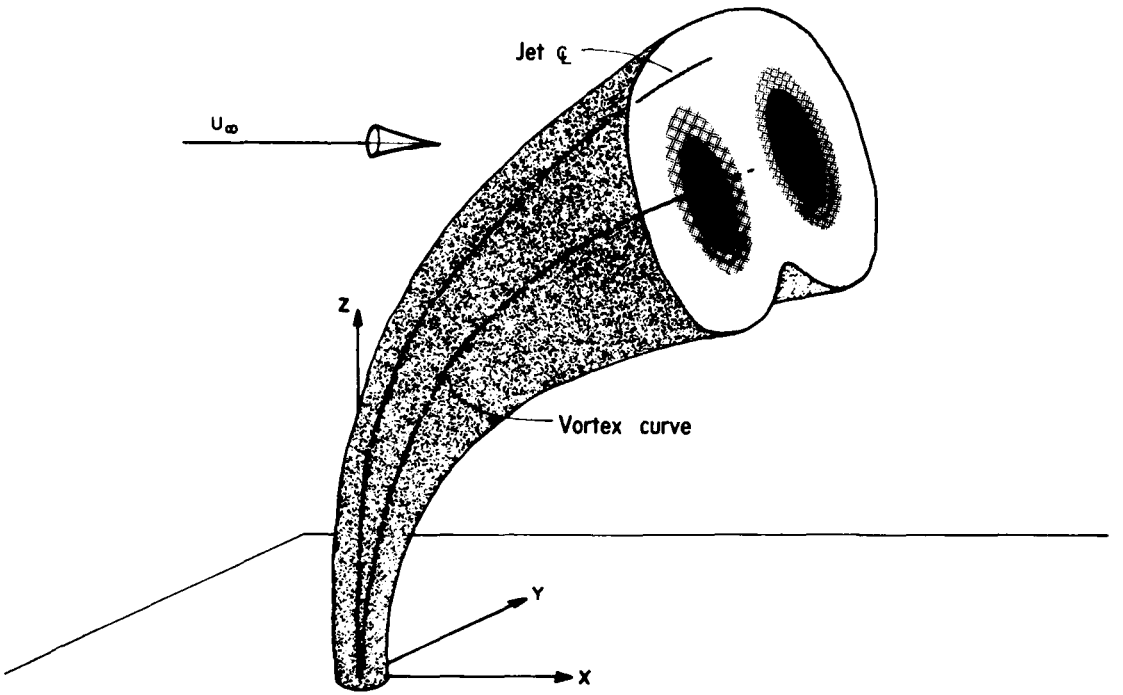

Figure 1.- Sketch of a jet in a crossflow

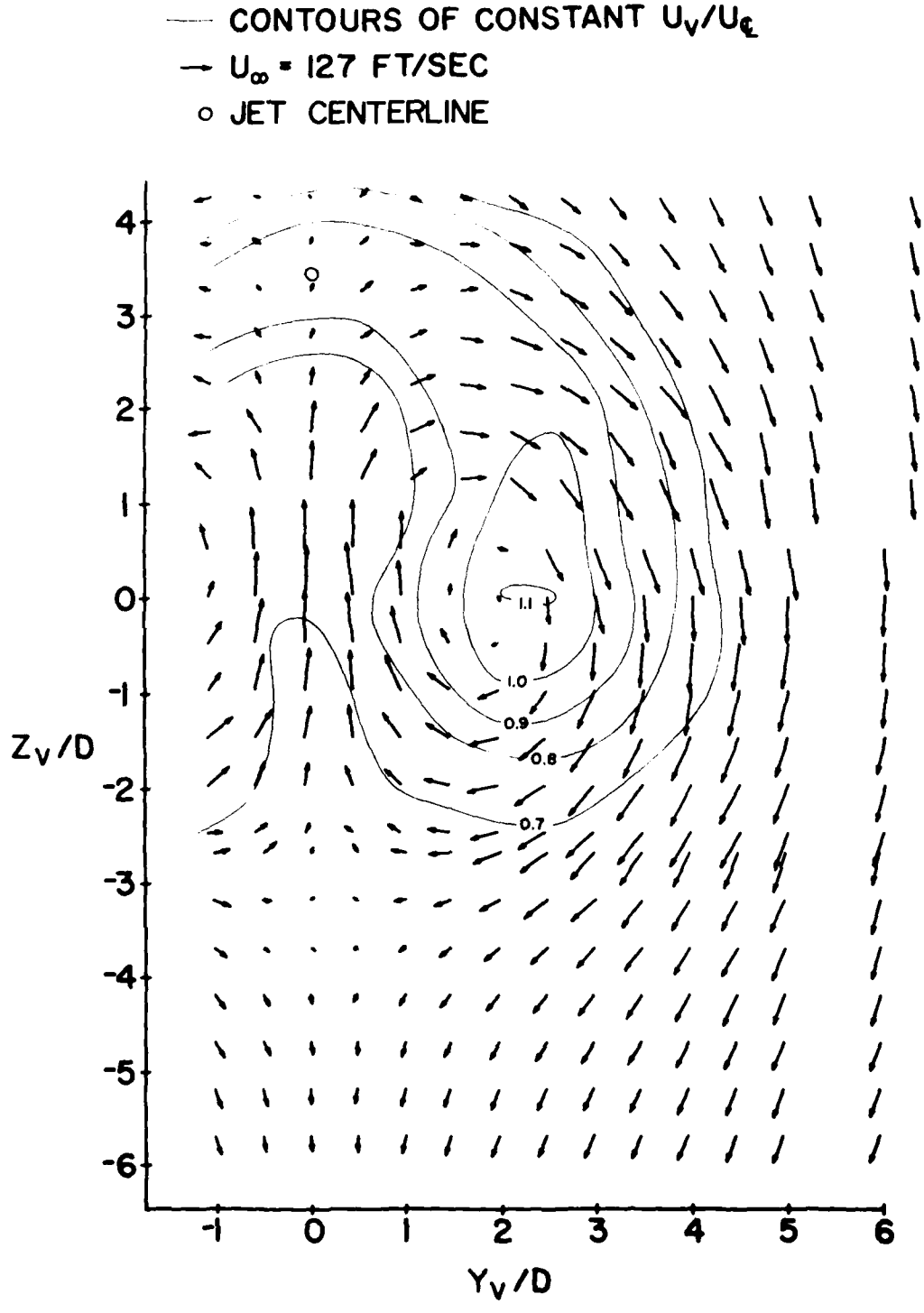

Figure 2.- Measured velocities. R=8, X/D=10.0, z/D=5.31.

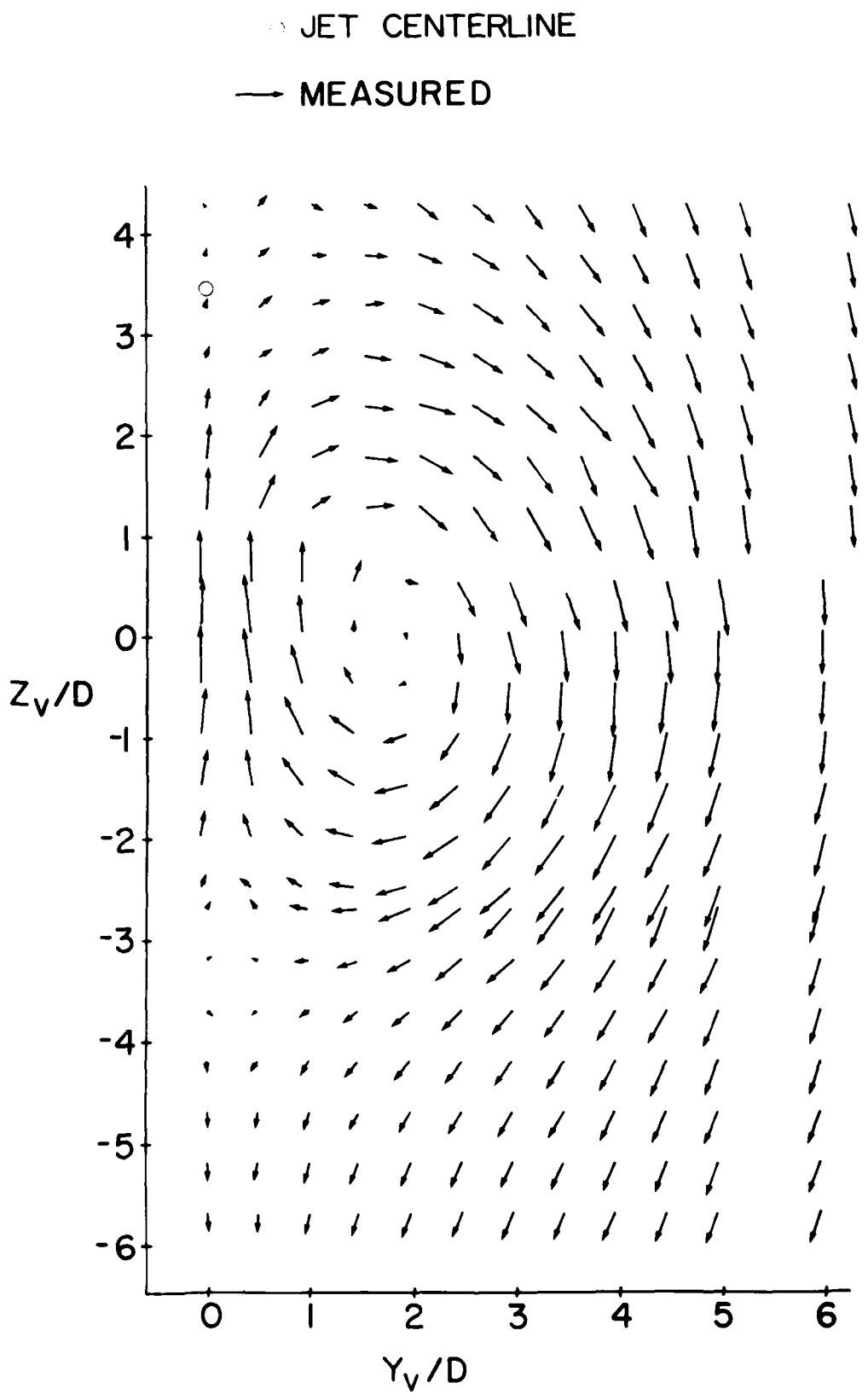

Figure 3.- Projections of measured velocities on cross section, R=8, X/D=10.0, z/D=5.31.

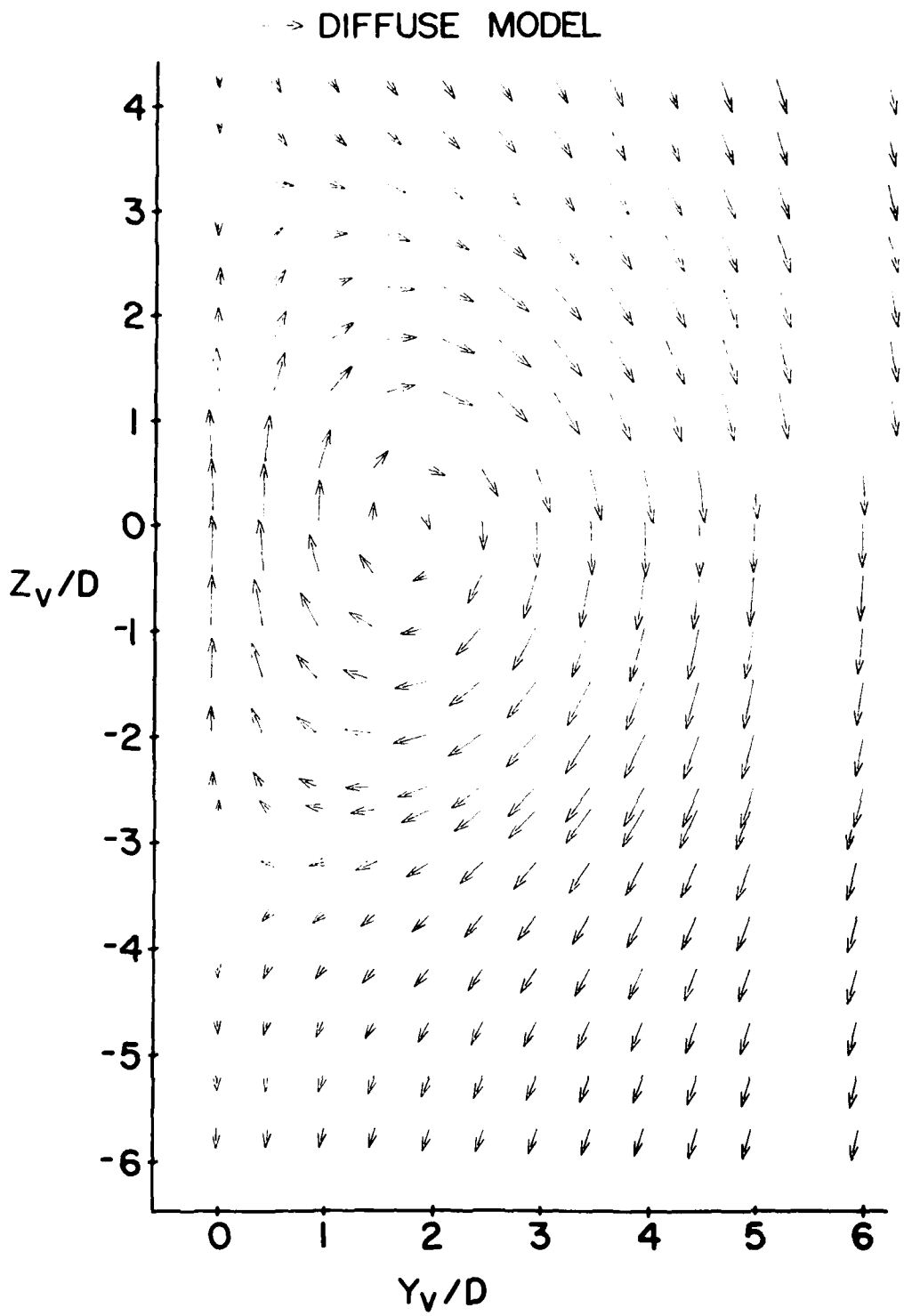

Figure 4.- Velocities calculated from diffuse vortex model at locations of measurement. R=8, X/D=10.0, z/D=5.31.

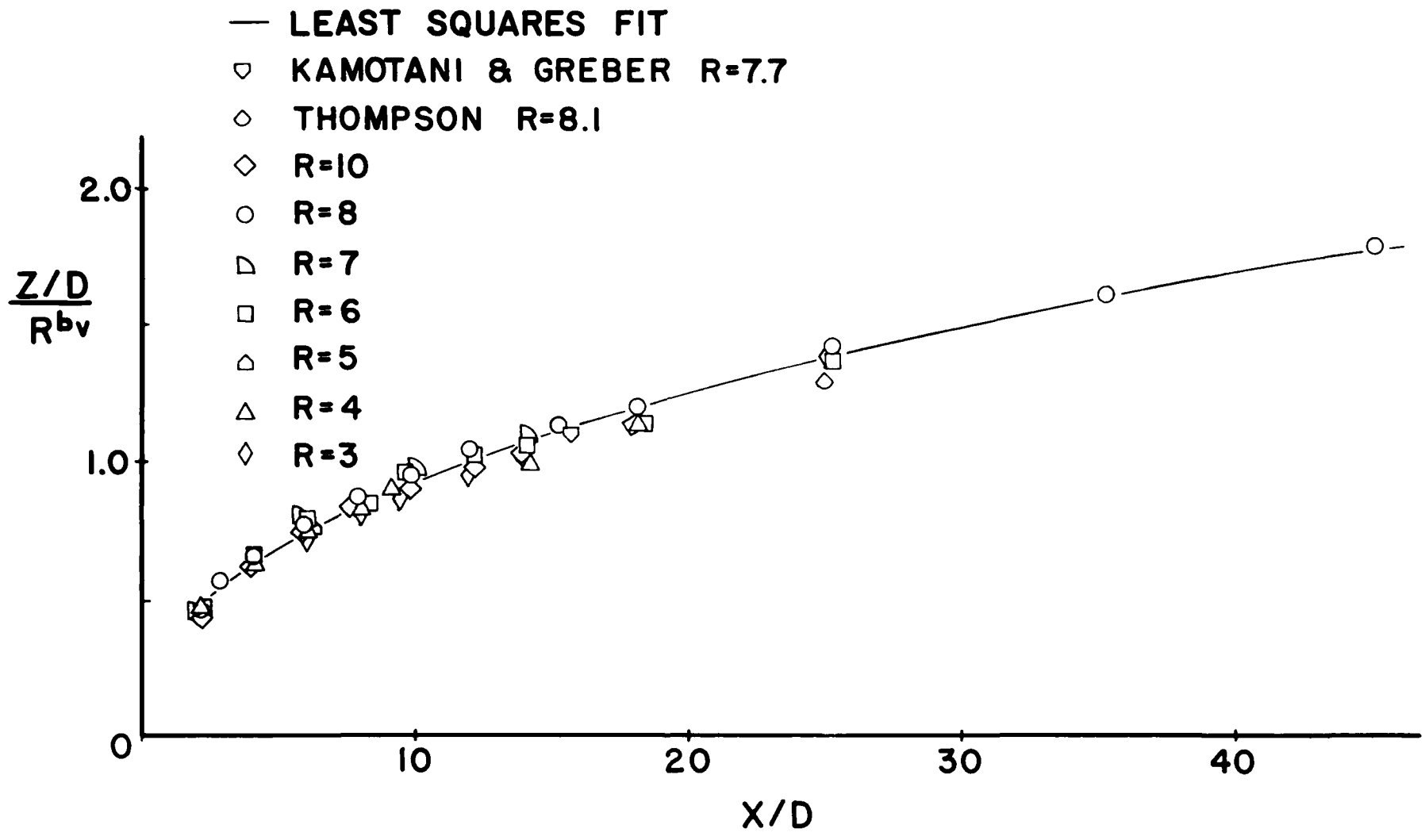

Figure 5.- Vortex curve

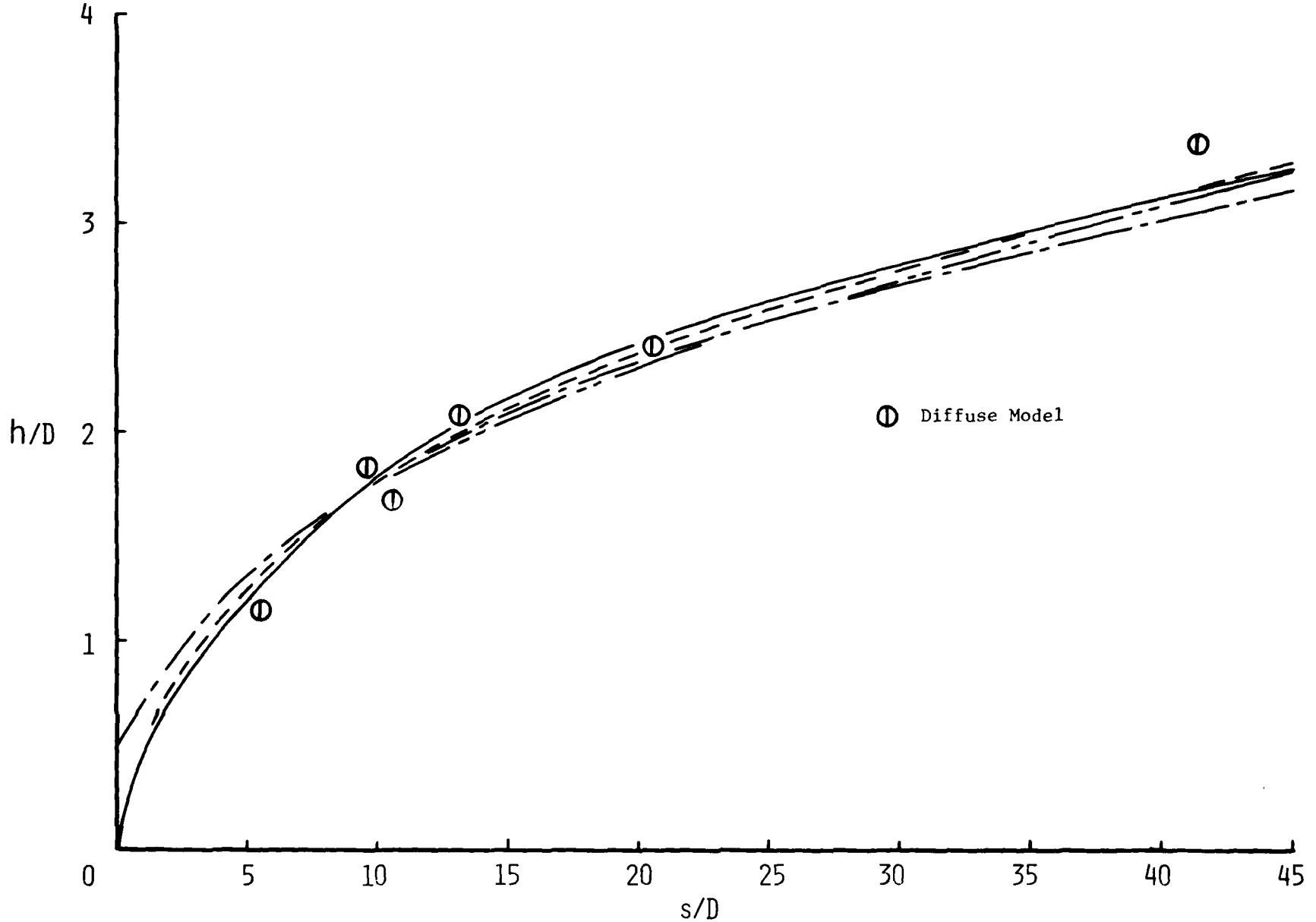

Figure 6.- Effective Vortex Spacing, R=8.

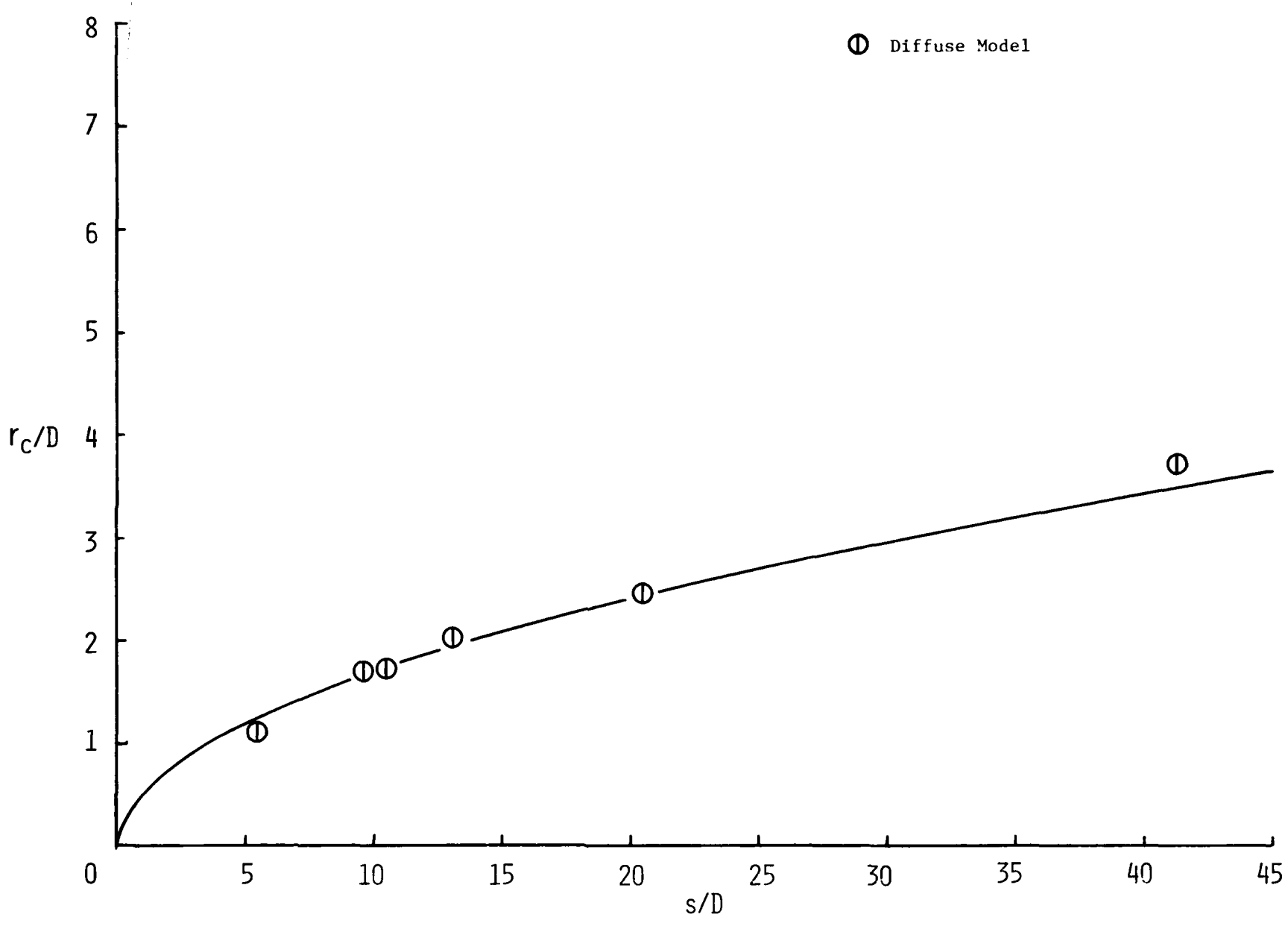

Figure 7.- Vortex Core Size, R=8.

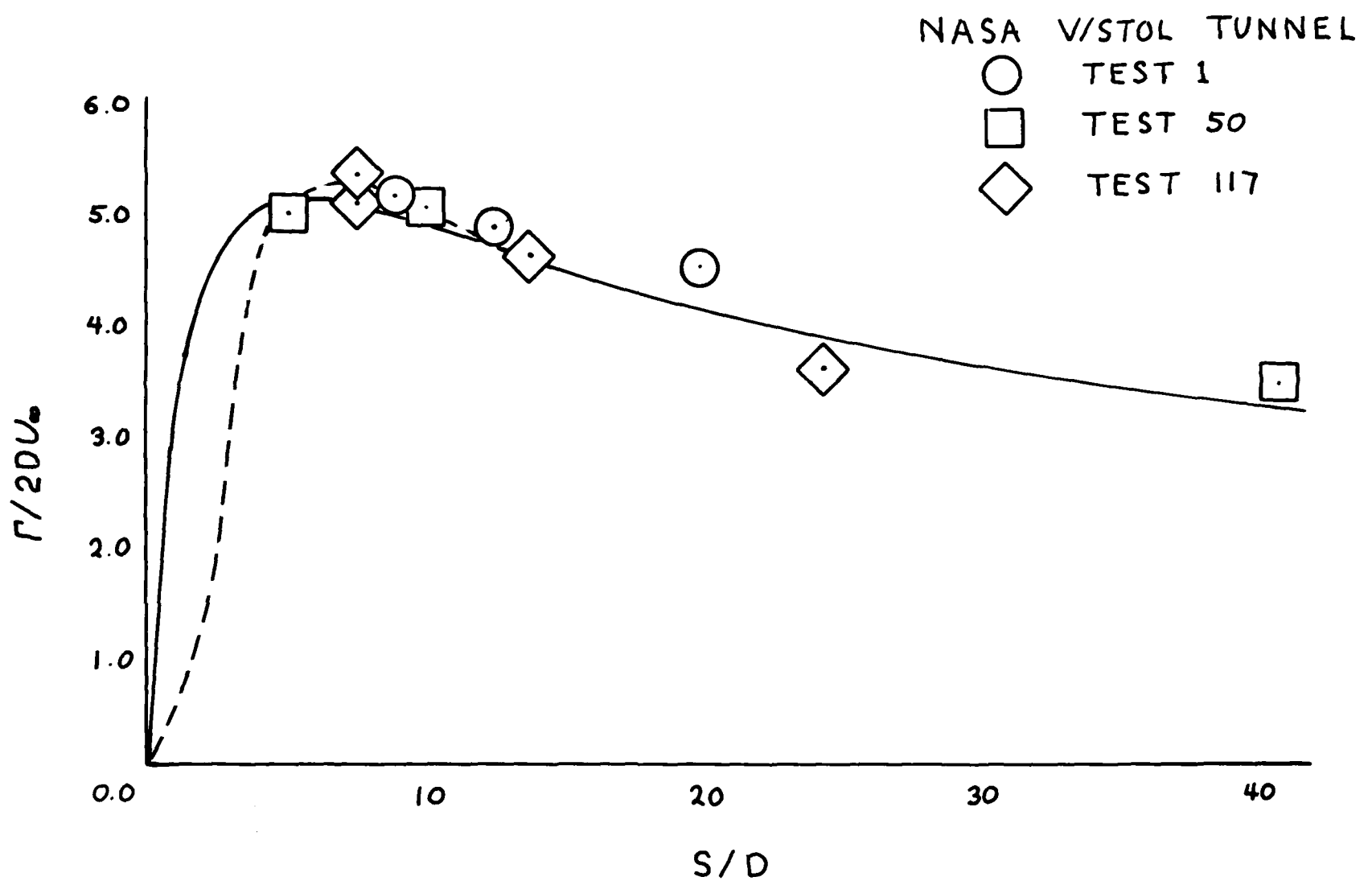

Figure 8.- Vortex Strength, R=8.

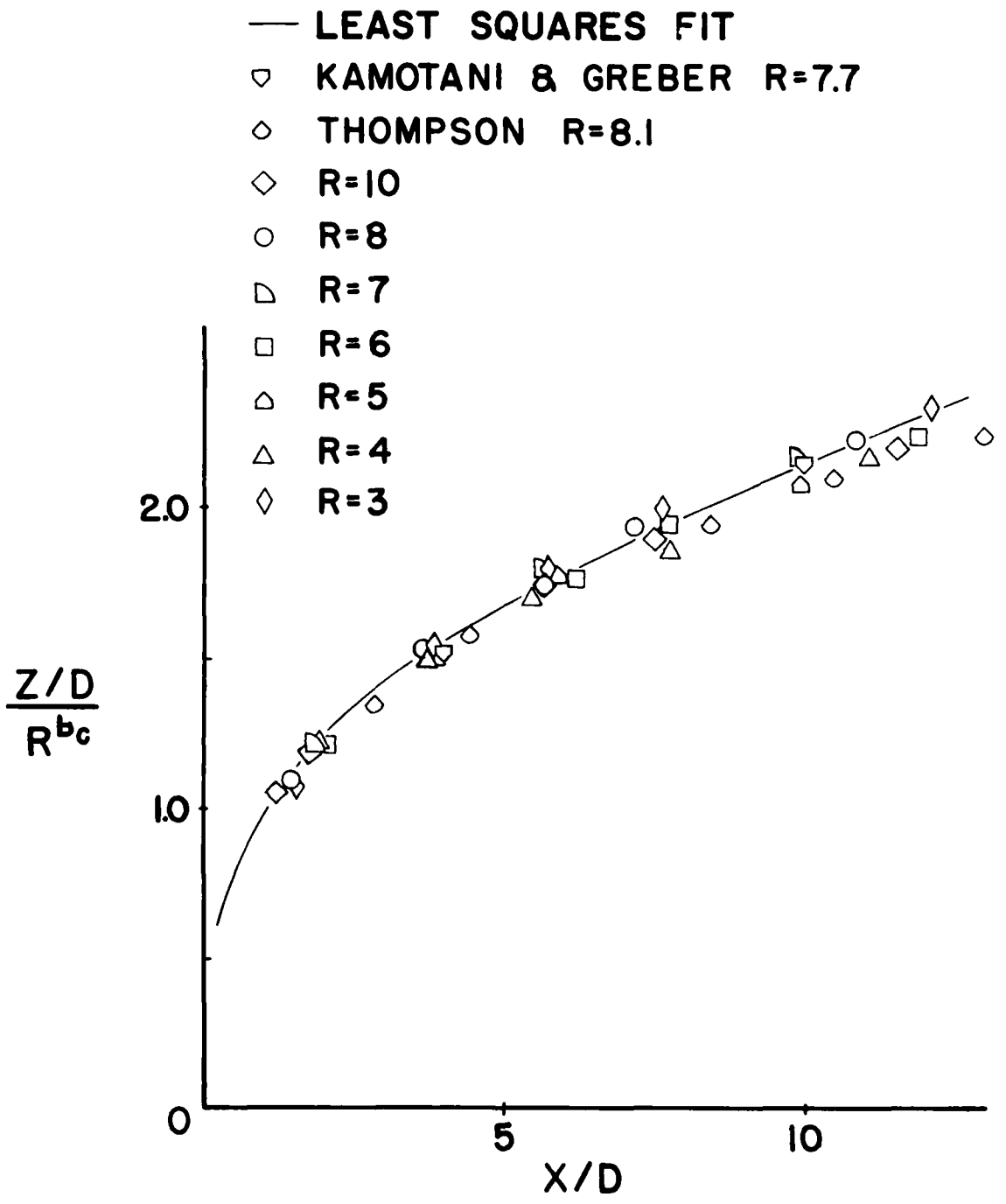

Figure 9.- Jet Centerline.

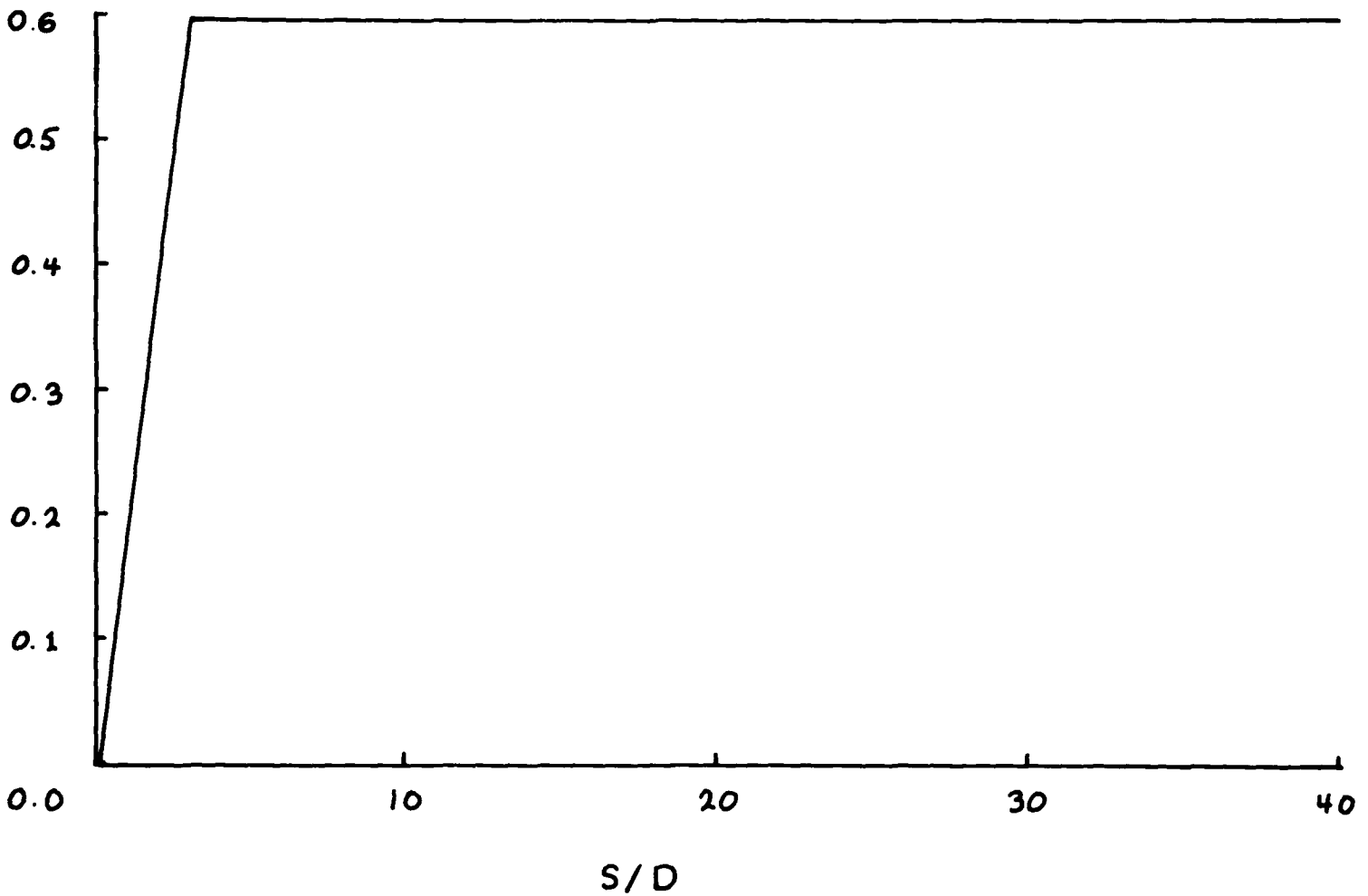

Figure 10.- Entrainment, R=8.

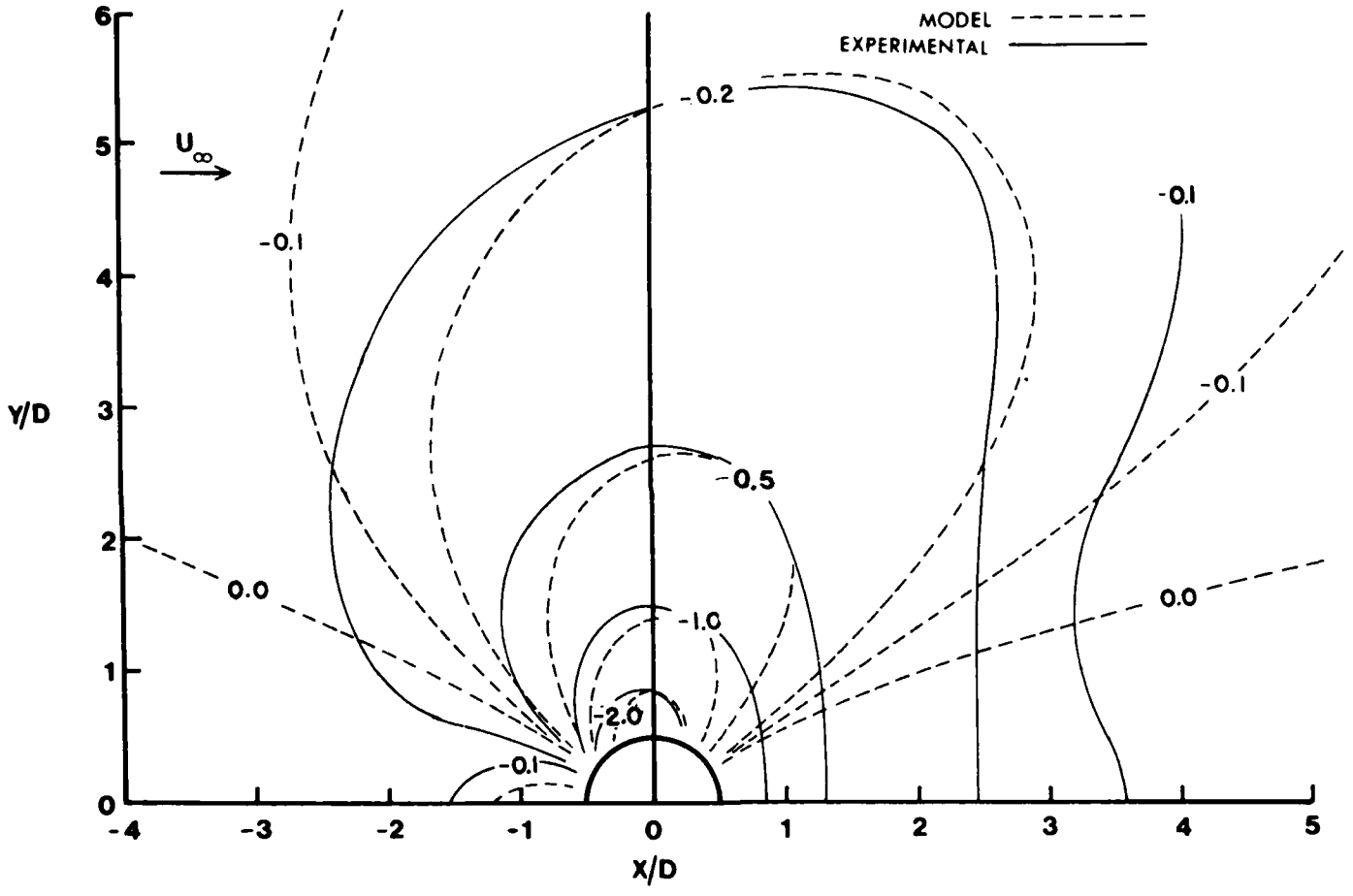

Figure 11.- Comparison of Model Results with Experimental Pressure Contours for Zero Entrainment.

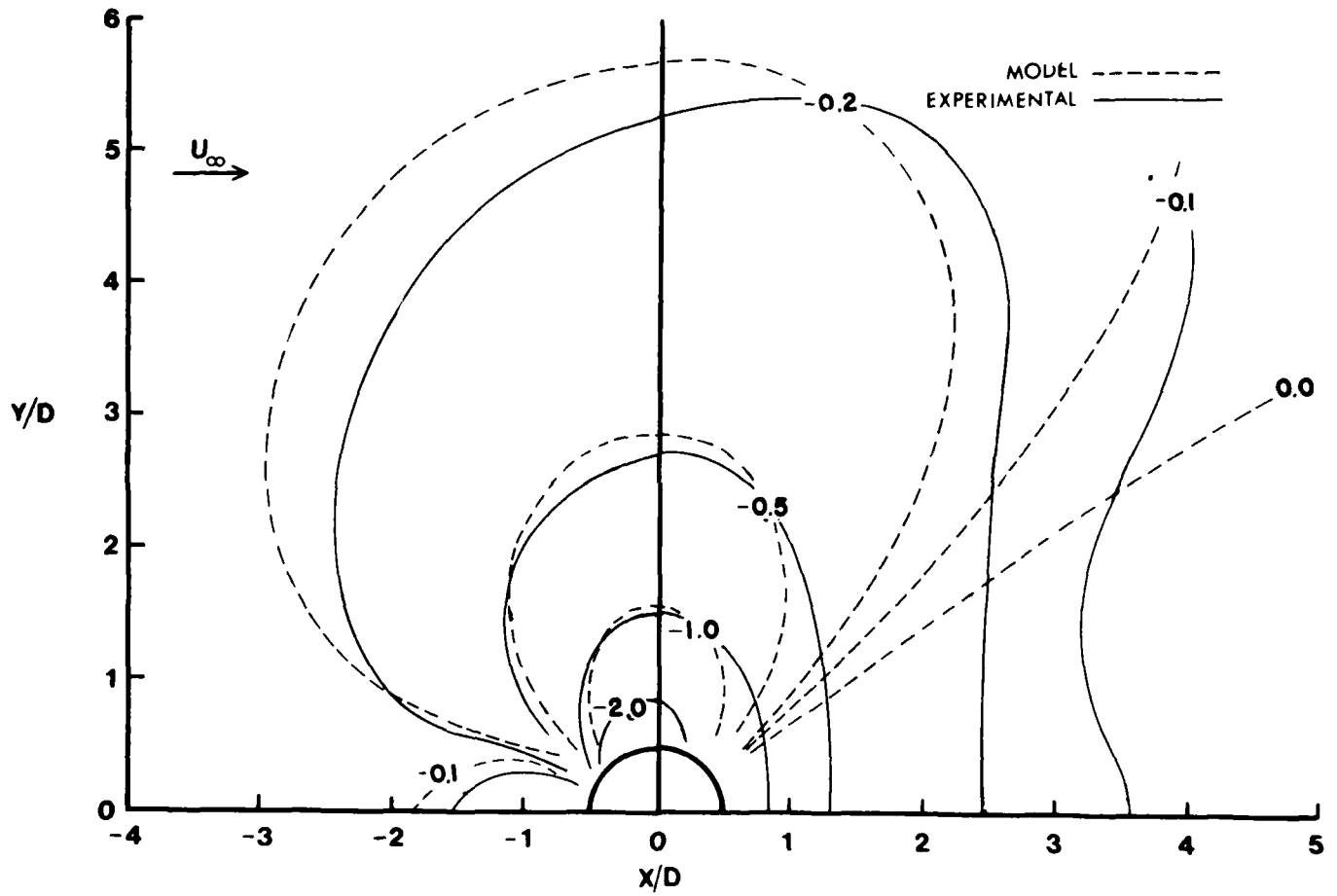

Figure 12.- Comparison of Model Results with Experimental Pressure Contours for E=0.6.

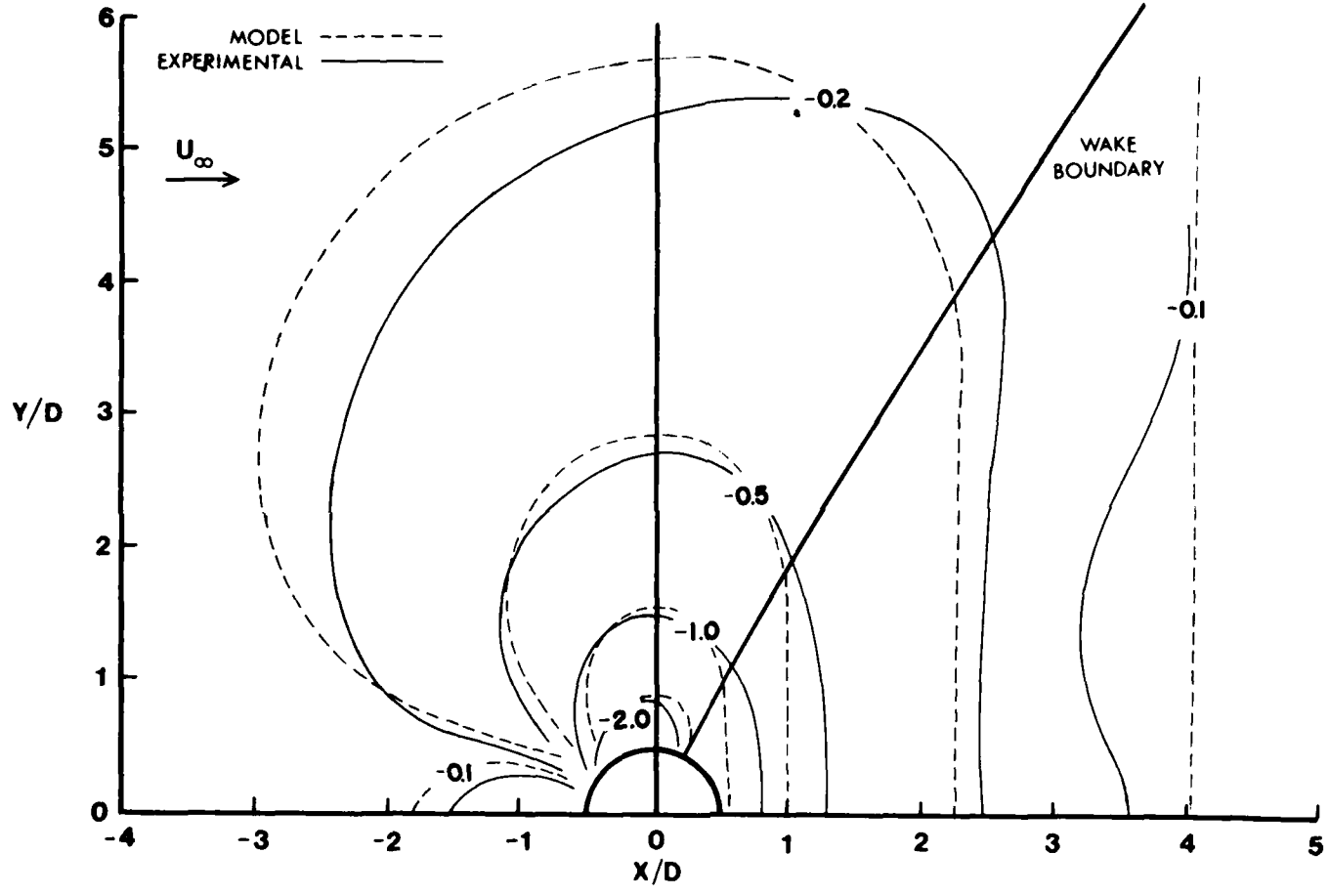

Figure 13.- Comparison of Model Results with Experimental Pressure Contours with Application of Wake Region Assumption (E=0.6)

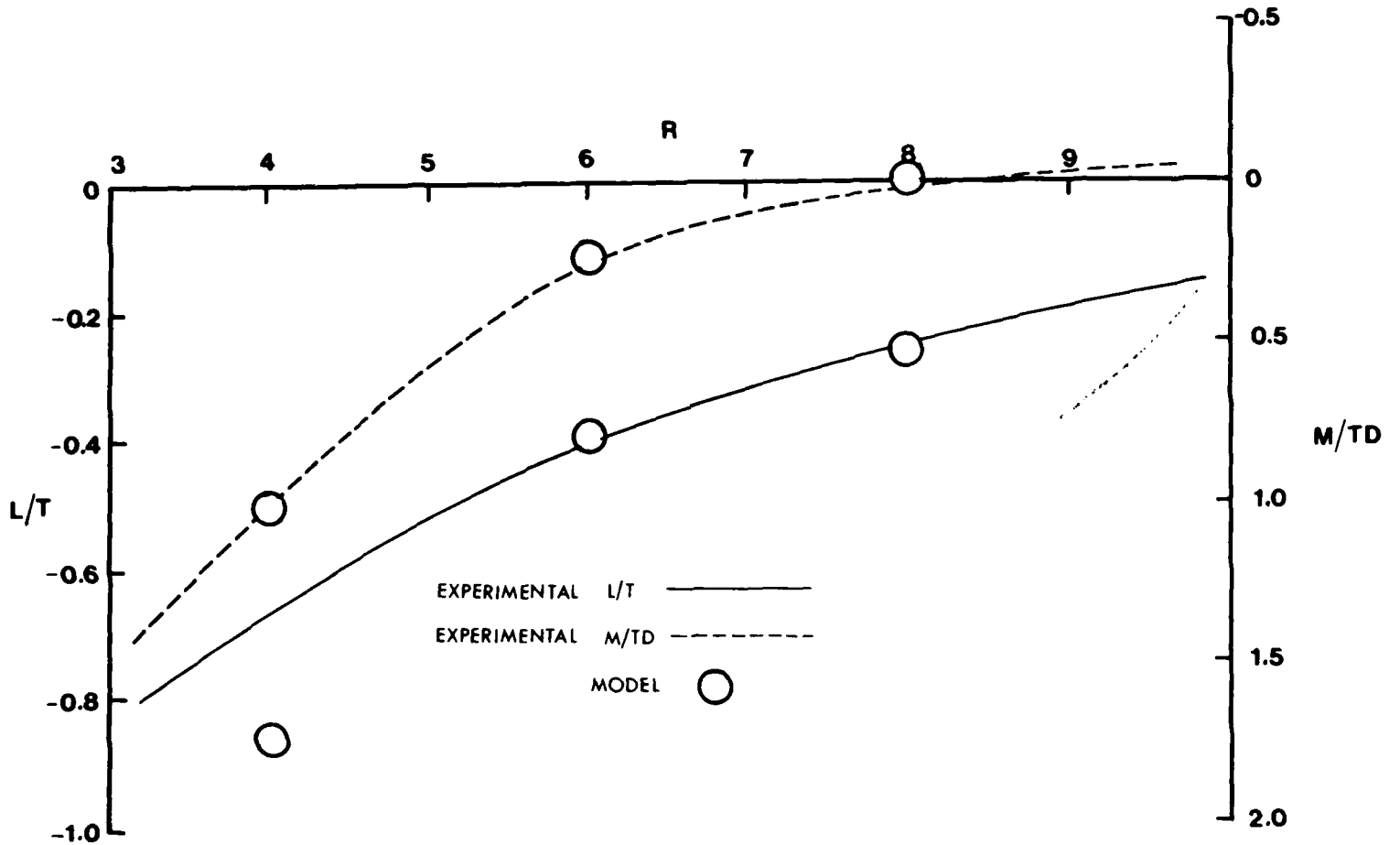

Figure 14.- Comparison of Model Results and Experimental Lift and Moment on the Flat Plate

A PREDICTION METHODOLOGY FOR PROPULSIVE INDUCED FORCES AND MOMENTS IN TRANSITION AND STOL FLIGHT

by

T. D. Beatty

Vought Corporation

Dallas, TX

This paper describes the V/STOL Aircraft Propulsive Effects Computer Program (VAPE), developed at the Vought Corporation under Navy Contract number N62269-78-C-0036 for determining the flow field about an arbitrary V/STOL configuration in the transition and/or STOL regions of flight.

The VAPE program is capable of evaluating:

- o effects of relative wind about the aircraft
- o effects of propulsive lift jet entrainment and flow blockage
- o effects of engine inlet suction on the aircraft flow field

The jet induced effects are evaluated by use of three different jet models:

- o the Wooler-Ziegler Jet Method for circular jets
- o the Weston-Dietz Jet Method for circular jets
- o the Thames Jet Method for rectangular jets

Emphasis in this paper is on comparing the various jet methods in terms of approach used, and results obtained. The modifications made to the Weston-Dietz Method to make it applicable to multiple jets is also discussed. In addition, a summary of the experimental tests performed by Dr. Thames on rectangular jets is presented along with a description of the jet model developed.

INTRODUCTION

V/STOL concepts currently being investigated for Navy missions employ various arrangements of lift and/or lift/cruise engines. The experimental data on V/STOL configurations obtained to date indicate that sizable propulsion induced force and moment characteristics can occur in the V/STOL flight mode. These effects are dependent upon jet efflux geometry and arrangements of the jets relative to aerodynamic surfaces. The presence of these effects poses a problem to the aircraft designer in the conceptual and preliminary design stage, since the designer must account for the effect of the propulsive jets to obtain the best performance.

These propulsive induced effects have caused considerable efforts to be expended throughout the aircraft industry to develop analytical and empirical prediction methods. Most of these efforts have been concentrated into two basic categories: (1) In Ground Effect (IGE) and (2) Out of Ground Effect (OGE). Various techniques have been developed to simulate the propulsive jet and its influence upon the aircraft.

The program to be discussed in this paper, the Vought Aircraft Propulsive Induced Effects Computer Program (VAPE), is concerned with the flight regime where the aircraft is transitioning from conventional forward flight to vertical hovering flight. The VAPE method is applicable for both IGE and OGE as long as the jet geometry and jet to freestream velocity ratio are within certain specified boundaries.

DISCUSSION

Several years ago, Vought initiated an in-house funded program to establish analytical and experimental techniques for analyzing and designing V/STOL aircraft. The experimental efforts conducted resulted in the construction of a 15 x 20 foot V/STOL test section in the Vought low speed wind tunnel facility, a small ground effect facility for preliminary testing, and a large ground effect facility for testing models which are compatible with the V/STOL test section.

The analytical effort identified several methods available in the industry which were applicable to V/STOL aircraft analysis. These methods were designed for various aspects of the V/STOL problem such as hovering in ground effect, the transition region out of ground effect, and engine inlet analysis techniques. These methods were all basically "stand alone" techniques which required input from other programs or supplied output data which had to be used in other methods. There did not exist one program which could provide the total flow field about a V/STOL aircraft. Therefore, Vought proceeded in the formulation of the Vought V/STOL aircraft propulsive effects program, VAPE, for the transition region of flight and various other techniques for other flight regimes. The VAPE program which resulted from these efforts utilizes several of these stand alone methods which were available in the literature. These methods, as will be discussed later, were extensively modified at Vought in order to develop the unified procedure utilized in VAPE.

The VAPE program is currently being modified under a contract from the Naval Air Development Center. The program is being extended to perform an analysis on V/STOL aircraft in the STOL region of flight, and additional jet models are being added to generalize the configurations which can be analyzed and to improve the program accuracy. The program which will be discussed in this paper is this latest version of VAPE.

It is noted that throughout this paper where reference is made to a method such as the HESS program, it is the Vought revised method which is being discussed and the name used is purely for reader identification.

VAPE PROGRAM

The Vought V/STOL aircraft propulsive effects program system is a union of five potential flow computational techniques: (1) the Hess three dimensional analysis program, (2) the Stockman inlet analysis program, (3) the Wooler-Ziegler jet model, (4) the Weston-Dietz jet model and (5) the Thames rectangular jet model. These programs are used in conjunction with geometry models to form a very general and very efficient program for determining the propulsive induced effects. A schematic of the program options and the basic program logic is presented in figure 1. The configuration geometry is digitized using the geometry module with the plot and symmetry modules used to facilitate model formulation. This model is then input to the Hess potential flow program where the actual aerodynamic characteristics of the aircraft are determined.

The geometry is also input to the stockman inlet module. The inlet module determines the velocity on the inlet face needed to obtain the correct mass flow through the nacelle. These velocities are then transferred to the Hess program to be used as boundary conditions on the inlet face.

A jet model determines the induced velocities due to the jet exhaust on the panels of the model. These velocities are then converted to a normal velocity acting at the centroid of each panel to be used as boundary conditions in Hess. The Hess solution is then executed with the above boundary conditions producing the aerodynamic forces on the aircraft which include inlet and jet exhaust effects.

Major modules of VAPE are discussed in the following text. These modules are:

- o Geometry
- o Hess potential flow
- o Stockman inlet analysis
- o Wooler-Ziegler jet model
- o Weston-Dietz jet model
- o Thames rectangular jet model

GEOMETRY MODULE

The geometry module consists of several routines developed to assist in paneling a configuration for input into the Hess potential flow program. Historically, the biggest expense involved in utilizing a panel method like Hess is not necessarily the computer time but the engineering hours required to digitize

an aircraft configuration. Therefore, to help alleviate this problem, Vought developed several geometry routines as shown in figure 2. These routines presented are used to perform the tasks shown in table 1.

Subroutine	Description
JUNCPAN	Find intersection between lifting and non-lifting bodies and repanel non-lifting body
CIRCLE	Generates circular bodies and distributes panels. Also panels inlets
CONIC	A general routine for describing and paneling non-circular bodies
AIRFOIL	Generates wings from airfoil shapes and distributes panels
PLOTTING	There are two plotting routines: (1) Subroutine HESPLOT generates calcomp plots of input configuration (2) Subroutine HESIGS is an interactive routine which plots data on the Tektronic low cost graphic scope and permits input modification
SYMMETRY	This routine converts a body defined about a plane of symmetry into a complete body

TABLE 1

Hess Potential Flow Program

The HESS potential flow program, Reference 1, is the primary module of the VAPE system. This program calculates the flow field characteristics about any arbitrary three-dimensional configuration. This method is currently used throughout industry and at several government facilities.

The HESS method is "exact" in the sense that no approximations are made in the basic formulation, as is done in small-perturbation or lifting-surface theories. The basis of this method is a distribution of source density over the surface of the body about which flow is to be computed. Application of the normal-velocity boundary condition on the surface of the body yields an integral equation for the distribution function of the source density, where the domain of integration is the body surface. Once this equation is solved for the source distribution, flow velocities both on and off the body surface can be calculated. An aircraft configuration in HESS is composed of non-lifting and lifting bodies, where a lifting body is defined as one which possesses definite trailing edges and contains bound vorticity. This program is explained in detail in reference 1 and 2 and will not be described in any further detail in this paper.

Stockman Inlet Analysis

The jet exhaust flow induces a change of pressure on parts of the aircraft as will be discussed later. In addition, the inlet also effects the flow field about the configuration. This effect must be considered if a good description of the flow field is to be obtained, even for flow-through nacelles when using a panel method to assure the correct flow into the nacelle. Quantitative results on this aspect of the flow modeling will be presented later in this discussion.

The Stockman program, reference 3, as it is currently utilized in VAPE is restricted to axisymmetric inlets. This program utilizes the HESS axisymmetric potential flow program together with a finite difference boundary layer program to obtain the inlet flow field solution for a specified mass flow.

In the VAPE system, this program also supplies input to a routine to determine the inlet forces and moments as will be discussed in a subsequent session of this workshop.

The Stockman routine operational at Vought has also undergone in-house modifications. Vought has overlayed the routines into one program with the viscous iterative procedure automated.

Jet Models

The flow field produced by a jet issuing into a crossflow is shown schematically in figure 3. As can be seen, a pair of counter-rotating vortices are formed by the interaction of the jet and the crossflow. The jet methods contained in VAPE attempt to model this flow field by two different techniques as explained in the following sections.

Wooler-Ziegler Jet Model

The method of Wooler-Ziegler (ref. 4) is divided into two parts: (a) calculation of the jet envelope, and (b) calculation of velocities induced by the jets on the flow outside the jets. The analysis of part (a) assumes incompressible and inviscid flow, except for the viscous phenomenon of mass entrainment by the jet. The analysis of part (b) is obtained by replacing the jet with sinks, sources, and doublets, and performing a potential flow analysis about these singularities.

Equations for conservation of mass, and conservation of momentum of the jet flow in directions tangential and normal to the local jet centerline direction are used for the jet envelope calculations. Jet cross sections in planes normal to the jet centerline are assumed to be ellipses. Entrainment rates of ambient air into the jet are assumed to vary along the jet trajectory. An empirical equation is used for the prediction of these rates.

Figure 4 shows elements that are used to represent effects of the jet on flow around the jet. Jet blockage is represented by a series of doublets and sources placed along the jet centerline. Jet entrainment is represented by sinks placed across the jet at an angle of 90 degrees to the free stream direction as shown in Figure 5. Doublet strengths depend upon local dimensions of the jet cross section, jet centerline inclination to the onset flow, and free stream velocity. Source strengths depend on local curvature of the jet centerline. Sink strengths match

local entrainment of the jet. Expressions from three-dimensional potential flow theory are used to calculate induced velocities at points on the aircraft surface for each flow singularity used in the analysis. These velocities are summed vectorially to get the total velocity increment caused by the jets on the onset flow.

The Wooler-Ziegler method is capable of dealing with single or two jet configurations. For the two jet configuration mutual interference effects between the jets as well as the results of a merger of the jets are analyzed. Restrictions on the relationship of the jet injection angles relative to the aircraft onset flow are minor. The only requirement is that the velocity vectors at the nozzle exits must not be parallel to the onset flow vector.

The Wooler-Ziegler analysis as described in reference 4 applies for aircraft altitudes out of ground effect. Vought has revised the Wooler-Ziegler computer program to account for ground blockage effects when an aircraft is operating within the altitude range of 10 to 25 equivalent nozzle diameters. Equivalent nozzle diameter is defined as the diameter of a single nozzle with an exit flow area equal to the total exit flow area of all the lift engine nozzles on an aircraft. The revision uses images of the jet singularities below the ground plane to force normal components of velocity to be zero at the ground plane. The real and image singularity system used in the revision is illustrated in Figure 5. The Wooler-Ziegler method described above [part (a) of the analysis] is used to determine envelopes of the real jets, and strengths of the doublets, sources and sinks associated with the real jet. Each source, sink or doublet of the image system is the mirror image with respect to the ground plane of a source, sink, or doublet of the real system with the same strength.

The Weston-Dietz Jet Model

The Weston-Dietz jet method, references 5 and 6, unlike Woolers approach attempts to model the counter-rotating vortices by placing vortex filaments along experimentally derived vortex lines. These vortices account for the flow blockage while the entrainment is accounted for in a manner similar to Woolers using sinks along the jet centerlines. Figure 7 presents a schematic indicating the relative location of the jet centerline and the projected vortex curves. The basic Weston-Dietz method is for a single jet, based on a very extensive experimental data base of measured locations of vortex and jet curves and detailed values of vortex strength reported in reference 5. This data is reduced to equations which are universal for the ranges of data obtained. This data base was extended by Fearn, reference 7, for injection angles other than 90 degrees.

This method has been extended at Vought to handle multiple jets by using the techniques of Wooler. This approach assumes that the front jet in a jet pair, i.e., jet 1 in figures 8(b) and 8(c) acts independently of the second jet and thus the equations for a single jet are appropriate. The aft jet is assumed to operate in a reduced dynamic pressure field produced by the blockage of the front jet. The magnitude of this reduction in dynamic pressure is a function of the amount of blockage as discussed in reference 4. For the case shown in Figure 8a no mutual interaction effects are assumed for the extended Weston-Dietz model. Figure's 9 through 11 present a comparison of the experimental

data of Wooler compared to the predicted jet path centerline of both Wooler and the extended Weston-Dietz method. As can be observed both methods predict similar curves which agree fairly well with the experimental data.

The Weston-Dietz method is also being modified at Vought to perform calculations for V/STOL aircraft in the STOL (short takeoff/landing) regime. This modification requires the addition of methodology to predict the effects of the wall jet which is formed when the jet efflux impinges on the ground. The approach which is being used is applicable whenever the aircraft is moving with sufficient velocity and with the jets deflected away from the vertical enough to ensure that no fountain is formed and that no jet wash is reflected back to the airplane surfaces. The technique employed is to determine the limits of the ground plane wall jet using an empirical relation developed by Colin, reference 8, which determines the forward stagnation line. A schematic of this relationship is shown in figure 12. The impingement points are found by installing a ground plane in the HESS model and searching the jet centerline path until intersection with the ground is determined. The stagnation line is then determined and the region in front of this line is treated as a simple ground plane. The region aft of this line is analyzed using techniques from reference 9 and 10 to determine the entrainment rate. This is then converted into a normal velocity using relationships from reference 9 and used as a boundary condition in the HESS program.

Thames Rectangular Jet Method

This is a program developed at Vought by Thames, reference 11, which calculates the flow field about rectangular jets issuing into a cross wind. This contractual effort was supported jointly by NASA Langley Research Center and the Naval Air Development Center. The model contained in VAPE is very similar in formulation to the Weston-Dietz circular jet model. The only difference is the numerical techniques for utilizing the wind tunnel data to obtain the proper vortex location and strengths. This method is limited to one jet due to the nature of the available wind tunnel data.

A schematic of the model formulation is presented in figure 13. This figure presents some of the differences between the Weston-Dietz circular jet model and the Thames rectangular jet model. There are several curves used for the source sink lines in the rectangular jet model due to its aspect ratio. One interesting result which has been observed in this model is that if the sink lines are converted to source lines, the flow field is essentially the same everywhere except in the wake region where the agreement with the experimental data is improved. This is acceptable since the model is being developed to predict the flow field, and it is not really necessary to model the complete physics of the flow. This change has also been tried in a preliminary form in the Weston-Dietz model and has shown some improvement in the wake region in this model also.

RESULTS

The foregoing was a brief description of the major components of the VAPE system. The following will present some results obtained using this program for various configurations.

Flat Plate Analysis

The flat plate configuration tested by Weston, reference 5, was analyzed using both the Wooler-Ziegler and the Weston-Dietz method. Figures 14 and 15 present the results for pressure coefficient for two angular positions as a function of distance from the jet exit. The θ of ninety degrees is directly lateral from the jet exit while the θ's of 135 and 180 are in the lee of the jet. These results indicate that both methods are in agreement and predict the experimental levels fairly accurately except in a region between θ of 135 and 180 degrees in a region close to the jet exit. The flow in this area as indicated in the experimental data is separated; and since neither method includes any separation effects, agreement should not be expected. Modifications are in progress to alter the Weston-Dietz method to try to account for this separation region, to altering the vortex and/or sink lines in this region.

Effects of Lift on Jet Model

The majority of the experimental data obtained on the jet in a crossflow has been for a circular jet issuing from a flat plate. This ignores lift effects and therefore raises the question of how lift or different body geometry affects the experimental data. There are two recent tests which were performed to try and isolate the effects of non-flat plate body configurations on jet data. The first was performed by Vought personnel at NASA LRC, reference 11, where a blunt body was tested with a rectangular jet issuing from the rear. The second was data recently published by McMaham and Antani, reference 12, for a jet issuing from a lifting wing. Considering this second set of data, the authors show the effects of varying the circulation about an airfoil and how it changes the various parameters associated with the Weston-Dietz jet model. Subsequently, this data was analyzed at Vought where an interesting conclusion was reached. If the value of jet velocity ratio, R, from Weston's model is modified to account for the local flow conditions at the jet exit, then the equation used for predicting jet vortex and centerline locations also predict the experimental data of reference 12 very well. Figures 16 and 17 present the experimental vortex and jet centerlines locations from reference 12 compared to the predicted values of the modified Weston-Dietz method. The results indicate that the Weston-Dietz method can predict the correct trajectories for the vortex and the jet, with lift effects, if the local conditions at the jet exit are used for reference instead of freestream. No analysis has been performed on the other parameters of vortex strength or spacing to see if this is true for these parameters also.

V/STOL AIRCRAFT CONFIGURATION

The last results are for a V/STOL model tested at NASA Langley, reference 13. Figure 18 presents a computerized plot of the configuration as modeled for input to the HESS program. It was mentioned above that the inlet can cause considerable changes in the results obtained by using a HESS type solution. The test data indicated a valve of velocity on the inlet between .8 and 1.0 as for the case of no jet. Figure 19 shows that as the inlet velocity is increased above this level the total airplane lift decreases considerably. This is due primarily to a change in the pressures on the forebody since the wing flow field is not altered appreciably.

The moments are therefore also effected by this inlet flow to a large degree. Therefore, it is important that a good estimate of the inlet flow field be obtained and used as an input to the HESS program when considering a V/STOL type aircraft since the inlets are normally very large and effect a large part of the flow field.

A comparison of experimental and VAPE calculations for the total forces on this configuration as a function of jet velocity ratio are presented in figures 20 and 21. The results presented in figure 20 for the zero angle of attack case show that at the lower values of jet velocity ratio, the comparisons are very good; but at higher values of jet velocity ratio, the results diverge from the experimental values. However, the trends are correct even to predicting the non-linear characteristics of the L/T curve. Figure 21 presents comparisons for ten degrees angle of attack showing similar results as presented in figure 20. These calculations were performed with a preliminary version of the VAPE program using the Wooler-Ziegler Jet model, which do not include any attempt at modeling the wake behind the jet. In addition, the velocity imposed on the inlet face was considered a constant across the face instead of being variable as will be done in the final VAPE program. It is anticipated that when these effects are included, the results will improve.

CONCLUDING REMARKS

A general method has been developed for the prediction of propulsive induced effects on V/STOL configurations in both the transition and the STOL flight regimes. This method gives very good predictions for a wide variety of configurations, thus providing the aircraft designer with a technique for predicting the effects of different propulsion systems on the aircraft aerodynamic characteristics. The VAPE method, with the inclusion of the Thames rectangular jet method, even allows the designer to assess the relative effects of two-dimensional and circular nozzles. By using the VAPE program the designer can significantly improve the basic aircraft design before starting the wind tunnel testing phase of configuration development.

REFERENCES

1. Hess, J. L., "The Problem of Three-Dimensional Lifting Potential Flow and its Solution by Means of Surface Singularity Distribution," Computer Methods in Applied Mechanics and Engineering, Vol. 4, 1974, North Holland Publishing Co.

2. Hess, J. L., "Calculation of Potential Flow About Arbitrary Three-Dimensional Lifting Bodies," Final Technical Report, McDonnell Douglas Report No. MDC 55679-01, Oct. 1972, also AD755480.

3. Stockman, N. O. and Button, S. L., "Computer Programs for Calculating Potential Flow in Propulsion System Inlets," NASA TMX-68278, 1973.

4. Wooler, P. T. and Ziegler, H., "Analysis of Stratified and Closely Spaced Jets Exhausting into a Cross Flow," NASA CR-132297, Nov. 1973.

5. Weston, R. P., "Induced Pressure Distribution of a Jet in a Crossflow," NASA TN 0-7916, July 1975.

6. Dietz, W. E., "A Method for Calculating the Induced Pressure Distribution Associated with a Jet in a Cross Flow," Masters Thesis, University of Florida, 1975.

7. Fearn, R. L.; Krausche, D.; and Weston, R. P.; "A Round Jet in a Cross-flow--The Influence of Jet Injection Angle on Vortex Properties," to be published by AIAA.

8. Colin, P. E.; and Olivari, D.: "The impingement of a Circular Jet Normal to a Flat Surface With and Without Crossflow," AD688953, Jan. 1969.

9. Kotansky, D. R.; Durando, J. A.; and Bristol, D. R.; "Multi-jet Induced Forces and Moments on VTOL Aircraft Hovering In and Out of Ground Effect," Naval Air Development Center, Report No. NADC-77-229-30, June 1977.

10. Siclari, M. J.; Barche, J.; and Migdal, D.; "V/STOL Aircraft Prediction Technique Development for Jet-Induced Effects," Naval and Propulsion Test Center Report No. PDR-623-18, April 1975.

11. Thames, F. C., "Development of an Analytical Model to Predict Induced Effects of Aspect Ratio 4.0 Rectangular Nozzles in a Subsonic Cross-wind," To be published as NASA CR.

12. McMahon, H. M. and Antani, D. L.: "Experimental Study of a Jet Issuing From a Lifting Wing," Journal of Aircraft, Volume 16, Number 4, April 1979.

13. Mineck, R. E. and Schwendemann, M. F.: "Aerodynamic Characteristics of a Vectored-Thrust V/STOL Fighter in the Transition-Speed Range," NASA TND-7191, May 1973.

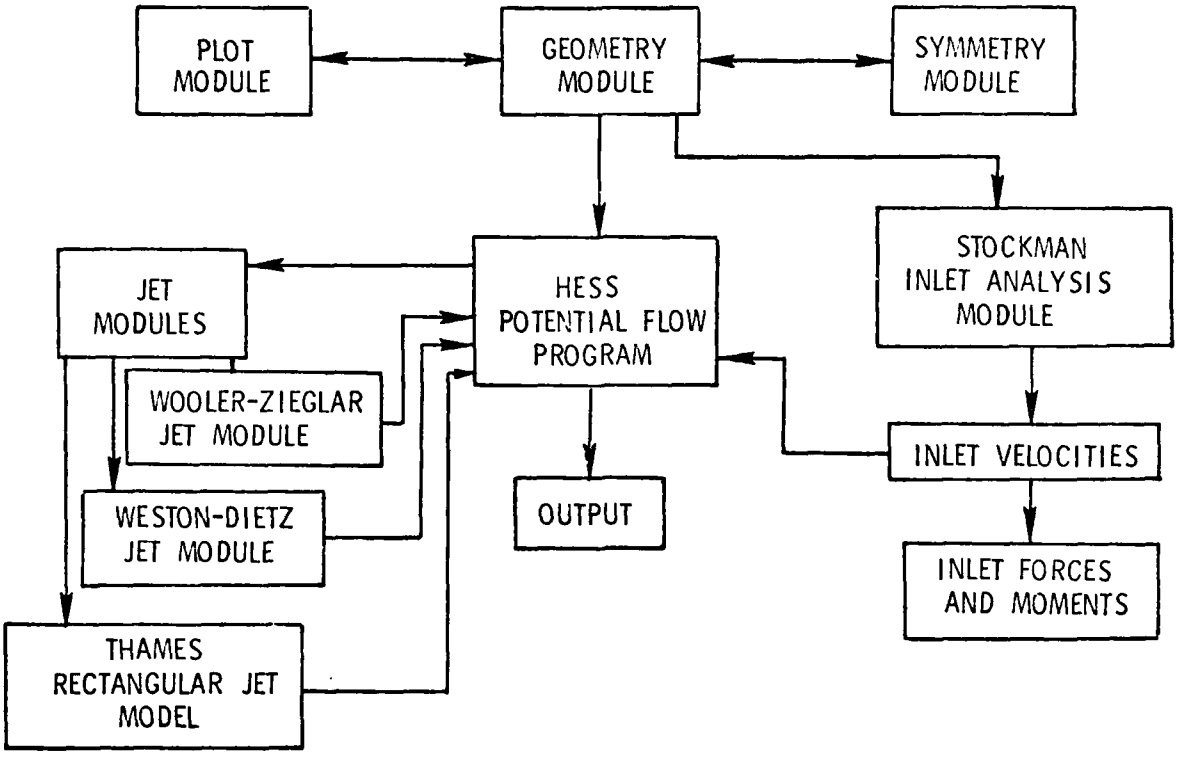

Figure 1. Schematic of program interaction for VAPE

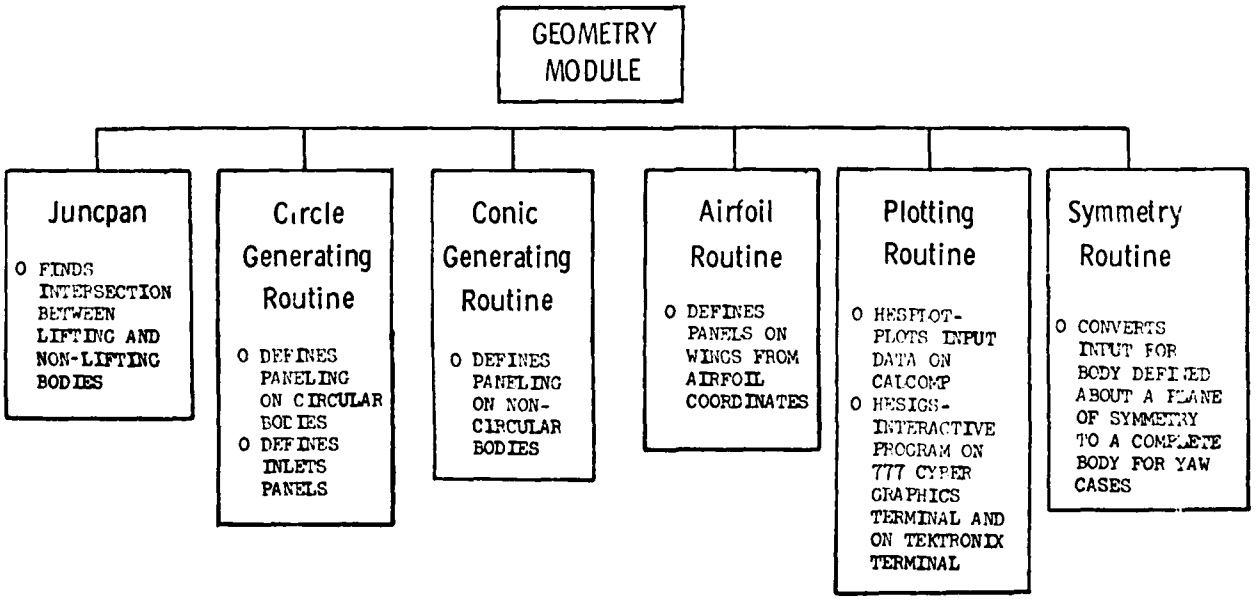

Figure 2. Components contained in Geometry module

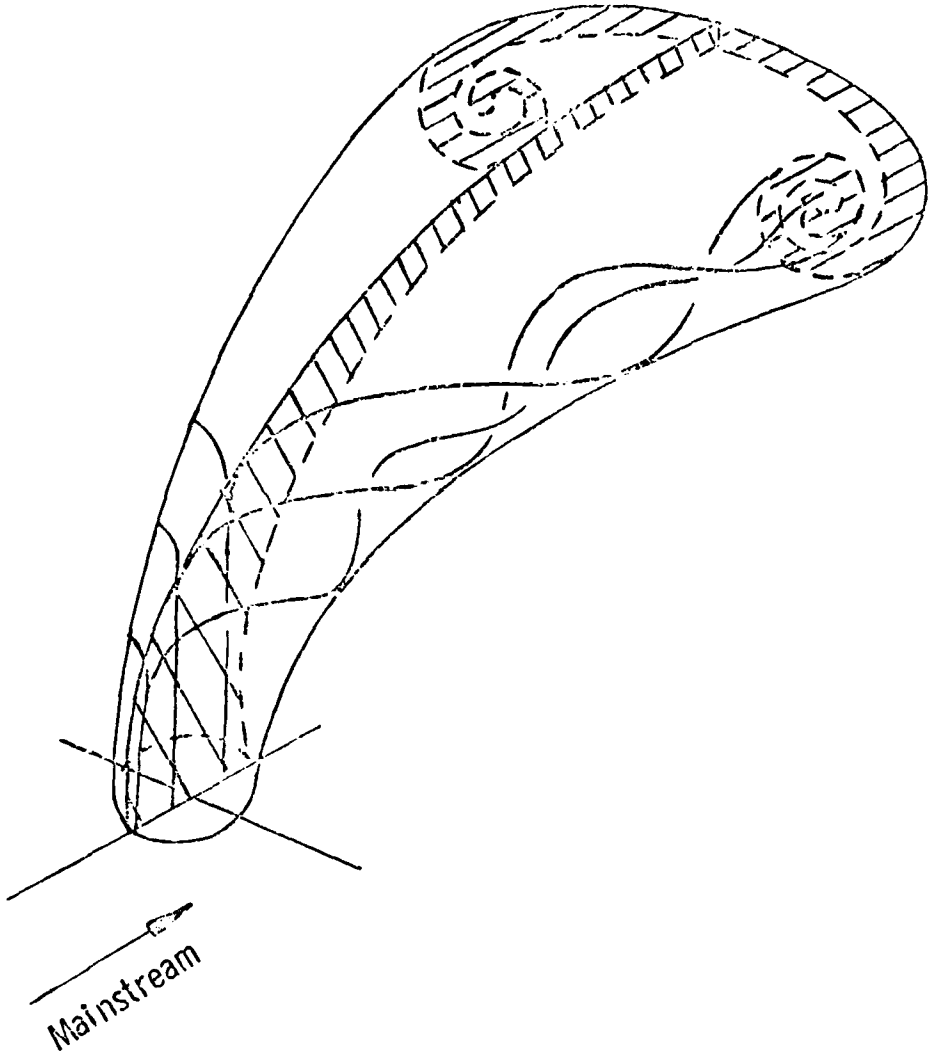

Figure 3. Schematic of flow field produced by a jet issuing into a crossflow

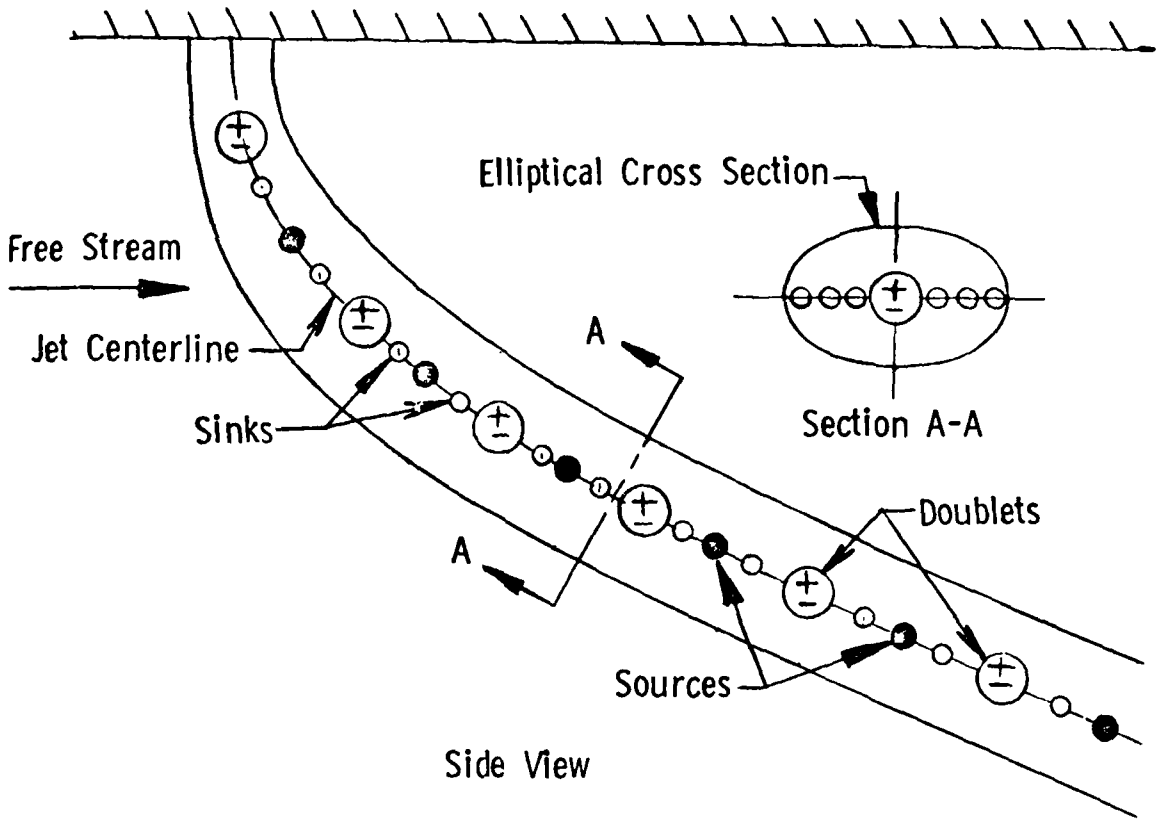

Figure 4. Wooler-Zieglar jet model singularities- bottom view

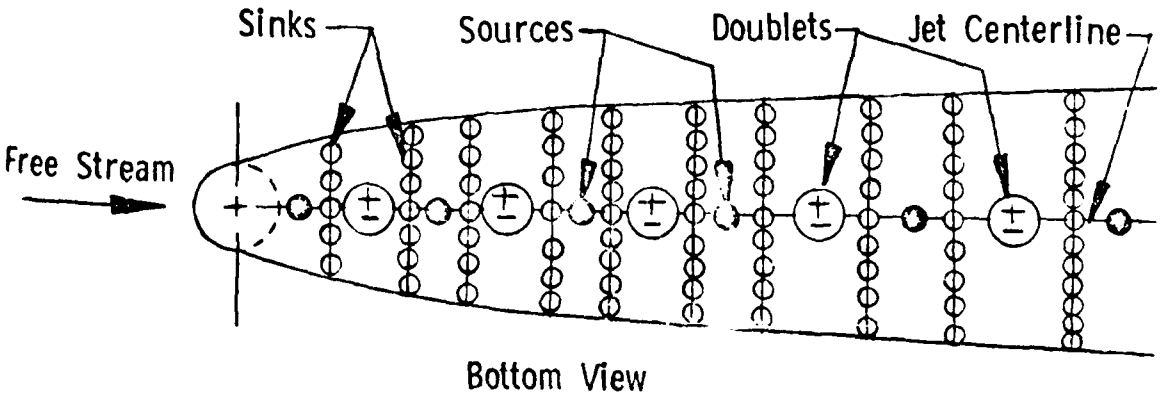

Figure 5. Wooler-Zieglar jet model singularities- top side view

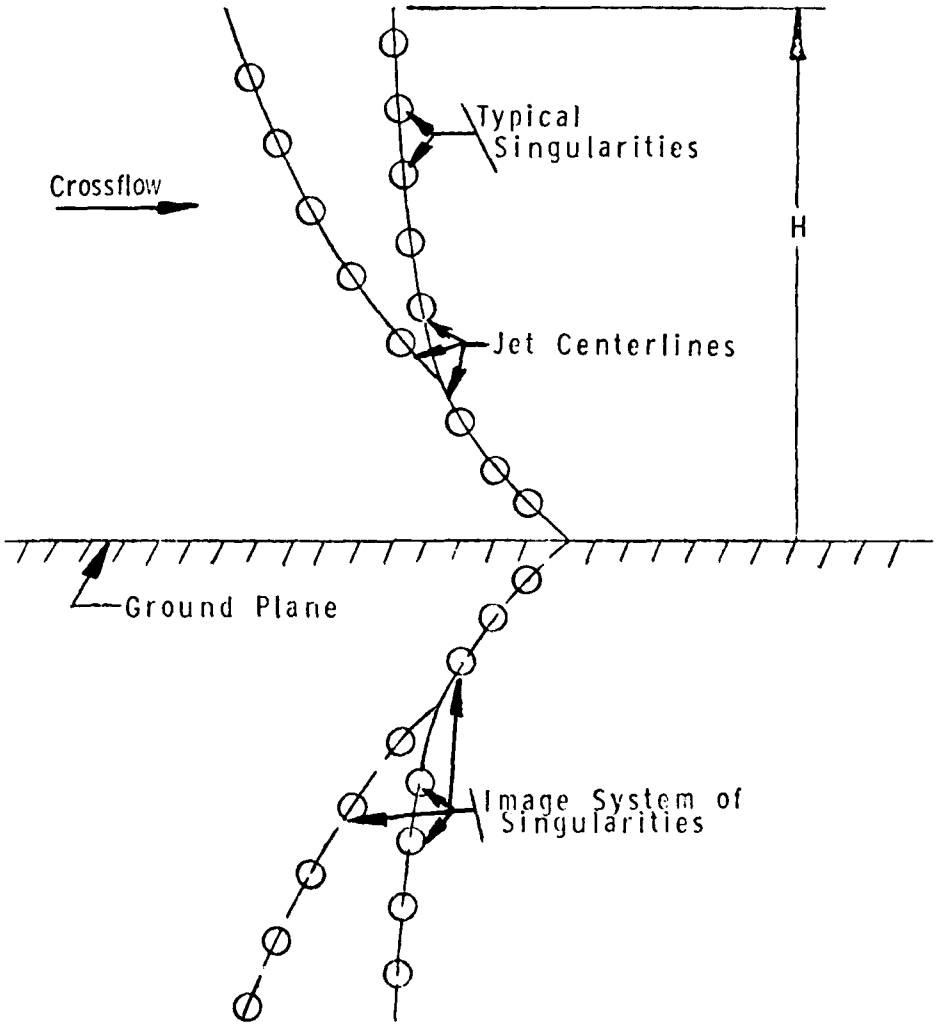

Figure 6. Image system for intermediate altitude ground effects calculation.

AD-A079 115 NAVAL AIR DEVELOPMENT CENTER WARMINSTER PA F/G 1/3
PROCEEDINGS OF A WORKSHOP ON V/STOL AIRCRAFT AERODYNAMICS, VOLU--ETC(U)
MAY 79 C HENDERSON, M F PLATZER

UNCLASSIFIED NL

2 OF 7
AD
A079115

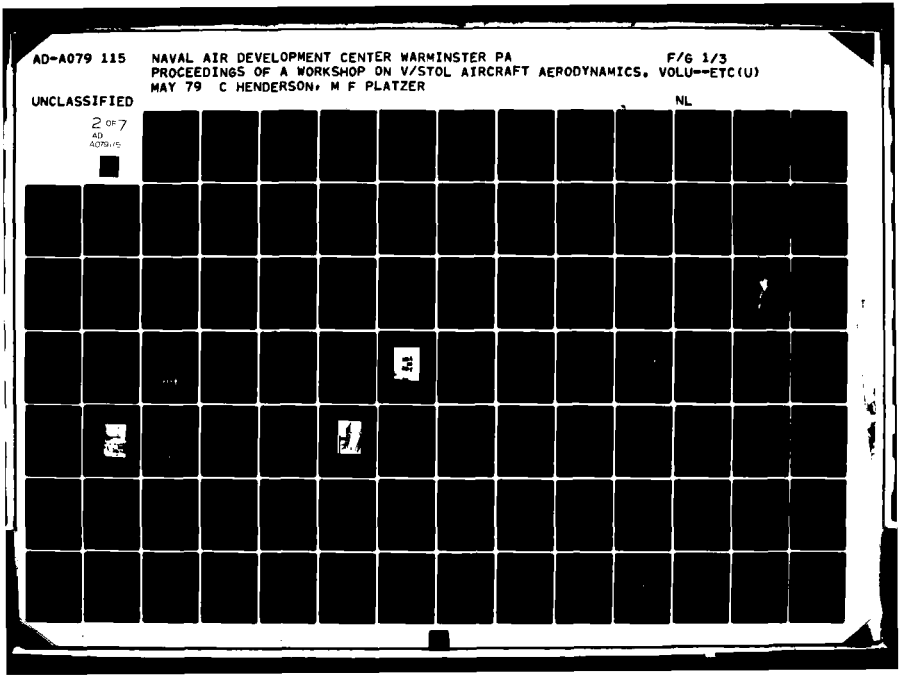

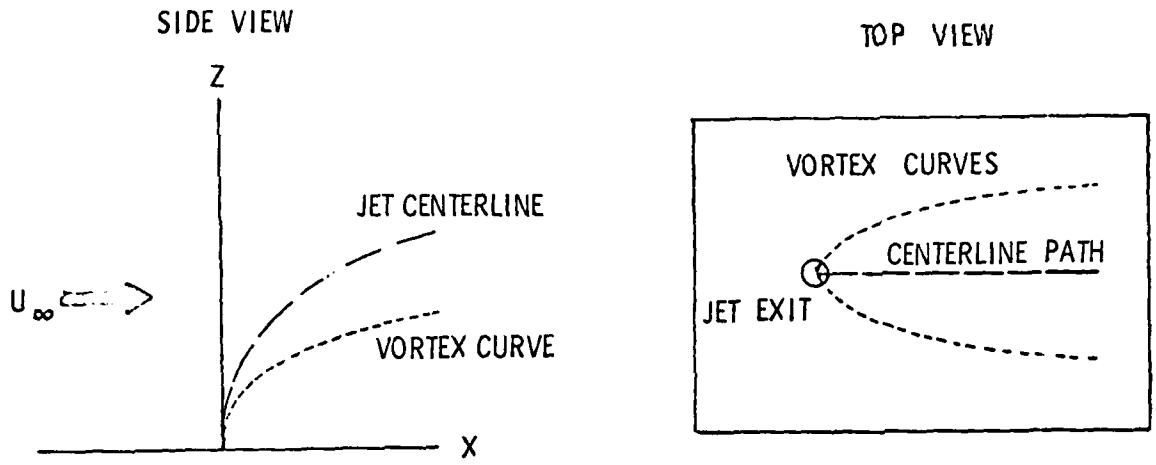

Figure 7. Schematic of jet centerline and vortex curves for Weston-Dietz jet model

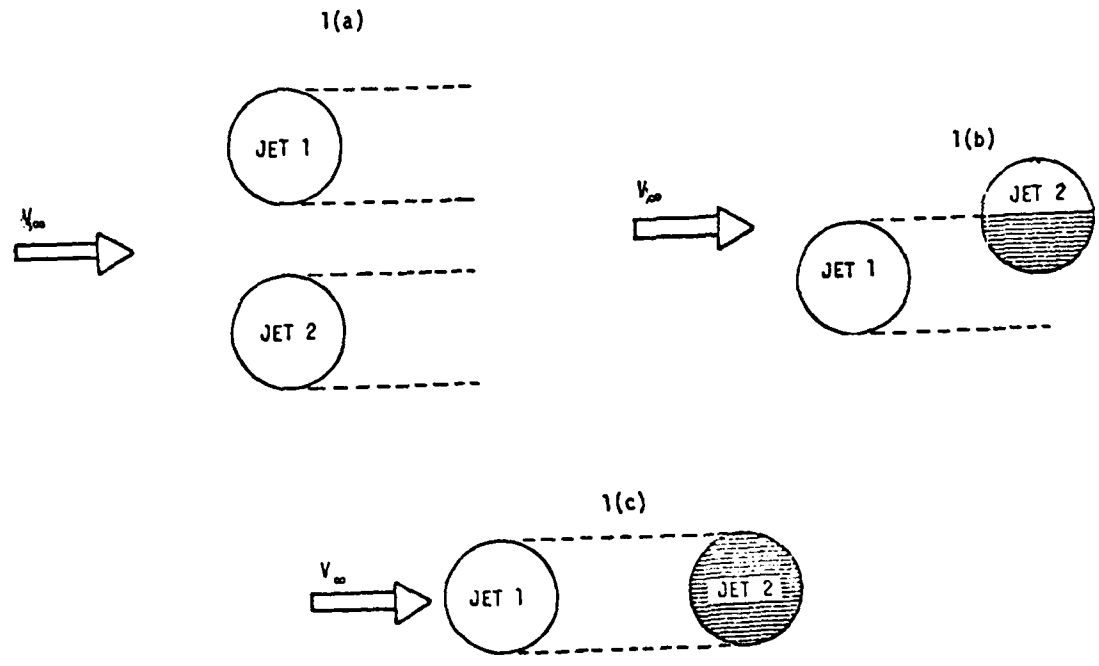

Figure 8. Schematic of blockage effects utilized in both Wooler-Zieglar and the revised Weston-Dietz jet models

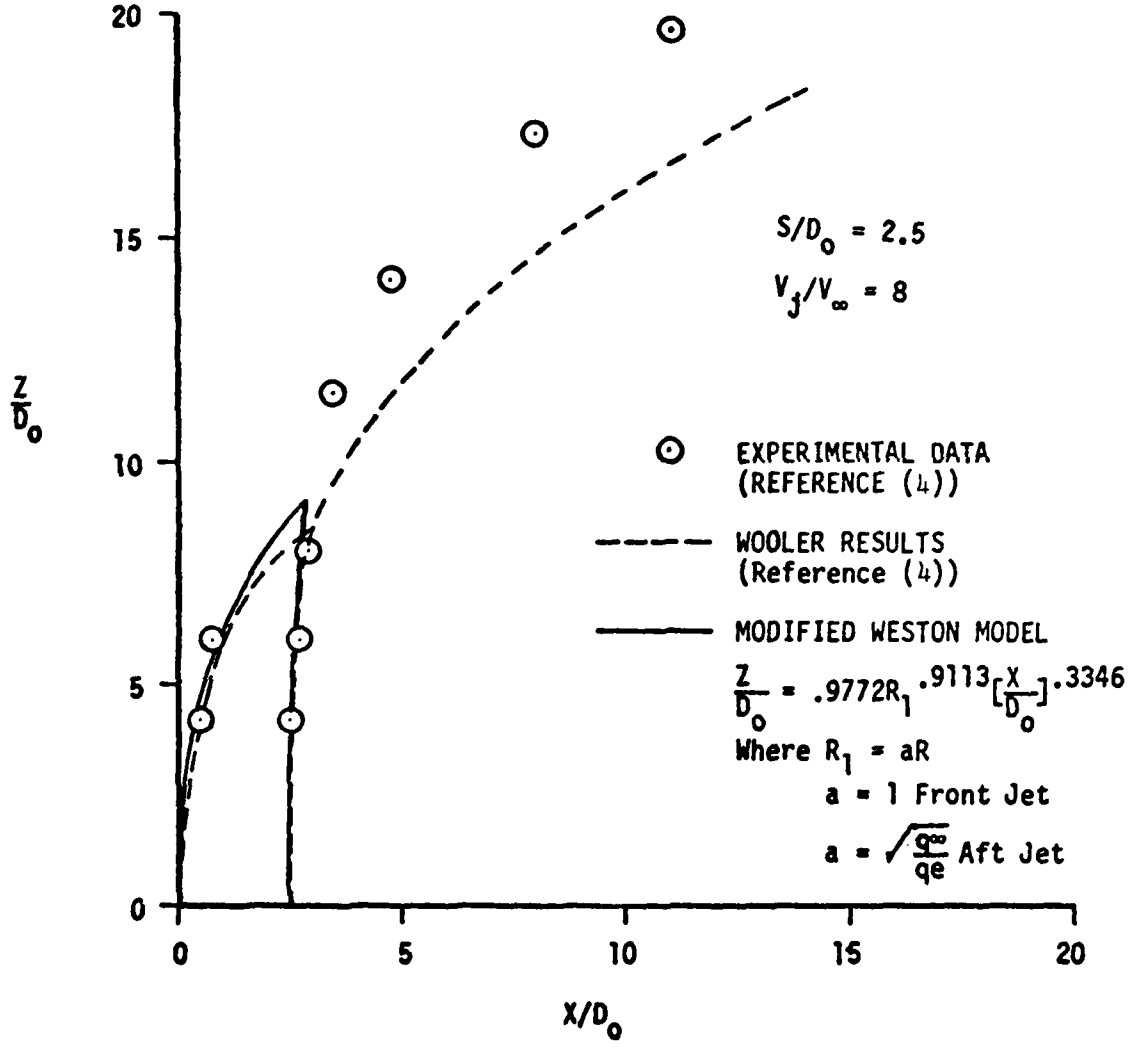

Figure 9. Comparison of calculated and experimental jet path centerlines, jet spacing = 2.5 diameters, jet velocity ratio, R, = 8

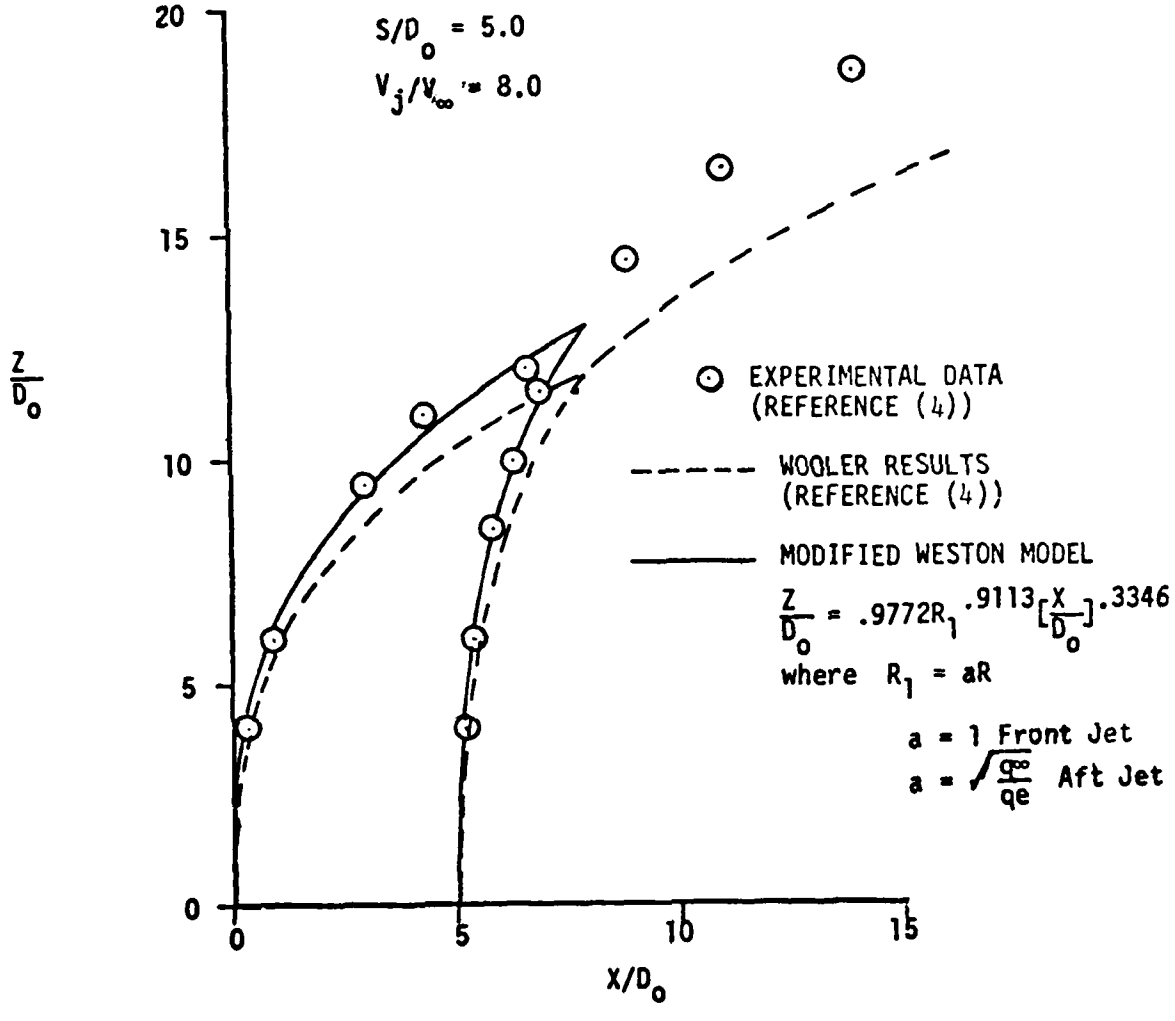

Figure 10. Comparison of calculated and experimental jet path centerlines, jet spacing = 5.0 diameters, jet velocity ratio, R, = 8

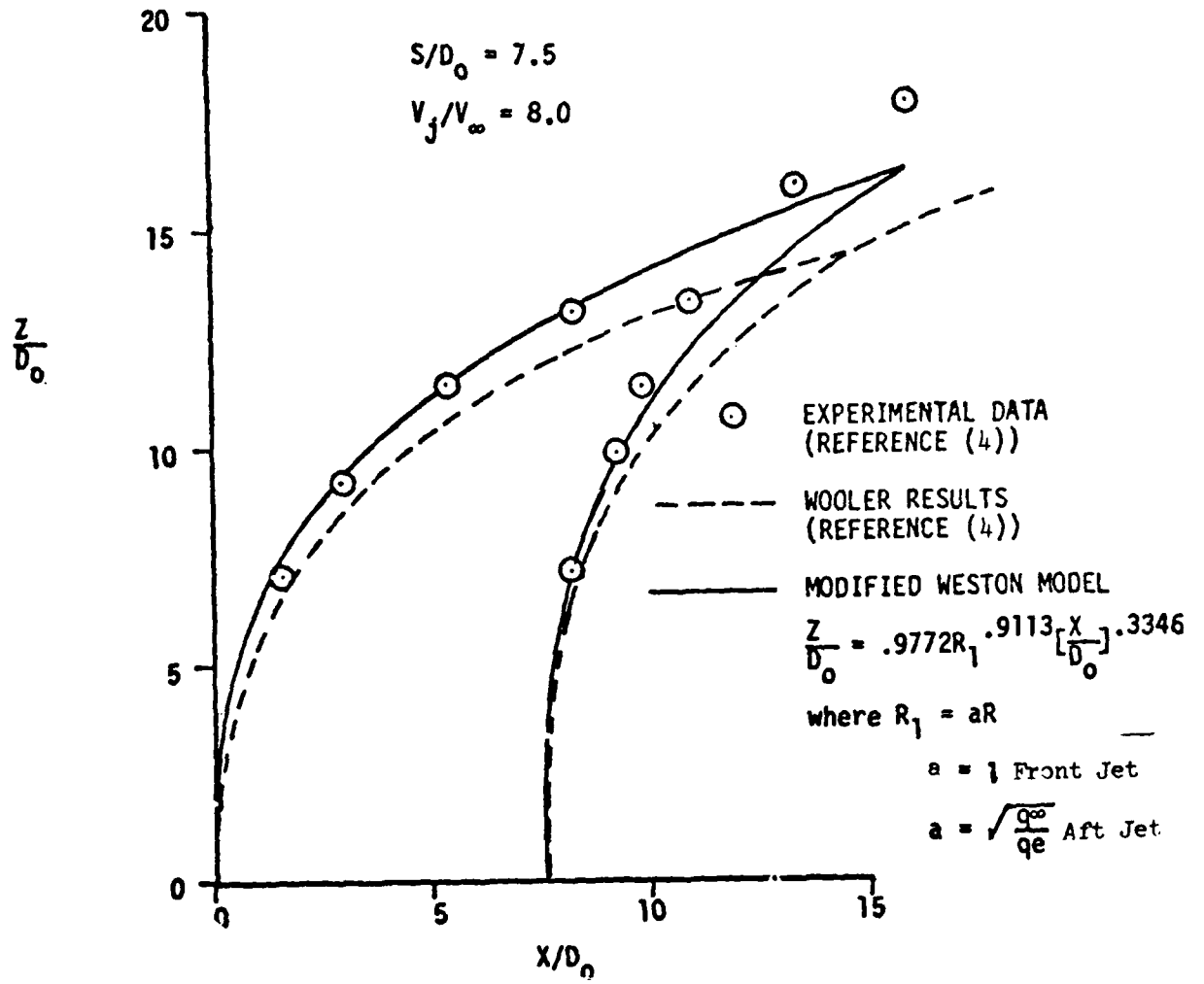

Figure 11. Comparison of calculated and experimental jet path centerlines, jet spacing = 7.5 diameters, jet velocity ratio, R, =8

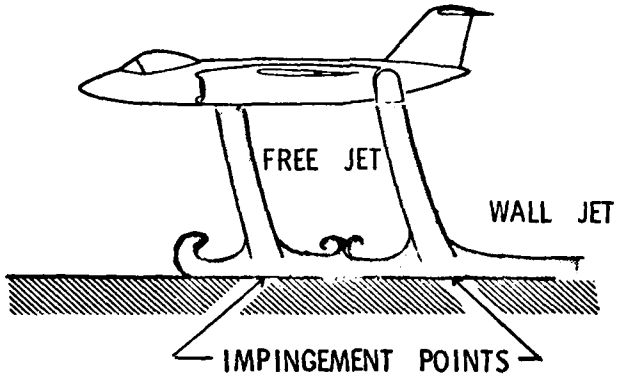

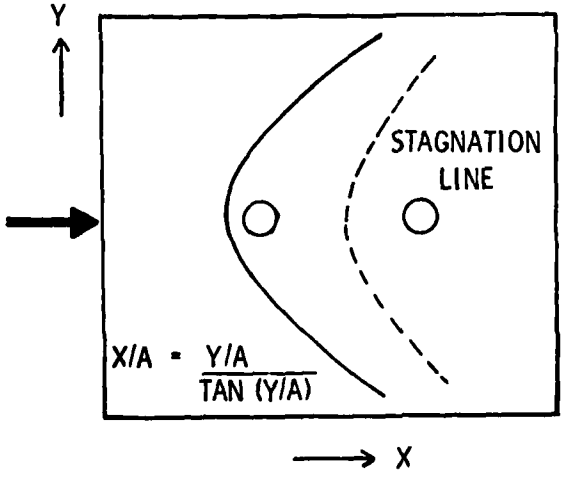

$$A = 1.03 \left[V_{jexit} / V_{\infty} \right]$$

Figure 12. Schematic of model utilized for STOL calculations in VAPE

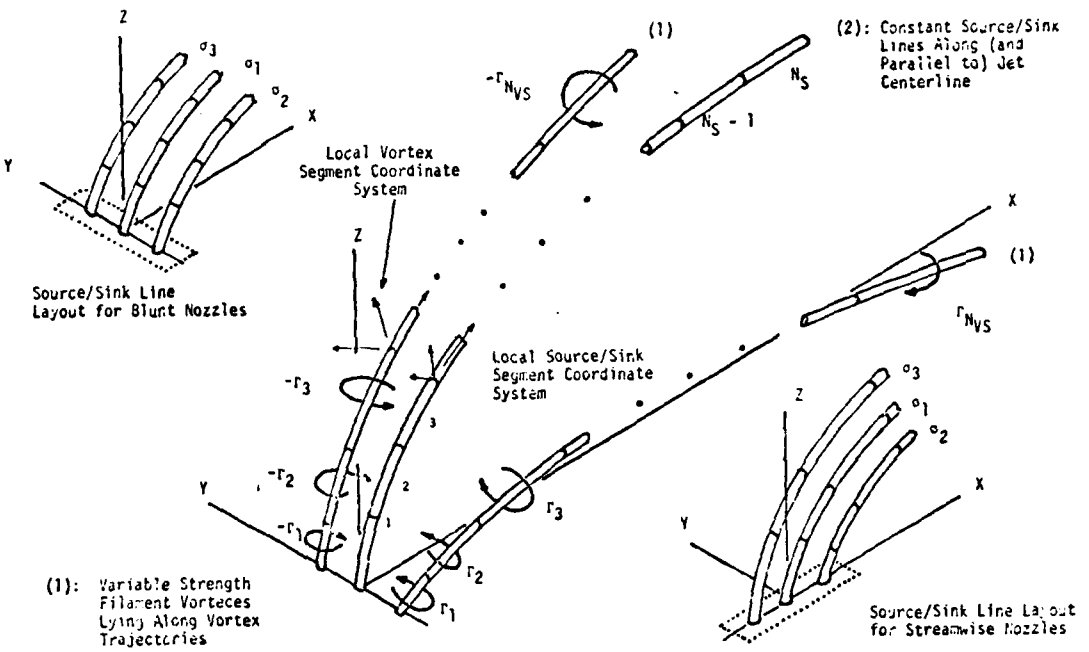

Figure 13. Schematic of model formulation for Thames rectangular jet model

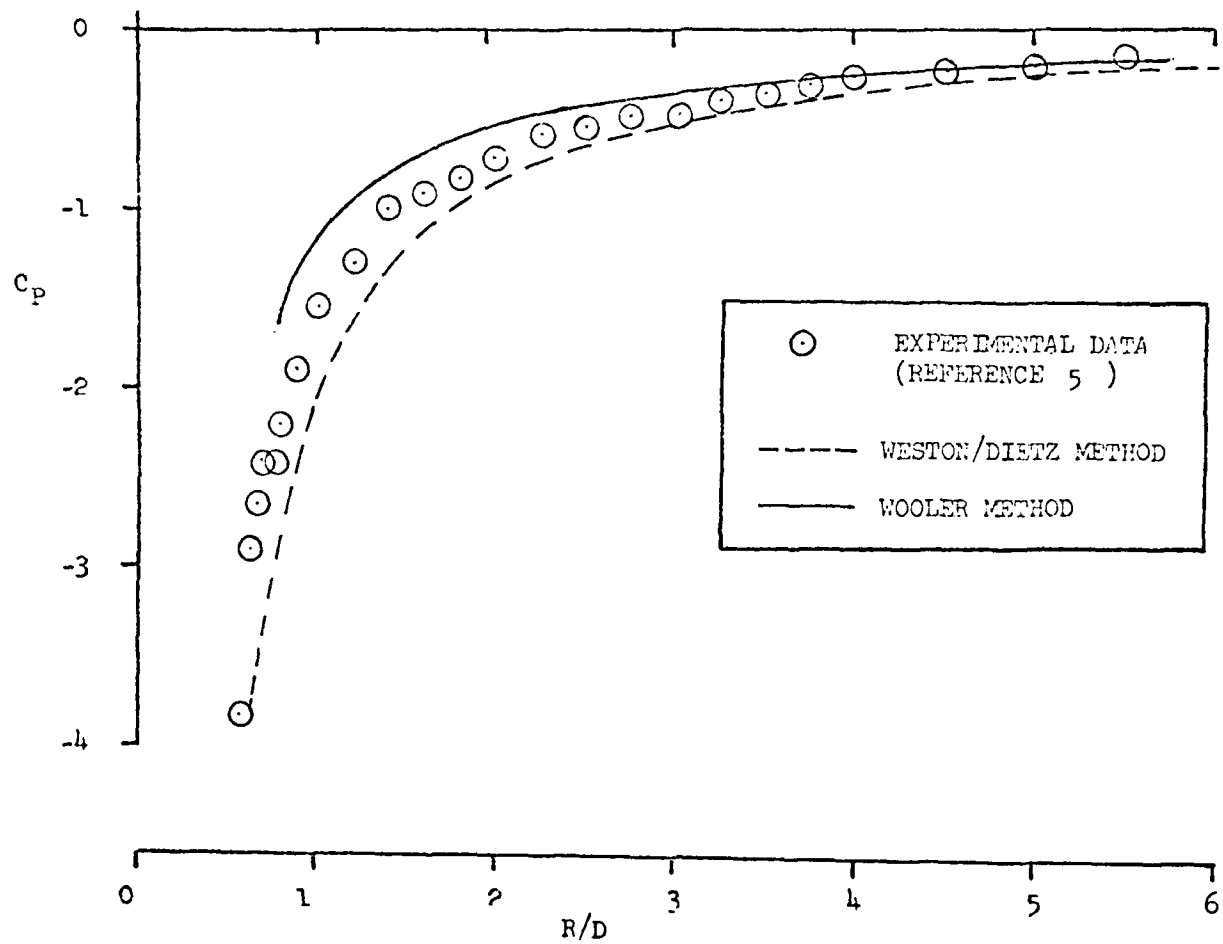

Figure 14. Comparison of experimental and calculated flat plate pressures induced by a jet. R = 8, M_{jet} = .93, 90

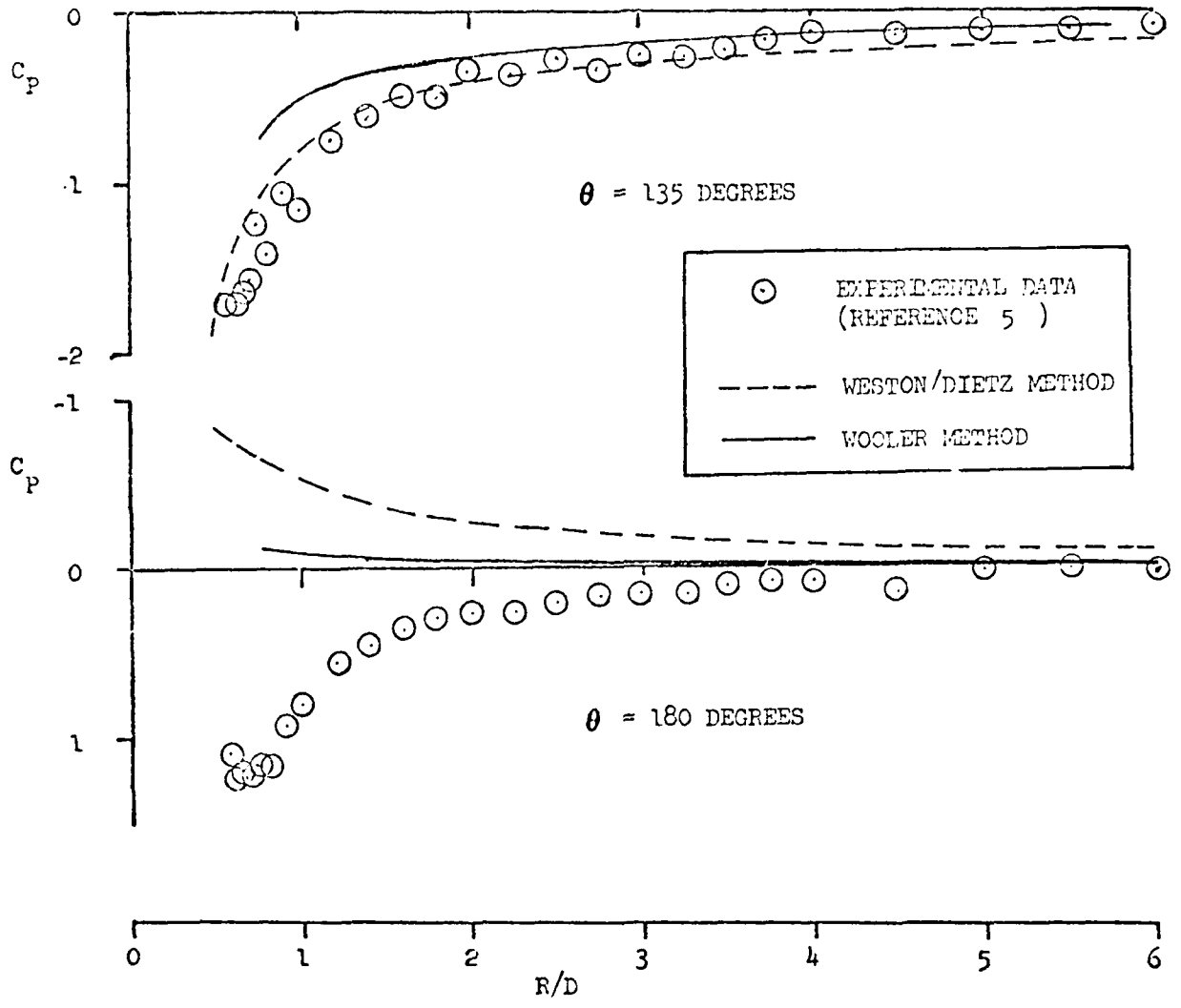

Figure 15. Comparison of experimental and calculated flat plate pressures induced by a jet. R = 8, Mjet M_{jr} M_{jet} = .93 135 180

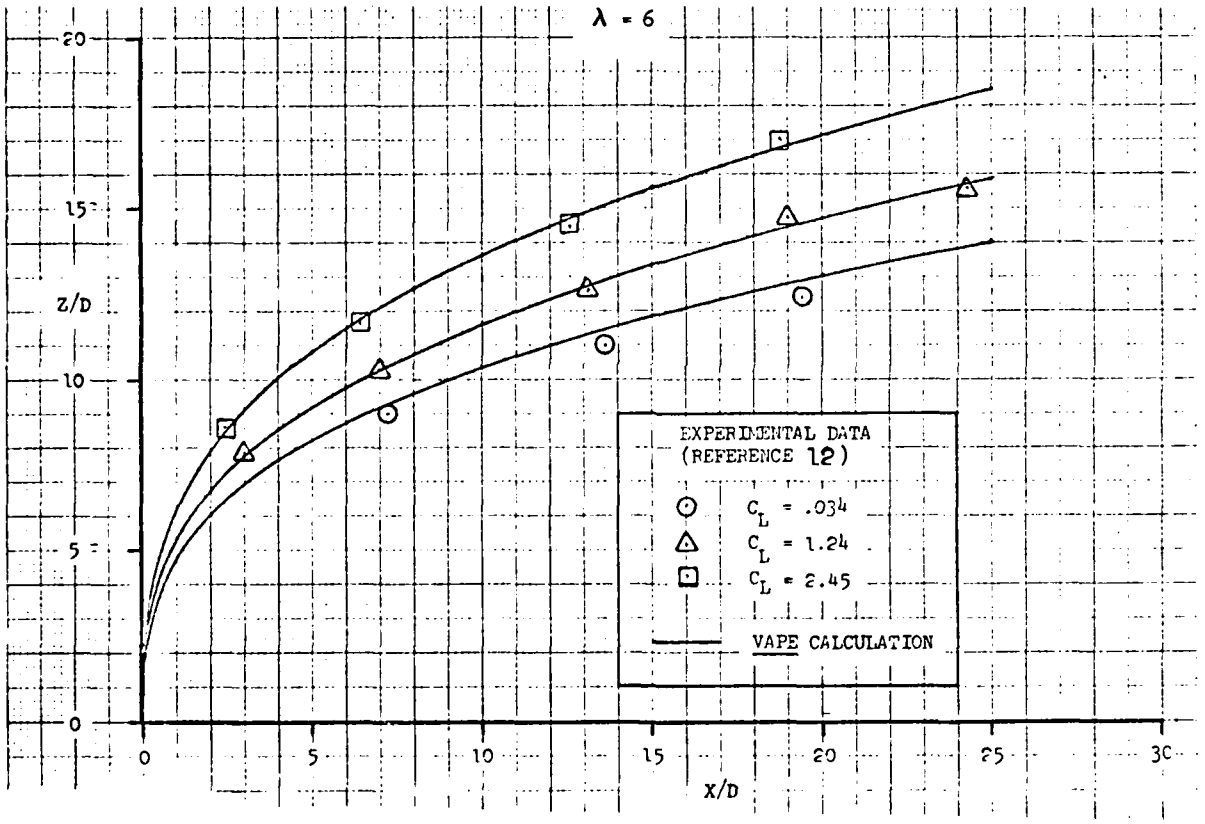

Figure 16. Comparison of experimental and VAPE predicted jet centerline path with lift effects.

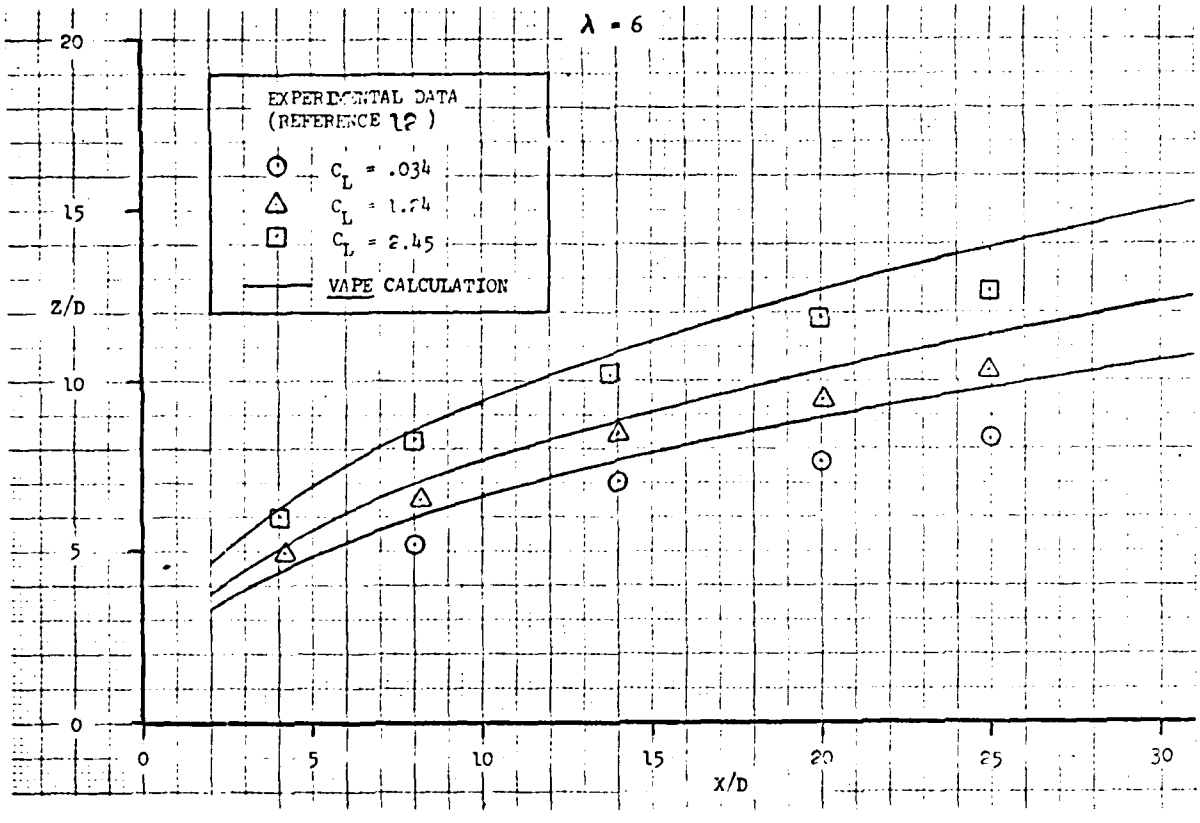

Figure 17. Comparison of experimental and VAPE predicted vortex curves with lift effects

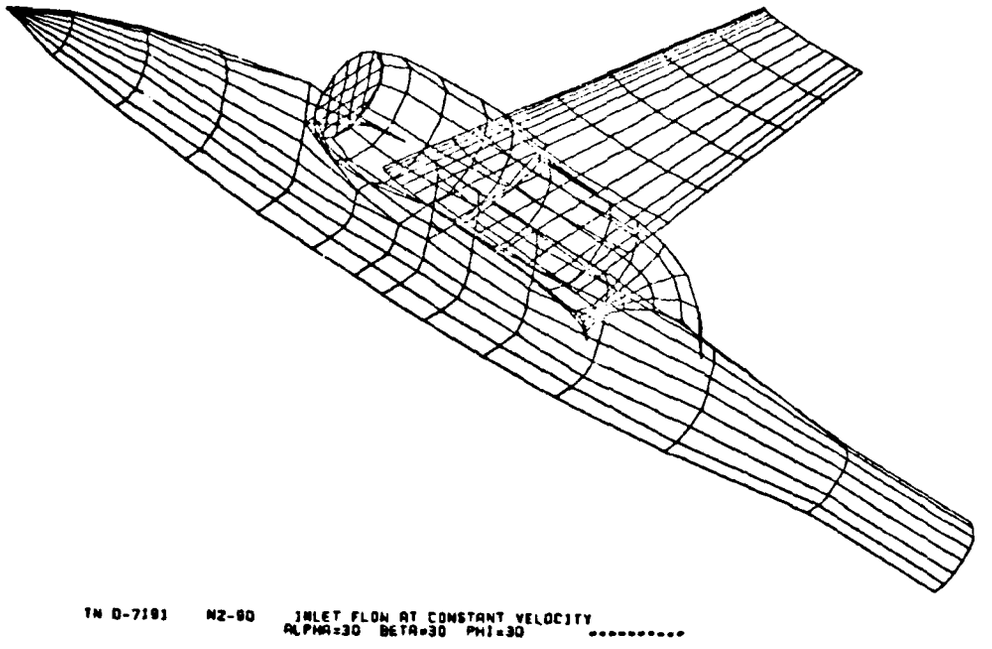

Figure 18. Computer generated graph of VAPE input geometry for V/STOL model of Reference 13.

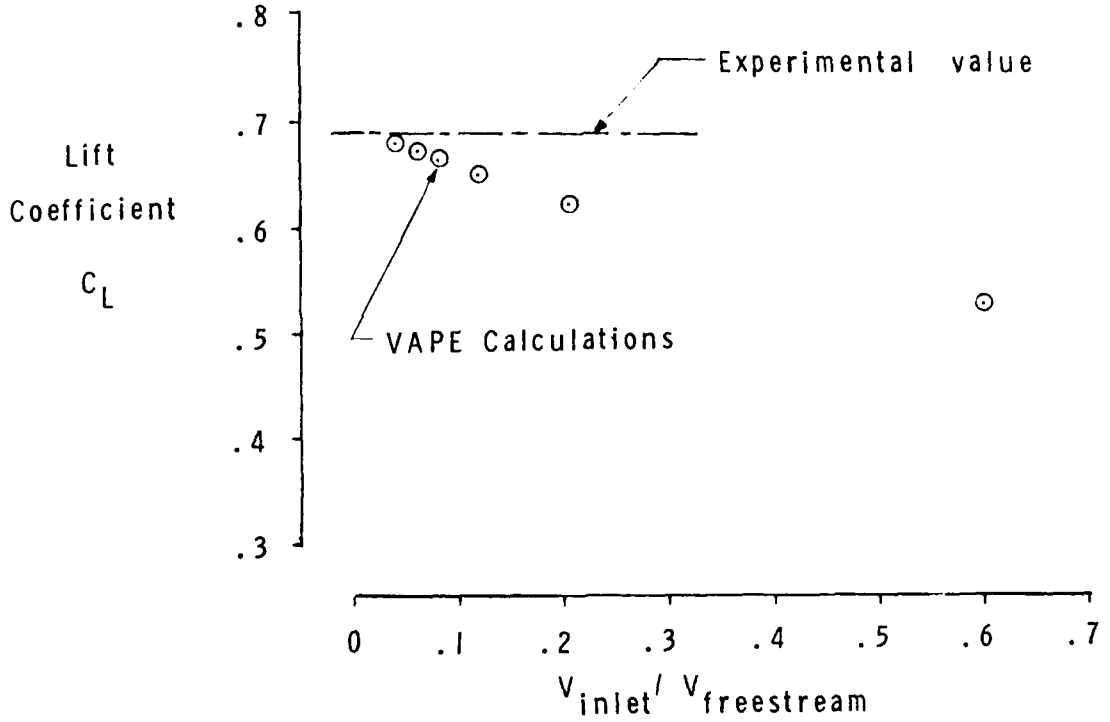

Figure 19. Effect of inlet velocity on VAPE calculations for V/STOL model of Reference 13. No jet operating

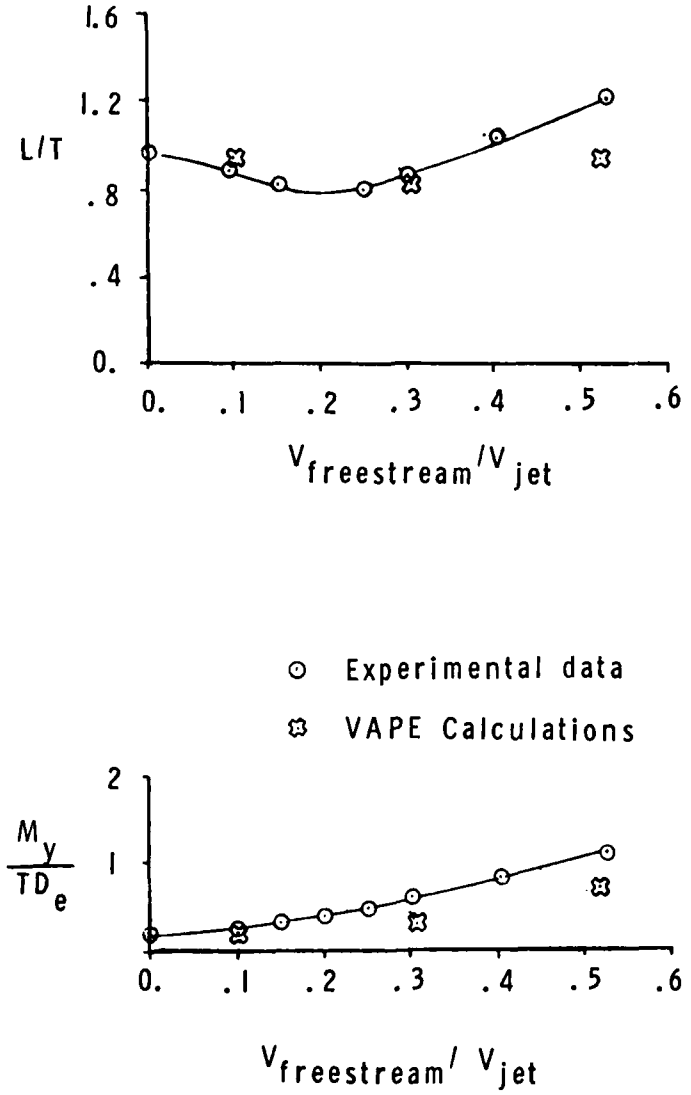

Figure 20. Comparison of experimental and predicted forces and moments for the model from TND-7191, angle of attack = 0 degrees

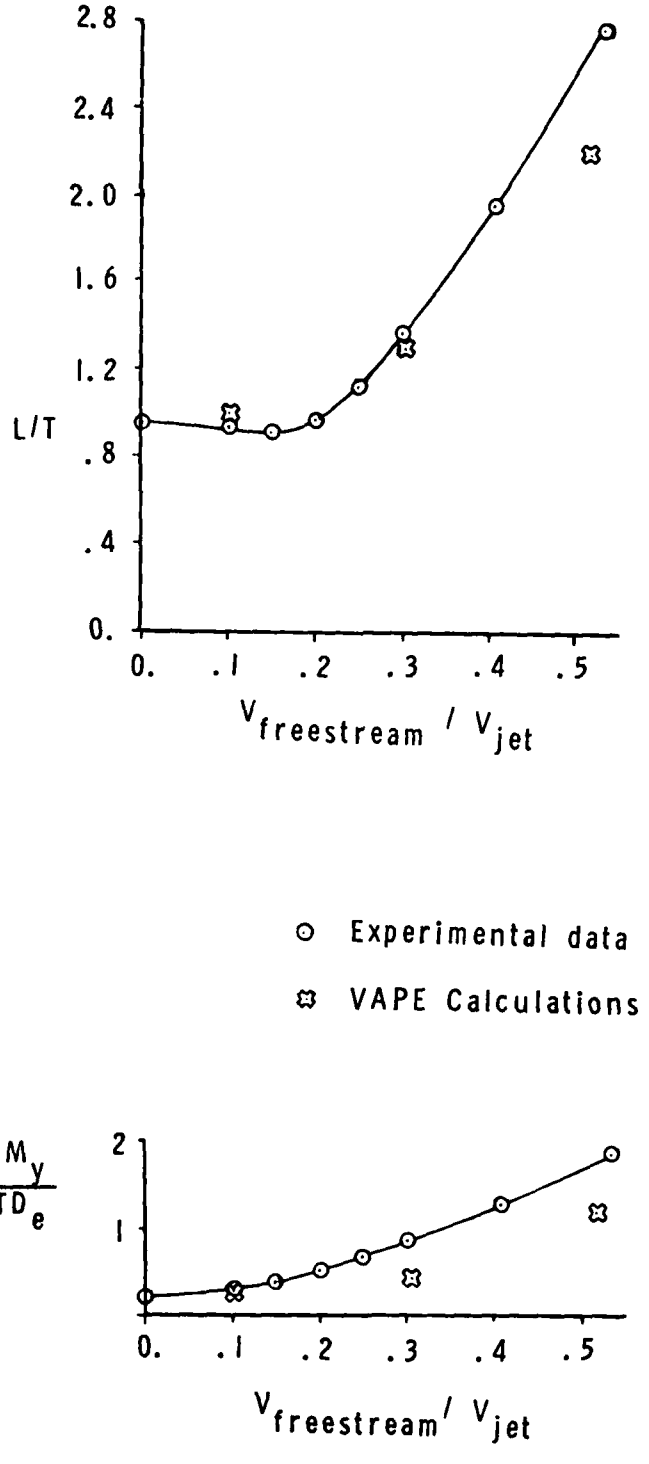

Figure 21. Comparison of experimental and predicted forces and moments for the model from TND-7191, angle of attack = 10 degrees

A REVIEW OF SOME FUNDAMENTALS OF LIFTING JET INTERFERENCE WITH PARTICULAR REFERENCE TO U.S. NAVY TYPE A AND B CONCEPTS

P. G. Knott
British Aerospace,
Warton Division,
Wind Tunnel Dept.

ABSTRACT

Wind tunnel test results are presented showing some of the fundamental characteristics of lifting jet interference. These are discussed in conjunction with recent test data from U.S. Navy type A and B concepts.

Some pitfalls in presentation and interpretation of test results are discussed. Questions are raised concerning little understood or anomalous data.

The application of a computational method to a simple case is presented and obstacles to progress in developing computational methods of wider applicability are discussed.

The majority of BAe Warton experience is with combat aircraft configurations having fuselage buried engines of low by-pass ratio. For these configurations lift jet interference cannot be ignored, but acceptable characteristics can be developed.

A high by-pass ratio engined configuration tested, which is pertinent to Navy type A, shows very low levels of lift jet interference. For this type it seems likely that the engine inlet flow may have a measurable effect on the aerodynamics. Some comments on inlet flow effects are made.

ACKNOWLEDGEMENT

Grumman Aerospace Corporation permission to present and discuss results of tests carried out for them at BAe Warton, is gratefully acknowledged.

CONTENTS

1. INTRODUCTION

In the context of V/STOL Aerodynamics 'jet interference' is defined as the force or moment or pressure coefficient increment induced by the engine exhaust flow when directed at a relatively large angle to the free stream. In Wind Tunnel parlance this is usually defined as the difference between the force or moment on the configuration 'power on' relative to a 'power off' condition (Fig. 1).

This definition can lead to difficulties in application to aircraft design (because the power off state is not a very practical datum) and in comparison with computational methods (which considers the total flow field around the body), but it is a convenient basis for the evaluation of configuration variables, which is the main purpose of this paper.

The Wind Tunnel is still the major tool in the study of this subject. Work at Warton started in the late 1950's, and in the early 1960's a big low speed tunnel was built specially for this work. This facility, as it is to-day, is shown on figure 2, and the associated test techniques are the subject of reference 1.

As a result of some two decades of wind tunnel testing it is now widely appreciated that jet interference effects can be large and unfavourable and hence cannot be neglected in the design, development and performance assessment of jet and fan lift V/STOL aircraft.

Analytically the subject is a complex and difficult one, characterised by multi-variable and non-linear behaviour. As a result the Wind Tunnel has not so far been able to provide an adequately reliable data base from which to develop prediction methods of wide applicability. It has however given us a useful understanding of the fundamentals mainly as a by-product of supporting numerous project investigations.

At the risk of covering some well trodden ground this paper reiterates some of these fundamentals and attempts to relate these to recent tests on U.S. Navy type A and B study projects.

2. HOVER, IN AND OUT OF GROUND EFFECT

To describe the mechanics of lift interference in hover it is convenient to distinguish between ground proximity and heights above which the presence of ground has no influence.

2.1 Out of Ground Effect

The mechanism is entirely one of jet entrainment, the secondary flow induced by the jet causing negative pressure on the underside of all surrounding surfaces (fuselage and wings). There is no practical way that the lift interference can be other than unfavourable. These unfavourable effects are however usually small, but not always so,

and since they impact directly on installed thrust for V.T.O. it is essential to confirm the level by testing.

Figure 3 shows a selection of model test results covering the extremes of hover lift loss measured. Simple flat plates with central single jets give 'suck down' as low as 1% of thrust or less. A type A configuration with tilting nacelles also falls in this low bracket because the engine exhausts are relatively remote from the lifting surfaces. Configurations more typical of type B combat aircraft tend to have multiple jets relatively close to lifting surfaces. These configurations generally fall in the 3% to 5% range.

It is as well to be aware that the 'suck down' can be sensitive to near field jet properties and to near exit geometry. Small variations exist due to thrust level or pressure ratio which are attributed to changes in the jet entrainment characteristics. Fig. 3 also shows some unusual results in which the addition of longitudinal fences to the lower surface close to the jet exits, produced 'suck down' as high as 10%. The mechanism was never understood, but speculated to be due to local vorticity, and is shown here merely to illustrate that such things can happen.

Fig. 4 shows some results from NASA tests (reference 2) together with some B.A.C. data superimposed. The analysis clearly shows that there is a relationship between jet free air decay rate and suck down. It is interesting to note however that the relationship is different for the two sets of data.

In aircraft design terms these differences are not serious but they do suggest that it is advisable to represent the characteristics of the full scale jet in the model tests as far as possible, and essential to represent local geometry e.g. fences, gear doors, cavities and other protuberances.

2.2 Ground Effect

In the presence of ground the flow is more complex and hence the results more difficult to quantify. In addition to free jet entrainment there is also wall jet entrainment, and an impacting jet cushion or 'fountain effect' in the case of multi-jets.

Single or very closely spaced multiple jet layouts exhibit progressively increasing 'suck down' over and above the 'out of ground' value as ground is approached because of the added wall jet and the closer boundary confines of the lifting surface and ground. Fig. 5 shows data from simple flat plates with single jets. A practical example of this type is the U.K. research aircraft S.C.1. Fig. 5 shows an early R.A.E. correlation (reference 3) with NASA and BAC data superimposed. The data is well fitted by a 'reciprocal of height squared' law, but like the out of ground correlation described above, the data sets have different constants.

The closely spaced central jet configurations are of very limited practical interest because the 'gear' height 'suck down' is so large. Figure 6 presents some early BAC jet lift V.T.O. fighter developments, showing how the relative location of a basic 8 lift engine cluster can influence the gear height losses. Providing areas between the jets allows ground effect cushion or fountain effects which tend towards a limiting case represented by the hovercraft or ground effect machine. Fig. 7 shows how this cushion effect can be strengthened by the addition of fences. As described earlier this particular experiment produced adverse effects away from ground. The very modest pitching moments induced for quite significant changes in lift confirm that there is a fairly well balanced distribution and hence no trimming problems.

Fig. 8 shows some results from practical combat aircraft configuration testing. A Harrier model test exhibits good characteristics in which the ground cushion wins the fight against the free jet/wall jet 'suck down' at gear height. The effect of toe-ing the jets out by 30^{o} is depicted in the BAC '4 poster' design. The ground cushion is greatly weakened to the extent that at gear height the losses have changed from 1% to 10%. This is a possible problem that has to be faced in changing the Harrier nozzle layout for, for example, P.C.B. re-ingestion reasons. The third curve is from a BAC 'lift + lift/cruise' (L + L/C) concept study and shows one of the problems associated with this concept. The lift and lift/cruise nozzles are remote from each other such that favourable ground effects are almost non-existent i.e. the pairs of nozzles act like remote single jets.

A much better configuration in this respect is that giving rise to the lower set of curves which show results from tests on a Grumman 'sea-control ship' study, L + L/C configuration. The rear lift/ cruise nozzles have some space between them and in addition the two lift engines are split into four nozzles with significant surface area between. The lift characteristic show a ground effect which arrests the lift droop as ground is approached. Without toe-out the 'suck down' takes over before gear height is reached but with 10^{o} of toe-out the characteristic at gear height is considerably improved, approaching more closely the ideal, which would be the out of ground figure.

More recent L + L/C design trends have departed from rotating cascade lift/cruise nozzles in favour of rectangular ('2 dimensional') nozzles integrated with the wing T.E. together with a lift engine, 'bleed-burn' or ejector augmented (R.A.L.S.) lift nozzle in the forward fuselage. Figure 9 shows some results from a low speed model of one such layout from tests carried out for Grumman. It is interesting to note that there is a significant favourable ground effect generated at intermediate heights which can only be the result of the spanwise gap between the vectored lift/cruise nozzles creating the 'fountain effect'. At gear height the suck down takes over however, leading to values of the order of 10%. The isolated lift nozzle in the nose does not help in this respect.

In generating favourable ground effect contributions by optimising the ground 'cushion' or ground 'fountain' effects it has to be remembered that this may introduce adverse effects due to hot gas re-ingestion.

In the late 1950's during the development of the S.C.1 aircraft various types of take-off platform surfaces were tested at model scale by the R.A.E. (reference 5). One such successful technique was the ribbed ground mat. Figure 9 shows that this technique is very effective in producing a good hover characteristic with negligible gear height losses. The associated pitching moment increments are within $\pm$ 3% of $\bar{c}$ and hence do not constitute a problem. The lift improvements produced by the ribbed mat are very sensitive to the angular position of the ribs and the aircraft on this configuration.

The Navy type A requirement gives rise to a different type of configuration. A model of one such proposal is shown on figure 10. This particular configuration is characterised by a remoteness of the engine exhausts from the lifting surfaces.

Figure 11 shows some results from tests on this model. Note the much expanded vertical scale in order to show the changes at gear height. The most improtant feature of this configuration from the hover point of view is that the engine exhausts are well below the high wing, resulting in very low levels of 'suck down' (less than 1% out of ground effect). In all cases tested, gear height values were within $\pm$ 5%, very much less than the type B configurations. These results are presented here to also demonstrate the sensitivity to local geometry on the under-fuselage region, and show that it is not difficult to produce favourable lift interference at gear height or at worst confine 'suck down' to 1% or less, on this configuration.

3. JET INTERFERENCE AT FORWARD SPEED

The main purpose of this section of the paper is to examine trends and orders of magnitude typical of jet lift solutions to Navy type A and B requirements. Before doing so it is useful to try to get a feel for the importance of jet induced lift, how best to present test results and some of the difficulties facing attempts to develop computational methods for predicting jet interference.

3.1 The Importance of Jet Induced Lift

The significance of particular values of jet induced lift at forward speed is not as immediately obvious as it is in hover. It is therefore worthwhile to try to decide, for example, what penalty is paid for loss of lift due to jet interference before attempting to discuss trends and orders of magnitude due to configuration variables.

To this end some short take-off and climb out calculations with various lift interference assumptions have been carried out. The results of one such calculation is shown on figure 12. Two levels of

lift loss assumptions, B and C, were made, together with the other assumptions listed and the ground roll and climb out distances compared with a zero lift loss assumption. Ground roll is performed with all thrust horizontal until a condition is reached where, nozzle vectoring and rotation to incidence produces a 1.1 g normal acceleration and 0.15 g tangential acceleration.

The losses assumed are not excessive but they have a marked effect on lift off speed and ground roll distance. The climb out to a 15 m screen height is somewhat less affected once the lift acceleration has been established.

In practice the ground effect and out of ground lift will differ, whereas they have been assumed the same in this example. Conditions at unstick are critical and it is the highest losses that matter because the use of relatively favourable ground effect for early unstick could result in climb out difficulties.

A transition from V.T.O. will depend only on 'out of ground effect' values but the required normal and tangential accelerations have to be satisfied from the very lowest forward speed. If increased power over that required to hover or a diving transition is to be avoided, the condition to be satisfied is that the initial rate of decrease of lift due to jet interference must be no greater than the ability to increase lift on the wings due to incidence and forward speed.

Clearly lift losses of the order of 10% to 15% of thrust in the speed range V_E = 0.1 to 0.2 do matter to the V/STOL fighter and effort applied to reduce such levels within the constraints imposed by other disciplines is justified.

3.2 Presentation of Results

In hover the most obvious way to express jet interference is in terms of proportion of thrust i.e. $\Delta L/T$. At forward speed the best way to express the results is not so obvious. Figure 13, which is taken from reference 1, is used here to illustrate the problem.

The familiar $\Delta L/T$ v V_E for a L + L/C configuration tested at forward speed in ground effect, shows the hover value, but as V_E is increased the data becomes progressively less meaningful because lift proportional to thrust becomes less significant and lift proportional to wing lift i.e. C_L more so. This presentation exaggerates the lift interference as V_E increases because of non-dimensionalising by a decreasing $C\mu$. In addition the power-off C_L cannot be shown.

The same results in terms of 'airframe' C_L v $C\mu$ is also shown. At the origin the 'power-off' lift is shown and the changes in C_L induced by the power at low $C\mu$ are now more meaningfully expressed. Not so the high $C\mu$ end however, where the large loss of C_L looks alarming but is in fact only about 8% of thrust as seen by the $\Delta L/T$ plot. Note that

the slope of the C_L v $C\mu$ graph at high $C\mu$ approximates to the hover lift loss. The left hand side of both plots are most meaningful therefore, and a unique presentation showing the desired information over the whole $C\mu$ range has yet to be found. These presentations are for a single model attitude (incidence, sideslip, height, jet vector angle) and presenting the variation with these parameters is an additional consideration.

The lower plot shows how the results would look if presented as total lift, including the vector component of $C\mu$ ($C\mu'$). Although this helps to put the data into perspective in that it shows how much the lift is thrust dominated at high $C\mu$, it has little else to recommend it. This form of results presentation also serves to indicate the potential resolution problem if the total lift were measured directly on the model balance, but this is outside the scope of this paper and is discussed in reference 1.

3.3 Calculation of Jet Induced Lift

Clearly one would like to be able to compute the pressure distribution around an arbitrary wing/body/multi-jet configuration at any attitude, jet angle, and thrust coefficient, including ground effects.

By the early 1960's work had commenced along this ambitious path, and a sink-doublet jet model for use with lifting surface theory was developed. What follows is a description of the state of the art reached by 1972 when work ceased at the then British Aircraft Corporation (B.A.C.) (about a decade).

The simplest case of a wing with single central lift jet was chosen for the initial study. The method commenced with empirical data on the maximum total pressure path of the jet, which is primarily a function of the discharge angle θj and the cross flow velocity ratio V_E. The example described is for 90^o discharge angles. The external influence of the deflected jet is represented by combinations of sink and doublet distributions along the jet path. Experimental surface pressure distributions on infinite flat plates are used to determine the singularity strengths, by trial and error. The application of this jet model to the computation of pressures on a finite wing is then facilitated by the use of a, then (1969), new lifting surface theory developed at Warton and a wing pressure coefficient definition which included velocity cross product terms, to enable comparisons to be made with experimental data from a thick wing. Comparisons were made at two values of V_E, 0.125 and 0.25.

Figure 14 shows the comparison at $V_E = 0.125$. The large negative pressure increment near the jet is quite well represented. Behind the jet comparison is poor as would be expected since no provision for viscous wakes are made in the model except that implied by the doublet vorticity. At the leading edge comparison is disappointing and may in some way be due to the large curvature on the experimental model surface or quite possibly to deficiencies in the sink strength near the wing surface.

In the course of developing the sink and doublet distribution strengths based on infinite wall data, it was found that there was a considerable change in the relative strengths of these singularities with velocity ratio (V_E). In one limiting case, however, the jet can be represented by sinks alone. The average doublet strength therefore tends to increase with increased velocity ratio and the distribution of doublet strength along the jet path increases from an origin value equivalent to a solid cylinder at the wing surface independent of V_E.

The jet model could be much improved by a more detailed knowledge of the relative strengths of entrainment and vorticity in the deflected jet and very detailed measurements of jet properties in cross flow are included in the total U.K. jet lift interference research programme.

The relatively recent developments of 'panel methods' to solve the Newmann boundary condition for lifting potential flow, made possible by the development of large capacity, high speed computers, now offers a much more suitable tool than the lifting surface theories, and further progress could usefully be made with this facility.

The big obstacle to progress is the multi-jet problem, giving rise to partial screening from the free stream of one jet by another and the complexity of coalescing jets. The jet path and sink doublet strengths and distributions along the jet path would then be multi-variable. The trends are understood and can be predicted but expressing these accurately and reliably over a wide range of applicability seems a daunting task and indicates the need to remove much of the empiricism from the definition of cross flow jets.

Wooler et al, reference 6 and 7 under AFFDL and NASA contracts has extended his pioneering work on single jets which started in the U.K., to two and three jets in-line with modest success, but this still leaves the capability well short of an adequate universal method. Additionally it is apparent that the free turbulent jet is far from unique so that it is particularly difficult to obtain a good 'near field' representation applicable to a wide range of nozzles and jet Mach numbers.

3.4 Combat Aircraft Configurations

3.4.1 Harrier Types

As the only in-service VSTOL combat aircraft in the Western World the characteristics of the Harrier (AV8) and other possible future derivatives to meet Navy type B or U.K. V/STOL fighter requirements are of considerable interest. In concept Harrier types are essentially lift/cruise (L/C) engined with a 'four-poster' vectoring nozzle system, as distinct from lift plus lift/cruise (L + L/C) types which are discussed later.

Figure 15 shows some jet lift interference data from model tests. Data is shown for 60° jet vector angle, out of 'ground effect'. The AV8A and 8B curves have been taken from reference 3. The AV8A curve agrees well with estimates for Harrier and with some test data from a B.A.C. model similar to Harrier. The level of lift loss shown is clearly not negligible, and not surprising therefore that developments of the aircraft like AV8B should include improved jet lift characteristics amongst the objectives.

The result of development to AV8B shown in Figure 15 is quite remarkable in that a large improvement in lift for relatively small changes in geometry appear to have been achieved. Experience shows that jets located aft relative to planform tend to be favourable (jet flap effects) and forward locations are adverse. Combined they cannot be linearly added with any certainty as the forward jets tend to dominate. Figure 15 shows the effect of a 20% shift in nozzles location. The rearward shift is favourable but not to any great extent. The AV8B development includes a much more powerful flap and optimisation of rear nozzles and flap interference, together with extension of the forward nozzle outer shrouds. These developments can all be expected to be favourable to lift interference but, considering that there still exists a pair of jets well forward on the planform, the result is remarkable.

Encouraged by these results, further tests have recently been carried out at Warton on B.A.C. Model 26. This programme was concerned with the feasibility of wing tilt (for both pilot visibility and lift interference improvement) and the effect of jet lift in the post stall regime in general. Some interesting results were obtained, a summary of which is shown on figure 16. It is apparent that wing tilt does reduce the lift losses, but it is also interesting to note, that an even better result was obtained without tilting the wing but simply by rotating the aircraft to the same wing attitude, keeping the jet to free stream angle constant. This does nothing for pilot visibility of course, but leaving that aside a number of interesting points emerge regarding the aerodynamics:-

Firstly, the wing tilt affects the 'power off' lift which does not show in this presentation. Hence the need for figure 17 where the significant data is plotted as C_L v C_μ.

It has been found that below the stall the lift interference increment is not generally sensitive to wing incidence at constant jet to free stream angle. This is apparently not so post-stall. Even at high angles of attack in attached flow it might be expected that some reduction in unfavourable lift loss might result because of the change in geometry (jets pointing more aft relative to wing). Post-stall it is not difficult to imagine that blowing from the underside of the wing will have some influence on the stall pattern, apparently to reduce its extent. Certainly the concept of lift interference as being a positive or negative circulation effect (essentially an attached flow concept) no longer applies uniquely.

Not shown but also of note is the fact that the 'four-poster' L/C types exhibit significant lift losses at cruise nozzles setting ($\theta_j = 0^o$) i.e. pointing the jets aft relative to wing induces an attached flow circulation type lift loss, but at post stall this is counteracted by a favourable effect in the form of some flow re-attachment due to blowing.

Ground effect at forward speed is not shown for the Harrier, AV8A, since the characteristics depend very much on variables like fuselage fences and nozzle toe angle, which do not have much influence out of ground, and have been the subject of developments of the aircraft. Data without detailed geometrical definition would be misleading but it does seem that it is not difficult to generate favourable effects at gear height in hover and these should have some carry over to forward speed.

3.4.2 Lift + Lift/Cruise Types

The lack of positive thinking applied to jet lift interference has been a criticism made by designers. The question, they said, was "how to obtain favourable jet lift interference" and not simply "how to reduce lift losses". Consequently when serious work started on the design of lift + lift/cruise V/STOL fighters in the early 70's this was one of the objectives.

Away from ground effect, the need to balance lift thrust about the aircraft C.G. and with operation at essentially low value of V_E (high $C\mu$) and large vectoring angles, the scope for favourable lift interference was limited.

Figure 18 shows some of the results obtained from small scale tests on a basic fighter model to confirm and extend data on the effects of nozzle location. Comparison of nozzle locations (4), (A) and (D) shows that only with nozzles located behind the wing planform were really low levels of lift loss generated. Moving the nozzles to the fuselage side at the rear (configuration X) produced favourable effects at the high end of the V_E range of interest. To minimise the adverse effects of the balancing lift engines, comparison between configuration (3) and (4) shows that the jets should be in-line rather than side by side when in the forward location. Combining the best pairs to give (3X) still resulted in lift losses of 5% to 15%, the resultant being dominated by the front lift engines. This layout was to have been the basis of a configuration around which more detailed studies to optimise and improve the characteristics were to be carried out, but by which time interest had declined in the U.K. and effort was directed towards supporting more detailed configuration development by Grumman.

The first of these studies is shown in figure 19. The rear nozzle arrangement was similar to the B.A.C. 'X' configuration but the forward lift engines although in line had side by side vectoring

nozzles. Figure 20 shows that the rear nozzles produced very favourable effects tail-off, and very low levels of loss tail-on. The front nozzles were not as bad as might have been expected and the complete configuration was quite pleasing because the lift nozzle configuration also produced good ground effect characteristics. Figure 21 shows that 10^{o} of nozzle toe-out was of great benefit in ground effect, which, coupled with other developments for good hover characteristics, produced favourable lift interference at gear height over the V_E range of interest. Out of ground effect the losses were still up to 15% in the worst condition of interest.

The rear nozzle alone tests had shown that the rear nozzle and tail interfered adversely and in the course of studies of trim 'power on' the results shown on figure 22 were obtained. 'Power off' -10^{o} of tail setting was required to trim. 'Power on' results at this setting indicated that the tail was stalled, and this was confirmed by tuft studies showing downwash at the root end of the $\frac{1}{4}$ chord station of 25^{o}. The reduced lift loss shown with tail stalled is not of any practical significance because the reduction occurs mostly at the less effective higher V_E values and is associated with a 'power off' C_L reduction of 0.1.

In more recent times U.S. Navy type B requirements have introduced some new technology concepts to the L + L/C types, notably underwing nacelle engines with trailing edge integrated rectangular vectoring nozzles, designed particularly to give good cruise/manoeuvre aerodynamics rather than V/STOL. One such configuration is shown on figure 23. The relative forward location of the L/C nozzles permits less balancing thrust in the forward fuselage which must be beneficial to lift interference. Vectoring the L/C nozzles at the wing trailing edge should also be beneficial.

Figure 24 shows the effect of small (half a nacelle width) variations in spanwise location on the lift interference at gear height appropriate to STOL operation, the most outboard position of the L/C nacelle being the best.

Early on in the tests on this configuration it was found that the L/C vector nozzle had significant lateral spread of the jet due to vectoring, which caused increased entrainment and lift loss at the low values of V_E. Side plating of the nozzles thus became the standard configuration. The lower graph of figure 24 also shows that side plating of the lift nozzle when vectored gives a useful reduction in lift loss. In this case the deflection of the jet is from 90^{o} to 40^{o}.

The basic out of ground effect lift and pitch interference and the effect of jet vector angles are shown on figure 25. Despite the favourable features of this configuration the lift losses are relatively high. The reason for this is thought to be due to the

forward lift engine and the substantial after-body planform area behind the L/C nozzles. It should be emphasised that these tests were of a preliminary, exploratory nature and depending upon the importance of these characteristics to the aircraft performance further work may be desirable.

3.4.3 Lift Interference and V.I.F.F.

The use of thrust vectoring for manoeuvre purposes, on Harrier/AV8A in particular, has provoked considerable interest in recent years. After the initial optimistic claims it is now somewhat better understood that vectoring in forward flight is probably more effective in terms of rapid rates of fore and aft speed and acceleration changes than in terms of normal forces.

In generating lift by thrust vectoring two fundamental considerations apply:- firstly as the forward speed increases the vectored thrust as a force coefficient gets progressively less; secondly lift losses due to thrust vectoring may not be negligible and hence will erode the effectiveness of vectoring.

Consider the Harrier with 90^{o} thrust vectoring and a reasonably optimistic assumption about lift loss ($\Delta L/T = -0.4$). At a forward speed of $M_{\infty} = 0.4$ a 50% increase in lift coefficient can be achieved, but by $M_{\infty} = 0.8$ this has reduced to about 15%. Without lift losses these gains would be 70% and 25% respectively (Figure 26).

Lift interference data pertinent to the low thrust coefficients of high subsonic Mach number operations is scant and extrapolating the high thrust coefficient data is difficult. The NASA tests on a Kestrel model (reference 9) and some B.A.C. data on model 26 indicate that the lift loss $\Delta L/T$ does not continue to fall with increased V_E (reduced $C\mu$) as has sometimes been assumed, but bottoms out around $\Delta L/T = -0.5$ and stays approximately constant over the $C\mu$ range of interest.

As previously described, model tests show a lift loss at zero vector angle, and the lift loss due to vectoring should be taken relative to this datum rather than the 'power off' value. The level of lift loss for Harrier/AV8A is therefore probably around about $\Delta L/T = -0.4$.

On the basis of the results presented in reference 8, it would be expected that some lift augmentation due to thrust vectoring would occur on the AV8B. In addition the wing will have a higher usable C_L max than AV8A. At the lower combat Mach numbers (0.4, 0.5) there is a useful increase in manoeuvre lift to be obtained on both AV8A and AV8B by thrust vectoring.

3.4.4 A Navy Type A Configuration

The powered lift model of one design in response to Navy type A specification is shown on figure 10, and the hover lift characteristics are briefly discussed in section 2, where it is shown that this particular layout leads to very small lift interference effects.

Figure 27 shows that the lift interference is also very small at forward speed. Out of ground effect, the lift interference is negative by virtue of the forward location of the lift jets relative to planform but very small by virtue of the vertical displacement of the engine exhausts below the wing. On this figure the lift for a nacelle angle of 45^{o} is presented both as $\Delta L/T$ and C_L. At the very low speed end of the transition range the lift losses are of the order of 2% to 3% and at the conversion to wing borne flight ΔC_L is of the order of -0.1.

The effect of nacelle tilt angle in and out of ground effect is shown on figure 28. Out of ground at 60^{o} the lift losses rise above 5% whereas at 30^{o} the interference goes favourable both in and out of ground effect. In a transition or S.T.O.L. the large deflection angles are only used at near hover conditions so that typically in such operations the lift interference will vary between about $-2\frac{1}{2}\%$ and $+2\%$. These levels will not have any significant effect on performance and can possibly be ignored in performance assessment.

Figure 29 shows the range within which the pitching moment and drag interference effects lie. The jet induced pitching moments at large nacelle anagles are significant but the jet effects on drag are very small compared with the intake ram drag.

The majority of testing done on this model has been with a non-metric inlet. Some preliminary tests were done with the inlet metric and these indicate, as expected, that the inlet effects dominate the drag and considerably increase the nose up pitching moment. The aircraft thrust based control system is of course designed to cope with these. The intake effect on lift does not appear to be significant but it should be emphasised that these tests are very preliminary and the intake effects shown are only indicative of the order of magnitude. Much further testing is required in order to define the inlet contributions. It is considered that jet only testing of configurations of this type is not adequate since it is difficult, if not impossible, to estimate the inlet contribution to pitching moment and not entirely safe to assume that the only intake effect on drag is the intake momentum or ram drag term. Furthermore it has not been clearly demonstrated that the inlet flow does not have any lift interference effects.

Just how to set about measuring these effects in the tunnel and the associated book-keeping inevitably leads to arguments about total forces and component forces techniques, such arguments are outside the scope of this paper. The model built and tested at Warton has air breathing simulators so that both inlet and exhaust flows are present, but since the majority of testing was done without the inlet metric, the inlet effects have not been adequately obtained to date.

4. CONCLUSIONS

Experimental results show that jet interference can be large and unfavourable on configurations which are suitable for combat aircraft and of relevance to U.S. Navy type B requirement.

It has however been demonstrated that it is possible to produce favourable lift interference in ground effect and out of ground effect in certain circumstances at the higher speed end of transition. Further work is clearly desirable to optimise lift interference, within the constraints of the configuration, and in particular more work is necessary at high angles of attack where some separation on the wings occurs.

Navy type A requirements give rise to configurations which are more likely to have low jet interference effects. The use of high-by-pass ratio engines on such configurations does however give rise to the likelihood of possible intake flow effects which have yet to be adequately investigated.

Progress on a computational method for jet interference has been slow and as yet no universal method has been developed. Some better tools needed for such a method are now available and it would seem timely to launch another attack on the problem.

It is fundamental that vectoring in forward flight (V.I.F.F.) is more effective the lower the flight speed that it is employed and that lift interference will have some influence on its effectiveness at any speed. With future V/STOL fighter aircraft is should be a practical proposition to obtain favourable lift interference effects at effective V.I.F.F. speeds.

REFERENCES

1. P. G. Knott — V/STOL Aerodynamic testing techniques at British Aircraft Corporation. Journal of Aircraft, Vol. 15, No. 6 June 1978

2. Gentry and Margason — Jet induced lift losses on VTOL configurations hovering in and out of ground effect. N.A.S.A. TN-D 3166 1966

3. L. A. Wyatt — Static tests of ground effect on planforms fitted with a centrally located round lifting jet. R.A.E. TN 2862 1962

4. W. P. Nelms — Studies of aerodynamic technology for V/STOL fighter/attack aircraft. A.I.A.A. paper 78-1511 August 1978

5. L. A. Wyatt — Tests on the loss of vertical jet thrust due to ground effect on two simple VTOL planforms with particular reference to the Short S.C.1 aircraft. R.A.E. Aero Report 2607 May 1968

6. P. T. Wooler et al — V/STOL Aircraft aerodynamic prediction methods investigation. Vol. 1. Theoretical Development of prediction methods. Technical Report A.F.F.D.L.-TR-26 Vol. 1 Jan 1972

7. Ziegler and Wooler — Analysis of stratified and closely spaced jets exhausting into a crossflow. N.A.S.A. CR-132297 Nov 1973

8. Lacy and Miller — The AV8B wing: Aerodynamic concept and design. A.I.A.A./N.A.S.A. Ames V/STOL Conference paper 77-607 June 1977

9. Margason, Vogler and Winston — Wind tunnel investigation at low speeds of a model of the Kestrel (XV-6A) vectored thrust V/STOL airplane. N.A.S.A. TN-D 6826 July 1972

NOMENCLATURE

A_j		jet exit area
AR		wing aspect ratio $= \frac{b^2}{s}$
b		wing span
$\bar{c}$		wing geometric mean chord
C_L		airframe lift coefficient
C_L power on		airframe lift coefficient with jets blowing
C_L power off		" " " without jets blowing
$C\mu$		jet thrust coefficient $= \frac{T}{q_o\ s}$
$C\mu'$		thrust coefficient vector in lift direction
Cp		airframe surface pressure coefficient
Cp power on		airframe surface pressure coefficient with jets blowing
Cp power off		" " " " without jets blowing
ΔCp	=	Cp power on - Cp power off
ΔC_L	=	C_L power on - C_L power off
$\bar{D}$	=	diameter of a circle of the same area as an arbitrary lifting surface area
dj	=	jet exit diameter
D	=	airframe drag
ΔD	=	charge in airframe drag due to jet interference D power on - D power off
$\frac{\Delta D}{T}$	=	jet interference drag as a proportion of jet thrust
h	=	height of airframe reference point above the ground
L	=	airframe lift
$\frac{L}{D}$	=	airframe lift to drag ratio
$\frac{\Delta L}{T}$	=	jet induced lift as a proportion of jet thrust $= \frac{\Delta C_L}{C\mu}$

$\left(\frac{\Delta L}{T}\right)_o$ = jet induced lift in hover out of ground effect

M = airframe pitching moment

ΔM = change in airframe pitching moment due to jet interference

M_∞ = free stream mach no.

q_o = free stream dynamic pressure

$\frac{q}{q_o}$ = maximum jet dynamic pressure at any downstream location as a proportion of the maximum jet dynamic pressure at the exit plane

s = airframe reference planform area

T = jet thrust

$\frac{T}{W}$ = thrust to weight ratio

$\frac{T_L}{T_{LC}}$ = lift engine thrust to lift/cruise engine thrust ratio

V_E = effective free stream to jet velocity ratio = $\left(\frac{\rho_o V_o^2}{\rho_j V_j^2}\right)^{\frac{1}{2}}$

V_o = free strem velocity

V_j = jet velocity

$\frac{W}{s}$ = airframe wing loading

$\frac{x}{c}$ = chordwise location as a percentage of local chord

$\frac{x}{d_j}$ = distance downstream of the jet exit plane in jet diameters

α = angle of incidence of the airframe to free stream

θ_j = jet thrust vector angle at the jet exit relative to the aircraft horizontal datum

$\frac{\theta_L}{\theta_{LC}}$ = lift engine thrust vector as a proportion of the lift/cruise engine thrust

ρ_o = free stream density

ρ_j = jet stream density

LIST OF FIGURES

LIST OF FIGURES Continued

Fig. 1 **Definition of Jet Interference**

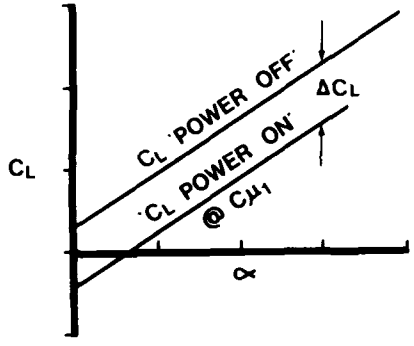

$$V_E = \left(\frac{\rho_o V_o^2}{\rho_j V_j^2}\right)^{1/2} = \left(\frac{2}{C\mu \; S_{A_j}}\right)^{1/2} \longrightarrow$$

$$\frac{\Delta C_L}{C\mu} = \frac{\Delta L}{T} \downarrow$$

$$\frac{\Delta L}{T} = \frac{C_L \text{ POWER ON} - C_L \text{ POWER OFF}}{C\mu}$$

Fig. 2 V/S.T.O.L. Tunnel

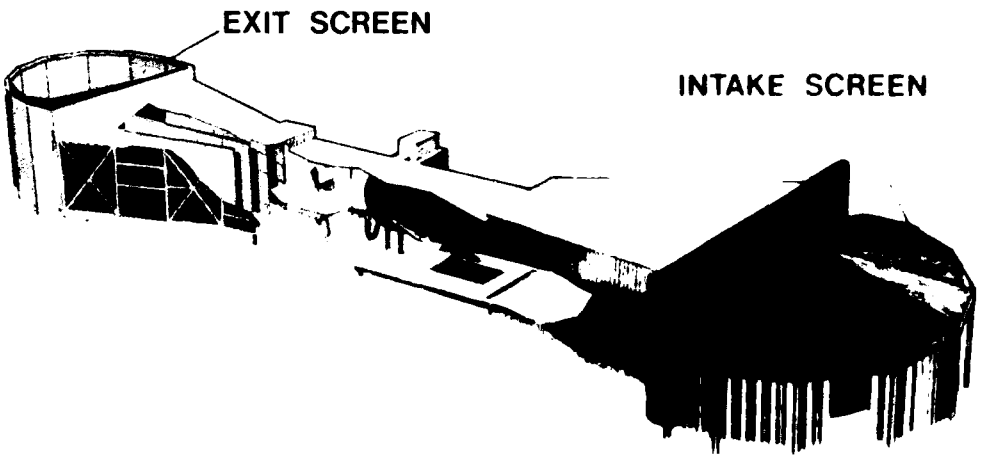

Fig. 3 Hover (Out of Ground Effect) Lift Loss. (From Model Tests)

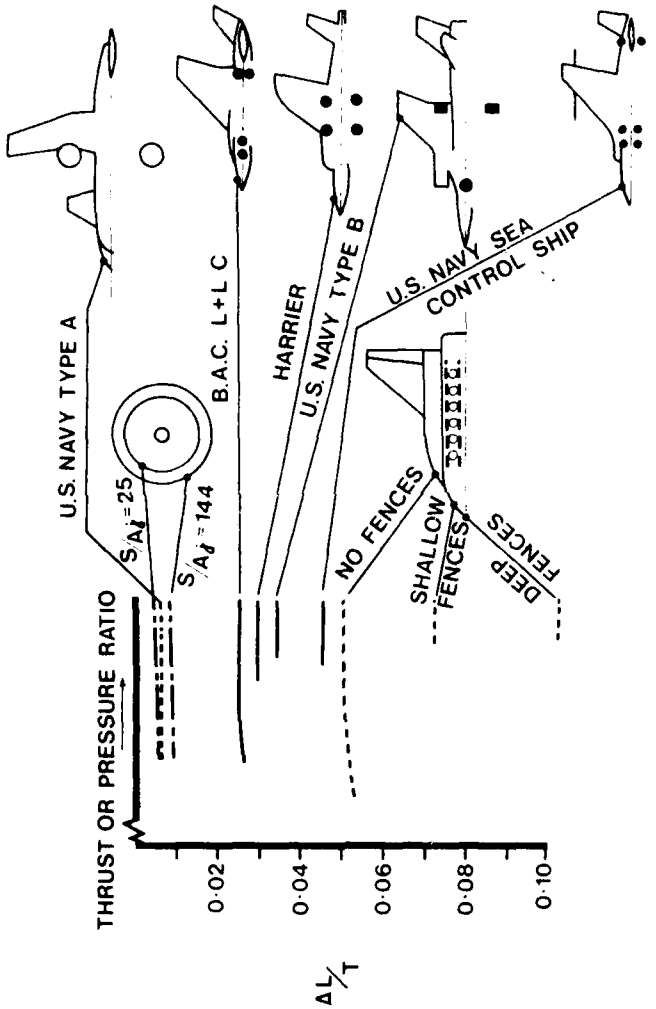

Fig. 4 Influence of Jet Entrainment on Hover Lift Loss

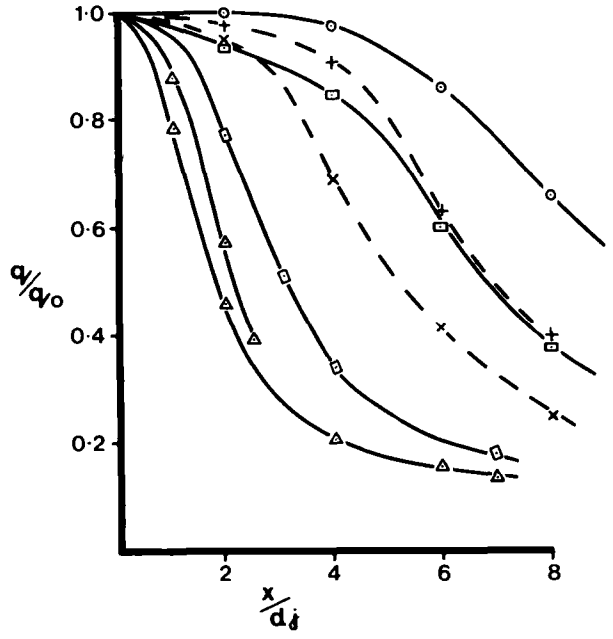

JET DYNAMIC PRESSURE DECAY
FOR DIFFERENT JETS

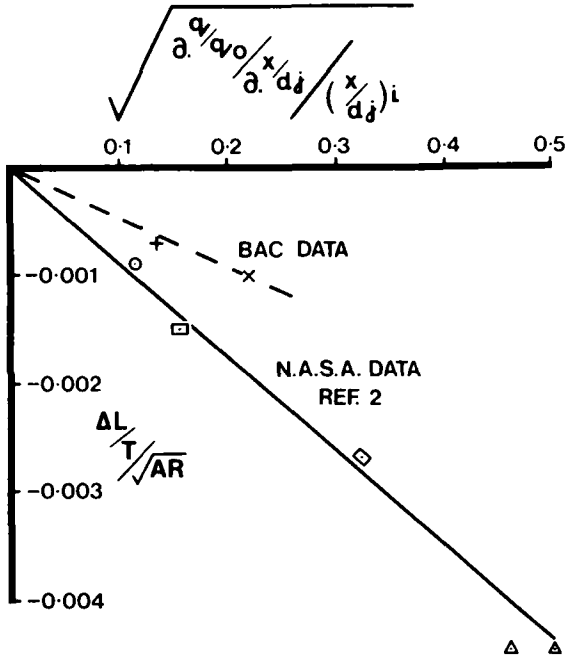

LIFT LOSS AS A FUNCTION
OF JET CHARACTERISTICS

Fig. 5 **Ground Effect Correlation for Single, Centrally Located Jets**

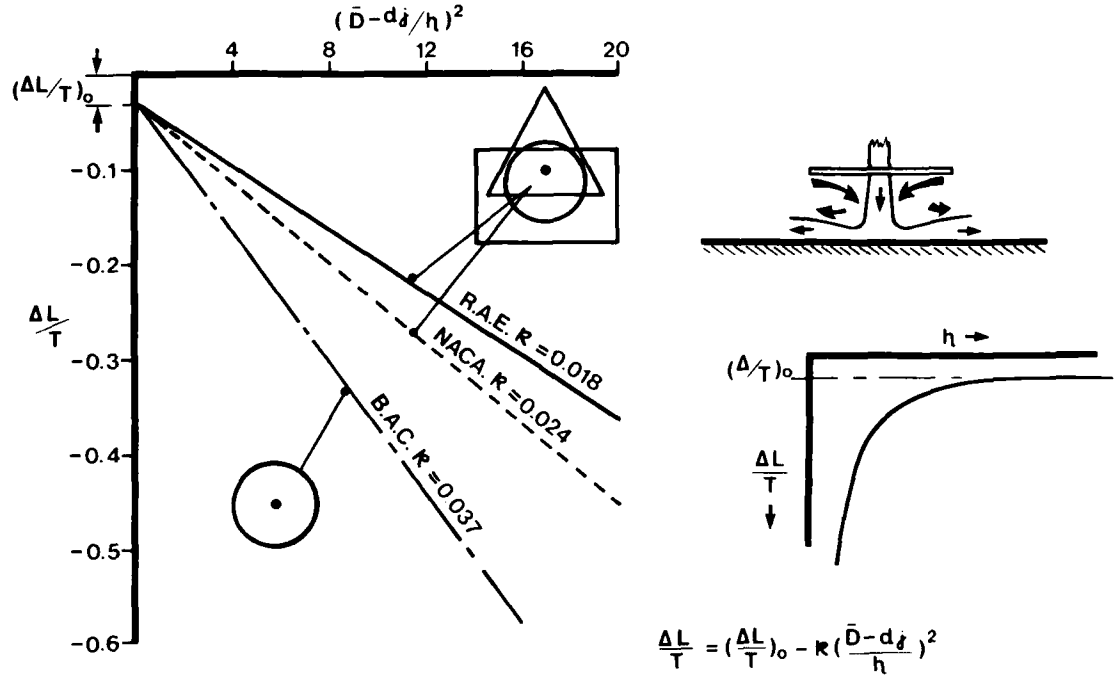

Fig. 6 The Influence of Multi-Jet Location on Ground Effect

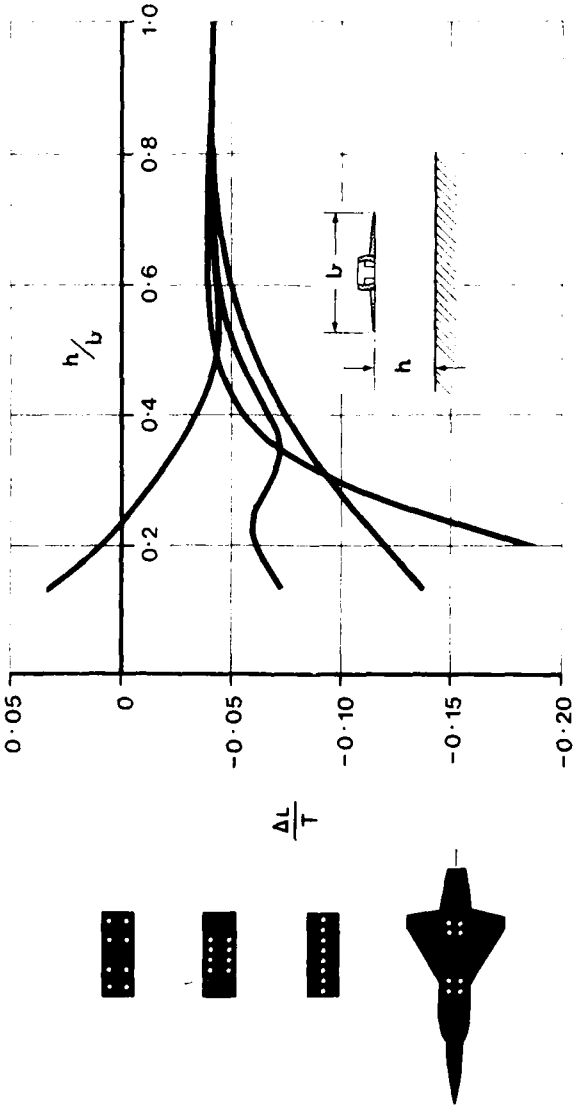

Fig. 7 The Effect of Fuselage Fences on Hover

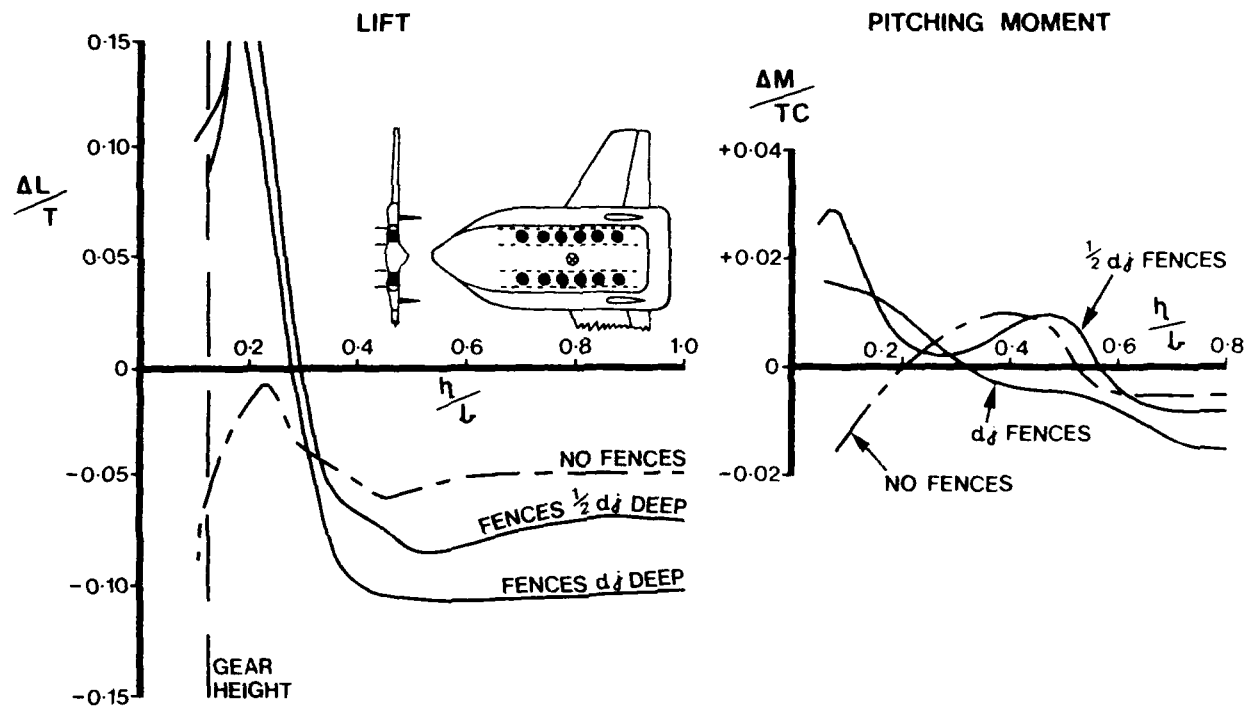

Fig. 8 Ground Effects on L/C and L + L/C Configurations

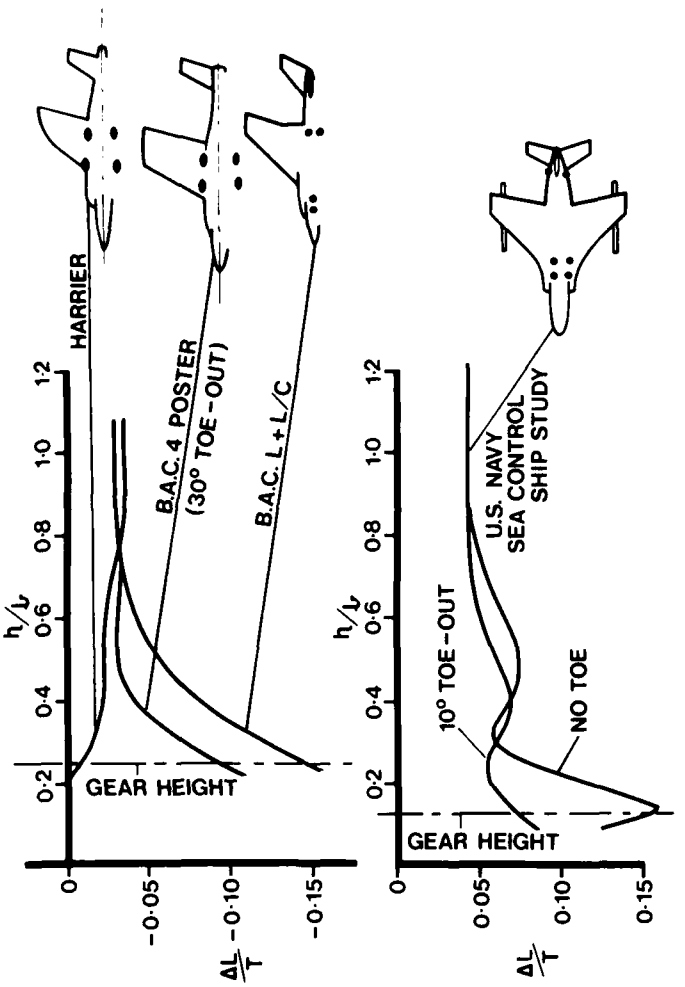

Fig. 9 Effect of Ribbed Ground Mat on Lift Loss at Gear Height
(Ribs aligned spanwise)

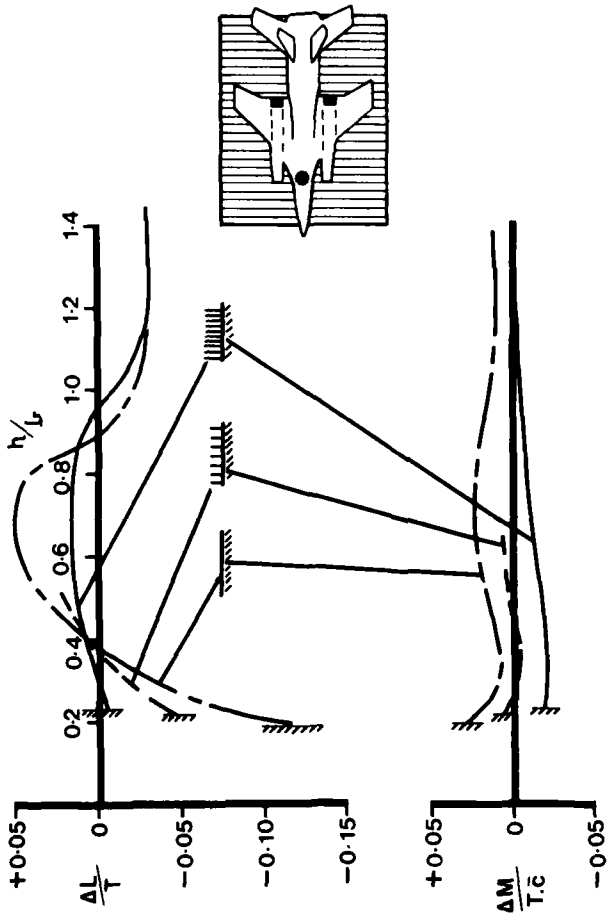

Fig. 10 A Navy Type 'A' Configuration in Hover

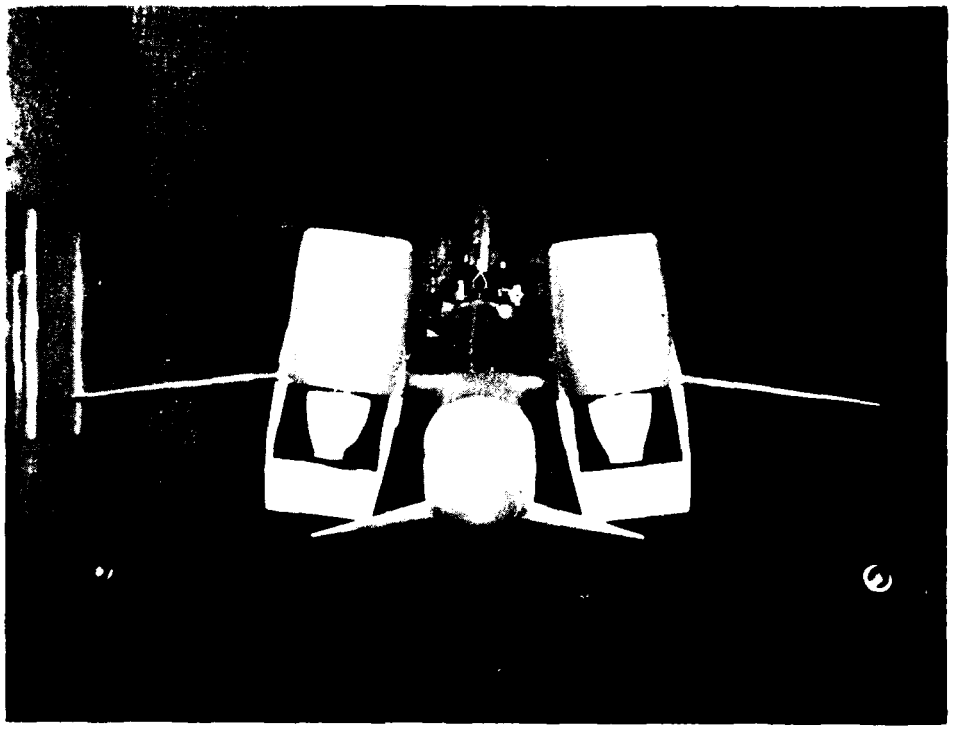

Fig. 11

A Navy Type 'A' Configuration V.T.O.L. Ground Effect on Lift (h measured to fuselage bottom.)

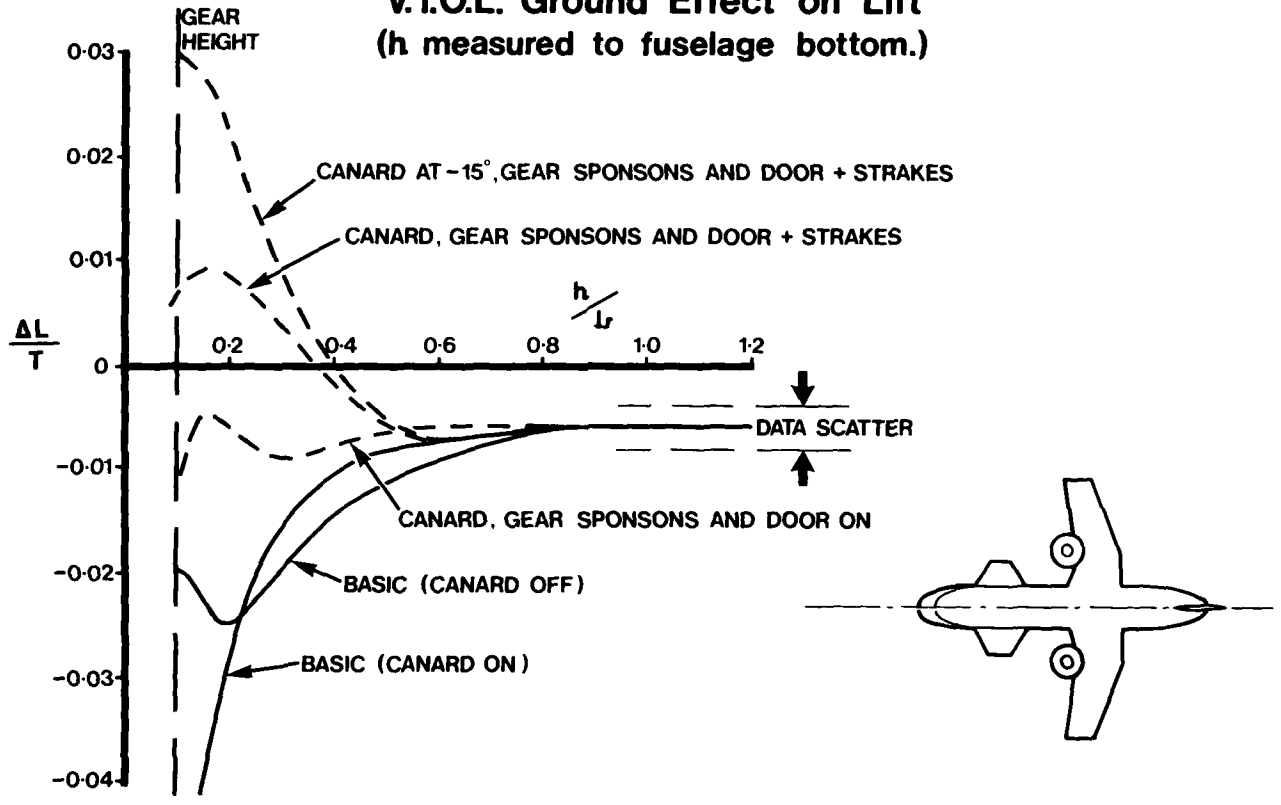

Fig. 12 Effect of Lift Losses on S.T.O. Performance

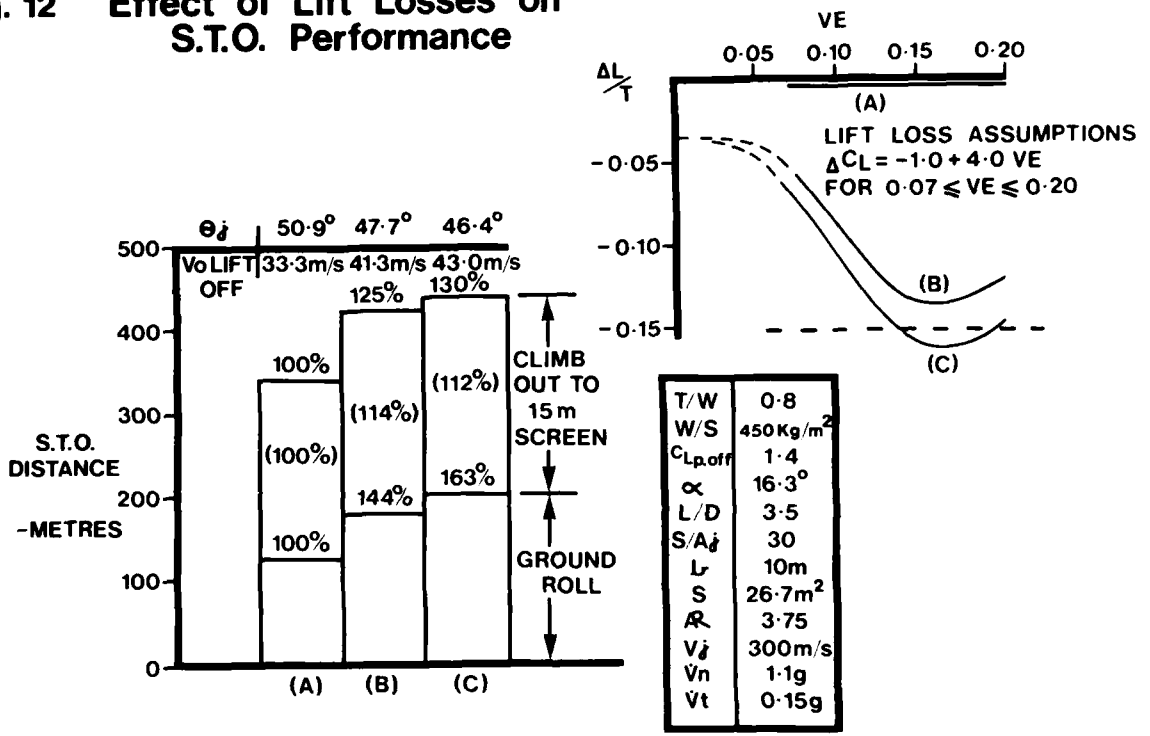

Fig. 13

Presentation of Results

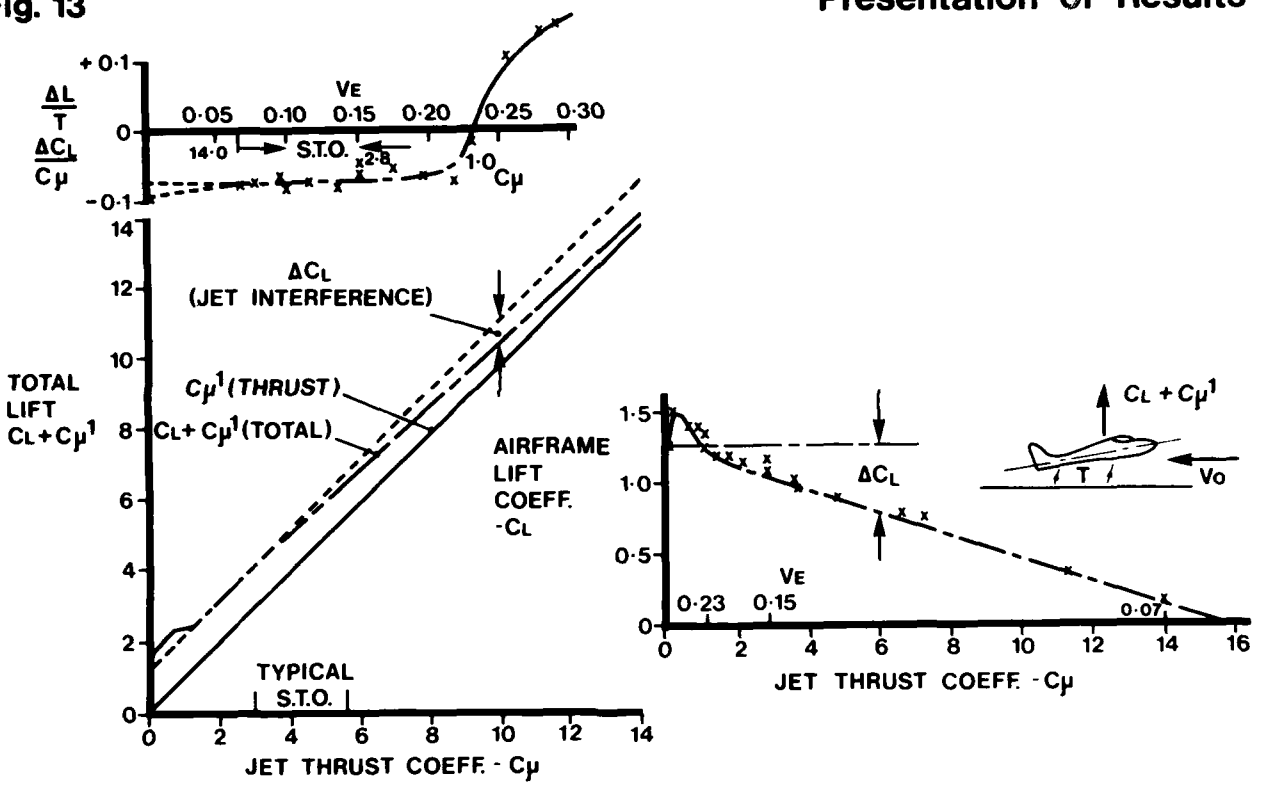

Fig. 14 **Jet Induced Lower Surface Pressures**
$V_E = 0{\cdot}125$

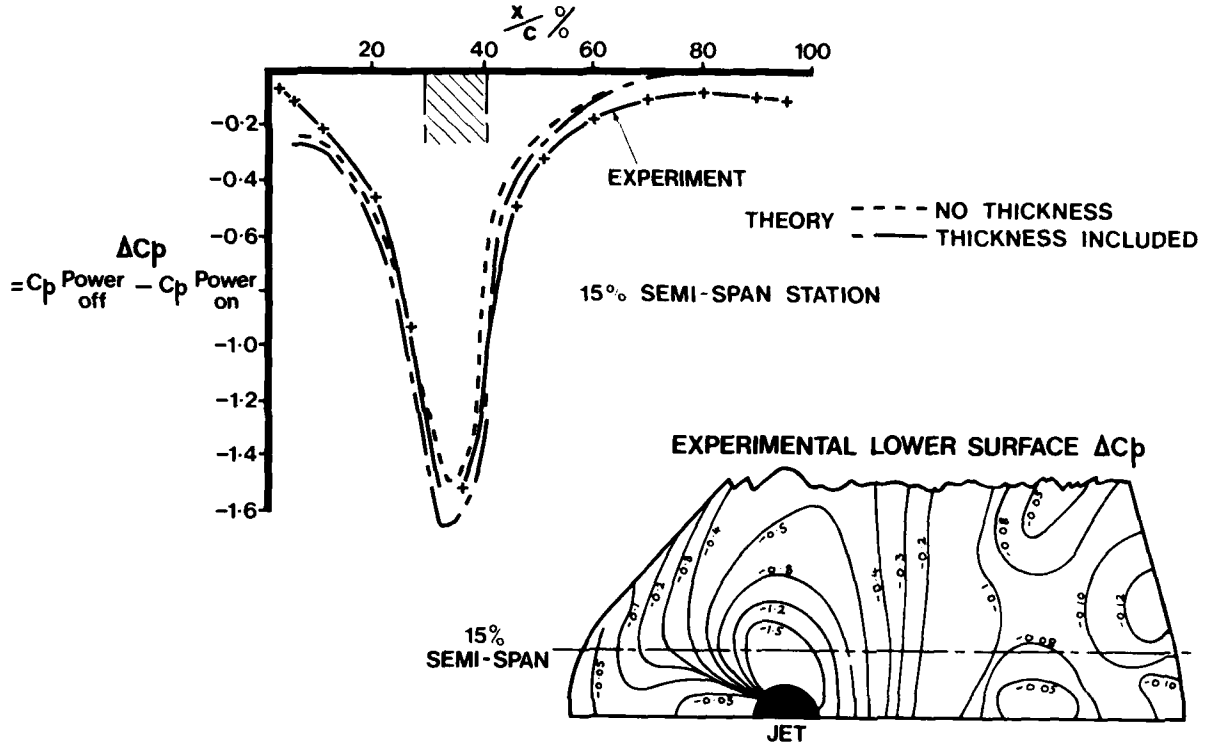

Fig. 15

4 Nozzle L/C Types.
O.G.E. Lift Interference at Fwd. Speed.
$\theta_j = 60°$

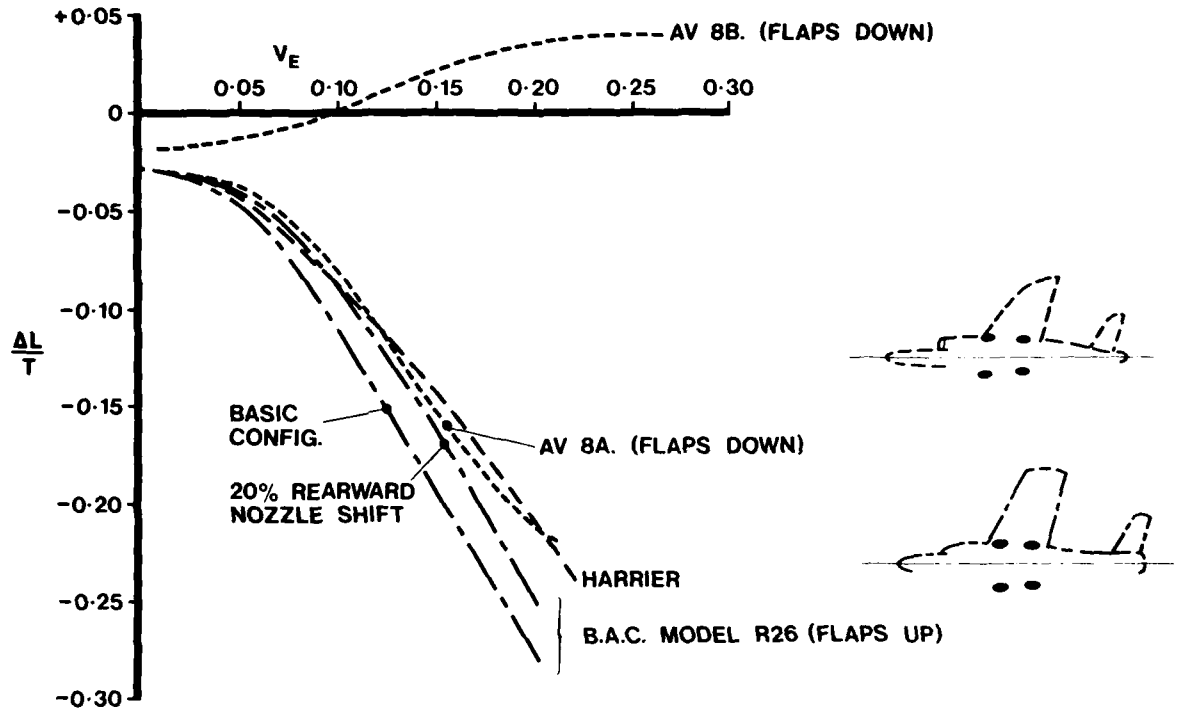

Fig. 15 **The Effect of Wing Tilt and High Incidence on Harrier Type Lift Interference**

B.A.C. model R26 with tilt wing ~ $\theta_j = 90°$

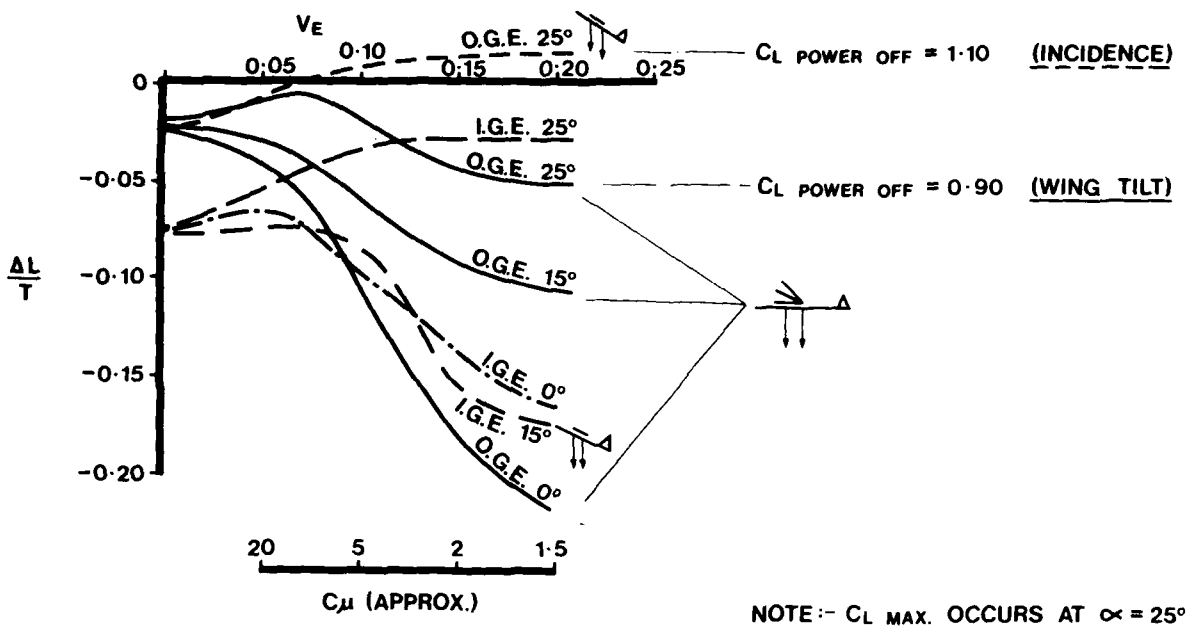

NOTE :- $C_{L\ MAX.}$ OCCURS AT $\alpha = 25°$ WITH PARTLY STALLED WING.

Fig. 17

C_L v $C\mu$ Presentation for Model 26 with Tilt Wing - Post Stall Lift (Power On)

$\propto$ Wing = 25° θj = 90°

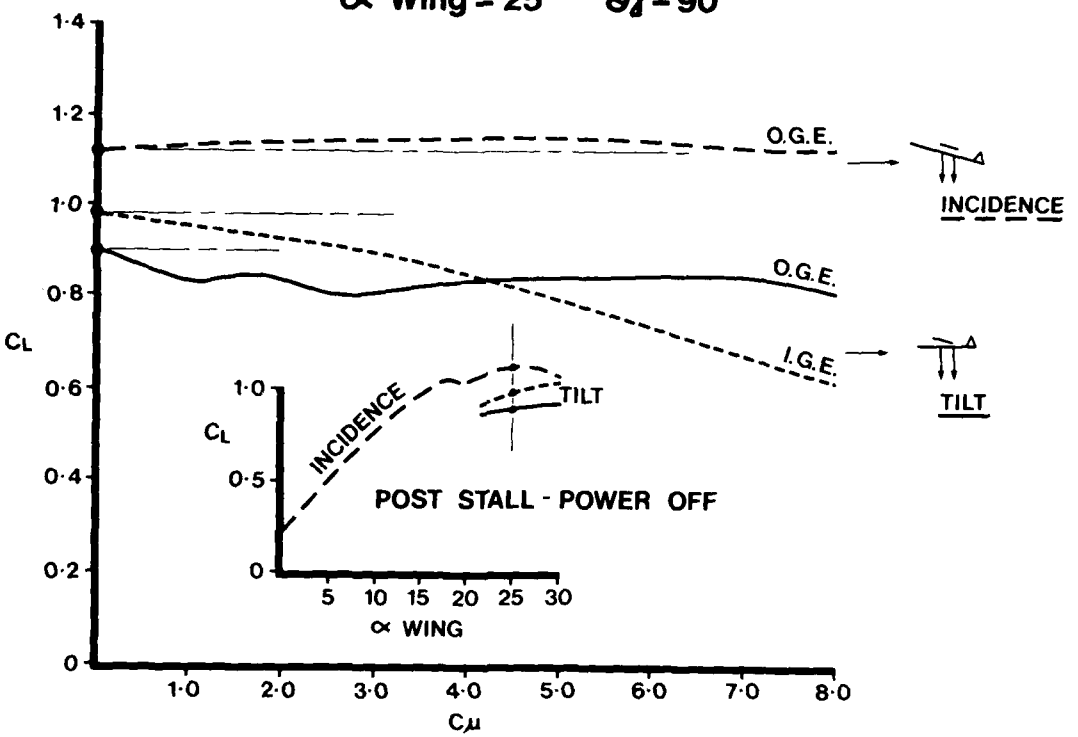

Fig. 18 The Effect of Jet Location on Lift Interference
Clean Wing. Out of Ground Effect.
$\alpha = 0°$ $\theta_j = 90°$

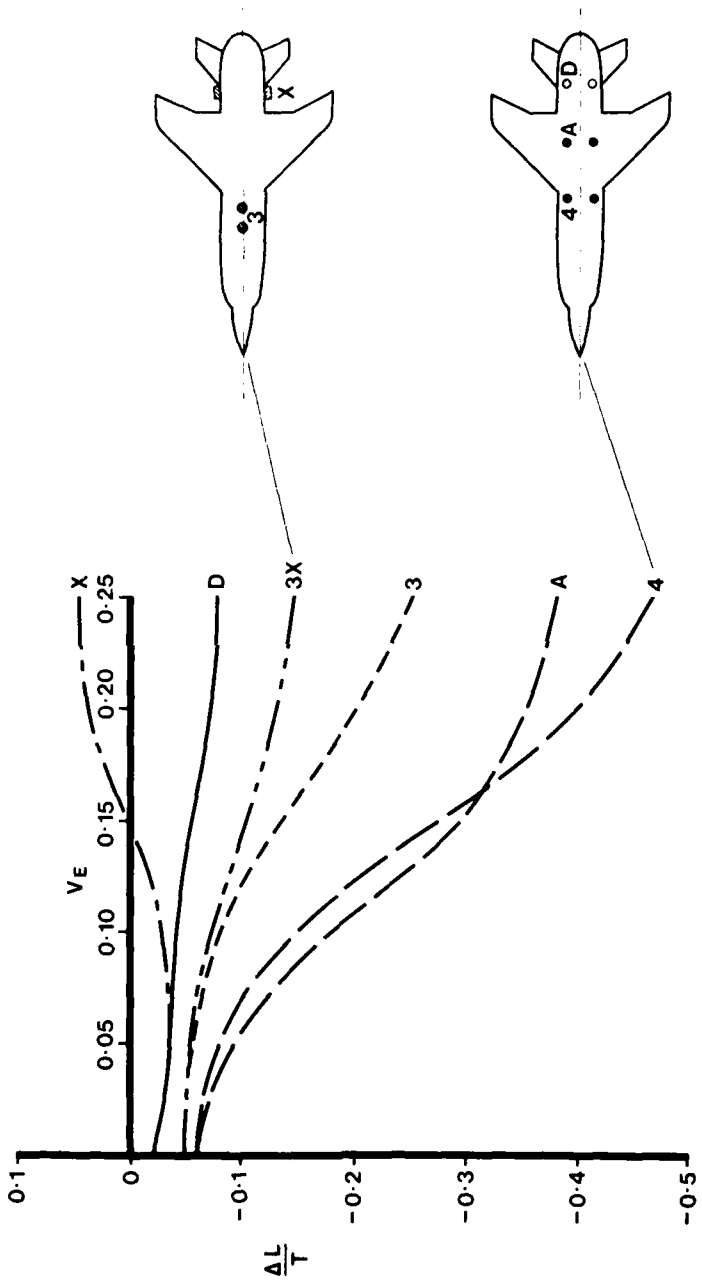

Fig. 19 Grumman 'Sea Control Ship' Study
Configuration - 607

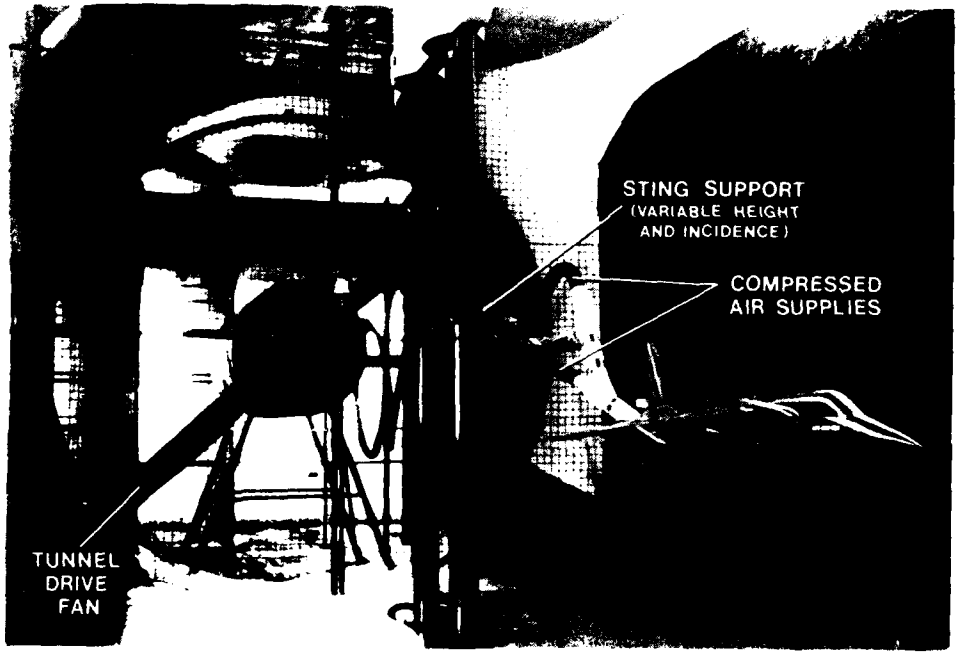

Fig. 20 Grumman 607 - Lift Interference. Out of Ground Effect
$\alpha = 0°$ $h/b = 1{\cdot}0$

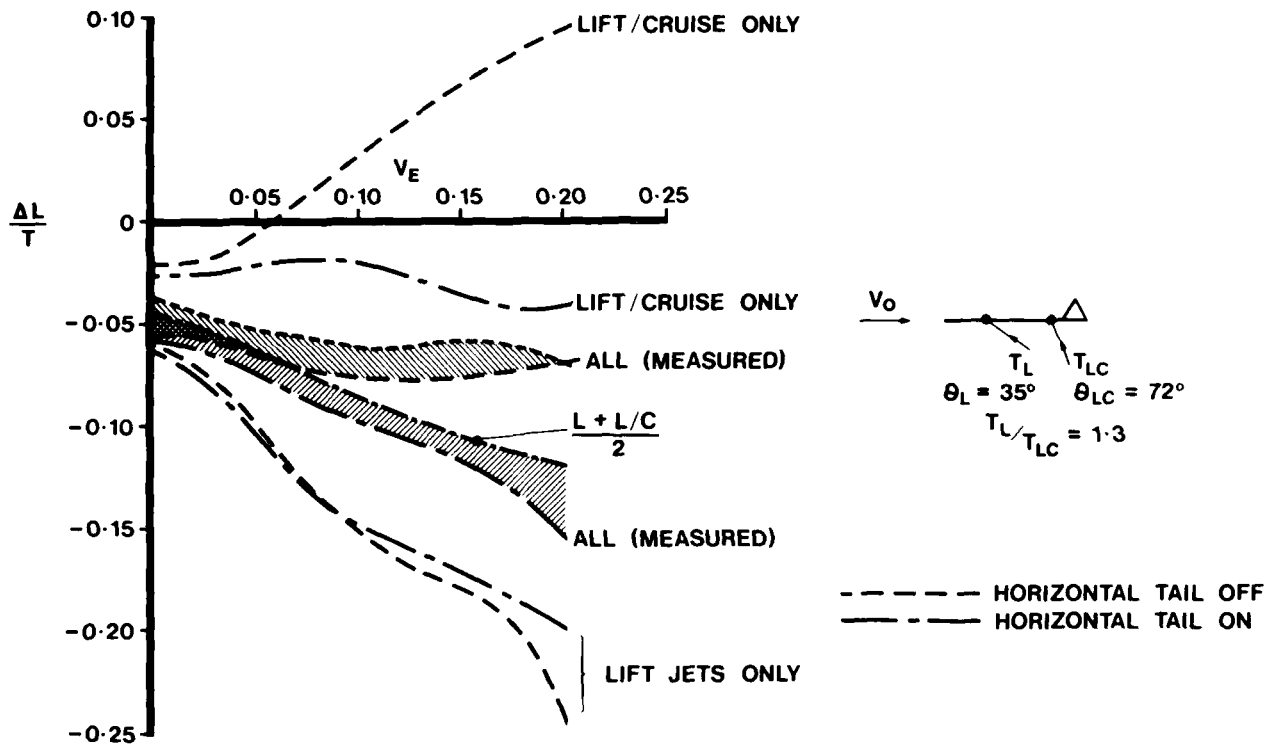

Fig. 21

Effect of Toe-out on Lift

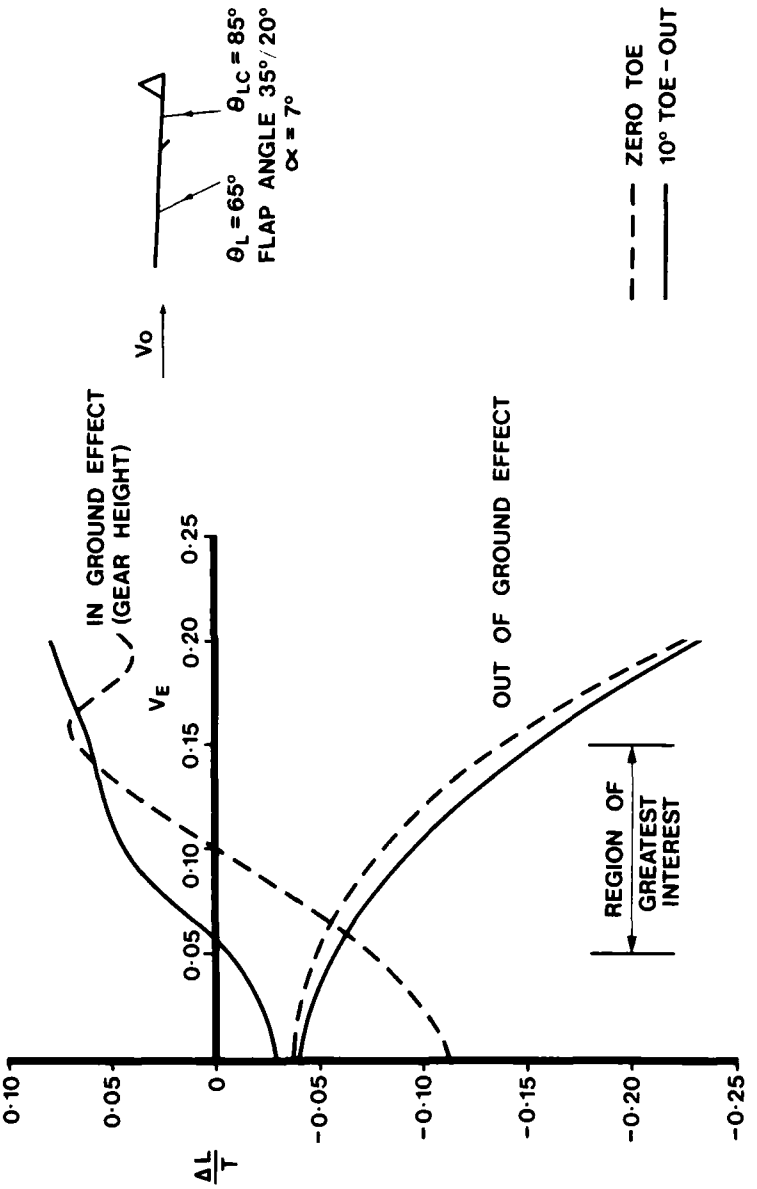

Fig. 22 **Jet Interference with the Horizontal Tail**
$\alpha = 7°$. Flap angles 35°/20°.

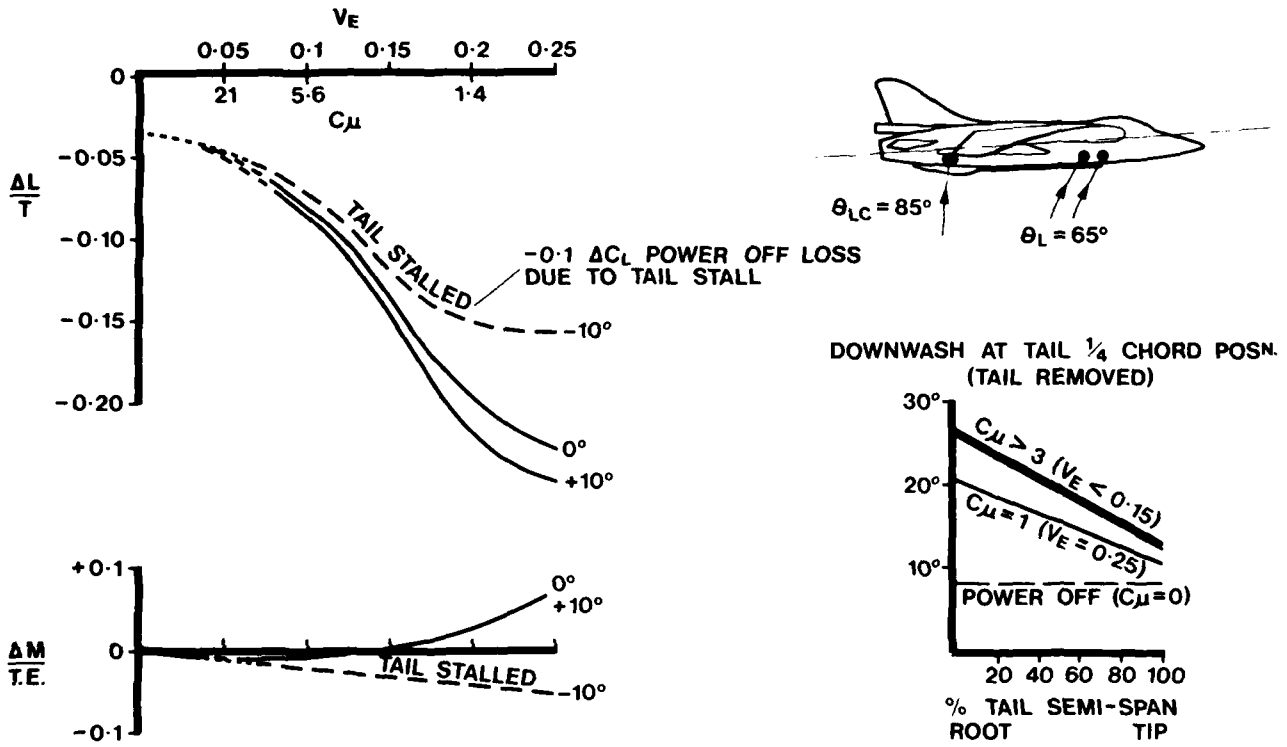

Fig. 23 Grumman 623 Configuration

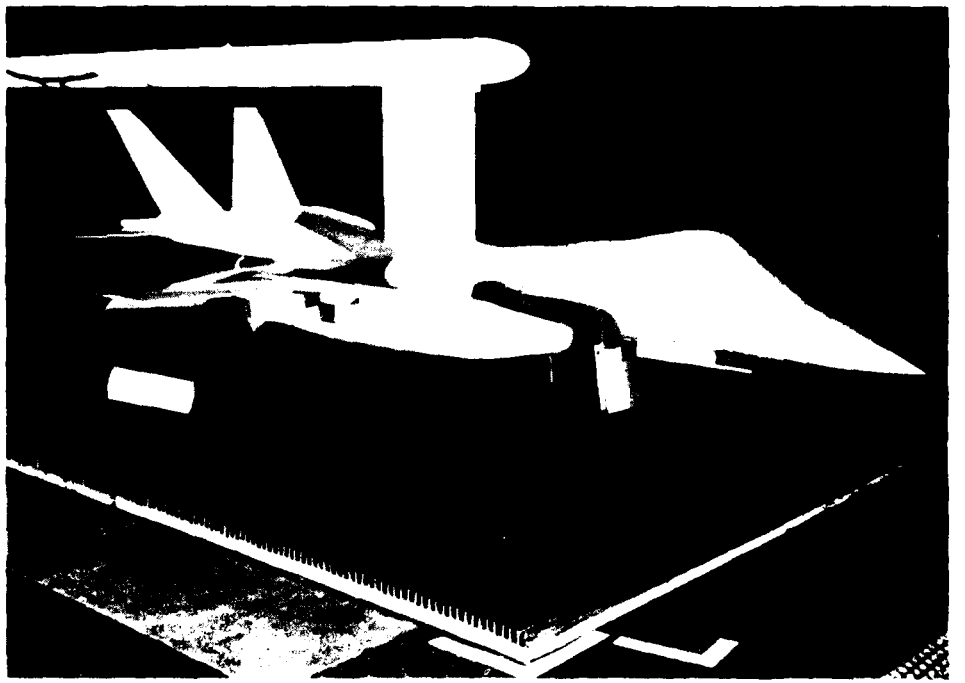

Fig. 24 The Effect of Spanwise Location of the L/C Nacelle

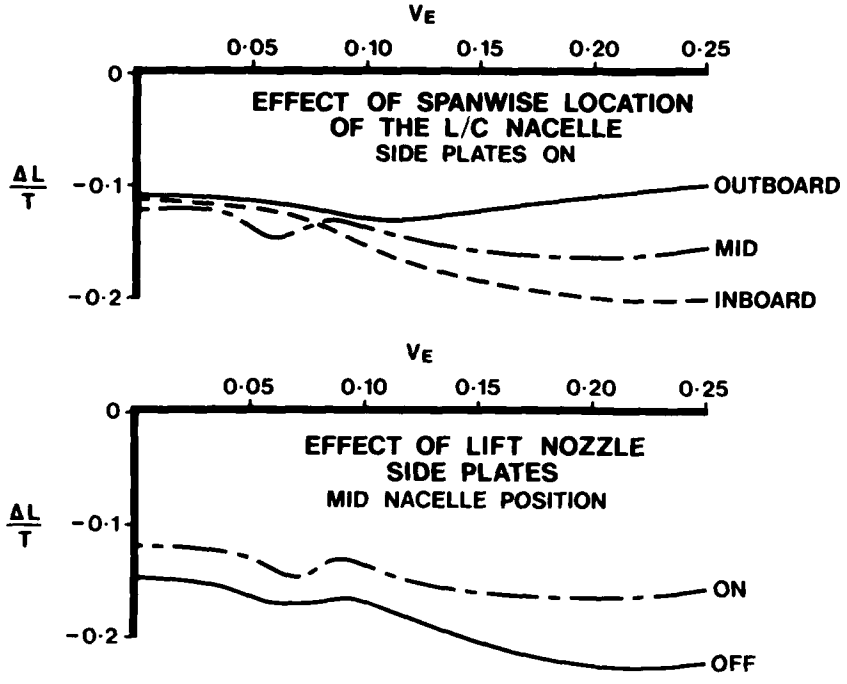

623 CONFIGURATION

θ_L/θ_{LC} = 40°/40°

T_{L}/T_{LC} = 0·35

h/l_r = 0·2 (I.G.E. - GEAR HEIGHT)

Fig. 25

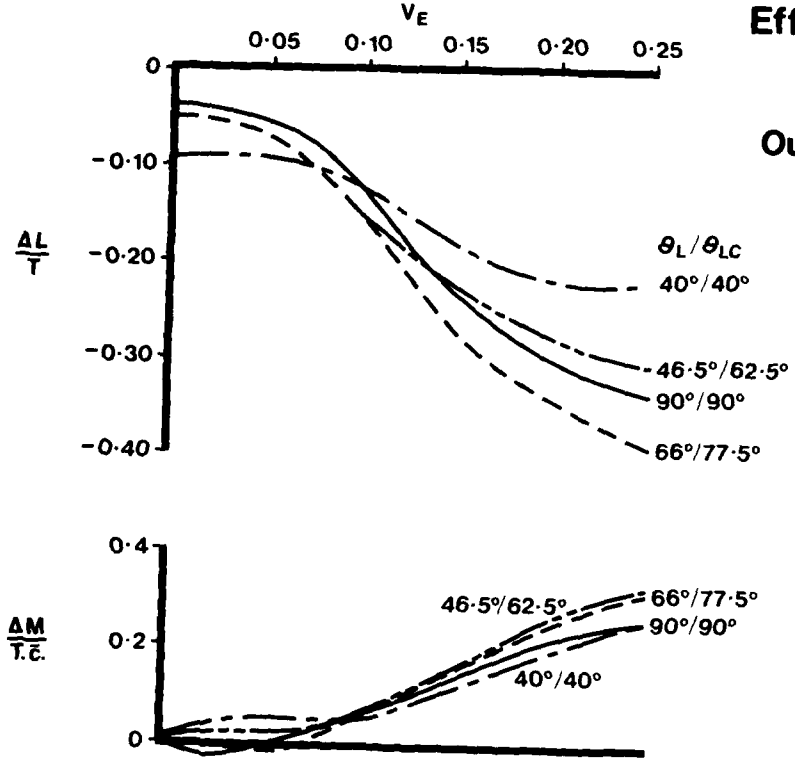

623 Configuration
Effect of Jet Vector Angle.
Out of Ground Effect.
$T_L / T_{LC} = 0·57$
Outboard lift / cruise nozzles.
Side plates on.

Fig. 26 Harrier - Lift Force Due to V.I.F.F.
$\theta_j = 90°$

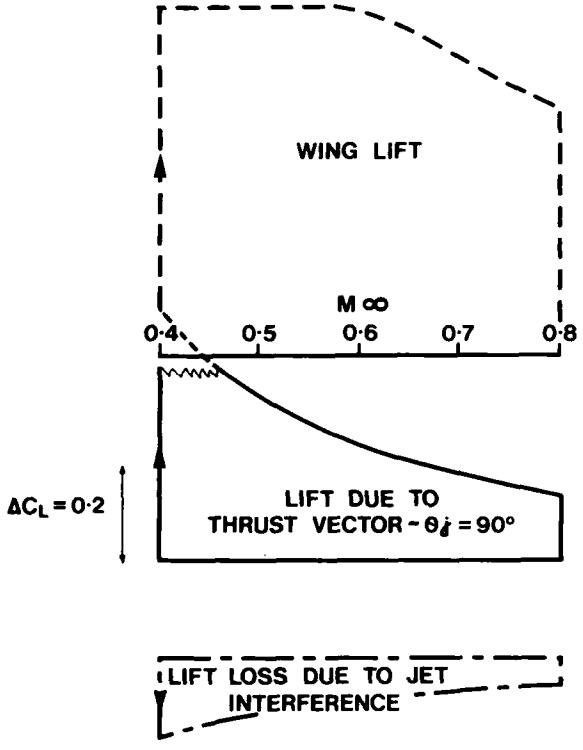

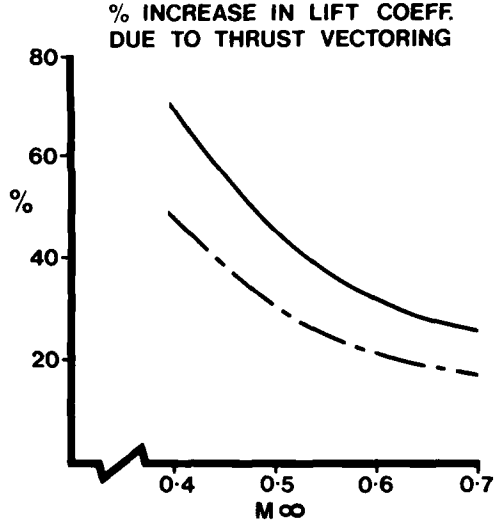

Fig. 27 Type 'A' Configuration. Out of Ground Effect Lift
$\theta_j = 45°$ $\alpha = 5°$

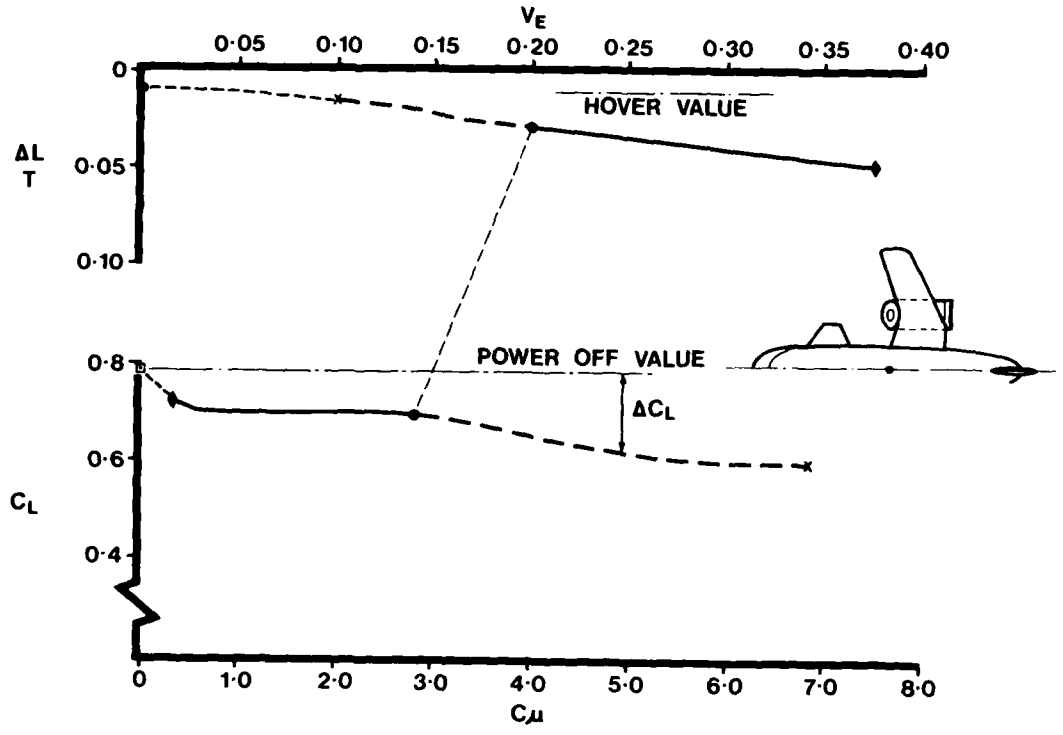

Fig. 28 Type 'A' Configuration. - Effect of Nacelle Angle θ_j on Lift
$\alpha = 5°$

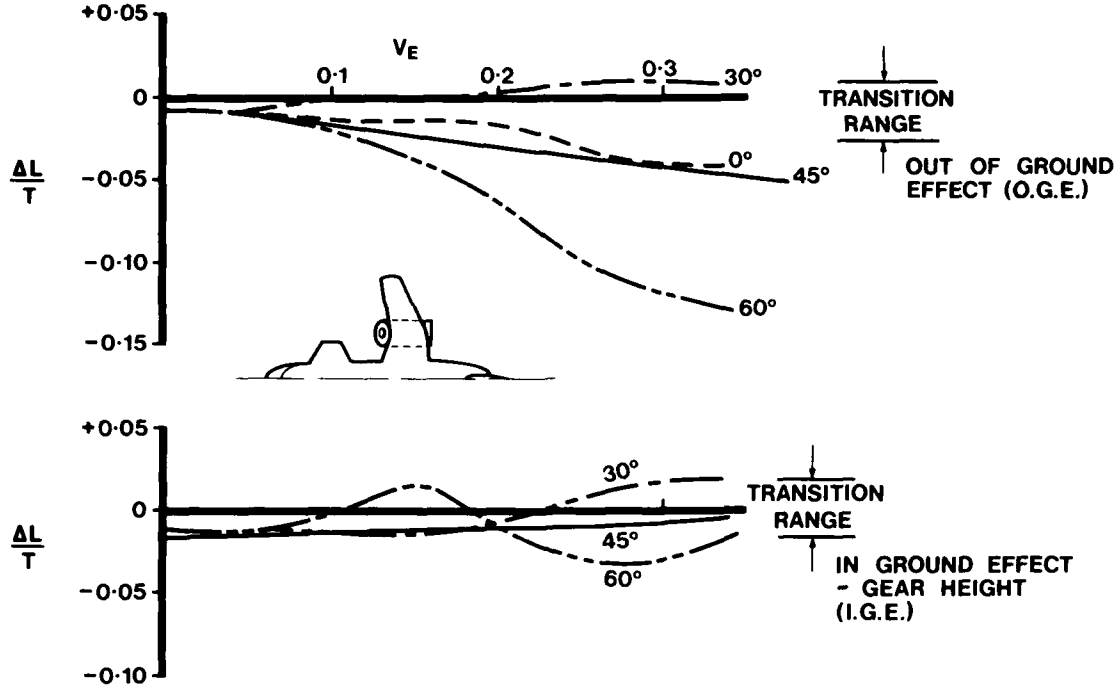

Fig. 29 Type 'A' Configuration - Pitching Moment and Drag

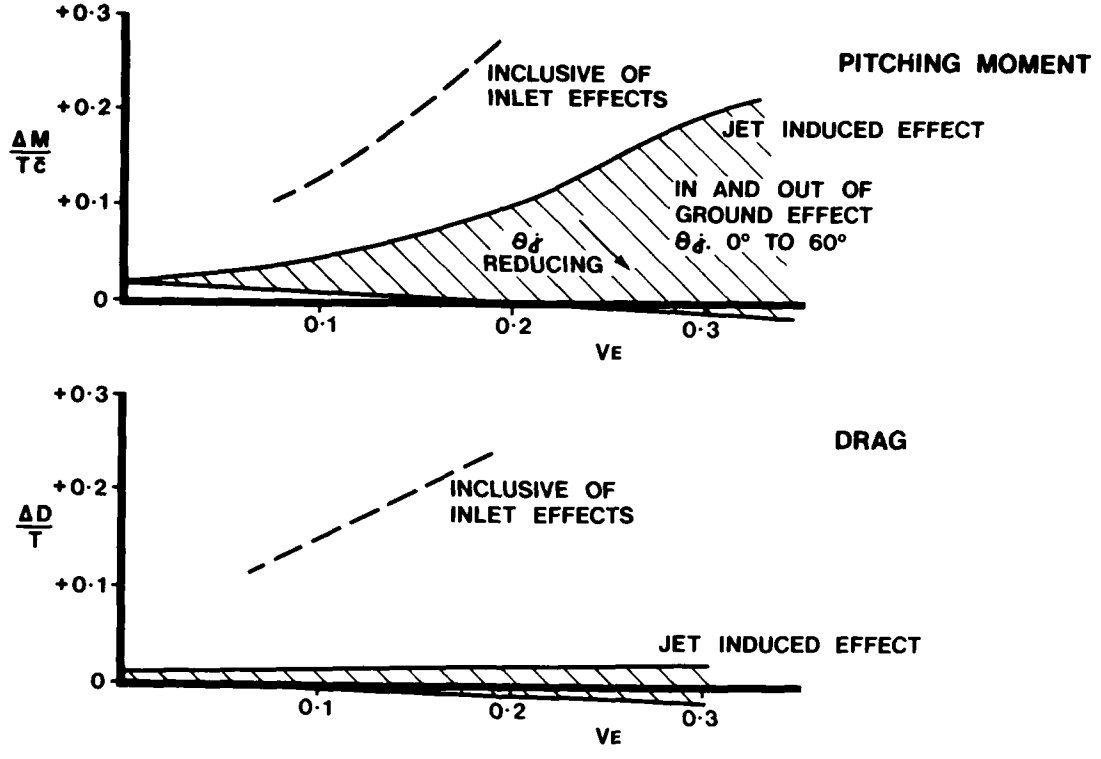

SURFACE PRESSURE DISTRIBUTION ON A FLAT PLATE OR BODY OF REVOLUTION FROM WHICH A JET IS ISSUING

S. C. Perkins, Jr. and M. R. Mendenhall
Nielsen Engineering & Research, Inc.

ABSTRACT

A correlation method to predict pressures induced on an infinite plate by a jet issuing from the plate into a subsonic free stream has been developed. The complete method consists of an analytical method which models the blockage and entrainment properties of the jet and a correlation which accounts for viscous effects. The method has been developed for jets exhausting normal to the plate, and is presently being extended to jets exhausting at an angle to the plate and to jets exhausting from a body of revolution.

INTRODUCTION

During the past several years there has been an increased interest in V/STOL configurations which utilize lift-jet engines mounted in wings and/or the fuselage. While these configurations usually exhibit improved lift characteristics, the interaction of the jet and the free stream can result in undesirable aerodynamic loading characteristics influencing lift and stability. This situation arises during transition from hovering to horizontal flight, when the configuration has attained some forward speed but must still rely on the jet for lift. Investigation of the effects of a lift jet on the pressure distribution on an infinite flat plate or on a body of revolution, as presented in this paper, is a first step in understanding the jet-wing and jet-fuselage interference problem.*

Experimental investigations of jet interference effects on an infinite flat plate (refs. 1-5) have shown that the jet produces a region of positive pressure upstream of the jet and regions of negative pressure downstream and to each side of the jet. The negative pressure field has been found to intensify as the jet velocity ratio (V_j/V_∞) is increased. Oil film tests, such as those done by Mosher (ref. 5), show a strong viscous region immediately downstream of the jet. It is in this viscous dominated region that most analytical methods fail to predict the pressure distribution on the plate.

In recent years, several theoretical and empirical methods to predict the jet induced pressures on a flat plate have been developed (e.g. refs. 6 through 10). Predicted pressure distributions from these methods are generally in good agreement with experiment in the region upstream of the jet. However, accurate prediction of the pressure distribution on the plate in the viscous dominated region to the side and downstream of the jet was not obtained by these methods. Since purely analytical methods have not been successful in predicting the viscous effects of the jet, an empirical approach seems appropriate.

The pressure prediction method presented in this paper consists of an analytical model and an empirical correlation factor to account for viscous effects. The analytical model utilizes a sink distribution to represent entrainment effects and a distribution of vortex quadrilateral panels on the jet boundary to represent blockage effects. The jet boundary and position are determined from empirical observations. The viscous correction factor is obtained from a correlation of the difference between analytically predicted surface pressures and measured results. Details of the method as developed for a jet issuing normal to the plate are presented in reference 11, where correlation factors are shown for jet velocity ratios up to twelve, and predicted pressure distributions are compared with experimental data for several velocity ratios within this range. This paper presents a summary of the prediction method and comparisons of measured and predicted pressure distributions for two jet velocity ratios.

---

*Sponsored by NASA/Ames under Contract NAS2-9509.

SYMBOLS

A_i	area of sector or segment of circular flat plate
b	half-width of the jet mixing region
C_m	pitching-moment coefficient
C_n	normal-force coefficient
C_p	pressure coefficient, $\frac{p - p_\infty}{q_\infty}$
D	jet diameter at the exit plane
$\vec{n}$	unit normal at the centroid of a vortex quadrilateral panel
p	static pressure
Q_a	sink intensity, volume per unit time
q_a	local sink intensity, volume per unit time
q'_a	nondimensional sink intensity, $q_a/V_\infty D$
q_∞	dynamic pressure, $\frac{1}{2}\rho V_\infty^2$
r	radial distance along the plate from the center of the jet to any field point on the plate
r_a	vector from a sink to each field point, $\sqrt{(x_j-x_a)^2 + (y_j-y_a)^2 + (z_j-z_a)^2}$
r_{max}	radius of the circular plate
s_a	curve length of the jet axis

t	local jet width in x_j-z_j plane
U_x, U_y, U_z	velocity components due to entrainment in the jet coordinate system
u, v, w	velocity components in the X, Y, and Z directions, respectively
V_j	jet velocity at the exit plane
V_∞	constant free-stream velocity
X, Y, Z	plate coordinate system fixed at the center of the jet exit plane, positive X is upstream
x_a, y_a, z_a	coordinates of the jet axis in the jet coordinate system
x_j, y_j, z_j	jet coordinate system fixed at center of the jet exit plane, positive x_j is downstream
z'_a	normalized vertical coordinate of jet axis, z_a/D
α	local slope of jet centerline; dz_j/dx_j, $\alpha = \delta_j$ at exit
β	polar angle, measured clockwise from the positive X-axis in the plate X-Y plane
$(\Delta C_p)_{viscous}$	correlation increment of pressure coefficient
δ_j	initial inclination angle of jet centerline, measured from the positive x_j axis in the x_j-z_j plane, $\delta_j = 90° - \theta$
θ	initial inclination angle of jet centerline, measured from the positive z_j axis in the x_j-y_j plane, $\theta = 0°$ for a jet issuing normal to the free stream
μ_∞	absolute viscosity of free stream
ρ_∞	free-stream density

Subscripts

a	jet centerline quantity
max	maximum value
∞	free-stream quantity

APPROACH

A sketch of an expanding jet of initial velocity V_j and initial inclination angle δ_j emerging from an infinite plate into a subsonic crossflow of velocity V_∞ is shown in figure 1. Predicted pressure distributions on the plate tend to compare well with data in the region of positive pressure upstream of the jet ($0° \leq \beta < 90°$), where viscous effects are small; but downstream of this angle, the viscous effects are strong and present theoretical methods cannot predict plate pressures accurately.

One approach to the problem of predicting pressures in a viscous region is to correlate the pressure difference between analytical results without viscous effects and available data. Assuming such a correlation can be made, the pressure coefficient at each point on the plate is expressed as

$$C_p = C_p\Big|_{\text{potential}} + \Delta C_p\Big|_{\text{viscous}} \tag{1}$$

where $\Delta C_p|_{\text{viscous}}$ is the correlation factor which represents viscous effects. The potential portion of the above equation is calculated using the Bernoulli equation in the form

$$C_p = 1 - \left\{ \frac{(V_\infty + u)^2 + v^2}{V_\infty^2} \right\} \tag{2}$$

A discussion of the jet model and the pressure correlation is presented in the following sections.

Jet Model

Details concerning the specification of the jet centerline path, the blockage and entrainment models, and the spreading rate of the jet for a jet exhausting normal to a flat plate are presented in this section. Aspects of the model which are different for jets exhausting at an angle to the plate and for jets exhausting from a body of revolution are discussed at the end of each section.

Centerline shape

The jet centerline, at initial inclination angle δ_j to the plate, is shown in figure 1. The path of the jet centerline is specified using the following empirical relation developed by Margason (ref. 12)

$$\frac{x_j}{D} = \frac{1}{4\sin^2\delta_j}\left(\frac{V_\infty}{V_j}\right)^2\left(\frac{z_j}{D}\right)^3 + \frac{z_j}{D}\cot\delta_j \qquad (3)$$

This calculated centerline shape compared well with jet wake vapor flow visualization data for a wide range of velocity ratios ($1 \le V_j/V_\infty \le 10$) throughout the inclination angle range of interest ($30° \le \delta_j \le 90°$). The centerline shapes for a jet exhausting at an angle to the plate are obtained using Eq. (3), while experimentally determined jet paths will be used for the body of revolution case.

Blockage model

A jet exhausting from an infinite plate into a subsonic free stream has been observed to exhibit a displacement effect as though the jet boundary were behaving as a solid surface, particularly near the surface of the plate (refs. 7 and 10). The effect of the solid jet boundary is obtained by representing the specified wake surface with a series of vortex quadrilateral panels on which a boundary condition of flow tangency due to the free stream is enforced. The vortex quadrilateral panel blockage model described herein is based on a method developed by Maskew (ref. 13).

The boundary of the jet wake, specified by the centerline path and the wake radius along the centerline, is divided into length segments as illustrated in figure 2. Each length segment is further divided into a number of circumferential segments. A slice through the wake, normal to the centerline, shows the circular cross section wake to be represented by a series of straight segments. The control point on each panel is located at the centroid of the panel, and the vector $\vec{n}$ is the unit normal to the panel, positive when directed outward. The boundary condition satisfied at each control point is

$$\vec{V} \cdot \vec{n} = 0 \qquad (4)$$

where $\vec{V}$ is the vector sum of the free-stream velocity and the velocity induced at a panel control point by all vortex quadrilateral panels making up the blockage model. Implementation of this boundary condition results in a set of linear simultaneous equations in terms of the unknown vortex quadrilateral strengths.

After obtaining the vortex strengths for each panel, the field point velocity induced by a single quadrilateral vortex ring is obtained by summing the contribution from each of the four sides of the ring. A summation over all the

panels representing the jet surface will produce the velocity induced at a point by the complete blockage model.

As with all finite panel methods, tne representation of the flow around a solid body is better the further the point of interest is from the body. For practical problems of interest in this work; that is, flow around circular cross section jets with small diameters compared to their length, a good rule of thumb is that the point of interest should not be nearer to the surface than one panel width. This rule has been verified for the flow around a cylinder. All results presented in this paper were obtained using twenty panels around the circumference of the jet.

This blockage model is also being used for jets exhausting at an angle to the plate and for jets exhausting from a body of revolution.

Entrainment model

A jet exhausting from an infinite plate into a subsonic free stream will entrain air from the free stream and accelerate it in the direction of the jet. The induced flow external to the jet boundary can be represented by sinks distributed along the jet axis. One approach to this method of modeling entrainment was developed by Yeh (ref. 7) and is described herein.

The potential of a three-dimensional sink is:

$$\phi = \frac{1}{4\pi}\frac{Q_a}{r_a} \tag{5}$$

where Q_a is the sink intensity and r_a is the vector distance from the sink to each field point. If the sink distribution lies on the jet axis, the potential can be found by integrating a variable sink intensity over the length of the jet axis. The expression for the potential becomes

$$\phi(x_j,y_j,z_j) = \frac{1}{4\pi}\int_0^\infty \frac{q_a\,ds_a}{\left[(x_j-x_a)^2 + (y_j-y_a)^2 + (z_j-z_a)^2\right]^{1/2}} \tag{6}$$

where q_a is the local sink intensity and s_a is the curve length along the jet axis. In order to obtain velocity components, the potential is differentiated with respect to each coordinate direction. Yeh approximates the variable sink distribution by assuming an equation of the form:

$$q'_a = \frac{q_a}{V_\infty D} = ae^{bz'_a - c(z'_a)^2} \tag{7}$$

By use of empirical correlation, Yeh obtains expressions for a, b, and c in terms of V_j/V_∞. Substituting the expressions for these coefficients into Eq. (7), a relation for the local sink intensity as a function of z_a is obtained. The induced velocities are obtained by integrating the expressions for $\partial\phi/\partial x_j$, $\partial\phi/\partial y_j$, and $\partial\phi/\partial z_j$ (U_X, U_Y, and U_Z, respectively) along the jet axis. Since the distance along the axis (s_a) is a function of z_a, Eq. (3) for the jet centerline must be used in conjunction with these expressions to obtain U_X, U_Y, and U_Z.

In order for U_Z to be zero in the X-Y plane to satisfy the no-flow condition at the plate, the entrainment model is imaged below the Z = 0 plane. The effect of this imaging is to double the X- and Y-components of the induced velocities in the Z = 0 plane and cancel the Z-component of velocity.

The integral which defines the potential for a distribution of sinks along the jet axis, given by Eq. (6), does not have an analytical solution and must be solved numerically. Since the integration cannot be carried out to infinity, a practical jet length must be chosen to produce an accurate solution. Studies of the effect of jet length on the entrainment results showed a jet length of 20 initial jet radii to produce consistent results. Consequently, 20 initial jet radii is the upper integration limit for all results presented in this paper.

The above entrainment model equations can be used only when $V_j/V_\infty \geq 2.35$. At lower jet velocity ratios, the empirically determined coefficients produce a singularity in the sink strength equation. It is known that blockage effects are dominant at low velocity ratios, while the entrainment effects are more important at high velocity ratios. The velocity ratio at which entrainment effects begin to have an influence on the pressure distribution on the plate is not known, but some comparisons with data, to be discussed in the RESULTS section, provide some indications in this regard.

Investigations to date indicate that the entrainment for a jet exhausting at an angle to the plate probably lies between the entrainment for a normal jet and that for a co-flowing jet. An attempt to obtain a correlation for the entrainment based on available data is presently being made. The preliminary jet model for jets exhausting from a body of revolution uses the same entrainment model for jets exhausting normal to a plate.

Spreading rate

As a circular jet exhausts from an infinite plate into a subsonic crossflow velocity, the jet interaction with the free-stream velocity causes the boundary to expand or spread with increasing distance along the jet. Some knowledge of the extent of the jet boundary is important in predicting the displacement or blockage effect of the jet. In actuality, the jet expands and its cross section distorts into a kidney shape as shown in sketch 1. The distortion of the jet and its roll-up into a pair of vortices is described in references 15, 16, 17, and 18. This condition occurs near the end of the potential core of the jet. The modeling of the vortex pair is very important if flow-field

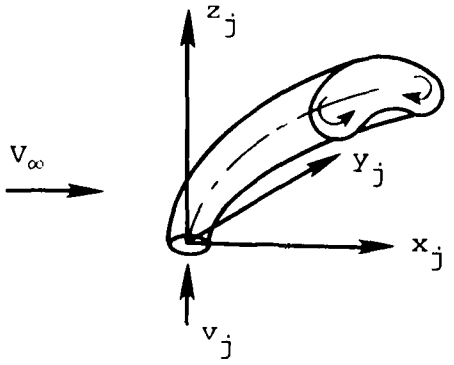

Sketch 1.- Jet cross section

velocities in the vicinity of the downstream portion of the jet are desired, but for purposes of calculating the pressure distribution on the plate near the jet, the displacement effect is more important. For this reason, the authors have chosen to neglect the formation of the vortex pair in the model presented in this paper.

Numerous investigators have studied the spreading rates of jets in a crossflow using both experimental and analytical methods. The results in references 14 and 19 will be used to calculate the required spreading rates in the following manner. Bowley and Sucec (ref. 19) assume the crossflow velocity to be a shear layer velocity with a specified profile; however, for purposes of the present work, the crossflow velocity will be assumed uniform. They assume the jet to be co-flowing with an external velocity $V_\infty \cos \alpha$, where $V_\infty \cos \alpha$ represents the local component of the free-stream flow along the jet centerline. Treating the jet as a planar jet of local thickness t, the spreading rate in the x_j-z_j plane is determined using Abramovich's results (ref. 20) for plane turbulent jets with a co-flowing external stream. The spreading rate for the initial region, which extends from the jet exit plane to the end of the potential core, is a function of V_j/V_∞ and the local slope of the jet centerline (α). The spreading rate for the main region is a function of the free-stream velocity (V_∞), the local slope of the jet centerline, and the local centerline velocity of the jet (V_m). Figure 3 shows a side view of a planar jet exhausting into a crossflow and indicates the initial and main regions.

The expressions for spreading rates were developed by Bowley and Sucec for rectangular shaped jets using the plane jet results of Abramovich. Since the expressions obtained by Abramovich (ref. 20) for axisymmetric jets are nearly identical to those for plane jets, the plane jet expressions are used to represent the spreading rate boundary for the present circular cross section jet model. The axisymmetric jet assumption is best in the region near the plate where the jet has not had the opportunity to spread a large amount. The spreading model will deteriorate at large distances from the plate; however, at large distances from the plate, the displacement effect on the plate and the induced pressure on the plate will be small.

Assuming an initial region length of 3 jet diameters, based on available data, and using experimental data from Keffer and Baines (ref. 14) to obtain the local centerline velocity along the jet axis, expansion rate curves were obtained for jet velocity ratios of 4.0, 6.0, and 8.0. Spreading rate curves for velocity ratios other than these were obtained by interpolation or extrapolation of the known curves. The expansion rate curves presented in figure 4 are used to determine the blockage model for the predicted results in this paper. This same blockage model is also being used for a jet exhausting at an angle to the plate and from a body of revolution.

Correlation

The purpose of the correlation is to isolate the viscous effects of the jet on the plate or body. It is expected that the predicted potential pressure distribution away from the jet and within the range $0° \leq \beta \leq 60°$ will be in good agreement with experiment. The predicted pressures near the jet and within the range $60° \leq \beta \leq 180°$ will likely be in poor agreement with experiment due to viscous effects. Assuming that the measured pressure distribution is given by a potential part and a viscous part, the viscous part can be determined by a differencing technique.

$$\Delta C_p\Big|_{\text{viscous}} = C_p\Big|_{\text{experiment}} - C_p\Big|_{\text{potential}} \tag{8}$$

Correlating this quantity as a function of jet velocity ratio and position on the plate or body, the predicted pressure induced by a jet exhausting from the plate or body into a crossflow is given by

$$C_p = C_p\Big|_{\text{potential}} + \Delta C_p\Big|_{\text{viscous}} \tag{9}$$

The success of this correlation, as with any correlation, is dependent on the quantity of data available and how well these data compare with one another. In regions where multiple sets of data are in good agreement with one another, the correlation method results should compare well with these and other data. In regions where the data sets are in poor agreement, it is impossible to obtain a correlation which will provide good results with all data.

In comparing data sets having the same velocity ratio, it is necessary to note that other parameters, such as jet size, jet Mach number, initial jet velocity profile, jet turbulence level, free-stream Mach number, and Reynolds number based on run length (Re_ℓ) are seldom the same for any two data sets. Although it is felt that the velocity ratio is the dominant parameter in determining the pressure on the plate, these other parameters may indeed have secondary effects.

It was impossible to find two sets of data for which the range of experimental parameters was identical. Given adequate data, the correlation could include

any of the aforementioned parameters; however, in the absence of these data, the correlation presented in this study is based only on the jet velocity ratio.

The correlation curves presented in this report were obtained in the following manner. First, theoretical pressure distributions were obtained using the blockage model alone for $V_j/V_\infty < 2.35$ and the blockage plus entrainment model for $V_j/V_\infty \geq 2.35$ as discussed in a previous section. Next, a $(\Delta C_p)_{viscous}$ was obtained by comparing these results with experimental data. In cases where more than one data set exists for a particular V_j/V_∞, $(\Delta C_p)_{viscous}$ is found by averaging the correlation values obtained from each data set. By determining a $(\Delta C_p)_{viscous}$ for each chosen position, a data base is set up which consists of a $(\Delta C_p)_{viscous}$ array for each jet velocity ratio. Linear interpolation is used to determine correlation values for the plate at any V_j/V_∞, β, and r/D values for which correlation curves have not been determined. Some results are described in the following section.

RESULTS

The predicted potential pressure distribution on the upstream side of a jet is compared with experiment in figure 5. At a low velocity ratio ($V_j/V_\infty = 2.2$), the comparison in figure 5(a) indicates that the blockage model alone is sufficient to give reasonable results in the region of the plate where viscous effects are small. This is in agreement with the jet velocity ratio limitations discussed in a previous section in connection with the entrainment model. Data comparisons using the blockage model alone and blockage plus entrainment model for $V_j/V_\infty = 8.0$ are shown in figure 5(b). Large entrainment effects exhibited at $V_j/V_\infty = 8.0$ improve the blockage alone results and show excellent agreement with data at $\beta = 0°$ and 30°. These results serve to illustrate the ability of the potential flow model to predict the pressure distribution on the plate in the absence of large viscous effects.

Correlation curves for a flat plate were determined for jet velocity ratios 1.0, 1.67, 2.2, 3.33, 3.9, 5.0, 6.1, 8.0, 10.0, and 12.0. The correlation values were determined at $\beta = 0°$, 30°, 60°, 90°, 120°, 150°, and 180° and r/D = 0.75, 1.0, 1.5, 2.0, 3.0, and 5.0. Figure 6 shows the correlation curves which are used to obtain predicted pressure distributions for $V_j/V_\infty =$ 3.33 and 10.0. Correlation curves for the other jet velocity ratios are found in reference 11.

The systematic variation of $(\Delta C_p)_{viscous}$ seen in figure 6 is typical of that seen at each velocity ratio; however, the actual shape of each correlation curve changes somewhat with changing velocity ratio. The correlation factors are presented as a function of β for constant radius values because the systematic nature of the $(\Delta C_p)_{viscous}$ values is more obvious than when presented as a function of radius for constant β values.

An attempt was made to collapse all the correlation curves at a given velocity ratio onto a single curve, but this effort was not successful. It proved impossible to find a common normalizing parameter which was applicable for all velocity ratios. As a result of this investigation, the correlating

factors were maintained in data base form as shown in figure 6. Any required factor can be obtained by interpolating between curves at a given velocity ratio and interpolating between velocity ratios.

The pressure prediction method, made up of the blockage model, the entrainment model, and the viscous correction factor, will now be applied to two flow conditions for which data are available for comparison. The available data are the same data used to develop the viscous correlation factors; thus the quality of the agreement in reality depends on the degree of agreement between different sets of data. It would be more useful to compare the prediction method with independent data, but adequate additional data are not available at the present time. Additional flat plate data will soon be available from Ames Research Center. These data will be compared with results from the prediction method as a check of the accuracy of the method. Then the data will be included in the correlation to improve the viscous correlation factors.

Data comparisons of C_p vs. r/D at β = constant for V_j/V_∞ = 3.33 and 10.0 are presented in figures 7 and 8, respectively. In figure 7, predicted pressure distributions with and without the correlation correction are included to illustrate the effect of the correction factor at various positions around the jet. The uncorrected results are not shown in figure 8.

Varying degrees of success were obtained using the data correlation prediction method. As mentioned above, the success is dependent on how well the various sets of data agree with one another. In regions where the data sets are in good agreement, the prediction method results agree well with all experimental results. In general, comparisons with data are in good agreement over a wide range of flow conditions.

An interesting means of comparing measured and predicted results is to compare the total force and distribution of force on a finite plate with the jet at its center. The normal force is obtained by integrating pressures on a circular finite plate whose diameter is dependent on the location of the outermost data points. The circle is divided into sectors and segments, as shown in figure 9(a), and the pressure coefficient at the area centroid of each of these segments is used to determine a force on that segment. These forces are summed to obtain a total normal force, and moments are taken about the Y-axis to obtain a pitching moment. The positive sense of the normal force and pitching moment is shown in figure 9(b). The measured and predicted force and moment coefficients are compared in figure 10.

A circular plate with a radius of 5.5 jet diameters was used to obtain results for the references 1 and 4 data comparisons. A smaller plate with a radius of 4.25 jet diameters was used for the reference 5 comparisons. The good agreement for both normal force and pitching moment coefficients indicates that, while the correlation method pressure distribution results are not in perfect agreement with experiment, the method produces accurate integrated force and moment results.

CONCLUDING REMARKS

A correlation method was developed to include viscous effects in the predicted pressures on an infinite flat plate from which a jet is issuing into a subsonic crossflow. Correlation values of viscous induced pressure coefficients were defined as the difference between pressures predicted by a potential model and those obtained from experimental data. Jet blockage and entrainment effects were accounted for in the potential model using a vortex quadrilateral panel model and a sink distribution model, respectively. The viscous effects of the jet were represented by the correlation values.

Comparisons of measured and predicted plate pressures in the vicinity of normal jets ($\theta = 0°$) over a wide range of jet velocity ratios were generally good. Comparisons of measured and predicted normal-force and pitching-moment coefficients on a finite plate were also in good agreement.

The correlation method described in this report could be improved and made more general in several areas. The first improvement to the method as it exists now would be the infusion of additional data at the same flow conditions used to determine the present correlation factors. This would verify the factors and give additional confidence in their application to pressure prediction in the vicinity of jets exhausting from a plate. Also, if additional data were available which had a systematic variation of parameters including jet inclination angle, jet Mach number, and plate Reynolds number, these parameters could be included in the correlation curves.

REFERENCES

1. Vogler, R. D.: Surface Pressure Distributions Induced on a Flat Plate by a Cold Air Jet Issuing Perpendicularly from the Plate and Normal to a Low-Speed Free-Stream Flow. NASA TN D-1629, Mar. 1963.

2. Bradbury, L.J.S. and Wood, M.N.: The Static Pressure Distribution Around a Circular Jet Exhausting Normally from a Plane Wall Into an Airstream. Aeronaut. Res. Council C.P. No. 882, Aug. 1965.

3. Ousterhout, D.S.: An Experimental Investigation of a Cold Jet Emitting from a Body of Revolution into a Subsonic Free Stream. NASA CR-2089, Aug. 1972.

4. Fearn, R.L. and Weston, R.P.: Induced Pressure Distribution of a Jet in a Crossflow. NASA TN D-7916, June 1975.

5. Mosher, D.K.: An Experimental Investigation of a Turbulent Jet in a Cross Flow. Georgia Inst. of Tech. Rept. GIT-AER-70-715, Dec. 1970 (Ph.D. Thesis).

6. Dietz, W.E., Jr.: A Method for Calculating the Induced Pressure Distribution Associated with a Jet in a Crossflow. NASA CR-146434, 1975.

7. Yeh, B.T.: Calculation of the Pressure Distribution Induced by a Jet on a Flat Plate. ESRO-TT-159, May 1975.

8. Heltsley, F.L. and Parker, R.L., Jr.: Application of the Vortex Lattice Method to Represent a Jet Exhausting from a Flat Plate into a Crossflowing Stream. AEDC-TR-73-57, June 1973.

9. Hackett, J.E. and Miller, H.R.: A Theoretical Investigation of a Circular Lifting Jet in a Cross-Flowing Mainstream. AFFDL-TR-70-170, Jan. 1971.

10. Chang, H.S. and Werner, J.E.: Analysis of an Entrainment Model of the Jet in a Crossflow. NASA CR-132324, Nov. 1972.

11. Perkins, S.C., Jr. and Mendenhall, M.R.: A Correlation Method to Predict the Surface Pressure Distribution on an Infinite Plate from which a Jet is Issuing. NASA CR-152160, May 1978.

12. Margason, R.J.: The Path of a Jet Directed at Large Angles to a Subsonic Free Stream. NASA TN D-4919, Nov. 1968.

13. Maskew, B.: Calculation of the Three-Dimensional Potential Flow Around Lifting Nonplanar Wings and Wing-Bodies using a Surface Distribution of Quadrilateral Vortex Rings. Report TT-7009, Loughborough University of Technology, Sept. 1970.

14. Keffer, J.F. and Baines, W.D.: The Round Turbulent Jet in a Cross-Wind. J. Fluid Mech., Vol. 15, Pt. 4, Apr. 1963, pp. 481-497.

15. Fearn, R.L. and Weston, R.P.: Vorticity Associated with a Jet in a Crossflow. AIAA Journal, Vol. 12, No. 12, Dec. 1974, pp. 1666-1671.

16. Kamotani, Y. and Greber, I.: Experiments on a Turbulent Jet in a Cross Flow. AIAA Journal, Vol. 10, No. 11, Nov. 1972.

17. Pratte, B.D. and Baines, W.D.: Profiles of the Round Turbulent Jet in a Cross Flow. J. Hydraulics Div., Proceedings of the ASCE, Vol. 92, No. HY6, Nov. 1967, pp. 53-64.

18. Camelier, I., Karamcheti, K., and Hodder, B.: An Experimental Study of the Structures and Acoustic Field of a Jet in a Cross Stream. AIAA Paper No. 75-460, Mar. 1975.

19. Bowley, W.W. and Sucec, J.: Trajectory and Spreading of a Turbulent Jet in the Presence of a Crossflow of Arbitrary Velocity Distribution. Presented at 14th Annual Gas Turbine Conference and Products Show, ASME Paper 69-GT-33, Mar. 1969.

20. Abramovich, G.N.: The Theory of Turbulent Jets. M.I.T. Press, 1963.

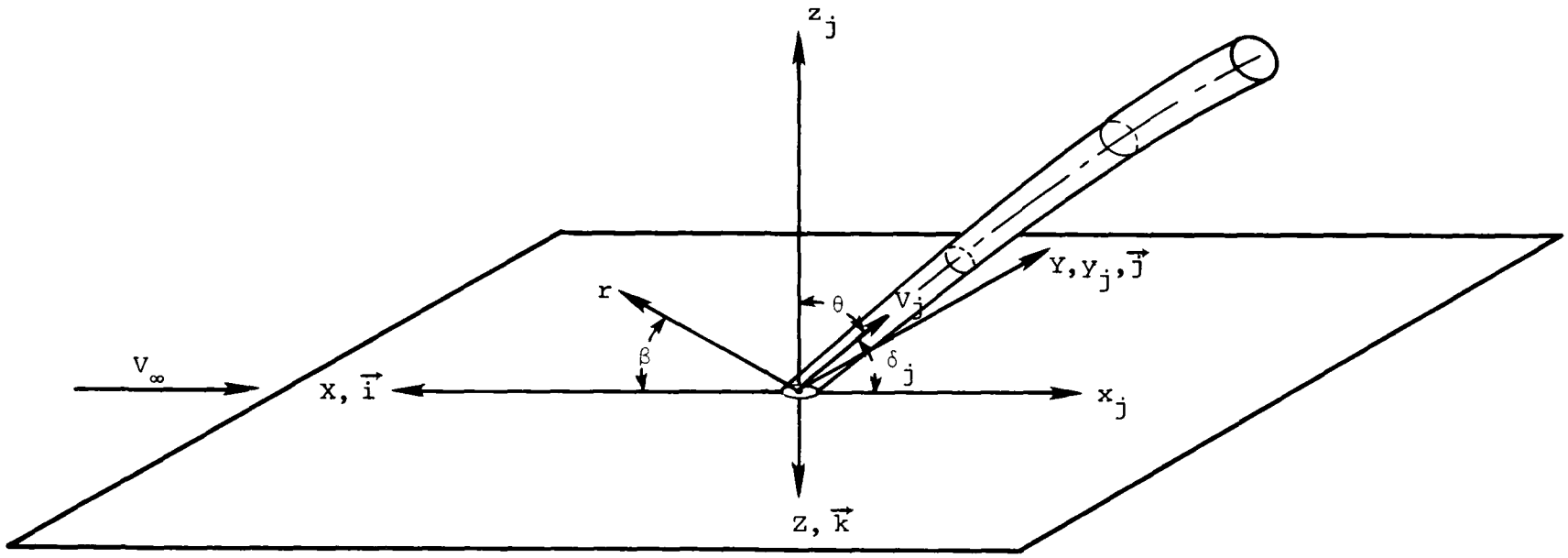

Figure 1.- Coordinate system for a jet issuing from a flat plate into a subsonic crossflow (isometric view).

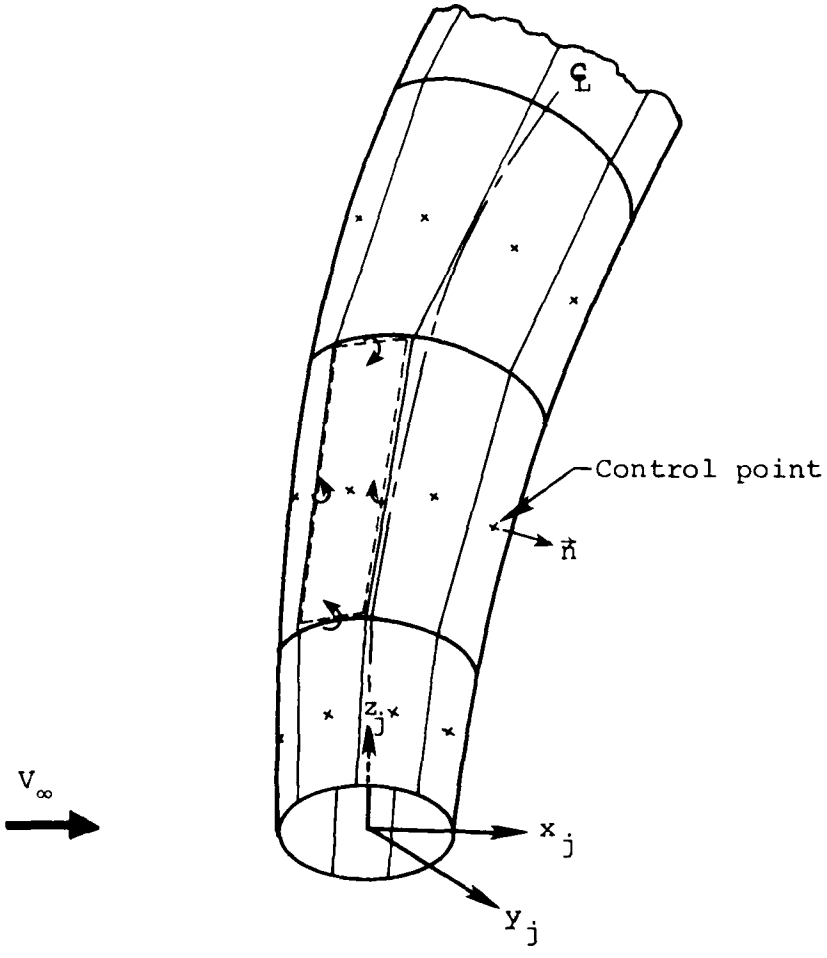

Figure 2.- Vortex quadrilaterals on wake surface.

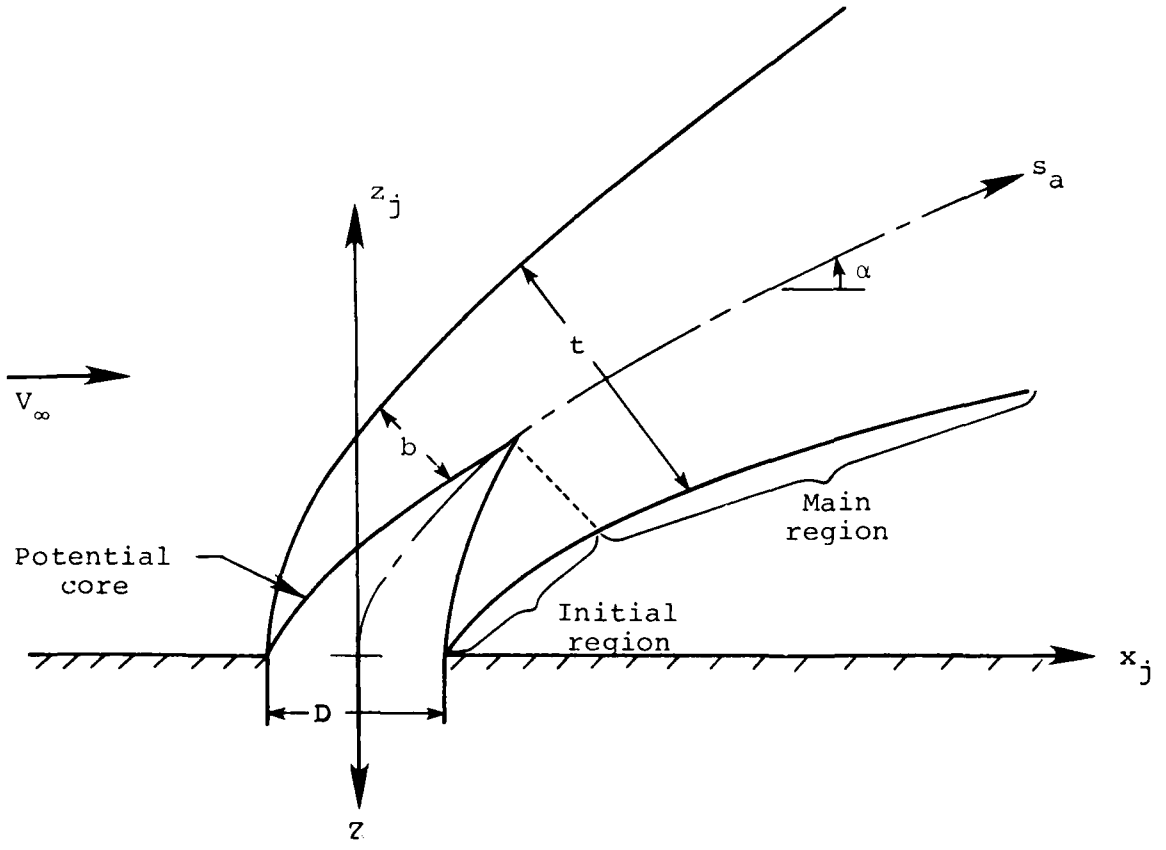

Figure 3.- Side view of an expanding jet indicating initial and main regions.

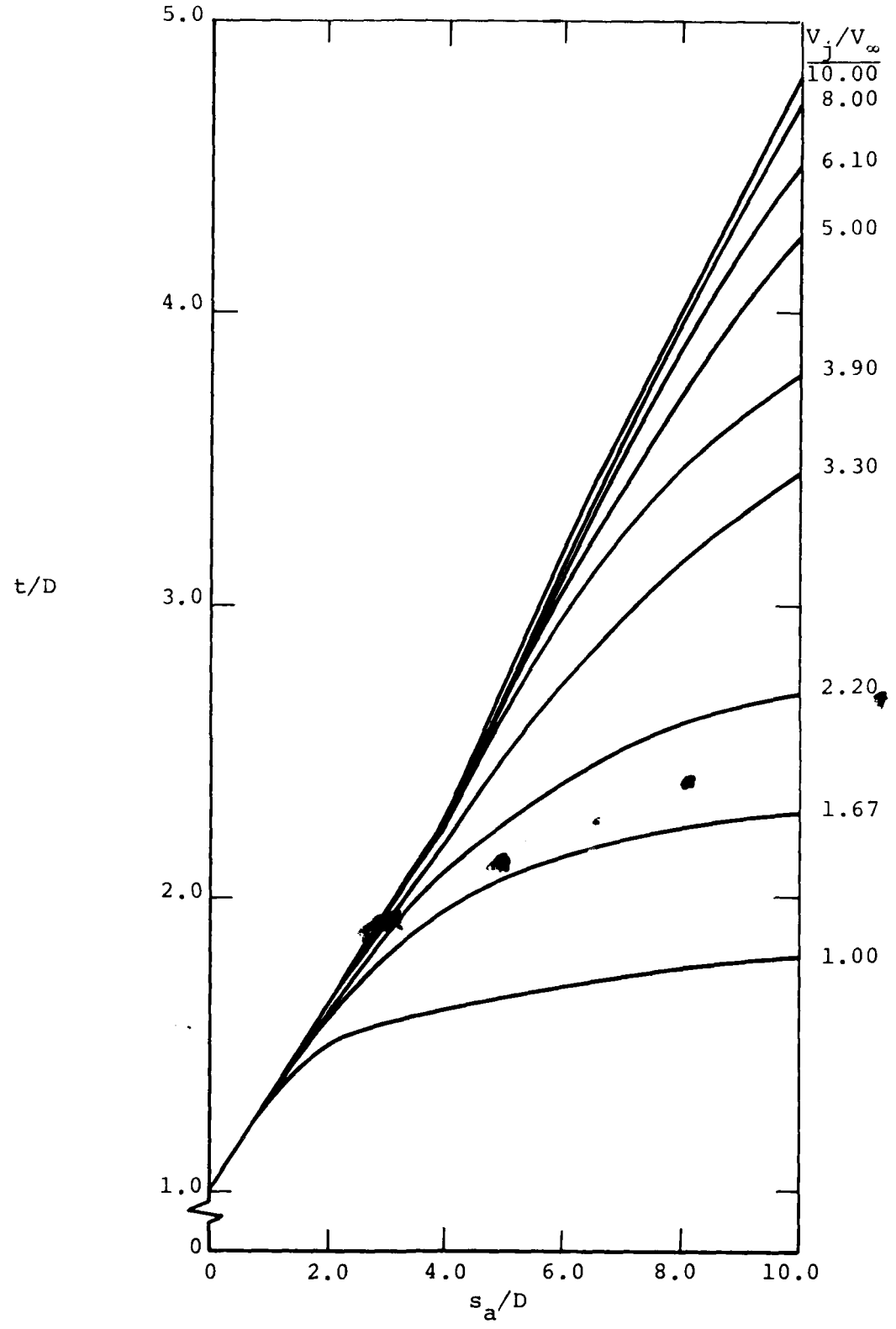

Figure 4.- Jet expansion curves.

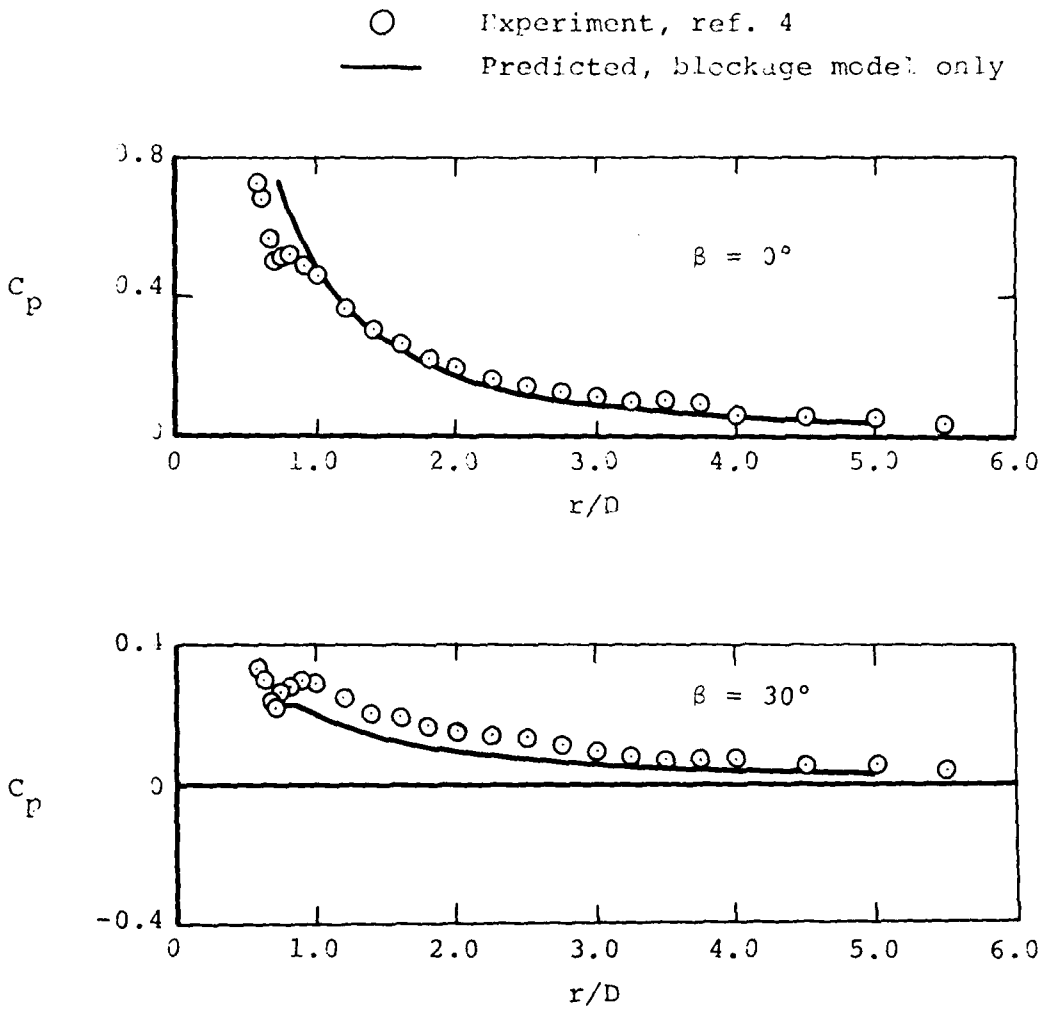

(a) $V_j/V_\infty = 2.2$

Figure 5.- Comparison of measured and predicted pressure distribution.

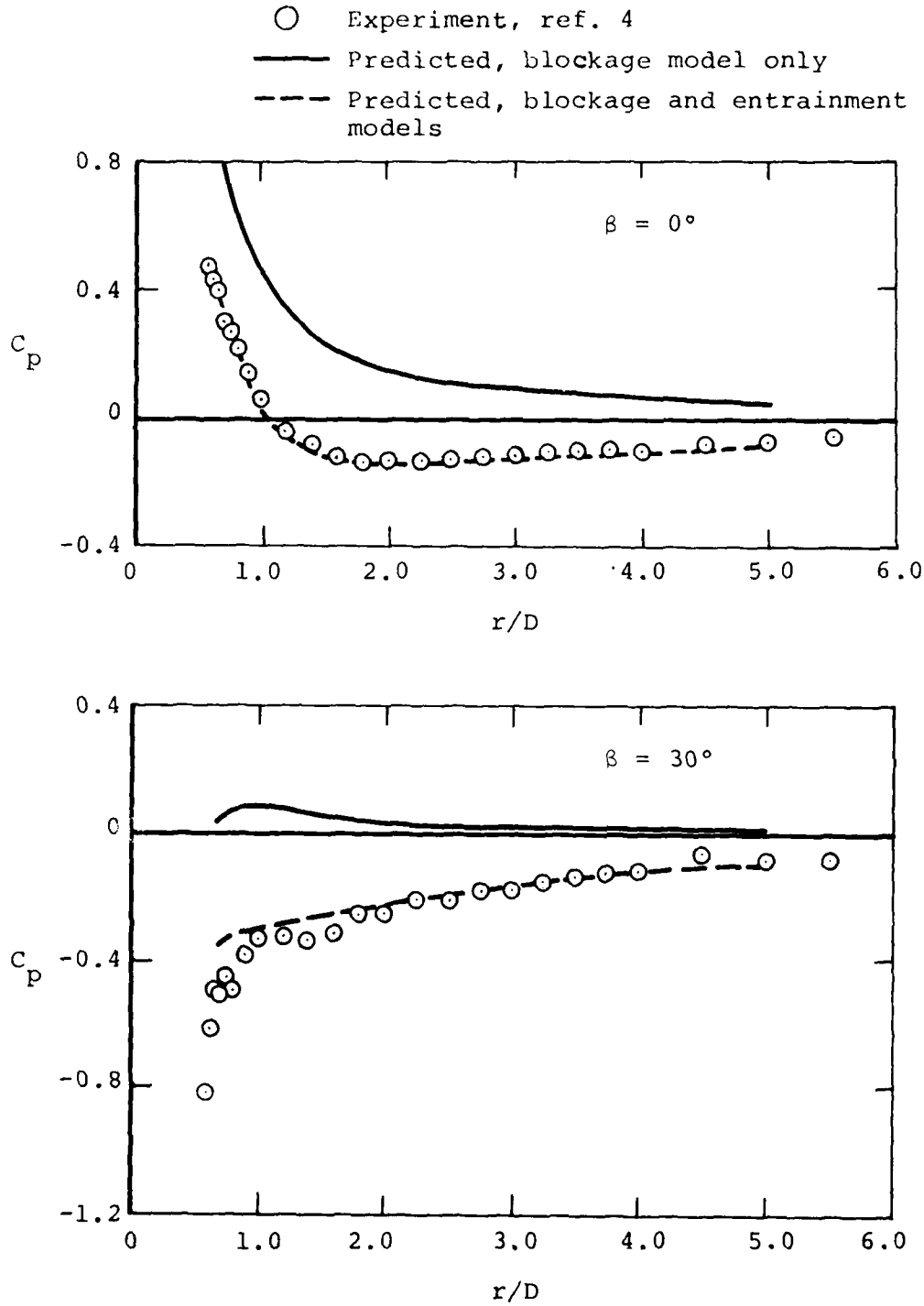

(b) $V_j/V_\infty = 8.0$

Figure 5.- Concluded.

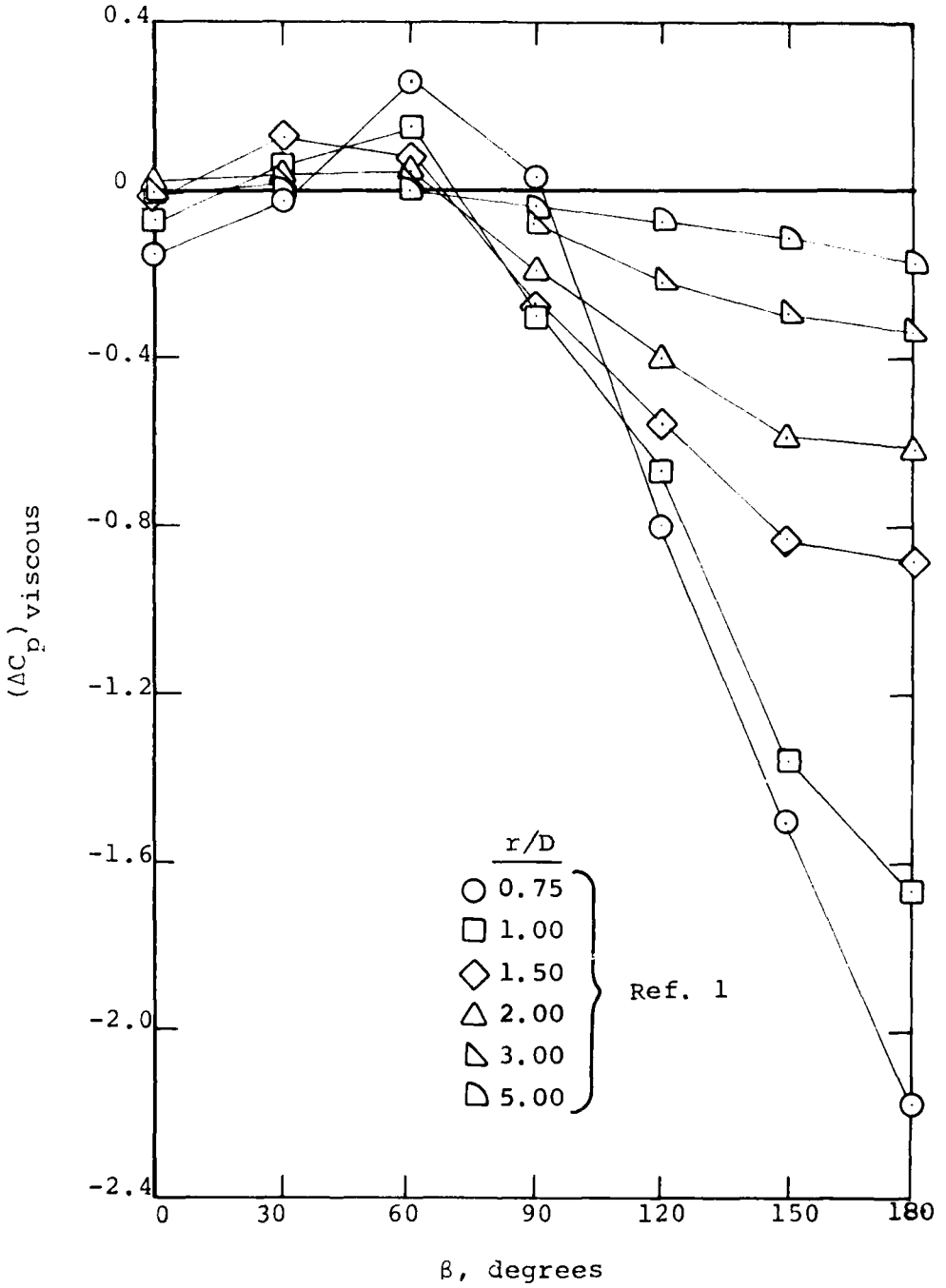

(a) $V_j/V_\infty = 3.33$

Figure 6.- Correlation factor for viscous portion of the pressure coefficient induced on a flat plate by a jet exhausting into a crossflow, $\theta = 0^o$.

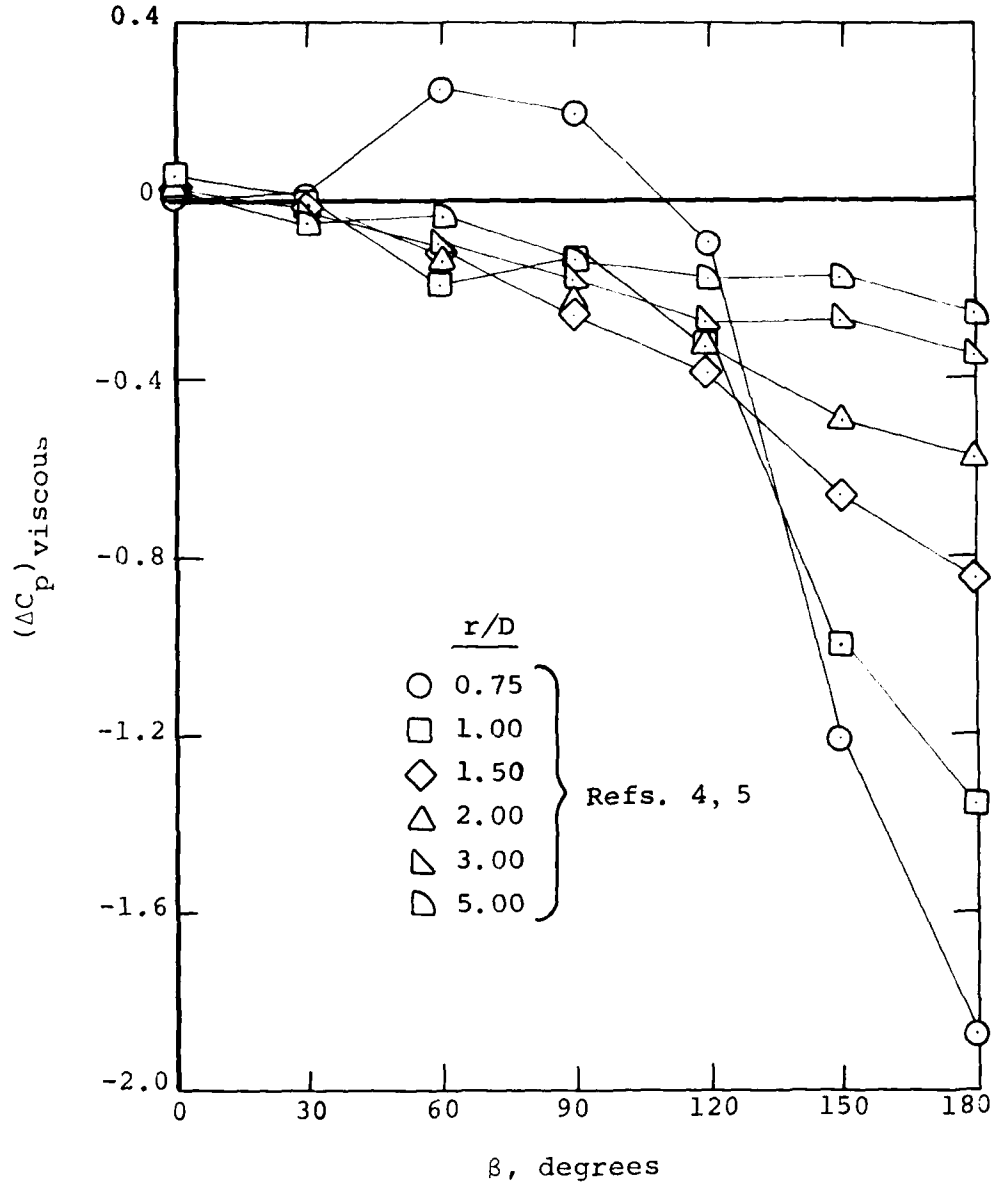

(b) $V_j/V_\infty = 10.0$

Figure 6.- Concluded.

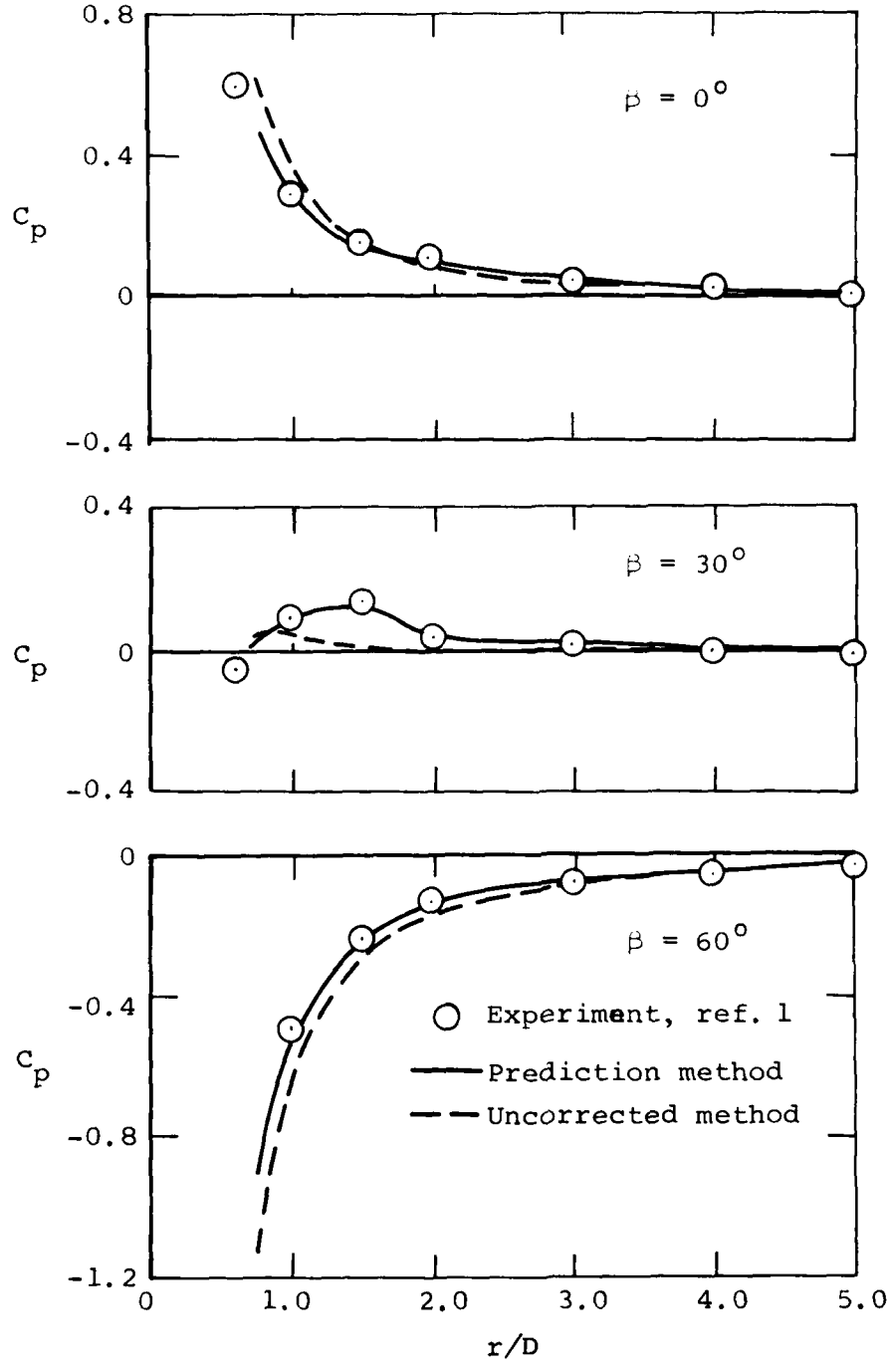

Figure 7.- Comparison of measured and predicted plate pressure distribution, $V_j/V_\infty = 3.33$.

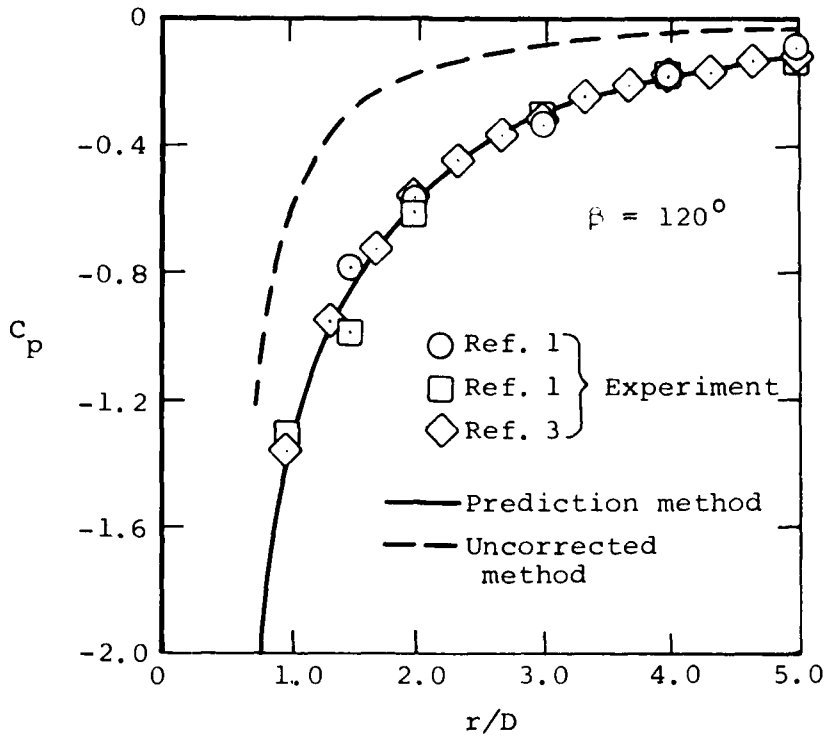

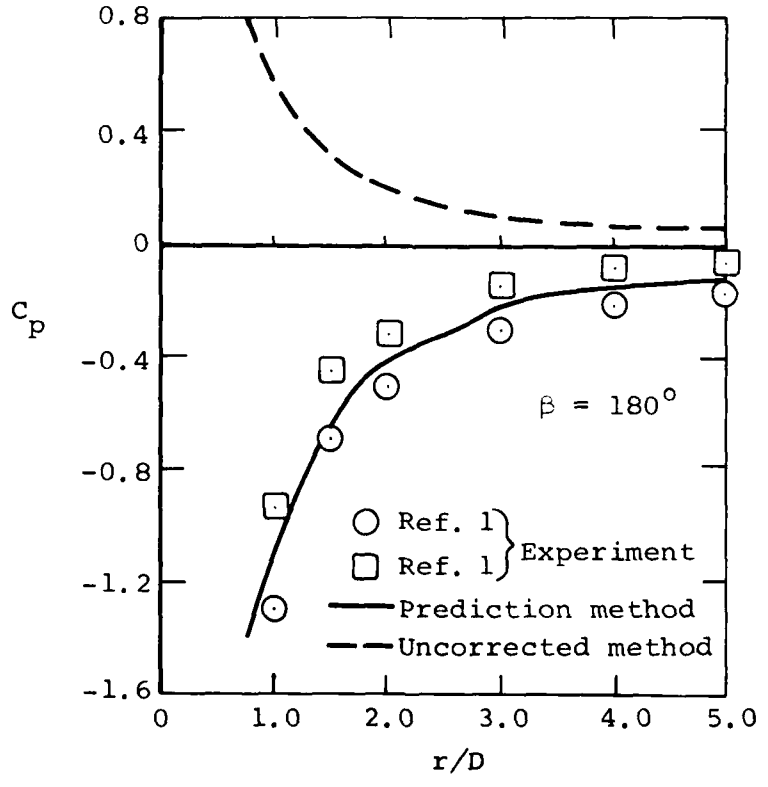

Figure 7.- Concluded.

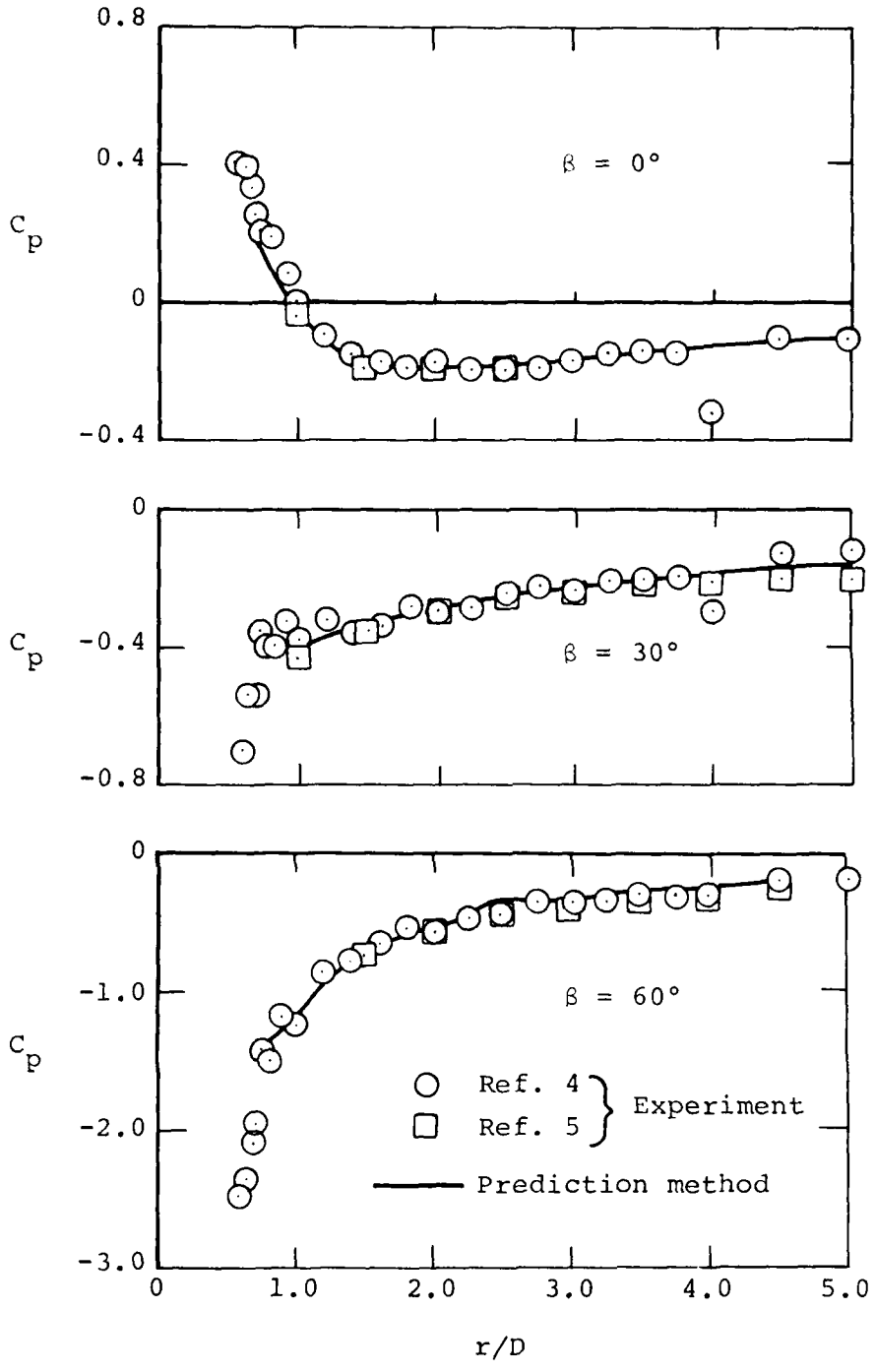

Figure 8.- Comparison of measured and predicted plate pressure distribution, V_j/V_∞ = 10.0.

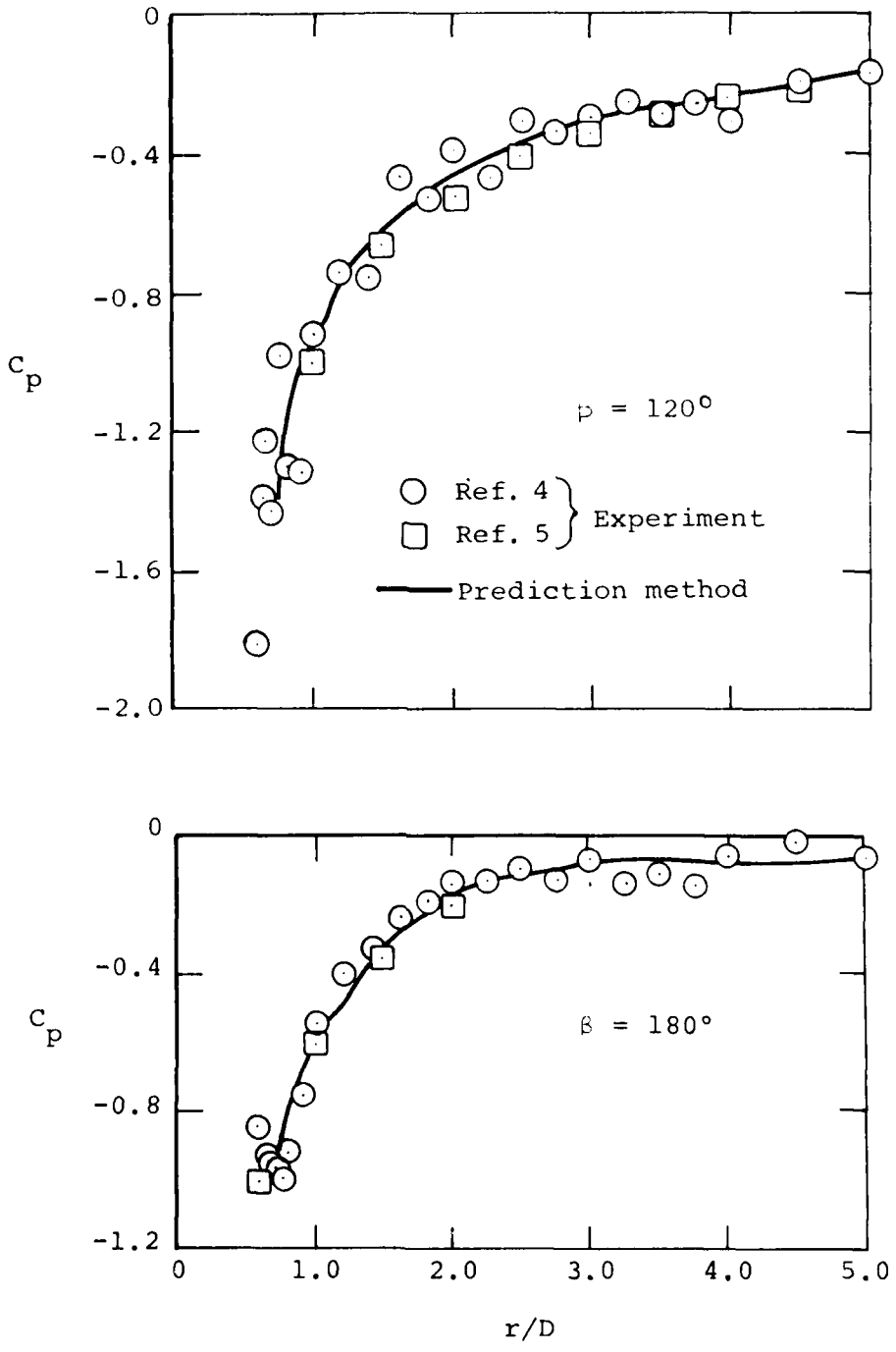

Figure 8.- Concluded.

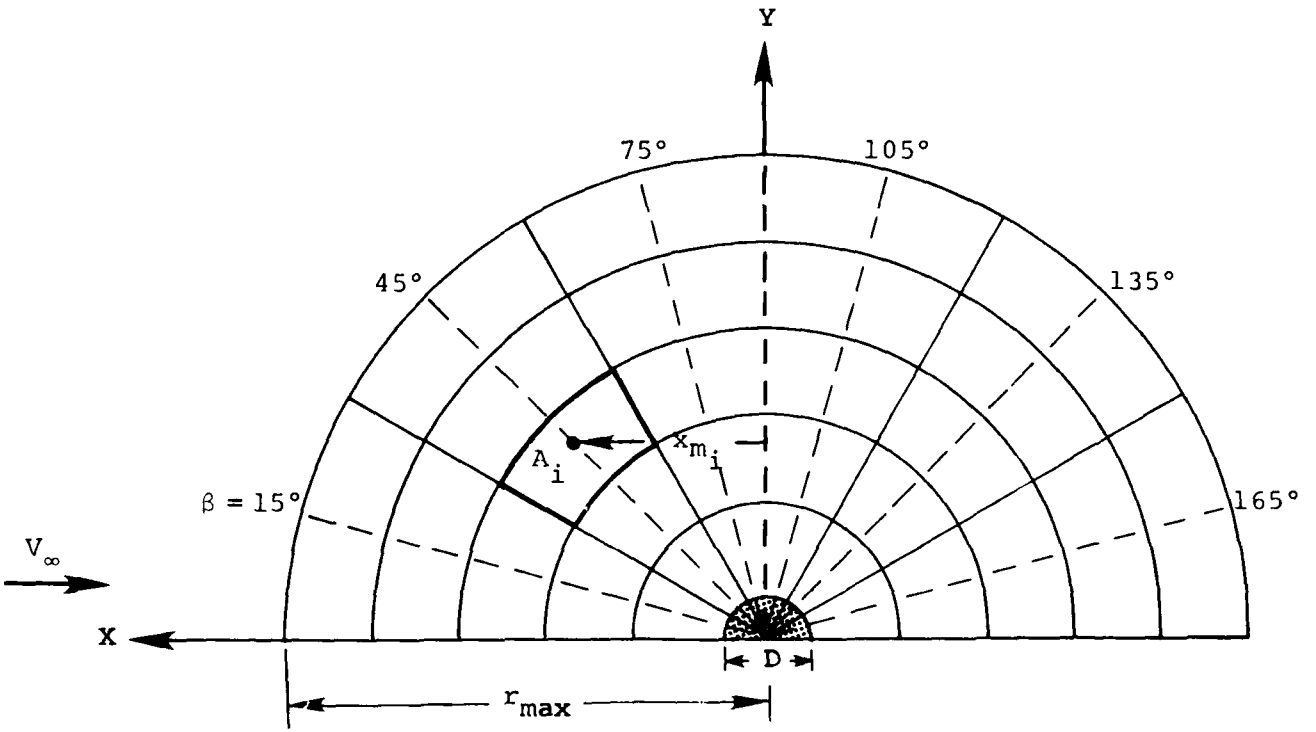

(a) Typical grid layout.

Figure 9 .- Finite circular plate.

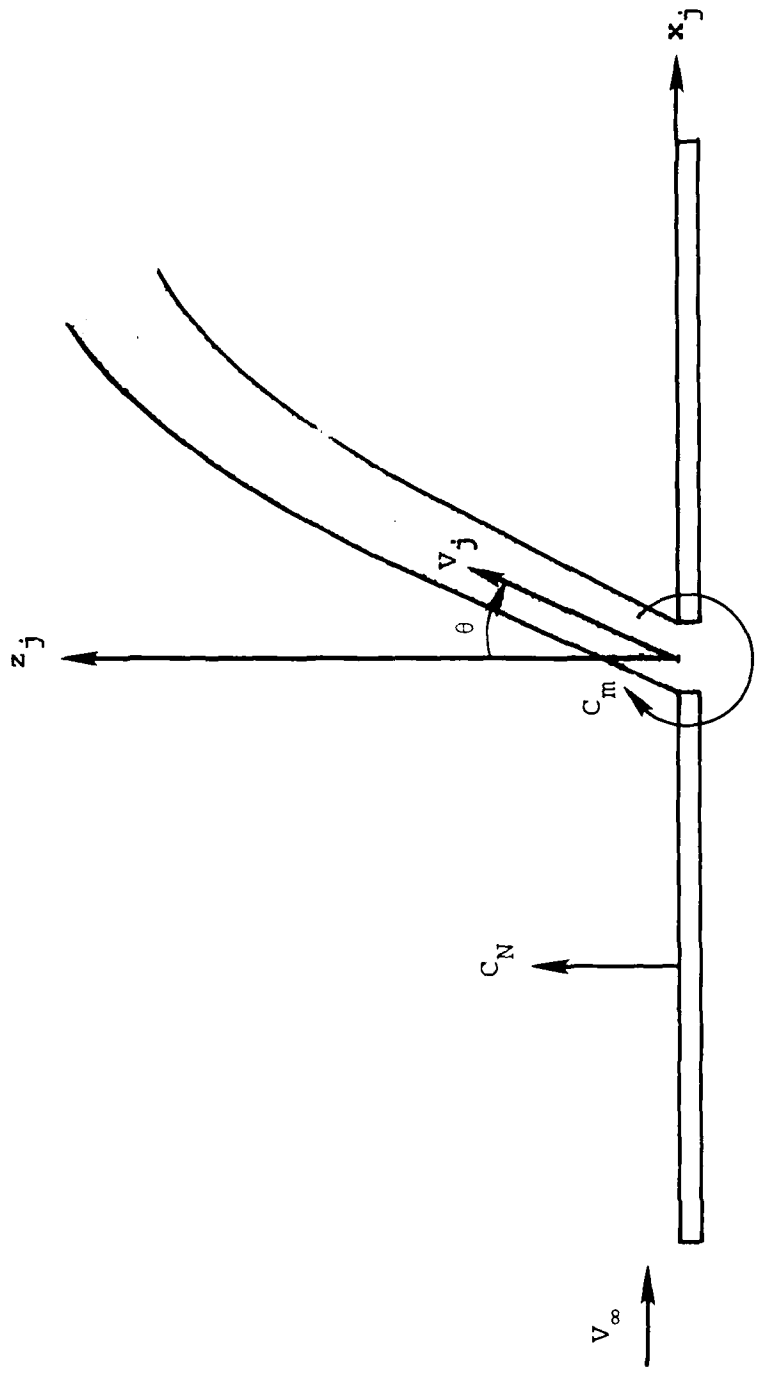

(b) Force and pitching moment nomenclature.

Figure 9.- Concluded.

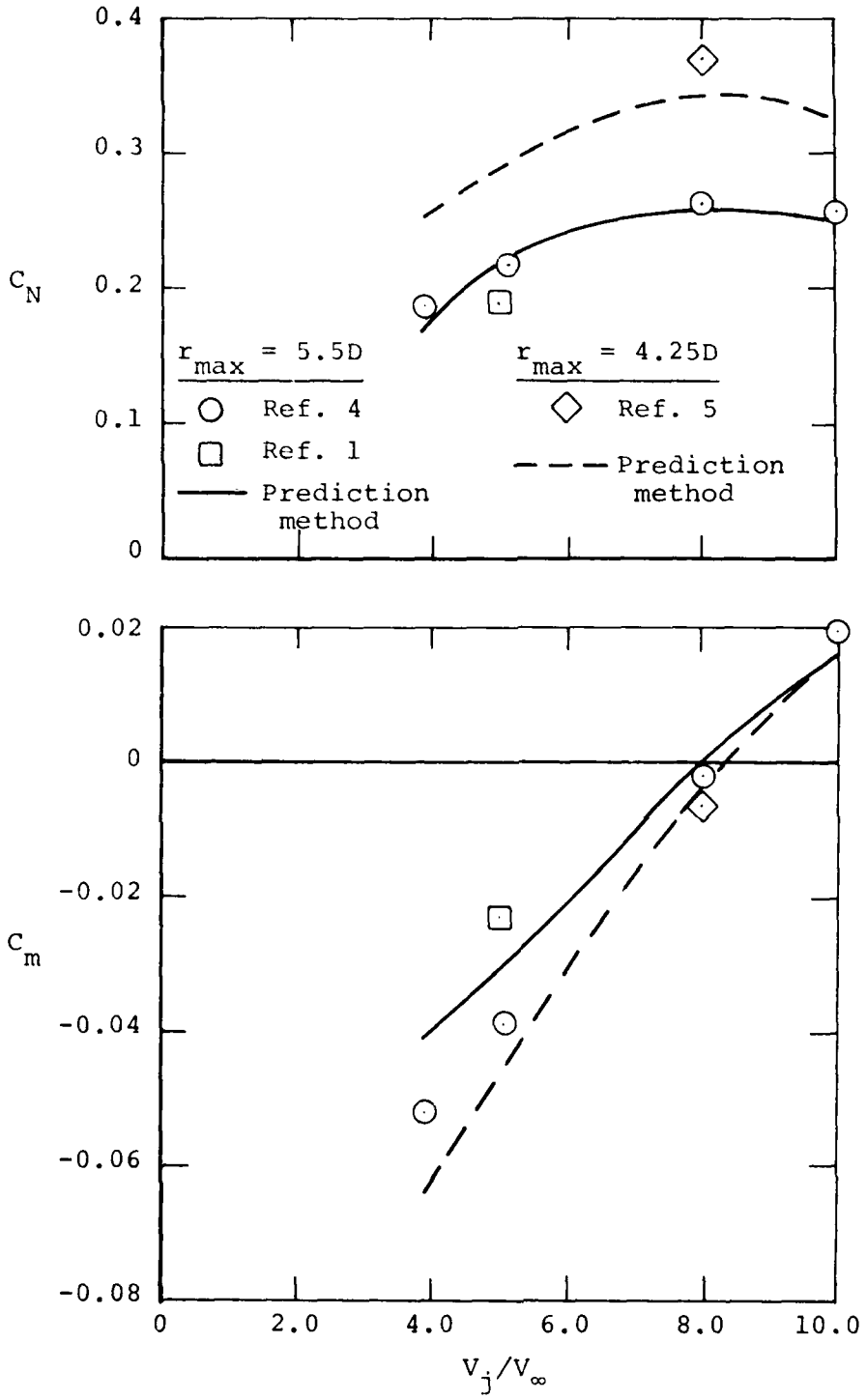

Figure 10.- Comparison of normal force and pitching moment on a plate obtained from measured and predicted pressure distributions.

PROPULSION-INDUCED EFFECTS ON A SUPERSONIC VSTOL FIGHTER/ATTACK AIRCRAFT

P.T. Wooler
Northrop Corporation, Aircraft Group
Hawthorne, California

Abstract

Propulsion-induced longitudinal and lateral aerodynamic characteristics have been evaluated for a supersonic VSTOL fighter/attack aircraft. The clipped delta wing configuration features close-coupled canard surfaces mounted on 2-D side inlets. The primary engine nozzles are vectorable 2-D nozzles, with the direct lift mode the bypass air from both engines feed a single remote augmentor nozzle, located in the nose.

Jet-induced aerodynamic characteristics for thrust vectoring to maneuver in the cruise/combat regime and for the transition flight phase have been evaluated by determining the jet-induced flow field and computing forces and moments due to the induced flow field. The jet-induced flow field is obtained by utilizing an entrainment model for jets exhausting into a crossflow, which solves continuity and momentum equations for the jet path and represents the entrainment and blockage effects of the jet with a sink-doublet singularity distribution. Jets of initial elliptical cross section serve as an approximation to the rectangular cross-section jets from the 2-D primary nozzles.

Forces and moments are computed by employing a vortex-lattice method of representing lifting planforms. To determine power-induced longitudinal aerodynamic characteristics, a camber distribution is introduced on the planform to satisfy flow tangency conditions in the presence of the jet-induced velocity field. Induced rolling moments for the configuration in a cross-wind condition are obtained by imposing asymmetric cambering on the planform to reflect the asymmetry of the induced flow field. In the transition flight phase, corrections for the jet wake effect from the lift jet are applied.

Symbols

A_j	jet cross-sectional area
A_{j_1}	total exit area of two primary engines
A_{j_2}	exit area of remote augmentor nozzle
b	wing span
$\bar{c}$	mean aerodynamic chord
C	circumference of jet cross section
C_D	crossflow drag coefficient of jet
C_T	thrust coefficient
d	length of major axis in elliptical representation of jet cross section
d_0	jet exit diameter
E_1, E_2, E_3	entrainment coefficients
F_1	main engine thrust
F_2	forward nozzle thrust

AD-A079 115 NAVAL AIR DEVELOPMENT CENTER WARMINSTER PA F/G 1/3
PROCEEDINGS OF A WORKSHOP ON V/STOL AIRCRAFT AERODYNAMICS. VOLU--ETC(U)
MAY 79 C HENDERSON, M F PLATZER

UNCLASSIFIED NL

3 OF 7
AD
A079115

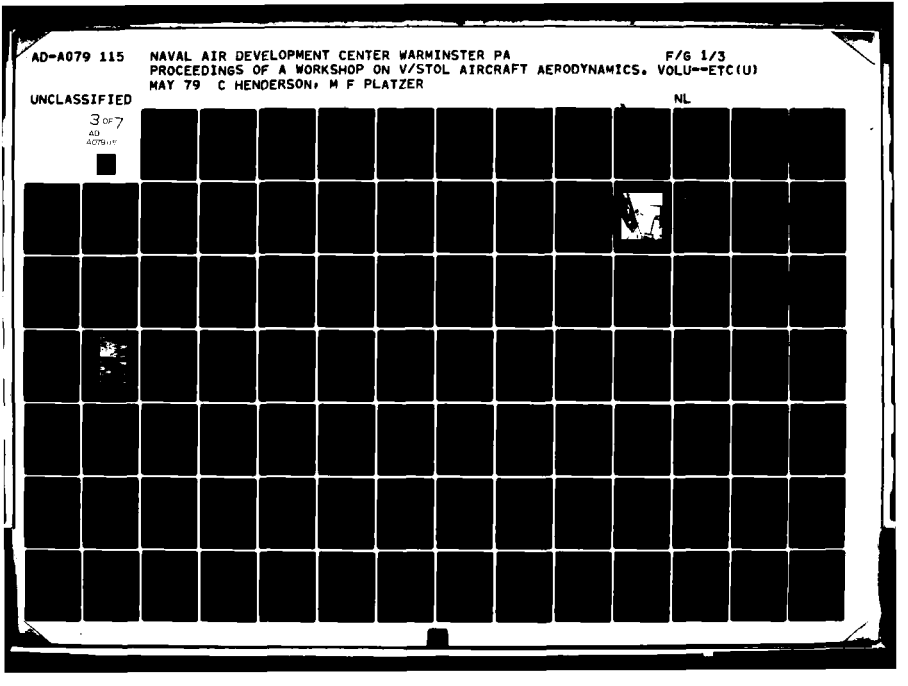

q_∞	freestream dynamic pressure
q_e	effective freestream dynamic pressure
R	local jet radius of curvature
s	coordinate along jet centerline; distance between jet exits
S	wing reference area
T	total thrust
U_∞	freestream speed
U_j	mean jet speed
U_{jo}	jet exit speed
ΔC_L	induced lift coefficient
ΔC_m	induced pitching moment coefficient
ΔC_ℓ	induced rolling moment coefficient
ΔL	induced lift
α	angle of attack
β	angle of sideslip

Introduction

VSTOL concepts being investigated for Navy missions employ various arrangements of lift and/or lift/cruise engines. The interaction of the propulsion system exhaust with the freestream can have a significant effect on the aerodynamics of the aircraft. Propulsion-induced forces and moments, which are a function of jet efflux geometry and arrangements relative to aerodynamic surfaces, affect the performance, stability and control requirements of the aircraft.

Vectoring the nozzles for maneuvering at angle of attack increases the angle between the vectoring lift/cruise engine efflux and the freestream and tends to magnify these interaction effects. During the transition phase, when the aircraft is not yet fully supported by the aerodynamic forces on the wing as in conventional flight, the jets are directed at large angles to the freestream, leading to significant propulsion-induced forces and moments. Propulsion system interactions with a non-uniform crossflow, typical during initial and final flight phases in carrier-based operations where perturbations due to flow off the superstructure may be present, can further magnify these interference effects.

In this paper, an approach to evaluating propulsion-induced aerodynamic characteristics by determining the jet-induced flow field and computing the forces and moments due to the induced flow field is presented. This approach will be applicable to future Navy aircraft which employ lifting jet and/or vectored thrust concepts.

Discussion of Approach

The approach presented here evolves from a technology base of analytical engineering methods developed at Northrop for use by design personnel during the preliminary design and evaluation of VSTOL aircraft.

Due to the complexity of the problem of predicting the propulsion-induced effects on VSTOL aircraft, Northrop's approach is to develop the methods in modular form. This allows for easier updating of the modular elements as progress is made in the component technical areas. The modular approach also permits the selection of a combination of modules to satisfy the need for

engineering methods which may be used in the early stages of design. Northrop's modular approach is summarized below:

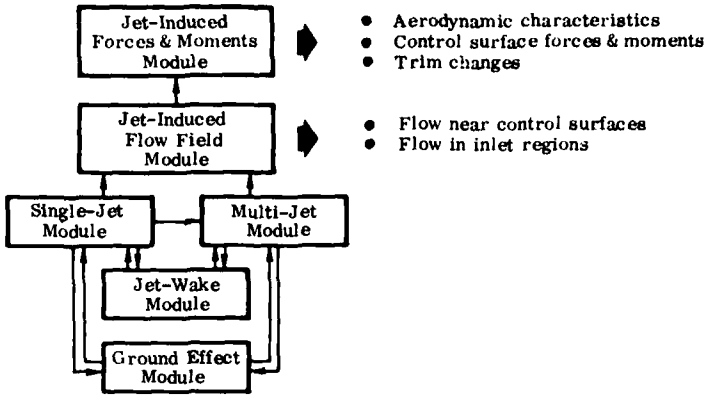

By employing a sequential operation, rather than having combined the computational procedures directly, any component in the sequence may be replaced to incorporate improvements in the theoretical models as they may be developed further.

Determination of Jet-Induced Flow Field

The entrainment model of Reference 1, which has been utilized extensively in predicting aerodynamic interference effects on adjacent lifting surfaces in References 2-4, has been employed in the evaluation of the jet-induced flow field.

Circular Jet Model. Consider a circular jet exhausting at a right angle into a uniform freestream, as shown below:

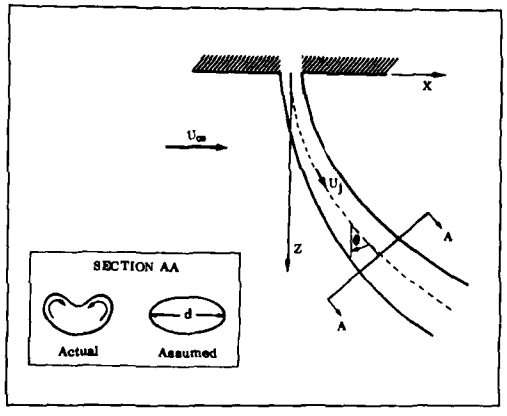

The jet model is incompressible and neglects viscous effects other than the entrainment caused by this mechanism. The entrainment of mainstream fluid into the jet and the pressure forces on the jet boundary govern the equations of motion of the jet, which can be written using the coordinate system above,

continuity $$\rho(d/ds)(A_jU_j) = E \tag{1}$$

momentum $$\rho(d/ds)(A_jU_j^2) = EU_\infty \sin\theta \tag{2}$$

force $$\rho A_jU_j^2/R = EU_\infty\cos\theta + C_D\tfrac{1}{2}\rho U_\infty^2\cos^2\theta\, d \tag{3}$$

$$= \rho A_jU_j^2X'/\left[1 + (X')^2\right]^{3/2}$$

where the entrainment of mainstream fluid into unit length of the jet is assumed to be:

$$E = \rho E_1U_\infty d\cos\theta + \frac{\rho E_2(U_j - U_\infty\sin\theta)C}{1 + E_3U_\infty\cos\theta/U_j} \tag{4}$$

The entrainment parameters E_1, E_2, E_3 of Equation(4) were obtained from test data. A functional relationship between the cross-sectional area of the jet and the jet growth is established, based on experimental observations of the jet development. An ellipse with a ratio of minor to major axis of 1/4 is chosen to represent the fully developed region of the jet. In the development region, the ratio of minor to major axis decreases linearly with distance from the jet orifice.

After substitution of these geometric relationships into Eqs 1-3, a set of differential equations for U_j^*, d^*, X^*, is obtained in terms of Z^*, the entrainment coefficients, and the crossflow drag coefficient used to account for the net force acting on the jet boundary as a result of the pressure differential around the jet. U_j^*, d^*, X^* are the mean jet speed, jet diameter and displacement of the jet centerline in nondimensionalized form. With initial conditions at the jet exit given, the equations of motion can now be integrated for a specified jet exit velocity ratio, $m = U_{j_0}/U_\infty$.

Although the equations of motion for the jet model of Reference 1 were written for a jet exhausting normally into a crossflow, they are valid for any jet, in a local coordinate system oriented with the X axis in the freestream direction and the XZ plane defined by the freestream flow vector and the jet exhaust vector. Thus, the jet model is seen to be general with respect to jet exhaust angle, angle of attack, and sideslip.

To obtain the induced velocity field due to the jet interference, the entrained fluid is represented by a uniform sink distribution along an axis normal to the freestream. The integrated strength of this sink distribution is given by Equation(4). The blockage effect of the jet is represented by a doublet distribution along the jet centerline. The strength of this distribution of doublets is obtained from the coefficient of the $1/\bar{z}$ term in the complex velocity potential expansion $W(\bar{z})$ for the two-dimensional flow past an ellipse. From these sink and doublet distributions, the jet-induced velocity components at a given point external to the jet can now be evaluated by integrating over the extent of the jet.

Jet in Non-Uniform Crossflow. For the purpose of treating non-uniform crossflow, a scheme that treats the exhausting jet in a number of segments can be employed, as shown in the following sketch. Velocities $\bar{u}_1$, $\bar{u}_2$ are perturbations which, when combined with the constant crossflow $\bar{U}_\infty$, create a non-uniform crossflow.

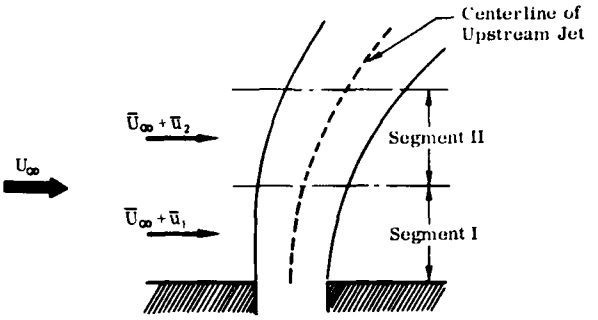

The direction cosines of the freestream vector, $\bar{U}_\infty+\bar{u}_1$, are determined and the local coordinate system aligned with the freestream vector anf the jet exhaust vector is established for segment I. Using the effective jet exit velocity ratio for segment I, the equations for U_j^*, d^*, X^* may now be integrated over the extent of segment I.

The last point of segment I then becomes the origin of the next segment (i.e., next discrete jet) with a diameter $d_{O_2} = d_1^* d_{O_1}$, where d_1^* is the last computed value of the non-dimensionalized jet diameter in segment I.

At this point the direction cosines of $\bar{U}_\infty+\bar{u}_2$ are determined and a new local jet-oriented coordinate system is established. The initial value for dX^*/dZ^* is determined in this coordinate system from the known direction of the jet centerline at the end of segment I. The effective jet exit velocity ratio for segment II is:

$$m_{2eff} = \frac{U_{jo_2}}{U_\infty}\left(\frac{U_\infty}{U_\infty + u_2}\right) = U_{j_1}^* m_1 \left(\frac{U_\infty}{U_\infty + u_2}\right) \qquad (5)$$

The equations for mean jet speed, jet diameter and centerline displacement in non-dimensionalized form may now be integrated over the extent of segment II.

After integration over the extent of the entire jet, the flow field induced by the jet can now be determined by replacing the jet (i.e., the number of discrete jet segments) by the representative singularity distribution of sinks and doublets.

Two-Jet Model. The basic single-jet analytical model has been applied to the computation of the interaction flow field due to a two-jet configuration in Reference 2. A two-jet configuration is treated as a combination of discrete jets. The equations of motion for each of the two exhausting jets are integrated utilizing the appropriate initial conditions for each jet.

The upstream jet is assumed to develop independently of the downstream jet, and the downstream jet is assumed to exhaust into a crossflow of reduced dynamic pressure which it "sees" as the result of blockage by the upstream jet. Thus, the influence of the upstream jet on the downstream jet is introduced into the computations as a reduced freestream velocity, $U_e/U_\infty = (q_e/q_\infty)^{1/2}$, in the equations governing the development of the downstream jet. The extent of overlap between the two jets is the principal parameter in determining the degree of blockage experienced by the downstream jet. Test data of Reference 5 were used to obtain an empirical relationship for the dynamic pressure q_e which the downstream jet "sees" as the result of the crossflow blockage by the upstream jet, in terms of the crossflow dynamic pressure q_∞, and the spacing between the two

jets, s, as shown in the following schematic.

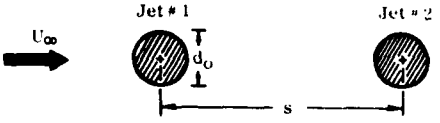

This empirical relationship is given in Reference 3 as

$$\sqrt{\frac{q_e}{q_\infty}} = \frac{s/d_o - 1}{s/d_o + .75} \qquad \{s/d_o > 1\} \tag{6}$$

and is used as a limiting value, when the computation of the overlap between the two jets shows that the downstream jet element is completely in the zone of influence of the upstream jet element (as, for example, in the case of two jets aligned in the crossflow direction). When the two jets are not aligned, an effective crossflow dynamic pressure, q_β (which is a weighted mean of q_e given above and q_∞), is utilized. The weighting of the dynamic pressure is determined from the degree of overlap between the upstream and the downstream jet elements as shown below.

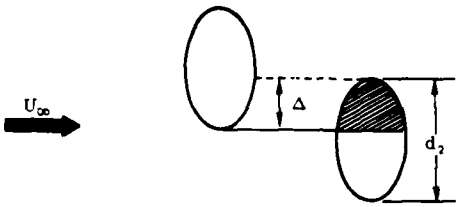

Thus,

$$\sqrt{q_\beta} = \frac{\Delta\sqrt{q_e} + (d_2 - \Delta)\sqrt{q_\infty}}{d_2} \tag{7}$$

As the equations of motion for the two exhausting jets are being integrated, the distance between the two jet centerlines is continually checked. When intersection of the two jets is indicated, initial conditions for the merged jet which results are determined from continuity and momentum considerations, as detailed in Reference 3. These intial conditions are then employed in integrating the set of differential equations for the merged jet.

The velocity field induced by a two-jet configuration can now be determined by replacing each jet (including the jet resulting from the coalescence of the two exhausting jets) by its representative singularity distribution of sinks and doublets.

By treating the two-jet configuration as a combination of discrete jets, the generality of the single-jet model with respect to angle of attack and sideslip is retained for each jet. However, in order to keep computational complexity involved in checking the overlap between the two jets along the jet path at a tractable level, the jet exhausts are constrained to lie in parallel planes. This has not proven to be a restriction in the treatment of practical aircraft configurations.

Non-Axisymmetric Jets. Correlation of test data indicates that the extent of the region in which a jet of initial circular cross section deforms into a kidney shape (represented here as an elliptical one) is a function of the jet exit to freestream velocity ratio, U_{j_0}/U_∞. The extent of this region may be expressed as $0 \leq (Z/d_0)(U_\infty/U_{j_0}) \leq 0.3$.

Thus, for the circular jet model, in the development region of the jet the ratio of minor to major axis decreases linearly from 1 at $Z/d_0 = Z^* = 0$ to 1/4 at $Z^* = 0.3(U_{j_0}/U_\infty)$. This leads to

$$\text{minor axis/major axis} = 1 - 5/2\ Z^*(U_\infty/U_{j_0}) \tag{8}$$

with the circumference and area of the developing jet expressed in terms of this diameter ratio:

$$C = \frac{\pi d\left[1 + (1 - 5/2\ Z^* U_\infty/U_{j_0})^2\right]^{1/2}}{2} \tag{9}$$

$$A_j = \pi(1 - 5/2\ Z^* U_\infty/U_{j_0})d^2/4 \tag{10}$$

In order to obtain a better representation of the effects of high aspect ratio rectangular cross section jets, the basic model has been modified to provide for treatment of jets with an initial minor-to-major axis ratio of less than 1. This is done by setting an intial condition of $Z^* > 0$ at the jet exit. Thus, a value of Z^* corresponding to a given jet exit exit axis ratio may be determined from Equation(8) and the integration of the equations of motion carried out as before. While this represents a relatively minor modification of the computational procedure, it allows treatment of jets of initial elliptical cross section with minor-to-major axis ratio of down to 1/4, and hence a better approximation to the rectangular cross section jet.

Evaluation of Induced Forces and Moments

The latest version of the computer program developed originally in Reference 6 for estimating subsonic aerodynamic characteristics of complex planforms is utilized to evaluate propulsion-induced forces and moments on the configuration.

The program represents the lifting planforms with a vortex lattice. These complex planforms include wings with variable-sweep outer panels, wings with changes of dihedral across the span, wings with twist and/or camber, and a wing in conjunction with either a tail or a canard. Good agreement with experimental has been achieved for wing-body combinations by including the planform of the body in the overall planform.

To evaluate power-induced longitudinal aerodynamic characteristics, a camber distribution is introduced on the planform to satisfy the flow tangency condition at the 3/4-chord of the horse-shoe vortices in the lattice representation in the presence of the power-induced velocity field. Aerodynamic coefficients at zero angle of attack represent propulsion-induced effects.

This program has been utilized to improve upon results obtained as part of the prediction methods investigation documented in Reference 3. During that investigation, the vectored thrust model shown in Figure 1 was tested with vectored thrust nozzles in forward and aft positions as indicated. Comparisons

between theory and experiment for induced lift were made. The computations used the two-jet model as outlined previously to predict the interference velocity field and a lifting surface method restricted to wing-alone configurations.

Good agreement was obtained with the nozzles in the aft position, with the dominant effect expected to be the jet-wing interaction. However, for the nozzles in the forward position, the wing-alone computation resulted in poor correlation, due to jet-induced uploads on the large nacelles and the body ahead of the jet exits. This can be seen as part of Figure 2. The improvement in correlation which has been obtained by taking advantage of the extended capability of the vortex lattice approach to include the planform of the body and nacelles is also shown.

Additional computations have been carried out to determine the jet-induced aerodynamic characteristics of the body/nacelle-alone configuration using the vortex lattice lifting surface approach. Comparison with experimental data is shown in Figure 3.

In evaluating the propulsion-induced aerodynamics of a configuration with components significantly three-dimensional (i.e., body, nacelle), the choice of vertical location for the placement of the lifting planform is obviously critical, since this will significantly affect the induced velocity field which in turn dictates the flow tangency conditions for the lifting planform. Establishment of guide lines for this purpose offers significant potential for improvement in the application of the vortex lattice method.

The results of Figures 2 and 3 were obtained by specifying the flow tangency conditions in terms of the downwash angle $\delta = \tan^{-1}(w/U_\infty)$. The freestream velocity U_∞ can be modified to incorporate jet-induced changes, due to the potential jet model. Thus, for instance, the correlation in Figure 3 can be improved at the higher velocity ratios, where the induced flow in front of the jets tends to decrease the freestream velocity, in effect increasing the upwash angle and resultant upward load on the nacelles.

Propulsion-induced aerodynamics for configurations in cross-wind condition (i.e., at sideslip) are evaluated by taking advantage of the asymmetric planform capability of the vortex-lattice program. The jet-induced velocity field will, of course, be asymmetric at sideslip. This can be accounted for by resorting to asymmetric cambering of a symmetric planform to reflect the asymmetry of the induced flow field.

Employing a vortex lattice lifting surface method to evaluate propulsion-induced aerodynamic forces and moments is suitable in an approach aimed at the conceptual and preliminary design stage. While it does not treat details of a configuration in the manner of a full paneling method, its ease of application and efficiency are assets at a stage where the relative merits of a number of configurations have to be evaluated. The output from the jet-induced flow field module could be arranged to allow substitution of a paneling method for detailed analysis of a design at a later stage, in much the same manner as the vortex lattice method has been substituted for the wing-alone lifting surface approach.

Application to Supersonic VSTOL Fighter Configuration

Propulsion-induced longitudinal and lateral aerodynamic characteristics have been evaluated for the supersonic fighter/attack concept shown in Figure 4. The clipped delta wing design, featuring close-coupled canard surfaces mounted on 2-D side inlets, has a lift/cruise propulsion system which divides the

engine airflow into separate exhausts forward and aft of the center of gravity. The primary engine nozzles are vectorable 2-D nozzles, with both engines feeding a single remote augmentor nozzle, located in the nose, in the direct lift mode. Details of the design may be found in Reference 7.

The nomenclature used in the discussion of propulsion-induced aerodynamic characteristics is summarized in the following schematic representation of the efflux from the primary nozzles and the RALS nozzle.

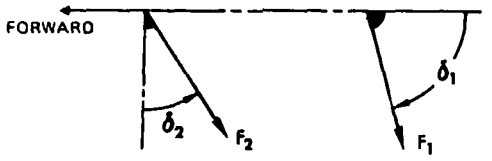

Propulsion-induced effects have been computed for two flight regimes:

- Cruise/combat flight regime where thrust vectoring for maneuvering is employed
- Transition flight phase where the presence of the RALS jet must be accounted for

Since the jet model of Reference 1 is a potential flow model which neglects viscous effects other than entrainment, an empirical correction to the induced aerodynamic characteristics is presented for the jet wake effect from the RALS jet.

Cruise/Combat Flight Regime

Effects of deflecting the thrust of the two primary nozzles on the longitudinal aerodynamic characteristics of the configuration were evaluated at a fixed deflection angle for a range of angle of attack and velocity ratio representative of thrust vectoring for maneuvering. The velocity ratio is defined in terms of the thrust coefficient of the two primary nozzles as,

$$\frac{U_\infty}{U_{jo}} = \left(\frac{2A_{j_1}/S}{C_T}\right)^{1/2} \qquad (11)$$

where A_{j_1} is the total nozzle exit area of the two engines, U_∞/U_{jo} is the ratio of freestream velocity to jet exit velocity.

Figure 5 shows the effect of thrust deflection ($\delta_1 = 15°$) on induced lift as a function of angle of attack, for a velocity ratio of 0.3. Experimental data from Reference 8 are included for comparison. Sufficient similarity between the model of the experimental investigation and the present design, in terms of the wing-canard planform and relative location of the two-dimensional nozzles with respect to the lifting surfaces, exists to make the comparison meaningful. Computed induced lift coefficients, ΔC_L, are compared with interpolated experimental data from Reference 8. The relative invariance of induced lift with velocity ratio, displayed by the experimental data of Reference 8, is also predicted quite well in Reference 7.

Induced lift as a function of velocity ratio at constant α is shown in Figure 6. The results are presented in terms of the induced lift coefficient and the

nondimensionalized induced lift, $\Delta L/T$, where

$$\frac{\Delta L}{T} = \Delta C_L \frac{S}{2A_{j_1}} \left(\frac{U_\infty}{U_{jo}}\right)^2 \tag{12}$$

Figure 7 shows induced pitching moment at the same operating conditions. The computation of the nondimensionalized pitching moment follows from Equation (12) substituting C_m for C_L. Trends and magnitudes in computed induced pitching moment are consistent with the experimental data of Reference 8.

Transition Flight Regime

In the transition flight phase, the RALS jet contributes to the jet-induced flow field and must be accounted for. The jet model of Reference 1 was utilized to evaluate the induced flow field due to the efflux from the primary nozzles and the RALS nozzle. Negligible interference effects between the RALS jet and the primary jets, due to the large separation, permit a direct superposition of the two induced flow fields (Reference 3).

For a fixed velocity ratio of the primary jets, U_∞/U_{jo}, the velocity ratio of the RALS jet is expressed as

$$\left(\frac{U_\infty}{U_{jo}}\right)_R = \left(\frac{F_1/F_2}{A_{j_1}/A_{j_2}}\right)^{1/2} \left(\frac{U_\infty}{U_{jo}}\right) \tag{13}$$

where F_1/F_2 is the thrust split between the primary nozzles and the RALS nozzle and A_{j_2} is the exit area of the RALS nozzle. The nondimensionalized induced lift, $\Delta L/T$, is now computed as

$$\frac{\Delta L}{T} = \Delta C_L \frac{S}{2A_{j_1}} \frac{1}{(1+F_2/F_1)} \left(\frac{U_\infty}{U_{jo}}\right)^2 \tag{14}$$

Induced lift and pitching moment have been computed as a function of velocity ratio for a number of jet deflection angles and thrust splits representative of the transition flight phase in Reference 7.

The rolling moment induced at a sideslip angle of 10° for one representative set of operating conditions in the transition flight phase is presented in Figure 8.

Immediately downstream of the jet efflux there is a wake region which has not been accounted for in the prior discussions. The primary propulsion exhaust is located at the trailing edge of the wing so that its wake has no significant aerodynamic effect. However, the RALS jet exhausts well forward of the wing and its wake interacts with the fuselage lower surface, and at sideslip can be directed under the canard and wing. Theoretical analysis methods are not available, but an empirical method (Reference 3) has been developed for estimating these effects. Charts were generated in Reference 3 for the lift and moment increments due to a normally exhausting jet as a function of velocity ratio and wake length.

These charts have been used to obtain longitudinal aerodynamic increments and incremental rolling moment for the configuration in Reference 7. The incremental rolling moment for a sideslip angle of 10° is presented in Figure 9. There is a lift loss, nose down pitching moment and a negative rolling moment for positive sideslip due to the wake of the RALS jet.

Refinement of Approach: Analytical Jet Wake Model

The substitution of an analytical jet wake model for the empirical corrections which presently constitute the jet-wake module offers significant potential for improvement in the prediction methodology as well as extending its range of application.

An existing two-dimensional Neumann program for computing the flow about an arbitrary cross section has been used to predict the pressure distribution in the wake of a jet as illustrated below:

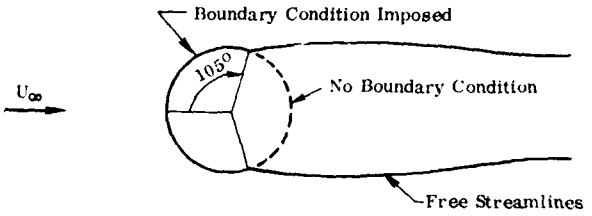

A partial circular cylinder was specified, causing the program to satisfy tne boundary condition of no flow through the surface up to 105° from the free-stream flow. This causes a free streamline to separate from each end of the cylinder definition. This condition is somewhat similar to the boundary layer separation which can be expected to occur from crossflow about an exhausting jet.

Since the computer program distributes sources and sinks about the partial cylinder, a net outflow of fluid exists aft of the cyclinder. This condition, while unrealistic from a physical viewpoint, causes the pressure in the simulated wake region to more closely approach the conditions of real wake flow than does potential flow about a closed circular cylinder. A similar approach is reported in Reference 9, where separation streamlines are imposed on a circular cylinder and a base pressure is imposed. The jet wake model discussed here does not require that the base pressure be predetermined.

To determine how closely this simple model can reproduce pressure distributions occurring in a jet wake, velocity components induced by the jet were determined, based on the potential flow jet model. These velocity components have as one of the terms of generation the velocity induced by a two-dimensional circular cylinder in potential flow. To incorporate wake effects by the suggested method, the velocities predicted by the Neumann program for the partial cylinder were substituted for the closed cylinder values. The results obtained, when corrected for the presence of an infinite flat plate in the plane of the jet exit, are shown in Figures 10 and 11.

The test data are pressure coefficients on a flat plate from which a jet issues normally into the freestream. The pressure coefficients predicted by the analytical jet wake model show considerable improvement over the potential flow predictions in the region directly behind the jet.

Conclusions

- The present approach of evaluating propulsion-induced aerodynamic characteristics has given good results for subsonic and supersonic VSTOL fighter/attack configurations.
- The prediction methodology is suitable for the conceptual and preliminary design phase.
- The modular approach permits easy substitution of improved theoretical models as they become available.
- The development of a suggested analytical jet wake model offers potential for improvement over the empirical corrections presently used.

References

1. Wooler, P.T., Burghart, G.H. and Gallagher, J.T., "Pressure Distribution on a Rectangular Wing with a Jet Exhausting Normally into an Airstream," Journal of Aircraft, Vol. 4, No. 6, November-December 1967, pp. 537-543.
2. Ziegler, H. and Wooler, P.T., "Multiple Jets Exhausting into a Crossflow," Journal of Aircraft, Vol. 8, No. 6, June 1971, pp. 414-420.
3. Wooler, P.T., Kao, H.C., Schwendemann, M.F., Wasson, H.R. and Ziegler, H., "VSTOL Aircraft Aerodynamic Prediction Methods Investigation," AFFDL-TR-72-26, Vols I,II, January 1972.
4. Ziegler, H. and Wooler, P.T., "Analysis of Stratified and Closely Spaced Jets Exhausting into a Crossflow," NASA CR-132297, November 1973.
5. Fricke, L.B., Wooler, P.T. and Ziegler, H., "A Wind Tunnel Investigation of Jets Exhausting into a Crossflow," AFFDL-TR-70-154, December 1970.
6. Margason, R.J. and Lamar, J.E., "Vortex-Lattice Fortran Program for Estimating Subsonic Aerodynamic Characteristics of Complex Planforms," NASA TN D-6142, February 1971.
7. Brown, S.H., "Study of Aerodynamic Technology for VSTOL Fighter/Attack Aircraft- Horizontal Attitude Concept," NASA CR-152130, May 1978.
8. Yip, L.P. and Paulson, J.W., Jr., "Effects of Deflected Thrust on the Longitudinal Aerodynamic Characteristics of a Close-Coupled Wing-Canard Configuration," NASA TP 1090, December 1977.
9. Parkinson, G.V. and Jandali, T., "A Wake Source Model for Bluff Body Potential Flow," Journal of Fluid Mechanics, 1970, Vol. 40, part 3, pp. 577-594.
10. Wu, J.C., McMahon, H.M., Mosher, D.K. and Wright, R.A., "Experimental and Analytical Investigations of Jets Exhausting into a Deflecting Stream," Journal of Aircraft, Volume 7, No. 1, January-February 1970, pp. 44-51.
11. Bradbury, L.J.S. and Wood, I.N., "The Static Pressure Distribution Around a Circular Jet Exhausting Normally from a Plane Wall into an Airstream," RAE Technical Note AERO 2978, August 1964.

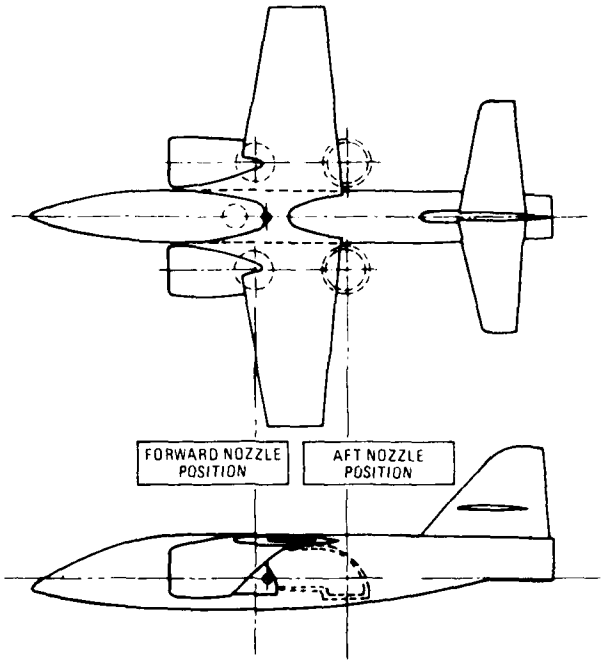

FIGURE 1. WIND TUNNEL MODEL OF SUBSONIC VSTOL FIGHTER CONCEPT

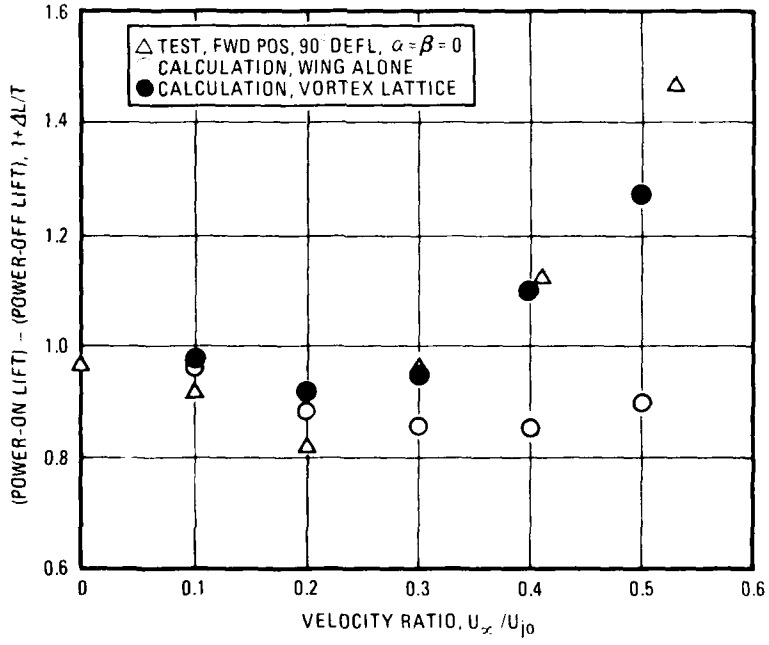

FIGURE 2. PROPULSIVE LIFT FOR WING/BODY/NACELLE

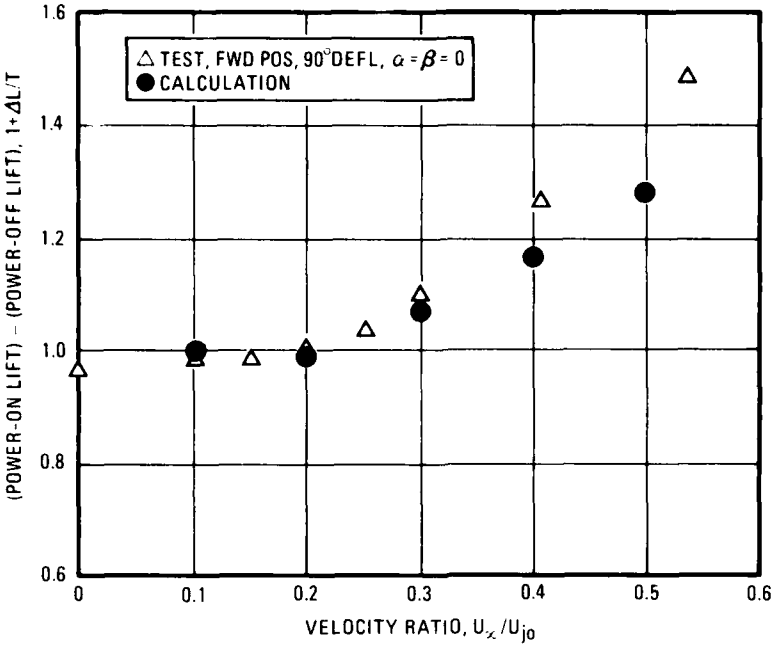

FIGURE 3. PROPULSIVE LIFT FOR BODY/NACELLE

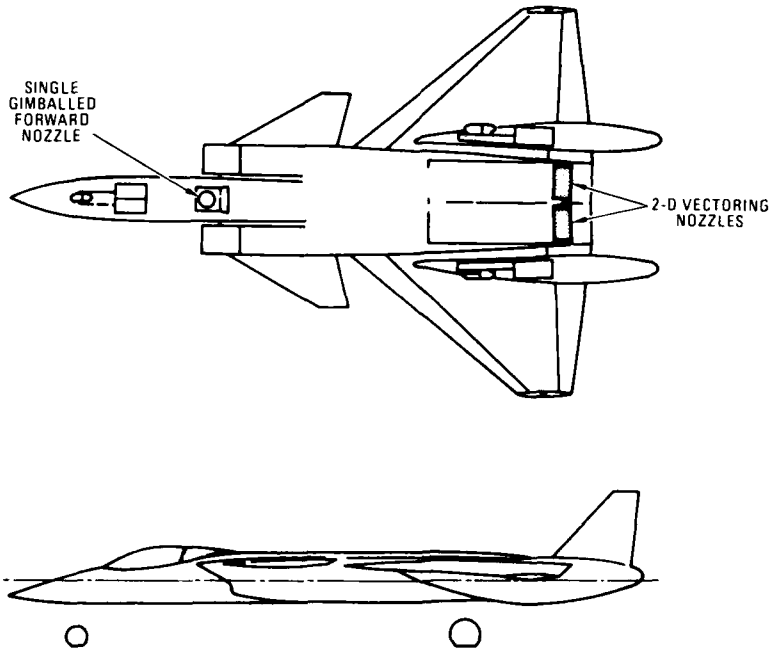

FIGURE 4. SUPERSONIC VSTOL FIGHTER/ATTACK CONCEPT

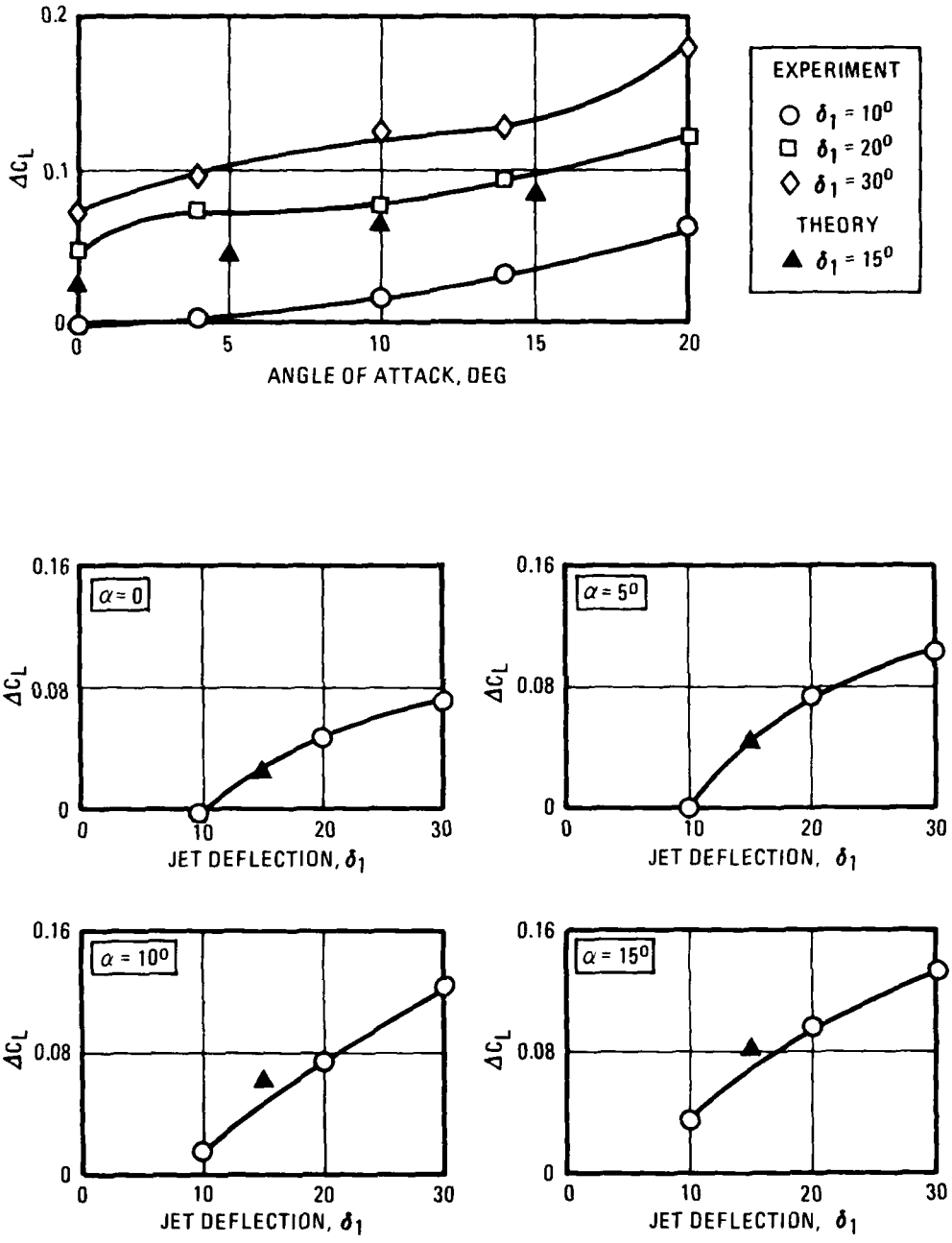

FIGURE 5. EFFECT OF DEFLECTED THRUST ON LIFT ($U_\infty/U_{jo} = 0.3$)

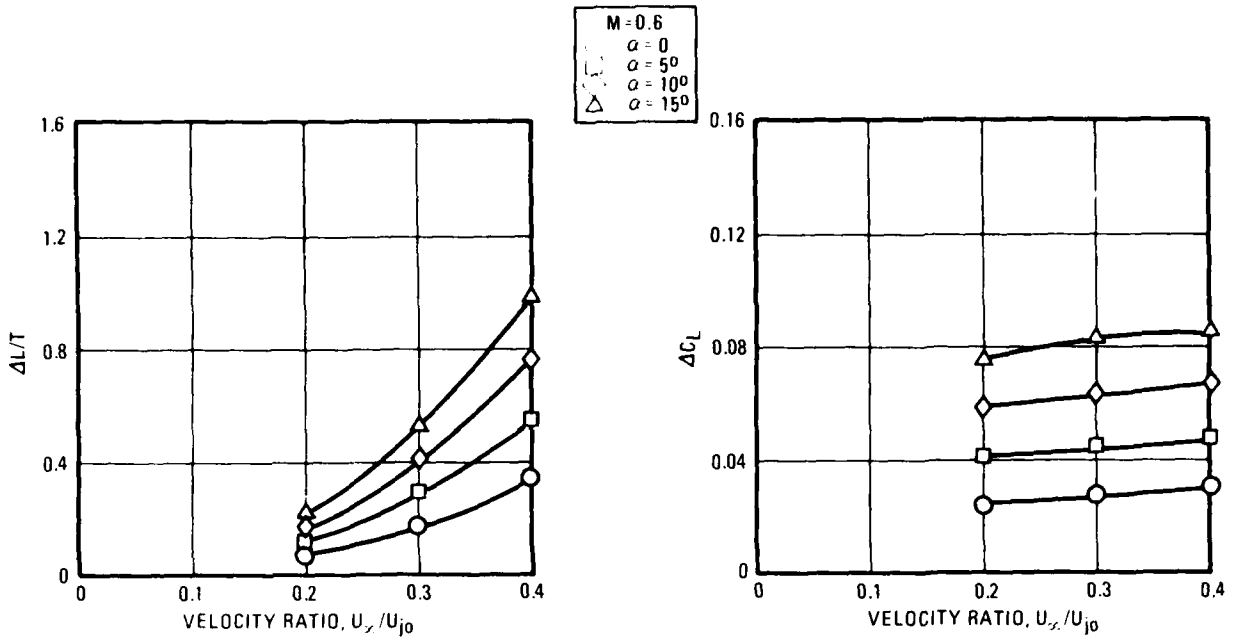

FIGURE 6. INDUCED LIFT DUE TO THRUST VECTORING ($\delta_1 = 15^o$)

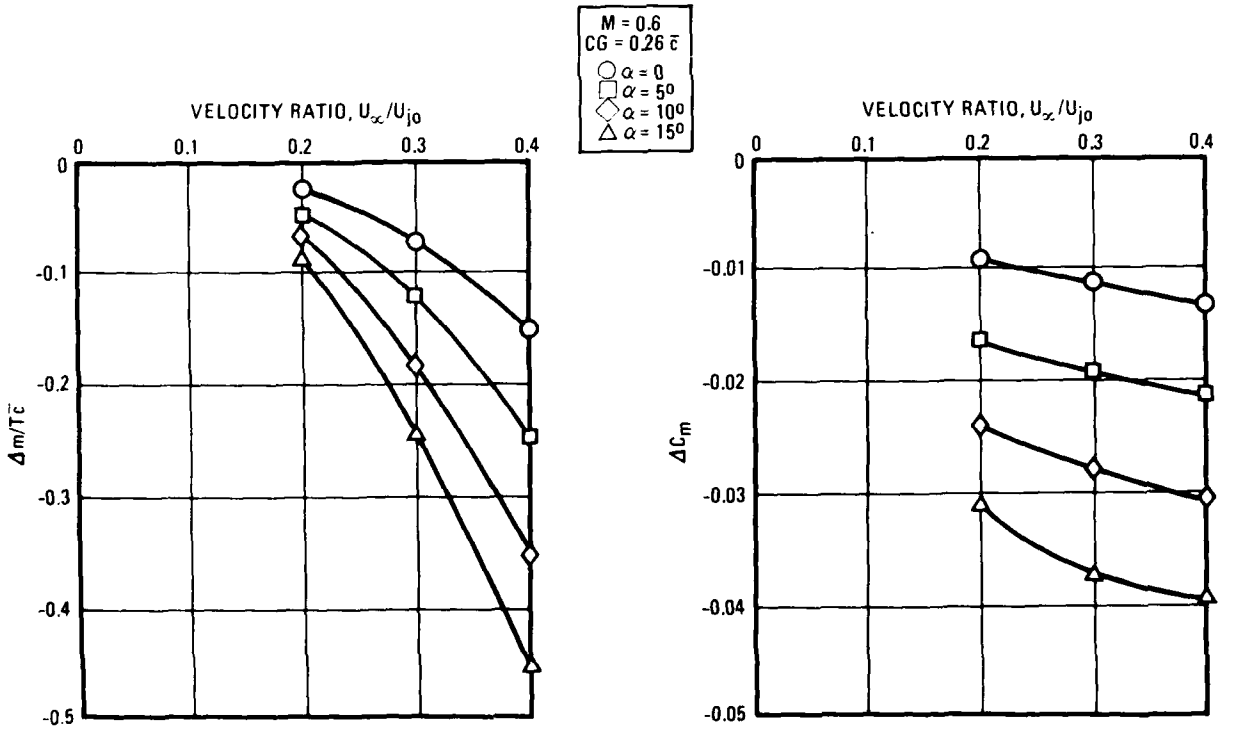

FIGURE 7. INDUCED PITCHING MOMENT DUE TO THRUST VECTORING ($\delta_1 = 15^o$)

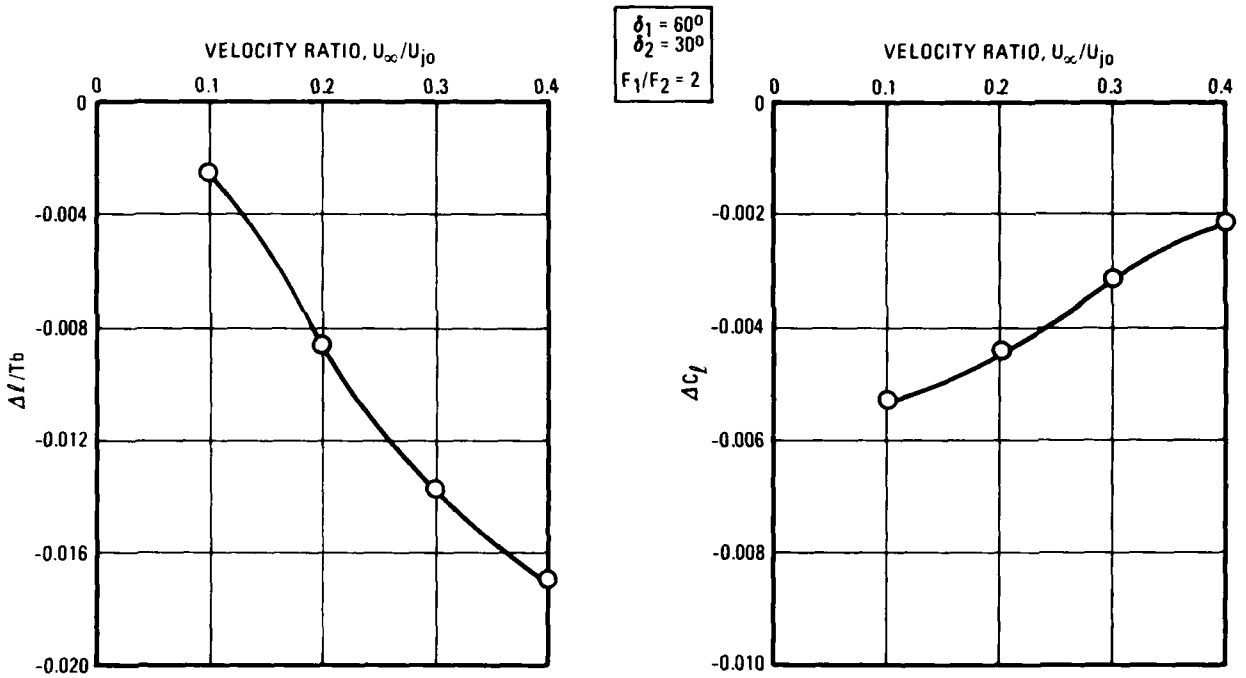

FIGURE 8. PROPULSION-INDUCED ROLLING MOMENT IN TRANSITION ($\beta = 10^o$)

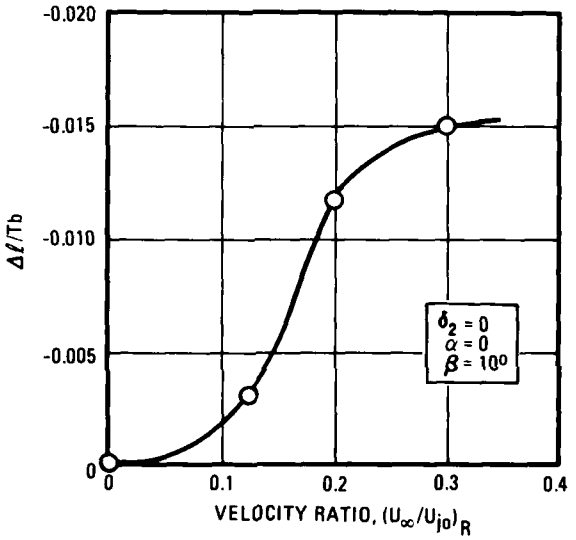

FIGURE 9. RALS WAKE CONTRIBUTION TO PROPULSION-INDUCED ROLLING MOMENT ($\beta = 10^o$)

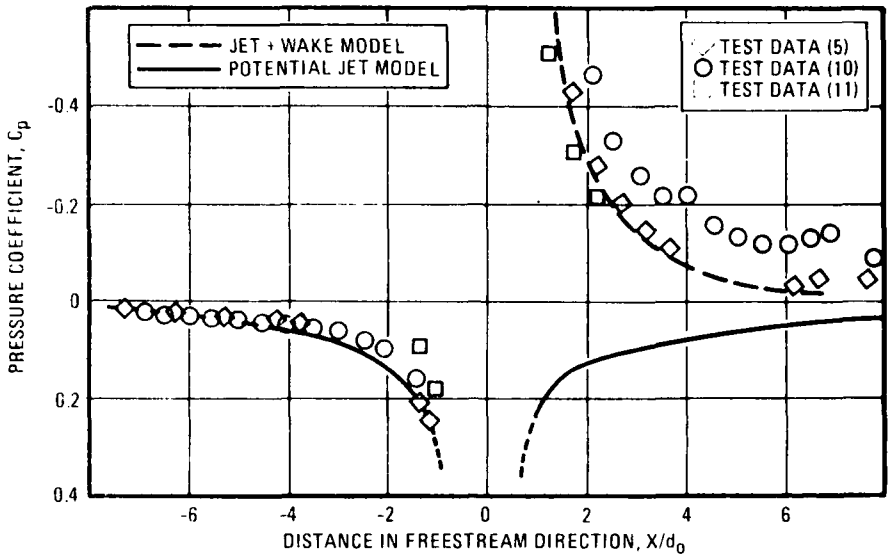

FIGURE 10. JET WAKE PRESSURE PREDICTION ($Y/d_0 = 0$, $U_\infty /Ujo = 0.25$)

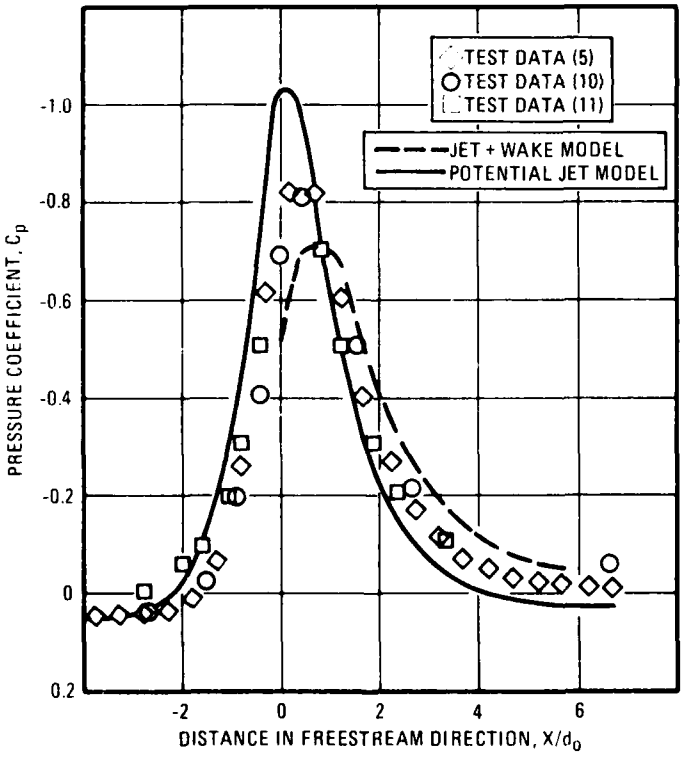

FIGURE 11. JET WAKE PRESSURE PREDICTION ($Y/d_0 = 1.5$, $U_\infty /Ujo = 0.25$)

FLAP SURFACE PRESSURES BEHIND A JET ISSUING FROM A WING IN CROSS FLOW

by

Howard M. McMahon
Georgia Institute of Technology

ABSTRACT

Surface pressures were measured on a two-dimensional wind tunnel model consisting of an NACA 0021 airfoil fitted with a 30% chord NACA 4415 flap. A round turbulent jet (exit diameter/wing chord = 0.10) issued from the wing lower surface at the 65% chord location. Measurements of chordwise surface pressure distributions on the flap were made in the plane of symmetry and up to 4 jet radii spanwise for three different combinations of wing angle of attack and flap deflection and at three different values of jet velocity/free stream velocity ratio.

The results indicate that, at the largest flap deflection angle (15^{o}), the effective flap angle and hinge moment in the plane of symmetry are reduced significantly by the influence of the jet, and a significant interference extends spanwise to at least four jet radii. A comparison with another investigation done with a jet exit located below the wing indicates that the interference effect may be sensitive to the vertical location of the jet exit relative to the flap.

INTRODUCTION

The surface pressures and forces on a two-dimensional wing containing a round turbulent jet exhausting from the wing surface were studied by Mikolowsky (Ref. 1). Later, this same wing model was used in studying the behavior of the deflected jet (and in particular the strength and location of the contrarotating vortices) in the presence of varying amounts of wing lift. In order to increase the maximum lift coefficient, the wing model was fitted with a flap. The results of these studies of the deflected jet are found in Ref. 2.

The flap was instrumented with surface pressure taps in the region downstream of the jet exit. During the course of the deflected-jet experiments, these flap pressures were monitored, and the resulting pressure data form the basis for the present discussion.

APPARATUS AND TEST CONDITIONS

The experiments were conducted in the Georgia Tech 9-foot wind tunnel at an indicated freestream velocity of 100 ft/sec, which corresponds to a Reynolds number (based on wing chord) of 8.15×10^{5}.

The wing-flap model as installed in the wind tunnel is shown in Fig. 1. The view is from upstream, looking upward. The rake and actuator shown in the picture were used in the jet plume studies and were not present during the surface pressure measurements.

The two-dimensional wing had a span of 7.12 feet and was installed between flat sidewalls. The wing had a chord (C) of 15.37 inches and had an NACA 0021 section modified such that it had a straight line contour from the 80% chord station to the trailing edge. A transition strip 0.38 in. wide was located at 5% chord on both the upper and lower surfaces. The jet plenum chamber was supplied by air piped internally in the wing.

The flap had an NACA 4415 section with a chord (C_f) of 4.61 in. (i.e. 30% of wing chord) and was attached to the wing at four points located 15 in. and 39 in. on either side of the wing centerline. The flap was rotated about its leading edge. Pressure taps were installed in a chordwise row from the leading edge to $0.65C_f$ in the plane of symmetry (Y = 0) and at three other spanwise locations.

The jet exit in the wing was 0.75 in. in radius (r_j), hence the ratio of jet diameter to wing chord was $d_j/C = 0.10$. The exit was flush with the wing surface at the 65% wing chord location, with the jet flow at the exit being normal to the wing chord. The jet exit was located at mid-span (Y = 0). The quality of the turbulent jet outflow is discussed in Ref. 1.

Since the primary aim of the experiment was to investigate the influence of wing circulation on the properties of the deflected jet, data were taken at three values of wing lift which were achieved by three different combinations of wing angle of attack (α) and flap deflection angle (δ). These combinations were: $\alpha = 0^o$, $\delta = -5^o$ (minimum lift, $C_L = 0.034$); $\alpha = 6^o$, $\delta = 0^o$ (intermediate lift, $C_L = 1.24$); and $\alpha = 8^o$, $\delta = 15^o$ (maximum lift, $C_L = 2.45$).

The effective velocity ratio of the jet, λ, is defined as the square root of the ratio of the jet dynamic pressure to the freestream dynamic pressure,

$$\lambda^2 = \frac{\rho_j V_j^2}{\rho_\infty V_\infty^2}$$

Data were taken for each of the three lift cases at $\lambda = 0$, 4, 6, and 8.

The wing-flap configuration for maximum lift is shown in Fig. 2. Also shown are the jet centerline (the locus of points of maximum total pressure in the plane of symmetry Y = 0) and the vortex curve (the projection of the vortex trajectories onto the symmetry plane Y = 0) for the smallest effective jet velocity ratio, $\lambda = 4$ (Ref. 2). At larger values of λ, the deflected jet is, of course, further away from the wing and flap.

The details of the flap location relative to the wing trailing edge are shown in Fig. 3. The flap location was suggested by NASA Langley Research Center based upon computer optimization studies for maximum lift coefficient with this wing-flap combination.

RESULTS AND DISCUSSION

Since, as has been mentioned, the primary purpose of the experiment with the wing-flap was a study of the deflected jet, there was no systematic variation of flap angle and wing angle of attack, nor was the spanwise coverage of flap surface pressure as extensive as would be desirable for a control surface study. However, those flap pressure distributions which were measured did indicate that the influence of a jet in proximity to a flap or control surface may be significant.

Figure 4 shows the flap pressure coefficient $C_p = (p - p_\infty)/q_\infty$ plotted versus flap chordwise location (in the plane of symmetry) at the maximum lift condition for $\lambda = 0$ (jet off) and $\lambda = 8$. The effect of the presence of the jet is to reduce the effective flap deflection angle by about 5 degrees. The hinge moment about the flap leading edge was calculated by using only the C_p contribution to $0.65C_f$ and also by extrapolating the data to $C_p = 0$ at the trailing edge. Both methods indicated a reduction in section hinge moment of 24% due to the presence of the jet.

The pressure data may also be presented in the form of interference pressure coefficient, ΔC_p, where $\Delta C_p = C_p(\text{Jet on}) - C_p(\text{Jet off})$. This is the formulation as given in Fig. 5 (note that the graphs of ΔC_p have the ordinate positive upward). Figure 5 shows the effect on the flap interference pressure distribution due to varying the jet velocity ratio at the maximum lift condition. The interference on the upper surface is quite insensitive to jet velocity ratio, while the interference on the lower surface of the flap decreases with decreasing velocity ratio but is still substantial at the lowest velocity ratio tested.

The interference effect on the flap at the minimum lift condition ($\alpha = 0^\circ$, $\delta = -5^\circ$) was quite different from that at the largest flap angle, as is seen in Fig. 6. The character of the interference on the upper surface is the same as at $\alpha = 8^\circ$, $\delta = 15^\circ$. Thus, the upper surface behaved as if the flap were at a decreased (more negative) angle of attack. However, the interference on the lower surface is now positive (increased angle of attack) rather than negative as it was at maximum lift. Data for the intermediate lift case ($\alpha = 6^\circ$, $\delta = 0^\circ$) indicated a small positive interference on the lower surface over the first 30% of the flap chord and essentially zero interference thereafter. The upper surface again had a positive interference.

Thus, the interference over the upper surface of the flap was consistently positive at all conditions tested, while the interference on the lower surface changed sign as the flap angle changed. There were not enough data taken to explain this difference. It seems reasonable that the slot between the wing trailing edge and the flap became less effective because of the blockage of the jet wake, with a corresponding decrease in velocity and increase in pressure over the flap upper surface at all flap angles. Also, since the interference effect of the jet on the wing surface pressures behind the jet exit was negative, one might expect this interference pattern to have extended to the flap lower surface. However, this was not the case for the smaller flap defection angles ($\delta = 0^\circ$ and $\delta = -5^\circ$). Hence, the jet interference effect cannot be represented simply as an effective change in flap angle at all values of flap deflection.

The spanwise extent of the jet interference is shown in Fig. 7 for the high-lift case at $\lambda = 8$. It is seen that the interference effect remains significant out to at least four jet radii; the hinge moment at 2.6 r_j was reduced by 20%. At $\lambda = 4$, the spanwise decay of interference was more pronounced, expecially on the upper surface. This might be expected, since surface oil film patterns behind a jet issuing at right angles to a flat plate (e.g. Ref. 3) have shown that the wake width behind the jet decreases as λ decreases.

The interference pressure distributions on the flap reported here may be compared to those measured by Carter (Ref. 4) with a jet exit located some distance below the wing surface. The present configuration and that used by Carter are contrasted in Fig. 8. The model used in Ref. 4 was a body of revolution with a high wing of NACA 4415 section fitted with a 30% chord airfoil flap of the same section. The wing and flap had one row of chordwise pressure taps located 0.75 wing chord lengths outboard of the symmetry plane of the model. An ejector (drawn to scale) on an external sting was moved to various locations around the model while interference pressures and forces were measured. The jet exit location nearest to that used in the present work was one at 0.75C downstream of the wing leading edge and 0.64C below the wing chord line.

A comparison of the results taken from Ref. 4 and those observed in this experiment is shown in Fig. 9. It is perhaps presumptuous to label this figure as one illustrating the effect of jet exit location, since the test conditions were not identical in other respects. The data from the present work are for $\alpha = 8^o$, $\delta = 15^o$, $\lambda = 8$, $d_j/C = 0.10$ while those from Ref. 3 are for $\alpha = 0^o$, $\delta = 40^o$, $\lambda = 6.7$, $d_j/C = 0.25$. However, it is not the magnitude of the interference that is compared, but the sign. The interference on the upper surface is positive in the present tests, as it was for all flap angles and all values of λ. The interference as reported in Ref. 4 is negative on the upper surface for all values of λ between 4 and 10. There is a similar sign difference over the first 20% of the flap chord on the lower surface. The sign difference in the upper surface interference may not be surprising, since the wake of the jet in the present tests served to block the slot between the wing trailing edge and the flap, while the jet wake in Ref. 4 did not. This comparison of the two experimental results indicates that the interference effect of a jet on a flap may be sensitive to the vertical location of the jet exit relative to the flap.

CONCLUSIONS

Since the flap data taken during the course of these experiments were limited, no definitive statements can be made regarding the effectiveness of a flap or control surface in the presence of a deflecting jet. However, the following observations are presented regarding the influence of a jet in crossflow issuing from a wing surface upstream of a flap:

(1) At large flap deflection angles, the effective flap angle and hinge moment in the plane of symmetry are reduced significantly, and a major interference effect extends spanwise to at least four jet radii.

(2) The interference effect on a flap caused by a jet in crossflow may be sensitive to the vertical location of the jet exit relative to the flap.

ACKNOWLEDGEMENT

The work reported here was done in collaboration with D. L. Antani, who is presently at the Northrop Corporation. His contribution is gratefully acknowledged. The research was supported by NASA under Grant NSG 1257, with R. P. Weston acting as Technical Officer.

REFERENCES

1. Mikolowsky, W. T.: An Experimental Investigation of a Jet Issuing from a Wing in Crossflow. Ph.D. Thesis, Georgia Institute of Technology, Atlanta, Georgia, 1972. A condensed version of this work appeared in AIAA Journal of Aircraft, Vol. 10, No. 9, pp. 546-533, 1973.

2. McMahon, H. M. and Antani, D. L.: Experimental Study of a Jet Issuing from a Lifting Wing. AIAA Journal of Aircraft, Vol. 16, No. 4, pp. 275-281, 1979.

3. Mosher, D. K.: An Experimental Investigation of a Turbulent Jet in a Crossflow. Ph.D. Thesis, Georgia Institute of Technology, Atlanta, Georgia, 1970.

4. Carter, A.: Effects of Jet-Exhaust Locations on the Longitudinal Aerodynamic Characteristics of a Jet V/STOL Model. NASA TN D-5333, 1969.

FIG.1 WING AND FLAP

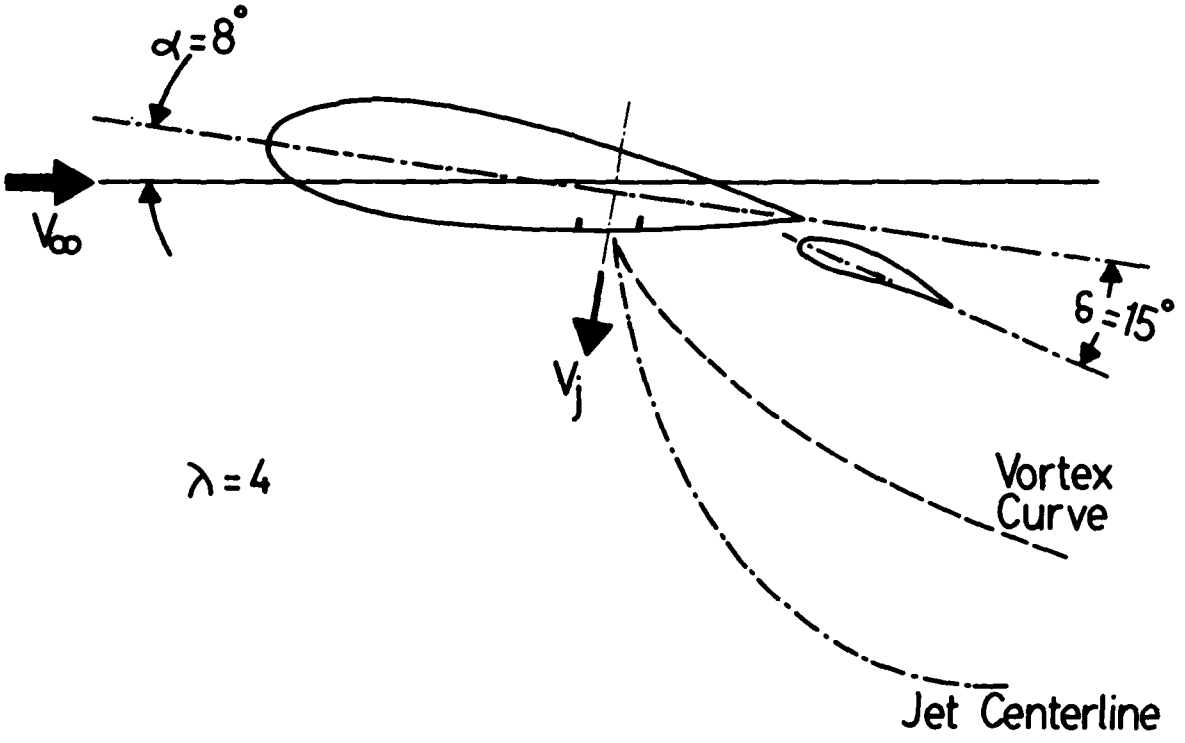

FIG. 2 JET PATH

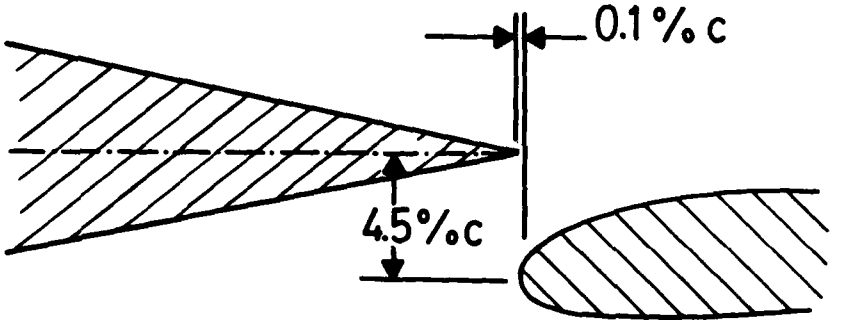

FIG. 3 FLAP SPACING

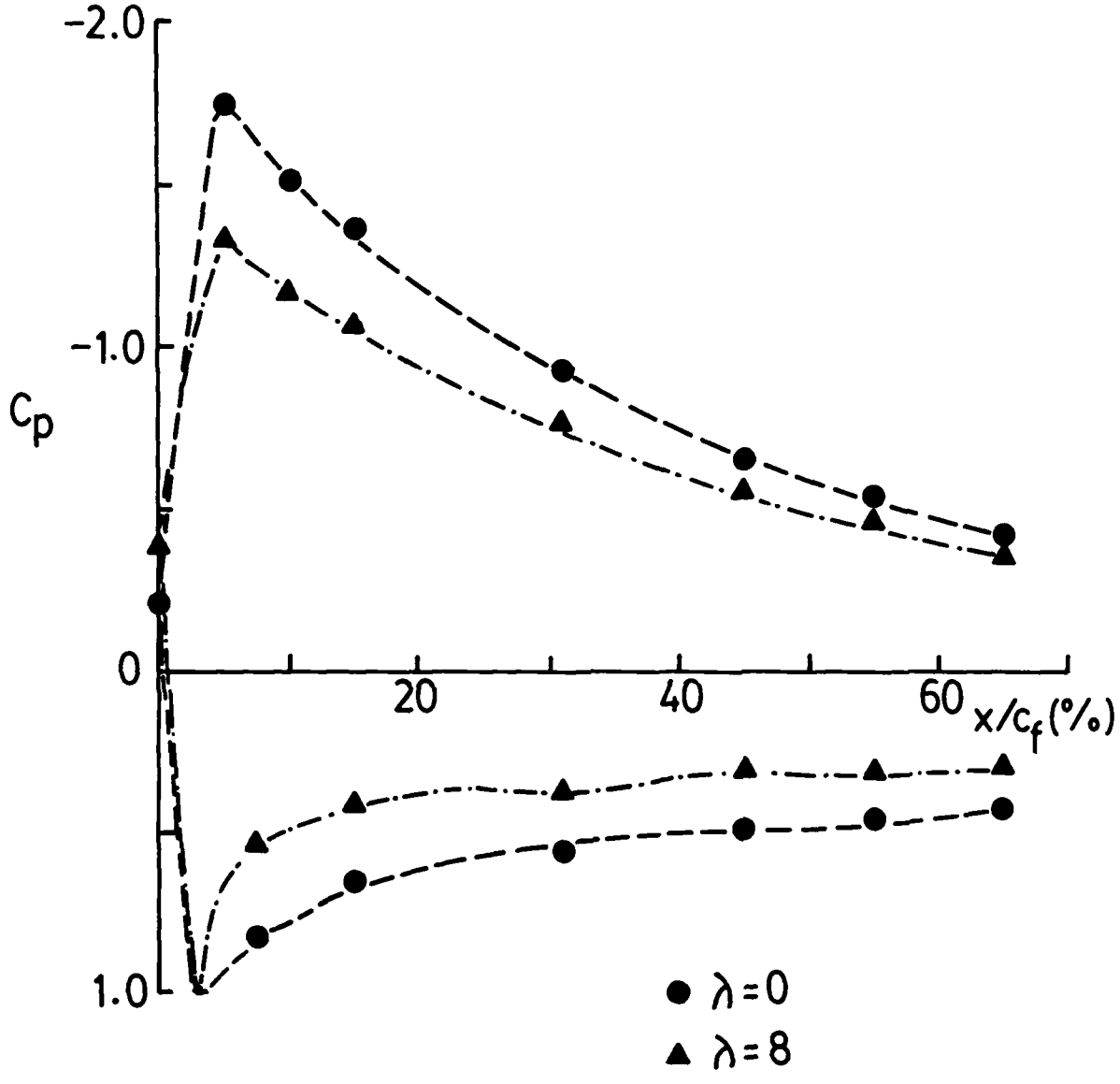

FIG.4 JET EFFECT (Y=0)
($\alpha = 8°$; $\delta = 15°$)

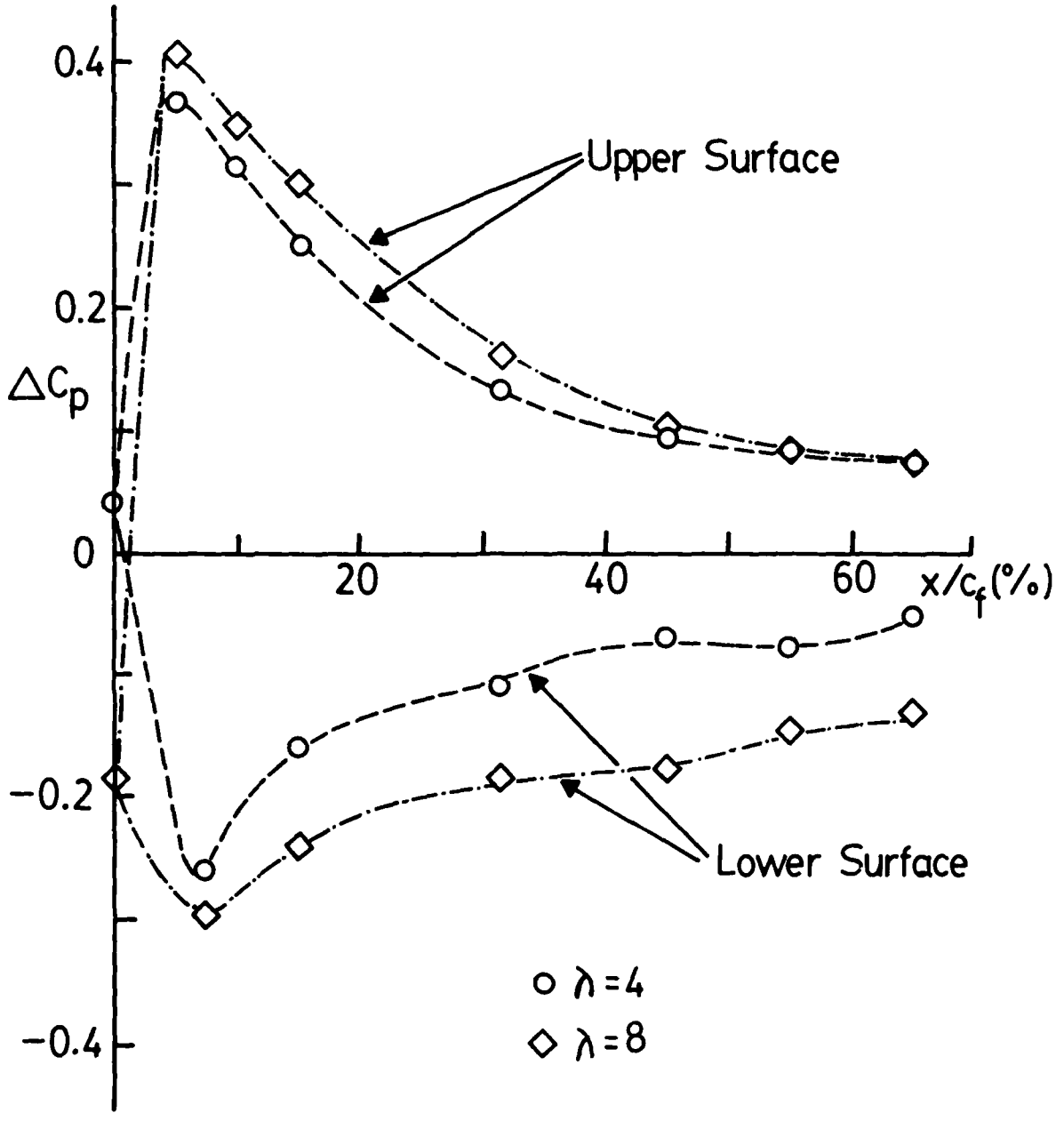

FIG.5 JET INTERFERENCE (Y=0)
$\alpha = 8^\circ$; $\delta = 15^\circ$

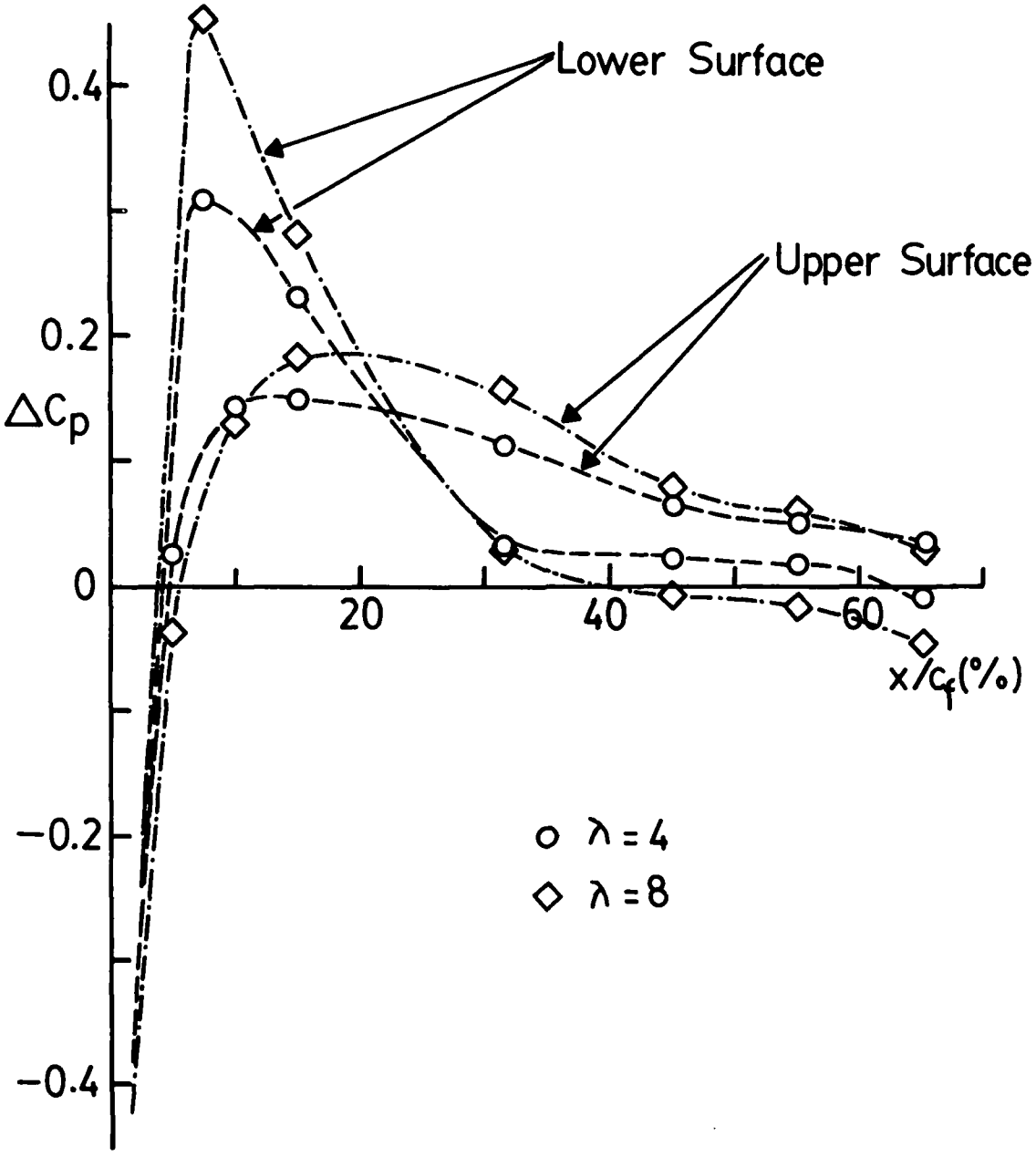

FIG.6 JET INTERFERENCE (Y=0)

$\alpha = 0^\circ$; $\delta = -5^\circ$

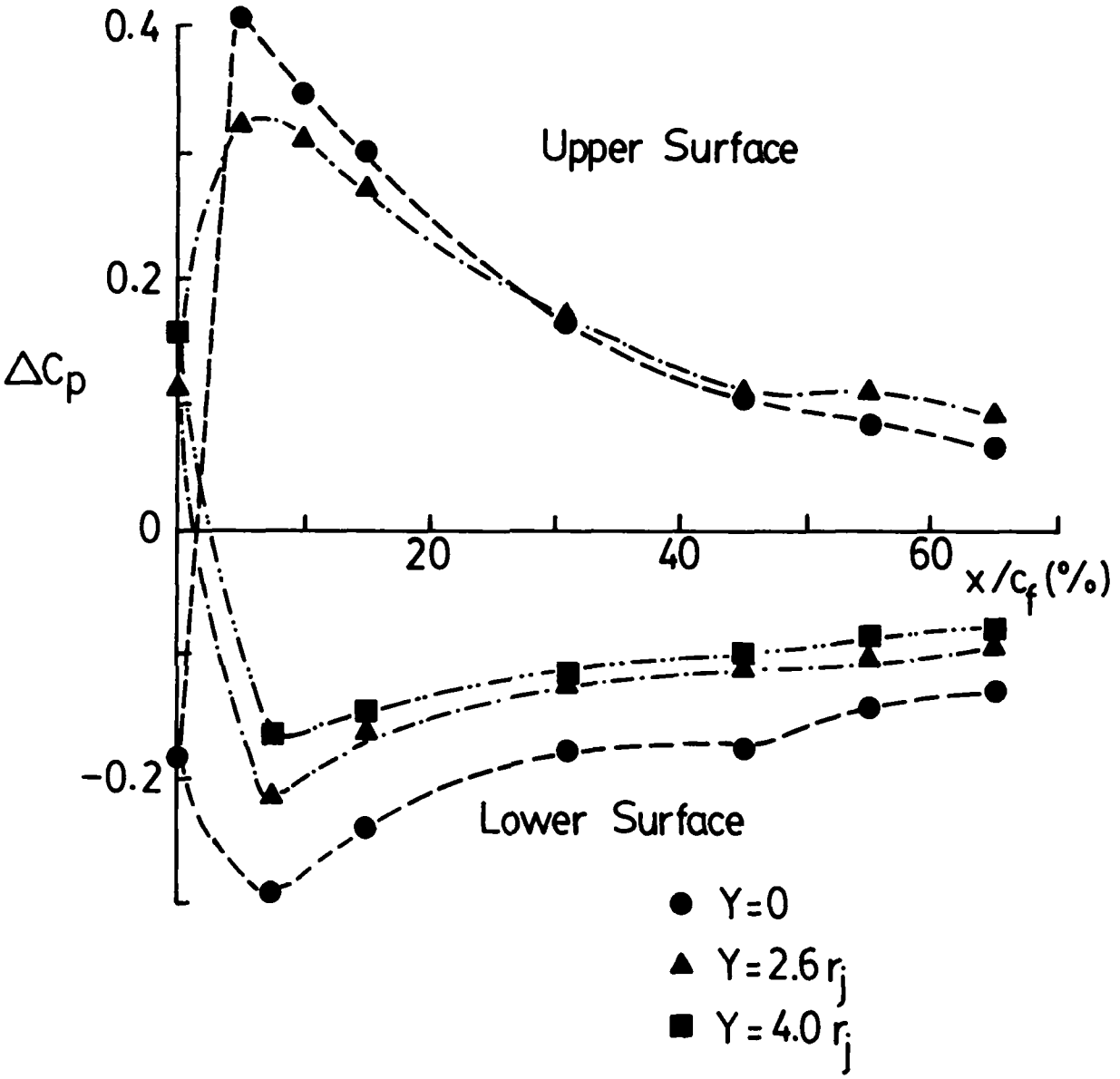

FIG. 7 JET INTERFERENCE (Spanwise)
$\lambda = 8$
($\alpha = 8^\circ$; $\delta = 15^\circ$)

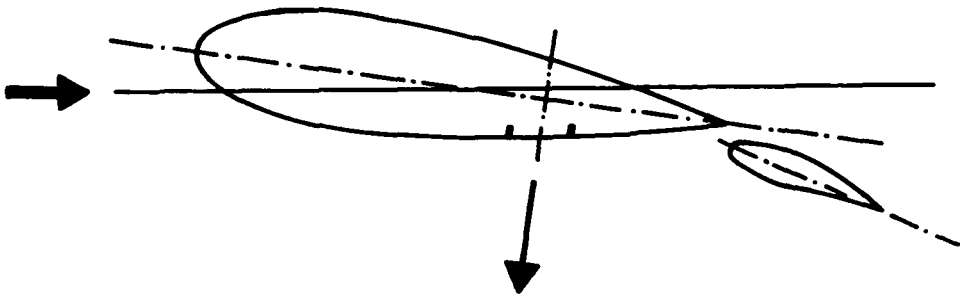

a) Present Work

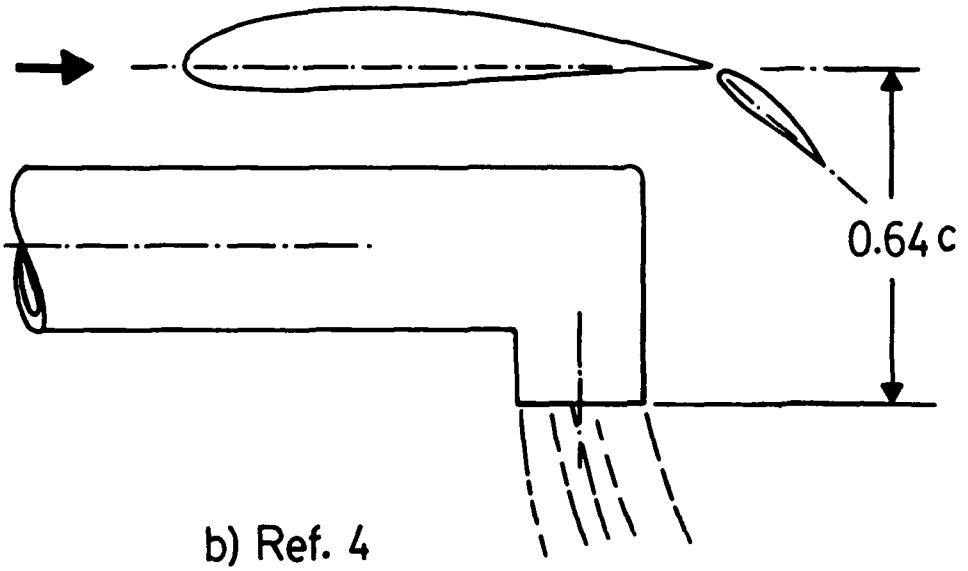

b) Ref. 4

FIG.8 JET EXIT LOCATIONS

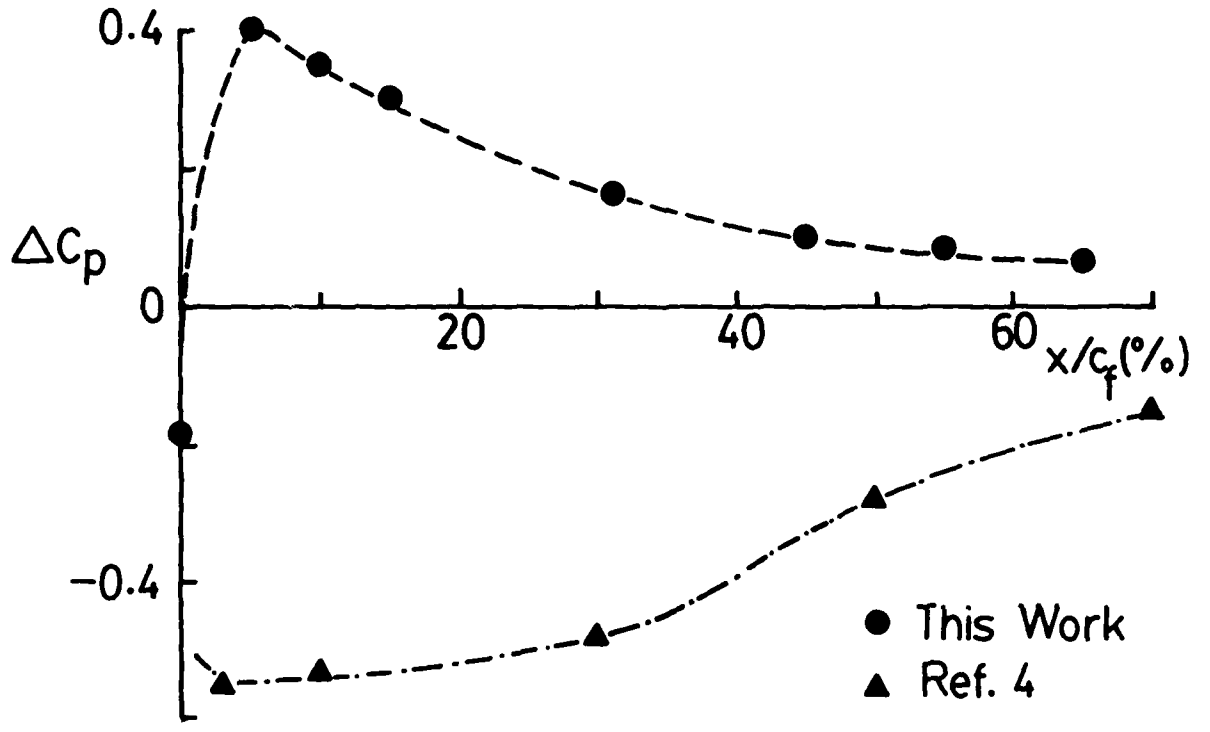

(a) Upper Surface

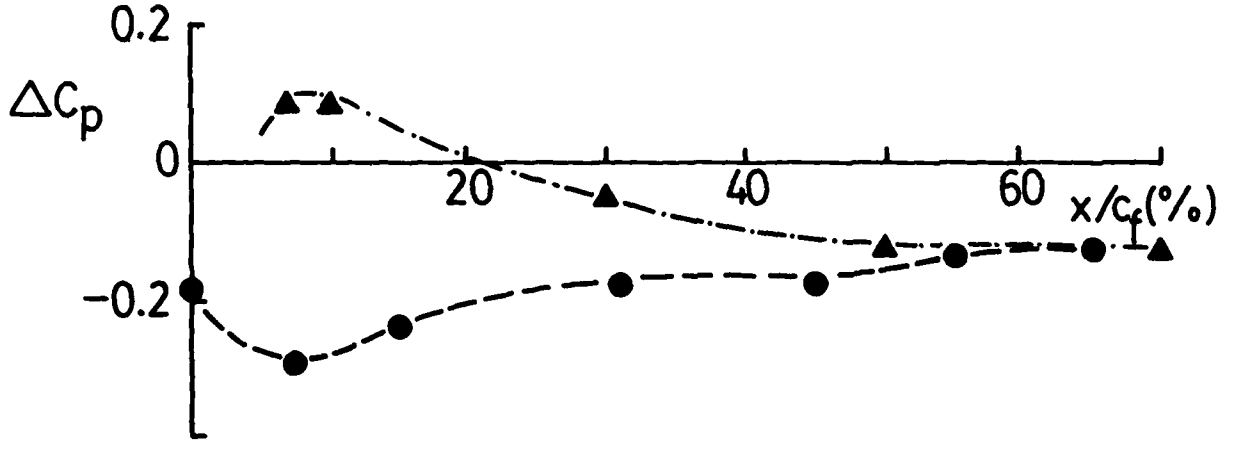

(b) Lower Surface

FIG.9 EFFECT OF JET EXIT LOCATION

A NUMERICAL INTERACTION ALGORITHM FOR PREDICTION OF VSTOL JET-INDUCED FLOWFIELDS[†]

By

A. J. Baker and P. D. Manhardt,

Computational Mechanics Consultants, Inc.

Knoxville, TN

And

K. T. Yen, Naval Air Development Center

Warminster, PA

ABSTRACT

A viscous-inviscid interaction algorithm is derived for numerical determination of the three-dimensional flowfield surrounding and entrained into the wake of a V/STOL jet issued orthogonally into a subsonic crossflow bounded on one plane by an aerodynamic surface. The dominant influence parameter coupling the three-dimensional external potential flow analysis, and the imbedded three-dimensional viscous and turbulent analysis of the jet and near-field-wake, is the entrainment flow induced into the jet region and its influence on the potential flow. The two distinct solution domains are pressure coupled, and the entrainment-induced mass flux addition to the wake is the primary iteration variable of the global algorithm. A key element of the algorithm is definition of a surface defining the coincident boundary of the dual analyses. Numerical studies have confirmed existence of the interface surface for the test case of a circular jet, and estimation of the entrainment velocity distribution thereon. The three-dimensional jet region description is contained within the parabolic Navier-Stokes equations yielding detailed evolution of the turbulent flow. The turbulence closure model involves all six components of the Reynolds stress tensor, and finite element numerics are employed throughout.

[†]This research was supported by the Naval Air Development Center under NADC Contract No. N62269-77-C-0491.

INTRODUCTION

In the transition from hover to wing-borne flight, a significant fraction of the lift of a V/STOL aircraft is furnished by direct engine thrust. The resultant injection of a high-velocity jet of exhaust (or air), at almost right angles to the aerodynamic surface, and to the cross-flow induced by the aircraft forward flight, produces an extremely complicated three-dimensional flowfield which can significantly alter the aircraft aerodynamic characteristics. Since the basic phenomena of transverse jet injection is so fundamental to V/STOL performance, it is crucially important that a firm understanding of cause and effect be established. This paper derives and computationally evaluates the key features of a three-dimensional viscous-inviscid flow interaction numerical solution algorithm for the near-field of a V/STOL jet.

Since the transverse injected jet is fundamental to many physical processes, in addition to V/STOL aircraft, a comprehensive base of experimental data and linearized theoretical analyses has become established. The first consequential theoretical study was reported in the dissertation of Chang (Ref. 1), who employed potential flow theory and bound vortex filament concepts to predict roll-up of the separation boundary between a parallel onset flow and a perpendicular cylindrical jet. Her results clearly illustrate flow evolution to the hallmark horse-show cross-sectional shape, and the basic concept (application of potential flow theory) has been expanded upon and refined to a great extent, c.f., Ref. 2, 3. Experiments (Ref. 4) on a round jet confirmed the horse-shoe cross-section contours, and also noted that the jet siphoned the transverse flow boundary layer into the jet wake region. This is not a dominant feature of a jet issued from an isolated pipe (Ref. 5), and has become recognized as perhaps a most consequential contributor to performance alterations of V/STOL aircraft. This phenomenon is termed "entrainment" and is properly interpreted as the total effect of vortex roll-up plus the induced turbulent mixing. Conversely, "blockage" is simply the potential characteristics for inviscid flow around an equivalent solid body.

The significant interest in the V/STOL jet problem has prompted the conducting of numerous experimental projects to probe the associated three-dimensional velocity fields to well downstream of injection and to record induced surface pressure distributions. It is this later phenomenon that is perhaps the singularly important analysis requirement since in practice the injection plate becomes a (lifting) aerodynamic surface, c. f., Ref. 6, 7. McMahon and Mosher (Ref. 8) published oil flow streaklines, see Figure 1, that provide dramatic evidence of the induced flowfield difference between a V/STOL jet and the equivalent-diameter solid blockage. For the latter, Figure 1a, definite stagnation points exist both upstream and downstream on the centerline and are connected by an apparent inviscid flow streamline. Outside this streamline, the exterior flow apparently remains irrotational and simply responds to the blockage induced by the body.

Conversely, the plate streamlines for the circular V/STOL jet, Figure 1b, are consequentially different (the concentric circle is part of the experimental apparatus and not a streakline). The appearance of the upstream stagnation point region is not consequentially different indicating blockage-dominance. However, in the mid-chord region of the jet, the surface flow becomes directed almost radially inwards. Two streamlines are symmetrically oriented downstream which separate the complex wake interior flow from the deflected freestream.

The incoming streamlines, which divide the flow region into entrained and deflected segments, intersect the downstream-dividing streamlines symmetrically, and a weak stagnation line appears to connect these two points (essentially on top of the circle). A rear stagnation point, which must be induced by flow impinging the plate from above (anti-parallel to the jet axis) is clearly evident. Interior to this envelope, the flow appears directed radially inwards towards the jet, which (from conservation of mass) must turn parallel to the jet and form the characteristic wake. It is quite apparent, therefore, that blockage dominance for the V/STOL jet is confined to a small upstream region, and that the majority of the near-jet surface flow is highly rotational, turbulent and three-dimensional. Therefore, one might expect that potential flow models would encounter considerable difficulty in addressing the nearfield flow of a V/STOL jet.

Figure 2 is an interpretation of the jet roll-up process and establishment of the counter-rotating vortex pair. Mosher (Ref. 9) and Kamotani and Greber (Ref. 10) extensively probed the jet flowfield vicinity in three-dimensions for the circular jet of velocity ratio $\lambda = 8$. Considerable data interpretation was pursued in reference 9, in particular determination of the orientation along the jet path of the plane with unit normal parallel to the local dominant axial velocity component. Plotting data in vertical planes produced the familiar horse-shoe profiles previously determined. However, when the local velocity vector is resolved into scalar components in the local normal-transverse plane coordinate system, the local jet cross-section shape and transverse plane counter-rotating flow immediately becomes apparent. For example, Figure 3 illustrates the symmetric half-plane distribution of the normal mean axial jet velocity for $\lambda = 8$, at downstream stations $x_1/d = 7$ and 23, where x_1 is the curvilinear coordinate parallel to the curved jet path with origin at the plate surface, and d is the jet initial diameter. Note the characteristic horse-shoe shape has become the (equally) familiar "kidney" shape in this representation. Since the jet is basically axially symmetric at the point of injection, the combined influence of blockage plus entrainment is to rapidly erode the jet potential core and to eventually establish the axial velocity maxima near the center of each transverse plane vortex, Figure 3b.

ANALYSIS

These experimental results indicate that the non-potential character of the near-field jet flow is the dominant determinor of the essential V/STOL jet character. Therefore, it seems rather optimistic to assume that a viscous correction to a potential flow-derived model could adequately describe near-field phenomena without an intractible number of adjustable parameters. This is the base assumption of this reported analysis, as has been concluded by others. Specifically, a numerical solution of some form of partial differential equations for viscous, rotational flow is required. The analysis of the experimental data clearly indicates that three-dimensionality is absolutely intrinsic to the flowfield development; hence, there is no lower dimensional description that can yield meaningful results. The jet and near-field flow is rotational, viscous and undoubtedly highly turbulent. Therefore, for a prediction methodology to be adequate, it must be obtained using some form of the three-dimensional time-averaged Navier-Stokes equations. Furthermore, since the three-dimensional analysis is required, the complete Reynolds stress tensor must be considered.

Remote from the plate there is indication of an inviscid flow streamline connecting upstream and downstream transverse-plane velocity stagnation points. Both the initial jet and onset cross-flow velocities are steady and the dominant scalar component of the jet velocity vector is uni-directional, parallel to the curvilinear jet axis.

These observations have guided the reported analysis which yields derivation of a three-dimensional, viscous-inviscid interaction algorithm for detailed prediction of the near-field flow associated with a V/STOL jet injected transverse to a subsonic crossflow. Table 1 briefly summarizes the major phases of the concept. Following Input, a sequence of inexpensive two-dimensional potential flow solutions are conducted at the injector surface. These yield estimates of the interface contour separating the potential and viscous-turbulent solution domains. A relatively inexpensive three-dimensional potential flow solution, Phase C, determines the first estimate of the inviscid pressure distribution on the plate and on the viscous jet region domain boundaries. For Phase D, a modestly inexpensive computational sequence yields the initialization of all variables required solved in the three-dimensional turbulent flow solution, plus distribution of the pressure fields which interconnect the two solution domains. Step E is a relatively expensive solution of the complete three-dimensional parabolized viscous and turbulent jet flowfield equations. The solution is acceptable when the potential flow entrainment is in agreement with that predicted by the viscous jet region solution, as affected by entrainment everywhere perpendicular to the jet axis.

Table 1

SUMMARY OF THREE-DIMENSIONAL V/STOL JET INTERACTION ALGORITHM

PHASE	OPERATION	DESCRIPTION
A.	Input	Problem specified by: U_∞ = crossflow velocity U_j, d_j, r_j = jet velocity, diameter, trajectory
B.	2D Potential Flow Computation	1. Find C_p for blockage contours on injector plate 2. Extract entrainment velocities at plate
C.	3D Potential Flow Computation	1. Interpolate interaction surface 2. Distribute entrainment 3. Compute plate and surface C_p
D.	2D Viscous And Turbulent Jet Region Solution	1. Initialize jet region axial velocity 2. Compute transverse plane velocity distributions 3. Compute turbulence correlation distributions 4. Compute interior pressure distribution
E.	3D Turbulent Jet Region Computation	1. Integrate complete 3D jet region equations 2. Stop at top of 3D domain of Step C. 3. Compare turbulent jet axial velocity to negative of inviscid entrainment, Step C.2. 4. Repeat analysis starting at Step C.1 if required

The viability of an interaction algorithm is based solely upon identification of a surface within the flowfield upon which inviscid potential flow boundary conditions can be specified. Based upon the available experimental data, this appears a valid concept for the V/STOL jet problem only if the interface is not impervious. The data confirm that, for a circular jet at $\lambda = 8$ for example, the inviscidly-impervious surface develops within 4-5 jet diameters downstream of injection, as confirmed by existence of an apparent streamline connecting two stagnation points. The stagnation points exist on the symmetry plane at about ± 4 jet diameters from the defined center of the jet flow region, and the region extends laterally about the same distance. Hence, for this case at least, the region of viscous-dominated rotational flow appears bounded by a nominal cylinder of top radius equal to approximately 4 jet diameters. The cross-sectional shape of the cylinder near the plate surface must be determined from the analysis and is not an inviscid streamline, c.f., Figure 1. The oil-flow photographs do provide some guidance however.

The key element in the algorithm is pressure coupling between the inviscid and viscous flow analyses. Due to the developed parabolization, the transverse plane pressure distribution and axial pressure gradient become locally solvable as a function of distance along the jet trajectory. This is accomplished using differential equations obtained from the divergence of the transverse plane mean flow momentum equations. The detailed development is presented elsewhere (Ref. 11). Defining the limited tensor index summation convention, $1 \leq j \leq 3$ and $2 \leq k, \ell \leq 3$, where x_ℓ is the coordinate system spanning the plane transverse to the local jet direction, with unit normal parallel to the x_1 coordinate, the differential equation governing the jet-region pressure distribution is

$$L(\bar{p}) = \frac{\partial}{\partial x_\ell}\left[\frac{\partial \bar{p}}{\partial x_\ell} + \frac{\partial}{\partial x_j}(\bar{\rho}\tilde{u}_j\tilde{u}_\ell) - \frac{\partial}{\partial x_k}(\bar{\sigma}_{\ell k} - \overline{\rho u_\ell' u_k'})\right] = 0 \qquad (1)$$

The overbar and over-tilde in equation (1) signify time-averaged and mass-weighted time-average respectively, and $\bar{p}$ is pressure, $\bar{\rho}$ is density, $\tilde{u}_i$ is velocity vector, $\bar{\sigma}_{\ell k}$ is the Stokes viscous stress tensor, and $\overline{\rho u_\ell' u_k'}$ is the Reynolds stress tensor. The solution for equation (1), a linear elliptic Poisson equation, consists of complementary and particular contributions as

$$\bar{p}(x_i) = p_c(x_i) + p_p(x_i) \qquad (2)$$

By definition, the complementary solution satisfies the homogeneous equation

$$L(p_c) = \frac{\partial^2 p_c}{\partial x_\ell^2} = 0 \qquad (3)$$

Subject to the known boundary conditions for pressure $\bar{p}(x_i)$. The interface inviscid flow pressure distribution is everywhere known, Phase C, yielding

$$\bar{p}(\bar{x}_\ell) = p^I(\bar{x}_\ell) = p_c(\bar{x}_\ell) \tag{4}$$

In equation (4), $\bar{x}_\ell$ indicates x_ℓ constrained to the interfacial boundary of the viscous solution domain, and p^I is the inviscid flow pressure level distribution. Elsewhere, on the jet region central symmetry plane the boundary condition is vanishing normal gradient.

$$\ell(p_c) = \frac{\partial}{\partial x_\ell} p_c \cdot \hat{n}_\ell = 0 \tag{5}$$

Therefore, solution of equations (3)-(5) determines the pressure distribution interior to the viscous jet region as induced by the impressed cross-flow velocity distribution. Hence, the required pressure coupling of the interaction algorithm is facilitated.

The particular pressure distribution p_p modifies the computed complementary pressure distribution to account for viscous and turbulence modifications within the jet region. The particular solution p_p is any function satisfying equation (1) with homogeneous boundary conditions on interface segments coincident with p^I known. The appropriate Poisson equation for p_p is the inviscid form (Ref. 11).

$$L(p_p) = \frac{\partial}{\partial x_\ell}\left[\frac{\partial p_p}{\partial x_\ell} + \frac{\partial}{\partial x_j}\left(\bar{\rho}\tilde{u}_j\tilde{u}_\ell + \overline{\rho u_\ell'' u_k''}\right)\right] = 0 \tag{6}$$

Equations (1)-(6) define the pressure coupling algorithm as well as determination of pressure distributions in the three-dimensional parabolic viscous flow solution.

The partial differential equation system assumed appropriate for the three-dimensional viscous and turbulent flow region prediction is the three-dimensional parabolic Navier-Stoke's system (Ref. 12)

$$L(\bar{\rho}) = \frac{\partial}{\partial x_i}(\bar{\rho}\tilde{u}_i) = 0 \tag{7}$$

$$L(\bar{\rho}\tilde{u}_1) = \frac{\partial}{\partial x_i}(\bar{\rho}\tilde{u}_i\tilde{u}_1) + \frac{\partial \bar{p}}{\partial x_1} - \frac{\partial}{\partial x_\ell}\left[\frac{\bar{\mu}}{Re}\frac{\partial \tilde{u}_1}{\partial x_\ell} - \overline{\rho u_1'' u_\ell''}\right] = 0 \tag{8}$$

$$L(\bar{\rho}\tilde{u}_2) = \frac{\partial}{\partial x_i}(\bar{\rho}\tilde{u}_i\tilde{u}_2) + \frac{\partial \bar{p}}{\partial x_2} - \frac{\partial}{\partial x_\ell}\left[\frac{\bar{\mu}}{Re}\left(\frac{\partial \tilde{u}_2}{\partial x_\ell} + \frac{\partial \tilde{u}_\ell}{\partial x_2}\right) - \overline{\rho u_2' u_\ell'}\right] = 0 \tag{9}$$

$$L(\bar{\rho}\tilde{u}_3) = \frac{\partial}{\partial x_i}(\bar{\rho}\tilde{u}_i\tilde{u}_3) + \frac{\partial \bar{p}}{\partial x_3} - \frac{\partial}{\partial x_\ell}\left[\frac{\bar{\mu}}{Re}\left(\frac{\partial \tilde{u}_3}{\partial x_\ell} + \frac{\partial \tilde{u}_\ell}{\partial x_3}\right) - \overline{\rho u_3' u_\ell'}\right] = 0 \tag{10}$$

$$L(k) = \frac{\partial}{\partial x_i}(\bar{\rho}\tilde{u}_i k) - \frac{\partial}{\partial x_i}\left[\bar{\rho}\left(\frac{\bar{\nu}}{Re} + C_k \frac{k}{\varepsilon}\overline{u_i' u_k'}\right)\frac{\partial k}{\partial x_k}\right] + \overline{\rho u_i' u_k'}\frac{\partial \tilde{u}_k}{\partial x_i} + \bar{\rho}\varepsilon = 0 \tag{11}$$

$$L(\varepsilon) = \frac{\partial}{\partial x_i}(\bar{\rho}\tilde{u}_i\varepsilon) - \frac{\partial}{\partial x_i}\left[\bar{\rho}\left(0 + C_\varepsilon \overline{u_i' u_k'}\frac{k}{\varepsilon}\right)\frac{\partial \varepsilon}{\partial x_k}\right]$$

$$+ C_\varepsilon^1 \overline{\rho u_i' u_\ell'}\frac{\varepsilon}{k}\frac{\partial \tilde{u}_k}{\partial x_\ell} + C_\varepsilon^2 \bar{\rho}\varepsilon^2 k^{-1} = 0 \tag{12}$$

Recall the index limited summation convention, $1 \leq i \leq 3$ and $2 \leq k, \ell \leq 3$. The variables appearing in equations (7)-(12) are the mass-weighted, time-averaged density, pressure, velocity and dynamic Reynolds stress tensor, and Re is the reference Reynolds number. Equations (11)-(12) are the three-dimensional parabolic form of the transport equations for turbulence kinetic energy k and isotropic dissipation function ε, defined as

$$k \equiv \frac{1}{2}\overline{u_i' u_i'} \tag{13}$$

$$\frac{2}{3}\delta_{ij}\varepsilon \equiv 2\bar{\nu}\overline{\frac{\partial u_i'}{\partial x_k}\frac{\partial u_j'}{\partial x_k}} \tag{14}$$

The dynamic Reynolds stress is assumed the product of the time-averaged density and the kinematic Reynolds stress tensor, the parabolic components of which in principal coordinates are (Ref. 12).

$$\overline{u_1'u_1'} = C_1 k$$

$$\overline{u_2'u_2'} = C_3 k - 2C_4 \frac{k^2}{\varepsilon} \frac{\partial \tilde{u}_2}{\partial x_2} - C_2 \frac{k}{\varepsilon} C_4 \frac{k^2}{\varepsilon} \left[\frac{\partial \tilde{u}_1}{\partial x_2}\right]^2$$

$$\overline{u_3'u_3'} = C_3 k - 2C_4 \frac{k^2}{\varepsilon} \frac{\partial \tilde{u}_3}{\partial x_3} - C_2 \frac{k}{\varepsilon} C_4 \frac{k^2}{\varepsilon} \left[\frac{\partial u_1}{\partial x_3}\right]^2$$

$$\overline{u_1'u_2'} = - C_4 \frac{k^2}{\varepsilon} \frac{\partial \tilde{u}_1}{\partial x_2}$$

$$\overline{u_1'u_3'} = - C_4 \frac{k^2}{\varepsilon} \frac{\partial \tilde{u}_1}{\partial x_3}$$

$$\overline{u_2'u_3'} = - C_4 \frac{k^2}{\varepsilon} \left[\frac{\partial \tilde{u}_2}{\partial x_3} + \frac{\partial \tilde{u}_3}{\partial x_2}\right] - C_2 \frac{k}{\varepsilon} C_4 \frac{k^2}{\varepsilon} \frac{\partial \tilde{u}_1}{\partial x_2} \frac{\partial \tilde{u}_1}{\partial x_3} \qquad (15)$$

The various C_i and C_q^α are correlation constants of the turbulent closure model.

Equations (8)-(12) are five initial-value, two-dimensional elliptic boundary value, non-linear partial differential equations written on the dependent variables of jet region velocity $\tilde{u}_i$ and turbulence correlations k and ε. Equation (7) is a constraint enforcing conservation of mass, which is inserted directly into the right-hand non-homogeniety of the particular pressure Poisson equation (6). The solution domain for equations (7)-(12) is the three-dimensional domain interior to the interface surface and closed from below by the injection plate. The domain is open-ended in the downstream jet direction, the result of the parabolizing simplification. Hence, the 3DPNS system is initial-value on the x_1 curvilinear coordinate, and the solution is started at the injection plate surface. As a consequence, initial-condition distributions are required specified for all dependent variables $\{q\} \equiv \{\bar{\rho}, \tilde{u}_i, k, \varepsilon\}$ at this location. This in itself is a consequential computational problem since in reality all that is known is the (nominal) jet velocity $\tilde{u}_1$, on a circle of diameter d, and the distribution of the tangential and entrainment velocity components of $\tilde{u}_\ell$ on the interface surface. Procedures have been developed to meet the differential equation requirements, however, and are discussed with the numerical results. Boundary conditions are required appropriately specified everywhere on the (two-dimensional) interface surface (Ref. 11).

The remaining solution requirements are met using the familiar Laplacian differential equation governing potential flow

$$L(\phi) \equiv \nabla^2 \phi = 0 \qquad (16)$$

where the dependent variable is the perturbation potential function ϕ,

$$\vec{u} \equiv \vec{U}_\infty - \nabla\phi \qquad (17)$$

Boundary conditions on ϕ are everywhere required specified, and determined from equation (17). Should the boundary not be an inviscid streamline, then $\vec{u}\cdot\hat{n}$ equals the inviscid "onset" velocity component u_p^I, and

$$\nabla\phi\cdot\hat{n} = \vec{U}_\infty\cdot\hat{n} - u_p^I \tag{18}$$

The developed equation systems are all well-posed initial boundary value problems and amenable to solution using any consistent numerical algorithm. A finite element algorithm has been developed that facilitates some degree of geometric flexibility, and is presented in detail in reference 11.

RESULTS

The primary evaluational requirement for the developed three-dimensional interaction algorithm is verification that an interfacial surface, separating the irrotational and rotation-dominated flow regimes, can be quantized. For the circular jet at $\lambda = 8$, the intersection of the interfacial surface with the jet injection plane was assumed a nominal airfoil, and a Phase B solution domain established. Figure 4 illustrates the macro-domain discretization and boundary conditions as well as the computational finite element domain. Following extensive numerical studies (Ref. 11), it was determined that the pressure recovery associated with a conventional trailing edge could not be sufficiently diminished, irrespective of thickness ratio and/or trailing edge bluntness. For example, Figure 5 illustrates representative computed plate C_p, all of which compare poorly with experiment for the round jet at $\lambda = 8$, see Figure 6.

Therefore, the trailing edge must be replaced by a blunt base lying exterior to the interfacial surface. Additional numerical experimentation (Ref. 11) showed that for such a configuration, within close tolerance on location of the jet centerline and contour thickness ratio, the blockage-only induced C_p could be bounded uniformly by data. At least for the circular jet at $\lambda = 8$, therefore, the concept of an interfacial surface is verified, and the distribution of entrainment estimated from the envelope. The Phase C solution then yields the distribution of complementary pressure on the interface surface. Figure 7 illustrates a three-dimensional macro-element discretization for the circular jet. Figure 8 shows the resultant computed C_p distributions on the plate surface exterior to the interface intersection. The influence of entrainment is quite apparent; the results shown in Figure 8b. are in fundamental agreement with the experimental data (compare to Fig. 6). The pressure contours for the no-entrainment case, Figure 8a, compare particularly poorly within the low pressure region just off of the jet, further confirming that entrainment is a dominant influence in V/STOL performance.

The Phase D and E 3DPNS solution domain for the circular jet case at $\lambda = 8$ is shown in Figure 9. Figure 10 shows the interpolated distribution of jet flow axial velocity component $\tilde{u}_1$. Figure 11 shows the computed distributions of transverse velocity components within the domain, both with and without entrainment. Both contours are closed, but the entrainment-induced mass influx directly adjacent to the jet location is most noticeable. The 3DPNS entrainment-induced mass flux addition, through the continuity equation (7),

exerts a dominant influence on the local acceleration of the near-jet $\bar{u}_1$ velocity field. Figure 12 compares the distribution of acceleration for both cases. Note that without entrainment the dominant action is to retard the periphery of the jet (negative derivatives). Conversely, the entrained crossflow actually serves to accelerate the $\bar{u}_1$ velocity field to the side of the jet. Figure 13 is a plot of the computed $\bar{u}_1$ distribution at $x_1/d = 0.5$ in which the combined influences of entrainment and turbulence mixing are evident.

SUMMARY

A three-dimensional viscous-inviscid interaction algorithm has been derived for numerical determination of the detailed flowfield surrounding and entrained into the wake of a V/STOL jet issued orthogonally into a subsonic crossflow bounded on one plane by an aerodynamic surface. The dominant influence parameter coupling the three-dimensional external potential flow analysis, and the imbedded three-dimensional viscous and turbulent analysis of the jet and near-field wake, is the entrainment flow induced into the jet region and its influence on the potential flow. The two analyses are pressure coupled, and the entrainment-induced mass flux addition to the wake is the primary influence variable of the global algorithm. The key element of the algorithm is existence of a surface defining the coincident boundary of the dual analyses. Numerical studies have quantized the interface surface, for the case of a circular jet issued into a crossflow with velocity ratio equal to eight, including the specific geometry of the interface intersection with the injection plane and the entrainment velocity distribution thereon.

REFERENCES

1. Chang, H.-C., "The Roll-Up of A Cylindrical Jet in A Cross-Flow," Aerospace Research Laboratores Report ARL 73-0131, 1973

2. Wooler, P. T., "Development of An Analytical Model for the Flow of A Jet Into A Subsonic Cross-Wind," NASA SP-218, p. 101-118, 1968.

3. Schmidt, H., "Deflection of A Round Turbulent Jet in A Cross-Wind," Arch. Mech., Vol. 26, Pt. 5, p. 849-859, 1974.

4. Jordinson, R., "Flow in A Jet Directed Normal to the Wind," ARC Report and Memoranda No. 3074, 1956.

5. Moussa, A. F., Trischka, J. W. and Eskinazi, F., "The Near Field in the Mixing of A Round Jet with A Cross Stream," J. Flu. Mech., Vol. 80 Pt. 1, p. 49-80, 1977.

6. Vogler, R. D., "Surface Pressure Distributions Induced on A Flat Plate by A Cold Air Jet Issuing Perpendicularly from the Plate and Normal to A Low-Speed Free Stream Flow," NASA TN D-1629, 1963.

7. Bradbury, L. J. S., and Wood, M. N., "The Static Pressure Distribution Around A Circular Jet Exhausting Normally from A Plane Wall into an Airstream," C. P. No. 822, 1965, British Aero. Res. Council.

8. McMahon, H. M. and Mosher, D. K., "Experimental Investigation of Pressures Induced on A Flat Plate by A Jet Issuing into A Subsonic Crosswind," NASA SP-218, p. 49-62, 1968.

9. Mosher, D. K., "An Experimental Investigation of A Turbulent Jet in A Cross-Flow," Aerospace Engineering Report No. 70-7, Georgia Institute of Technology, 1970.

10. Kamotani, Y. and Greber, I., "Experiments on A Turbulent Jet in A Cross-Flow," AIAA J., Vol. 10, No. 11, p 1425-29, 1972.

11. Baker, A. J. and Manhardt, P. D., "A Numerical Viscous-Inviscid Interaction Algorithm for Prediction of Near-Field VSTOL Jet-Induced Flows," Report NADC-77167-30, 1979.

12. Baker, A. J., Manhardt, P. D. and Orzechowski, J. A., "A Numerical Solution Algorithm for Prediction of Aerodynamic Corner Flows," AIAA Paper No. 79-0073, 1979.

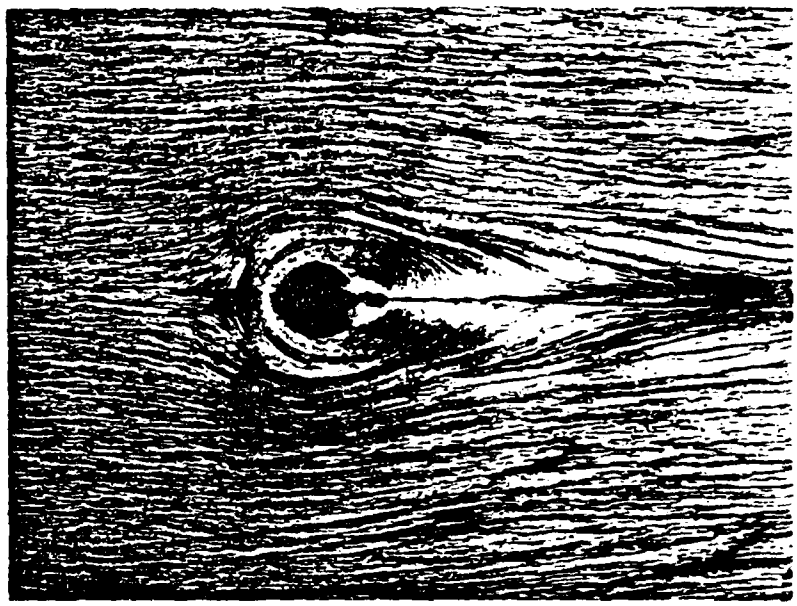

a) Solid Blockage

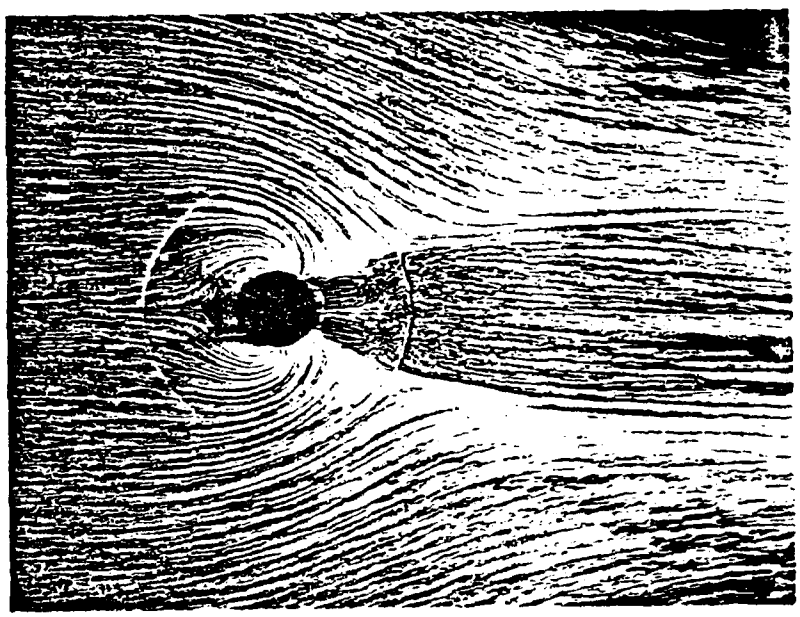

b) Circular Jet at $\lambda = 8$

Figure 1. Flow Patterns on the Injection Plate (Ref. 8)

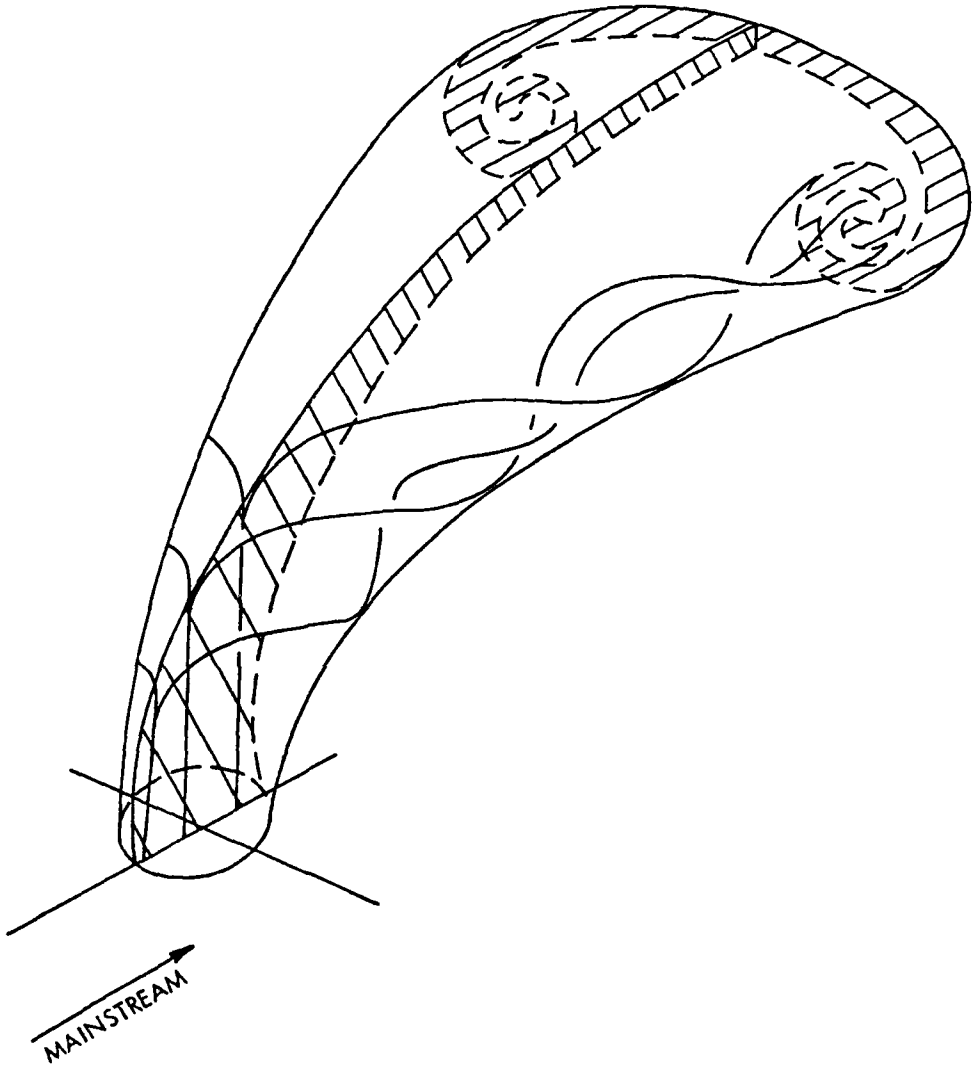

Figure 2. Illustration of Trailing Vortex Build-Up Behind Circular Jet

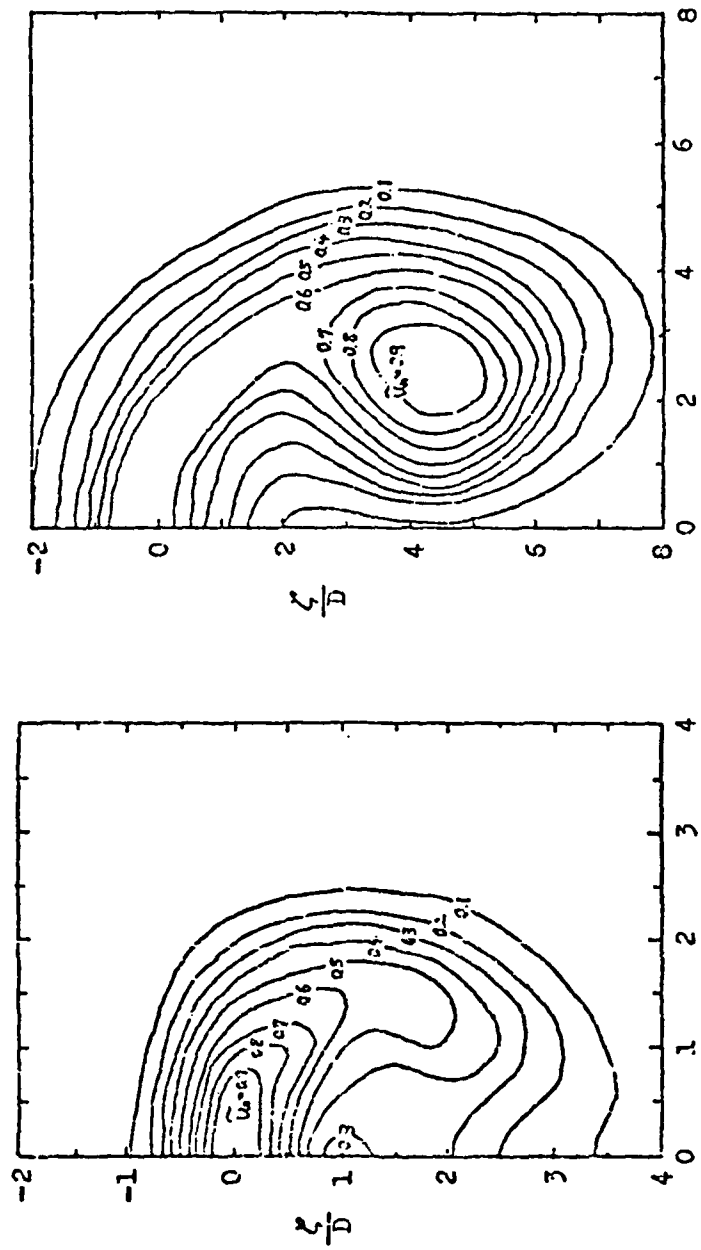

Figure 3. Transverse Plane Axial Velocity $\tilde{u}_1$ Contours (Ref. 10)

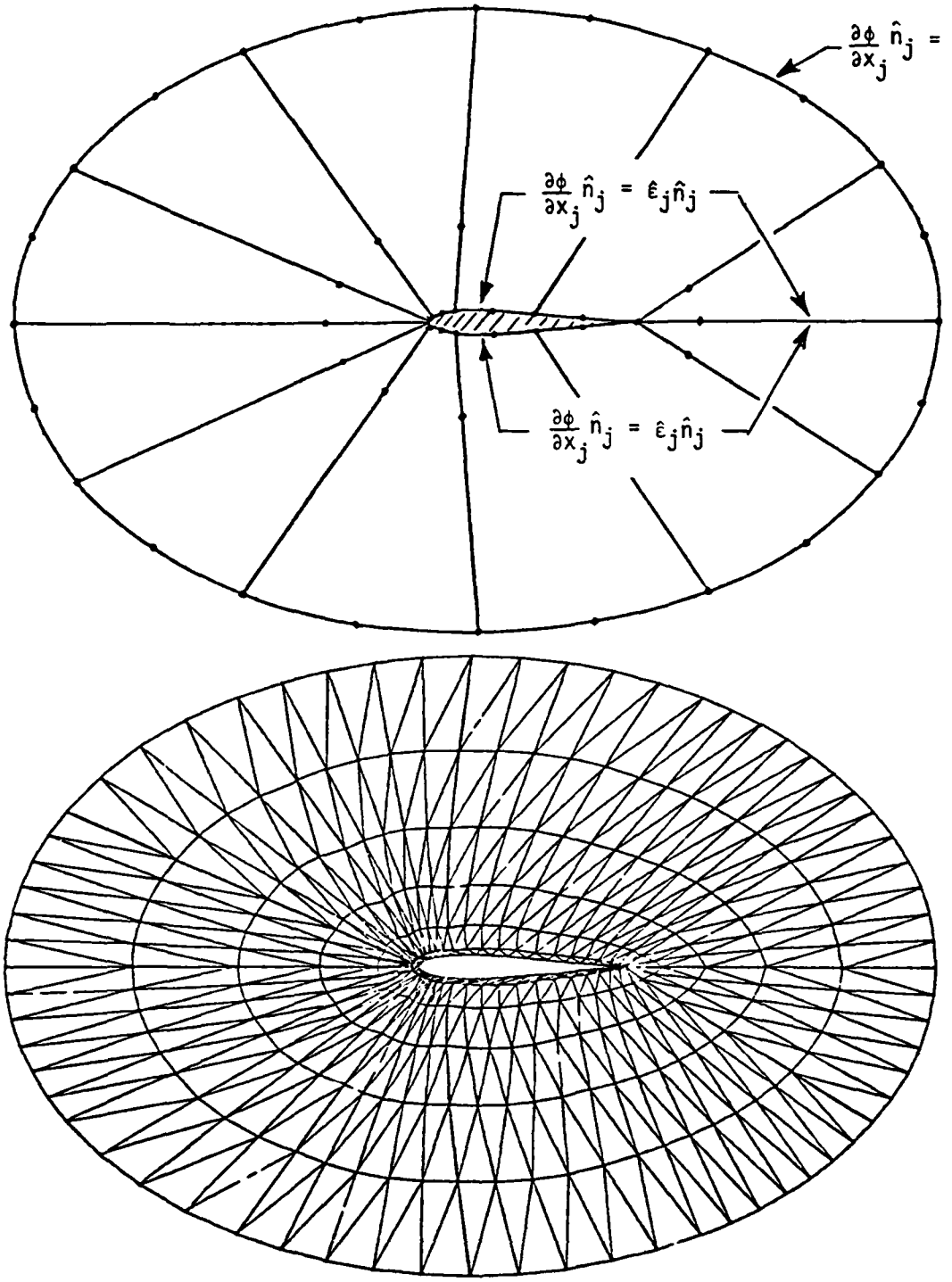

Figure 4. Macro Element and Finite Element Discretizations for Karman-Trefftz Potential Solutions

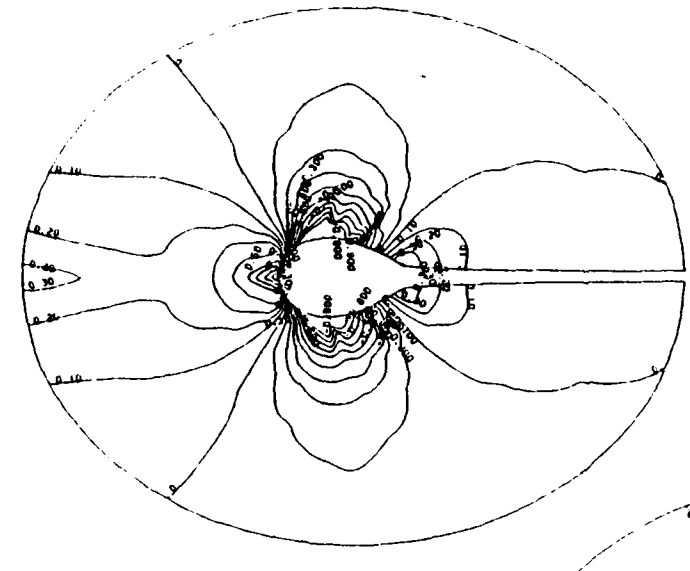

a) t/c = 0.88, Δ/c = 0.10

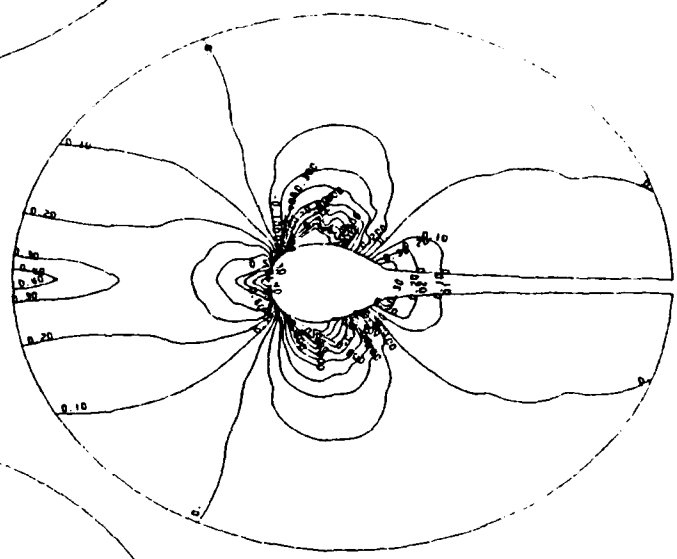

b) t/c = 0.88, Δ/c = 0.25

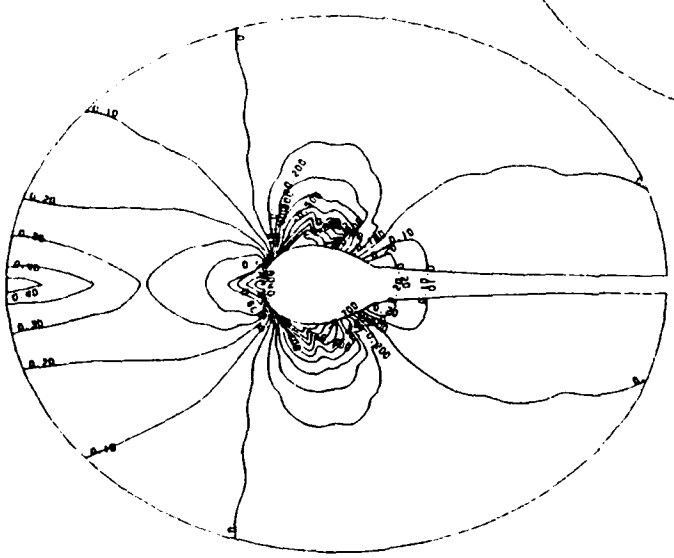

c) t/c = 0.88, Δ/c = 0.40

Figure 5. Computed Inviscid Pressure Distributions for Various Open Trailing Edge Airfoils

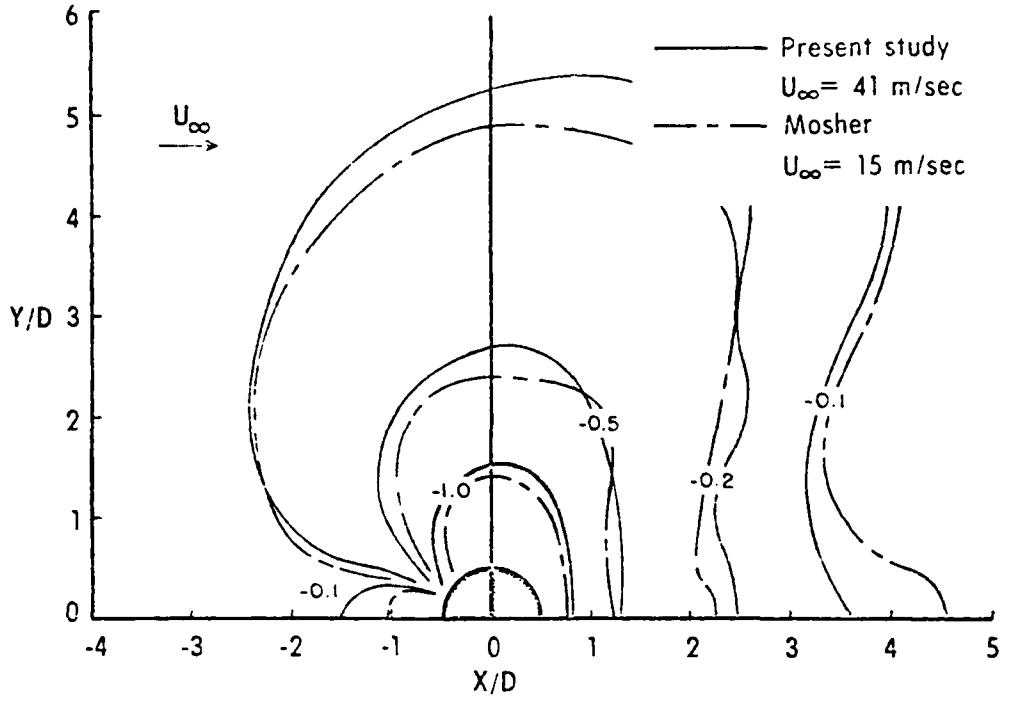

Figure 6. Experimental Contours of Constant Surface Pressure Distributions for Circular Jet, λ = 8 (Ref. 11)

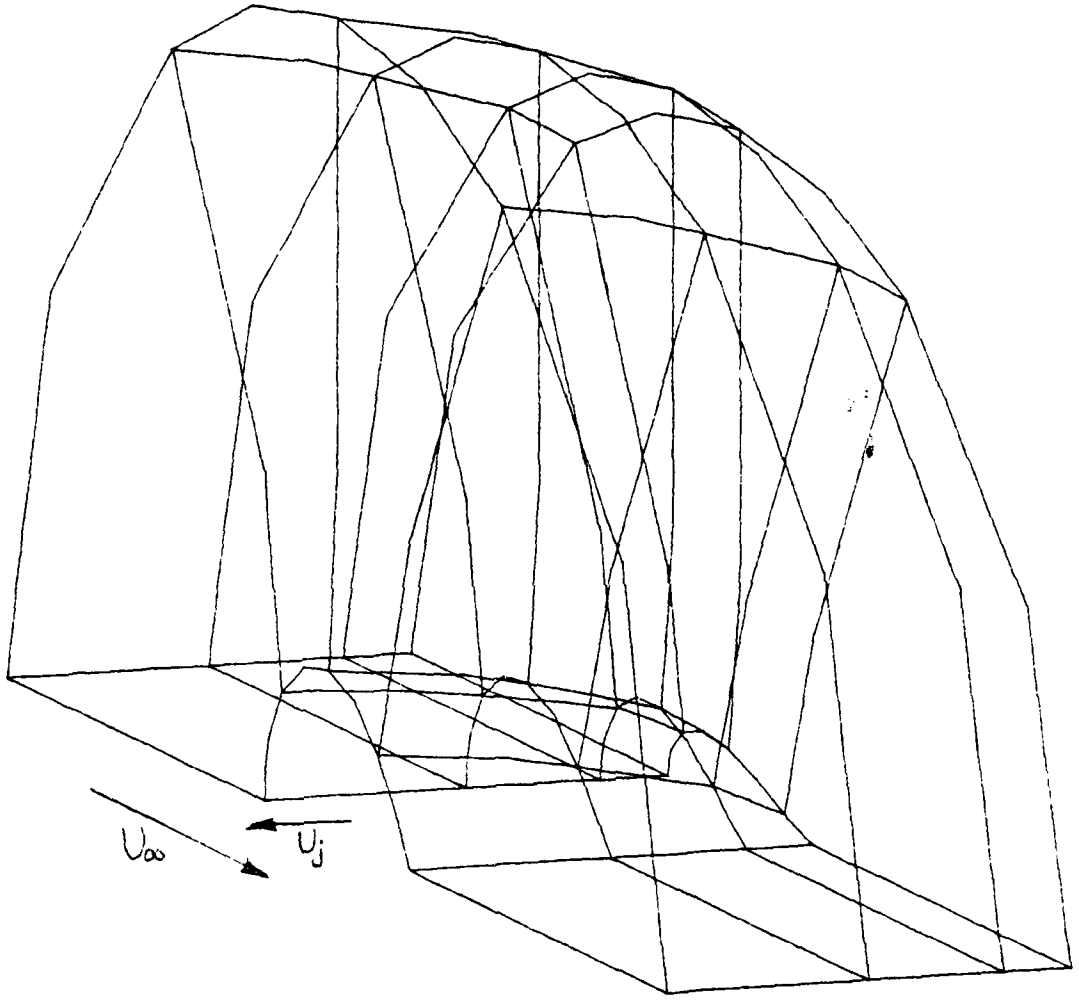

Figure 7. Three-Dimensional Potential Flow Solution Domain for Circular Jet, $\lambda = 8$, $U_\infty = 15$m/s

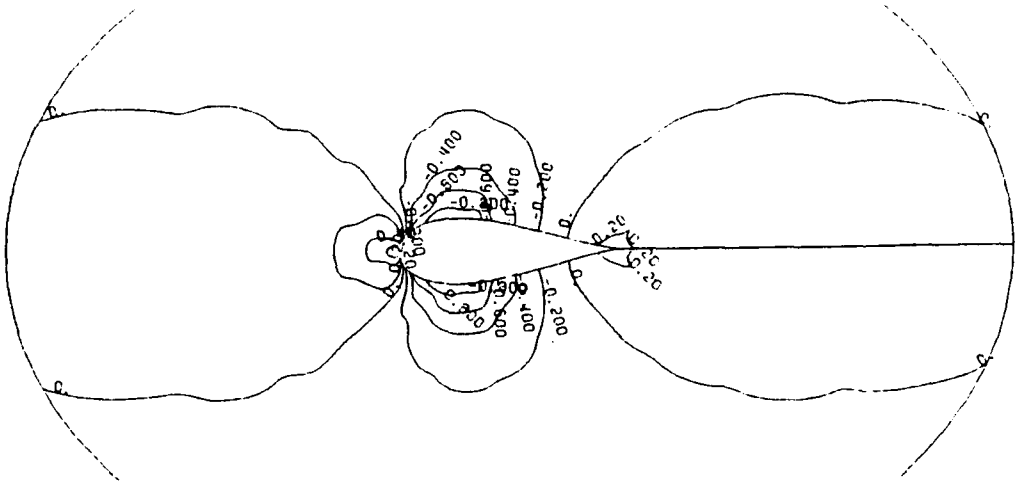

a.) Blockage flow, (no entrainment)

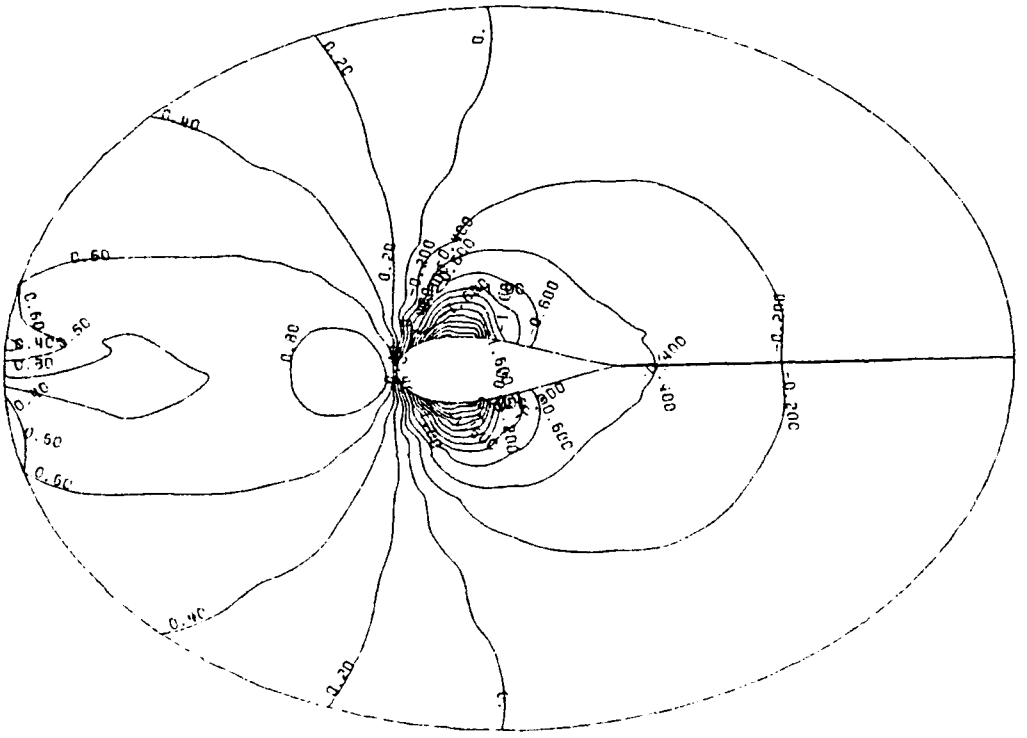

b.) Circular Jet with Entrainment, $\lambda = 8$

Figure 8. Computed Pressure Distribution on Injection Plane

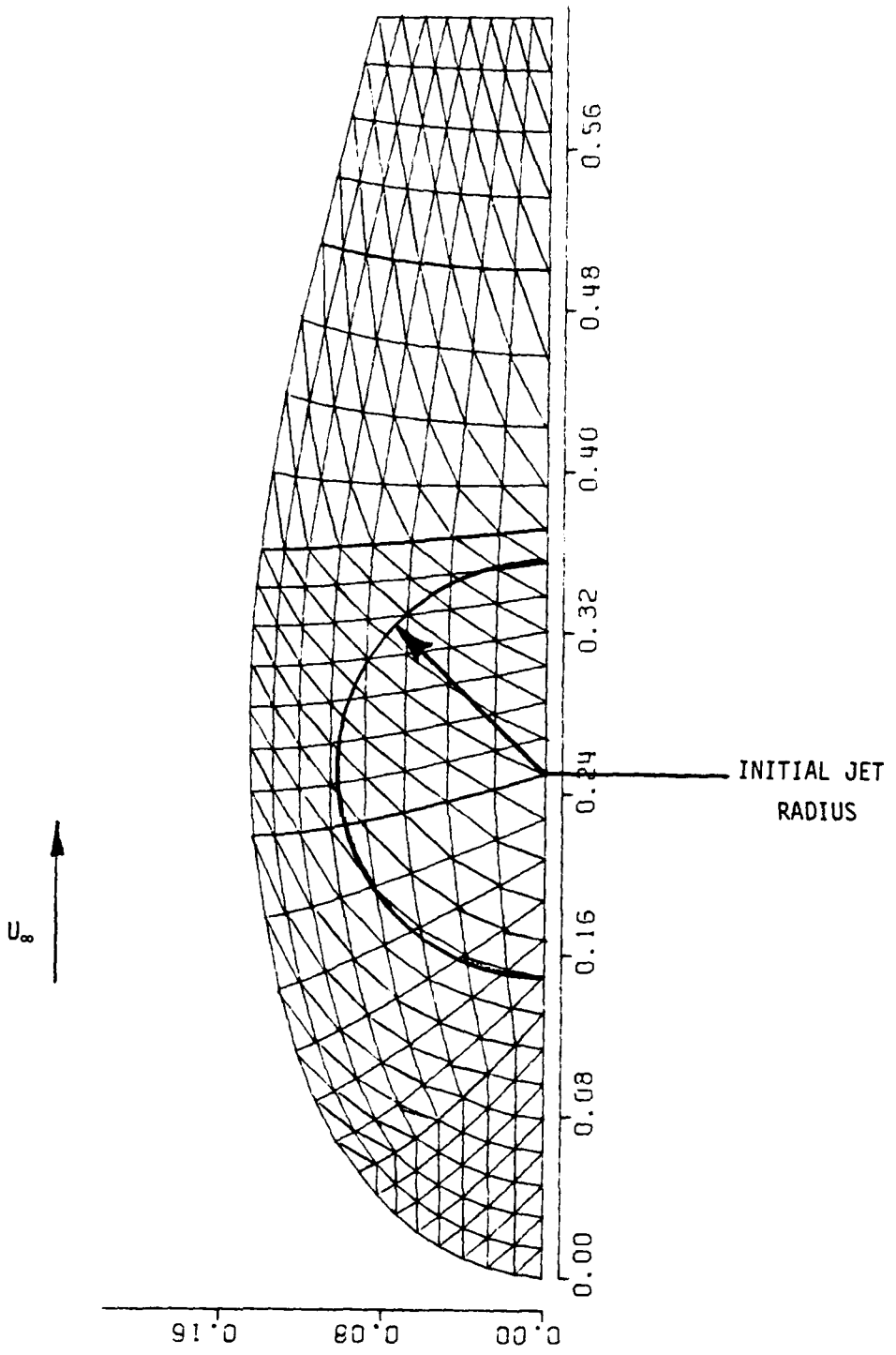

Figure 9. Generated Finite Element Discretization of 3DPNS Solution Domain

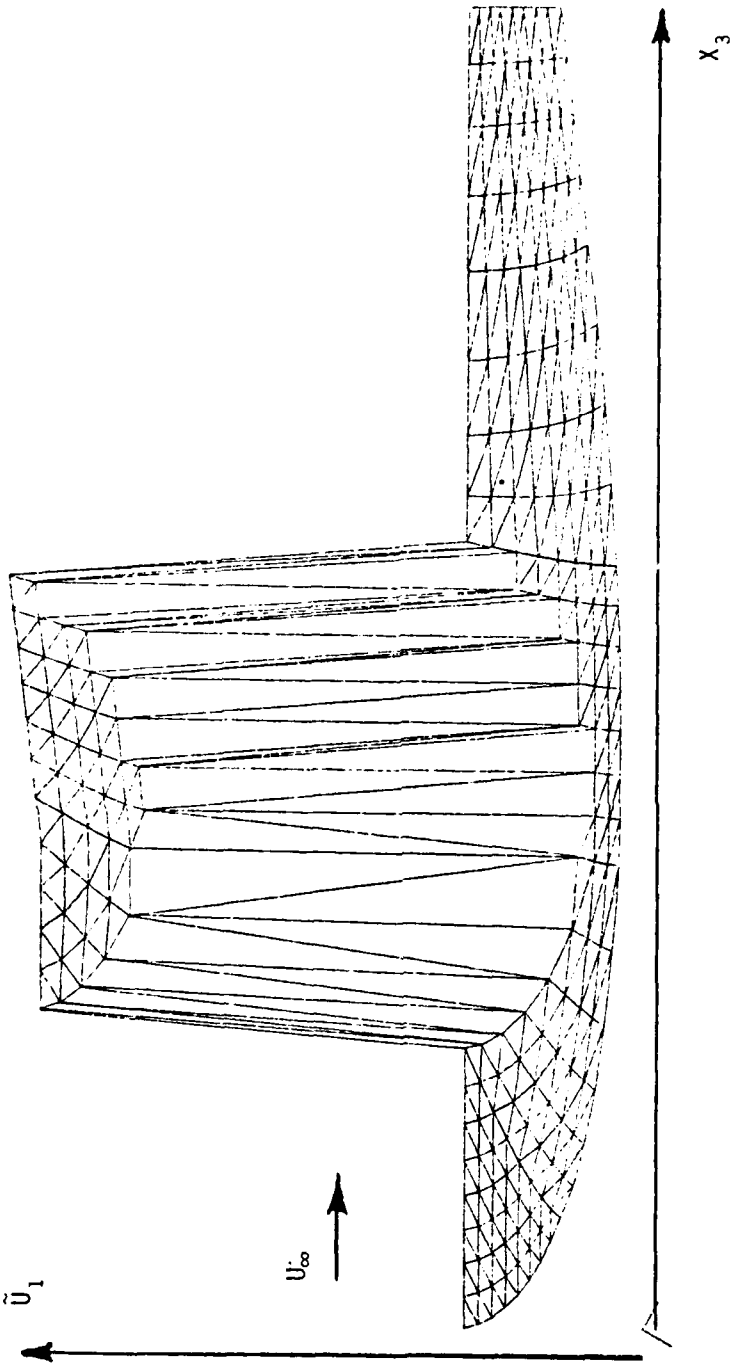

Figure 10. Initialized Distribution of 3DPNS Axial Velocity $\tilde{u}_1$ on S_1

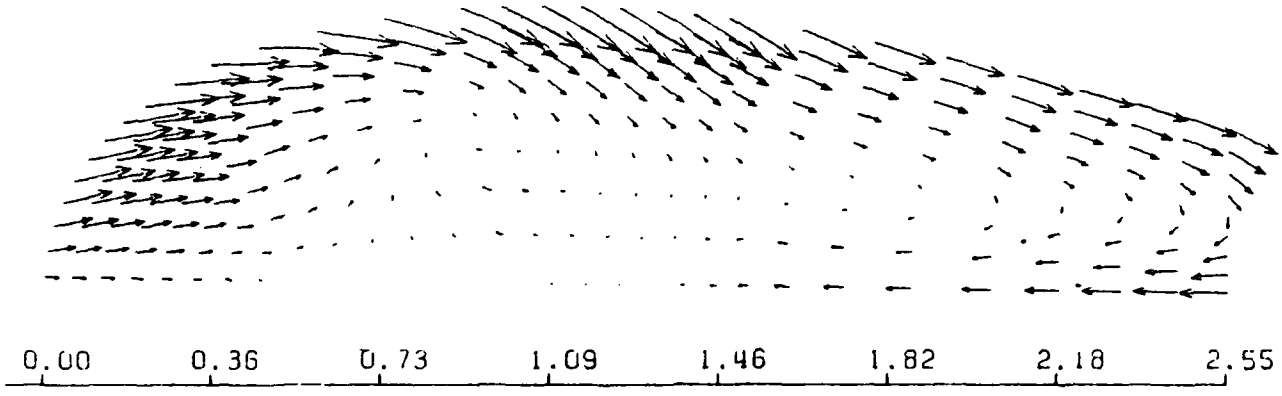

a) With Entrainment from Step B

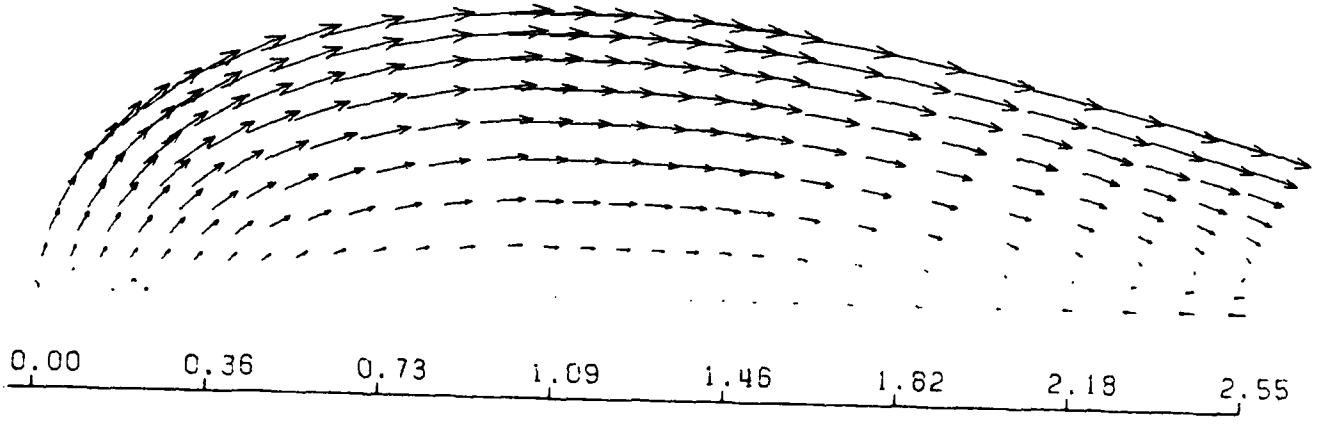

b) Without Entrainment

Figure 11. Computed Transverse Plane Velocity $\tilde{u}_\ell$ Vector Distributions on S_1

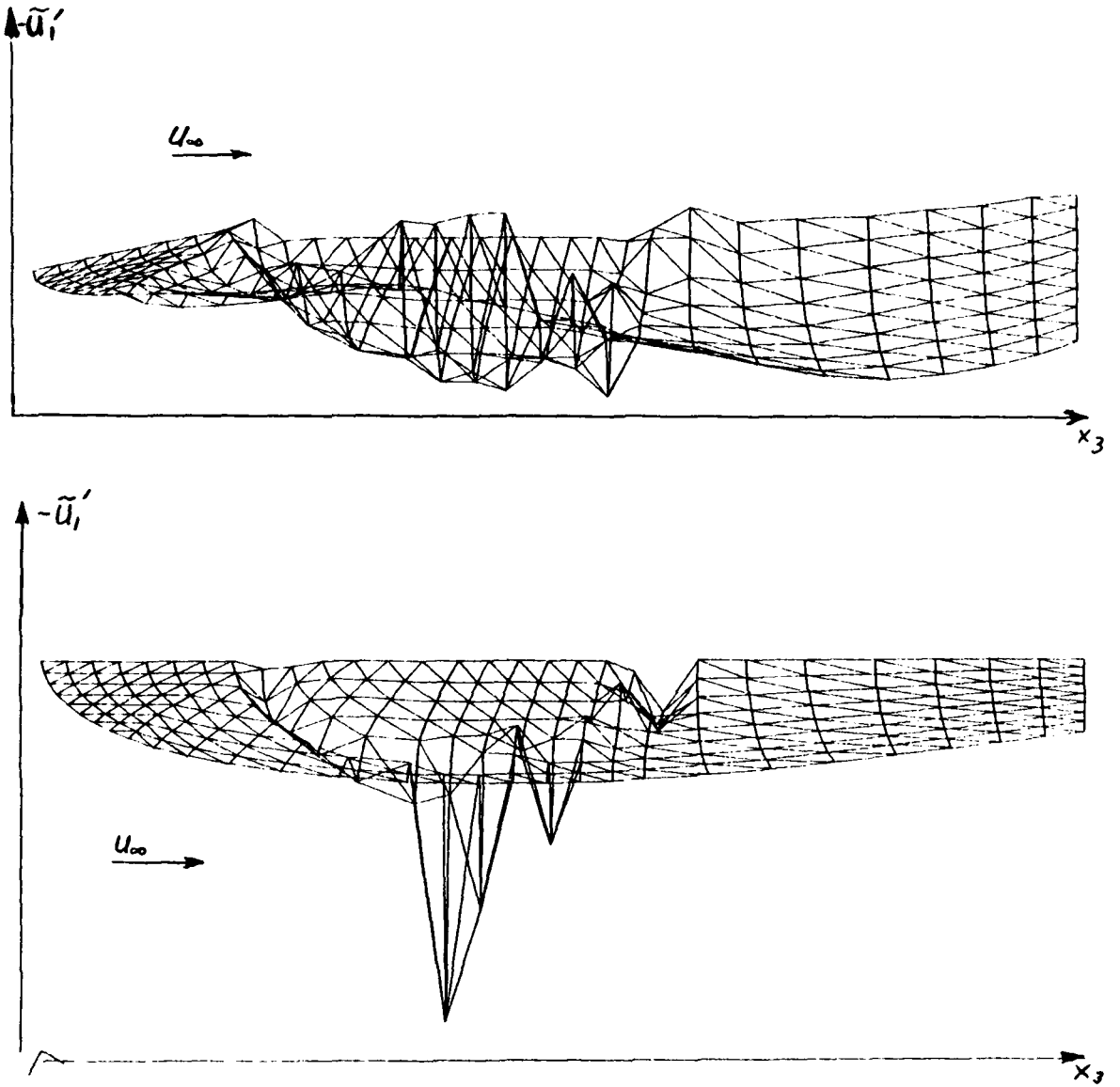

Figure 12. Computed Axial x_1 Derivative Distribution of Jet Region Velocity $\tilde{u}_\theta$ on S_1, a) with entrainment

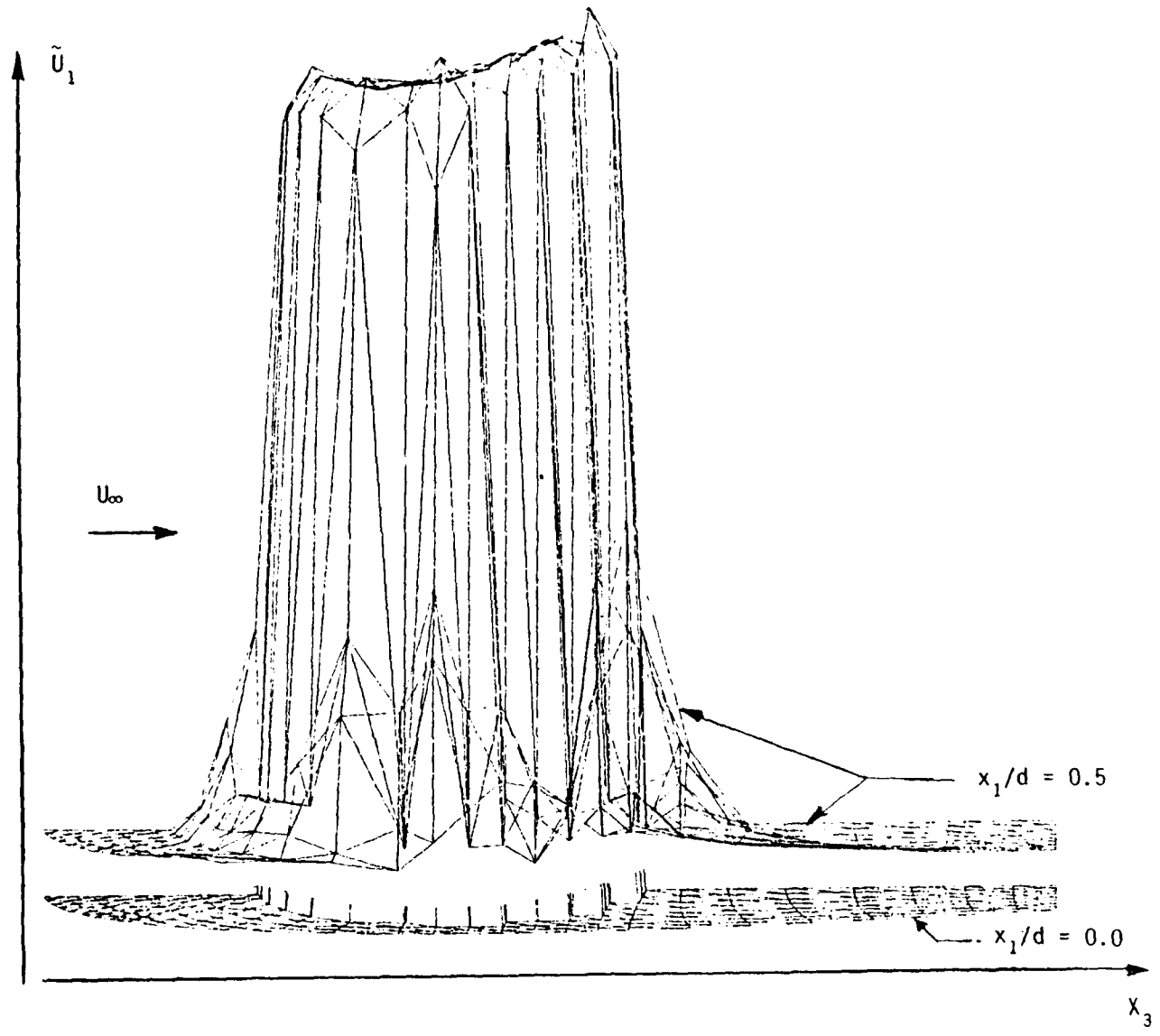

Figure 13. Computed Distribution of Jet Region Velocity $\tilde{u}_\theta$ on S_2, $x_1/d = 0.5$

SESSION II

AERODYNAMICS OF V/STOL AIRCRAFT IN HOVERING FLIGHT

Chairman:

Robert Weinraub
Naval Air Systems Command

AMPAC AEROSPACE MASS PROPERTIES ANALYSIS, INC.

AN EMPIRICAL METHOD FOR ESTIMATING JET-INDUCED LIFT LOSSES OF V/STOL AIRCRAFT HOVERING IN AND OUT-OF-GROUND EFFECT;

Effects of Planform and Arrangements of Multiple Jets on Low Wing, Vertical Jet Configurations

Richard E. Kuhn

ABSTRACT

A method for estimating the jet-induced lift losses experienced by Jet V/STOL aircraft in hovering flight in and out-of-ground effect has been developed by correlating available data. The method for single jet configurations is based on the original work by L.A. Wyatt which has been extended to include the effects of nozzle pressure ratio and wing height. The method for multiple jet configurations was developed by correlating available data on flat plate and low wing configurations. The methods are based on model data but comparisons are made with large-scale hot jet data where possible.

NADC Contract No. N62269 - 79 - C - 0231

2640 AMY DRIVE NORRISTOWN, PENNSYLVANIA 19403 (215) 539-1674

INTRODUCTION

The design, and the takeoff and landing performance, of VTOL aircraft require the ability to predict the lift losses inherent in the configuration in and out of ground effect. Gentry and Margason, in reference 1, developed a method for predicting the out-of-ground-effect lift losses and Wyatt in reference 2 developed a method for predicting the ground effects on single jet configurations. However, with multiple jets the flow field is much more complex and the designer must resort to experiments to determine the ground effects.

The present paper is the first step in an attempt to develop an empirical method for estimating the ground effects on multijet configurations that would be useful in the early preliminary design stage. The method is based on a correlation of available data for single and multiple jet configurations and, in its present form, is limited to vertical jets issuing from flat plates or low wing configurations.

This work was completed under contract to the Naval Air Development Center, Warminster, Pennsylvania, as part of their effort, under the technical direction of Mr. Campbell Henderson, to develop a V/STOL Aerodynamics and Stability and Control Handbook.

SUMMARY

A method for estimating the jet-induced lift losses experienced by Jet V/STOL aircraft in hovering flight in and out-of-ground effect has been developed by correlating available data. The method for single jet configurations is based on the original work by L.A. Wyatt which has been extended to include the effects of nozzle pressure ratio and wing height. The method for multiple jet configurations was developed by correlating available data on flat plate and low wing configurations. The methods are based on model data but comparisons are made with large-scale hot jet data where possible.

The data are presented in the following sections in a form and with paragraphs, equations, and figures numbered for direct inclusion in the Aerodynamics and Stability and Control Manual.

The methods for estimating the out-of-ground effect lift losses developed by Gentry and Margason and by McDonnell Aircraft need no further development and are included directly for completeness.

2.2 PROPULSION-INDUCED AERODYNAMICS

2.2.1 Hover

The induced lift experienced by a jet or fan-powered V/STOL aircraft in hovering flight is caused by the action of the issuing streams inducing pressures on the lower surface of the aircraft. Figure 2.2.1 (1) illustrates the phenomena. Out-of-ground effects, the free jet entrains air and lowers the pressure on the surface surrounding the nozzle. In-ground effects, the pumping action and induced pressures are greatly increased by the entrainment into the wall jet flowing along the ground outward from the point where the jet impinges on the ground. This causes the lift loss to increase rapidly as the ground is approached. With multiple jets, the flow field is much more complex and close to the ground the lift loss is reduced by positive pressures induced by the "fountain" flow generated when the outward flowing wall jets from two or more jets meet.

The present method for estimating the induced lift in hovering flight consists of three parts: 1) $\frac{\Delta L_\infty}{T}$, the jet-induced lift loss out-of-ground effect, 2) $\frac{\Delta L_s}{T}$, the lift loss of a single jet, or equivalent single jet configuration induced by the wall jet flow in-ground effect, and 3) $\frac{\Delta L_m}{T}$, the induced lift caused by the "fountain" flow generated by multi-jet configurations. The total induced lift is given by:

$$\frac{\Delta L_\infty}{T} = \frac{\Delta L}{T} + \frac{\Delta L_s}{T} + \frac{\Delta L_m}{T} \qquad 2.2.1\ (1)$$

The last term $\frac{\Delta L_m}{T}$ is in turn made up of three parts: $\frac{\Delta L_1}{T}$, the increase in lift loss caused by the increased pumping action due to the fountain flows that occur at heights above those where positive pressures are created and two terms that are used to estimate the effects of the positive pressures, $\frac{\Delta L_2}{T}$ and $\frac{\Delta L_3}{T}$. Thus, the multi-jet contribution is given by:

$$\frac{\Delta L_m}{T} = \frac{\Delta L_1}{T} + \frac{\Delta L_2}{T} + \frac{\Delta L_3}{T} \qquad 2.2.1\ (2)$$

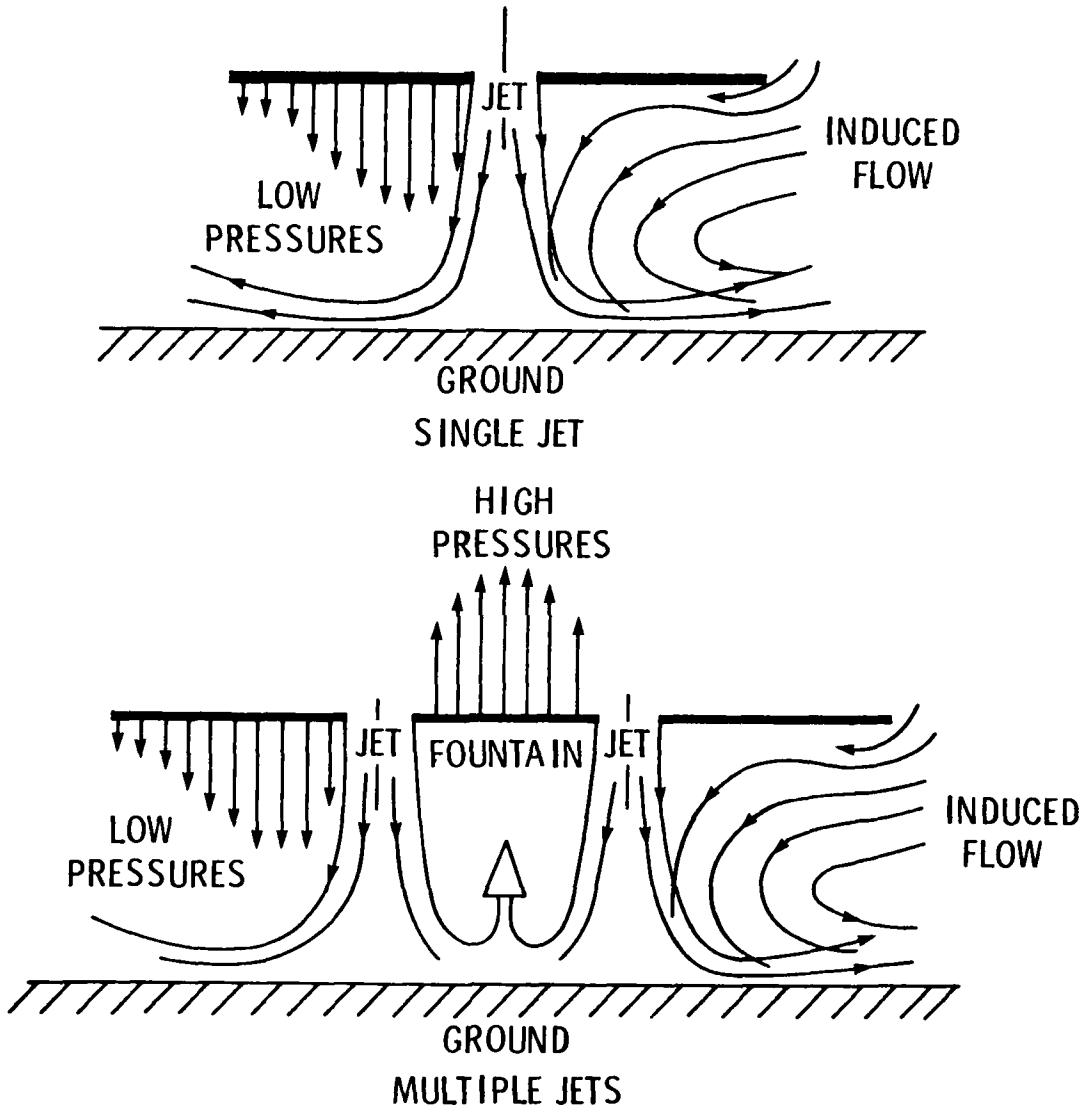

FIGURE 2.2.1 (1) - FLOW PATTERNS NEAR GROUND WITH SINGLE JET AND WITH MULTIPLE JETS

Figure 2.2.1 (2) presents the equations for calculating the induced lift terms and a schematic illustration of the manner in which they combine to give the total induced lift for a single jet and a multi-jet configuration. The following sections will discuss the development of these equations and the range and limitations of their applicability. The definitions of symbols used are given at the end of section 2.2.1 (1).

Out-of-Ground Effect - Method 1

The work of Gentry and Margason (Ref. 1) provides an empirical basis for estimating the jet-induced lift losses of single and multiple jet configurations out-of-ground effect. A major finding of that study was that the induced losses are a function of the jet decay rate. Higher decay rates result from more rapid entrainment of the ambient air. Increased entrainment induces higher suction pressures and a greater lift loss. A similar higher apparent decay rate occurs with multiple jets, when the axial distance x downstream from the nozzle is normalized to an equivalent single jet diameter, d_e, because multiple jets have a greater total surface area for mixing with ambient air than the equivalent single jet.

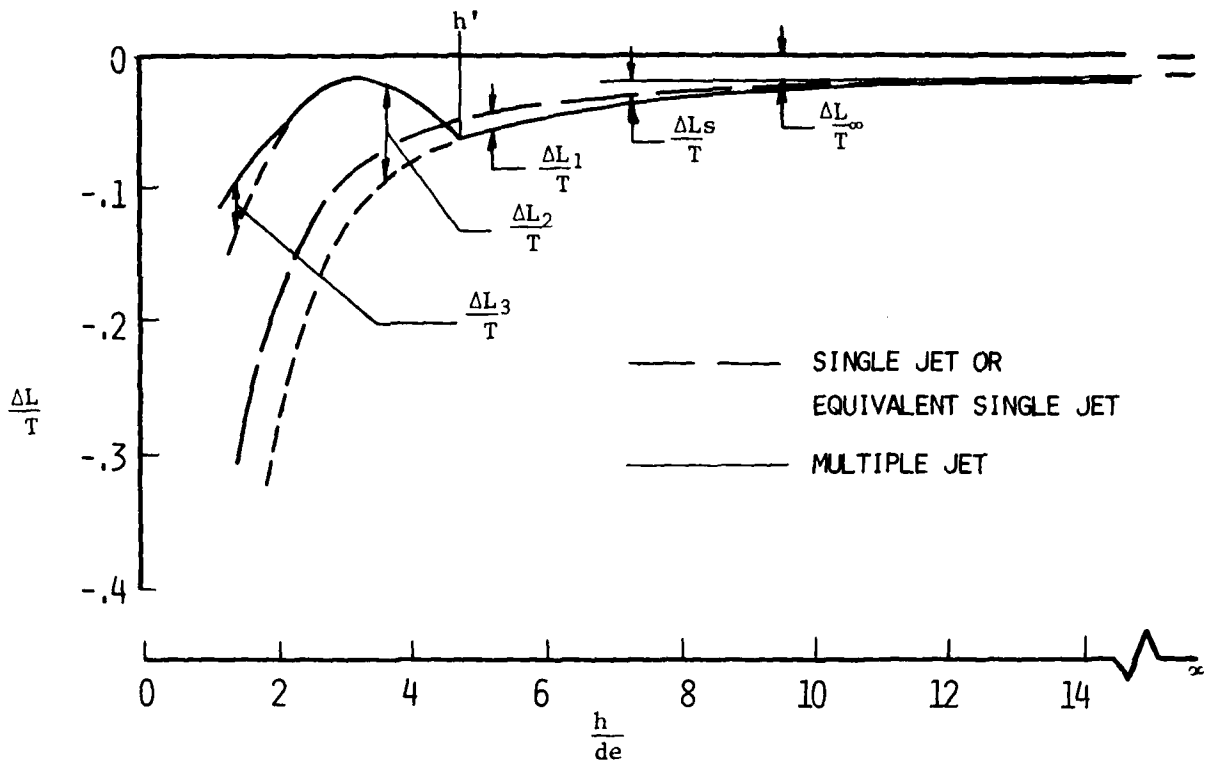

$$\frac{\Delta L_\infty}{T} = \sqrt{\frac{S}{A}}\left(.016\right)\left(\frac{P_N}{P}\right)^{-.64}\sqrt{-\left(\frac{\partial q/(P_n-p)}{\partial x/de}\right)_{max}\Big/\left(\frac{x}{d_e}\right)_i} \qquad 2.2.1\ (4)$$

or

$$\frac{\Delta L_\infty}{T} = \sqrt{\frac{S}{A}}\left(.0002528\right)\left[\left(\frac{P_n}{p}\right)^{-.64}\frac{\Sigma Pr}{d_e}\right]^{1.581} \qquad 2.2.1\ (6)$$

$$\frac{\Delta L_s}{T} = -.015\left[\frac{h/d_e}{\left(\frac{D}{d_e}-1\right)}\right]\left[-2.2-.24\left(\frac{P_n}{p}-1\right)\right] \qquad 2.2.1\ (7)$$

$$\frac{\Delta L_1}{T} = .5\,\frac{\Delta L_s}{T} \qquad 2.2.1\ (9)$$

$$\frac{\Delta L_2}{T} = \left(\frac{h'}{D} - \frac{h}{D}\right).135\,N^2\theta \qquad 2.2.1\ (11)$$

$$\frac{h'}{D} = 1.22\,\frac{1}{N}\left(\frac{D'}{d_e}\right)^{.65} \qquad 2.2.1\ (10)$$

$$\frac{\Delta L_3}{T} = 10\left(.9 - 10\,\frac{h}{D}\right) \qquad 2.2.1\ (12)$$

Note: $\frac{\Delta L_2}{T} = 0$ when $h > h'$, also $\frac{\Delta L_2}{T} = 0$ for two jet configurations

Figure 2.2.1 (2) - Schematic and Equations for Calculating Jet-Induced Lift in Hovering

The correlation of Ref. 1 provides an empirical expression for induced lift loss:

$$\frac{\Delta L_\infty}{T} = -.009 \sqrt{\frac{S}{A}} \sqrt{-\left(\frac{\partial qx/(P_n-p)}{\partial x/d_e}\right)_{max} \left(\frac{x}{d_e}\right)_i} \qquad 2.2.1\ (3)$$

where S = planform area

A = total jet exit area

d_e = diameter of an equivalent single nozzle having an area equal to the total of the areas of the multiple nozzles

$\left(\frac{\partial qx/(P_n-p)}{\partial x/d_e}\right)_{max}$ = maximum rate of decay of dynamic pressure

$(x/d_e)_i$ = downstream distance at which the dynamic pressure decay rate is maximum

The empirical basis for this out-of-ground effect lift loss equation is presented in Figure 2.2.1 (3) taken from Ref. 1.

A further refinement is developed in Reference 3 to account for the effects of nozzle pressure ratio $\frac{P_n}{p}$, given as:

$$\frac{\Delta L_\infty}{T} = -.016 \sqrt{\frac{S}{A}} \left(\frac{P_n}{p}\right)^{-.64} \sqrt{-\left(\frac{\partial qx/(P_n-p)}{\partial x/d_e}\right)_{max} \left(\frac{x}{d_e}\right)_i} \qquad 2.2.1\ (4)$$

These expressions apply to the case of equal jet thrust from each nozzle. For the case of substantially unequal thrust, the expressions can be applied to each jet, replacing d_e with d (of each jet) and summing the results as:

$$\frac{\Delta L_\infty}{T} = \left(\frac{\Delta L}{T_{j_1}}\right)\frac{T_{j_1}}{T} + \left(\frac{\Delta L}{T_{j_2}}\right)\frac{T_{j_2}}{T} + \text{- - - - - -} \qquad 2.2.1\ (5)$$

A difficulty experienced in the application of this method is knowledge of the actual decay characteristics of the jets from particular power plants planned for the vehicle design. However, if the exit conditions are known, the decay rate can be estimated from the data of Kleis and Foss, (Ref. 4).

Out-of-Ground Effect: Method 2

A more direct, easier to apply method for estimating out-of-ground effect jet-induced lift loss was developed by McDonnell Aircraft in Ref. 4. Correlation of data from various single and multiple jet configurations resulted in the following expression:

$$\frac{\Delta L_\infty}{T} = -.0002528 \sqrt{\frac{S}{A}} \left[\left(\frac{P_n}{p}\right)\right]^{-.64} \left(\frac{\Sigma P_r}{d_e}\right)^{1.581} \qquad 2.2.1\ (6)$$

where $\Sigma\pi d$ = total perimeter of all jets in the configuration. The basis of this equation is presented in Figure 2.2.1 (4). Again, for unequal jet thrust, the lift loss may be obtained by a superposition of individual jet effects. It should be noted that Method 2 implicitly accounts for the higher decay rate of multiple jet configurations in terms of equivalent jet diameter, d_e, but does not account for higher decay rates caused by jet exit conditions involving high mixing rates (as, for instance, when special supressor nozzles are used to reduce the temperature at ground level or to reduce ground erosion). If higher than normal turbulance levels and decay rates are involved, Method 1 must be used.

Both methods appear to correlate well with the limited amount of large scale data available (Ref. 6) as shown on Figures 2.2.1 (3) and 2.2.1 (4).

METHOD 1

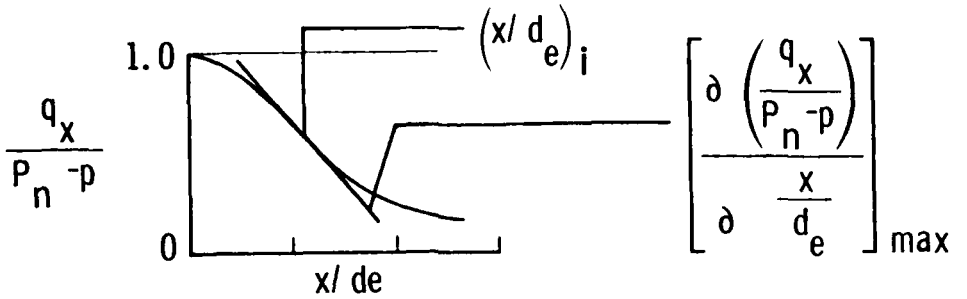

a) JET DECAY

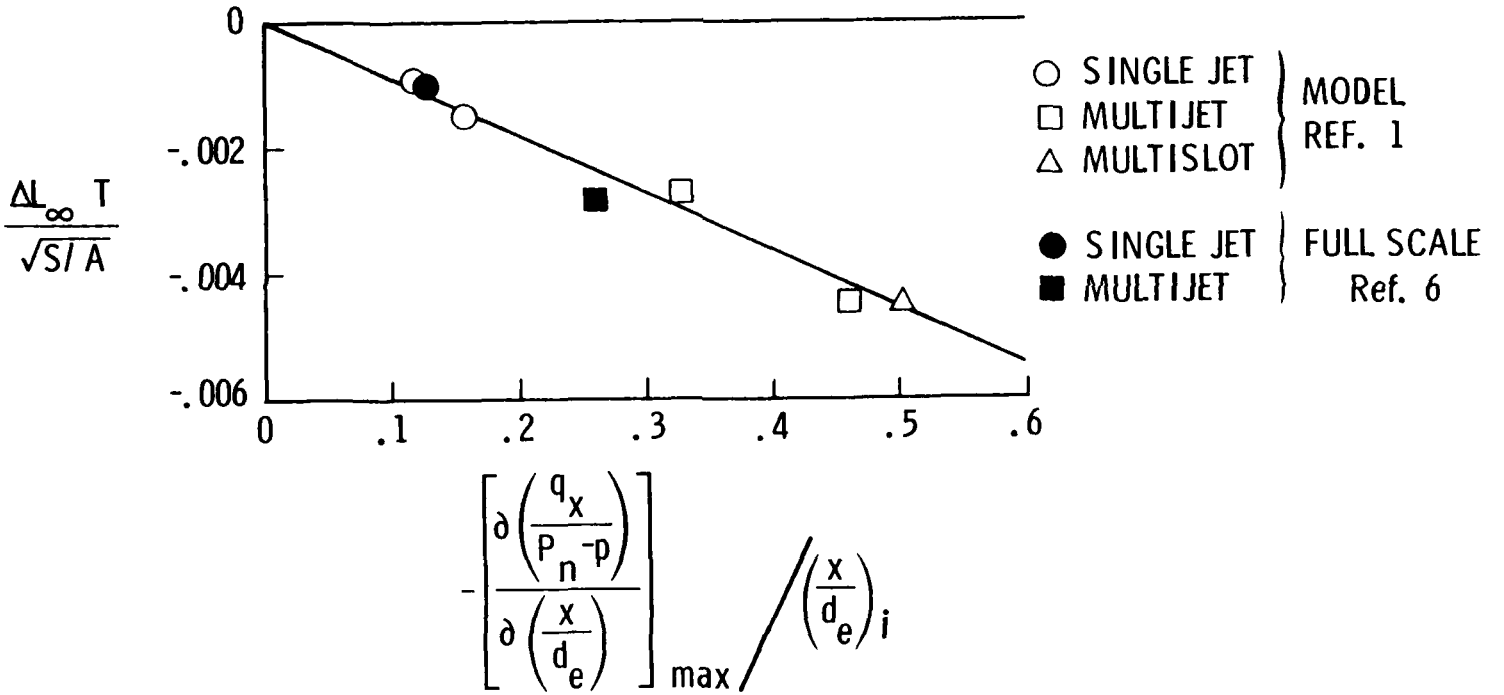

b) LIFT LOSS

FIGURE 2.2.1 (3) - CORRELATION OF INDUCED LOADS WITH JET DECAY PARAMETER (PRESSURE RATIO ≈ 2.0)

(METHOD 2)

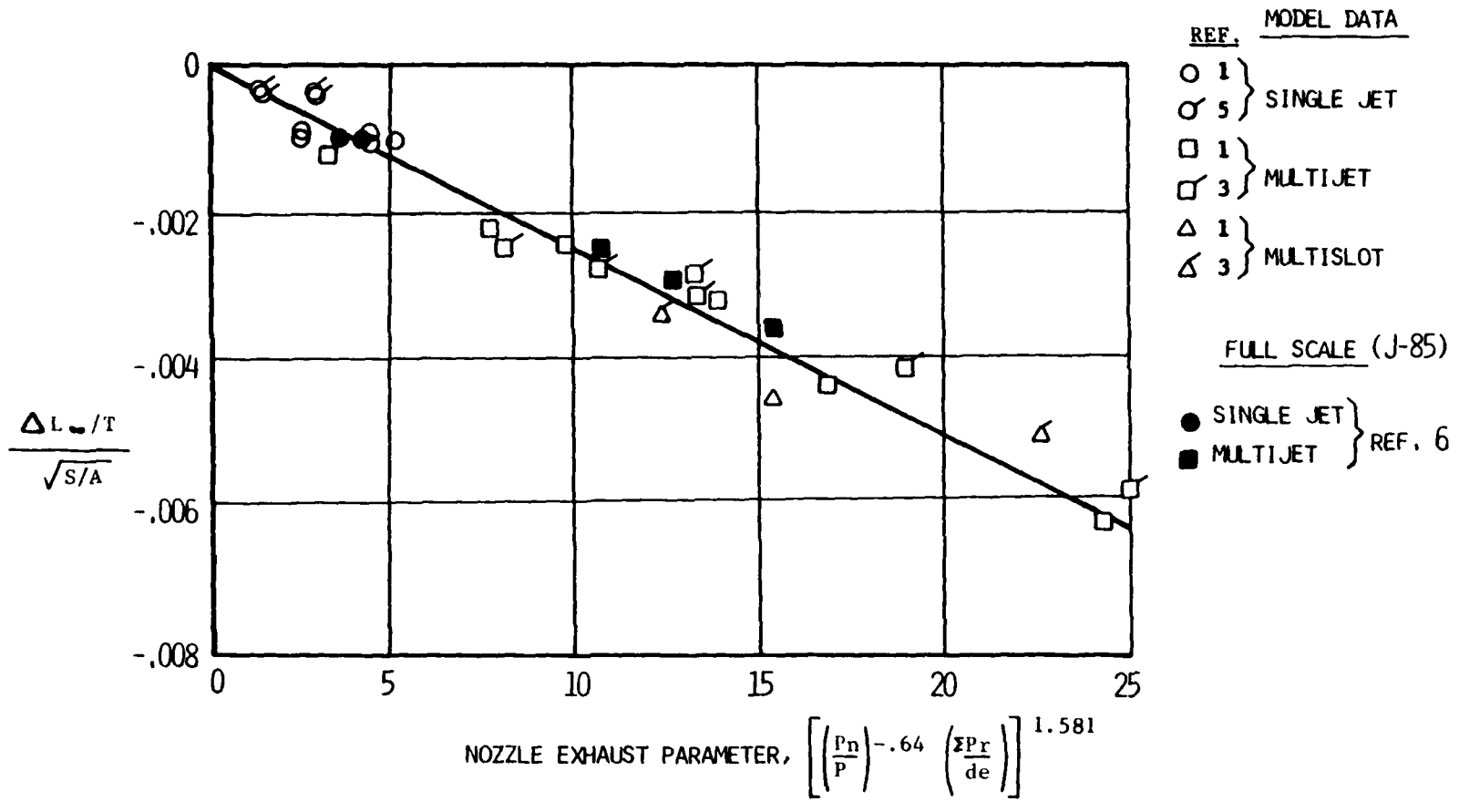

FIGURE 2.2.1(4) - Lift Loss Out of Ground Effect, Method 2

In-Ground Effect: Single Jet

The present, most widely accepted method for estimating the ground effects on single jet configurations is that originally developed by Wyatt, (Ref. 1). The method evolved from tests of single jets issuing from various circular, rectangular and triangular plates. The expression developed by Wyatt is:

$$\frac{\Delta L_s}{T} = -.012 \left(\frac{h}{\overline{D}-d}\right)^{-2.3}$$

where h = height of the blocking surface above the ground.

$\overline{D}$ = angular mean diameter of the blocking surface as defined below:

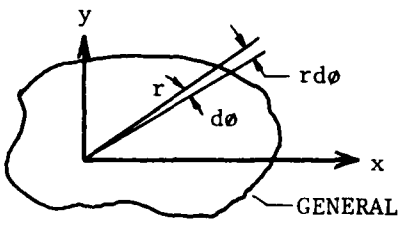

$$\overline{D} = \frac{1}{\pi}\int_0^{2\pi} r\,d\phi$$

For a centrally located jet in a circular planform $\overline{D} = D = 2\sqrt{\frac{S}{\pi}}$. Wyatt, in Reference 1, has computed the values of $\overline{D}$ for rectangular and triangular planforms of various aspect ratios with the jet origin on the center-line. These values are reproduced in Figure 2.2.1 (5).

Wyatt was unable to correlate his results with the data of Spreeman and Sherman (Ref. 7), and others (Ref. 8) have indicated an overprediction of the lift loss by the Wyatt expression at low heights. Wyatt's data were taken at low nozzle pressure ratios ($\frac{P_n}{p} < 1.5$), while much of Spreeman and Sherman's data and the data of more recent investigations were taken at pressure ratios of 2.0 and higher. When Wyatt's data are compared with other low pressure ratio data, a good correlation is obtained (Figure 2.2.1 (6)); however, the constant and exponent are changed slightly. Although there appears to be considerable scatter at the higher heights, almost all the data fall within ± 1%T of the correlation line.

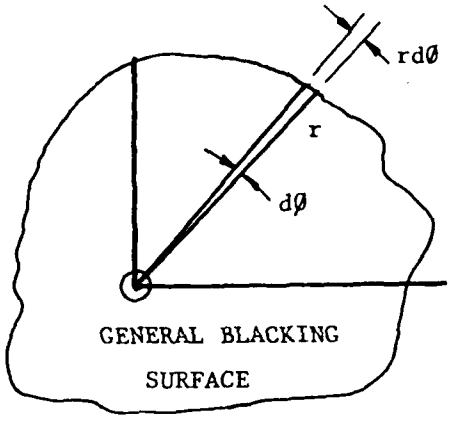

$$\bar{D} = \frac{1}{\pi} \int_{o}^{2} r d\emptyset$$

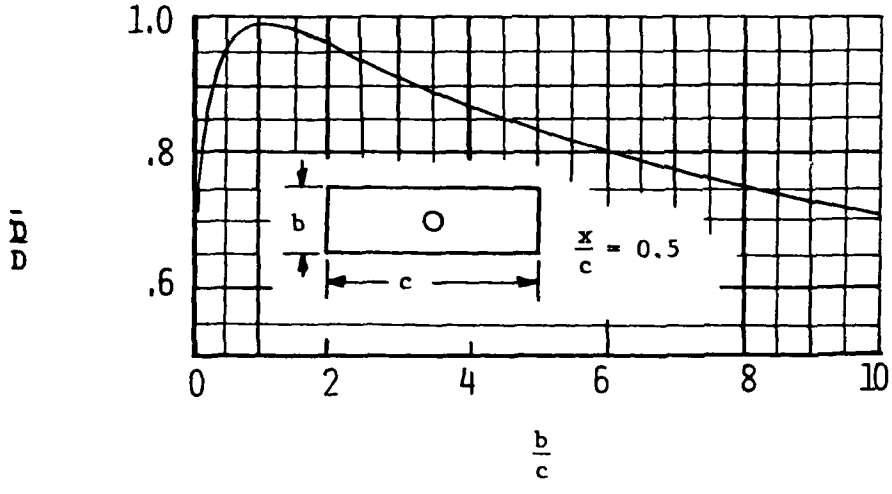

FIGURE 2.2.1 (5) - Values of D for Several Regular Planforms

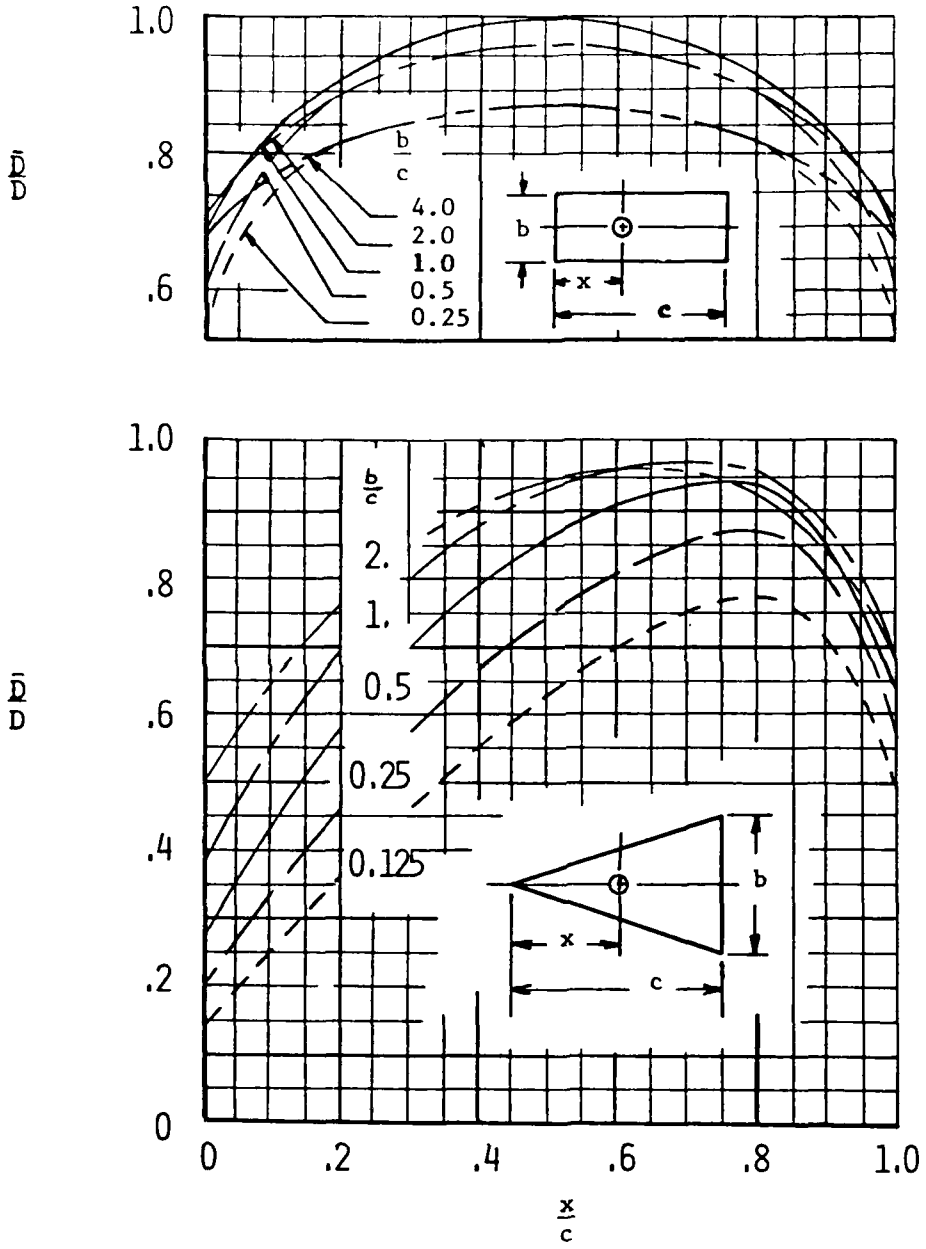

FIGURE 2.2.1 (5) - Concluded

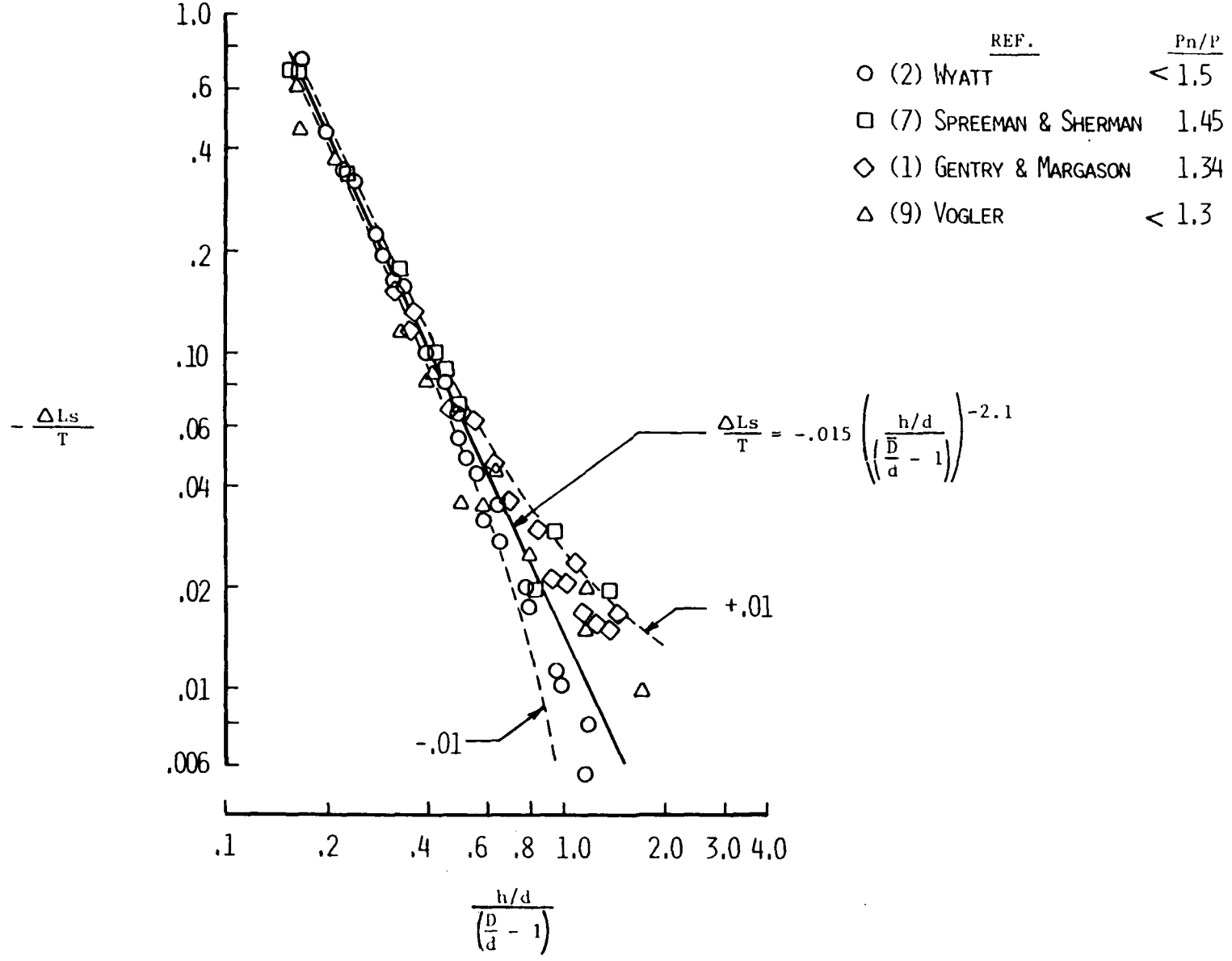

FIGURE 2.2.1 (6) - Ground - Induced Lift Loss on Single Jet Configurations at Low Pressure Ratios

At higher pressure ratios, the slope of the correlation line (that is the exponent in the lift loss equation) is reduced as illustrated in figure 2.2.1 (7). The variation of the exponent with nozzle pressure ratio is shown at the top of figure 2.2.1 (7). Within the scatter of the data, and considering the relatively poorer quality of the data of Reference 7, a linear variation of the exponent with pressure ratio is assumed. The resulting expression for the lift loss due to ground effect for single jet flat plate or low wing configurations is:

$$\frac{\Delta L_s}{T} = -.015 \left[\frac{h/d}{\left[\frac{\overline{D}}{d} - 1\right]} \right]^{-\left[2.2 - .24\left[\frac{P_n}{p} - 1\right]\right]} \qquad 2.2.1\ (7)$$

Figures 2.2.1 (8) to 2.2.1 (10) indicate the accuracy to which equation 2.2.1 (7) can predict data of various investigations.

The agreement between the calculations and the data for the two large-scale hot jet configurations (Figure 2.2.1 (9)) is good; for the X-14 airplane, the two jets were considered to be close enough together to act as a single jet. Figure 2.2.1 (9) also illustrates the importance of using the correct value of the mean angular diameter, $\overline{D}$, in calculating the lift losses. Although the total planform area to jet area ratio nature of the wing and fuselage of the X-14 lowers the value of $\overline{D}$. On the X-14 the height h was measured from the ground to the wing lower surface at the quarter chord of the mean geometric chord. The calculation included the effect of the lower height of the forward fuselage section as suggested in the following paragraph.

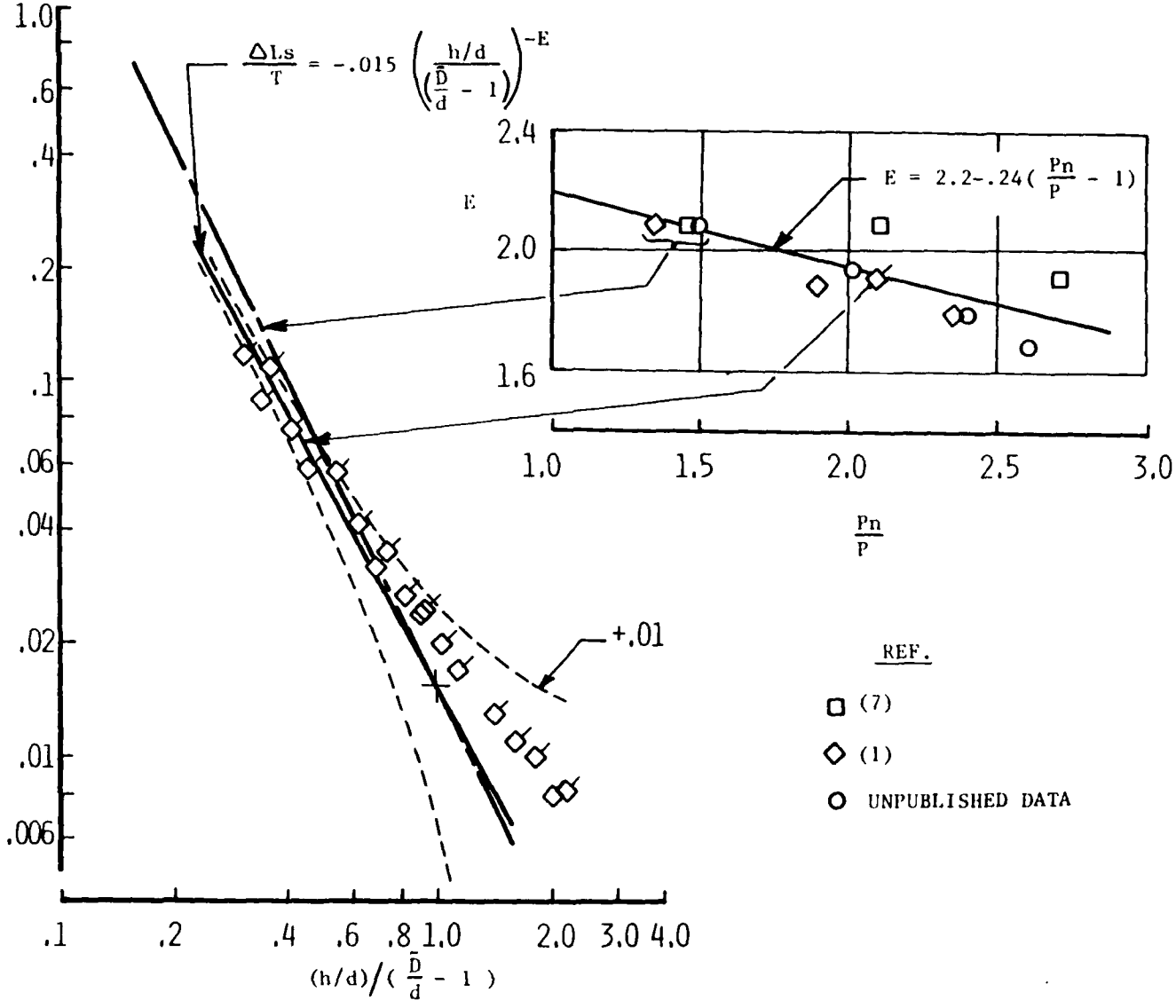

FIGURE 2.2.1(7) - Effect of Pressure Ratio on Single-Jet Configuration Lift Loss in Ground Effect

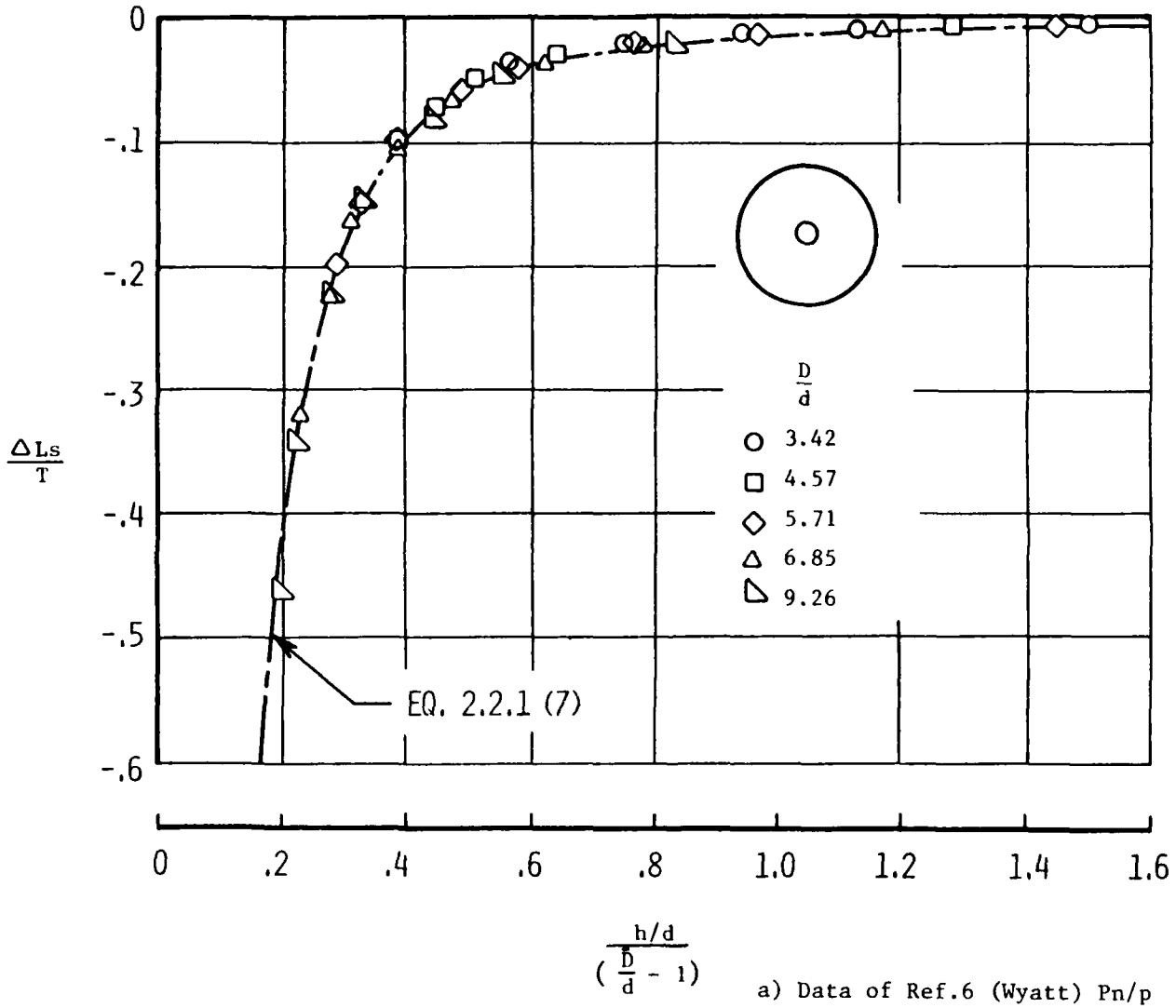

a) Data of Ref.6 (Wyatt) Pn/p 1.5

FIGURE 2.2.1 (8) - Comparison of Predicted Lift Loss With Data From Several Single Jet Investigations

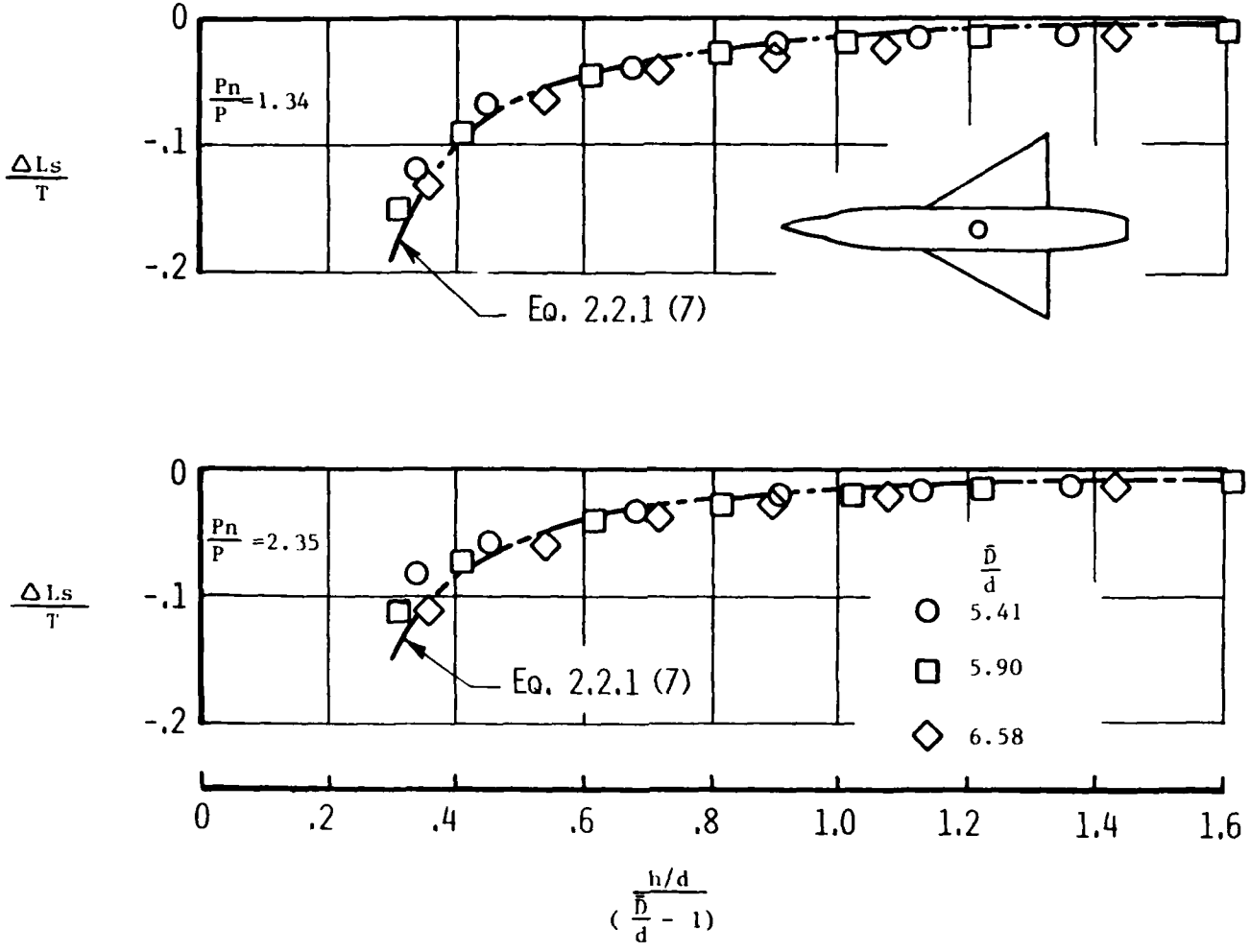

b) Data of Ref. 1 (Gentry and Margason)

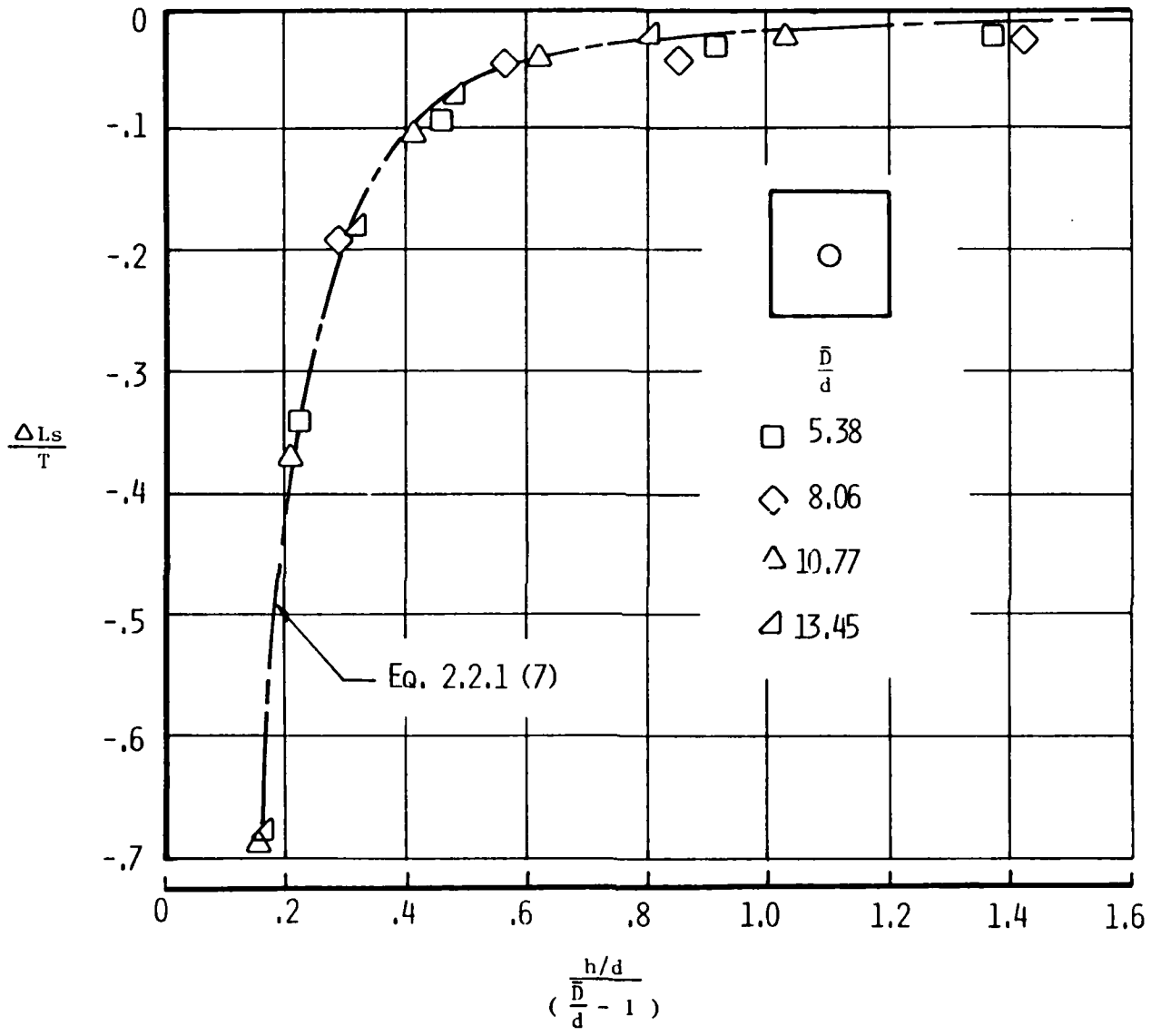

c) Data of Ref. 7 (Spreeman and Sherman) Pn/p = 1.45

FIGURE 2.2.1 (8) - Continued

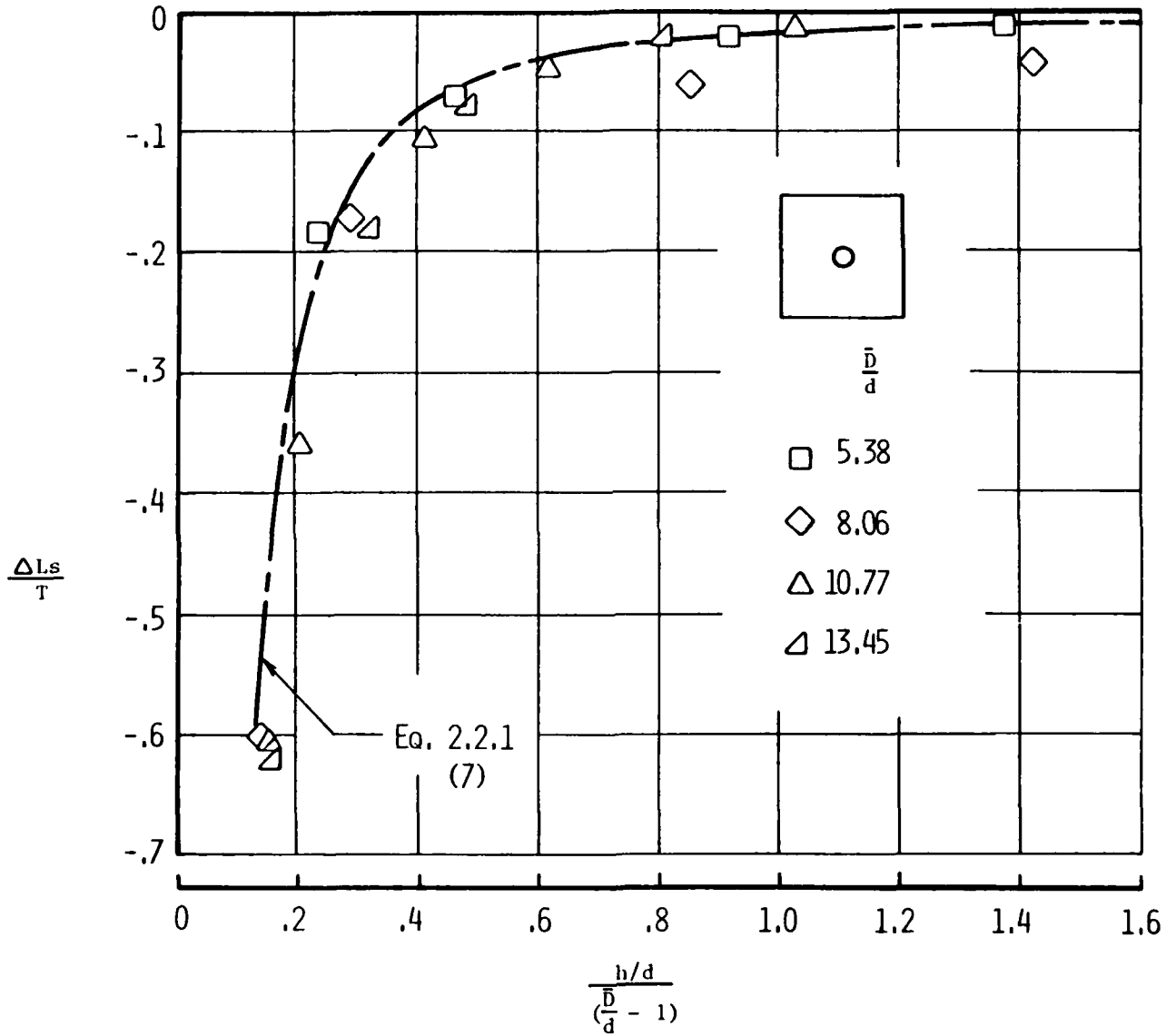

d) Data of Ref. 7 (Spreeman and Sherman) Pn/p = 2.7

FIGURE 2.2.1 (8) - Continued

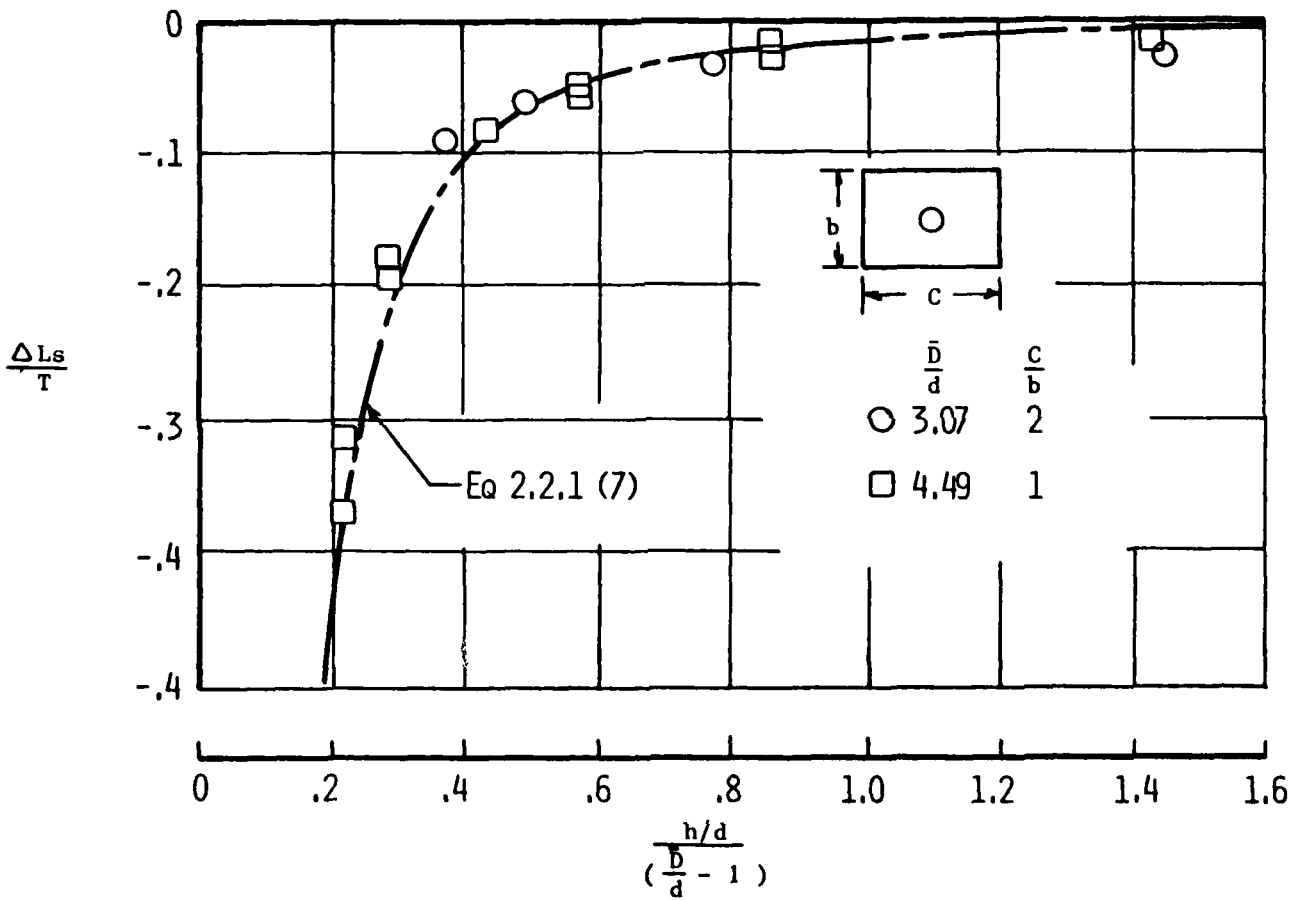

e) Data of Ref. 10 (Davenport and Spreeman) $P_n/P < 1.5$

FIGURE 2.2.1(8) - Concluded

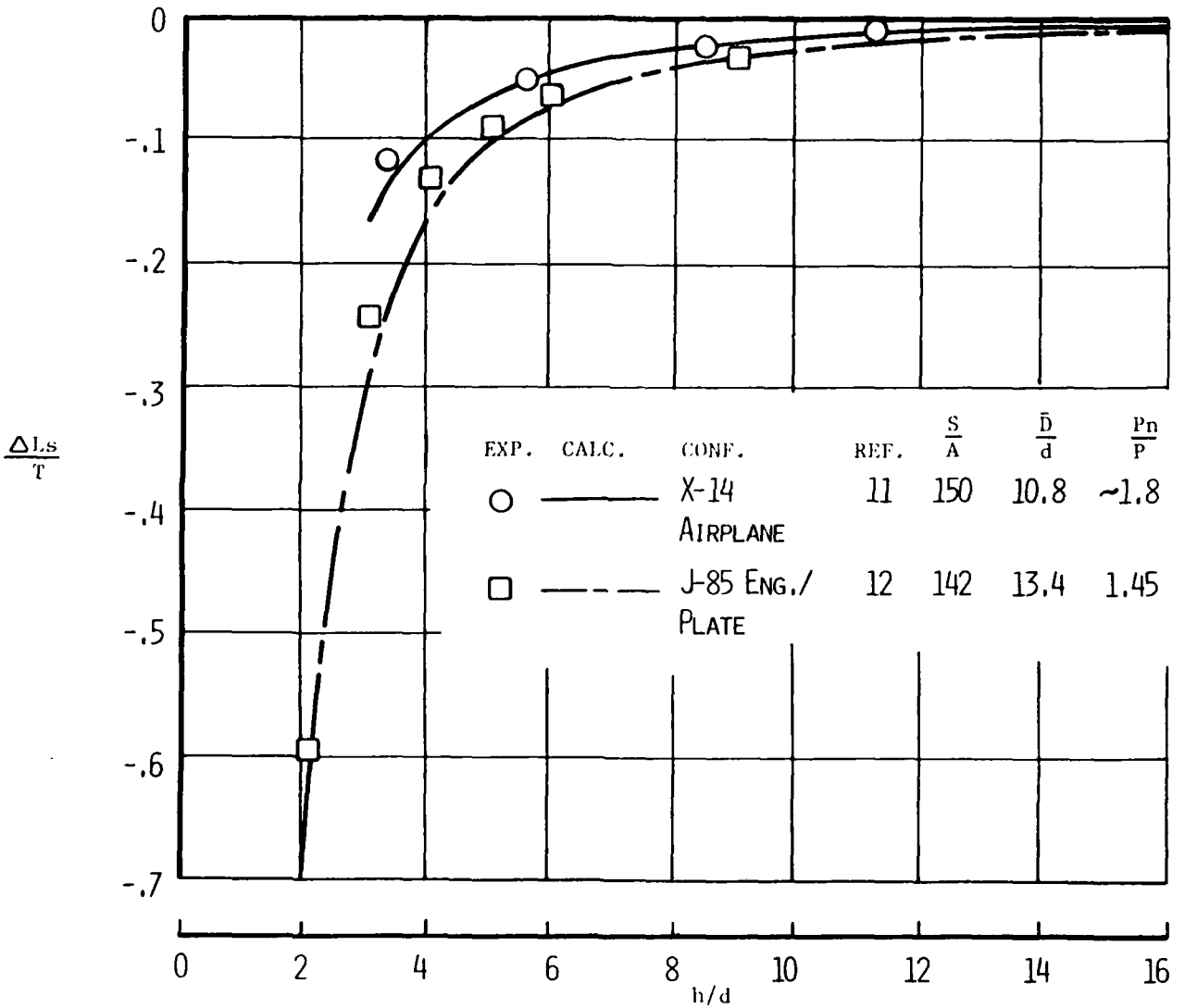

FIGURE 2.2.1 (9) - Comparison of Predicted Lift Loss With Data From Large-Scale Investigations

The effect of wing height is accounted for by the method suggested by Hammond in Reference 13 and illustrated below:

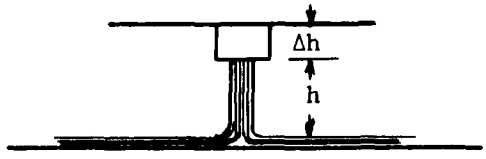

$$\left(\frac{\Delta L_s}{T}\right)_h = \left(\left(\frac{\Delta L_s}{T}\right)_{wb}\right)_{h+\Delta h} - \left(\left(\frac{\Delta L_s}{T}\right)_b\right)_{h+\Delta h} = \left(\left(\frac{\Delta L_s}{T}\right)_b\right)_h \qquad 2.2.1\ (8)$$

Where the subscript b signifies body alone and the subscript wb signifies wing-body, equation 2.2.1 (7) is used to compute the individual terms. Figure 2.2.1 (10) shows that this procedure predicts the lift losses for several high wing configurations of Reference 9 fairly well.

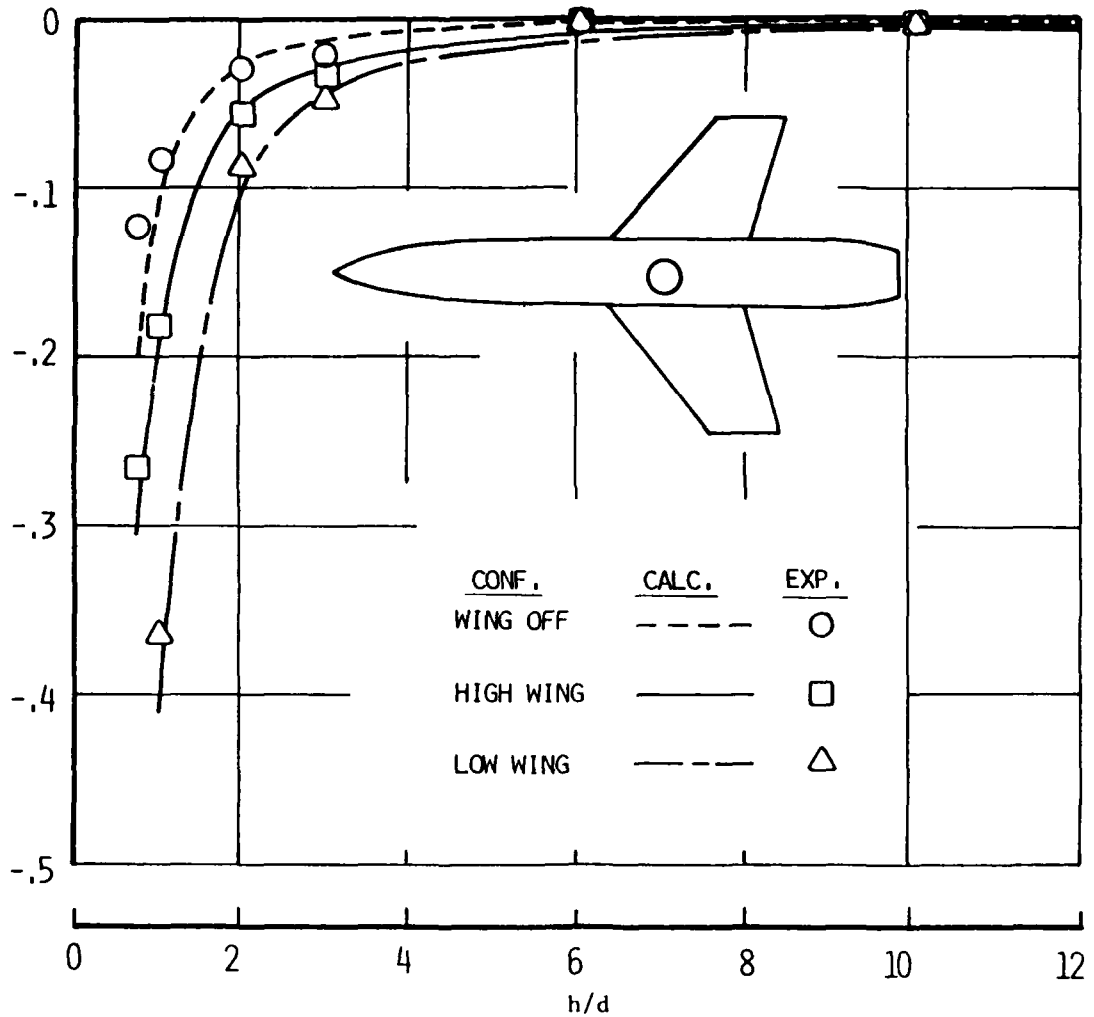

a) Intermediate Size Jet

FIGURE 2.2.1 (10) - Effect of Wing Hight, Single Jet Configurations

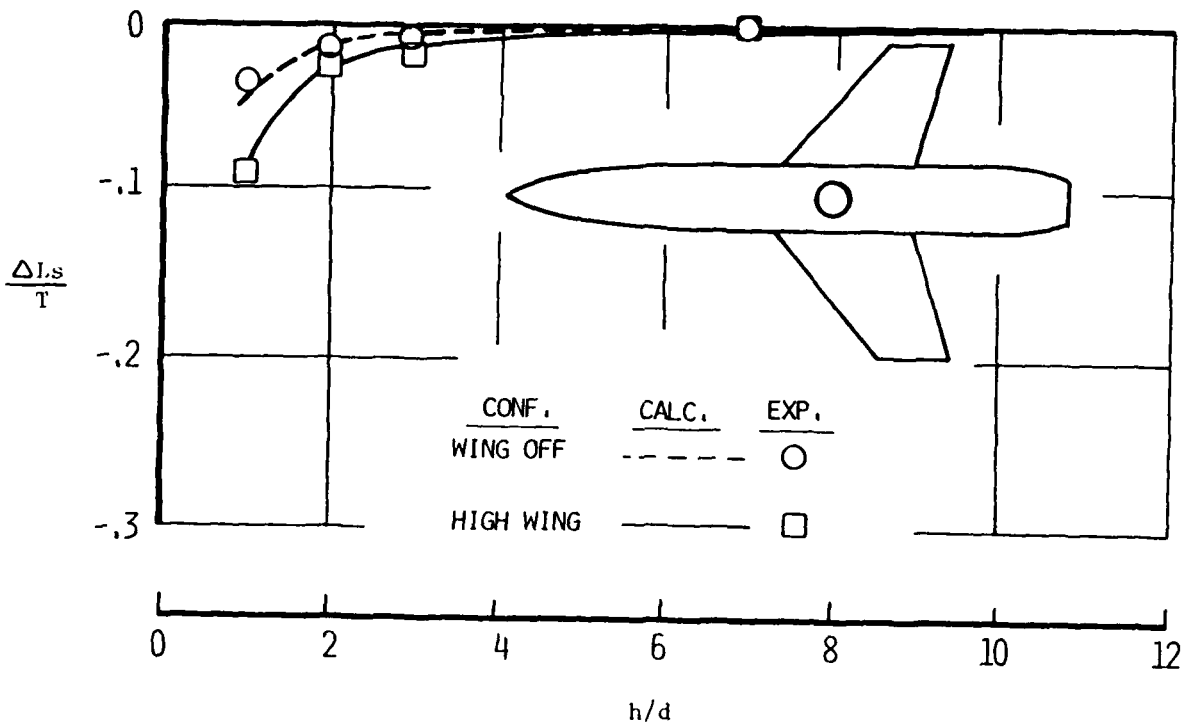

b) Large Jet

FIGURE 2.2.1(10) - Continued

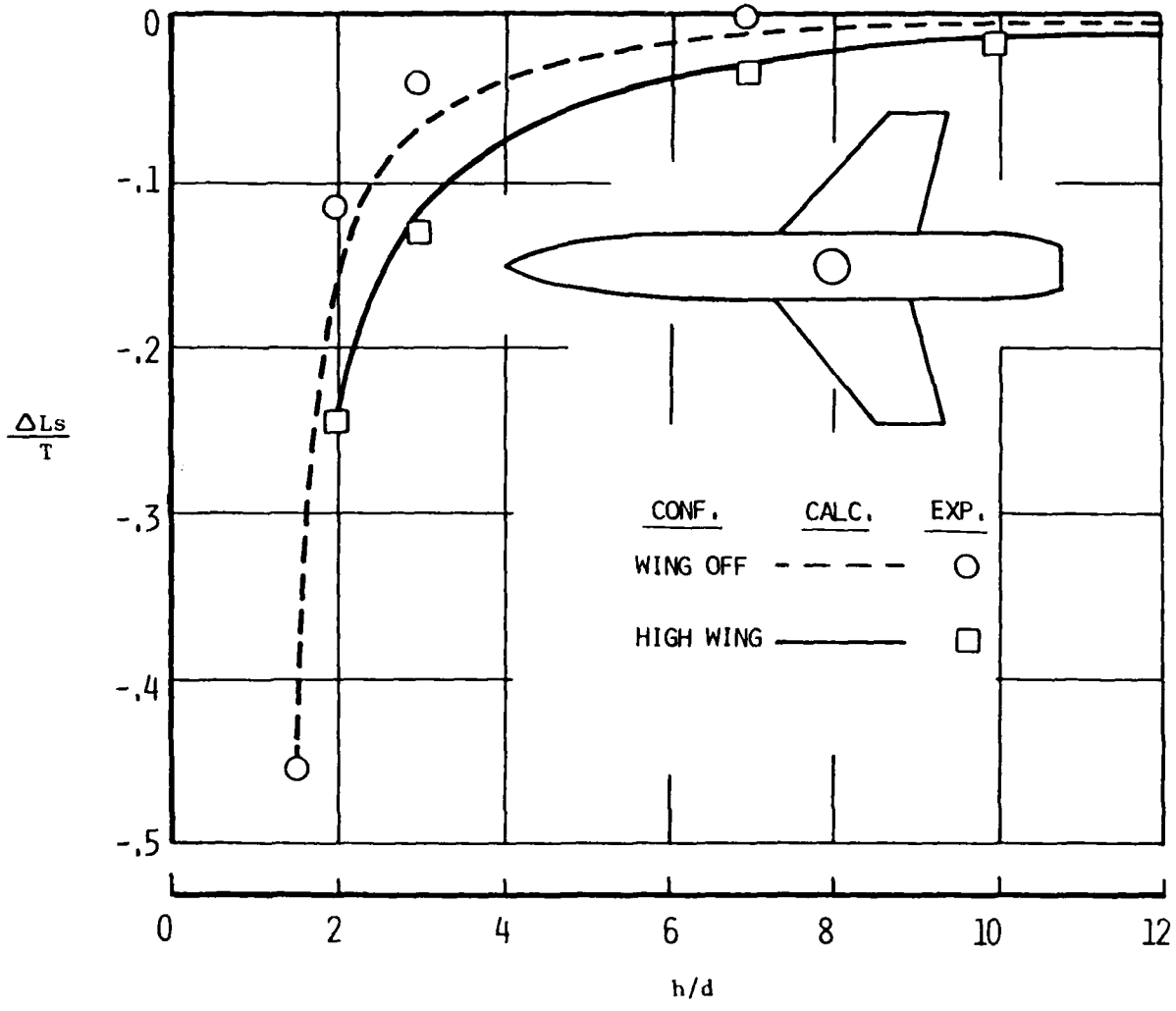

C) Small Jet

FIGURE 2.2.1(10) - Concluded

In-Ground Effect: Multiple Jet

With multiple jets the lift loss can be either increased or decreased depending on the configuration and the height above the ground as shown in Figure 2.2.1 (11). This figure compares data from a four-jet configuration from Reference 1 with a single jet configuration from the same reference having the same planform and total jet area. Below a height of three effect diameters, the expected fountain effect produces positive pressures to reduce the lift loss. However, above about three diameters the lift loss is actually increased. This increase in lift loss at intermediate heights is evident in other data, although there are few investigations where direct comparisons such as Figure 2.2.1 (11) can be made.

With multiple jets the flow field between the blocking surface and the ground and between the jets is much more complex than that for a single jet case. The work of Karemaa, et al., Reference 14, and the current work of Foley and associates at General Dynamics in surveying the actual flows between the jets in ground proximity is developing a much improved understanding of the phenomena involved. The present method for predicting the induced lift of multiple jet configurations uses the insight into the flow phenomena provided by Reference 14 to guide an empirical correlation of available data.

There appear to be three regions, as a function of height, involved. Above the height at which expected positive lifting pressures begin to manifest themselves, h', there is an increase in lift loss which appears to be proportional to the lift loss that would be expected from an equivalent single jet. This increase in suck-down is caused by the fountain

- [illegible] the blockage to the flow being entrained by the wall jet,
- [illegible] the induced suction pressures and the lift loss.

- [illegible] at which the positive lifting pressures are felt,
- [illegible] which the positive lift increases with height, and
- [illegible] logarithmically

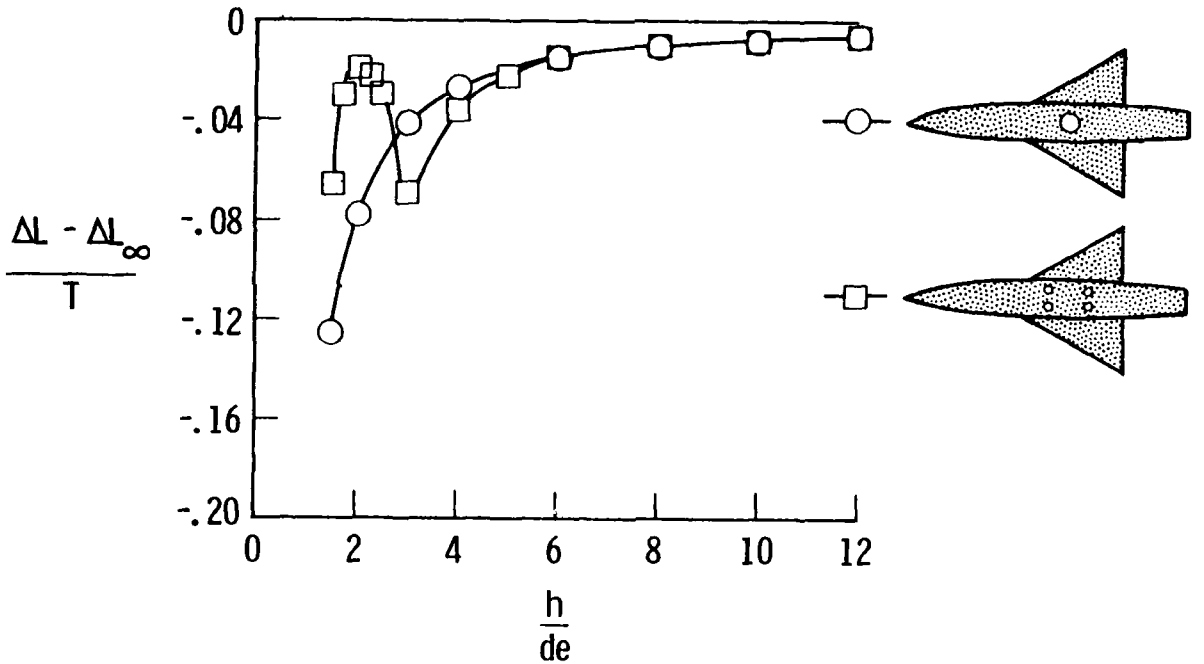

FIGURE 2.2.1 (11) - EFFECT OF MULTIPLE JETS

The present method is based on comparisons of the measured data from a variety of multiple jet configurations with the lift loss that would be expected for those configurations with a single jet of equal total area. The difference between the measured data and the lift loss calculated for an equivalent single jet is broken down into three terms: ΔL_1 derived from consideration of the flow involved in the upper region and ΔL_2 and ΔL_3 related to the lower regions.

For the highest region, where the lift loss is increased by multiple jets, an examination of the data of References 1, 9, 10, and 14 indicates that the lift loss is about 50% greater than would be calculated for an equivalent single jet. Therefore, the first term is defined as:

$$\frac{\Delta L_1}{T} = .5 \frac{\Delta L_S}{T} \qquad 2.2.1\ (9)$$

When this term is subtracted from the difference between the measured data and the lift loss calculated for an equivalent single jet, the result is, of course, the sum of ΔL_2 and ΔL_3. Only a few sets of data have enough data points to be of help in evaluating these later two terms. These data are plotted in Figure 2.2.1 (12).

The terms of ΔL_2 and ΔL_3 are positive and arise from upward pressures induced on the configuration by the fountain flows. While Reference 14 indicates that the fountains are considerably weakened by the entrainment action of the wall jet sheets flowing along the ground, a height is reached, nevertheless, where lifting pressures are generated as indicated by Figure 2.2.1 (12). This height, h', should be related to the size of the jet pattern and, as shown by the insert on Figure 2.2.1 (12), the present data indicate that this height can be estimated by the expression:

$$\frac{h'}{D} = 1.22 \frac{1}{N} \left(\frac{D'}{d_e}\right)^{.65} \qquad 2.2.1\ (10)$$

where D' is defined as the "bolt circle" diameter of the jet pattern as defined below:

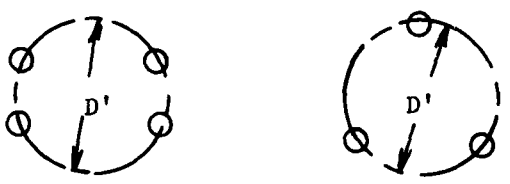

The strength of the lifting pressures should be a function of the number of fountains and, for the pressures contained within the jet pattern at least, to the solidity of the jet curtain, θ. The top insert in Figure 2.2.1 (12) indicates that the slope of the linear portion of the data (defined here as ΔL_2) is proportional to $N^2\theta$ and that the second term can be written as:

$$\frac{\Delta L_2}{T} = .133\, N^2\theta \left(\frac{h'}{D} - \frac{h}{D} \right) \qquad 2.2.1\ (11)^*$$

When ΔL_2 is subtracted from the data of Figure 2.2.1 (12), the remainder is defined as ΔL_3 and is plotted in Figure 2.2.1 (13). While the spread of the data indicates that there are several factors involved in determining the magnitude of ΔL_3, the data sample is too small to determine them and a single line is drawn through the data. The third term is defined as:

$$\frac{\Delta L_3}{T} = 10^{\left(.9 - 10 \frac{h}{D}\right)} \qquad 2.2.1\ (12)$$

The total induced lift is obtained by summing the proper terms as depicted by the schematic at the top of Figure 2.2.1 (2) and as defined below:

For a single jet configuration (or equivalent single jet) $\quad \frac{\Delta L}{T} = \frac{\Delta L_\infty}{T} + \frac{\Delta L_S}{T}$ 2.2.1 (13)

For multiple jet configurations $\quad \frac{\Delta L}{T} = \frac{\Delta L_\infty}{T} + 1.5 \frac{\Delta L_S}{T} + \frac{\Delta L_2}{T} + \frac{\Delta L_3}{T}$ 2.2.1 (14)

The agreement between the induced lift predicted by the above expression and experimental data from several multiple jet configurations is presented in Figure 2.2.1 (14). In order to depict the relative size of the configurations, their planforms are all drawn to the same scale relative to the equivalent single jet. The agreement is good, of course, for the configurations used in developing the method. The under-prediction of the lift at

*Note: For two jet or inline configurations there is no real "containment" of the pressure region and ΔL_2 is considered to be zero. The moderation of the suckdown pressures exhibited by these configurations is contained in ΔL_3.

the lowest heights for configuration 4 and the total failure to predict the large favorable increments at low heights for the eight closely-spaced jets of configuration 6 indicate the weakness in the last term, equation 2.2.1 (12). Also, the data of Figure 2.2.1 (14) d and e indicate that there are probably pressure ratio effects that are not included in the present method.

CONCLUDING REMARKS

The method presented does a reasonably good job of predicting the jet-induced lift for dispersed jets on flat plate and low wing configurations. Additional work is needed to develop methods to predict the effects of wing height, jet inclination, pressure ratio, and lower surface strakes or appendages designed to "contain" the fountain flow and augment the favorable lift.

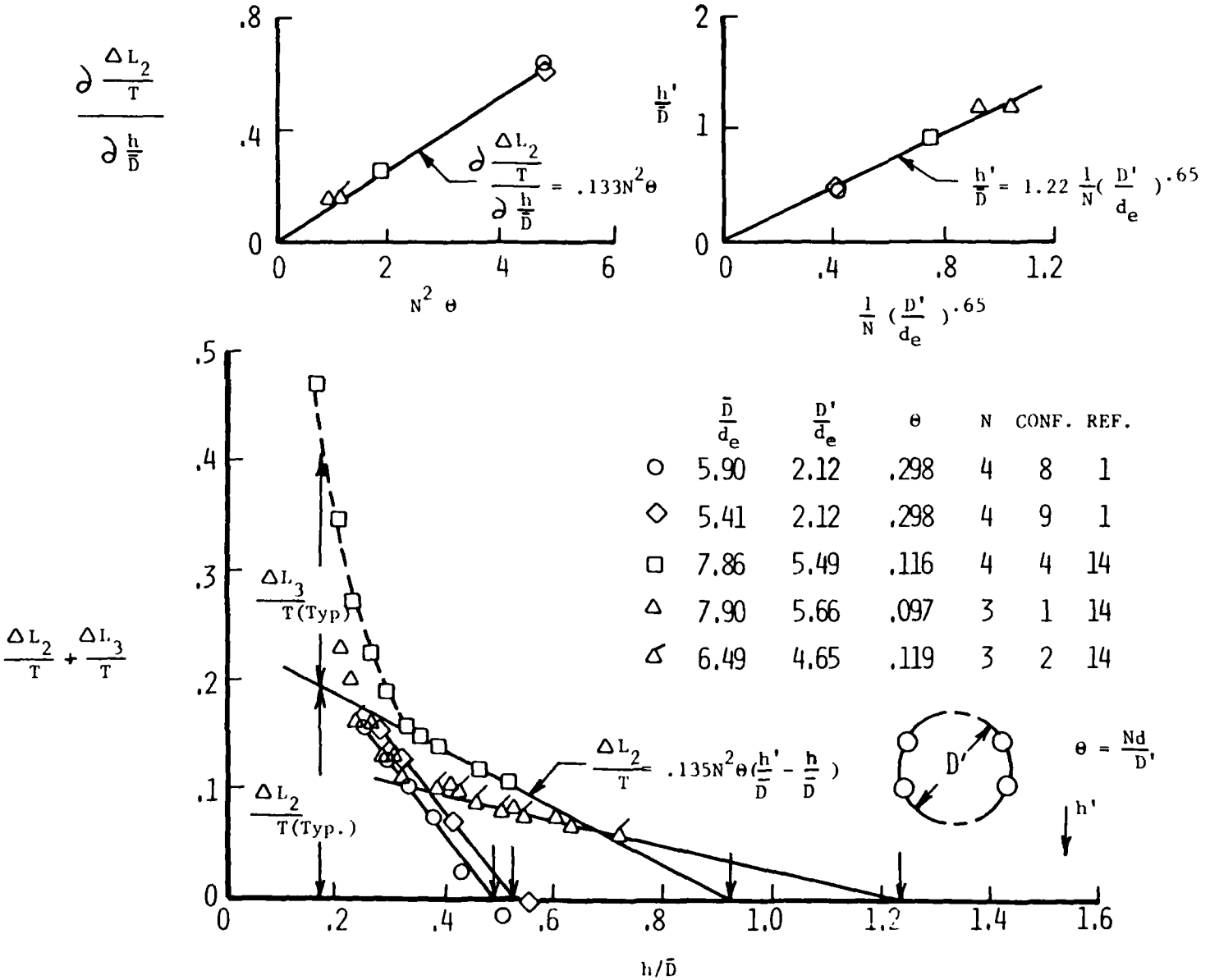

FIGURE 2.2.1 (12) - Derivation of the Expression for L_2/T

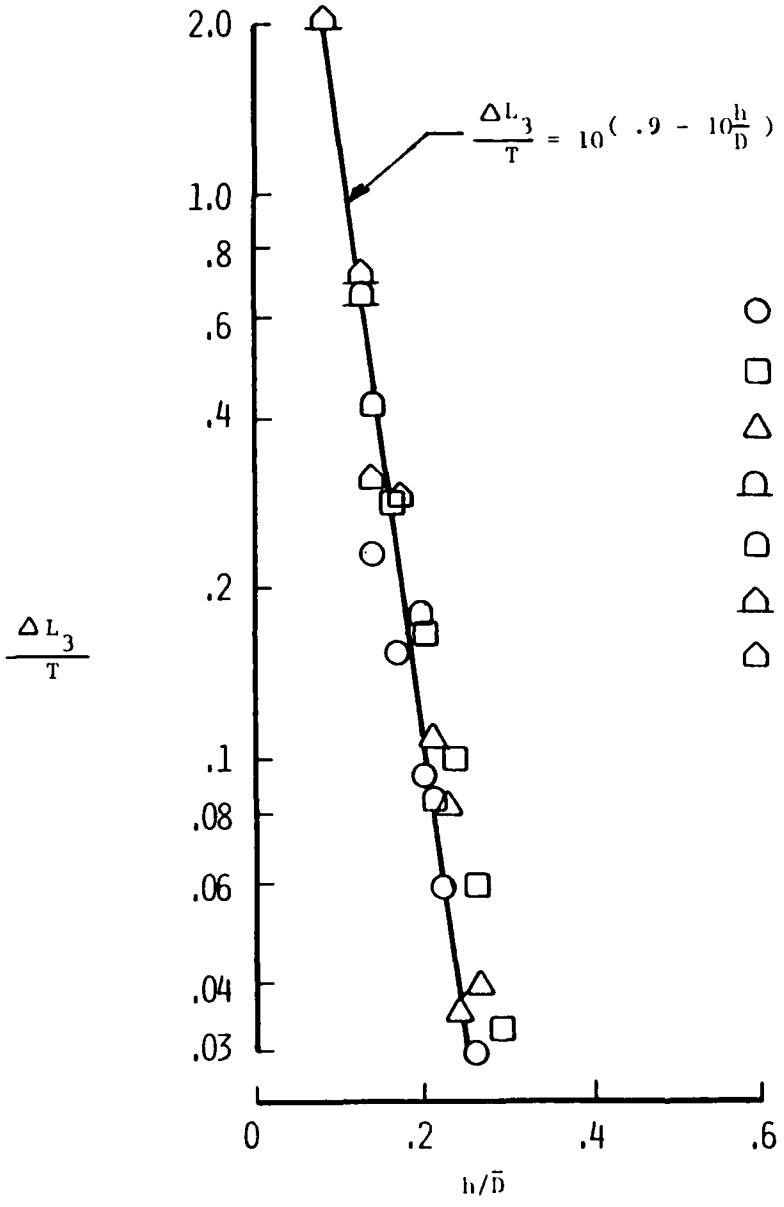

	N	$\frac{\bar{D}}{d_e}$	$\frac{D'}{d_e}$	θ	CONF.	REF.
○	2	12.55	—	—	3	14
□	4	7.86	5.47	.116	4	14
△	3	7.90	5.66	.097	1	14
⏢	4	5.74	2.26	.282	11	9
⏢	4	3.58	2.26	.282	10	9
⏢	4	5.74	2.14	.297	13	9
⏢	4	3.58	2.14	.297	12	9

FIGURE 2.2.1 (13) - Derivation of the Expression for L_3/T

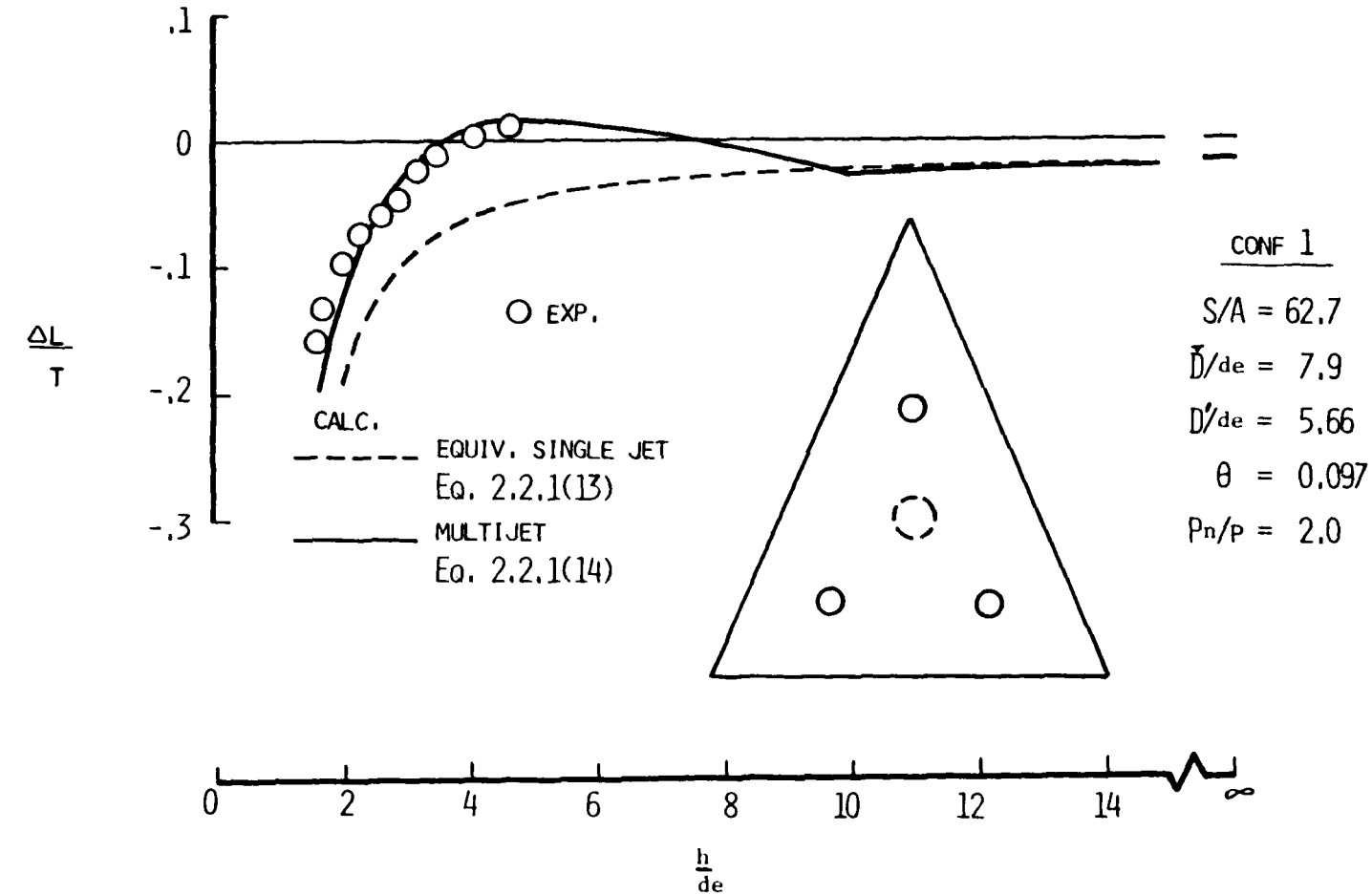

a) Triangular Planforms of Ref. 14

FIGURE 2.2.1 (14) - Comparison of Calculated and Measured Induced Lift for Several Multijet Configurations

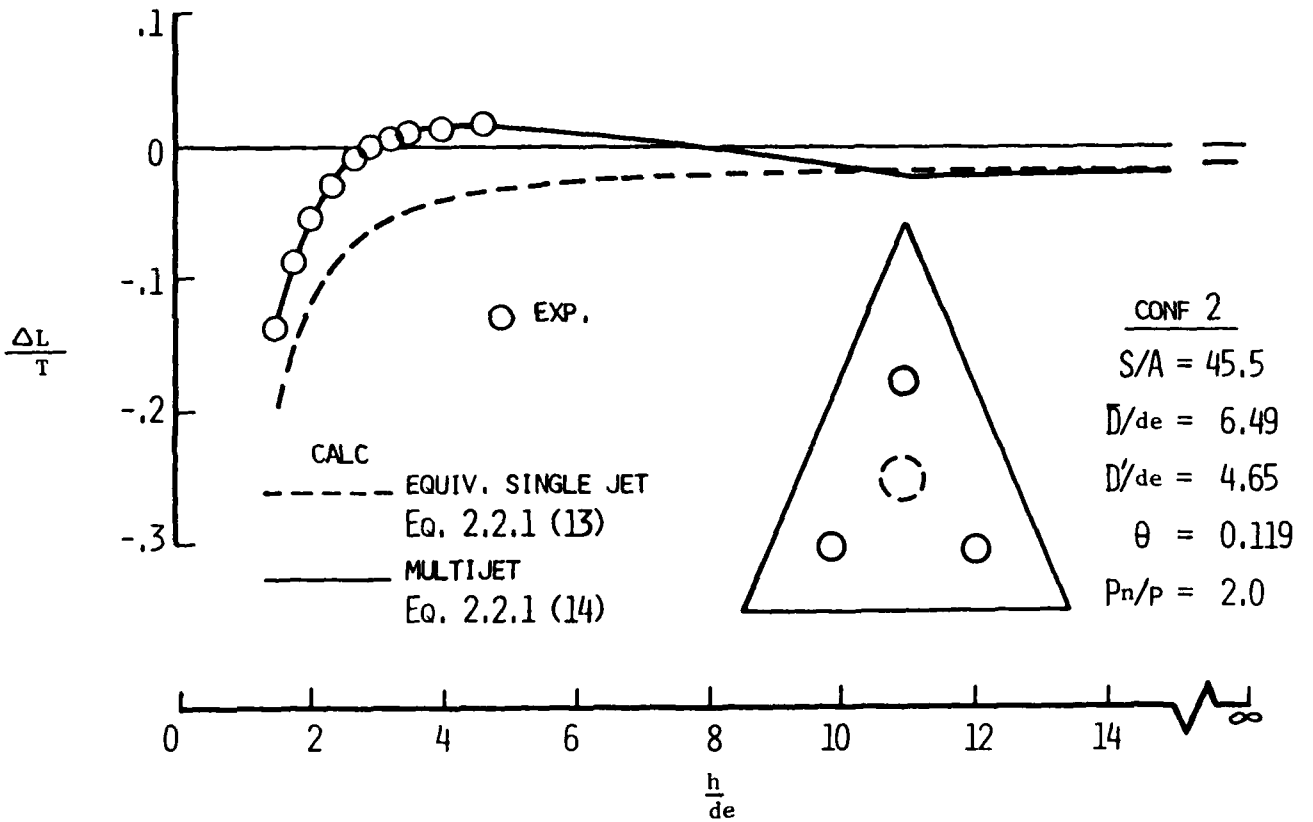

a) Concluded

FIGURE 2.2.1 (14) - Continued

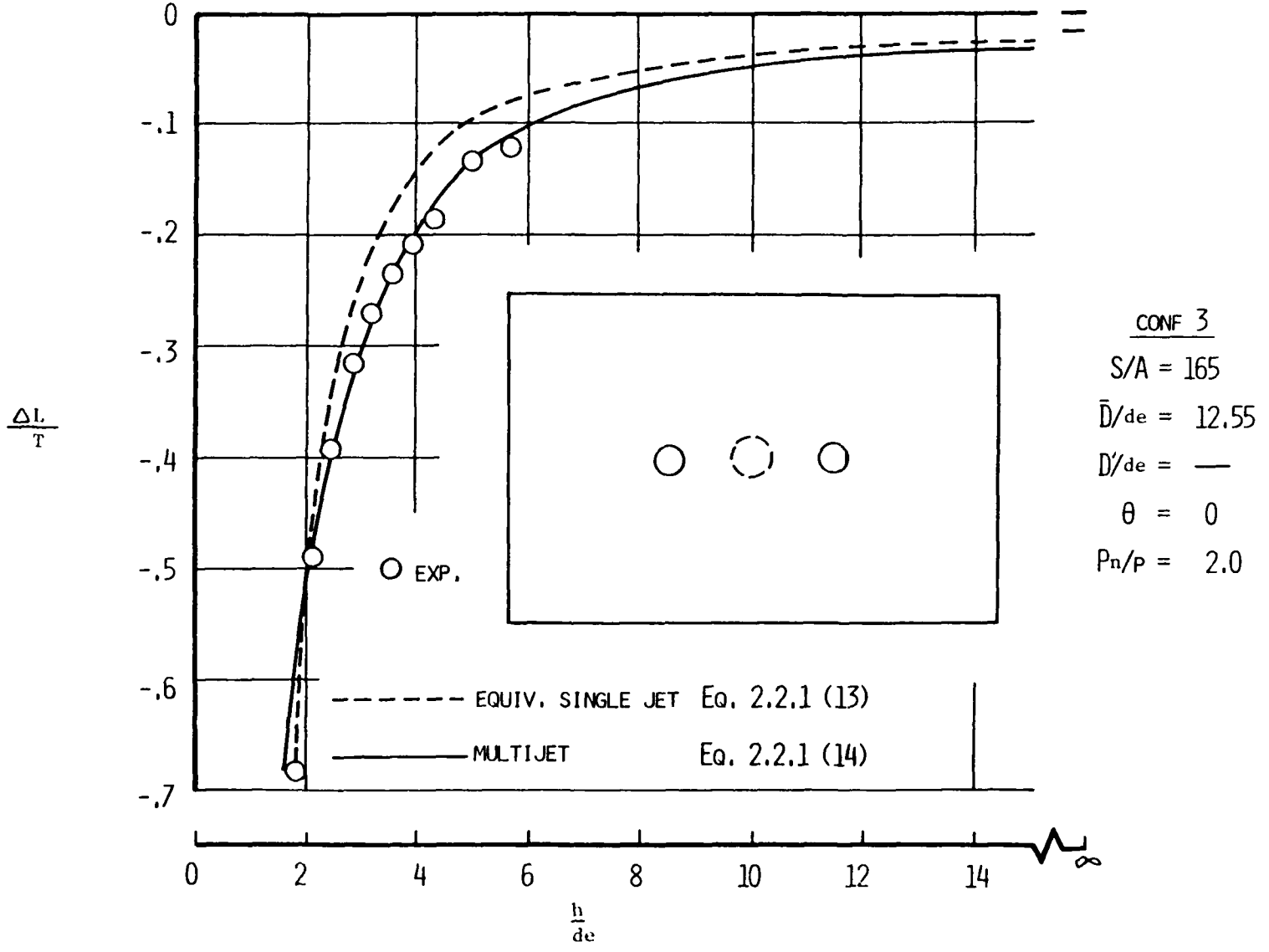

b) Rectangular Planforms of Ref. 14

FIGURE 2.2.1 (14)- Continued

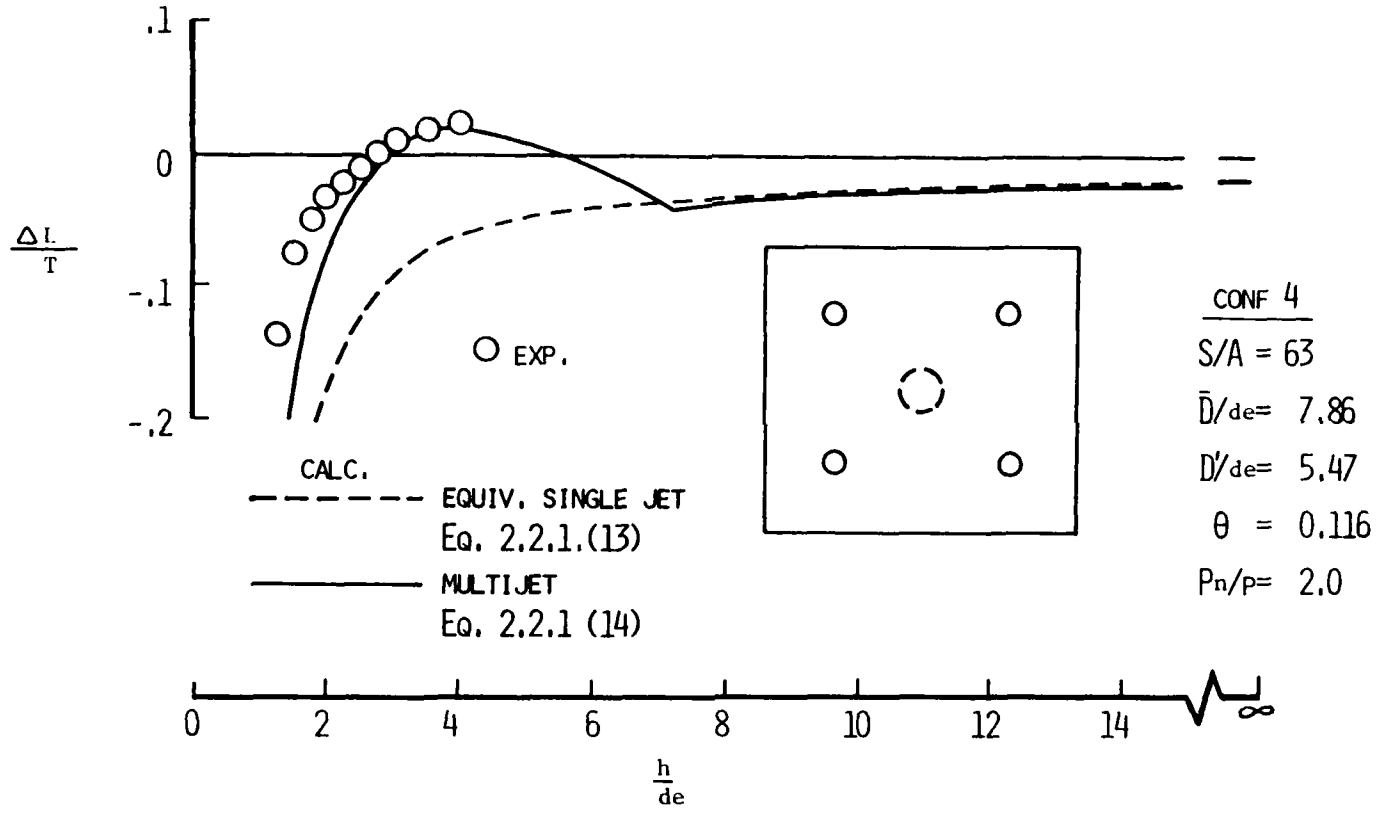

b) Concluded

FIGURE 2.2.1 (14) - Continued

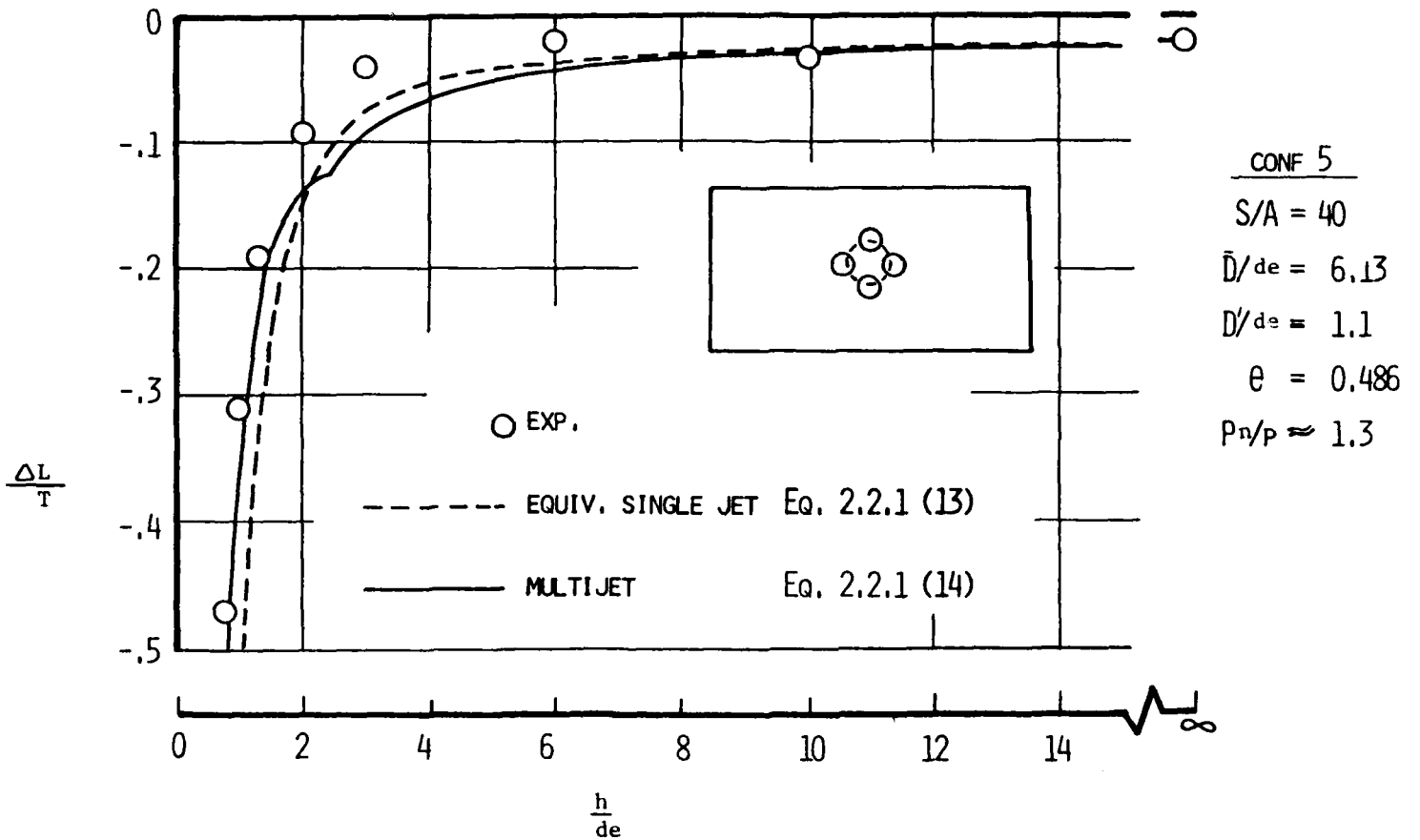

c) Rectangular Planforms of Ref. 10

FIGURE 2.2.1 (14) - Continued

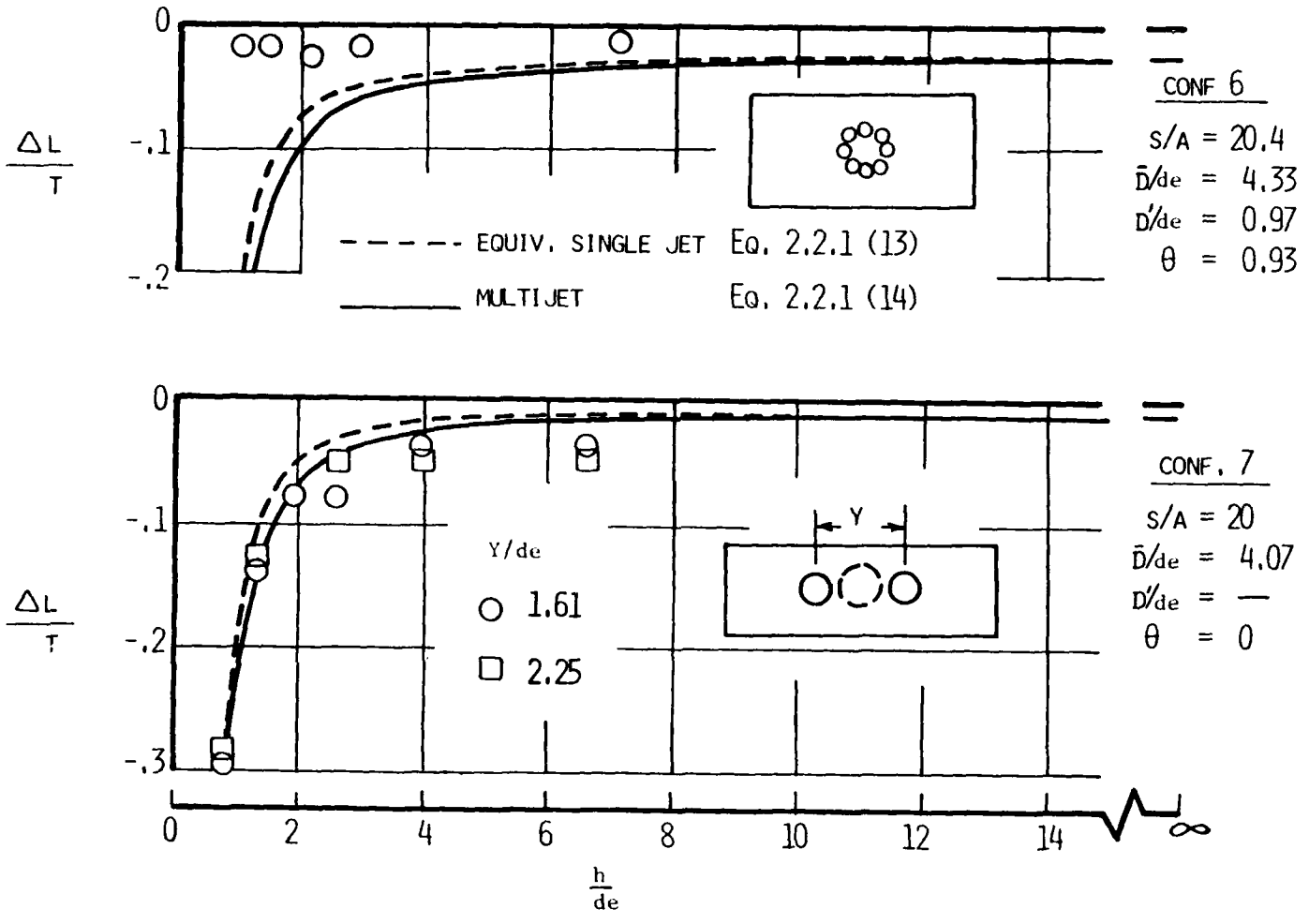

c) Concluded

FIGURE 2.2.1 (14) - Continued

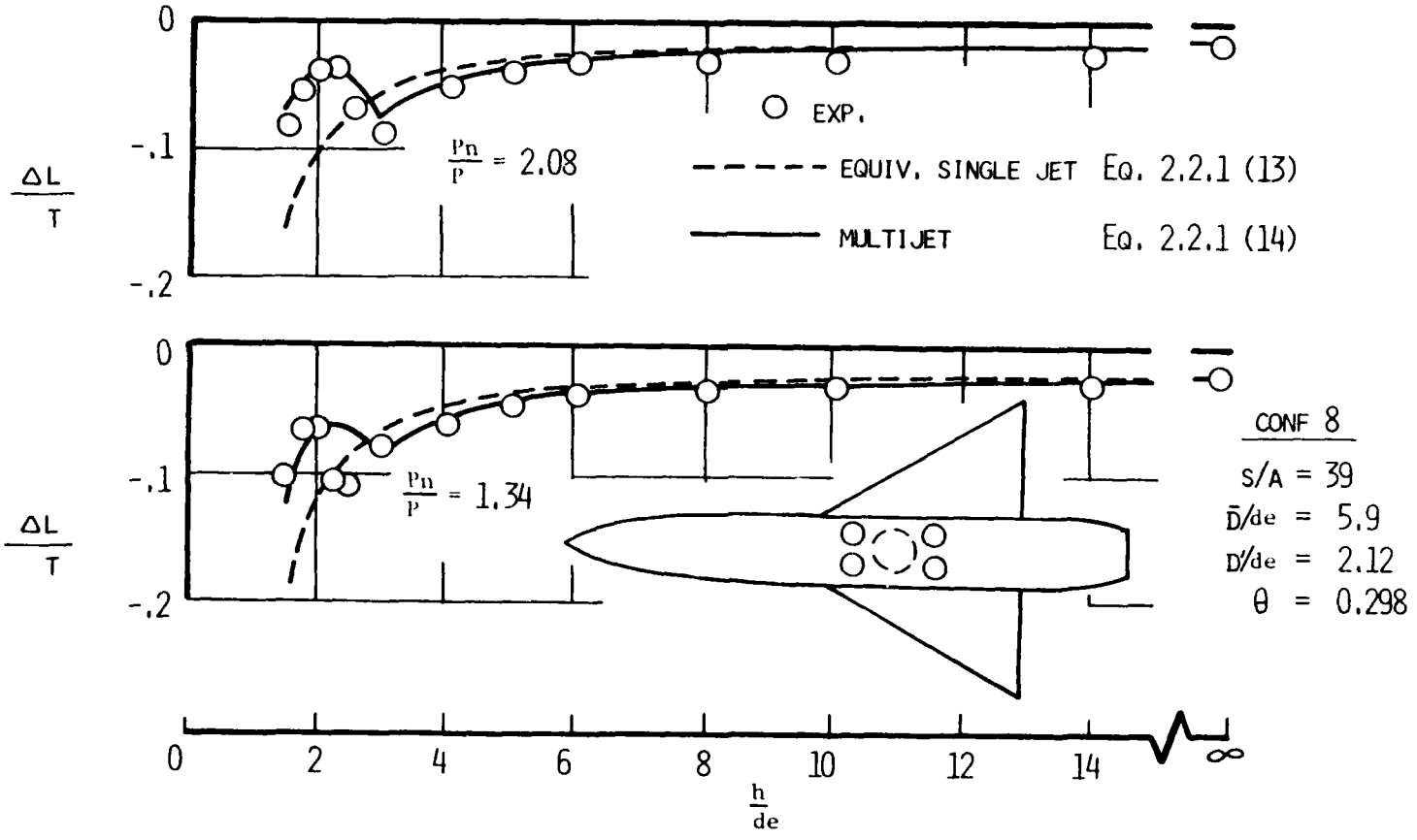

d) Low Wing Configuration of Ref. 1

FIGURE 2.2.1 (14) - Continued

AD-A079 115 NAVAL AIR DEVELOPMENT CENTER WARMINSTER PA F/G 1/3
PROCEEDINGS OF A WORKSHOP ON V/STOL AIRCRAFT AERODYNAMICS. VOLU--ETC(U)
MAY 79 C HENDERSON, M F PLATZER

UNCLASSIFIED NL

4 OF 7
AD A079115

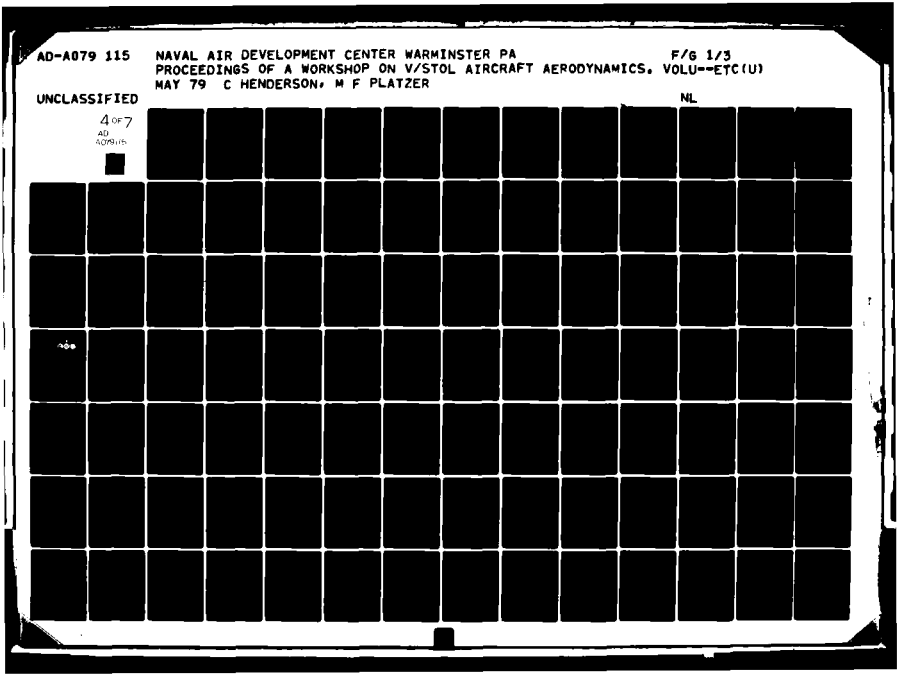

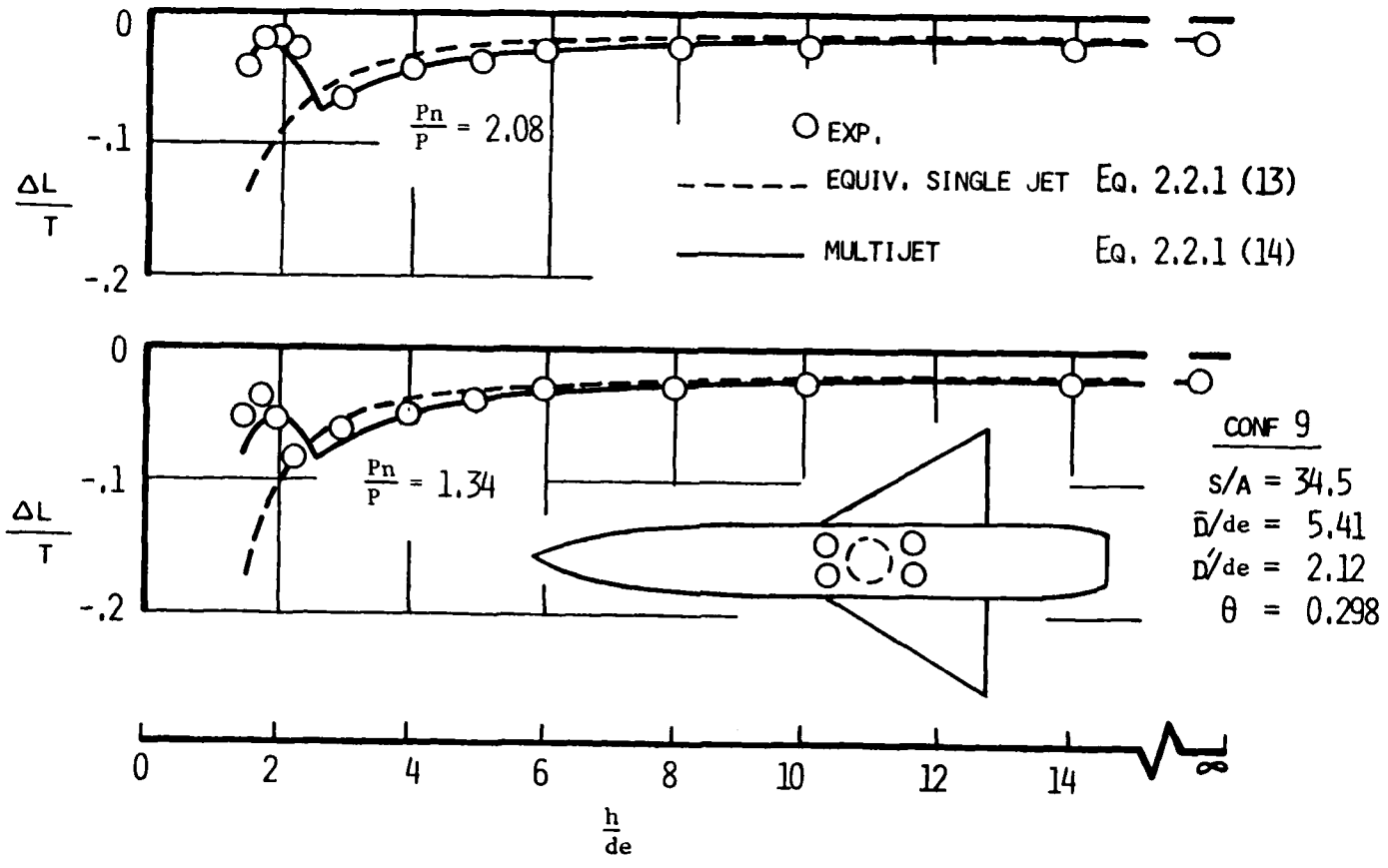

d) Concluded

FIGURE 2.2.1 (14) - Continued

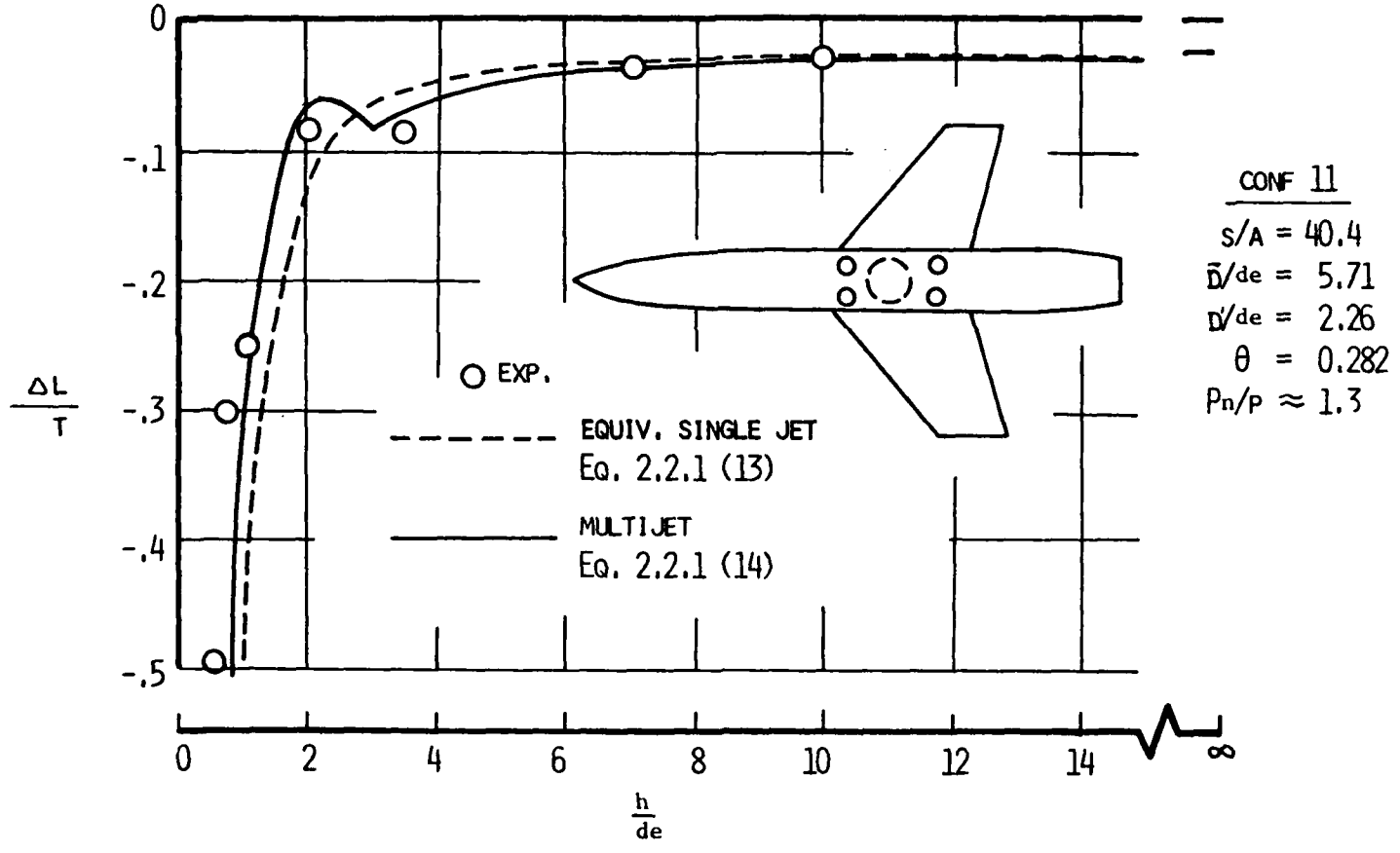

e) Low Wing Configuration of Ref 9

FIGURE 2.2.1 (14) - Continued

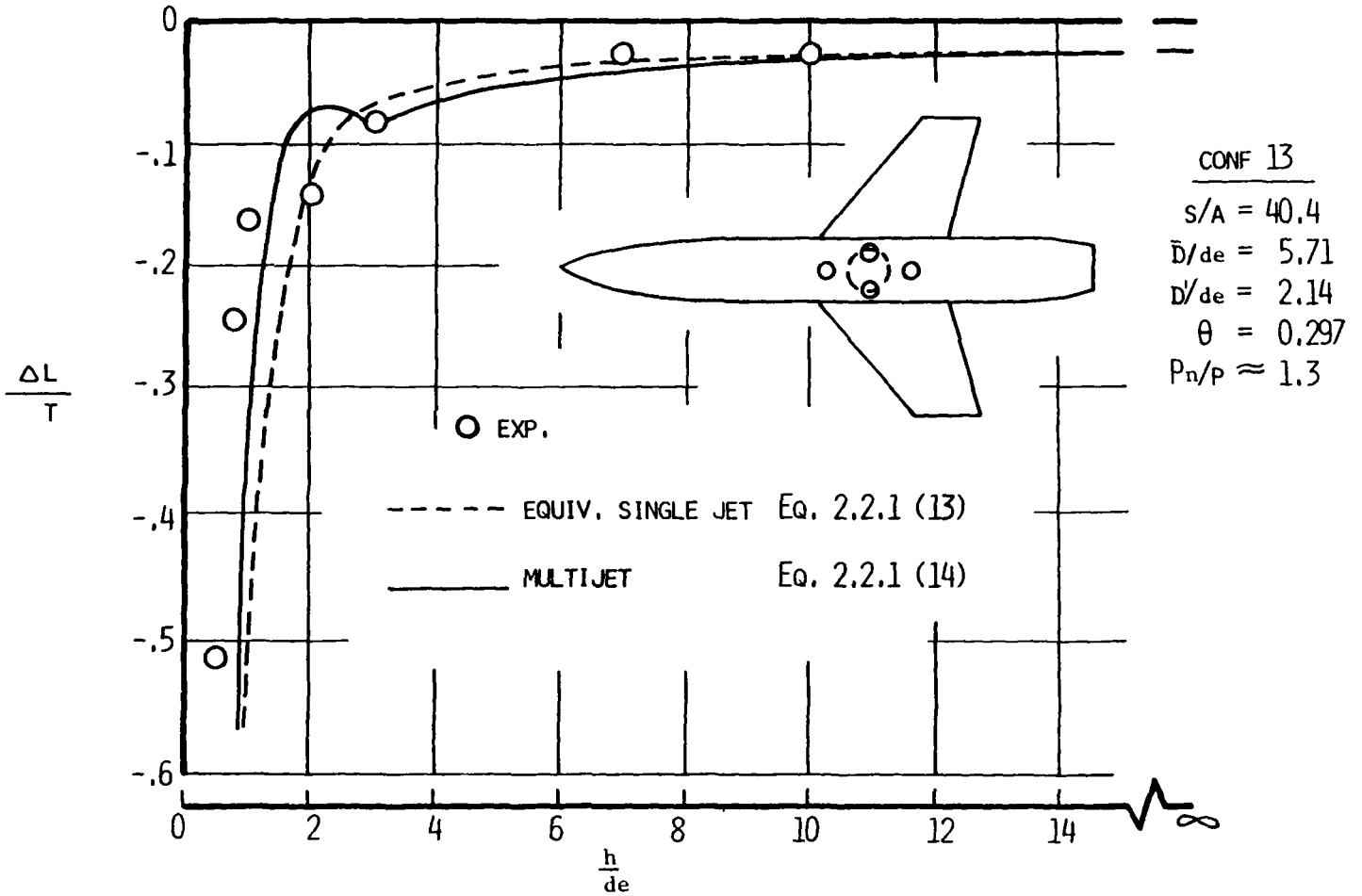

e) Concluded

FIGURE 2.2.1 (14) - Continued

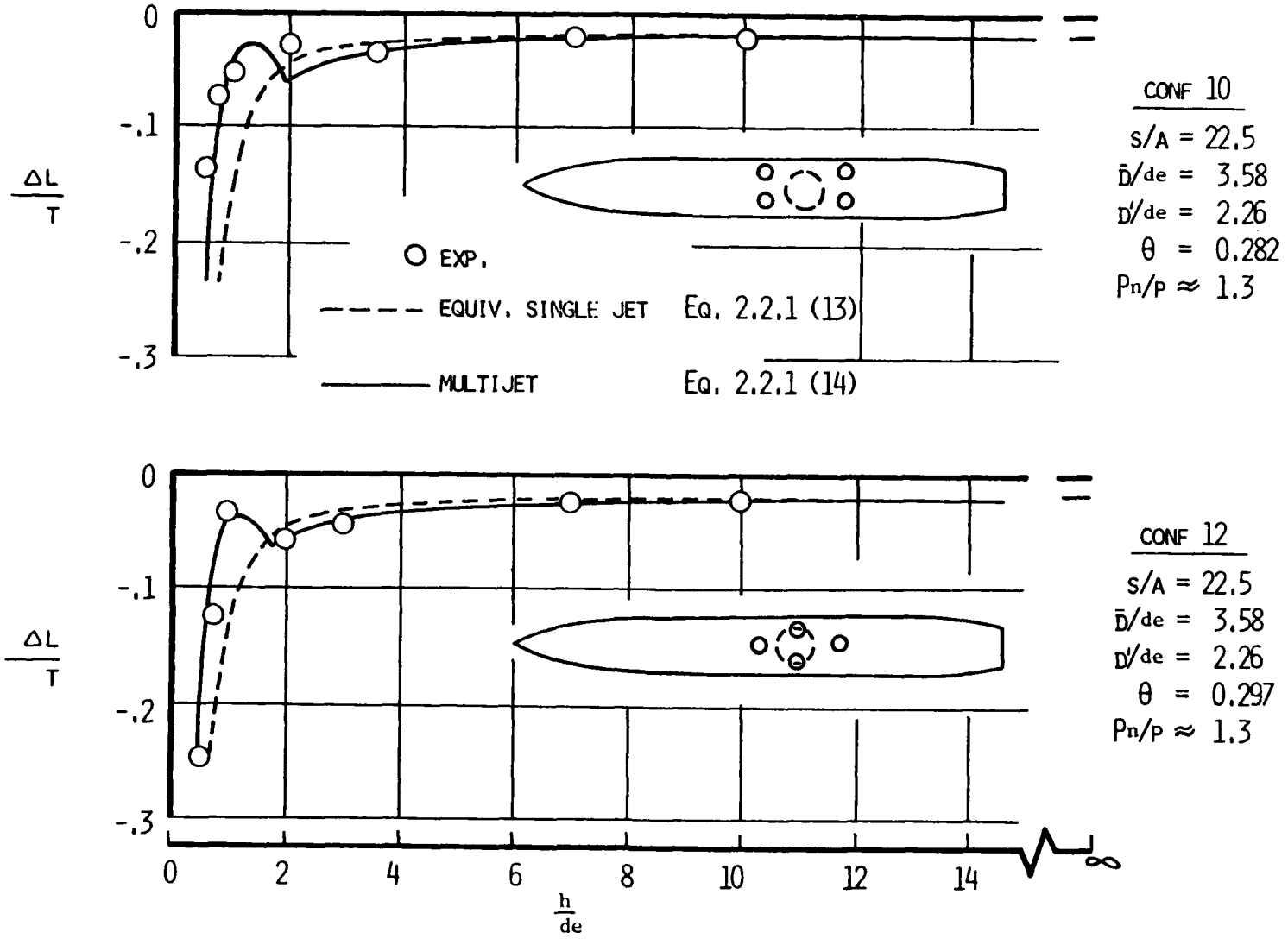

f) Fuselage alone Configuration of Ref. 9

FIGURE 2.2.1 (14) - Concluded

REFERENCES

1) Genrry, Carl L., and Margason, Richard J.: Jet-Induced Lift Losses on VTOL Configurations Hovering In and Out-of-Ground Effect, NASA TN D-3166, 1966.

2. Wyatt, L.A.: Static Tests of Ground Effect on Planforms Fitted With a centrally-located Round Lifting Jet. Ministry of Aviation, CP749, June, 1962.

3. Shumpert, P.K., and Tibbetts, J.G.: Model Tests of Jet-Induced Lift Effects on a VTOL Aircraft in Hover, NASA CR-1297, 1969.

4. Kleis, S.J., and Foss, J.F.: The Effect of Exit Conditions on the Development of an Axisymmetric Turbulent-Free Jet, Third Year Technical Report, NASA Grant NGR 23-004-068, Michigan State University, 15 May 1974.

5. McDonnell Aircraft: A Proposal to Develop Models for Propulsion-Induced Aerodynamics of High Aspect Ratio Jets, 1977.

6. McLemore, H. Clyde: Jet-Induced Lift Loss of Jet VTOL Configurations in Hovering Condition, NASA TND-3435, 1966.

7. Spreeman, Kenneth P. and Sherman, Irving R.: Effects of Ground Proximity on the Thrust of a Simple Downward-Directed Jet Beneath a Flat Surface, NASA TN 4407, 1958.

8. Louisse, Jan and Marshall, Frank L.: Prediction of Ground Effects for VTOL Aircraft With Twin Lifting Jets, AIAA Journal of Aircraft, February, 1976, pp. 123 - 127.

9. Vogler, R.D.: Interference Effects of Single and Multiple Round and Slotted Jets on a VTOL Model in Transition, NASA TN D-2380, August 1964.

10. Davenport, Edwin E. and Spreeman, Kenneth P.: Thrust Characterists of Multiple Lifting Jets in Ground Proximity, NASA TN D-513.

11. Rolls, Stewart L.: Jet VTOL Powerplant Experience During Flight Test of X-14A VTOL Research Vehicle, AGARDograph 103, pp. 543 - 557, October, 1965.

12. Hall, G.R.: Scaling of VTOL Aerodynamic Suck-Down Forces, AIAA Journal of Aircraft, July-August 1967, pp. 393 - 394.

13. Hammond, Alexander D.: Thrust Losses in Hovering For VTOL Aircraft, NASA SP-116, April 1966, pp. 163 - 176.

14. Karemaa, A., et al: The Aerodynamic and Thermodynamic Characteristics of Gountains and Some Far-Field Temperature Distributions, ONR Report, ONR-CR212-237-1F, July, 1978.

LIST OF SYMBOLS

A	total jet exit area, ft.^{2} (m^2)
S	total planform area, ft.^{2} (m^2)
d	diameter of individual jet, ft. (m)
d_e	diameter of equivalent single jet having area A, ft., (m) = $2\sqrt{A/\pi}$
D	diameter of equivalent circular planform having area S, ft., (m) = $2\sqrt{S\pi}$
$\overline{D}$	angular mean diameter of planform, ft. (m) $\frac{1}{\pi}\int_0^{2\pi} r\,d\phi$
D'	Diameter of "bolt circle" of multiple jet pattern, ft. (m)
h	height of lower surface of configuration above ground, ft. (m)
Δh	height of wing above configuration lower surface, ft. (m)
h'	height below which positive lifting pressures are experienced, ft. (m)
θ	fraction of jet pattern circumference blocked by individual jets
ΔL	total jet-induced lift, lb. (N)
ΔL_∞	lift increment induced out-of-ground effect, lb. (N)
ΔL_s	lift increment induced by single jet or equivalent single jet in-ground effect, lb. (N)
ΔL_m	lift increment induced by multiple jets in-ground effect, lb. (N)
$\frac{\Delta L_1}{T}$, $\frac{\Delta L_2}{T}$, $\frac{\Delta L_3}{T}$	terms used in calculating $\frac{\Delta L_m}{T}$
P_n	jet total pressure, lb./ft.^{2} (N/m^2)
p	ambient static pressure, lb./ft.^{2} (N/m^2)
T	total jet thrust of configuration, lb. (N)
$T_{j,1}$ & $T_{j,2}$	thrust of individual jets of multiple nozzle configuration, lb. (N)
N	number of jets and fountains in multiple jet configuration
q_x	maximum impact dynamic pressure measured at distance x downstream from nozzle exit plane, lb./ft.^{2} (N/m^2)
x	distance downstream from nozzle exit plane, ft. (m)
ΣP_r	summation of perimeter of all jets, ft. (m)

DEVELOPMENT OF AN EXPERIMENTAL BASIS FOR A HANDBOOK METHOD TO PREDICT GROUND-INDUCED FORCES ON A HOVERING V/STOL AIRCRAFT

By W. H. Foley

GENERAL DYNAMICS CORPORATION
Fort Worth, Texas

Abstract

As part of a program to develop a handbook method to predict ground-induced forces on a Hovering V/STOL aircraft for inclusion in the V/STOL Aerodynamic and Stability and Control Manual currently being written by NADC, an experimental program to measure suckdown and fountain characteristics is being conducted. The effects of planform contour, lift improvement devices, and nozzle exit conditions have been analyzed and are discussed.

Nomenclature

C_j, C_{fc}, C_{fi}	Extrapolation Coefficients
d	Nozzle Diameter
d_f	Distance From Nozzle ℄ To Fountain ℄
$\bar{D}$	Angular Mean Diameter (Ref. 4)
F_j	Nozzle Thrust
h	Altitude
h_j	Altitude Of Nozzle Exit Above Ground Plane
h_f	Altitude Of Fuselage Or LID Bottom Above Ground Plane
h_w	Altitude Of Wing Undersurface Above Ground Plane
LID	Lift Improvement Device
ΔL	Net Lift Loss (or Gain) In Ground Proximity
ΔL_j	Lift Loss Due To Suckdown
ΔL_{fc}	Lift Gain Due To Fountain/Planform Impact
ΔL_{fi}	Lift Loss Due To Fountain Interference
ℓ	LID Depth
NPR	Nozzle Pressure Ratio
W	Length Of Planform Which Is Impacted By The Fountain
ϵ	Characteristic Eddy Size
ϵ_o	Characteristic Eddy Size For A Clean Nozzle
∞	Out Of Ground Effect

INTRODUCTION

The flow field in the immediate vicinity of a hovering V/STOL aircraft can be divided into six more or less distinct regions (Figure 1). Of particular interest here are regions 1, 2, 3, and 5, i.e., those regions wherein the engine exhaust flows combine with induced ambient air flows to produce forces and moments upon the airframe. In the case of aircraft with high engine exhaust velocities combined with appreciable planform areas, such as the AV-8A and the VAK-191B, these forces and moments are almost invariably both large and unfavorable. Consequently, a considerable amount of theoretical and experimental work (e.g., References 1-10) has been devoted to the subject. During 1977 the Naval Air Development Center began work on a V/STOL Aerodynamic and Stability and Control Manual in order to reduce V/STOL test data and prediction methodologies to a form useful in a preliminary design environment - that is, to develop an engineering tool for doing rapid hand calculations of advanced aircraft performance during the conceptual stage of development. General Dynamics' Fort Worth Division is presently under contract to the Naval Air Development Center to conduct model tests and develop empirical formulations for hover-induced lift effects for application in the manual. The first phase of the program, the development of a methodology for the prediction of suckdown, has been completed. Suckdown is the flow phenomenon depicted in regions 5 and 6 of Figure 1 wherein ambient air, which is accelerated towards the aircraft because of entrainment by the exhaust flows, creates a low-pressure field under the aircraft and, consequently, a downward force on the planform.

METHODOLOGY DEVELOPMENT

The point of departure for the predictive methodology is the work of Karemaa, et al. (References 7, 8, and 11) wherein the net induced force upon a planform is divided into three parts, viz.

$$\Delta L/F_j = \Delta L_j/F_j + \Delta L_{fc}/F_j + \Delta L_{fi}/Fj \qquad 1$$

ΔL_j is a lift loss term due to pure suckdown, i.e., the suckdown which would be felt by a planform if no fountain jets were present. Physically, it may be measured on a model by operating each lift jet individually (so no fountain is produced), measuring the force on that portion of the planform adjacent to the operating nozzle, and summing the results for all jets. ΔL_{fc} is the buoyant force derived from the impact (if any) of the fountain jet upon the planform; ΔL_{fi} is a correction factor to account for the fact that the physical presence of the fountain interfers with the entrainment of ambient air by the exhaust flow and, thus, alters the single-jet suckdown ΔL_j.

The two-, three-, and four-jet data already obtained by use of simple, flat-plate planforms (References 7, 8, 11, and 12) will be used as the baselines for predicting the values of ΔL_{fc} and ΔL_{fi} for arbitrary aircraft; an empirical method, described below, will be used to predict ΔL_j. However, the baseline ΔL's must be extrapolated to account for variations in planform shape, planform undersurface contour, lift improvement devices, nozzle/planform area ratio, nozzle exhaust characteristics, and nozzle pressure ratio. Therefore, equation (1) is modified to read

$$\Delta L/F_j = C_j \Delta L_j/F_j + C_{fc} \Delta L_{fc}/F_j + C_{fi} \Delta L_{fi}/F_j \qquad 2$$

where C_j, C_{fc}, and C_{fi} are extrapolation coefficients.

RESULTS

(a) Suckdown

Empirical predictive equations for use in the manual have been developed for both C_j and $\Delta L_j/F_j$ (Reference 13) and are

$$C_j = C_{j1} \cdot C_{j2} \qquad 3$$

$$C_{j1} = .971 + .0295\, \epsilon/\epsilon_o \qquad 4$$

$$\left.\begin{array}{l} C_{j2} = 1.173 - .2495 \ln (NPR) \text{ if } NPR \leq 2 \\ = 1.061 - .0889 \ln (NPR) \text{ if } NPR \geq 2 \end{array}\right\} \qquad 5$$

$$\Delta L_{j\infty}/F_j = .0667 \cdot (d/\bar{D} - .420) \qquad 6$$

where, for rectangular planforms,

$$\frac{\Delta L_j}{F_j} = \frac{\Delta L_{j\infty}}{F_j} - (.00125\bar{D}/d + .0185) C_j \left[h/(\bar{D}-d)\right]^{-1.59} \qquad 7$$

and, for delta-shaped planforms,

$$\frac{\Delta L_j}{F_j} = \frac{\Delta L_{j\infty}}{F_j} - (.0072\bar{D}/d - .0166) C_j \left[h/(\bar{D}-d)\right]^{-1.28} \qquad 8$$

The above results were derived from data taken on flat-plate planform configurations, i.e., planforms where $h_j = h_f = h_w = h$. Often, this is not the case for actual aircraft. Therefore, as a check, the above equations were applied to the reference 14 configuration. Here a $\bar{D}$ was computed on the basis of exposed wing planform area and $\Delta L_j/F_j$ computed by equation 7 by use of $h = h_w$. To this an additional $\Delta L_j/F_j$ term, which was based on $\bar{D}$ for the

fuselage planform and used $h=h_f$, was added. Eddy-size data was unavailable, but it was assumed that the flow was at least as "clean" as that of the Reference 15 baseline, so $C_j=1$ was assumed. C_{j2} was calculated by equation 5 (NPR ≤ 2) for an NPR of 1.13 and is 1.14. The prediction is compared with the Reference 14 data on Figure 2; the agreement is reasonable.

(b) Fountain Buoyancy

It is apparent that C_{fc} will be a function of a number of variables. Reference 14 has indicated the importance of planform contour. References 14 and 16 indicate lift improvement devices must be included. Reference 15 has shown a nozzle exit condition effect and it is apparent that nozzle spacing, planform/nozzle area ratio, and fountain/planform capture area must yet be considered. Therefore, on the basis of the format developed for C_j,

$$C_{fc} = C_{fc1} \cdot C_{fc2} \cdot \ldots \cdot C_{fc7}, \qquad 9$$

although C_{fc5} - C_{fc7}, which reflect area variations, may not turn out to be independent of each other. These coefficients are enumerated in Table I. At this time, the data have been taken from which C_{fc1} and C_{fc2} will be derived (Reference 15), and tests are in progress at General Dynamics' Fort Worth Division, the results of which, when combined with data available in the literature, will form the basis for C_{fc5} and C_{fc6}. The derivation of C_{fc3}, C_{fc4}, and C_{fc7} has been completed; the remainder of this paper will discuss these results.

Tests conducted by Wohllebe and Migdal (Reference 14) showed that undersurface contour has a first-order effect on fountain buoyancy. The analogy of drag on blunt versus streamlined bodies is appropriate (Figure 3) but not exact; the change in fountain buoyancy, when the corners of a blunt fuselage are rounded, are much more dramatic than one would expect from predictions based on drag calculations. Undoubtedly, the cause lies in the fact that a fountain jet is of limited physical size and does not represent the infinite flow normally seen in drag work. Reference 14 considered somewhat modest corner roundings. Therefore, in order to extend the results of that work to cover a fuller range of surface contours, a model with three fuselage shapes was built and tested on General Dynamics' V/STOL Hover Test Facility (Figure 4). This model was tested at an NPR of 2.0 over a variety of altitudes (Figure 5) and, together with the Reference 14 data, was analyzed to determine $\Delta L_{fc}/F_j$. The results are shown in Figure 6 where $C_{fc3} = \Delta L_{fc}/F_j \div (\Delta L_{fc}/F_j)_{2r/w=0}$.

Closely related to planform contour is the subject of hover lift improvement devices (LIDs) (References 14 and 16). That they can be very effective in amplifying fountain lift can be seen from Figure 7 where model test data for a variety of LIDs installed on a General Dynamics Type A aircraft are shown. These devices work in a manner opposite to that shown in Figure 4, i.e., the LIDs force the fountain flow to reverse itself, thereby imparting additional vertical thrust to the aircraft planform (Figure 8). A comparison of the induced lift realized by a blunt fuselage and one with LIDs is shown in Figure 9. Two LID sizes were tested (ℓ/w = .50 and .25); little difference was observed between them (although, obviously, LID effectiveness must become negligible as $\ell \rightarrow 0$). Further, from both Figures 7 and 9, there is a substantial difference between LIDs that are completely closed (i.e., form a rectangle) and that are not (i.e., open at the ends). Although it seems unusual that removal in this manner of less than 10% of the LIDs should lower the induced lift by as much as 50%, it was observed during the tests that the removal of the ends provided a channel through which much of the flow proceeded fore and aft and was not turned as per Figure 8.

Calculated values of $\Delta L_{fc}/F_j$ for the cases of Figure 9 have been obtained and, using Configuration X1 as a baseline, C_{fc4} has been derived and is shown in Table II. In these cases, the LID length was quite long and probably represents a practical limit to the amount of a fountain that can be "captured" by LIDs. It is likely that actual aircraft, because of design or weight limitations, will be unlikely to use LIDs of this extent. Therefore, testing is continuing at General Dynamics in order to determine the sensitivity of C_{fc4} to LID length. Theoretically, the use of LIDs should be able to double the fountain lift in that the turn of the horizontally-flowing jet under the fuselage to the vertical direction should ideally produce the same reaction force as the initial fountain/planform impact. The value of C_{fc4} of 2.14 indicates that this is essentially achievable in practice. (The fact that $C_{fc4} > 2$ is not a repudiation of Newton. Rather, the difference likely represents a margin of experimental uncertainty).

A final point on the use of LIDs concerns the fact that they can be made too extensive. Figure 10a shows the results of the use of LIDs on a three-nozzle, delta flat-plate planform. The inner set (LID2) was positioned to capture most of the fountain; the outer (LID1) subtended the entire planform; both produced positive results. However, Figure 12a is somewhat deceptive in that, by using h_f as the pertinent altitude, the planforms of the LID configurations are not at the same height as that of the plane configuration for given h_f/d. Therefore, the data of Figure 10a has been replotted against h_j/d in Figure 10b. This represents the true effect of <u>adding</u> LIDs to this configuration.

Now, as h_j/d decreases, a point is reached where the physical presence of the devices blocks ambient air from access to the under-planform, and sizable vacuums are created. Thus, with LID1, at $h_j/d \leq 3.5$, performance is significantly worse than it was without LIDs.

Fountain capture area is defined as the portion of the fountain which can be intersected by the planform to produce fountain lift (see Figure 11). Two configurations that offered differing areas for fountain impact were tested and the ratios of the appropriate ΔL_{fc}'s obtained are plotted on Figure 12. If one considers the ground jet which spreads radially from each free jet which impacts the ground plane and asks what angular sector can ultimately impact the planform, one obtains from purely geometrical considerations, that this sector is bounded by the angles $-\theta'$ to θ' where

$$\theta' = \tan^{-1}\left(\frac{W/2}{d_f + h_f}\right) \qquad 10$$

for the symmetrical case under consideration. From Reference 7, then, the maximum fountain lift which can be realized (in the absence of LIDs) is $\int_{-\theta'}^{\theta'} \cos^2\theta \, d\theta$. In general, of course, the fountain lift actually realized will be somewhat less than this due to both fountain spreading normal to the θ-plane as well as fountain interference. Nonetheless, if one were to test, say, Configuration I0 and ask what the fountain lift would be on Configuration X0, a reasonable first approximation would be

$$\left(\frac{\Delta L_{fc}}{F_j}\right)_{X0} = \left(\frac{\Delta L_{fc}}{F_j}\right)_{I0} \times \frac{\left[\int_{-\theta'}^{\theta'} \cos^2\theta \, d\theta\right]_{X0}}{\left[\int_{-\theta'}^{\theta'} \cos^2\theta \, d\theta\right]_{I0}} \qquad 11$$

In fact, Figure 12 shows this to be reasonably accurate. Therefore, C_{fc7} is now defined, viz.

$$C_{fc7} = \left(\frac{\Delta L_{fc}}{F_j}\right) \div \left(\frac{\Delta L_{fc}}{F_j}\right)_{ref.}$$

$$= \left\{\int_{\theta_1'}^{\theta_2'} \cos^2\theta \, d\theta\right\} \div \left\{\int_{\theta_1'}^{\theta_2'} \cos^2\theta \, d\theta\right\}_{ref.} \qquad 12$$

Due to the fact that the integrals are functions of altitude as well as geometry, C_{fc7} is also a function of altitude.

CONCLUDING REMARKS

The foregoing presents the progress to date in the development of an empirical method to calculate the ground-induced

forces on a hovering V/STOL aircraft by dividing the net force into three components, each of which in turn are extrapolated by experimentally determined coefficients to correct for baseline configurations to arbitrary aircraft planforms. The analysis that has been completed to date indicates that the variables of nozzle exit conditions, planform contour, and lift improvement devices are relatively independent and can, accordingly, be described by independent coefficients. The major piece of work remaining is to determine the proper coefficients to describe the effects of the remaining geometric variables - nozzle spacing and planform/nozzle area ratio - as well as to generalize the results to three- and four-nozzle configurations.

REFERENCES

1. Spreeman, K.P. and Sherman, I.R., Effects Of Ground Proximity On The Thrust Of A Simple Downward Directed Jet Beneath A Flat Surface, NACA TN 4407, 1958.

2. Davenport, E.E. and Spreeman, K.P., Thrust Characteristics Of Multiple Lifting Jets In Ground Proximity, NASA TN D-513, 1960.

3. Vogler, R.D., Ground Effects On Single And Multiple Jet VTOL Models At Transition Speeds Over Stationary And Moving Ground Planes, NASA TN D-3213, 1966.

4. Wyatt, L.A., Static Tests Of Ground Effect On Planforms Fitted With A Centrally Located Round Lifting Jet, Ministry Of Aviation C.P. 749, 1962.

5. Kotansky, D.R., Durando, N.A., and Bristow, D.R., Jet-Induced Forces And Moments In and Out Of Ground Effect, McDonnell Aircraft Company Report, June, 1977.

6. Siclari, M.J., Barche, J., and Migdal, D., V/STOL Aircraft Prediction Technique Development For Jet-Induced Lift In Hover, Grumman Aerospace Corp. PDR 623-18, April, 1975.

7. Karemaa, A., Smith, C.W., Weber, H.A., and Garner, J.E., The Aerodynamic And Thermodynamic Characteristics Of Fountains And Some Far-Field Temperature Distributions, Office of Naval Research Report ONR-CR212-237-1F, July, 1978.

8. Smith, C.W., and Karemaa, A., Induced Effects Of Multi-Jet Fountains On Flat-Plate Surfaces, AIAA Paper No. 78-1516, August, 1978.

9. Kuhn, R., An Empirical Method For Estimating Jet Induced Lift Losses Of V/STOL Aircraft Hovering In And Out Of Ground Effect, Proceedings Of The Workshop On VSTOL Aerodynamics, May, 1979.

10. Siclari, J.J., Hill, W.G., and Jenkins, R.C., Investigation Of Stagnation Line And Upwash Formation, AIAA Paper No. 77-615.

11. Karemaa, A. and Ramsey, J.C., Aerodynamic Methodology For The Prediction Of Jet-Induced Lift In Hover, General Dynamics Report CASD-ERR-73-012, December, 1973.

12. Karemaa, A., Abbreviated Methodology For The Prediction Of Jet-Induced Lift In Hover, General Dynamics Report CASD-ERR-74-024, December, 1974.

13. Foley, W.H., Methodology For Prediction Of V/STOL Propulsion Induced Forces In Ground Effect, AIAA Paper No. 79-1281, June, 1979.

14. Wohllebe, E.A. and Migdal, D., Some Basic Test Results Of V/STOL Jet-Induced Lift Effect In Hover, AIAA Paper No. 79-0339, January, 1979.

15. Lummus, J.R., and Smith, C.W., Flow-Field Characteristics And The Effect Of Jet-Exhaust Simulation For VSTOL Vehicles Near The Ground, Proceedings Of The Workshop on VSTOL Aerodynamics, May, 1979.

16. Kamman, J.H., and Hall, C.L., Lift System Induced Aerodynamics Of V/STOL Aircraft In A Moving Deck Environment, McDonnell Aircraft Co. Report No. NADC-77-107-30, September, 1978,

TABLE I. FOUNTAIN CORE COEFFICIENTS

COEFFICIENT	INFLUENCING VARIABLE
C_{fc1}	Eddy Size
C_{fc2}	NPR
C_{fc3}	Planform Contour
C_{fc4}	Lift Improvement Devices
C_{fc5}	Nozzle Spacing
C_{fc6}	Planform/Nozzle Area Ratio
C_{fc7}	Fountain/Planform Capture Area

TABLE II. TWO-JET LID EXTRAPOLATION COEFFICIENTS

CONFIGURATION	C_{fc4}	STD. DEV. (AVERAGED OVER h_f)
Plane Planform	1.0	___
Full Longitudinal LIDs	1.64	.054
Full Longitudinal + Transverse LIDs	2.14	.022

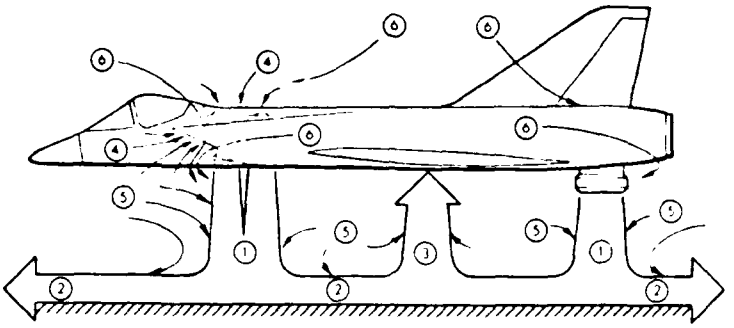

① EXHAUST FLOW (FREE JET)

② GROUND JET

③ FOUNTAIN JET

④ ENGINE INLET FLOW

⑤ & ⑥ ENTRAINED AMBIENT AIR

Figure 1 Flow Field Near a Hovering VTOL Aircraft

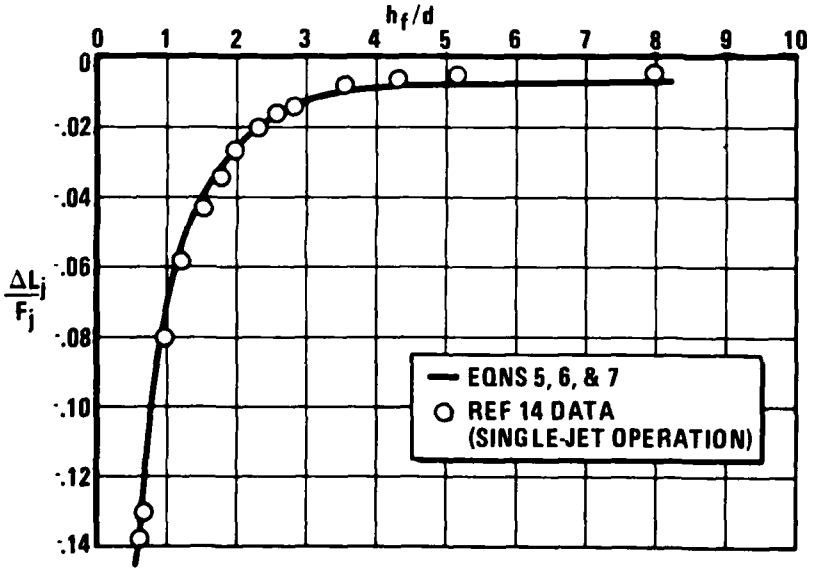

Figure 2 Empirical Suckdown Prediction Compared with Experiment

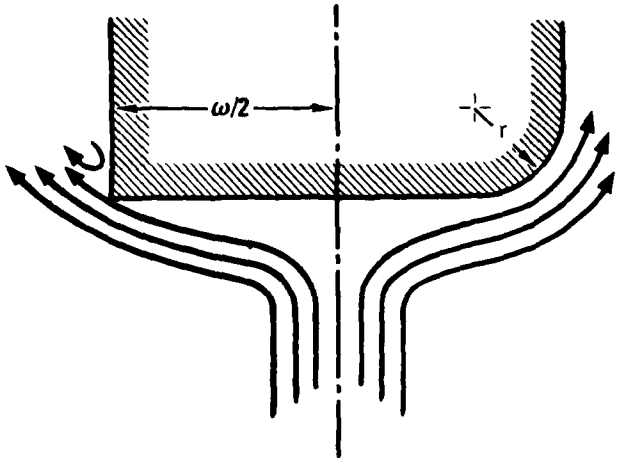

Figure 3 Fountain Streamlines Around Blunt and Semi-Rounded Fuselages

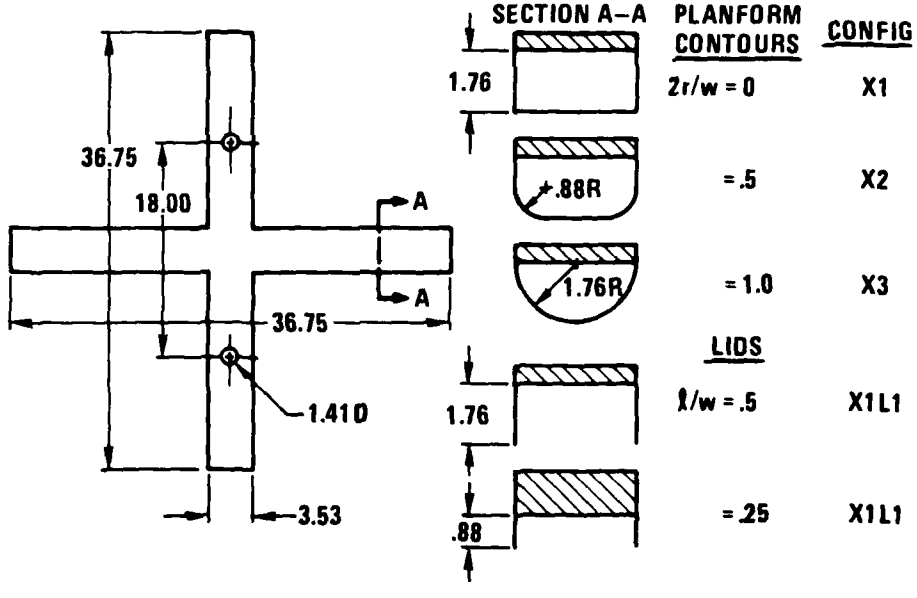

Figure 4 Cruciform Planform Models (All Dimensions in Inches)

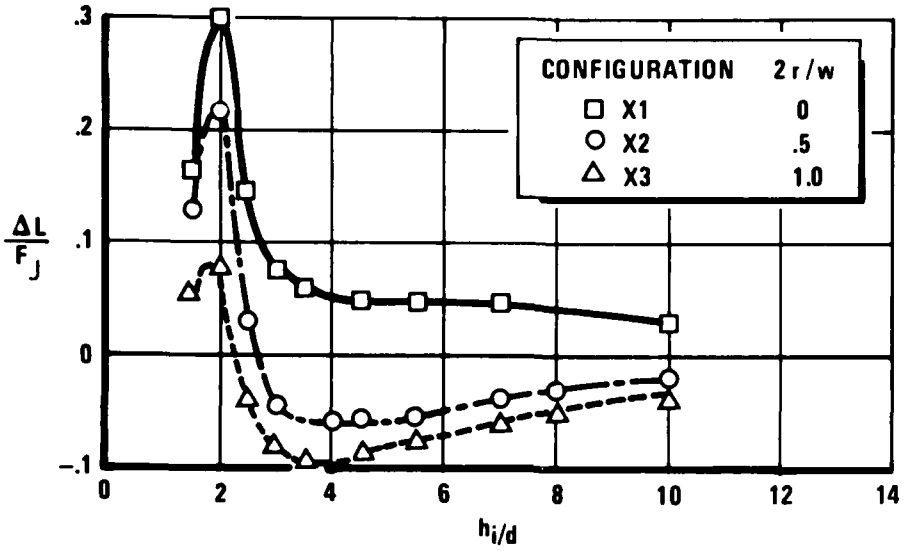

Figure 5 The Effect of Fuselage Contour on Induced Lift

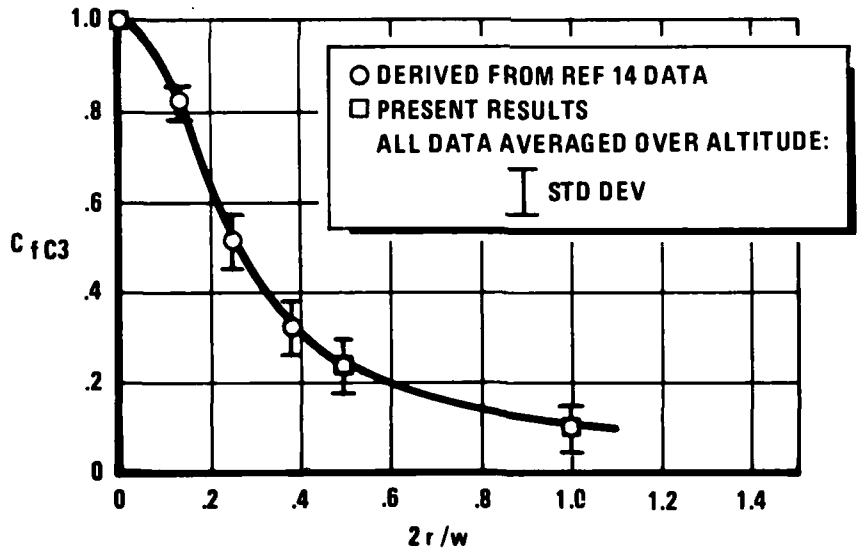

Figure 6 The Effect of Fuselage Contour on Fountain Core Strength

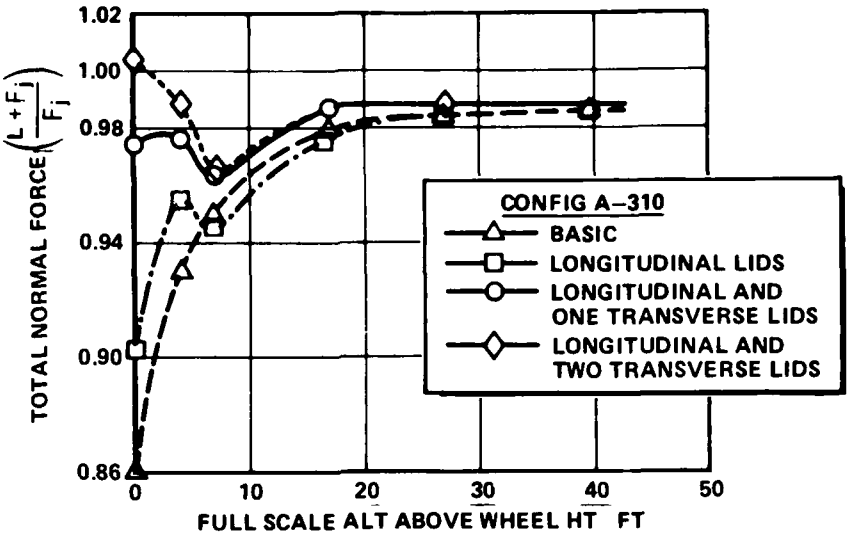

Figure 7 Effect of Lids on a Type A Configuration

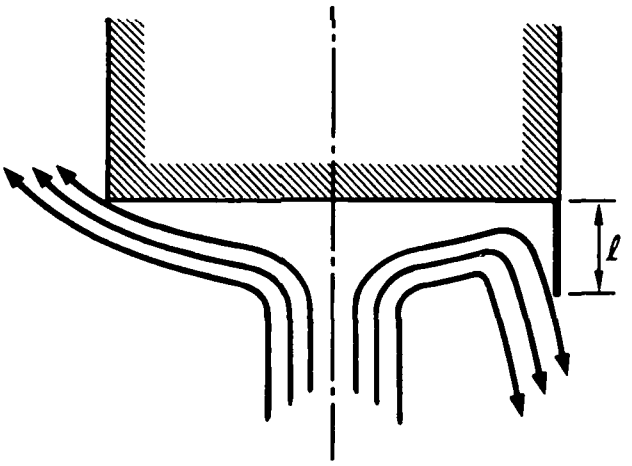

Figure 8 Fountain Streamlines Around a Blunt Fuselage and a Lid

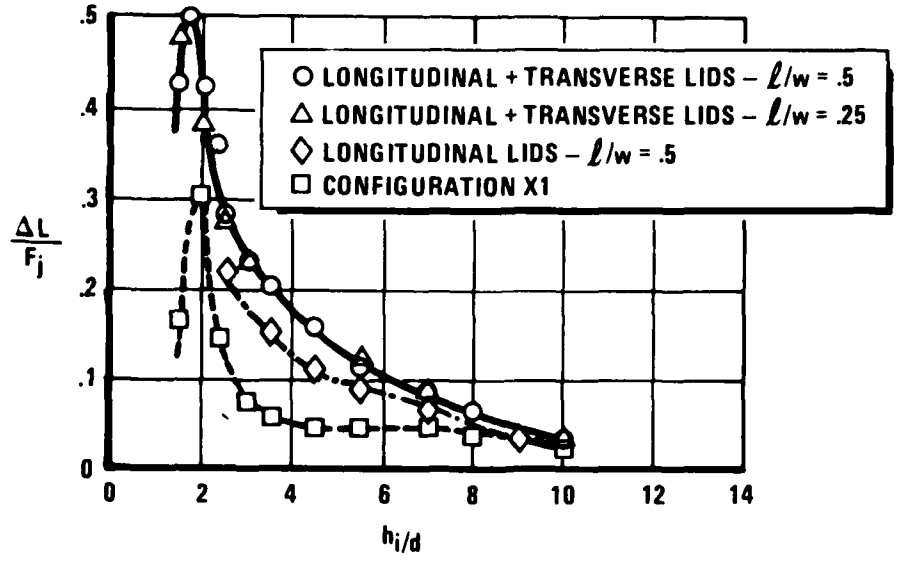

Figure 9 Cruciform Planform with Lids

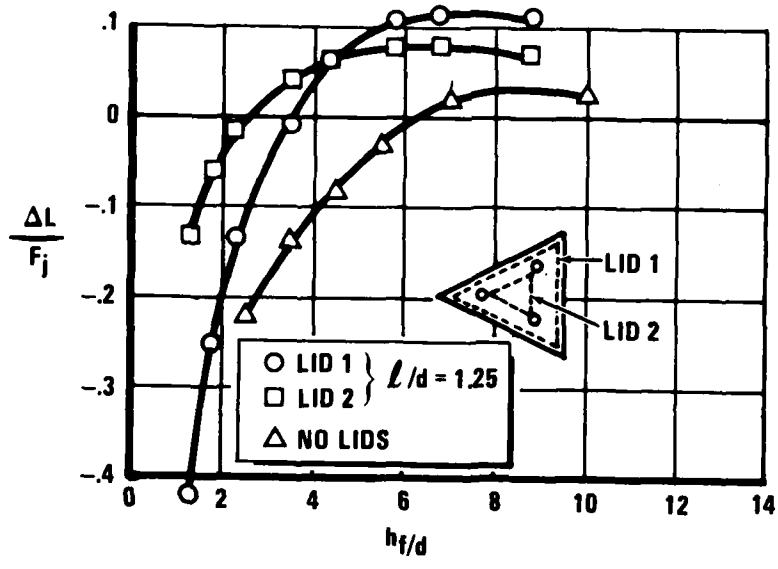

Figure 10a Effect of Lids on a Three Jet Configuration

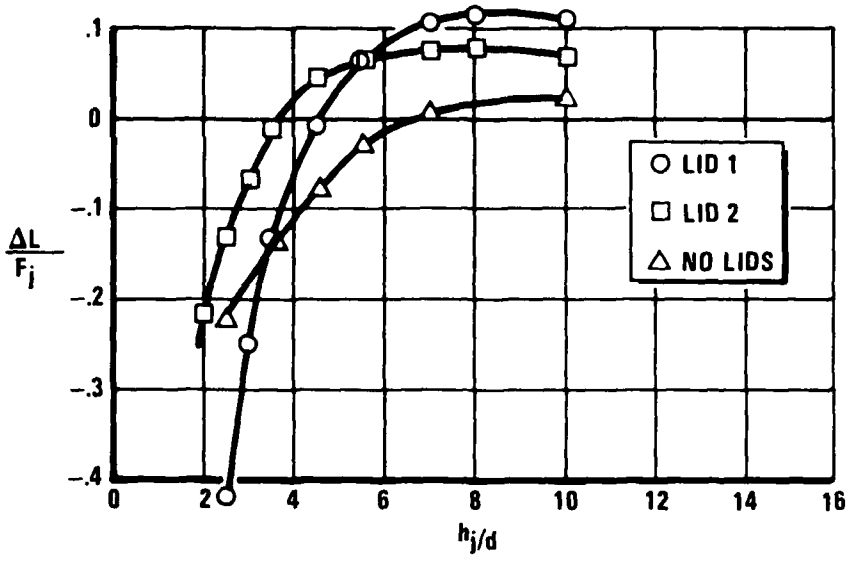

Figure 10b Effect of Lids on a Three Jet Configuration

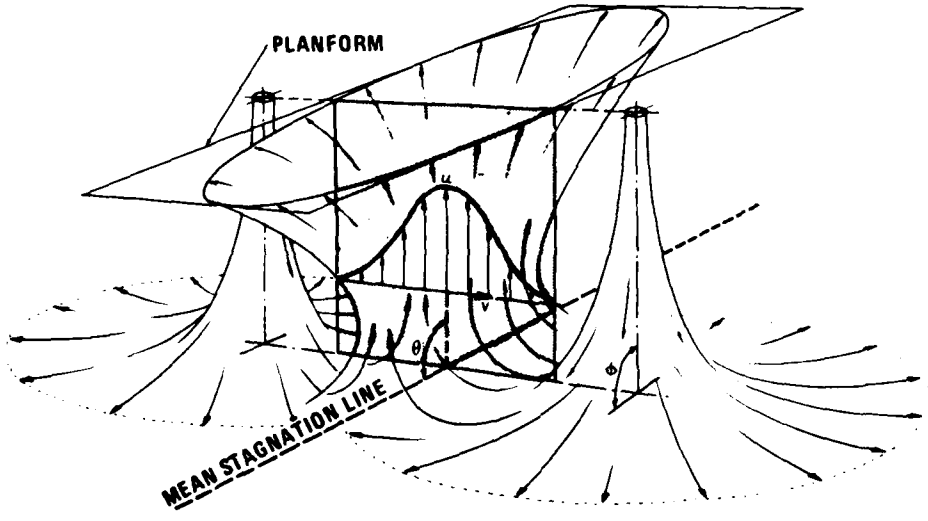

Figure 11 Fountain Jet Geometries

$$C_{fc_7} = \frac{(\Delta L_{fc}/F_j)_{10}}{(\Delta L_{fc}/F_j)_{X0}}$$

OR

$$\frac{\left(\int_{-\theta'}^{\theta'} \text{Cos}^2\theta d\theta\right)_{10}}{\left(\int_{-\theta'}^{\theta'} \text{Cos}^2\theta d\theta\right)_{X0}}$$

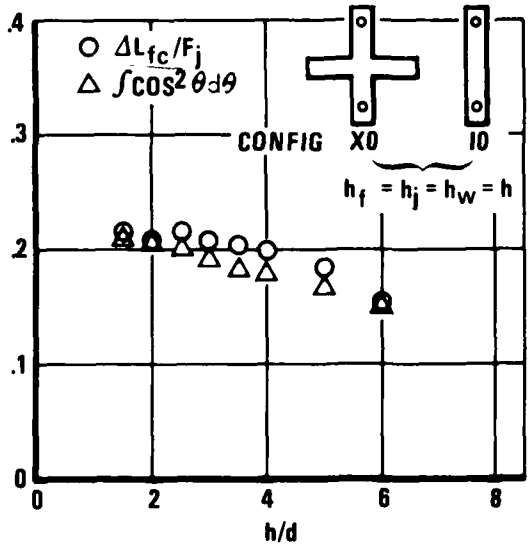

Figure 12 Fountain Lift and Capture Area

Flow-Field Characteristics and the Effect of Jet-Exhaust Simulation for VSTOL Vehicles Near the Ground*

J. R. Lummus, Senior Engineer
C. W. Smith, Engineering Specialist
General Dynamics Fort Worth Division
Fort Worth, Texas

Abstract

Induced forces due to VSTOL exhaust/ground plane interactions, on planforms represented by flat-plates, have been measured in a manner that allows the fountain effects to be isolated from the suckdown forces; two-, three-, and four-nozzle configurations have been tested. Pressure surveys of the fountains have been made to quantify fountain characteristics. Results are presented that show the relative magnitude of the fountain and suckdown contributions to the total induced forces acting on the blocking surfaces. In addition, results are presented that quantify the influence of nozzle exit conditions on the forces induced on the planforms.

*This research has been funded by the Office of Naval Research under Contract Nos. N00014-76-C-0698 and N00014-78-C-0384

Nomenclature

A	Area used in fountain integration
D	Nozzle-exit diameter
$\bar{D}$	Diameter of circle having equivalent planform area (Ref. 9)
d_f	Distance from one of two jets to the fountain on a line perpendicular to the fountain
ϵ	Largest physical dimension for turbulence generation; grid size for screens in this experiment
F	Force vector used in fountain integration
F_j	Total isolated thrust of all jet nozzles for single- or multiple-jet configurations
h	Height of the blocking surface above the ground surface
I	Turbulent intensity
ΔL	Total induced lift on the blocking surface, equal to the sum of the fountain and suckdown components
ΔL_F	Total incremental effect of the fountain on the induced lift, equal to the sum of the fountain core and fountain interference components
ΔL_{FC}	Lift of the fountain core obtained from integrations of the rake pressure data
ΔL_{fi}	Fountain interference lift
ΔL_j	Pure suckdown obtained with single nozzle
N_j	Nozzle designation where j = location of the plenum (see Figures 1 and 2)
Q_F	Dynamic pressure
T	Temperature
V	Velocity
X	Distance from the centroid of the nozzle configuration perpendicular to the rake path

Y	Distance from the centroid of the nozzle configuration along the rake path
Z	Distance above the ground plane
ρ	Density
S_1	Turbulence screen with element size = 0.125 in.
S_2	Turbulence screen with element size = 0.240 in.
P_1, P_2	Pressure distribution plates (see Figure 17)

Introduction

When two or more jets impinge normally on a plane surface, the resulting flow-field exhibits radially expanding jets along the surface (wall or ground jets). In addition, the wall jets from the different sources can meet to form a vertical-upflow region, or fountain. This fountain phenomena will accompany most hovering multiple jet V/STOL configurations. Under certain conditions, the fountain impacts the planform (blocking surface), produces lift, and, to some extent, can counteract the suckdown losses caused by the entrainment action of the ground jets. In addition, pressure fields are often produced as a result of the fountain which, by its physical presence, can block the entrainment of ambient air and interfere with the suckdown. This leads to additional lift losses or gains called fountain interference. Consequently, the fountain phenomenon is treated as being composed of two separate but additive effects - fountain core-associated lift gains and interference effects.

Development of empirical ground-effects methodology has been the subject of a continuing program at General Dynamics. Initial efforts[1, 2, 3] developed methods for the prediction of the free- and ground-jet characteristics. An extensive test program was then conducted to identify the fountain characteristics.[4, 5, 6] Specifically, this investigation was directed toward understanding the detailed nature of the fountain core, such as its momentum characteristics and the related flow angularities, interference effects, and entrainment characteristics. The force due to the fountain core was determined by pressure-rake surveys of the fountain. The difference between the fountain-core force and the total fountain increment (determined from the balance force measurements) is a measure of the fountain interference. Salient features are reviewed as Part I of this paper.

Flight tests of the VAK-191B VSTOL aircraft indicate that accurate modeling of engine exhaust conditions might be necessary so that model-measured ground-induced forces can be extrapolated to those of full-scale vehicles. In order to determine the criticality of these engine exhaust simulations, an experimental investigation has been conducted on the effects of varying nozzle-exit turbulence, total pressure distribution, and nozzle pressure ratio on the ground-induced forces for three of the model configurations discussed in Part I. The results of this investigation and their application to methods development for extrapolating model-to-full-scale ground-induced forces are reported in Part II of this paper.

I. FOUNTAIN FLOW-FIELD CHARACTERISTICS

Test and Model Description

These tests were conducted in the General Dynamics Low-Speed Wind Tunnel at San Diego. Forces and moments induced on flat plate planforms were measured by a six-component internal strain-gage balance system; fountain flow-field characteristics were measured with a traversing cone-probe pressure and temperature rake. The planforms used were triangular and rectangular flat plates with sharp 90-degree edges. One set of flat plates was designed for testing with two nozzles (Figure 1); three variations in distances between nozzles were provided. The three- and four-nozzle configurations tested are shown in Fugure 2.

Net Fountain Forces

The fountain-produced forces were measured by utilizing the capability of the model to attach various portions of the blocking surfaces to the balance. A two-nozzle configuration is discussed as an example of the approach (Figure 3). First, a rectangular flat plate equal to one-half of the total-plate area was placed on the balance and tested at various ground heights in the presence of its mirror image. Only the nozzle located on the metric side of the plate was operative. The resulting induced force was nondimensionalized with the thrust from the single nozzle and is defined as the pure suckdown, $\Delta L_j/F_j$, - that is, the suckdown which would be felt if no fountain was present during the full model test. The complete plate was then tested on the balance with both nozzles operating in order to determine the total induced force, $\frac{\Delta L}{F_j}$, including the fountain

effects, $\frac{\Delta L_F}{F_j}$. The difference between the total induced force and the pure suckdown equals the net fountain effect. This effect for two medium-spaced nozzles is shown in Figure 4. The fountain produces a net positive effect only at the low model heights ($h/D < 2.8$). The net fountain effects for two-, three- and four-nozzles at various spacings are summarized in Figure 5. With two nozzles, a large effect of nozzle spacing is apparent at the lower model heights. The close spacing ($d_f/D = 1.06$) shows a large lift loss indicating that the free jets have merged before striking the ground, thus eliminating the fountain but forming a strong reinforced ground jet. Both the medium and large spacings show the positive net effect of the fountain at low heights.

At moderate model heights three nozzles produce a stronger fountain effect than experienced with two nozzles (Figure 5). The different spacings result in similar curves with the closer spacing generally having a stronger fountain effect. A very strong fountain effect was obtained with the four-nozzle configuration, as shown in Figure 5.

Fountain Flow Characteristics

Fountain flow characteristics, as determined by the rake measurements, showed that the fountain formed between two nozzles can be represented by a rotation of the ground jets from each nozzle upward at a line along their intersection. A comparison between the measured flow angles for a typical two-nozzle case and the angles obtained by extending and rotating the ground jet is shown in Figure 6.

Three- and four-nozzle configuration fountain legs are present at low height in the fountain; however, as the flow rises in the fountain, the legs coalesce into a strong central core (Figure 7). Streamlines at the fountain centerline in the XZ-plane (Figure 8) illustrate the convergence of the flow at moderate heights in the fountain.

Fountain Core Force

The fountain momentum flux passing through a plane parallel to the ground at any height can be determined from the rake data. An estimate of the effective fountain core force, $\frac{\Delta L_{FC}}{F_j}$, at any height can be found by assuming that, if a solid surface were placed in the flow at that height without altering the flow, all of the momentum would be converted to a force on the plate with no losses.

The fountain core forces resulting from integrations of the rake data for two- and four-nozzle configurations are shown in Figures 9 and 10. Rake sweeps were conducted over slightly more than one-half of the fountain length. The net force is shown as a function of the length (Y-direction) of the fountain from the point of symmetry. Thus, the maximum force at each height in the fountain is the total core force for that configuration.

A strong decay in force with fountain height is evident for the two-nozzle case (Figure 9). The fountain force resulting from the four-nozzle configuration (Figure 10) shows the presence of the strong central core at the higher values of Z/D. Most of the force is experienced within two nozzle diameters from the centroid of the four nozzles.

The total fountain-core lift (maximum value of ΔL_{FC}, which occurs at Y/D values nominally of from 2 to 4) for the two- and four-nozzle configurations at each height in the fountain and at several blocking-surface heights is shown in Figure 11. Extrapolation of the data to the height of the blocking surface yields an estimation of the fountain core force that acts on the plates. There is no positive force on the plates for most of the two-nozzle configurations tested. In other words, the vertical component of momentum becomes zero before the fountain reaches the blocking surface. An exception is the medium-spaced nozzle configuration at low heights (h/d of 2.5) where a lift force approximately equal to 1% of the nozzle thrust is experienced. As a contrast, the strong fountain produced by the four-nozzle arrangement results in a positive force of 2-3% thrust at all model heights tested.

The fountain is a physical extension of the ground jet, and in this respect, it is expected to retain certain ground jet characteristics. This is especially true for the fountains between two nozzles. Here we would expect to find the usual lateral divergence of flow and entrainment of surrounding medium. The fountain test data, however, shows some surprising characteristics. A fountain between two nozzles, unlike the ground jet, does not gain mass but loses mass. In other words, the fountain is not entraining but is being entrained by a strong sink. This strong sink, with an appetite for the fountain, turns out to be the ground jet[6]. The fountain is blocking off one avenue through which the ground jet is normally supplied with ambient gases for entrainment. As a consequence of this blockage, the ground jet will entrain the relatively low energy gases of the fountain. The dissipation of the fountain is directly related to the height and size of the blocking surface. With a higher blocking surface location,

more of the entrained gas can be supplied through the opening around the edges (cross-hatched area of Figure 12) and the fountain will survive for a longer distance. Likewise, it will be shown in Part II that smaller blocking surfaces allow the formation of strong fountains, probably due to the additional gas available for entrainment into the ground jets.

Interference

A comparison of the fountain core force and the total fountain increment reveals a positive fountain interference effect, $\frac{\Delta L_{FI}}{F_j}$, Figure 13) for the cases where the fountain is sufficiently strong to reach the blocking surface. The exact nature of the flow-field that produces this positive effect is not known and will remain unanswered until the complete flow-fields surrounding the fountains are documented and understood. Contributions to the induced lift from free plus ground-jet entrainment, fountain core, and fountain interference are summarized in Figure 14 for the four-nozzle configuration. All three components are of significant magnitude and must be accounted for in the development of ground-effects prediction methodologies. It is particularly interesting that the fountain interference effect is as large (higher h/D) or larger (low h/d) than the fountain core force.

II. JET EXHAUST SIMULATION EFFECTS

Test And Model Description

The experimental investigation was conducted at the General Dynamics Fort Worth Division's Ground Effect Hover Test Facility. The flat-plate models of Figures 1 and 2 were utilized and provided two-, three-, and four-nozzle configurations. In addition, a cruciform plate was tested with the two-nozzle arrangement. Nozzle thrust and the planform induced forces and moments were measured with individual 5-component strain gage balances. Fountain flow-field characteristics were again measured with the traversing cone probe rake. The testing consisted of three phases - nozzle calibration, induced loads, and fountain surveys.

Nozzle Calibration Phase

With the flat-plate planforms removed, nozzle thrust was measured for variations in nozzle size, nozzle pressure ratio, nozzle exit turbulence, and total pressure distribution. One of the test

objectives was to cover the range of nozzle-exit flow parameters expected on real aircraft engines. To that end, nozzle pressure ratios (NPRs) of 1.5, 2.0, and 2.4 were tested, and simulations of exit pressure distributions and turbulence levels representative of turbojet and turbofan engines were obtained.

Turbulent intensity (I) was defined as the ratio of the area-weighted-average - RMS value of the fluctuating total pressure across the nozzle exit to the area-weighted-average total pressure (gage) across the nozzle exit. The fluctuating total pressure was measured by a high response subminature pressure transducer (Kulite) with an .08-inch-diameter transducer face; the signal was fed through a true RMS meter to provide an analog signal that was sampled at rates high enough and for long enough duration to ensure that, in the frequency ranges of interest (≤50 kHz), the total system error for intensity measurement was insignificant in terms of the objectives of this experiment (see footnote). The upper limit of turbulence considered was guided by turbulent intensity measurements of full-scale turbojet (Olympus 593) and turbofan (RB211) engines measured with a laser velocimeter that gave .01 to .02 for the turbojet and .01 in the core region and up to .20 in the fan region for the turbofan[7]. Turbulent intensity variations on the model were achieved by placing turbulence generating screens S_1 and S_2 (Figure 15) just upstream of the convergent nozzle section. Typical $P_{T_{RMS}}$ and P_T surveys for the baseline nozzle and S_2 turbulence generator at an NPR of 2.0 are shown in Figure 16. (The choke plate was always present well upstream within the nozzle body even for the baseline nozzle to provide uniform flow).

The error in turbulent intensity measurement due to the nonlinear frequency response characteristics of the Kulite transducer is reported by the manufacturer to be less than 3% for the turbulence frequency range of this experiment (<50 kHz) provided the turbulence characteristic length (eddy size) is greater than the diameter of the Kulite transducer face (.08 in); as this length approaches the size of the transducer face, the error increases. Since the turbulence screen S_1 and S_2 and pressure profile plates P_1 and P_2 used in this experiment all have characteristic lengths larger than the transducer face, the error in turbulent intensity measurement for these cases is considered negligible (<10%). For the baseline nozzle case (with choking plate), the eddy characteristic length is probably somewhat smaller than the transducer face diameter and a significant error may be produced (with indicated readings too low). However, since the turbulence intensities are low for the baseline nozzle case (<10%), large % errors in their measurement have little effect on the conclusions of this experiment.

Total-pressure-profile distributions were varied by placement of the P_1 or P_2 devices, shown in Figure 17, upstream of the nozzle section. These devices plus the baseline nozzle allowed a simulation of turbofan and turbojet nozzle pressure distributions as shown in Figure 18 for an NPR of 1.5. NPR is a somewhat arbitrary term when applied to non-uniform exit profiles like those produced by P_1 and P_2. Therefore, the NPRs for the non-uniform profiles were taken as those measured on the baseline, "top hat," profiles when the thrust produced by the non-uniform profiles matched that of the baseline. The screens S_1 and S_2 produced virtually uniform profiles so no analogous difficulty was present.

Induced Loads Phase

The net induced lift force, ΔL, on the model planform was measured while varying configuration, nozzle exit flow parameters, and model altitude.

For the two-nozzle configuration, NPRs of 1.5, 2.0, and 2.4 were tested; three- and four-nozzle configurations were tested at an NPR of 2.0. The turbulence screens and pressure distribution plates were tested with the two- and four-nozzle configurations; screen variations only were tested with the three-nozzle configuration.

To determine the effects of varying nozzle-exit conditions on the pure suckdown component of the net induced force, half of the two-nozzle plate was removed while operating that nozzle with half of the plate; induced loads were measured with the turbulence screens and plates and with variations in model altitude.

Fountain Survey Phase

The fountain rake was used to survey the fountains formed with the two- and four-nozzle configurations at an NPR of 2.0 to ascertain the effects on the fountain of the turbulence and pressure profile devices.

Results

Analysis of the experimental data is still in progress so results obtained to date are presented while remaining tasks and objectives are indicated.

Figure 19 shows the variation of I vs NPR obtained for the screens and plates. The high-velocity shear layers associated with the plate devices (as indicated by the pressure-profiles presented in Figure 18) resulted in even higher turbulent intensity levels than the screens. Turbulent intensity was found to decrease with increasing NPR for both the plates and screens.

In fact, it was noted that the same variation of intensity with NPR occurs with the baseline nozzle with a choking plate screen mesh (width of bars making up the mesh) of .05 in., S_1 of .125 in., and S_2 of .240 in.[8]

Variations in nozzle turbulence, nozzle pressure ratio, and nozzle total pressure distributions measurably affect the net induced forces, $\frac{(\Delta L)}{F}$, by altering the lift loss due to pure suckdown, the bouyant force produced by the impact of the fountain jet upon the planform, and fountain interference.

Effects on Net-Induced Forces

The magnitude of the maximum effect of nozzle turbulence on the net induced-force was found to be an 11% increase suckdown ($\frac{\Delta L}{F_j} = -.08$) for the two-nozzle configuration with the rectangular blocking surface over the range of NPRs tested (see, e.g. Figure 20). The maximum effect due to NPR variation was a 6% reduced suckdown ($\frac{\Delta L}{F_j} = +.04$) (from an NPR of 1.5 to 2.4). Varying the pressure distribution also increased the suckdown a maximum of 8% ($\frac{\Delta L}{F_j} = -.05$) near the ground (h/d = 2.5).

The variation due to turbulence for the three-nozzle configuration at an NPR of 2.0 is illustrated in Figure 21. Unlike the two-nozzle case, the maximum effect of the turbulence variation occurs at higher altitudes producing a large negative effect (50% change, $\frac{\Delta L}{F_j} = -.02$) but changes of similar magnitude are also observed at higher altitudes. Varying the pressure distribution produces the same maximum magnitude changes.

In Figure 23 the variation of net induced force ($\frac{\Delta L}{F_j}$) with screen and NPR for the two-nozzle configuration is displayed; this curve is typical of the trends that are obtained with pressure distribution and nozzle configuration variations.

Since the research blocking surfaces of Figures 1 and 2 are large and seem to dominate the flow field beneath them, it is of considerable interest to test a smaller plate that is more typical of realistic airplane configurations. To this end, a uniform plate with the same two-nozzle arrangement utilized above has been tested with the baseline nozzles and the S_2 screens, Figure 24. The suckdown is considerably less due to smaller plate size, but it is also evident that, unlike the larger rectangular plate (Figure 11), strong fountains are present. This is probably

because the cruciform plate makes more surrounding air available for entrainment into the ground jets, which then requires less air to be entrained away from the fountain, resulting in a stronger fountain. Changing the nozzle turbulence in the presence of the cruciform plate results in a very significant change in the net-induced force, Figure 24. This is probably due to a combination of effects. The increased turbulence increases the entrainment of the free and ground jets, which in turn decreases the fountain strength, both of which contribute to a more negative net-induced force.

Effects On Component Forces

In order to understand the flow mechanisms producing the changes described above on the net induced-force, the effects of varying the nozzle-exit conditions on the individual components of the net induced-force are being developed.

Pure Suckdown, $\frac{\Delta L_j}{F_j}$*

As part of an ongoing methodology development program, the data from this experiment have been correlated with the work of several previous experimenters[9, 10, 11] by Foley.[8] This correlation shows that there is "a fine structure" to suckdown that is a function of the implied area ratio, $\bar{D}/d$. Empirical relations have been developed allowing the prediction of pure suckdown as a function of altitude, $\bar{D}/d$, and planform shape for a reference NPR of 2.0 and a turbulent intensity level equal to that measured for the baseline nozzle case in this experiment. This value was then corrected for variations from baseline NPR and nozzle-exit conditions. Corrections for NPR and turbulence level have been derived from the test data of this experiment for a uniform total pressure distribution. With a uniform pressure distribution (baseline nozzle and screens), changing NPR causes different (independent) changes in turbulent intensity and suckdown than is obtained by changing the turbulence screens; these changes are each independent of altitude. Therefore, the pure suckdown that results from turbulent entrainment rate is proportional to turbulence, which can be characterized by the large eddy size, ϵ_e, associated with the turbulence and NPR. The large-scale eddy size (ϵ_e) is proportional to the largest physical dimension causing the turbulence, ϵ. If ϵ, or eddy "scale," is taken as the grid size of the screens, the pure suckdown (normalized by the NPR = 2.0, baseline nozzle case) variation with eddy size is not a function of altitude or NPR; conversely, the change in nondimensionalized suckdown with NPR is not a function of altitude or eddy size (viz Figure 19). Therefore, corrections to pure suckdown for NPR and

* The analysis presented in this section was funded by a contract from the Naval Air Development Center (Reference 8).

turbulence with uniform profile distribution were formulated by Foley as

$$\frac{\Delta L_j}{F_j} = C_{j_1} \cdot C_{j_2} \left[\frac{\Delta L_j}{F_j}\right]$$

NPR = 2.0
ϵ_o = .05"

where C_{j_1} and C_{j_2} are empirically derived functions from Figure 25 for the effects of eddy size and NPR, respectively, and are presented in Figures 26 and 27.

Foley's correlation of the effects of turbulence (for a uniform pressure profile) on pure suckdown has replaced turbulent intensity as the key variable with eddy scale and NPR. It presupposes that the effective eddy scale of the full-scale engine can be estimated by knowing the size of the turbulence-producing parts of the engine (say turbine blade size). This remains to be determined. The change in pure suckdown produced with a given change in turbulent intensity is less with the non-uniform pressure distribution. The mechanism of the effect of pressure distribution is not yet understood.

Fountain Core Lift, $\frac{\Delta L_{fc}}{F_j}$

Figure 28 shows that increasing the nozzle turbulence (and thereby increasing free-jet and ground-jet entrainment) reduces the fountain core force. However, for the two-nozzle configuration, varying nozzle turbulence has no effect on the fountain core lift at the blocking surface, $\frac{\Delta L_{FC}}{F_j}$, since it never reaches the planform. Although not measured, varying the pressure distribution is also expected to have no effect on $\frac{\Delta L_{FC}}{F_j}$ for this two-nozzle case for the same reason. Increasing the nozzle turbulence in the four-nozzle configuration causes a reduction in $\frac{\Delta L_{FC}}{F_j}$ at the blocking surface by 38% (Figure 28). Varying the total pressure distribution appears to have about the same effect (Figure 28).

Fountain Interference, $\frac{\Delta L_{Fi}}{F_j}$

The effect of varying the nozzle-exit conditions on the fountain interference will be developed for the two- and four-nozzle

configurations by subtracting the pure-suckdown and fountain-core increments from the net-induced forces. This task is now in progress.

Concluding Remarks

The results of a first test series that investigated fountain flow characteristics have been reviewed. It was determined that, for the large planforms tested, weak fountains are formed between two jets that dissipate before reaching the blocking surface except for the special case of low h/D and moderate nozzle spacing. Consequently, little or no positive lift is contributed to the hovering system. Conversely, multiple-nozzle arrangements (three and four) contribute stronger fountains that impact the blocking surface over a wide range of heights. However, the positive ground effect experienced derives as much or more of its lift from fountain interference as from the core of the fountain itself.

Variations in nozzle-exit turbulence, total pressure distribution, and pressure ratio produce noticeable changes with the large plates not only in the total net induced force measured by the usual ground effects model but also in the pure suckdown, fountain core, and fountain interference components. Changes of up to 10% of the nozzle thrust for each component were observed. Because the net induced force is often the sum of two relatively large-valued forces of opposite sign (suckdown and fountain lift), changes of this magnitude in the suckdown and fountain force could potentially result in first-order changes in aircraft sizing and performance. For example, the data for the cruciform plate, which more closely approximates a realistic aircraft planform, shows a dramatic change in net induced force due to turbulence that could significantly affect aircraft sizing.

References

1. Karemaa, A. and Ramsey, J.C., Aerodynamic Methodology for the Prediction of Jet-Induced Lift in Hover, General Dynamics Convair Aerospace Division Report CASD-ERR-73-012, December 1973.

2. Karemaa, A., Abbreviated Methodology for the Prediction of Jet-Induced Lift in Hover, General Dynamics Convair Aerospace Division Report CASD-ERR-74-024, December, 1974.

3. Gay, A., Jet-Induced Effects with Fundamental Geometries, General Dynamics Convair Aerospace Division Report, CASD-ERR-74-0044, December 1974.

4. Karemaa, A., Smith, C.W., Weber, H.A., and Garner, J.E., The Aerodynamics and Thermodynamic Characteristics of Fountains and Some Far-Field Temperature Distributions, Office of Naval Research Report Number, ONR-CR-212-237-1, May 1978.

5. Smith, C.W. and Karemaa, A., Induced Effects of Multi-Jet Fountains on Flat-Plate Surfaces, AIAA Paper No. 78-1516, August 1978.

6. Karemaa, A., Weber, H.A., and Smith, C.W., Aerodynamic and Thermodynamic Characteristics of Flow Fields Below VTOL Vehicles in Ground Proximity, AIAA Paper No. 79-0338 , January, 1979.

7. Smart, A.E. and Moore, C.J., "Aero-Enginer Applications of Laser Anemometry," AIAA Journal, Vol 14, No. 3, March 1976, pp 363-370.

8. Foley, W.H., Methodology for Prediction of Propulsion Induced V/STOL Forces in Ground Effect, AIAA Paper 79-1281, June 1979.

9. Wyatt, L.A., Static Tests Of Ground Effect On Planforms Fitted With A Centrally Located Round Lifting Jet, Ministry of Aviation CP. 749, 1962.

10. Spreeman, K.P. and Sherman, I.R., Effects Of Ground Proximity On The Thrust Of A Simple Downward Directed Jet Beneath A Flat Surface, NACA TN 4407, 1958.

11. Gentry, G.L. and Margason, R.J., Jet-Induced Lift Losses On VTOL Configurations Hovering In And Out of Ground Effect, NASA TN D-3166, 1966.

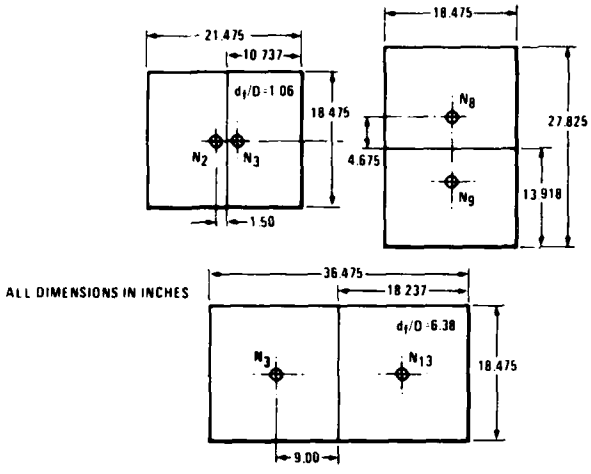

Figure 1 Rectangular Plate Blocking Surfaces for the Two Nozzle Configurations

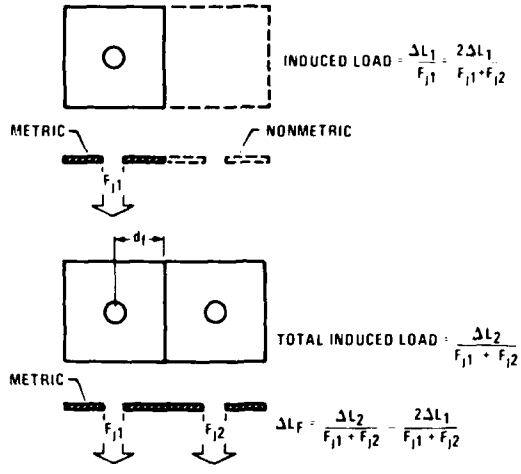

Figure 3 Scheme for Isolation of Fountain Incremental Effects

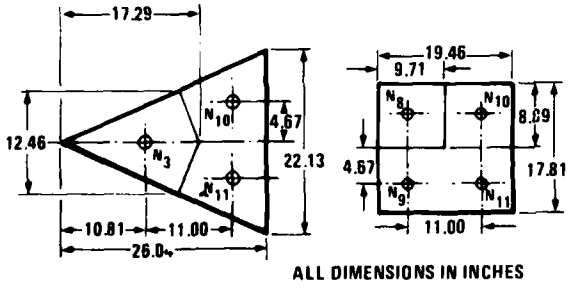

Figure 2 Triangular and Rectangular Plate Blocking Surfaces for the Three and Four Nozzle Configurations

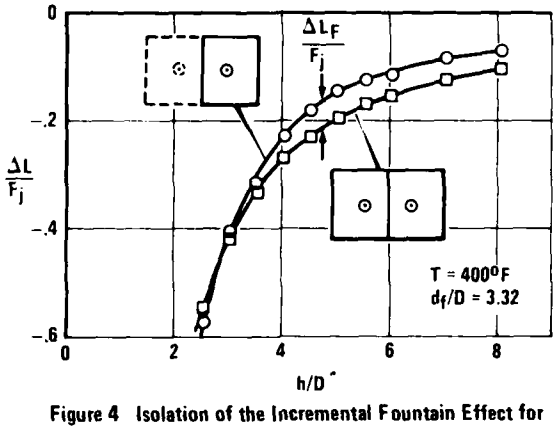

Figure 4 Isolation of the Incremental Fountain Effect for Two Nozzles

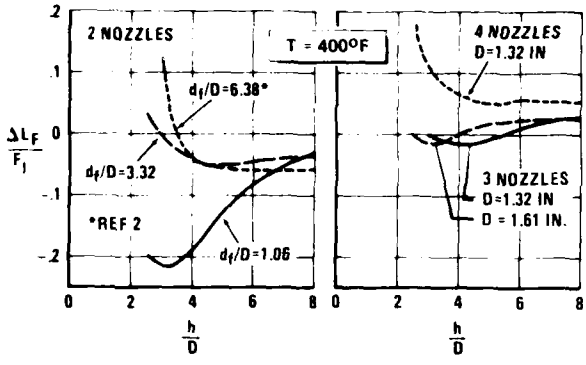

Figure 5 Incremental Fountain Lift for Two, Three and Four Nozzles

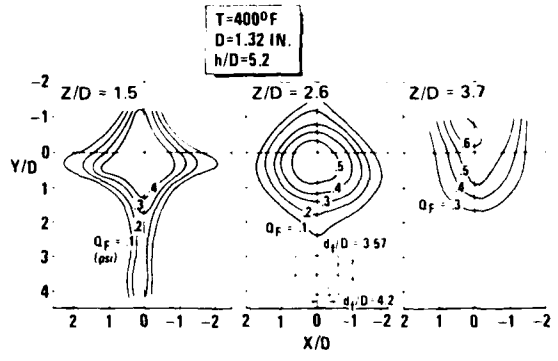

Figure 7 Dynamic Pressure Contours for the Four Nozzle Fountain

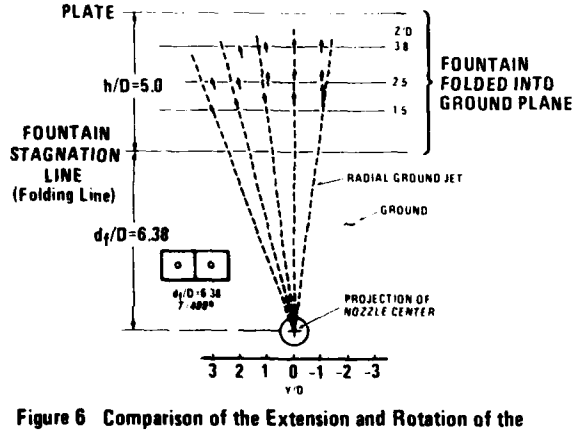

Figure 6 Comparison of the Extension and Rotation of the Ground Jet with Measured Fountain Flow Angularity

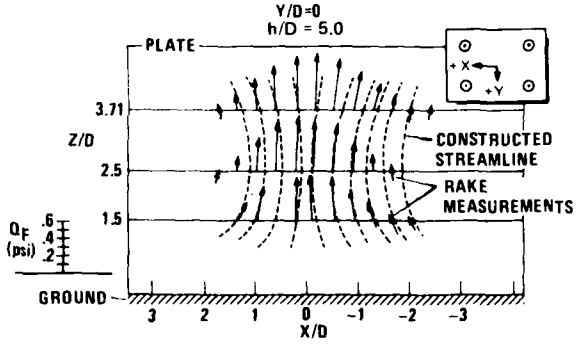

Figure 8 Flaw Angularity for the Four Nozzle Fountain

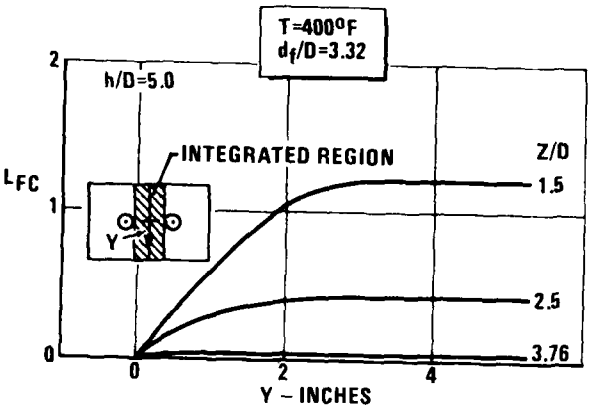

Figure 9 The Fountain Core Force with Two Medium Spaced Nozzles

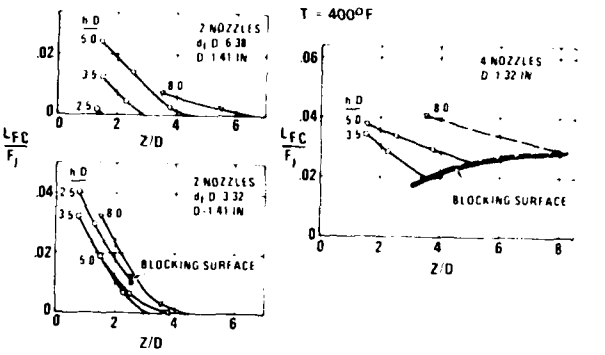

Figure 11 Extrapolation of the Fountain Core Force to the Blocking Surface

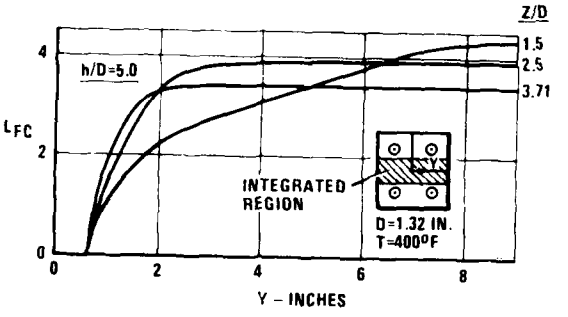

Figure 10 The Fountain Core Force with Four Nozzles

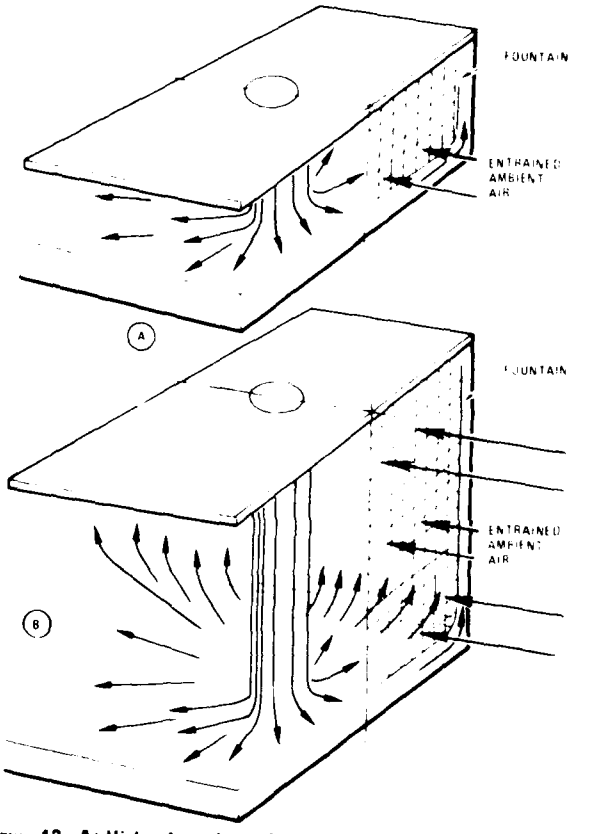

Figure 12 At Higher Locations of the Blocking Surface, Increasing Amounts of the Ambient Air Can Be Entrained through the Sides (Cross-Hatched Areas)

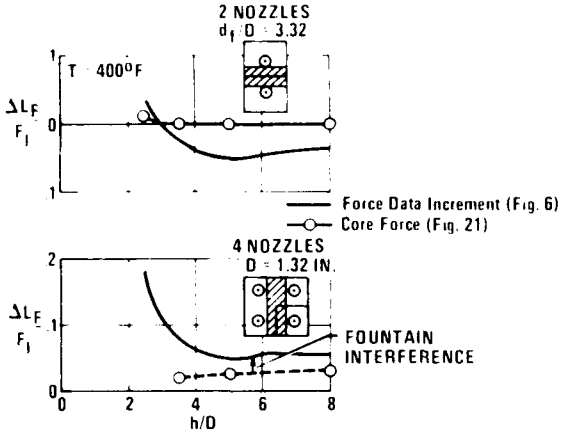

Figure 13 Comparison of the Fountain Core Force and the Total Fountain Increment

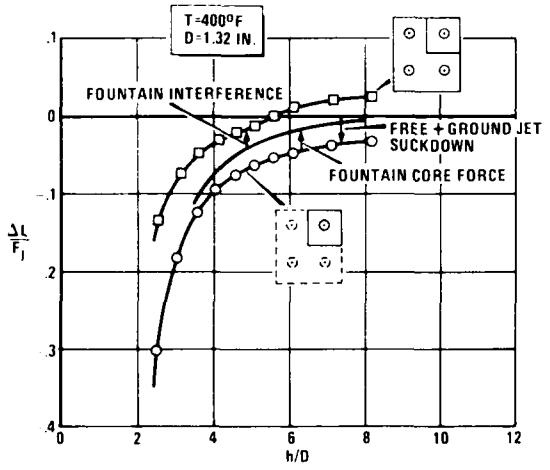

Figure 14 Component Buildup of Induced Lift Force Nozzles

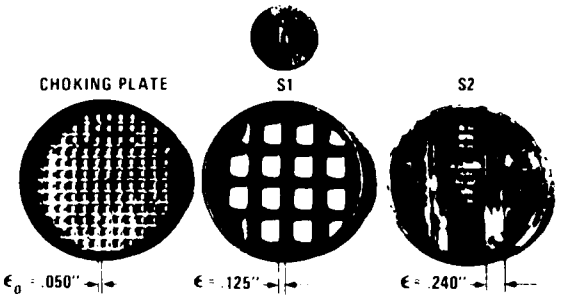

Figure 15. Turbulence Screens S1 and S2 Compared to Choking Plate

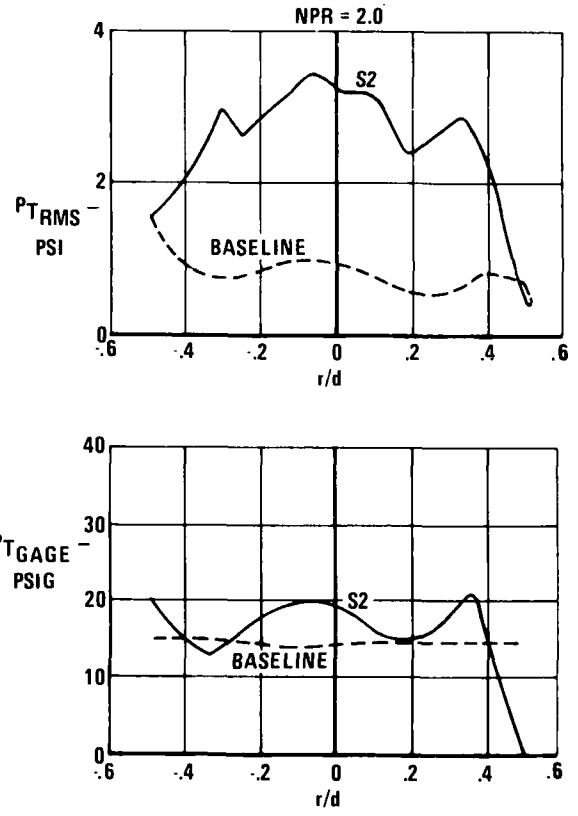

Figure 16. Typical Total Pressure and $P_{T_{RMS}}$ Surveys of Nozzle Exit for Baseline Nozzle and S2

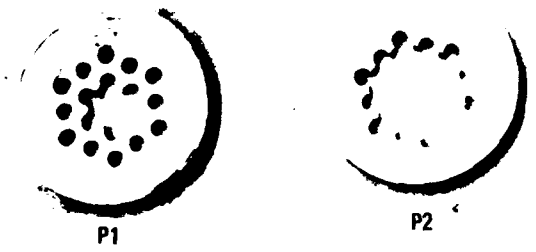

Figure 17. Pressure Provile Plates P1 and P2

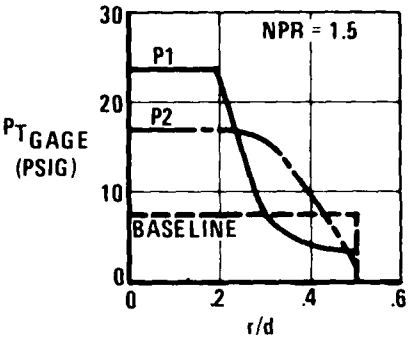

Figure 18. Nozzle Exit Total Pressure Distributions with Baseline Nozzle and Plates P1 and P2

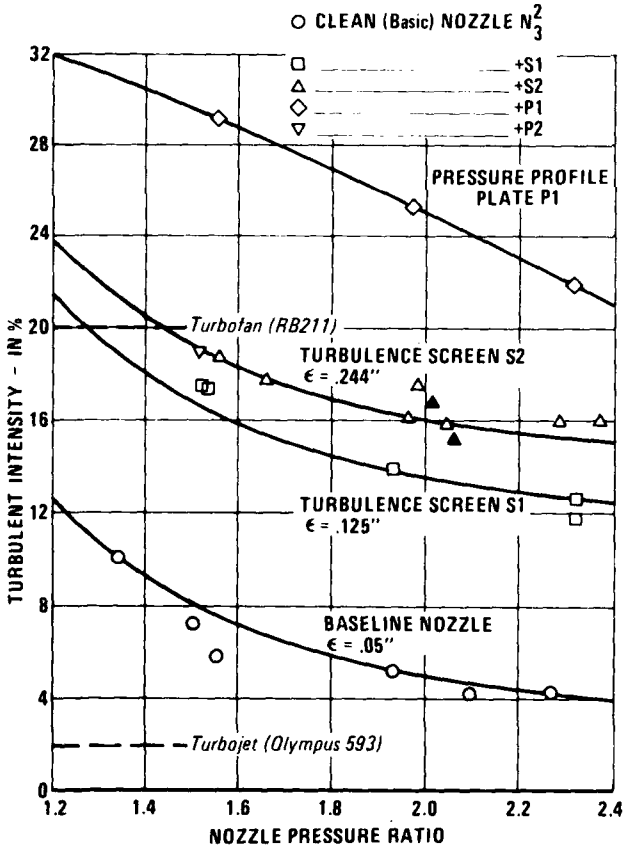

Figure 19. Turbulent Intensity vs. NPR for Screens and Plates

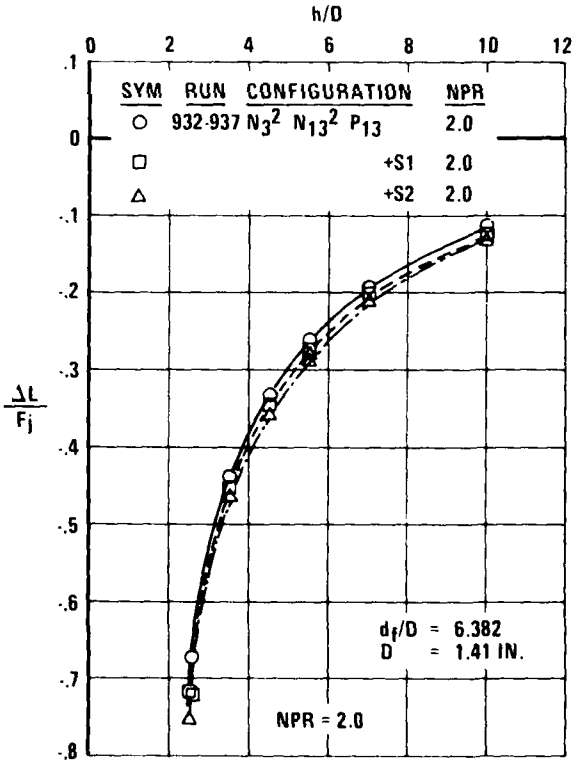

Figure 20. Effect of Varying Nozzle Turbulence with Screens S1 and S2 for 2 Nozzle Configuration

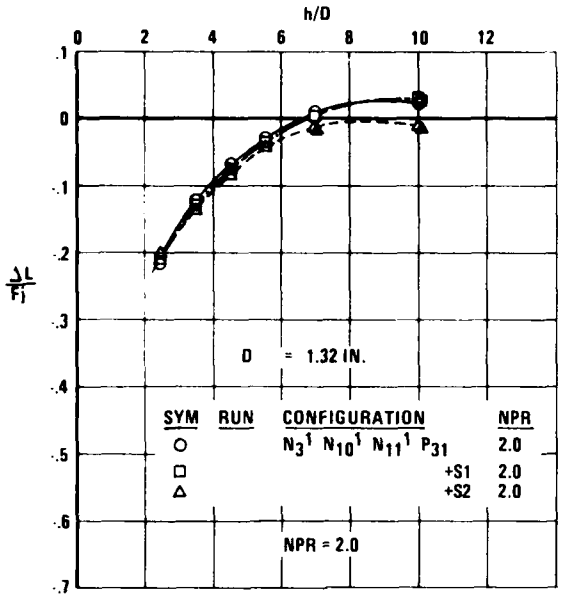

Figure 21. Effect of Varying Nozzle Turbulence with Screens S1 and S2 for 3 Nozzle Configuration

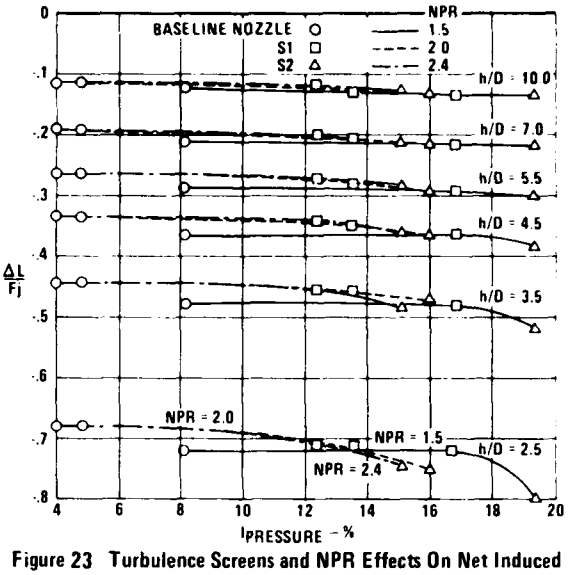

Figure 23 Turbulence Screens and NPR Effects On Net Induced Force Coefficient for Two Nozzle Configuration

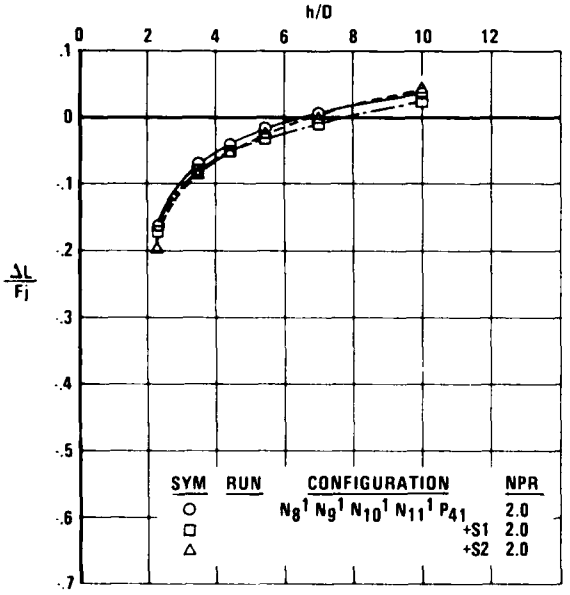

Figure 22. Effect of Varying Nozzle Turbulence with Screens S1 and S2 for Four Nozzle Configuration

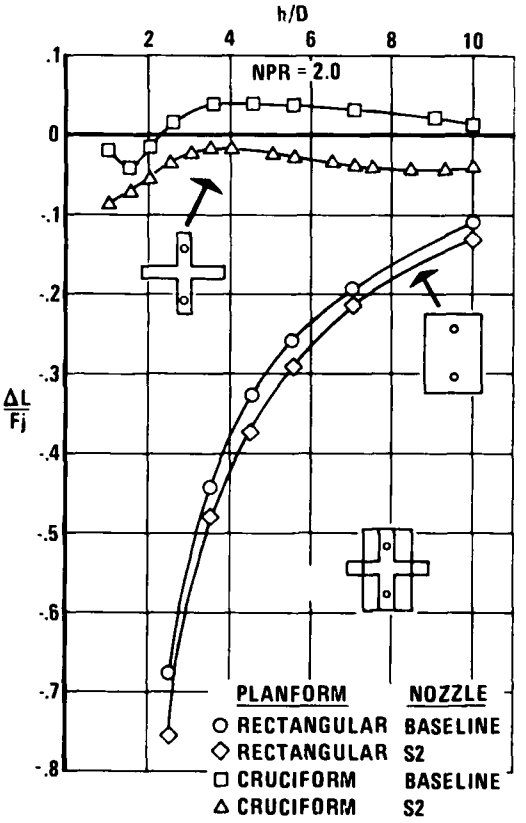

Figure 24 Effect of Nozzle Turbulence for Weak and Strong Fountain Cases Formed with 2 Nozzles

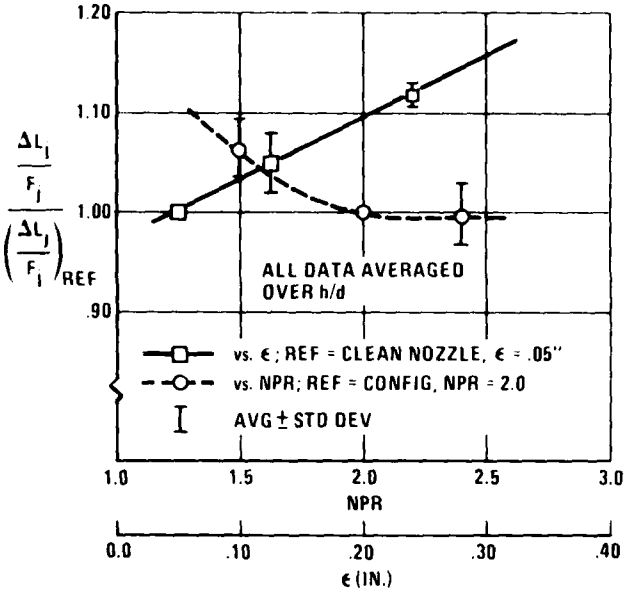

Figure 25. Effect of Nozzle Exit Pressure and Turbulence Scale On Suckdown

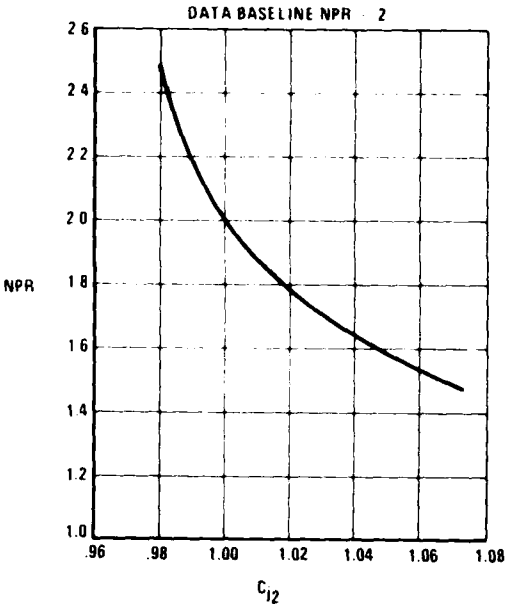

Figure 27 Effect of Nozzle Pressure Ratio On Suckdown

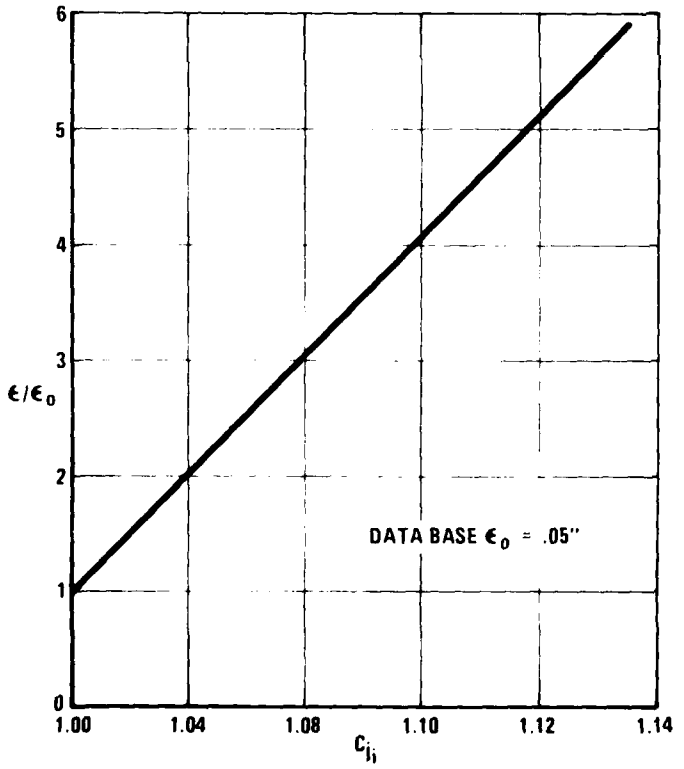

Figure 26 Effect of Eddy Size On Suckdown

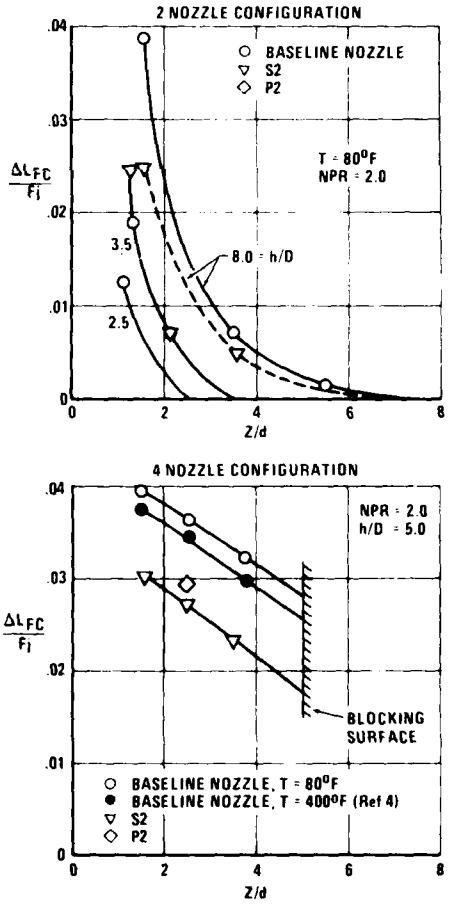

Figure 28. Effect of Varying Nozzle Turbulence and Pressure Distribution On Fountain Lift Increment, $\frac{\Delta L_{FC}}{F_j}$

DEVELOPMENT OF AN EMPIRICAL DATA BASE AND ANALYTICAL MODELING OF MULTIPLE JET V/STOL AIRCRAFT FLOW FIELDS IN GROUND EFFECT*

D. R. Kotansky and L. W. Glaze

McDonnell Douglas Corporation
McDonnell Aircraft Company

ABSTRACT

The accurate modeling and prediction of the three dimensional turbulent flow field below multiple lift jet V/STOL aircraft requires a substantial empirical data base because of the viscous nature of the jet impingement and fountain upwash flows. Key elements in the analytical modeling of these flow fields are the azimuthal distributions of turbulent wall jet radial momentum flux about the jet impingement points. These distributions determine the locations of the fountain bases and the amount of momentum flux entering the fountain formation region and subsequently entering the fountain upwash flow. These distributions have been determined for impinging rectangular jets of nozzle exit area aspect ratio four, six and eight for a range of jet impingement angles and nozzle exit heights above ground. Future work will include investigation of impinging jet flows from rectangular nozzles of aspect ratio one, two and three and measurement of fountain upwash flow formation and development.

*Portions of the experimental data presented herein were obtained by the McDonnell Aircraft Company under contract NAS2-9646 funded by NASA Ames Research Center.

INTRODUCTION

The design of V/STOL aircraft utilizing multiple jet powered lift systems requires a knowledge of the complicated viscous flow field interactions produced by such systems in ground effect. These interactions may result in the production of net forces on the airframe which may be either positive (providing additional lift) or negative. In addition, moments may be produced on the airframe resulting in significant stability and control problems.

The induced forces and moments usually result from one of two reasonably well defined viscous flow phenomena: jet entrainment and the formation of jet flow fountains. Jet entrainment causes otherwise static air to be set in motion, thus producing locally reduced static pressure regions on nearby airframe under-surfaces resulting in negative aerodynamic loads (suckdown). Although entrainment effects may occur both in and out of ground effect, and for either single or multiple jet systems, the formation of fountains requires an impingement surface and is peculiar to multiple jet systems. The fountains consist of the upwash flow resulting from the interaction of two or more wall jets on the ground surface. This upward convection of flow usually results in a positive aerodynamic lift, caused by the pressurization of the airframe undersurfaces containing and deflecting the fountain upwash flow. These flow field interactions are shown schematically in Figure 1. Motion of the aircraft and environmental cross winds additionally complicate this three dimensional flow field. Although most of the significant effects on V/STOL aircraft in ground effect are aerodynamic (associated with forces and moments on the airframe), a degradation of propulsion system performance frequently results from the upward convection of lift jet exhaust gas in the fountains which can be subsequently ingested into the engine inlets.

MULTIPLE JET FOUNTAINS

It is highly probable that VTOL aircraft with multiple jet lift systems can be configured to produce positive induced lift forces in ground effect. This problem and the influence of certain vehicle configuration variables on vehicle forces and moments in ground effect are discussed in Reference 1. A major consideration in configuration selection is the number and geometric arrangement of the lift jets in the aircraft lift system. Figure 2 shows an idealized multiple lift jet arrangement (eight jets in this case) spaced symmetrically about a hypothetical center of gravity. The octagonal central area circumscribed by the lines connecting the lift jet centerlines represents an idealized inner region. The remainder of the area constitutes the outer region. The interaction lines of the wall jets resulting from the lift jet pairs are shown as the dashed lines in Figure 2. These lines indicate the ideal locations of the fountain stagnation lines which form in both the inner and outer region. Figure 3 shows the maximum available fountain force as a function of the number of lift jets in an ideal multiple lift jet system. The lower curve in Figure 3 shows the maximum fountain force F_F available from the inner region only,

$$F_{F(\text{inner region})} = \left(\frac{1}{2} - \frac{1}{N}\right) F_T \qquad (1)$$

where F_T is the total lift system thrust and N is the number of jets in the lift system.

It should be noted that a two-jet ideal lift system has no inner region, by definition, and, therefore, all fountain force obtained from a two jet fountain is outer region force. The result shown in equation (1) is predicated on the assumption that all lift jet momentum flux that enters a volume below the aircraft whose planform is the inner region eventually is turned vertically and imparts this vertical momentum to the airframe. The upper curve in Figure 3 indicates the total available ideal fountain force including both the inner and outer region. The lift jet momentum flux entering the outer region volume is assumed to impinge on the airframe with an ideal angle of incidence resulting from the turning of the flow in an upward direction at the stagnation lines. Performing an integration of the vertical component of the outer region momentum flux and adding the result to the force from the inner region,

$$F_{F(\text{outer region + inner region})} = \left(\frac{1}{2} - \frac{1}{N} + \frac{1}{\pi}\right) F_T \qquad (2)$$

As noted in Reference 1, the potential benefits to be gained from additional fountain force resulting from the use of increasing numbers of jets up to 6 or 8 is obvious, but it must be realized that actual fountain forces are much less than the ideal values shown in Figure 3 by a factor of one third to one quarter based on the ideal inner plus outer region values.

A number of methodologies have been developed to aid the aerodynamicist in the understanding and the prediction of forces and moments on the V/STOL airframe in ground effect. Pertinent recent work in these areas is summarized in a "V/STOL Aerodynamic Technology Assessment" published by the Naval Air Development Center (NADC), Reference 2.

NON-CIRCULAR NOZZLE EFFECTS

Most of the experimental and analytical work to date has been concerned with multiple lift jet flows emanating from axisymmetric (round) nozzles, since these types of nozzles have been associated with CTOL and V/STOL aircraft historically. Only recently has serious effort been expended on the design and development of nonaxisymmetric nozzles. This is largely a result of investigations of potential benefits associated with the substitution of nonaxisymmetric nozzles for round nozzles in CTOL and lift-plus- lift-cruise V/STOL aircraft propulsion systems and the direct requirement for rectangular nozzles in certain STOL and VTOL systems such as upper surface blowing and thrust augmenting ejector systems.

The computation and prediction of the viscous (turbulent) flow field between a multiple jet V/STOL aircraft and the ground is strongly dependent on the mean structure (geometry) of the flows in the turbulent jets. The significant jet mean flow geometry and overall flow field geometry includes:

- The mean velocity distribution at the nozzle exit, $V_{je}(X_N, Y_N, Z_N = 0)$ (this specification includes nozzle exit shape);

- o Lift jet system arrangement including the number of jets, jet exit spacings and jet exit orientation with respect to the aircraft axes (including vector and splay angles); and

- o Aircraft surface geometry, orientation and height above ground.

Most of the above geometric variables were taken into account in the development of a ground flow field prediction computer program by the McDonnell Aircraft Company (MCAIR) for NADC which is described in detail in Reference 3. However, this work was based on the fundamental free jet flow development and impingement characteristics of round jets which, for the most part, were available in the published literature. Specifically, the free jet entrainment data of Kleis and Foss (Reference 4) and the geometric and kinematic properties of free and impinging round jets established by Donaldson and Snedeker (Reference 5) were utilized extensively. The data of Donaldson and Snedeker were also utilized to determine required analytical expressions for wall jet entrainment.

A key element in the modelling of the ground surface flow field below a hovering V/STOL aircraft is the local distribution of momentum flux about the individual jet impingement points on the ground plane. The data of Donaldson and Snedeker in Figure 4 show that this distribution for a round turbulent jet is sensitive to the jet impingement angle and relatively insensitive to the ratio of height above ground to nozzle exit diameter (H/D). These distributions of momentum flux together with the magnitudes of the total momentum fluxes emanating from the nozzle exits establish the location and (momentum) strength of the fountains in the flow field below the aircraft.

To establish a similar data base for rectangular jets, a study was conducted under the sponsorship of the NASA Ames Research Center to determine experimentally the azimuthal distributions of wall jet radial momentum flux about the impingement points of high aspect ratio rectangular jets as a function of nozzle exit area aspect ratio, jet impingement angle and nozzle exit height above ground. Additionally, Reynolds number effects, nonuniformities in rectangular jet exit velocity profiles and dual nozzle impingement including jet exit spacing effects were investigated.

This data base for high aspect ratio rectangular nozzles was then incorporated into the ground flow field computer program originally developed for round jets for NADC. This computer program together with the Douglas Neumann potential flow program modified for V/STOL applications (Reference 6) may then be used in the analysis and prediction of induced forces and moments on multi-jet V/STOL aircraft hovering in ground effect as described in Reference 3.

Experimental Test Program

The experimental test program was designed to provide data on the rectangular nozzle free jet characteristics and jet impingement characteristics for nozzle exit area aspect ratios of four, six and eight over a meaningful range of pertinent parameters associated with the operation of a V/STOL aircraft in the hover mode in ground effect.

Test Procedure

The desired wall jet momentum flux distributions about the rectangular jet impingement points were established by surveying the turbulent wall jet velocity profiles about the periphery of the jet impingement region for vertical and oblique jet impingement. In the oblique impingement experiments, pure pitch (rotation about the nozzle exit short axis) and pure roll (rotation about the nozzle exit long axis) were investigated, but combinaons of pitch and roll were not investigated. In the case of vertical impingement, one quarter of the periphery was surveyed since two planes of flow symmetry existed, and in the case of oblique jet impingement, one half of the periphery was surveyed since in this case only one plane of symmetry existed. The wall jets were surveyed at 15° increments in azimuth (ϕ) over the region of interest about the jet impingement point. Figure 5 defines the geometry and the coordinate systems for the jet impingement tests. It should be noted that the rectangular exit area nozzle width, D, was a fixed physical dimension of 2.0 cm. for all nozzles throughout the test program. The aspect ratio four, six and eight rectangular exit area nozzles used are shown schematically in Figure 6.

Hot Film Anemometer

The free jet and wall jet velocity profile surveys were accomplished with two component, directionally sensitive hot film anemometer probes. The selected probe configuration was the Thermo-Systems Model 1240-20 "Cross-Flow" probe used in conjunction with a two-channel Thermo-System Model 1050-2C anemometer unit. The plane of the sensor cross was parallel to the ground board resulting in the measurement of velocity and flow direction in the R, ϕ plane. Angularity was sensed with respect to a local ϕ = constant reference at the five ground board hole radial positions. The local angularity zeroing technique for the probe sensors is discussed in the Data Acquisition section. All probes were calibrated for mean flow velocity and flow angularity in a modified Thermo-Systems Model 1125 Calibrator. Angularity data were obtained with the calibrator supported on a manually adjustable turntable which allowed the calibrator to be rotated about the probe support axis. The zero angularity reference position for each probe was established by nulling out the difference between the two sensor outputs at a selected mean velocity level. Calibrations were performed at an anemometer overheat ratio of 1.5 for mean velocities in the range of 0 to approximately 90 m/sec and for yaw angularity, ψ, of $\pm 30°$ at four selected mean flow velocity magnitudes.

Experimental Results

Free jet surveys, performed to investigate the shape of the velocity profile at the nozzle exits and to examine the symmetry of the jet flows, proved that the quality of the flow issuing from the three rectangular nozzles was acceptable. Nondimensional wall jet velocity profiles revealed an independence from Reynolds number effects for the three Reynolds numbers (based on nozzle width, D) investigated: R_{e_D} = 146,000; 205,000 and 275,000.

Figures 7 and 8 present the azimuthal distribution of wall jet radial momentum flux for the L/D = 4 and L/D = 8 nozzles, respectively, in purely vertical impingement at nozzle to ground board height ratios, H/D, of 2.0 and 16.0. These data clearly indicate that the preferential direction of momentum flux is perpendicular to the long side of the rectangular nozzle exit (ϕ = 90° in Figures 7 and 8), and that this directional bias is a function of H/D, decreasing with increasing H/D. However, even at H/D = 16, this preferential direction is still present indicating that the impinging free jet was strongly non-axisymmetric even for the lowest aspect ratio nozzle.

The azimuthal distributions of wall jet radial momentum flux for oblique impingement caused by a rotation about the short axis of the nozzle exit (pitch) are shown in Figures 9 through 12 for jet impingement angles (α_j) of 60° and 75°. Figures 9 and 10 present the distributions for the L/D = 4 nozzle at H/D = 2.0 and H/D = 8.0, respectively; while the momentum flux distributions for the L/D = 8 nozzle are shown in Figures 11 and 12 at H/D = 4.0 and H/D = 8.0. For the pitch data, the angles ϕ = 0° and ϕ = 180° correspond to the directions perpendicular to the short sides of the nozzle exit with ϕ = 0° corresponding to the direction of the horizontal component of the free jet mean flow (see insert in Figure 9). The largest fraction of momentum flux appears in a direction approximately coincident with the magnitude of the impingement angle, and all significant flux of momentum occurs within the range of ϕ = 0° to ϕ = 120° of the impingement periphery. The exact location of the momentum flux peak is somewhat uncertain, however, since the wall jet profiles were obtained at fixed intervals of 15° in azimuth.

The azimuthal distributions of wall jet radial momentum flux for oblique impingement caused by a rotation about the long axis of the nozzle exit (roll) are shown in Figures 13-16, again for jet impingement angles (θ_j) of 60° and 75°. Figures 13 and 14 present the momentum flux distributions for the L/D = 4 nozzle at H/D = 2.0 and 8.0 while Figures 15 and 16 present the distributions for the L/D = 8 nozzle at H/D = 4.0 and H/D = 8.0. In roll, the angles ϕ = 0° and ϕ = 180° correspond to the directions perpendicular to the long side of the nozzle exit with ϕ = 0° defined as before. The roll data indicate strong distributions of momentum flux in the sectors of azimuth adjacent to perpendiculars to the long sides of the nozzle exit (ϕ = 0° and ϕ = 180°), with the strongest momentum flux occurring at the ϕ = 0° position as would be expected based on the simplest flow deflection model.

The wall jet radial momentum flux distributions for vertical and oblique impingement obtained as a result of this investigation were curve-fit in a piecewise manner (as shown in Figure 17 for oblique impingement in pitch) for inclusion in the ground flow field prediction computer routine described in Reference 3. This ground flow field program calculates wall jet stagnation line coordinates, in a ground based coordinate system, between jet pairs based on a balance of wall jet radial momentum flux. Originally developed for axisymmetric jets, this ground flow field program has thus been expanded to include rectangular jets with aspect ratios between 4 and 8.

Stagnation line locations for three two-jet sample cases are shown in Figures 18-20. Each case represents a two-jet configuration in which both nozzles have the same exit area and operate at the same nozzle pressure ratio (NPR) and exit conditions. In addition, each case presents stagnation line locations based upon two methods of computation: (1) the momentum flux method, described in Reference 3, and (2) the momentum flux density method of Reference 7. The large circles and rectangles in each figure represent the vertical projection of the nozzle exits onto the ground plane while the large asterisks represent the free jet impingement points. The origin of the ground surface X, Y coordinate system represents the vertical projection of the aircraft center of gravity onto the ground plane. Figure 18 simulates the case of two identical, axisymmetric jets symmetrically located about the center of gravity of an aircraft pitched at an angle of 10° (α_j = 80°) whose center of gravity is located at a height of six nozzle widths above ground (H/D = 6). The shift of the stagnation line toward the forward jet is a result of the non-symmetrical wall jet radial momentum flux distribution caused by oblique impingement of the axisymmetric jets (see Figure 4). Figure 19 represents the case of vertical impingement of one axisymmetric jet and of one rectangular jet with L/D = 8 in which the long axis of the rectangular nozzle exit is parallel to the aircraft centerline (τ = 0°). As indicated by Figures 8 and 4, the preferential direction of momentum flux is perpendicular to the long sides of the rectangular nozzle exit while the momentum flux is symmetrically distributed about the impingement point of the axisymmetric jet, thus the stagnation line is shifted toward the rectangular nozzle. Consequently, a 90° rotation of the rectangular nozzle (τ = 90°) results in a shift of the stagnation line toward the axisymmetric jet, as shown in Figure 20. It is also seen from these figures that the momentum flux method predicts a greater shift in stagnation line location than that predicted by the momentum flux density method. Comparisons with experimentally produced stagnation lines obtained through flow visualization techniques indicate that, in most cases, the momentum flux density method more accurately predicts stagnation line location.

ADDITIONAL RESULTS FOR RECTANGULAR NOZZLES

Additional analysis of the data obtained in the investigation conducted for NASA Ames resulted in the determination of the wall jet velocity distributions produced by the impingement of the high aspect ratio jets upon a ground plane. The maximum wall jet velocities (U_{max}) were normalized by the free jet center line velocity at an equivalent impingement plane (V_{jcI}). Figure 21 presents the wall jet velocity distributions for the L/D = 4, 6 and 8 nozzles at H/D = 2.0, 8.0 and 16.0. The wall jet velocity distributions for the three nozzles at impingement angles in pitch of 60° and 75° are shown in Figures 22 and 23 for H/D = 4.0 and 8.0, respectively. The effect of nozzle roll on the wall jet velocity distributions is shown in Figure 24, for H/D = 4.0, and in Figure 25, for H/D = 8.0.

Hot film anemometer surveys of the free jets provided free jet centerline velocity decay rates, free jet spreading characteristics and an indication of mass entrainment rates. The free jet centerline velocity decay for the rectangular nozzles is compared to that found by Donaldson and Snedeker for axisymmetric jets in Figure 26 where it can be seen that, for $Z_N/D \geq 6$,

the rectangular jets decay at a lesser rate than the axisymmetric jets. The free jet spreading characteristics in the two planes of symmetry of the rectangular jets are depicted in Figures 27 and 28. The jet spreading rate in the X_N, Z_N plane (Figure 27) is approximately linear for the range of Z_N/D's tested; and in the Y_N, Z_N plane (Figure 28), the jet spreading rate is approximately linear for $Z_N/D \geq 9.6$. Figure 28 also compares the variation of free jet width with distance from the nozzle of the rectangular jets with that shown in Reference 5 for axisymmetric jets. The free jet mass entrainment characteristics for the L/D = 4, 6 and 8 nozzles are compared with that found by Trentacoste and Sforza (Reference 8) for a L/D = 10 rectangular nozzle and with an axisymmetric jet (Reference 4) in Figure 29.

Additional fountain data was obtained in a recent MCAIR Internal Research and Development (IRAD) funded investigation of the effects of number of impinging jets and spacing on fountain upwash development. Hot film anemometer traverses were made through the fountains produced by the vertical impingement of two-, three- and four-jet configurations to obtain fountain velocity profiles. The effects of unequal nozzle thrust settings on two-jet fountain locations were also investigated. Figure 30 presents the fountain velocity profiles for a two-jet configuration in which both jets have the same thrust ($NPR_2/NPR_1 = 1.0$) and for the case of unequal thrust ($NPR_2/NPR_1 = 1.2$). It is evident from this figure that the fountain is inclined toward the weaker jet. Ground plane static pressure measurements also indicated a shift of the fountain base toward the weaker jet. Figure 30 indicates the effect of the presence of an inner region plate located at the nozzle exit plane on the development of a three-jet fountain. From this figure it can be seen that at this nozzle height (H/D = 8), the presence of an inner region plate has no effect on the peak velocity in the fountain up to a Z/D equal to half of the nozzle height. It was also observed that the peak fountain velocity was independent of jet exit height above ground for this configuration for jet exit height ratios of 2, 4 and 8.

FUTURE INVESTIGATIONS

Preparations are currently being made to conduct a follow-on study to the investigation of high aspect ratio rectangular nozzles conducted for NASA Ames to extend the empirical data base for nonaxisymmetric nozzles to include low aspect ratio rectangular nozzles with exit area aspect ratios (L/D) of 1, 2 and 3. The parametric study of the previous program will be extended to the low aspect ratio nozzles to obtain basic free jet, vertical impingement and oblique impingement data for low pressure ratio and, in addition, for choked and underexpanded nozzle exit flows. In addition, the effect of nozzle spacing on the strength of the fountain formed between two aspect ratio two nozzles will be investigated. Fountain impingement forces will be measured on a nozzle exit plane plate for various nozzle heights, nozzle pressure ratios and nozzle centerline spacings. The nozzle spacings have been chosen to permit free jet merging prior to ground impingement in order that the resulting effect on fountain strength may be determined. The nozzle exit plane plates will be supported on the upper side by a force balance. An additional exit plane plate, containing thirty-three static pressure taps between the two nozzle orifices, will be utilized to determine the pressure distribution resulting from fountain impingement.

Fountain development will be further investigated in a study to be conducted by MCAIR for the Office of Naval Research. The hot film anemometer will again be utilized to measure the wall jet and fountain upwash flows resulting from the impingement of two, turbulent, axisymmetric jets upon a ground plane. Jet nozzle exit diameters, nozzle pressure ratios and jet impingement angles will be varied to:

1. quantify the influence of the physical characteristics of interacting wall jet flows on:

    a. the magnitude of the wall jet radial momentum converted to fountain upwash momentum in the fountain formation process, and

    b. the local direction of the fountain upwash momentum at the exit of the fountain formation region as shown in Figure 1.

2. quantify the development of upwash flow in the fountain in terms of:

    a. the upwash mean flow velocity profile spreading characteristics, and

    b. the mass entrainment characteristics of the fountain.

Additionally, the influence of an upper surface plane upon which the fountain impinges will be investigated to determine the effects of the presence of the plane on fountain spreading and entrainment characteristics.

REFERENCES

1. Kotansky, D. R., "The Influence of V/STOL Vehicle Configuration Variables on Vectored Jet Induced Flow Fields in Ground Effect", AIAA Paper No. 78-1021 presented at the AIAA/SAE 14th Joint Propulsion Conference, Las Vegas, Nevada, 25-27 July 1978.

2. Walters, M., and Henderson, C., "V/STOL Aerodynamics Technology Assessment", Report No. NADC-77272-60, Naval Air Development Center, 15 May 1978.

3. Kotansky, D. R., Durando, N. A., Bristow, D. R., and Saunders, P.W., "Multi-Jet Induced Forces and Moments on VTOL Aircraft Hovering In and Out of Ground Effect", Report No. NADC-77-229-30, Naval Air Development Center, 19 June 1977.

4. Kleis, S. J., and Foss, J. F., "The Effect of Exit Conditions on the Development of an Axisymmetric Turbulent Free Jet", Third Year Technical Report, NASA Grant NGR 23-004-068, Michigan State University, 15 May 1974.

5. Donaldson, C. du P., and Snedeker, R. S., "A Study of Free Jet Impingement, Part I - Mean Properties of Free and Impinging Jets", Journal of Fluid Mechanics, Vol. 45, Part 2, pp 281-319, 1971.

6. Saunders, P. W., and Bristow, D. R., "Douglas Neumann Computations for Potential Flow About Arbitrary Three-Dimensional Bodies with Modifications for V/STOL Applications", McDonnell Douglas Corporation Report MDC A4707, 1 March 1977.

7. Private Correspondence, K. A. Green, Naval Air Development Center to D. R. Kotansky, 24 August 1978.

8. Trentacoste, N., and Sforza, P., "Further Experimental Results for Three-Dimensional Free Jets", A.I.A.A. Journal, Vol. 5, No. 5, p. 885, May 1967.

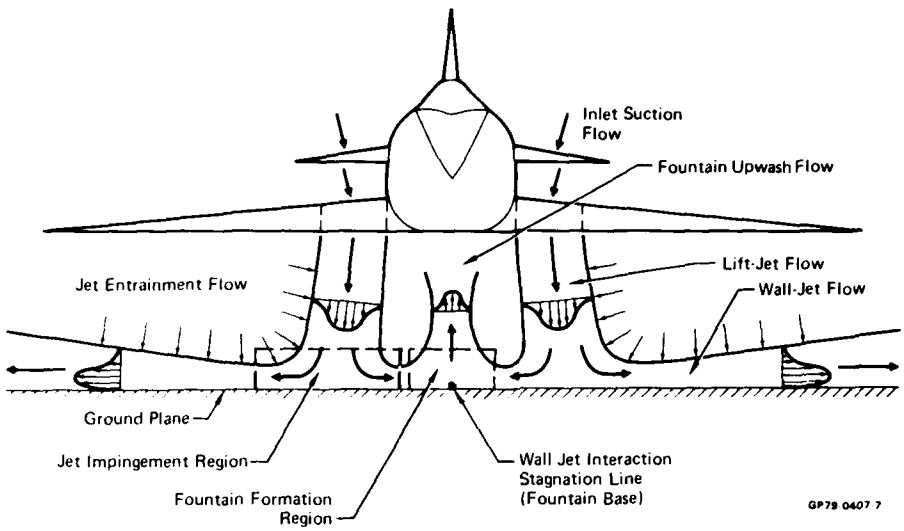

FIGURE 1
FLOWFIELD ABOUT A VTOL AIRCRAFT HOVERING IN GROUND EFFECT

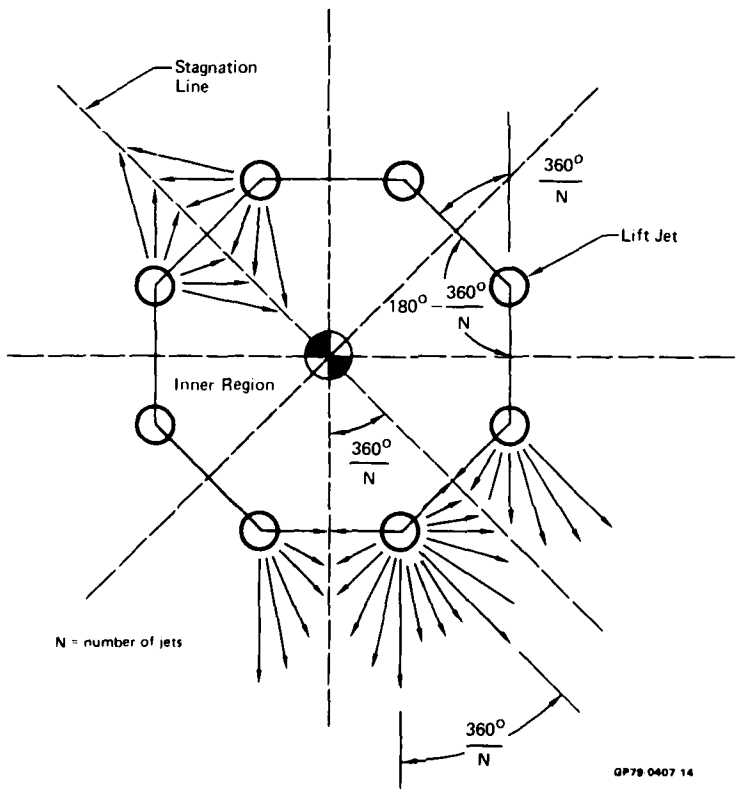

FIGURE 2
IDEAL 8-JET INNER REGION

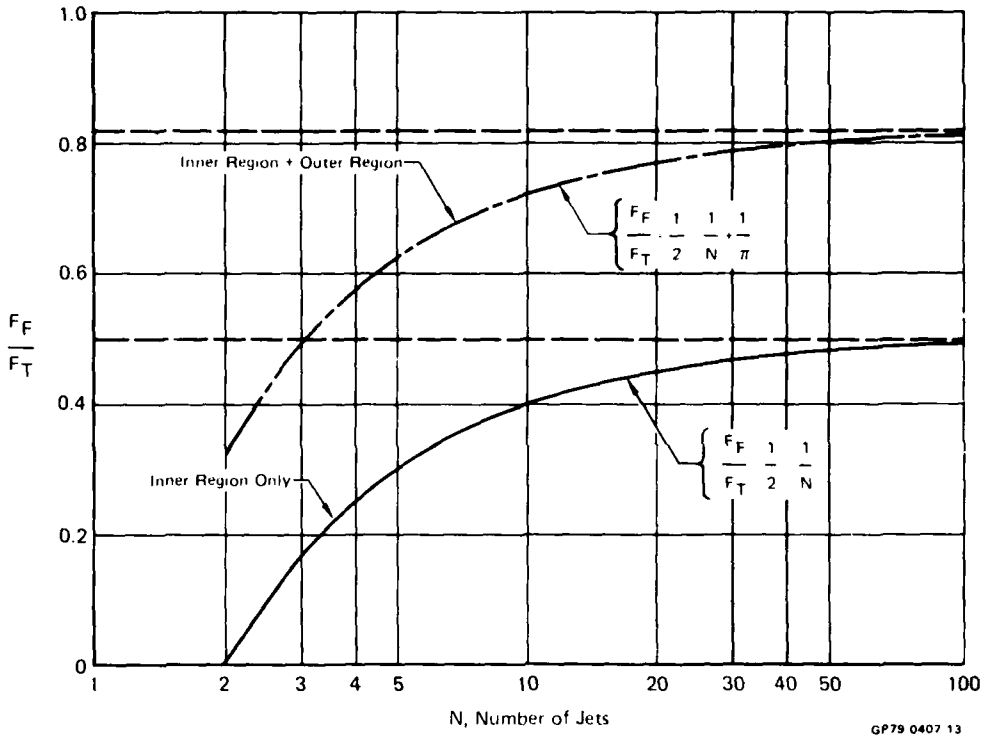

FIGURE 3
VARIATION OF MAXIMUM IDEAL FOUNTAIN FORCE WITH NUMBER OF JETS

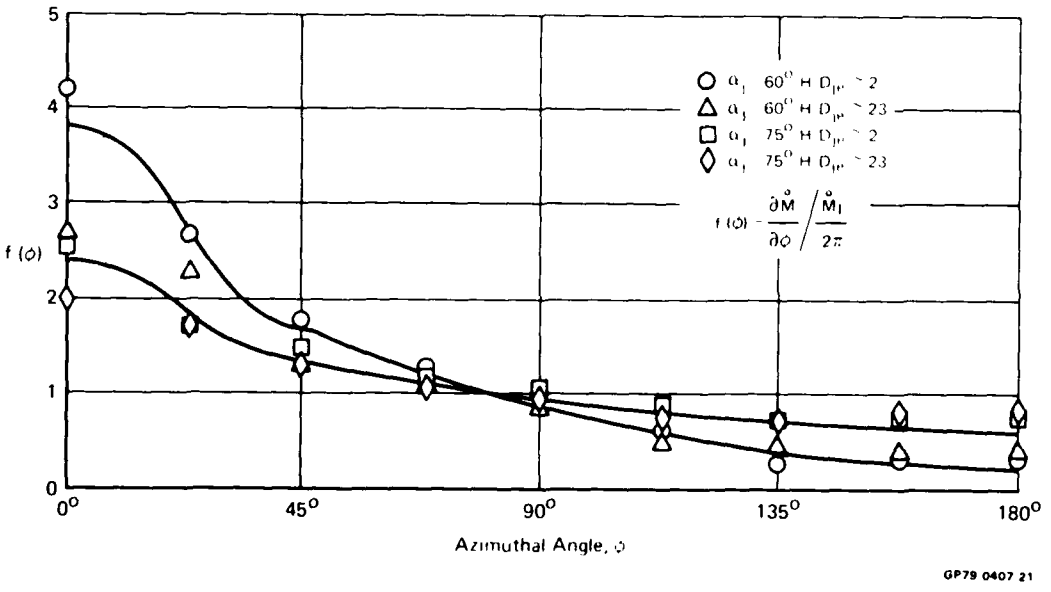

FIGURE 4
RADIAL MOMENTUM
Impinging Axisymmetric Jet

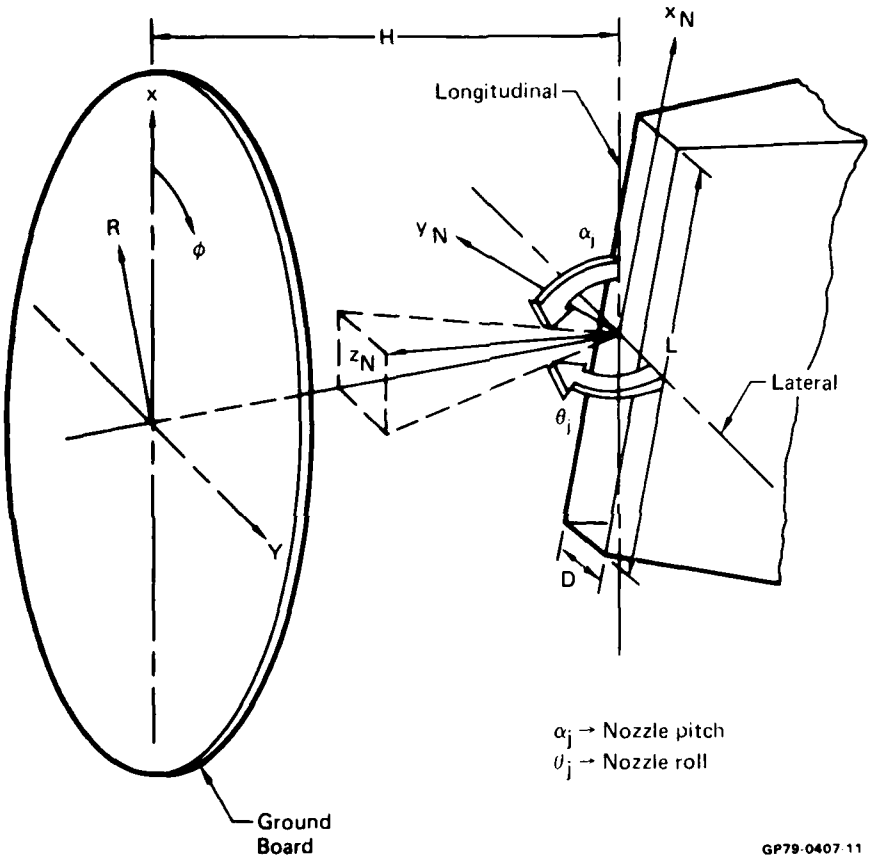

FIGURE 5
TEST NOMENCLATURE

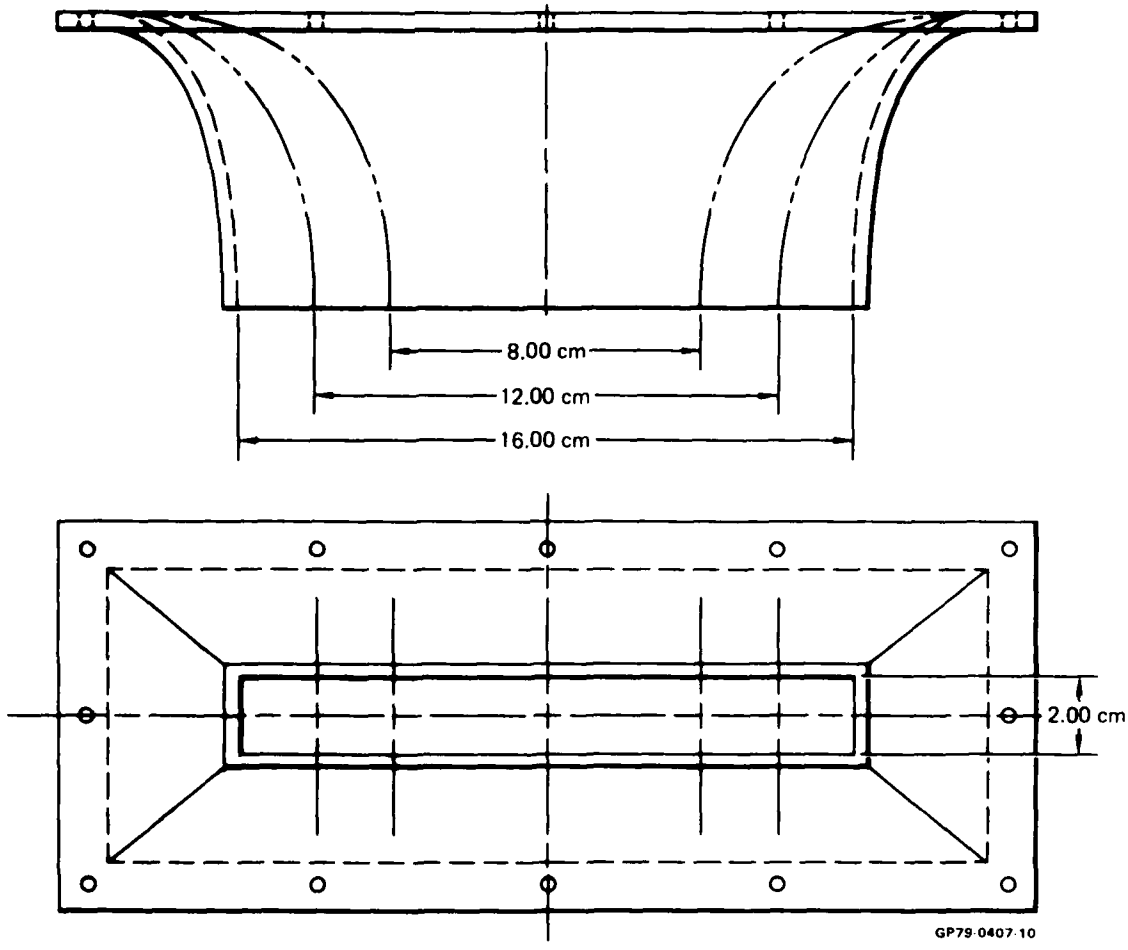

FIGURE 6
SINGLE NOZZLE CONFIGURATIONS

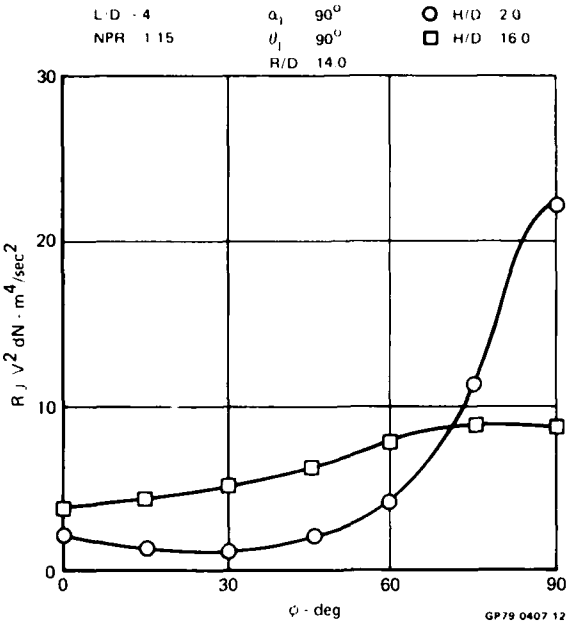

FIGURE 7
AZIMUTHAL DISTRIBUTION OF WALL JET RADIAL MOMENTUM FLUX
Vertical Impingement

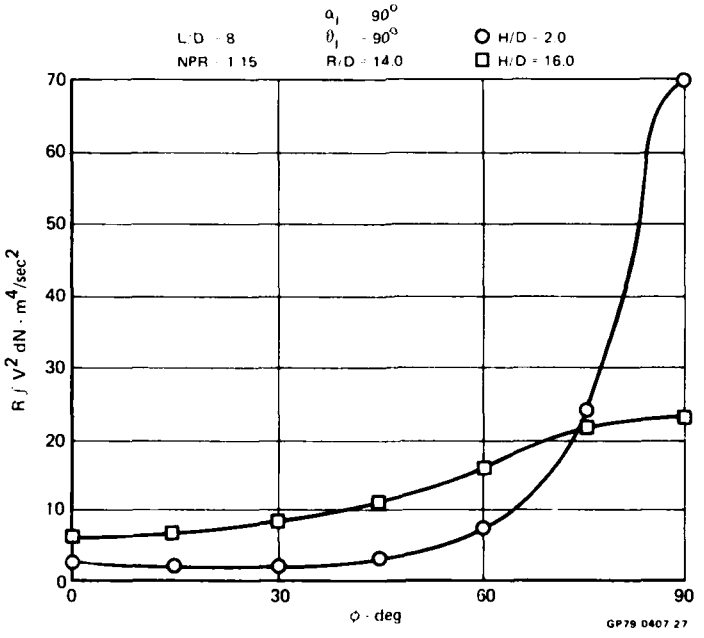

FIGURE 8
AZIMUTHAL DISTRIBUTION OF WALL JET RADIAL MOMENTUM FLUX
Vertical Impingement

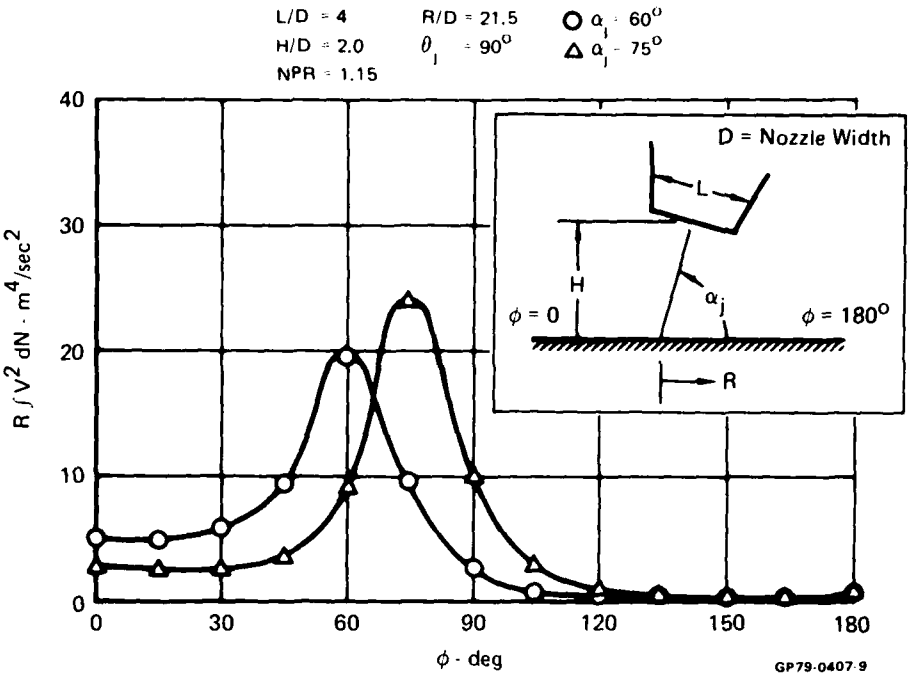

FIGURE 9
AZIMUTHAL DISTRIBUTION OF WALL JET RADIAL MOMENTUM FLUX
Oblique Impingement - Pitch

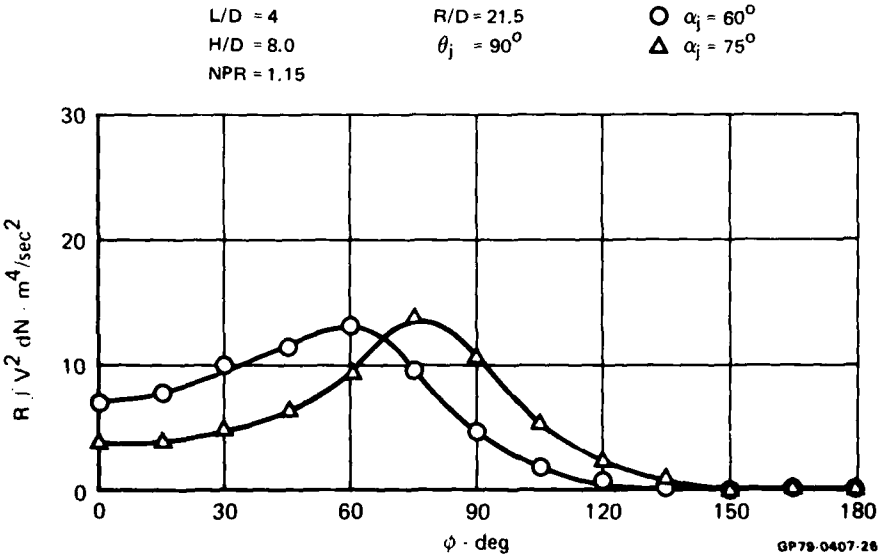

FIGURE 10
AZIMUTHAL DISTRIBUTION OF WALL JET RADIAL MOMENTUM FLUX
Oblique Impingement - Pitch

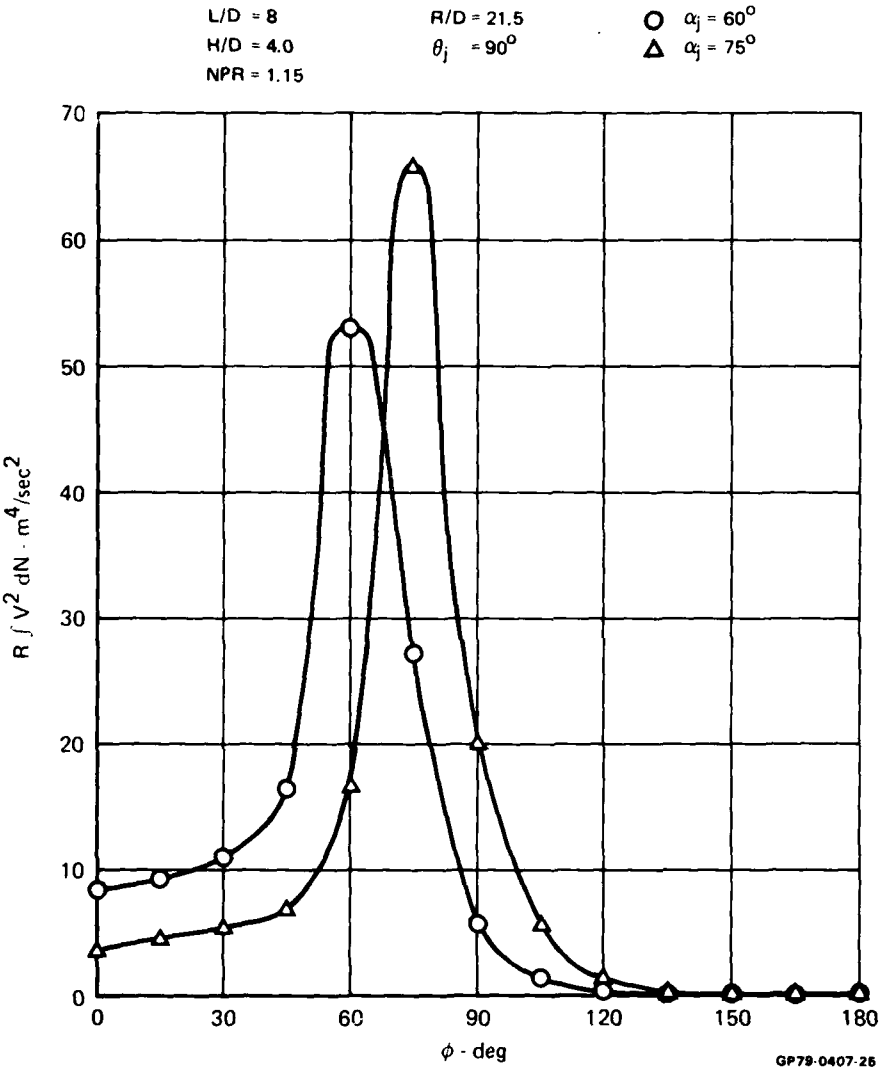

FIGURE 11
AZIMUTHAL DISTRIBUTION OF WALL JET RADIAL MOMENTUM FLUX
Oblique Impingement - Pitch

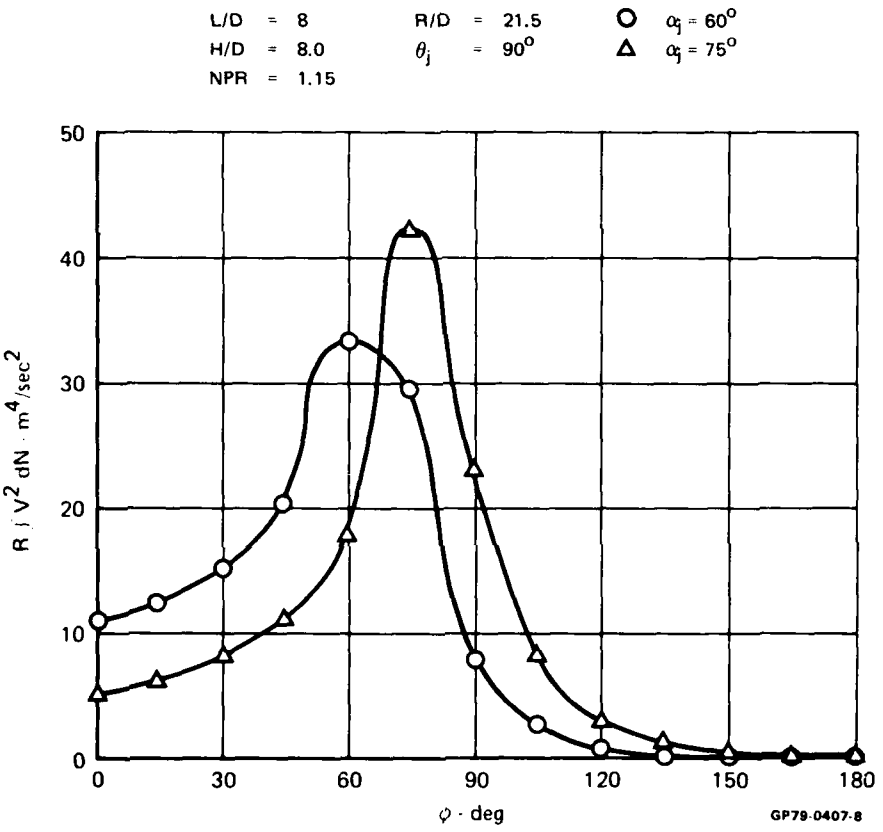

FIGURE 12
AZIMUTHAL DISTRIBUTION OF WALL JET RADIAL MOMENTUM FLUX
Oblique Impingement - Pitch

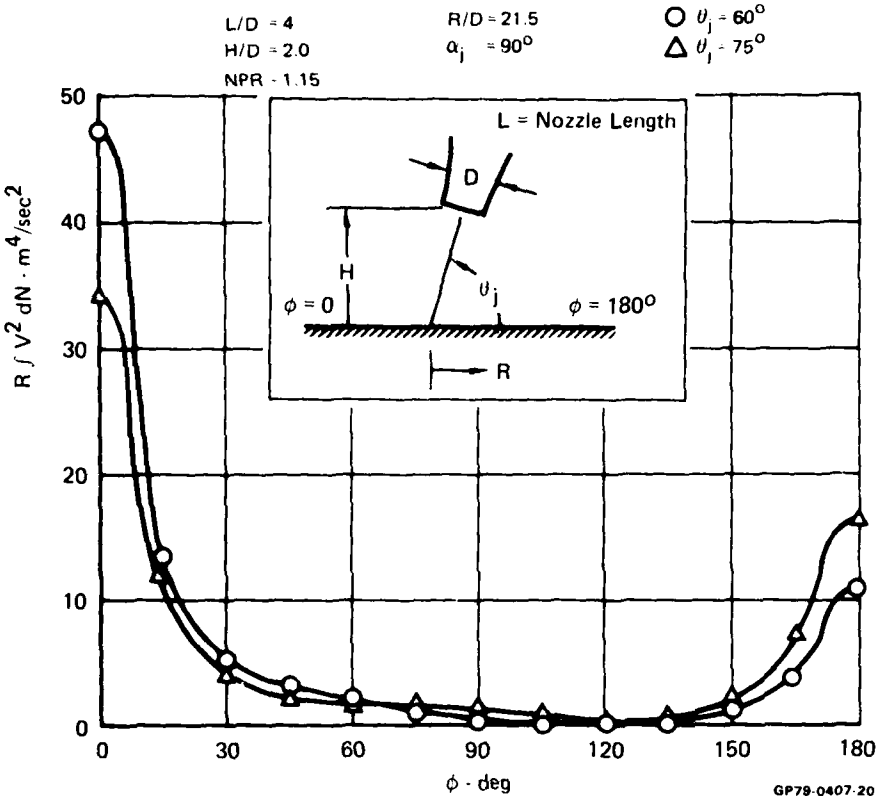

FIGURE 13
AZIMUTHAL DISTRIBUTION OF WALL JET RADIAL MOMENTUM FLUX
Oblique Impingement - Roll

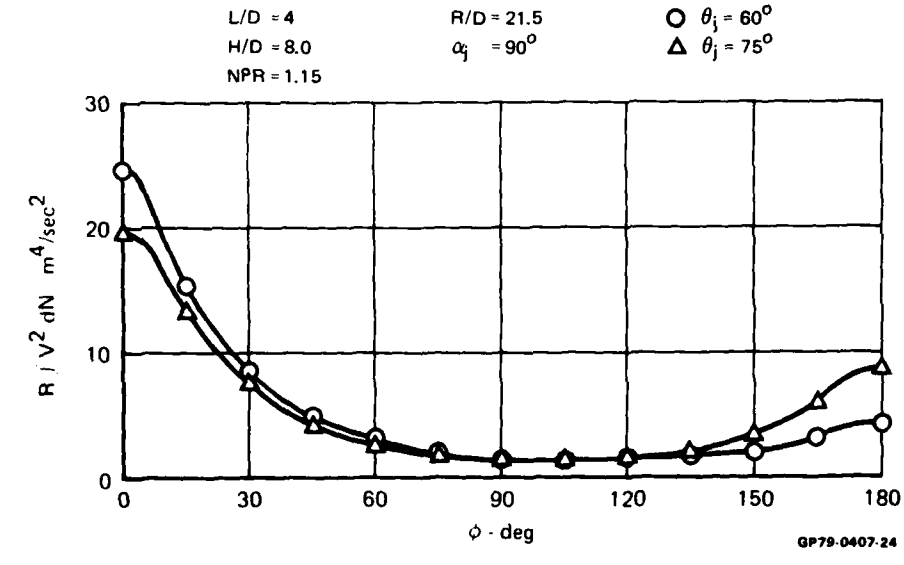

FIGURE 14
AZIMUTHAL DISTRIBUTION OF WALL JET RADIAL MOMENTUM FLUX
Oblique Impingement - Roll

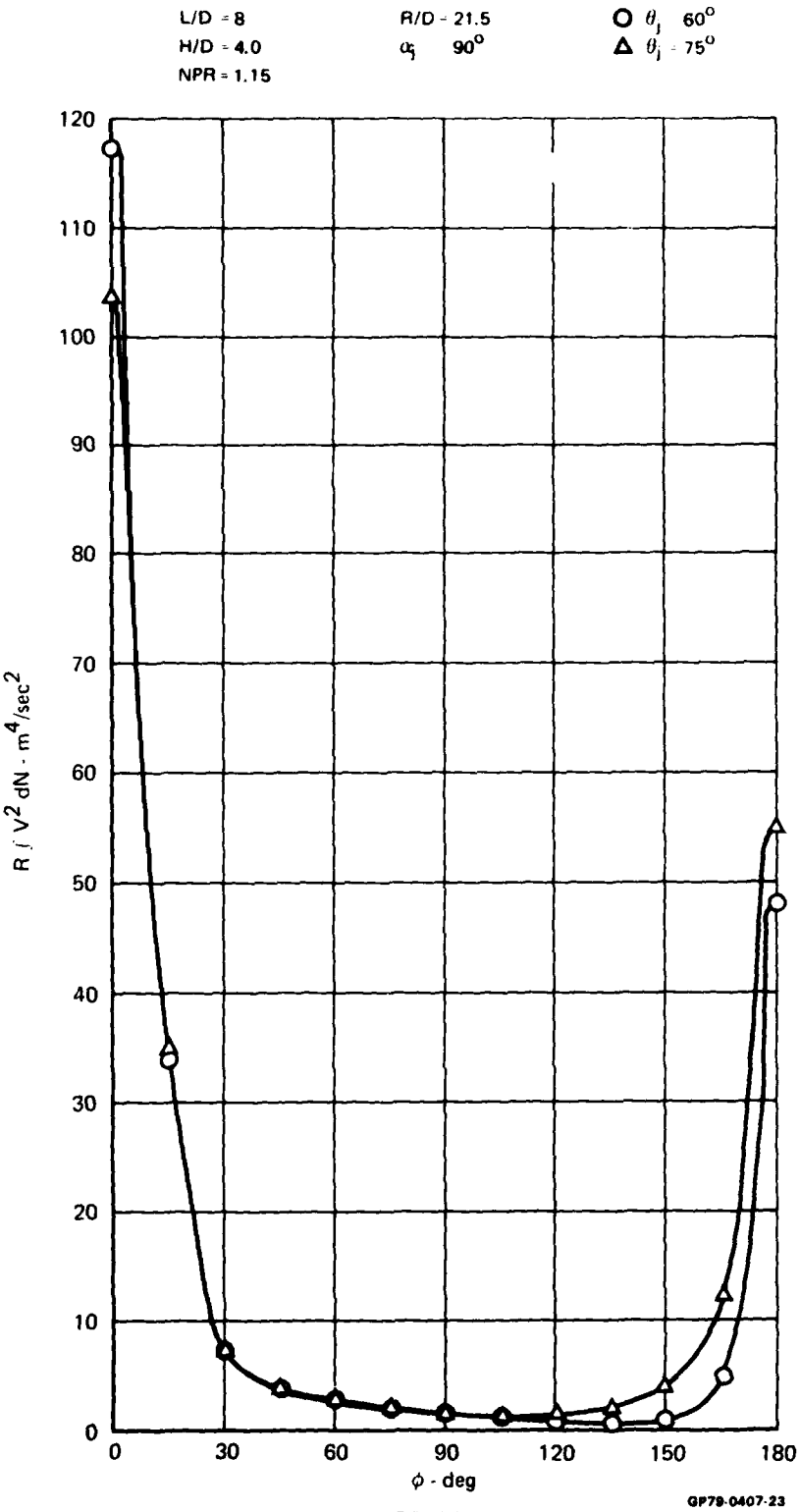

FIGURE 15
AZIMUTHAL DISTRIBUTION OF WALL JET RADIAL MOMENTUM FLUX
Oblique Impingement - Roll

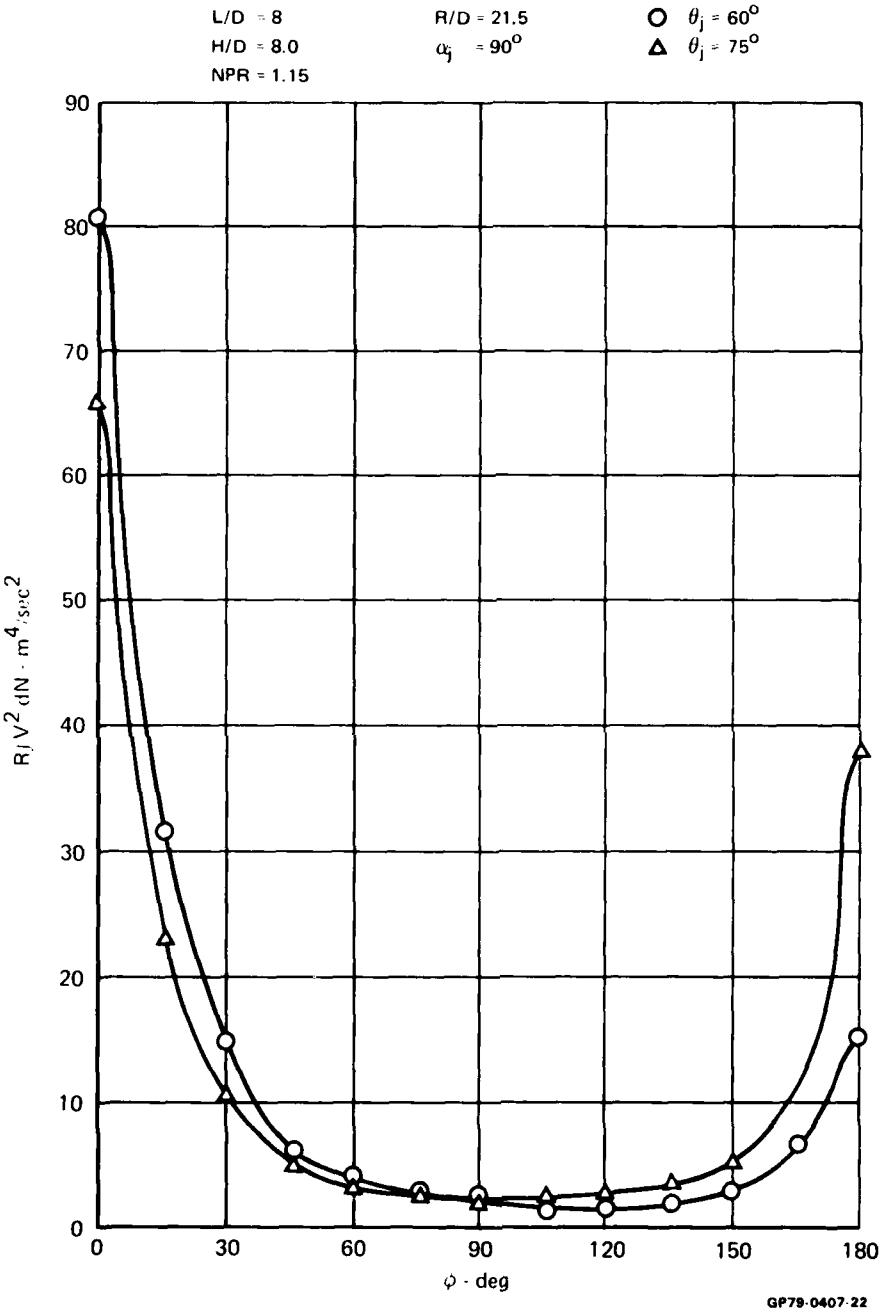

FIGURE 16
AZIMUTHAL DISTRIBUTION OF WALL JET RADIAL MOMENTUM FLUX
Oblique Impingement - Roll

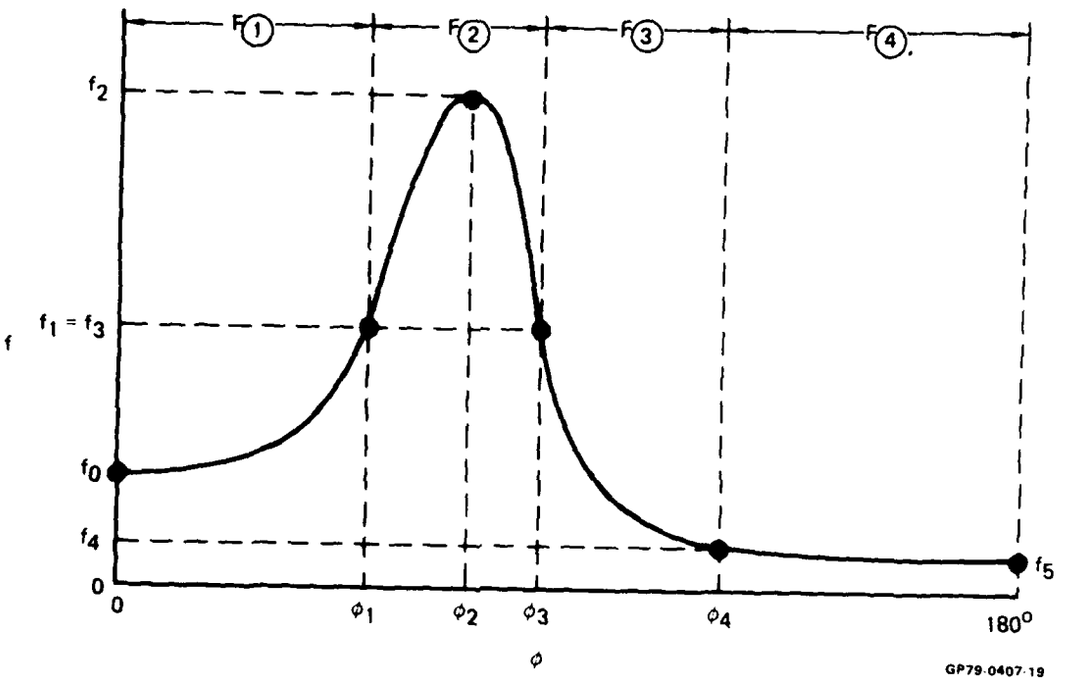

FIGURE 17
MOMENTUM FLUX DISTRIBUTION CURVE-FIT
Oblique Impingement - Pitch

	D	L	τ	Vector	Splay	NPR
Jet 1	3.192	–	0^o	90^o	0^o	1.80
Jet 2	3.192	–	0^o	90^o	0^o	1.80

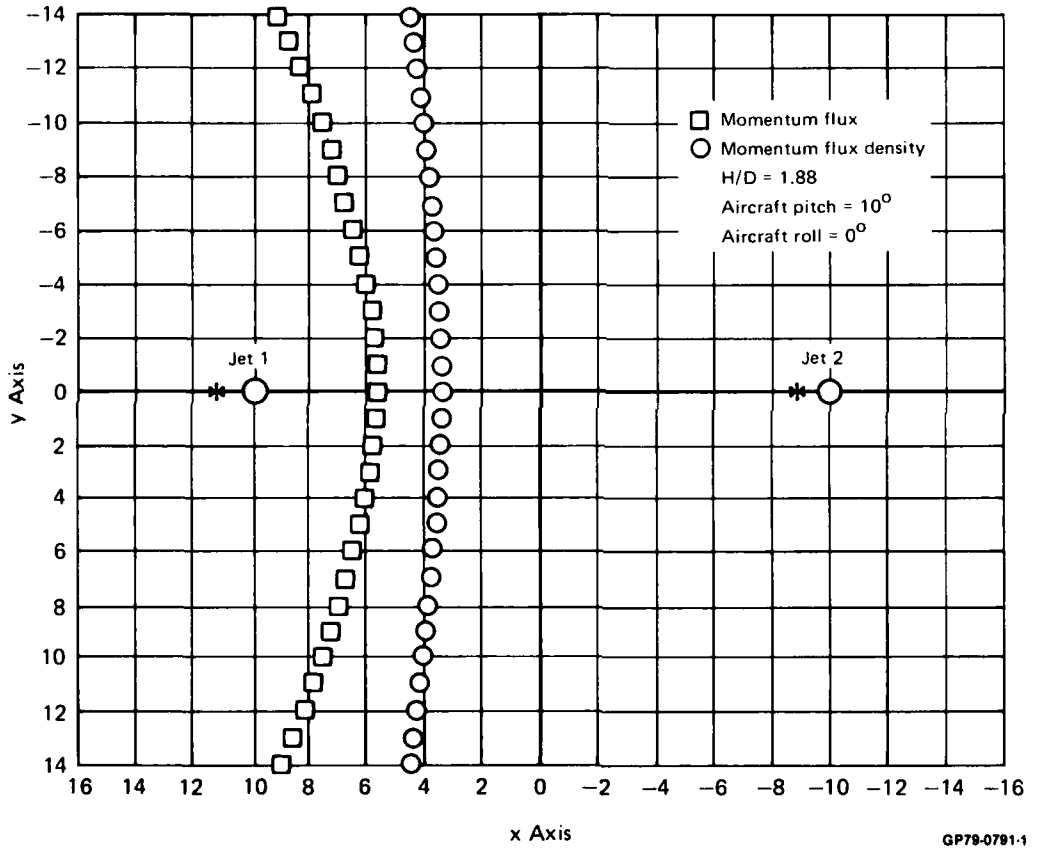

FIGURE 18
COMPUTED STAGNATION LINES

	D	L	τ	Vector	Splay	NPR
Jet 1	3.192	–	0°	90°	0°	1.80
Jet 2	1.000	8.000	0°	90°	0°	1.80

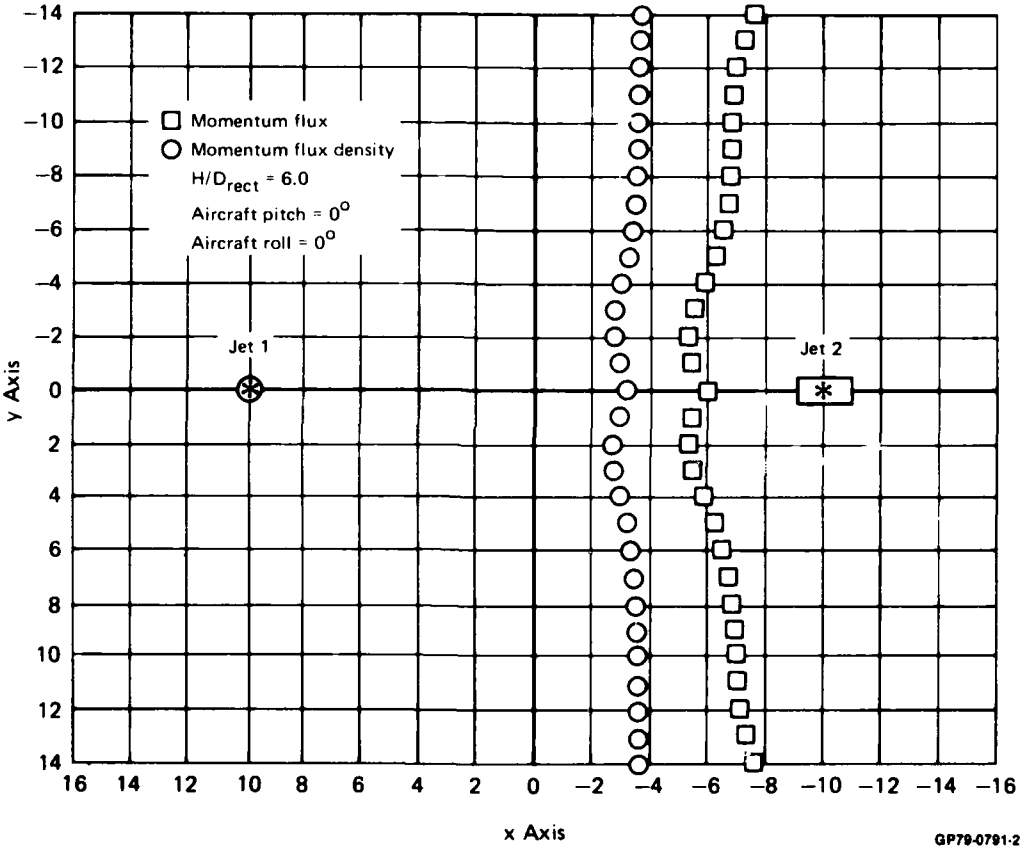

FIGURE 19
COMPUTED STAGNATION LINES

	D	L	τ	Vector	Splay	NPR
Jet 1	3.192	–	0°	90°	0°	1.80
Jet 2	1.000	8.000	0°	90°	0°	1.80

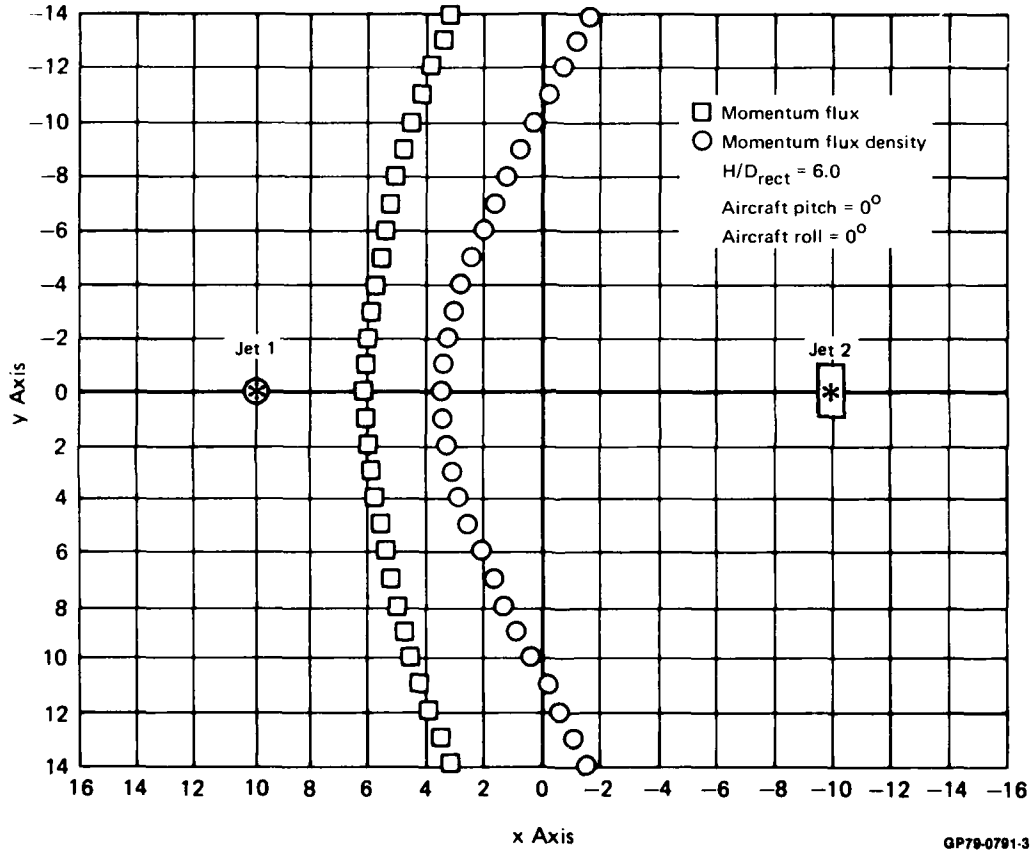

FIGURE 20
COMPUTED STAGNATION LINES

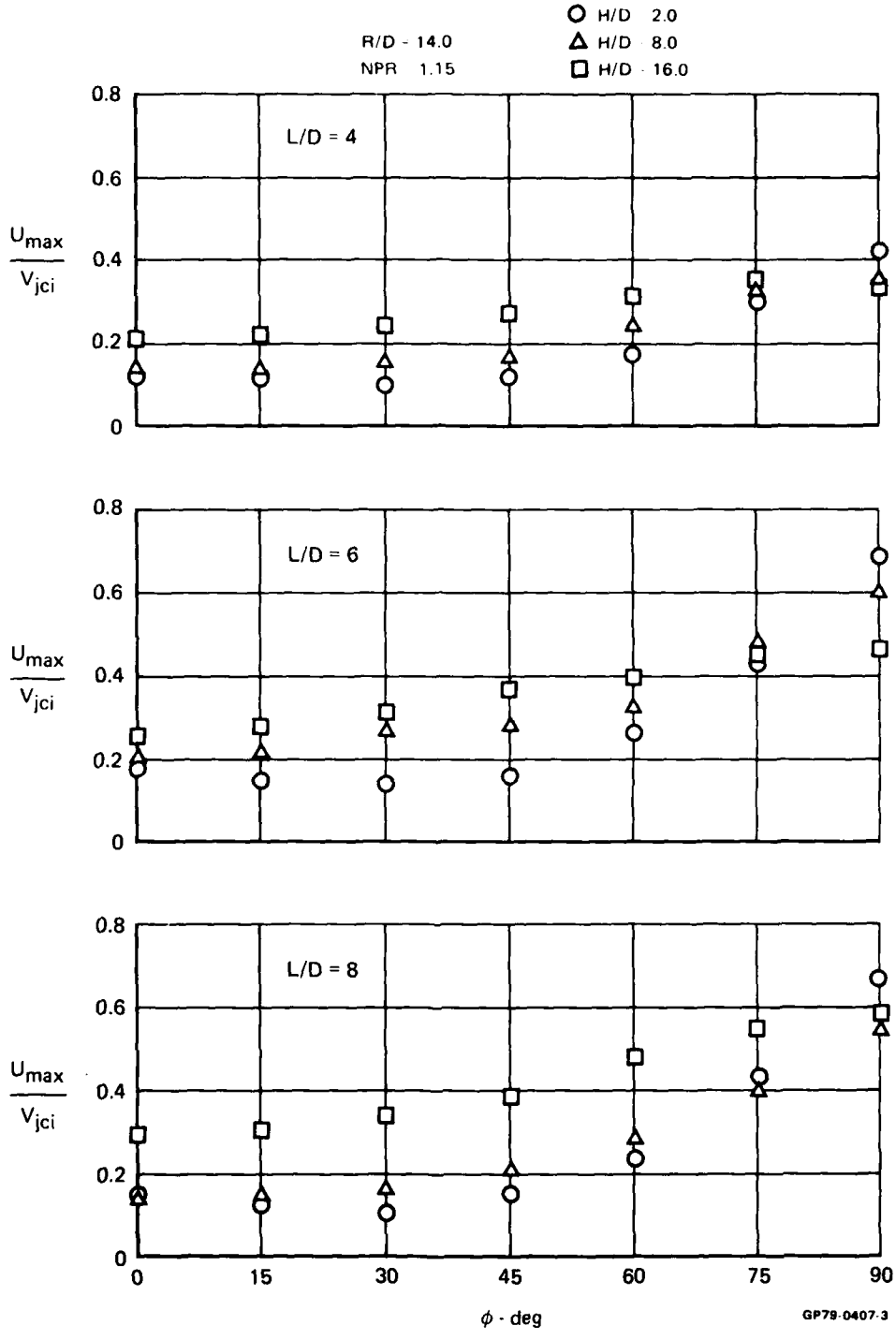

FIGURE 21
WALL JET VELOCITY DISTRIBUTION
Vertical Impingement

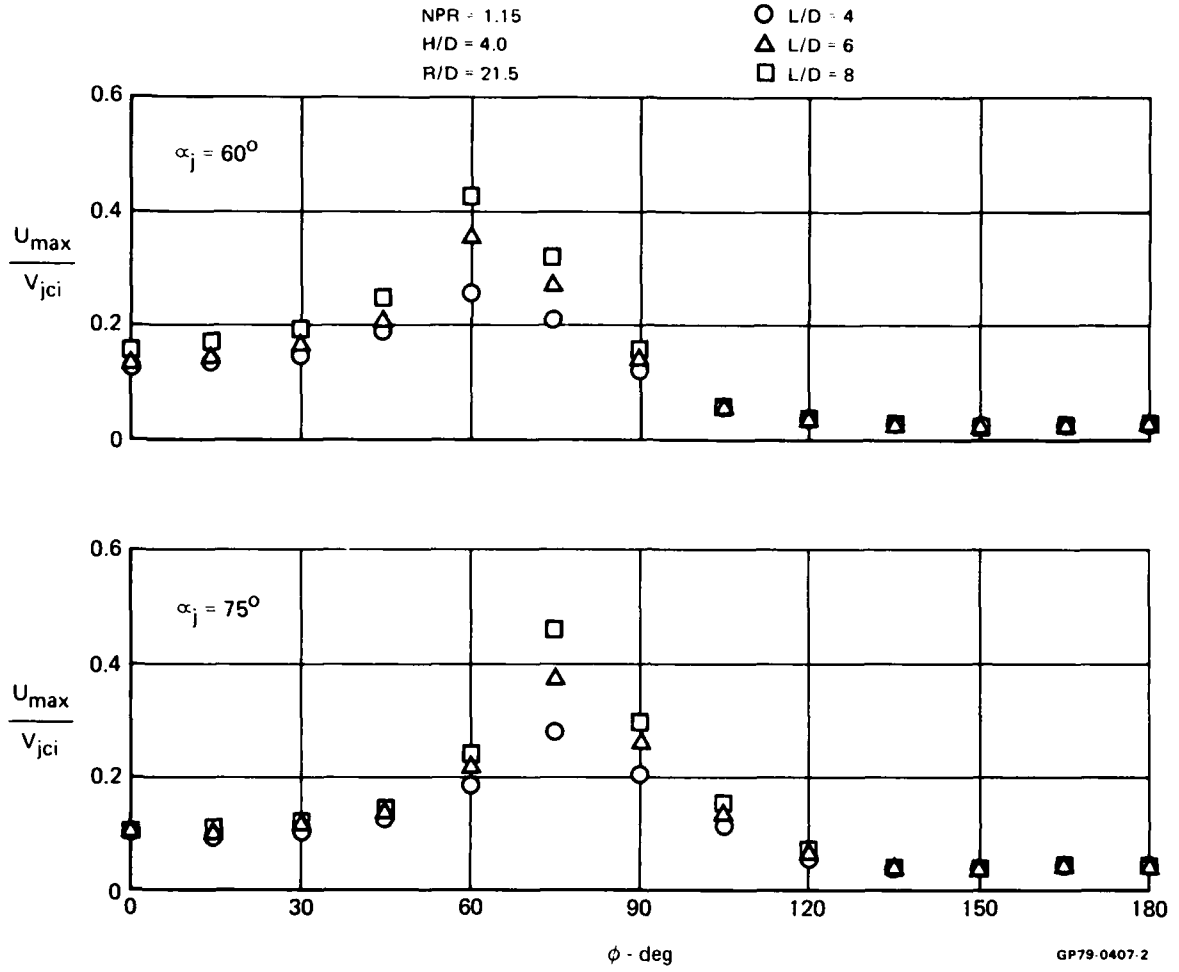

FIGURE 22
WALL JET VELOCITY DISTRIBUTION
Oblique Impingement - Pitch

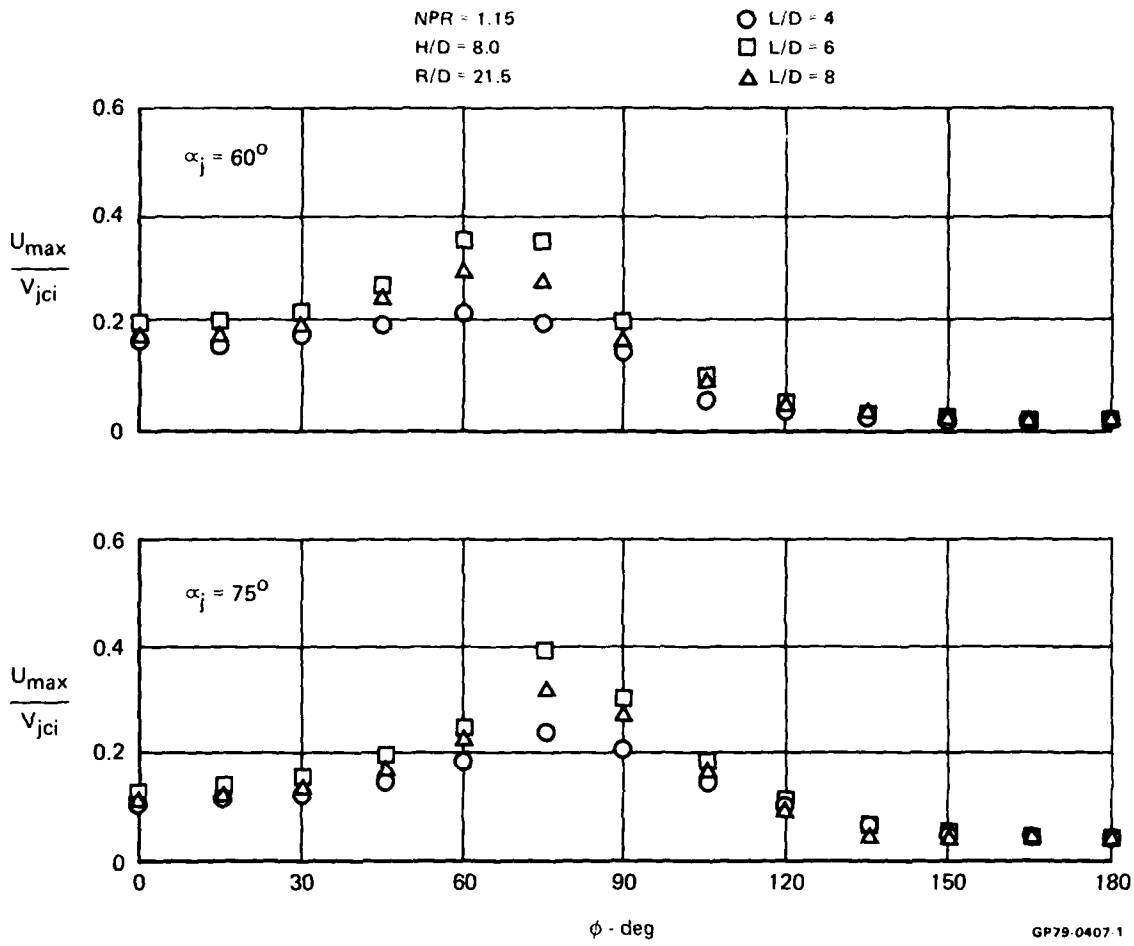

FIGURE 23
WALL JET VELOCITY DISTRIBUTION
Oblique Impingement - Pitch

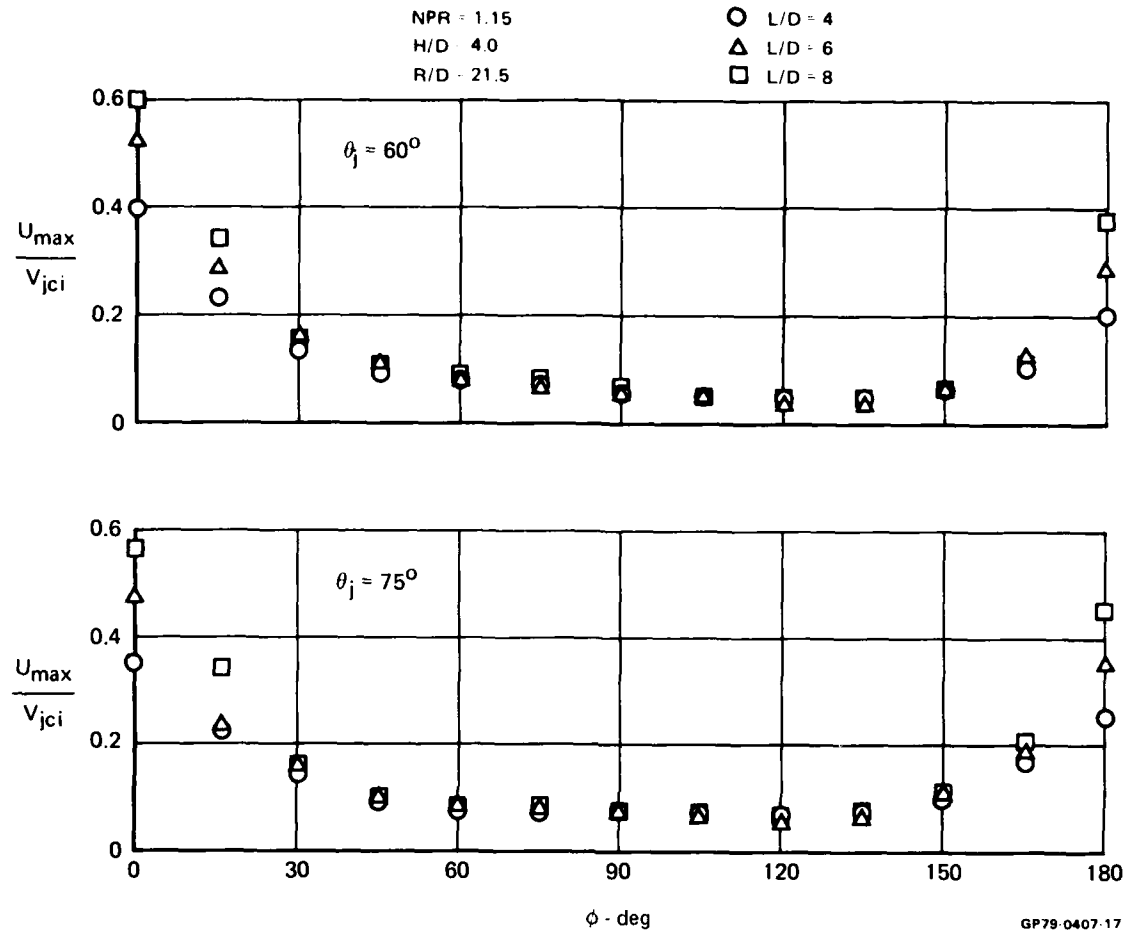

FIGURE 24
WALL JET VELOCITY DISTRIBUTION
Oblique Impingement - Roll

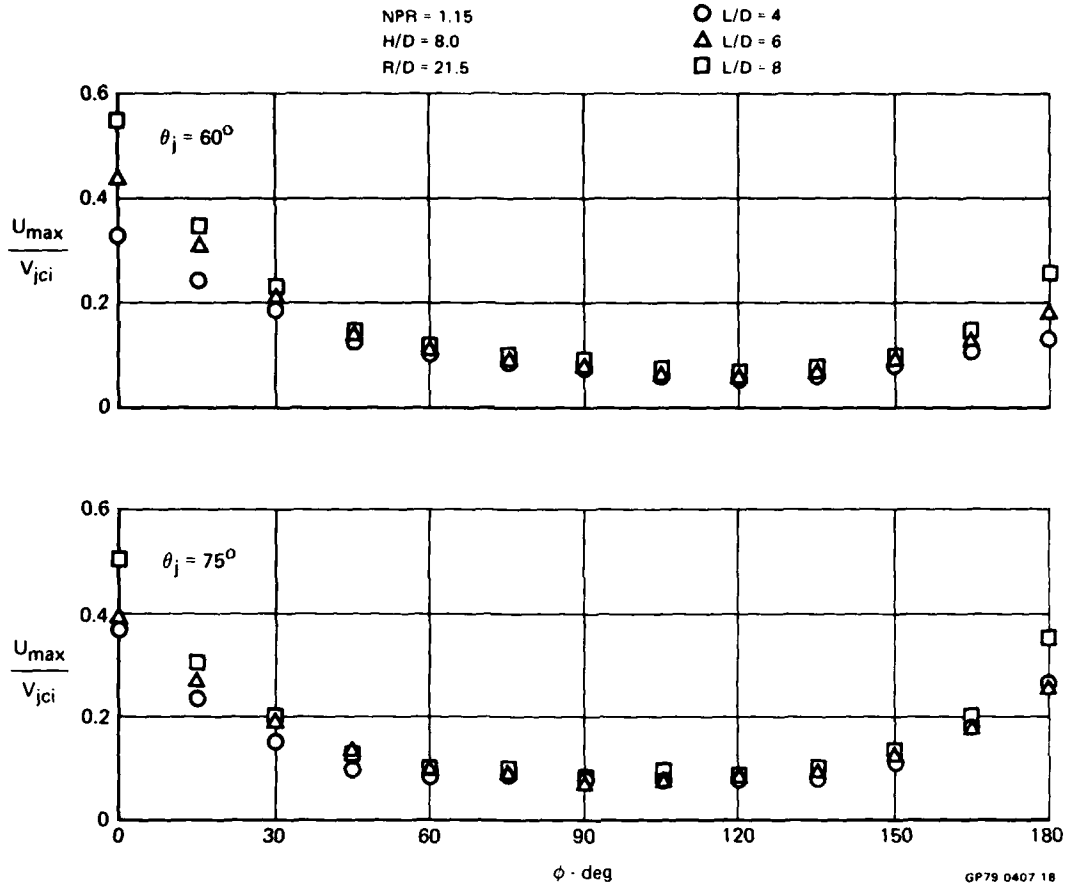

FIGURE 25
WALL JET VELOCITY DISTRIBUTION
Oblique Impingement - Roll

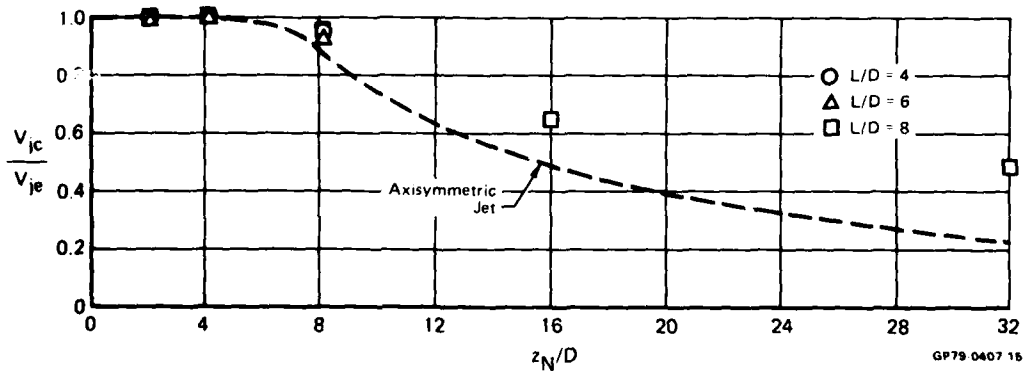

FIGURE 26
FREE JET CENTERLINE VELOCITY DECAY

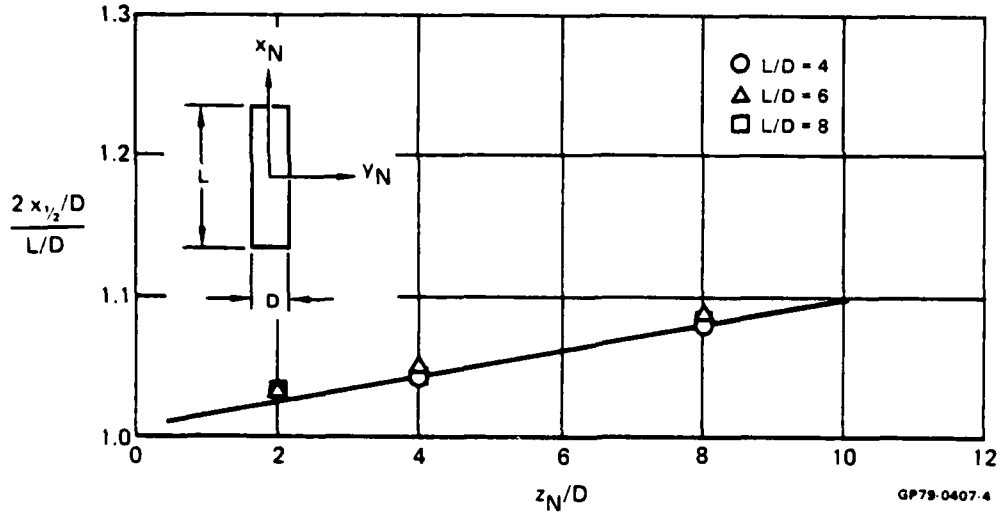

FIGURE 27
FREE JET SPREADING CHARACTERISTICS
x_N, z_N Plane

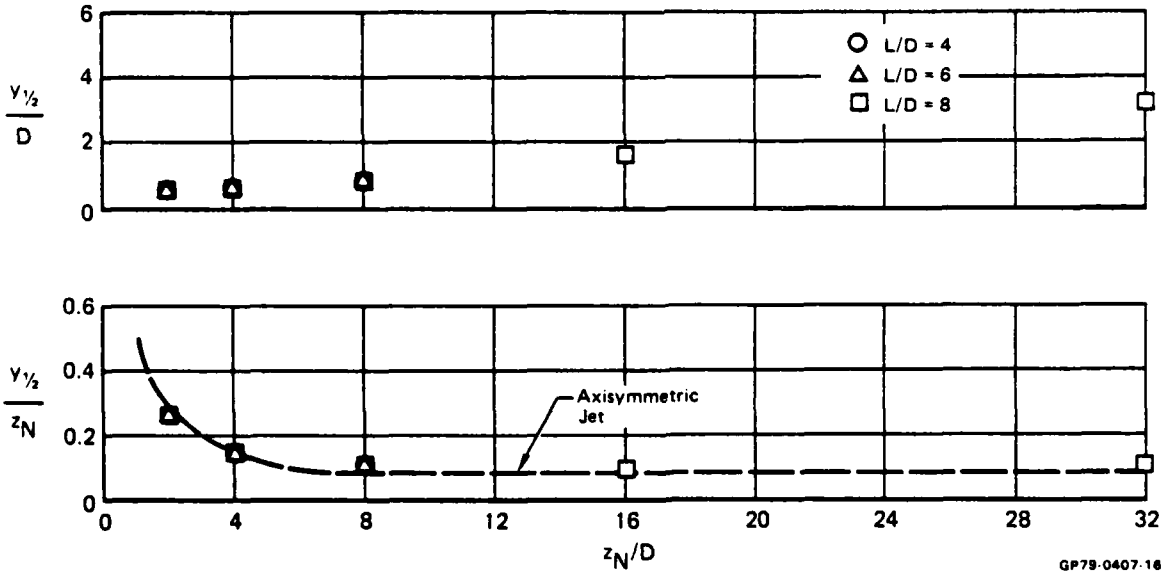

FIGURE 28
FREE JET SPREADING CHARACTERISTICS
y_N, z_N Plane

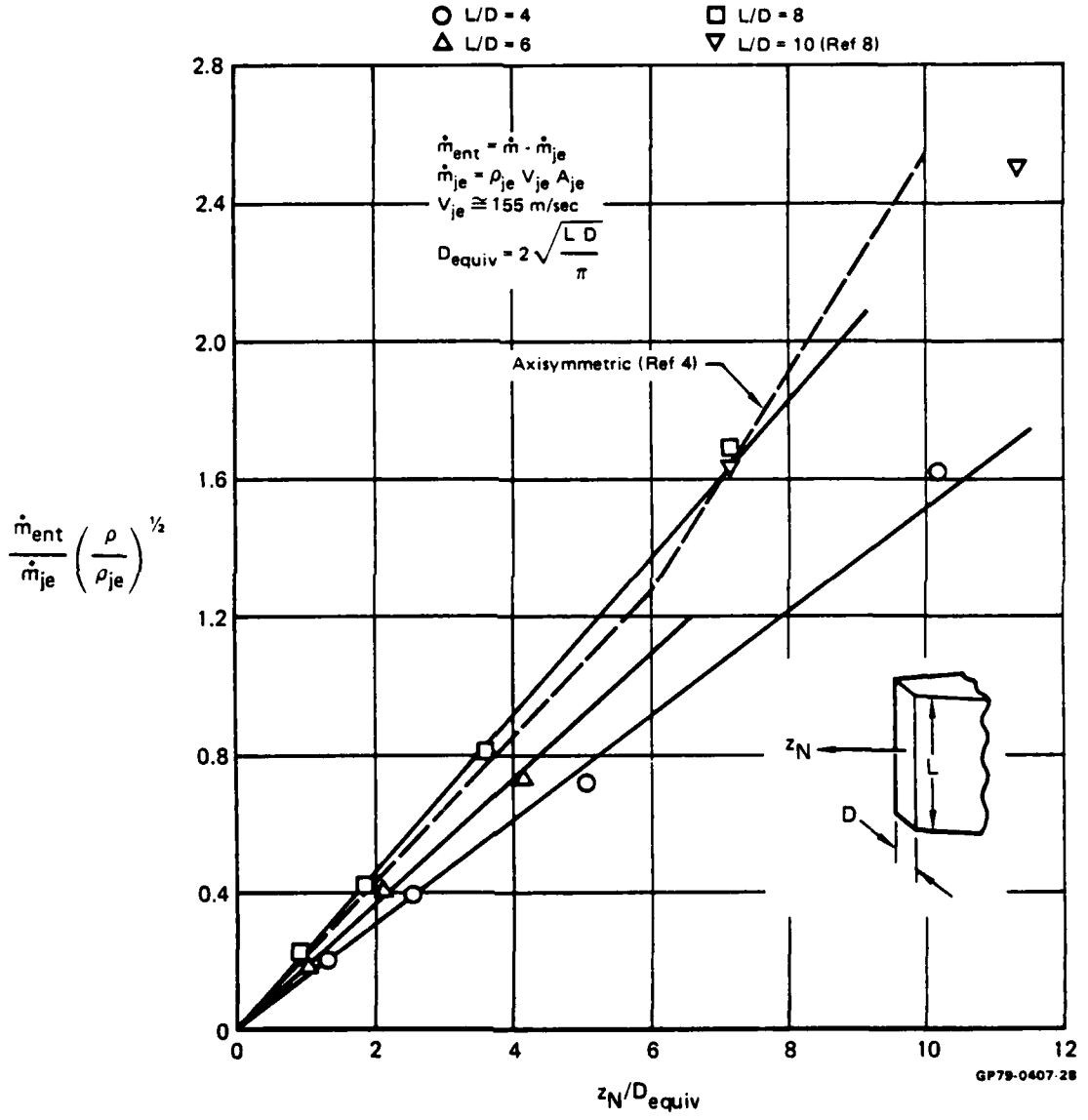

FIGURE 29
VARIATION OF MASS ENTRAINMENT WITH DISTANCE FROM NOZZLE

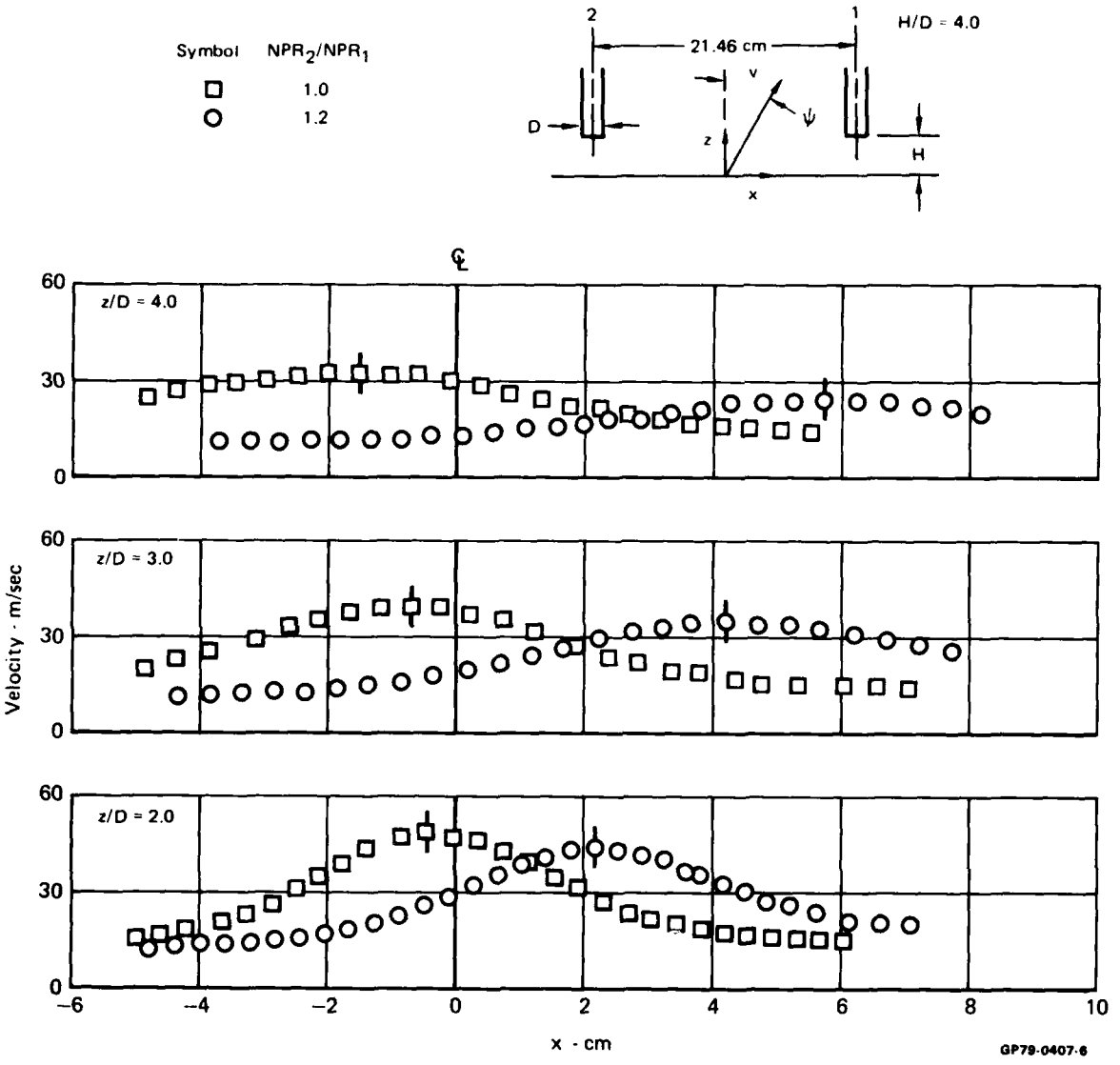

FIGURE 30
FOUNTAIN UPWASH - TWO IMPINGING JETS

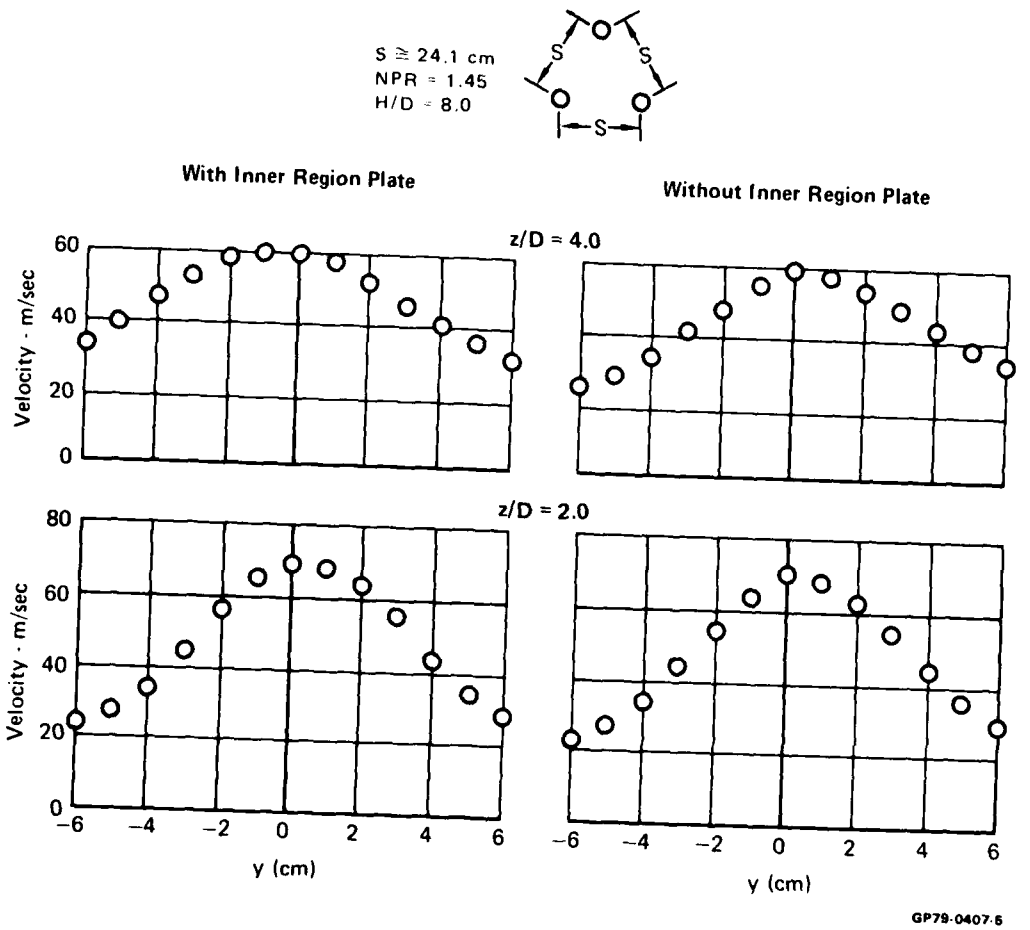

FIGURE 31
3-JET FOUNTAIN VELOCITY PROFILES

A THEORETICAL STUDY OF TWO- AND THREE-DIMENSIONAL IMPINGING JETS*

W.W. Bower†
R.K. Agarwal**
G.R. Peters***

McDonnell Douglas Corporation
St. Louis, Missouri 63166

Abstract

An important consideration for VTOL aircraft design is the aerodynamic interaction between airframe undersurfaces and the ground. In an effort to predict this phenomenon, a second-order-accurate, finite-difference scheme for solution of the two- and three-dimensional conservation equations of fluid mechanics, in combination with a turbulence model, is described. The solution technique is applied to a planar lift jet in ground effect for both incompressible and compressible flow and to two interacting incompressible jets with fountain formation. Fluid properties that characterize the jet impingement flowfields and comparisons with measured data are presented.

†*Scientist, McDonnell Douglas Research Laboratories.*

***Research Scientist, McDonnell Douglas Research Laboratories*

****Consultant, McDonnell Douglas Research Laboratories; Chairman, Department of Mathematics, Greenville College, Greenville, Illinois 62246.*

**This work was conducted in part under Office of Naval Research Contract N00014-76-C-0494 and in part under the McDonnell Douglas Independent Research and Development Program.*

Introduction

With the current interest in jet and fan-powered vertical-takeoff-and-landing (VTOL) military aircraft, there has been an increasing demand for improved performance-prediction methods. This demand is greatest for techniques to predict propulsion-induced aerodynamic effects in the hover mode of VTOL flight.

This task is not easy, however, since the hover mode of a VTOL aircraft is characterized by complex flow phenomena. Ambient air is entrained into the lift jets and the wall jets, leading to an induced downflow of air around the aircraft and a resulting suckdown force. In addition, the inward jet flows collide and create a stagnation region from which a hot gas fountain emerges and impinges on the lower fuselage surface. The fountain is a source of positive induced forces which, to some extent, counteract the large suckdown forces near the ground. However, the fountain also heats the airframe surface and can result in the reingestion of hot gas into the inlet.

The VTOL ground-effect flow is characterized by three-dimensionality, high turbulence levels, compressibility, strong pressure gradients, and regions of stagnation-point and separated flow. In order to gain a fundamental understanding of lift-jet induced flows, including entrainment and fountain characteristics, the McDonnell Douglas Research Laboratories (MDRL) has over the past three years conducted a theoretical investigation of two- and three-dimensional impinging jets, under contract to the Office of Naval Research (ONR).

In the first two years of the contract, attention was focused on a single, planar, unvectored lift jet in ground effect, illustrated schematically in Figure 1. The jet exits from a slot of width $\bar{D}$ in a contoured upper-surface a distance $\bar{H}$ above the ground plane. The region of interest extends a distance $\bar{W}$ on each side of the jet centerline. The jet flowfield can be characterized by the following three regions: a free-jet region in which the flow is essentially the same as that of a jet issuing into an unbounded region of the same fluid; the impingement region in which the flow changes direction with a large pressure gradient; and the wall-jet region in which the flow traverses the surface with zero pressure gradient. The fluid surrounding the jet is entrained at its boundaries in all three regions. This entrainment results in an induced secondary flow which can produce suckdown forces on the airframe undersurface and an associated lift loss.

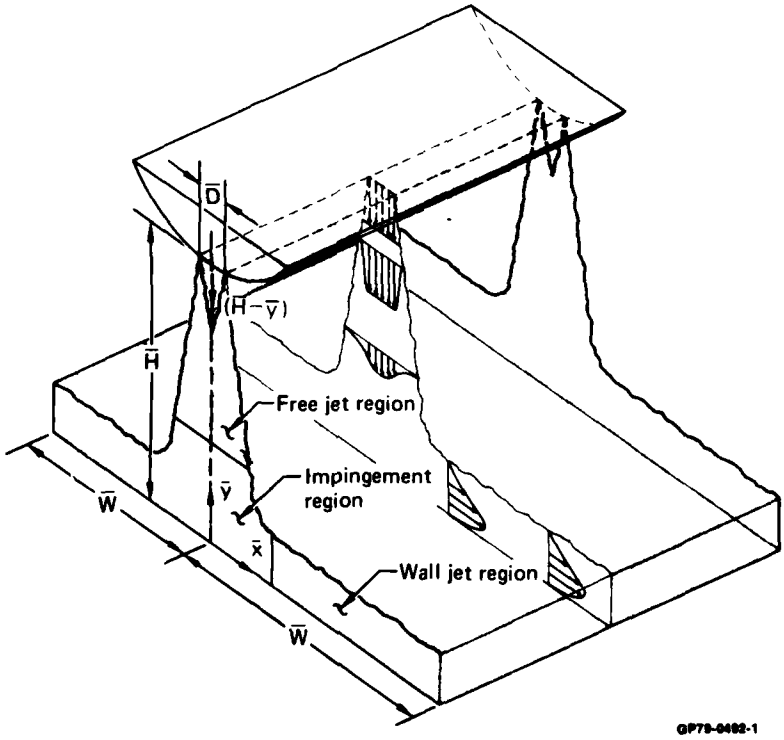

Figure 1. The planar impinging jet.

Isolated regions of the flowfield illustrated in Figure 1 can be analyzed with simplified techniques; for example, Rubel[1] has predicted the ground-plane pressure distributions in the impingement region using an incompressible, inviscid, rotational model for two-dimensional flow. Although good agreement has been obtained with measured ground-plane pressures, this approach cannot provide the fuselage undersurface pressure variation that is necessary to calculate the suckdown force.

A more rigorous analysis of the planar impinging jet, based on solution of the time-averaged Navier-Stokes equations in conjunction with a turbulence model, has been adopted by MDRL in its contract work with ONR. In the first year of this effort, an isolated, planar, incompressible lift jet in ground effect was analyzed, and in the second year this analysis was extended to compressible flow. In both endeavors, the time-averaged conservation equations, combined with an appropriate turbulence model, were solved in stream-function/vorticity form. A conformal mapping procedure was used to transform the nonrectangular physical plane into a rectangular computational plane, and a second-order-accurate, finite-difference scheme that is stable for all Reynolds numbers was applied to the transformed differential equations. The discretized system was solved iteratively using point relaxation for a range of the dimensionless parameters which characterize the problem.

In the third year of the contract work with ONR, MDRL extended its Navier-Stokes analysis of impinging jets to three-dimensional geometries. The configuration of primary interest, shown schematically in Figure 2, consists of two interacting, initially axisymmetric jets with fountain formation. The jets exit from two axisymmetric nozzles, each with diameter $\bar{D}$, whose centerlines are separated by a distance $\bar{L}$ and whose exit planes are a distance $\bar{H}$ above the ground. The width of the region of interest is the dimension $\bar{W}$, measured from the jet centerline. As in the case of the planar jet, the flowfield can be characterized by free-jet, impingement, and wall-jet regions. In addition, a fountain-upwash region is formed as a result of the interaction of the opposing wall jets. The inclination of the fountain is dependent on the geometry of the configuration and the ratio of the jet strengths. The fountain is a key element of the problem and the major motivation for analyzing this geometry, for as Walters and Henderson[2] conclude in an assessment of current methods to predict the aerodynamics of V/STOL aircraft, "a major deficiency exists both in available data base and prediction methods relative to fountain-induced effects."

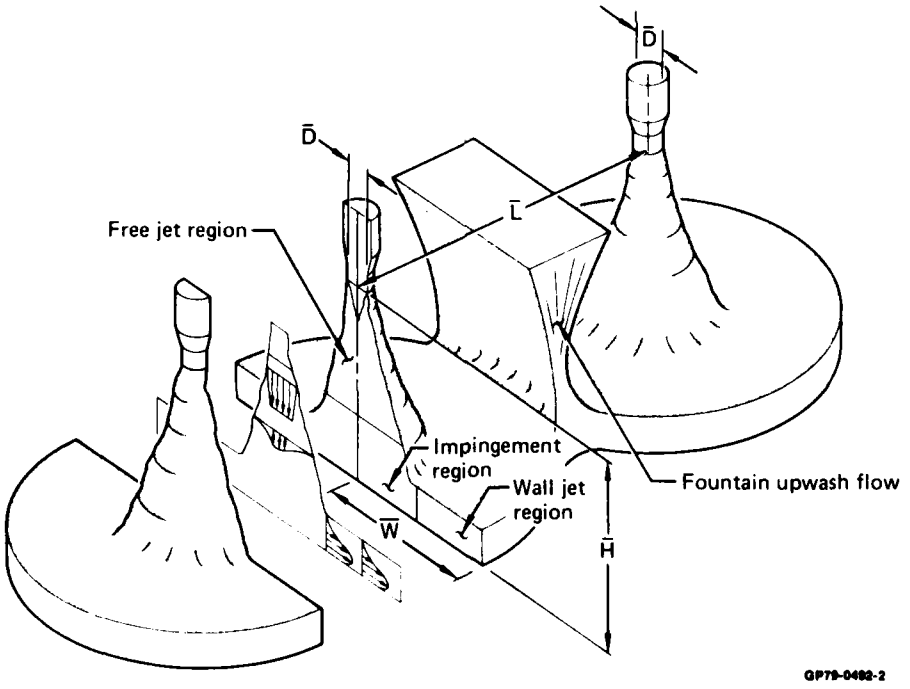

Figure 2. Two interacting, initially axisymmetric jets impinging perpendicularly on the ground with fountain formation.

An incompressible, inviscid, rotational flow model that is applicable to three-dimensional, jet-impingement problems has been described by Rubel[3]. This technique has been used to compute in a cartesian coordinate system an axisymmetric jet impinging perpendicular to the ground, but calculations of interacting jets with fountain formation have not been reported.

The basis of the MDRL approach adopted in the ONR contract for predicting three-dimensional, impinging jet flows is again a finite-difference solution of the time-averaged, Navier-Stokes equations with a complementary turbulence model. The conservation equations were solved in terms of scalar and vector potential functions and vorticity. Since the solution domain is a parallelepiped, a conformal mapping was not required. Solutions of the governing equations were obtained with an extension to three dimensions of the second-order-accurate, finite-difference algorithm used in the planar-jet analysis. An iterative solution of the discretized system of equations was obtained with line relaxation for selected dimensionless parameters which define the problem.

This paper describes the theoretical approach that has been adopted in the ONR contract work to compute two- and three-dimensional impinging jets. The flowfield model, numerical solution scheme, and representative results which illustrate the computed entrainment and fountain-upwash characteristics are presented. The direction of future MDRL work in the calculation of ground-effect flowfields is discussed.

Analysis of Two-Dimensional Impinging Jets

In this section, the procedure is described for computing the incompressible and compressible turbulent flowfields for the unvectored planar lift jet in ground effect shown in Figure 1. Contour plots of the calculated flow variables and comparisons with experimental data are presented.

The Governing Equations

The time-averaged continuity, momentum (Navier-Stokes), and thermal energy equations for steady compressible flow are given below in tensor notation for a space-fixed reference through which the fluid flows.

Conservation of mass:

$$\frac{\partial(\bar{\rho}\tilde{u}_j)}{\partial x_j} = 0 \tag{1}$$

Conservation of momentum in the $i^{\underline{th}}$ direction:

$$\frac{\partial(\bar{\rho}\tilde{u}_i\tilde{u}_j + \overline{\rho u_i'' u_j''})}{\partial x_j} = -\frac{\partial \bar{p}}{\partial x_i} + \frac{\partial \bar{\tau}_{ij}}{\partial x_j} + \bar{\rho}\bar{g}_i \tag{2}$$

Conservation of thermal energy:

$$\frac{\partial(\bar{\rho}\tilde{u}_j\tilde{J} + \overline{\rho u_j''h''})}{\partial x_j} = \frac{\partial}{\partial x_j}\left[\tilde{u}_i(\bar{\tau}_{ij} - \overline{\rho u_i'' u_j''}) + \overline{u_i''(\tau_{ij} - \frac{1}{2}\rho u_i'' u_j'')}\right] - \frac{\partial \bar{q}_j}{\partial x_j}. \tag{3}$$

In these equations, ρ denotes density, u_i the velocity component in the $i^{\underline{th}}$ direction, p the static pressure, τ_{ij} the shear stress in the $i^{\underline{th}}$ direction on a surface normal to the $j^{\underline{th}}$ direction, g_i the acceleration due to gravity in the $i^{\underline{th}}$ direction, J the total specific enthalpy, h the static enthalpy, and q_j the heat flux in the $j^{\underline{th}}$ direction.

Equations (1) through (3) are written in the form derived by Rubesin and Rose[4] in which ρ, p, τ_{ij}, and q_j are represented using the usual Reynolds decomposition and u_i, J, and h are represented using the mass-averaged

variables introduced by Favre[5]. Specifically, in the Reynolds decomposition, a general flow variable ϕ is expressed as the sum of a time-averaged component $\bar{\phi}$ and a fluctuating component ϕ':

$$\phi = \bar{\phi} + \phi' . \tag{4}$$

For the case of compressible flow, this approach is not the best for all variables because the resulting equations contain numerous explicit mean-product fluctuation terms arising from compressibility and do not have the same form as their incompressible counterparts. If, however, certain variables are written as mass-averaged variables, the resulting equations have virtually a term-by-term correspondence with the constant-property case. In the Favre system,

$$\phi = \tilde{\phi} + \phi'' , \tag{5}$$

where the tilde, ~, denotes a mass average defined in terms of the conventional time average and

$$\phi'' = \phi' - \frac{\overline{\rho'\phi'}}{\bar{\rho}} . \tag{6}$$

The time-averaged conservation Equations (1) through (3) have the same form as the instantaneous conservation equations with the exception of the Reynolds stress term $-\overline{\rho u_i'' u_j''}$, the Reynolds heat flux term $\overline{\rho u_j'' h''}$, and the mean-energy dissipation term $u_i''(\tau_{ij} - 1/2\,\rho u_i'' u_j'')$. Moreover, these equations essentially have the desired term-by-term correspondence with the incompressible time-averaged conservation equations. This correspondence can be significant, as pointed out in Reference 4, if the basic turbulence mechanisms in the compressible flow remain similar to those in the constant-property flow (the so-called Morkovin hypothesis) such that turbulence modeling information can be taken from incompressible flow data and applied to the compressible case.

In order to obtain a closed system of equations, the Reynolds stress term the Reynolds heat flux term, and the mean-energy dissipation term must be evaluated. In initial work on the planar jet, reported in References 6 and 7, one-equation models were used to represent the turbulence field (the Wolfshtein model[8] for the incompressible jet and Rubesin's extension of the Glushko model[9] for the compressible jet). Both of these approaches suffer because the turbulence length-scale distributions must be specified. For this reason, more recent analyses of the incompressible and compressible planar jets have used the two-equation Jones-Launder turbulence model[10] in which the length-scale variations are implicit in the analysis and need not be specified *a priori*.

When Equations (1) and (3) are expanded from tensor notation into cartesian coordinates (x,y) with the corresponding velocity components (u,v), the result is the so-called primitive-variable form of the time-averaged conservation equations for a compressible planar flow. In the present work the equations are not solved, however, in terms of the primitive variables (velocity components and static pressure). The reason for this, as indicated by Ghia et al. in Reference 11, is that the pressure does not appear as a dominant variable in the system of equations. Since only the first derivatives of pressure with respect to each of the coordinates are nested in the system and not the second derivatives, it is difficult in primitive-variable solutions of the Navier-Stokes equations to maintain the elliptic character of the pressure field.

Consequently, in the present approach, the governing equations are solved in terms of a dimensionless compressible stream function ψ defined by

(7)

(8)

and a dimensionless vorticity ω defined by

$$\omega = \frac{\partial \tilde{v}}{\partial x} - \frac{\partial \tilde{u}}{\partial y} \quad . \tag{9}$$

With this approach the stream function is computed from an equation derived by combining Equations (7) through (9), and the vorticity is computed from a transport equation derived by combining derivatives of the momentum equations in a manner that eliminates the pressure from the equation for ω.

The dimensionless governing equations in the present planar-flow analysis are given below:

Poisson equation for stream function:

$$\frac{\partial^2 \psi}{\partial x^2} - \frac{1}{\bar{\rho}} \frac{\partial \bar{\rho}}{\partial x} \frac{\partial \psi}{\partial x} + \frac{\partial^2 \psi}{\partial y^2} - \frac{1}{\bar{\rho}} \frac{\partial \bar{\rho}}{\partial y} \frac{\partial \psi}{\partial y} = -\bar{\rho}\omega \tag{10}$$

Transport equation for vorticity:

$$\tilde{\mu}_{eff} \left(\frac{\partial^2 \omega}{\partial x^2} + \frac{\partial^2 \omega}{\partial y^2} \right) + \left(2 \frac{\partial \tilde{\mu}_{eff}}{\partial x} - \mathrm{Re} \frac{\partial \psi}{\partial y} \right) \frac{\partial \omega}{\partial x} + \left(2 \frac{\partial \tilde{\mu}_{eff}}{\partial y} + \mathrm{Re} \frac{\partial \psi}{\partial x} \right) \frac{\partial \omega}{\partial y} = \mathrm{Re}\phi_1 - \phi_2 - \frac{\mathrm{Re}}{\mathrm{Fr}^2} \frac{\partial \bar{\rho}}{\partial x}, \tag{11}$$

where $\tilde{\mu}_{eff}$ is the effective viscosity and the functions ϕ_1, ϕ_2 (as well as the functions ϕ_3 through ϕ_{13} which appear in subsequent equations) are defined in the Appendix. The boundary conditions on Equations (10) and (11) follow from known velocity distributions at the boundaries of the solution domain.

Poisson equation for static pressure:

$$\frac{\partial^2 \bar{p}}{\partial x^2} + \frac{\partial^2 \bar{p}}{\partial y^2} = \frac{2}{\mathrm{Re}} \left(\frac{\partial^2 \tilde{\mu}_{eff}}{\partial x^2} \phi_3 + \frac{\partial \tilde{\mu}_{eff}}{\partial x} \phi_4 + 2 \frac{\partial^2 \tilde{\mu}_{eff}}{\partial x \partial y} \phi_5 + \frac{\partial \tilde{\mu}_{eff}}{\partial y} \phi_6 + \frac{\partial^2 \tilde{\mu}_{eff}}{\partial y^2} \phi_7 + \frac{4}{3} \tilde{\mu}_{eff} \phi_8 \right)$$

$$- 2\phi_9 + \frac{2}{\mathrm{Fr}^2} \frac{\partial \bar{\rho}}{\partial y} - \frac{4}{3} \bar{\rho} \left(\frac{\partial^2 \bar{k}}{\partial x^2} + \frac{\partial^2 \bar{k}}{\partial y^2} \right) - \frac{4}{3} \bar{k} \left(\frac{\partial^2 \bar{\rho}}{\partial x^2} + \frac{\partial^2 \bar{\rho}}{\partial y^2} \right) \quad , \tag{12}$$

where k is the turbulent kinetic energy.

The boundary conditions on the pressure are determined through the pressure gradients imposed by the component momentum equations,

$$\frac{\partial \bar{p}}{\partial x} = \frac{2}{\mathrm{Re}} \left(\frac{\partial \tilde{\mu}_{eff}}{\partial x} \phi_3 + \frac{\partial \tilde{\mu}_{eff}}{\partial y} \phi_5 + \frac{1}{2} \tilde{\mu}_{eff} \phi_4 \right) - 2\phi_{10} - \frac{4}{3} \left(\bar{\rho} \frac{\partial \bar{k}}{\partial x} + \bar{k} \frac{\partial \bar{\rho}}{\partial x} \right) \tag{13}$$

$$\frac{\partial \bar{p}}{\partial y} = \frac{2}{\mathrm{Re}} \left(\frac{\partial \tilde{\mu}_{eff}}{\partial x} \phi_5 + \frac{\partial \tilde{\mu}_{eff}}{\partial y} \phi_7 + \frac{1}{2} \tilde{\mu}_{eff} \phi_6 \right) - 2\phi_{11} + \frac{2}{\mathrm{Fr}^2} \bar{\rho} - \frac{4}{3} \left(\bar{\rho} \frac{\partial \bar{k}}{\partial y} + \bar{k} \frac{\partial \bar{\rho}}{\partial y} \right) \tag{14}$$

Transport equation for thermal energy:

$$\frac{1}{Pr}\frac{\tilde{k}_{eff}}{\tilde{c}_p}\left(\frac{\partial^2\tilde{h}}{\partial x^2}+\frac{\partial^2\tilde{h}}{\partial y^2}\right)+\left[\frac{1}{Pr}\frac{\partial}{\partial x}\left(\frac{\tilde{k}_{eff}}{\tilde{c}_p}\right)-Re\frac{\partial\psi}{\partial y}\right]\frac{\partial\tilde{h}}{\partial x}+\left[\frac{1}{Pr}\frac{\partial}{\partial y}\left(\frac{\tilde{k}_{eff}}{\tilde{c}_p}\right)+Re\frac{\partial\psi}{\partial x}\right]\frac{\partial\tilde{h}}{\partial y}$$
$$=\frac{Re}{2\bar{\rho}}\left(\frac{\partial\psi}{\partial x}\frac{\partial\bar{p}}{\partial y}-\frac{\partial\psi}{\partial y}\frac{\partial\bar{p}}{\partial x}\right)-\phi_{12}-\frac{Re}{Fr^2}\frac{\partial\psi}{\partial x}-\frac{2}{3}Re\bar{k}\left(\frac{\partial\bar{\rho}}{\partial y}\frac{\partial\psi}{\partial x}-\frac{\partial\bar{\rho}}{\partial x}\frac{\partial\psi}{\partial y}\right), \tag{15}$$

where k_{eff} is the effective thermal conductivity and c_p is the constant-pressure specific heat. The boundary conditions on the static enthalpy are determined through the temperature and heat flux distributions specified at the boundaries.

Transport equation for turbulent kinetic energy:

$$\tilde{\mu}_k\left(\frac{\partial^2\bar{k}}{\partial x^2}+\frac{\partial^2\bar{k}}{\partial y^2}\right)+\left(\frac{\partial\tilde{\mu}_k}{\partial x}-Re\frac{\partial\psi}{\partial y}\right)\frac{\partial\bar{k}}{\partial x}+\left(\frac{\partial\tilde{\mu}_k}{\partial y}+Re\frac{\partial\psi}{\partial x}\right)\frac{\partial\bar{k}}{\partial y}$$
$$=Re\left[\frac{\phi_{13}}{Re}+\frac{2}{3}\frac{\bar{k}}{\bar{\rho}}\left(\frac{\partial\bar{\rho}}{\partial y}\frac{\partial\psi}{\partial x}-\frac{\partial\bar{\rho}}{\partial x}\frac{\partial\psi}{\partial y}\right)+\bar{\rho}\epsilon_d+\frac{2\tilde{\mu}}{Re}\left(\frac{\partial\sqrt{\bar{k}}}{\partial y}\right)^2\right], \tag{16}$$

where ϵ_d is the turbulent dissipation. Quantities used in the Jones-Launder two-equation turbulence model are defined in Equation (18).

Transport equation for turbulent dissipation:

$$\tilde{\mu}_\epsilon\left(\frac{\partial^2\epsilon_d}{\partial x^2}+\frac{\partial^2\epsilon_d}{\partial y^2}\right)+\left(\frac{\partial\tilde{\mu}_\epsilon}{\partial x}-Re\frac{\partial\psi}{\partial y}\right)\frac{\partial\epsilon_d}{\partial x}+\left(\frac{\partial\tilde{\mu}_\epsilon}{\partial y}+Re\frac{\partial\psi}{\partial x}\right)\frac{\partial\epsilon_d}{\partial y}=Re\left\{-\frac{C_1\epsilon_d}{\bar{k}}\frac{\phi_{13}}{Re}+\frac{2}{3}\frac{C_1\epsilon_d}{\bar{\rho}}\right.$$
$$\left.\left[\frac{\partial\psi}{\partial x}\frac{\partial\bar{\rho}}{\partial y}-\frac{\partial\bar{\rho}}{\partial x}\frac{\partial\psi}{\partial y}\right]-\frac{2\tilde{\mu}\tilde{\mu}_t}{\bar{\rho}^3Re^2}\left[\frac{\partial^3\psi}{\partial y^3}-\frac{2}{\bar{\rho}}\frac{\partial\bar{\rho}}{\partial y}\frac{\partial^2\psi}{\partial y^2}+\frac{2}{\bar{\rho}^2}\frac{\partial\psi}{\partial y}\left(\frac{\partial\bar{\rho}}{\partial y}\right)^2-\frac{1}{\bar{\rho}}\frac{\partial\psi}{\partial y}\frac{\partial^2\bar{\rho}}{\partial y^2}\right]^2+\frac{C_2f_2\bar{\rho}\epsilon_d^2}{\bar{k}}\right\} \tag{17}$$

Jones-Launder turbulence-model relations:

$$\left.\begin{aligned}
&f_2=1-0.3e^{-R_t^2},\ \tilde{\mu}_t=\tilde{\mu}c_\mu f_\mu R_t\\
&f_\mu=\exp\left[\frac{-2.5}{1+R_t/50}\right],\ \tilde{\mu}_k=\tilde{\mu}+\lambda_k\tilde{\mu}_t\\
&\tilde{\mu}_\epsilon=\tilde{\mu}+\lambda_\epsilon\tilde{\mu}_t,\ \tilde{\mu}_{eff}=\tilde{\mu}+\tilde{\mu}_t\\
&\frac{\tilde{k}_{eff}}{\tilde{c}_p}=\frac{\tilde{k}_{mol}}{\tilde{c}_p}+\tilde{\mu}_t\frac{Pr}{Pr_t},\ R_t=Re\frac{\bar{\rho}\bar{k}^2}{\tilde{\mu}\epsilon_d}\\
&\lambda_k=1,\ \lambda_\epsilon=0.9091,\ Pr=0.72,\ Pr_t=0.9\\
&C_1=1.44,\ C_2=1.92,\ c_\mu=0.09
\end{aligned}\right\} \tag{18}$$

Either the turbulent kinetic energy and turbulent dissipation or their normal derivatives are specified at the boundaries.

The system of equations is completed with the equations of state,

$$p = 2\rho \left(\frac{\gamma - 1}{\gamma}\right) \tilde{h} \tag{19}$$

$$\tilde{h} = \tilde{c}_p \tilde{T}, \tag{20}$$

where γ is the ratio of specific heats and T is the static temperature, and with the temperature variation of the transport properties given by Worsøe-Schmidt and Leppert[12],

$$\tilde{\mu} = \left(\frac{\tilde{h}}{\tilde{h}_o}\right)^{0.67} \tag{21}$$

$$\tilde{k}_{th} = \left(\frac{\tilde{h}}{\tilde{h}_o}\right)^{0.71} \tag{22}$$

Equations (10) through (22) contain the following parameters which appear as a result of the normalization: $Re = \bar{\rho}_o \bar{V}_o \bar{D}/\bar{\mu}_o$, the Reynolds number; $Fr = \bar{V}_o/\sqrt{\bar{g}_o \bar{D}}$, the Froude number; and $Pr = \bar{c}_{p,o}\bar{\mu}_o/\bar{k}_{th,o}$, the Prandtl number. The reference conditions, denoted by the subscript, o, are taken to be the centerline values at the jet exit plane.

For the case of incompressible flow, $\rho = 1$, and the previous equations become greatly simplified both in form and number. The transport equation for thermal energy, the equations of state, and the temperature variations of the transport properties are not needed. In addition, the Poisson equations for static pressure need not be solved simultaneously with the Poisson equation for stream function and the vorticity transport equation.

The Numerical Solution Scheme

To solve the flowfield equations for a planar jet discharging from a curved upper surface, as shown in Figure 1, a conformal mapping technique is used to map the irregular physical plane into a rectangular computational plane. The governing equations are then rewritten in terms of the computational plane coordinates and solved using finite-difference procedures. Since there is geometric symmetry with respect to the jet centerline, only half of the flowfield need be treated.

The mapping technique, which is an inverse procedure, was devised at MDRL by G.H. Hoffman and is best explained with reference to Figure 3. Initially, a finite-difference computational plane with coordinates (ξ, η) is specified. The distance between nodes in the ξ direction is a and in the η direction is b, where a and b are not necessarily equal. Stretching functions can then be applied in each coordinate direction:

$$\mu = f_1(\xi), \tag{23}$$

and

$$\lambda = f_2(\eta). \tag{24}$$

With these relations, a mapping plane (μ, λ) is determined which permits finer resolution of the flowfield in regions where the gradients of the computed variables are severe. Finally, a conformal mapping given by

$$\mu + i\lambda = F(x + iy) \tag{25}$$

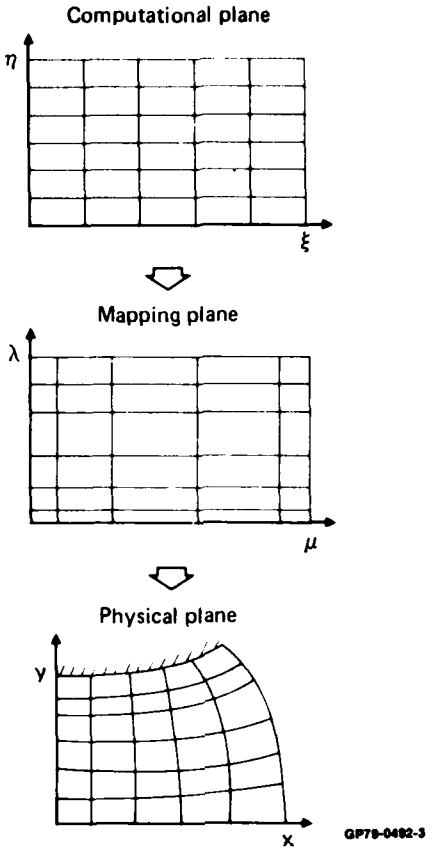

Figure 3. Inverse conformal mapping with stretching.

is introduced which specifies the physical plane (x, y). Since the mapping [Equation (25)] holds, it follows that both x and y obey Laplace's equation with coordinate stretching.

$$\frac{d\xi}{d\mu}\frac{\partial}{\partial\xi}\left(\frac{d\xi}{d\mu}\frac{\partial y}{\partial\xi}\right) + \frac{d\eta}{d\lambda}\frac{\partial}{\partial\eta}\left(\frac{d\eta}{d\lambda}\frac{\partial y}{\partial\eta}\right) = 0 \tag{26}$$

$$\frac{d\xi}{d\mu}\frac{\partial}{\partial\xi}\left(\frac{d\xi}{d\mu}\frac{\partial x}{\partial\xi}\right) + \frac{d\eta}{d\lambda}\frac{\partial}{\partial\eta}\left(\frac{d\eta}{d\lambda}\frac{\partial x}{\partial\eta}\right) = 0 \tag{27}$$

The boundary conditions imposed on Equations (26) and (27) follow from physical constraints when they are known at the boundaries, and from integration of the Cauchy-Riemann relations,

$$\frac{d\xi}{d\mu}\frac{\partial x}{\partial\xi} = \frac{d\eta}{d\lambda}\frac{\partial y}{\partial\eta}, \tag{28}$$

and

$$\frac{d\eta}{d\lambda}\frac{\partial x}{\partial\eta} = -\frac{d\xi}{d\mu}\frac{\partial y}{\partial\xi}, \tag{29}$$

when the x and y boundary distributions are not known.

The unique feature of the present mapping scheme is that instead of specifying the coordinate distributions in the physical plane and accepting whatever computational plane results, a numerically convenient computational plane is specified, and the corresponding coordinate distributions within the specified physical boundaries are computed. For this reason, the mapping scheme is an inverse procedure.

In the present analysis the mapping equations are discretized using conventional central-difference, finite-difference approximations to the derivatives. This discretization is not the case for the flowfield equations. The reason for this can be explained with reference to the following general form of the flowfield equations which appear in the analysis, where ϕ is an arbitrary flow variable, $\phi = \psi, \bar{p}, \omega, \tilde{h}, \bar{k}$, or ϵ_d:

$$\alpha \frac{\partial^2 \phi}{\partial \xi^2} + \gamma \frac{\partial \phi}{\partial \xi} + \beta \frac{\partial^2 \phi}{\partial \eta^2} + \delta \frac{\partial \phi}{\partial \eta} = \sigma. \tag{30}$$

The coefficients α, γ, β, and δ and the source term σ are functions of the flow variables.

The central-difference, finite-difference algorithm applied to Equation (30) provides diagonal dominance and thereby convergent solutions for only a limited range in the magnitudes of the coefficients γ and δ. This range is generally exceeded in the transport equations in which γ and δ contain the Reynolds number as a multiplicative factor. To ensure diagonal dominance for all values of γ and δ, Hoffman's augmented-central-difference algorithm[13] was applied to Equation (30). The central idea of this method can be explained by considering, for example, the derivative $\partial\phi/\partial\xi$. Using the point-of-the-compass notation shown in Figure 4 to designate the variable locations, this derivative can be evaluated at the central point P in terms of the adjacent east (E) and west (W) points with the following truncated Taylor-series representation and standard central-difference approximation to the first derivative:

$$\left.\frac{\partial \phi}{\partial \xi}\right|_P = \frac{\phi_E - \phi_W}{2a} - \left.\frac{a^2}{6}\frac{\partial^3 \phi}{\partial \xi^3}\right|_P - \left.\frac{a^4}{5!}\frac{\partial^5 \phi}{\partial \xi^5}\right|_P - \cdots \tag{31}$$

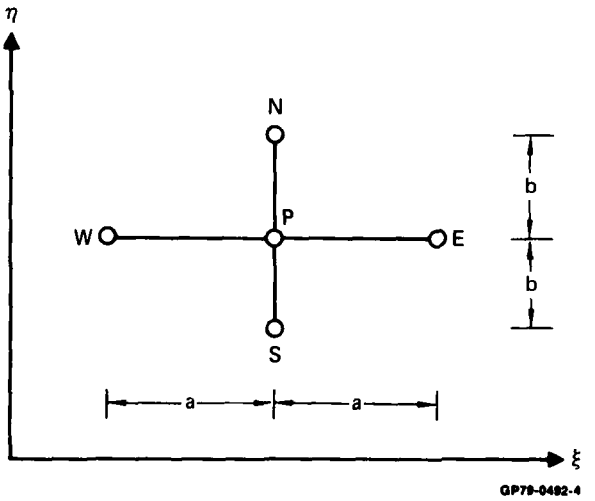

Figure 4. Five-point finite-difference stencil.

In the augmented-central-difference scheme, the derivative $\partial^3\phi/\partial\xi^3$ is retained and expressed in terms of lower-order derivatives by differentiating the governing transport equation with respect to ξ. The convective derivative $\partial\phi/\partial\eta$ is represented in an analogous fashion with the algorithm.

The finite-difference equations are solved using point relaxation. For each flow variable ϕ, a local residual is defined by $r_\phi = |\phi_{N+1} \quad \phi_N|$, where N is the iteration counter. Convergence is said to be achieved when $r_\phi < 10^{-6}$ everywhere in the flowfield.

The Computed Flowfields

Both incompressible and compressible flowfields have been calculated for the planar jet of Figure 1 using the computational region shown in Figure 5. The solution domain has a height H and a width W, where both dimensions are normalized by the jet width.

For the general case of compressible flow, the following boundary conditions are imposed: The vorticity, stream function, enthalpy, turbulent-kinetic-energy, and turbulent dissipation profiles are specified within the entering jet. On the upper surface, conditions result from the constraint of a no-slip, impermeable, isothermal wall; on the lower surface, conditions result from the constraint of a no-slip, impermeable, adiabatic wall. On the jet centerline the symmetry conditions are imposed, and at the right boundary the flow properties are taken to be uniform with respect to ξ, the transformed x coordinate. Pressure gradients at the boundaries are specified using Equations (13) and (14).

Flowfield calculations have been made for a range of the dimensionless parameters which define the problem, and representative solutions are shown in this section. Contour plots of the computed dimensionless variables are given in Figure 6 for the case of incompressible flow with H = 2, W = 3.68, and Re = 100 which were obtained with a 41 x 41 finite-difference grid. Computations have been carried out up to Re = 100 000, but since the truncation error of the finite-difference scheme is order Re^2h^2, where h = a = b, solutions for Re > 100 are not accurate with a 41 x 41 grid. This grid size was limited by the storage capacity of the CDC CYBER 175 used in the calculations. Future calculations will be performed on a CDC 7600, which has a larger storage capacity and will permit accurate computations at a higher Reynolds number.

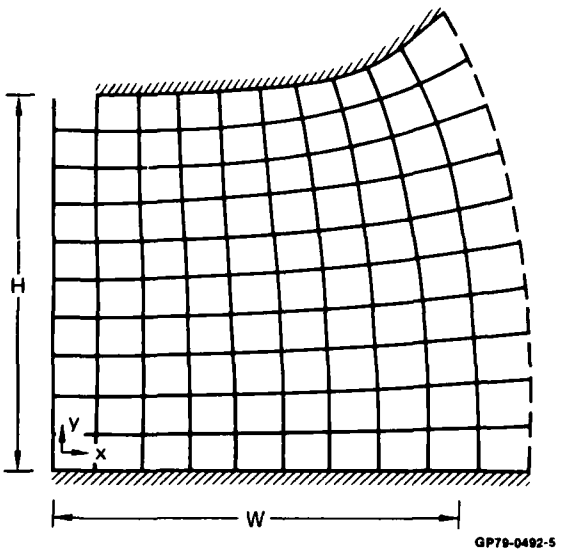

Figure 5. Definition of the computational region in the physical plane for a simulated fuselage undersurface in ground effect.

With reference to Figure 6, the stream function plot illustrates the turning of the jet and the mass entrainment. The vorticity distribution shows the convection of ω to the right and the development of the boundary layers on the upper wall (where separation occurs at the point of $\omega = 0$) and on the lower wall. The entrainment and recirculation zones are more clearly illustrated in the plots of the x- and y- velocity components. The static pressure plot shows an increase in p going toward the stagnation point where the value is set to unity. The distributions of the turbulent kinetic energy and the turbulent dissipation illustrate the decay in k and ϵ_d with distance from the jet exit plane. The length-scale contour, computed from the relation $L = k^{1.5}/\epsilon_d$, further reflects the relative turbulence levels in the flowfield.

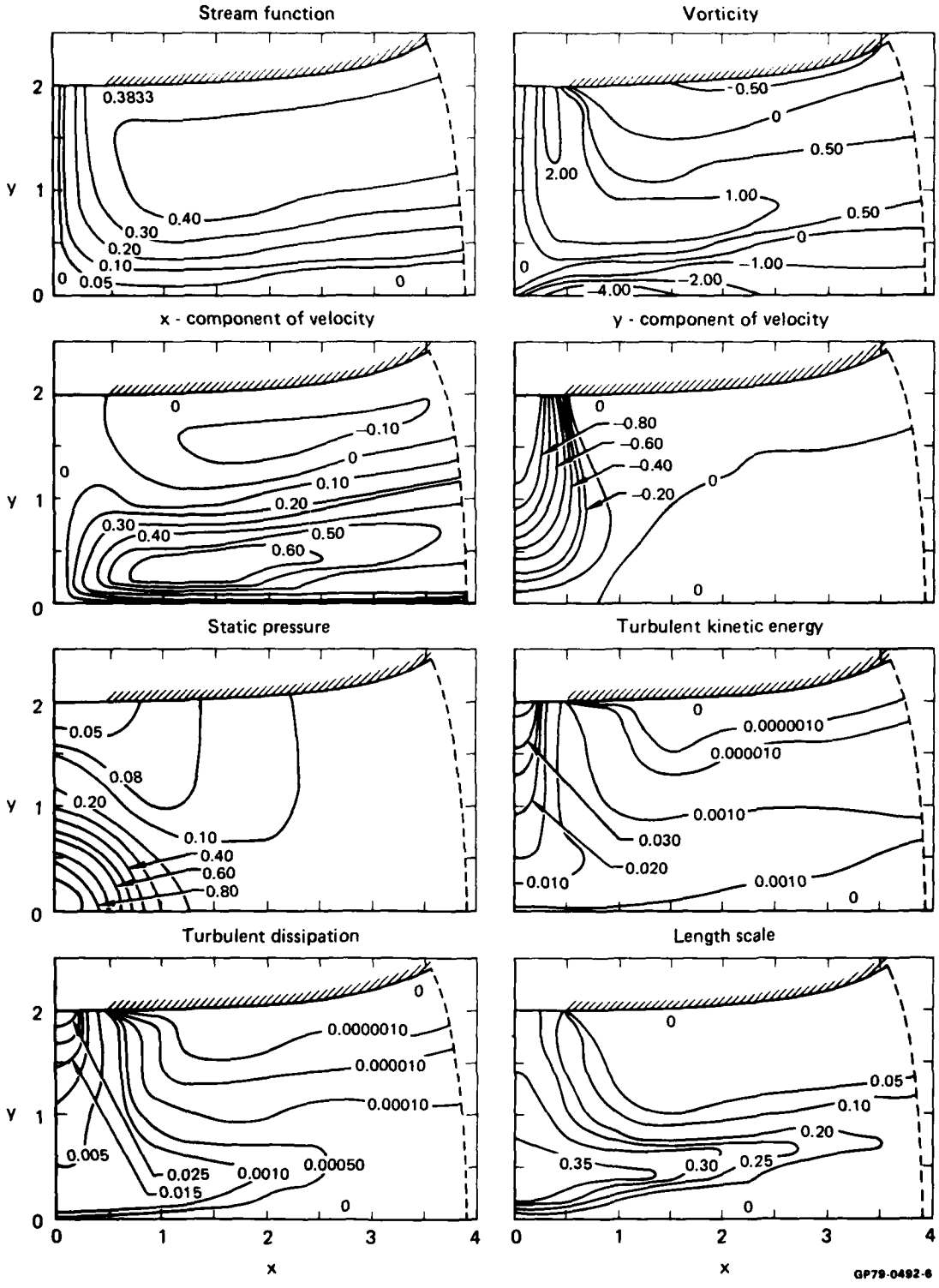

Figure 6. Property contours for the incompressible planar jet in ground effect (H = 2, W = 3.68, Re = 100).

Figure 7 shows the various contour plots calculated for the planar compressible jet in ground effect with H = 2, W = 3.68, Re = 100, Pr = 0.68, and Fr = 163. The stream-function, vorticity, and velocity-component profiles demonstrate the same basic form for the compressible case as for the incompressible case. The static pressure profile is also of the same form, but p at the stagnation point is not set to unity since its value is fixed by the equation of state. The static enthalpy contour shows the decay in temperature with distance from the jet core, and the density distribution reflects the variations in both the static enthalpy and pressure, with ρ increasing toward the upper boundary where the temperature is lowest. The k and ϵ_d profiles (the latter is not shown) have the same qualitative characteristics as for the case of incompressible flow, which is expected from the Morkovin hypothesis.

A comparison of the computed and measured pressure variations of the ground plane and simulated fuselage undersurface is shown in Figure 8. The data, which were obtained in a test program described in Reference 14, were measured at a Reynolds number of 130 000, while the computed values correspond to a Reynolds number of 100. Even with this large difference in Re, there is good agreement between the measured and computed centerline variations of the turbulent kinetic energy and velocity shown in Figure 9.

Analysis of Three-Dimensional Impinging Jets

In this section the procedure is described for computing the incompressible turbulent flowfield resulting from two interacting, initially axisymmetric jets with fountain formation as shown in Figure 2. Contour plots of the calculated flow variables are presented.

The Governing Equations

The time-averaged continuity and momentum equations which form the starting point in the three-dimensional, steady, incompressible flow analysis are Equations (1) and (2), which can be simplified with the condition of constant density. Turbulence closure is obtained by modeling the Reynolds stress term using the Glushko-Rubesin one-equation model for incompressible flow. A two-equation turbulence model is currently not used in the three-dimensional analysis because of storage limitations imposed by the CYBER 175 computer.

Equations (1) and (2) are expanded from tensor notation into cartesian coordinates (x, y, z) with the corresponding velocity components (u, v, w), but the equations are not solved in primitive-variable form. Rather, a potential-function/vorticity approach first proposed by Aregbesola and Burley[15] is adopted. In this technique, which is analogous to the stream-function/vorticity representation of the two-dimensional problem, the pressure is eliminated from the momentum equations in the formulation of a vorticity transport equation. The pressure field is then computed from a Poisson equation derived from the derivatives of the component momentum equations.

To identically satisfy the continuity condition, a scalar potential Φ and a vector potential A_i are introduced and the velocity field is given as

$$u_i = -\frac{\partial \Phi}{\partial x_i} + \epsilon_{ijk}\frac{\partial A_k}{\partial x_j}, \tag{32}$$

where ϵ_{ijk} is the alternating tensor. Hirasaki and Hellums[16] have shown that a unique vector potential A_i, within the gradient of an arbitrary harmonic function, exists such that

$$\frac{\partial A_i}{\partial x_i} = 0. \tag{33}$$

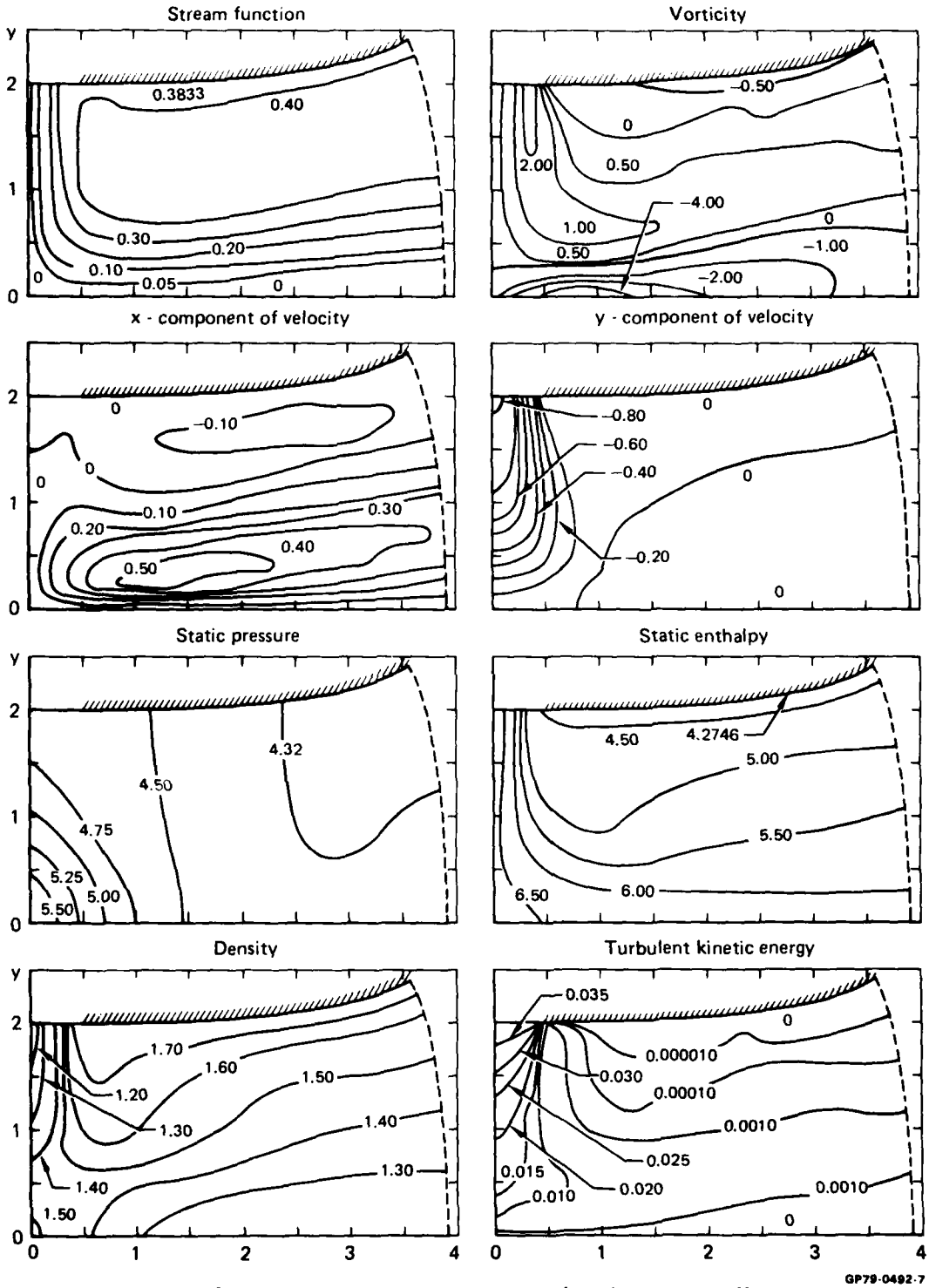

Figure 7. Property contours for the compressible planar jet in ground effect (H = 2, W = 3.68, Re = 100, Pr = 0.68, Fr = 163).

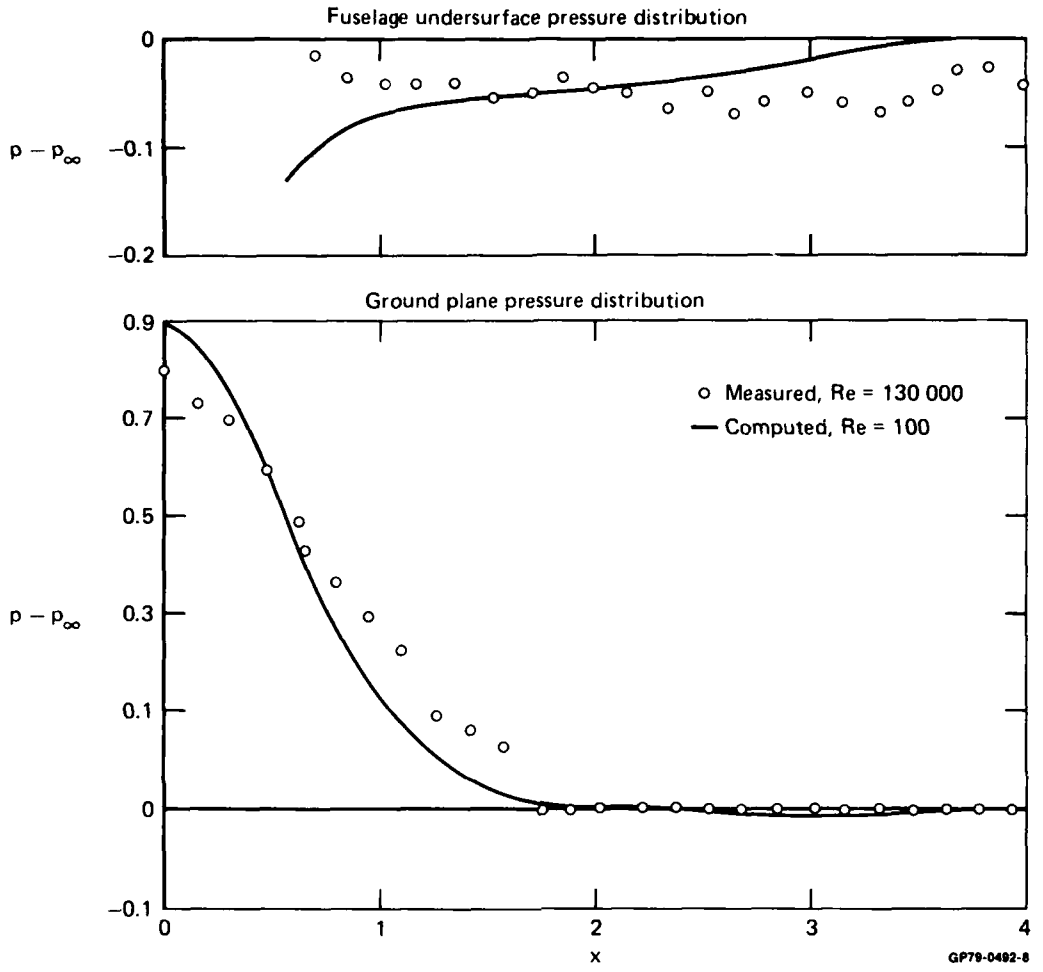

Figure 8. Comparison of experimental and theoretical pressure distributions for the incompressible planar jet in ground effect (H = 2, W = 3.68).

A differential equation for the vector potential is derived by taking the curl of Equation (32) and using Equation (33), which gives

$$\frac{\partial^2 A_i}{\partial x_j \partial x_j} = -\Omega_i , \tag{34}$$

where the vorticity is defined by

$$\Omega_i = \epsilon_{ijk} \frac{\partial u_k}{\partial x_j} . \tag{35}$$

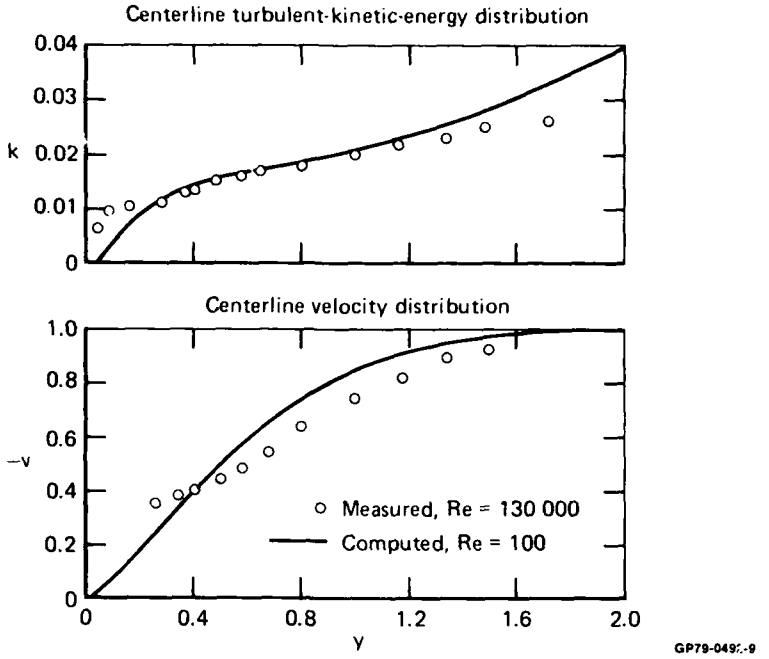

Figure 9. Comparison of experimental and theoretical centerline property distributions for the incompressible planar jet in ground effect (H = 2, W = 3.68).

A differential equation for the scalar potential is derived by taking the divergence of Equation (32),

$$\frac{\partial^2 \Phi}{\partial x_i \partial x_i} = 0. \tag{36}$$

The advantage of introducing a scalar potential is the convenience it offers in setting the boundary conditions on the velocity components. Since Equation (36) is independent of Reynolds number, it need be solved only once for a given geometry and set of boundary conditions.

The boundary values of the vorticity are evaluated from Equation (35), where u_i is calculated from Equation (32). The boundary conditions on A_i are chosen such that its tangential components are equal to zero; the conditions on the normal components are then determined by Equation (33). For a flat boundary the conditions become

$$\frac{\partial A_n}{\partial n} = 0, \; A_t = 0, \tag{37}$$

where n denotes the normal component and t the tangential. The normal velocity components are assumed to be known, and these values are used to compute the normal derivatives of the scalar potential on the boundary,

$$\frac{\partial \Phi}{\partial n} = n_j u_j. \tag{38}$$

The dimensionless governing equations in the present three-dimensional flow analysis are given below.
Poisson equation for scalar potential:

$$\frac{\partial^2\Phi}{\partial x^2} + \frac{\partial^2\Phi}{\partial y^2} + \frac{\partial^2\Phi}{\partial z^2} = 0 \tag{39}$$

Poisson equation for x component of vector potential:

$$\frac{\partial^2 A_x}{\partial x^2} + \frac{\partial^2 A_x}{\partial y^2} + \frac{\partial^2 A_x}{\partial z^2} = \Omega_x \tag{40}$$

Poisson equation for y component of vector potential:

$$\frac{\partial^2 A_y}{\partial x^2} + \frac{\partial^2 A_y}{\partial y^2} + \frac{\partial^2 A_y}{\partial z^2} = \Omega_y \tag{41}$$

Poisson equation for z component of vector potential:

$$\frac{\partial^2 A_z}{\partial x^2} + \frac{\partial^2 A_z}{\partial y^2} + \frac{\partial^2 A_z}{\partial z^2} = \Omega_z \tag{42}$$

Transport equation for x component of vorticity:

$$\begin{aligned}
[1+\epsilon(\bar{r})]\left(\frac{\partial^2\Omega_x}{\partial x^2} + \frac{\partial^2\Omega_x}{\partial y^2} + \frac{\partial^2\Omega_x}{\partial z^2}\right) &+ Re\left[\frac{1}{Re}\frac{\partial\epsilon(\bar{r})}{\partial x} - u\right]\frac{\partial\Omega_x}{\partial x} + Re\left[\frac{1}{Re}\frac{\partial\epsilon(\bar{r})}{\partial y} - v\right]\frac{\partial\Omega_x}{\partial y} \\
&+ Re\left[\frac{1}{Re}\frac{\partial\epsilon(\bar{r})}{\partial z} - w\right]\frac{\partial\Omega_x}{\partial z} = Re\left[\left(\frac{\partial v}{\partial y} + \frac{\partial w}{\partial z}\right)\Omega_x + \frac{\partial u}{\partial y}\frac{\partial w}{\partial x} - \frac{\partial u}{\partial z}\frac{\partial v}{\partial x}\right] \\
&+ \left[-\frac{\partial^2\epsilon(\bar{r})}{\partial x\partial y}\left(\frac{\partial w}{\partial x} + \frac{\partial u}{\partial z}\right) - 2\frac{\partial^2\epsilon(\bar{r})}{\partial y\partial z}\left(\frac{\partial w}{\partial z} - \frac{\partial v}{\partial y}\right) - \frac{\partial^2\epsilon(\bar{r})}{\partial y^2}\left(\frac{\partial w}{\partial y} + \frac{\partial v}{\partial z}\right)\right. \\
&- \frac{\partial\epsilon(\bar{r})}{\partial y}\left(\frac{\partial^2 w}{\partial x^2} + \frac{\partial^2 w}{\partial y^2} + \frac{\partial^2 w}{\partial z^2}\right) + \frac{\partial\epsilon(\bar{r})}{\partial z}\left(\frac{\partial^2 v}{\partial x^2} + \frac{\partial^2 v}{\partial y^2} + \frac{\partial^2 v}{\partial z^2}\right) \\
&\left. + \frac{\partial^2\epsilon(\bar{r})}{\partial x\partial z}\left(\frac{\partial v}{\partial x} + \frac{\partial u}{\partial y}\right) + \frac{\partial^2\epsilon(\bar{r})}{\partial z^2}\left(\frac{\partial w}{\partial y} + \frac{\partial v}{\partial z}\right)\right]
\end{aligned} \tag{43}$$

Transport equation for y component of vorticity:

$$[1+\epsilon(\bar{r})]\left(\frac{\partial^2\Omega_y}{\partial x^2} + \frac{\partial^2\Omega_y}{\partial y^2} + \frac{\partial^2\Omega_y}{\partial z^2}\right) + Re\left[\frac{1}{Re}\frac{\partial\epsilon(\bar{r})}{\partial x} - u\right]\frac{\partial\Omega_y}{\partial x} + Re\left[\frac{1}{Re}\frac{\partial\epsilon(\bar{r})}{\partial y} - v\right]\frac{\partial\Omega_y}{\partial y}$$

$$+ \mathrm{Re}\left[\frac{1}{\mathrm{Re}}\frac{\partial\epsilon(\bar{r})}{\partial z} - w\right]\frac{\partial\Omega_y}{\partial z} = \mathrm{Re}\left[\left(\frac{\partial u}{\partial x}+\frac{\partial w}{\partial z}\right)\Omega_y + \frac{\partial v}{\partial z}\frac{\partial u}{\partial y} - \frac{\partial v}{\partial x}\frac{\partial w}{\partial y}\right] + \left[\frac{\partial^2\epsilon(\bar{r})}{\partial x\partial y}\left(\frac{\partial w}{\partial y}+\frac{\partial v}{\partial z}\right)\right.$$

$$- \frac{\partial^2\epsilon(\bar{r})}{\partial y\partial z}\left(\frac{\partial v}{\partial x}+\frac{\partial u}{\partial y}\right) + \frac{\partial^2\epsilon(\bar{r})}{\partial x^2}\left(\frac{\partial w}{\partial x}+\frac{\partial u}{\partial z}\right) + \frac{\partial\epsilon(\bar{r})}{\partial x}\left(\frac{\partial^2 w}{\partial x^2}+\frac{\partial^2 w}{\partial y^2}+\frac{\partial^2 w}{\partial z^2}\right)$$

$$\left.\frac{\partial\epsilon(\bar{r})}{\partial z}\left(\frac{\partial^2 u}{\partial x^2}+\frac{\partial^2 u}{\partial y^2}+\frac{\partial^2 u}{\partial z^2}\right) - 2\frac{\partial^2\epsilon(\bar{r})}{\partial x\partial z}\left(\frac{\partial u}{\partial x}-\frac{\partial w}{\partial z}\right) - \frac{\partial^2\epsilon(\bar{r})}{\partial z^2}\left(\frac{\partial w}{\partial x}+\frac{\partial u}{\partial z}\right)\right] \tag{44}$$

Transport equation for z component of vorticity:

$$[1+\epsilon(\bar{r})]\left(\frac{\partial^2\Omega_z}{\partial x^2}+\frac{\partial^2\Omega_z}{\partial y^2}+\frac{\partial^2\Omega_z}{\partial z^2}\right) + \mathrm{Re}\left[\frac{1}{\mathrm{Re}}\frac{\partial\epsilon(\bar{r})}{\partial x} - u\right]\frac{\partial\Omega_z}{\partial x} + \mathrm{Re}\left[\frac{1}{\mathrm{Re}}\frac{\partial\epsilon(\bar{r})}{\partial y} - v\right]\frac{\partial\Omega_z}{\partial y}$$

$$+ \mathrm{Re}\left[\frac{1}{\mathrm{Re}}\frac{\partial\epsilon(\bar{r})}{\partial z} - w\right]\frac{\partial\Omega_z}{\partial z} = \mathrm{Re}\left[\left(\frac{\partial u}{\partial x}+\frac{\partial v}{\partial y}\right)\Omega_z + \frac{\partial w}{\partial x}\frac{\partial v}{\partial z} - \frac{\partial w}{\partial y}\frac{\partial u}{\partial z}\right] + \left[-\frac{\partial^2\epsilon(\bar{r})}{\partial x^2}\left(\frac{\partial v}{\partial x}+\frac{\partial u}{\partial y}\right)\right.$$

$$- \frac{\partial\epsilon(\bar{r})}{\partial x}\left(\frac{\partial^2 v}{\partial x^2}+\frac{\partial^2 v}{\partial y^2}+\frac{\partial^2 v}{\partial z^2}\right) - 2\frac{\partial^2\epsilon(\bar{r})}{\partial x\partial y}\left(\frac{\partial v}{\partial y}-\frac{\partial u}{\partial x}\right) + \frac{\partial\epsilon(\bar{r})}{\partial y}\left(\frac{\partial^2 u}{\partial x^2}+\frac{\partial^2 u}{\partial y^2}+\frac{\partial^2 u}{\partial z^2}\right)$$

$$\left.- \frac{\partial\epsilon^2(\bar{r})}{\partial x\partial z}\left(\frac{\partial w}{\partial y}+\frac{\partial v}{\partial z}\right) + \frac{\partial^2\epsilon(\bar{r})}{\partial y^2}\left(\frac{\partial v}{\partial x}+\frac{\partial u}{\partial y}\right) + \frac{\partial^2\epsilon(\bar{r})}{\partial y\partial z}\left(\frac{\partial w}{\partial x}+\frac{\partial u}{\partial z}\right)\right] \tag{45}$$

Transport equation for turbulent kinetic energy:

$$[1+\epsilon(\lambda\bar{r})]\left(\frac{\partial^2 k}{\partial x^2}+\frac{\partial^2 k}{\partial y^2}+\frac{\partial^2 k}{\partial z^2}\right) + \mathrm{Re}\left[\frac{1}{\mathrm{Re}}\frac{\partial\epsilon(\lambda\bar{r})}{\partial x} - u\right]\frac{\partial k}{\partial x} + \mathrm{Re}\left[\frac{1}{\mathrm{Re}}\frac{\partial\epsilon(\lambda\bar{r})}{\partial y} - v\right]\frac{\partial k}{\partial y}$$

$$+ \mathrm{Re}\left[\frac{1}{\mathrm{Re}}\frac{\partial\epsilon(\lambda\bar{r})}{\partial z} - w\right]\frac{\partial k}{\partial z} = \frac{Ck\,[1+\epsilon(\lambda\bar{r})]}{L^2} - \epsilon(\bar{r})\left[2\frac{\partial u}{\partial x}\frac{\partial u}{\partial x} + \left(\frac{\partial v}{\partial x}+\frac{\partial u}{\partial y}\right)\frac{\partial u}{\partial y} + \left(\frac{\partial w}{\partial x}+\frac{\partial u}{\partial z}\right)\frac{\partial u}{\partial z}\right.$$

$$\left. + \left(\frac{\partial v}{\partial x}+\frac{\partial u}{\partial y}\right)\frac{\partial v}{\partial x} + 2\frac{\partial v}{\partial y}\frac{\partial v}{\partial y} + \left(\frac{\partial w}{\partial y}+\frac{\partial v}{\partial z}\right)\frac{\partial v}{\partial z} + \left(\frac{\partial w}{\partial y}+\frac{\partial u}{\partial z}\right)\frac{\partial w}{\partial x} + \left(\frac{\partial w}{\partial y}+\frac{\partial v}{\partial z}\right)\frac{\partial w}{\partial y} + 2\frac{\partial w}{\partial z}\frac{\partial w}{\partial z}\right]. \tag{46}$$

where

$$\epsilon(\bar{r}) = H(\bar{r})\alpha\bar{r} \tag{47}$$

AD-A079 115 NAVAL AIR DEVELOPMENT CENTER WARMINSTER PA F/G 1/3
PROCEEDINGS OF A WORKSHOP ON V/STOL AIRCRAFT AERODYNAMICS, VOLU--ETC(U)
MAY 79 C HENDERSON, M F PLATZER

UNCLASSIFIED NL

5 OF 7
AD
A079115

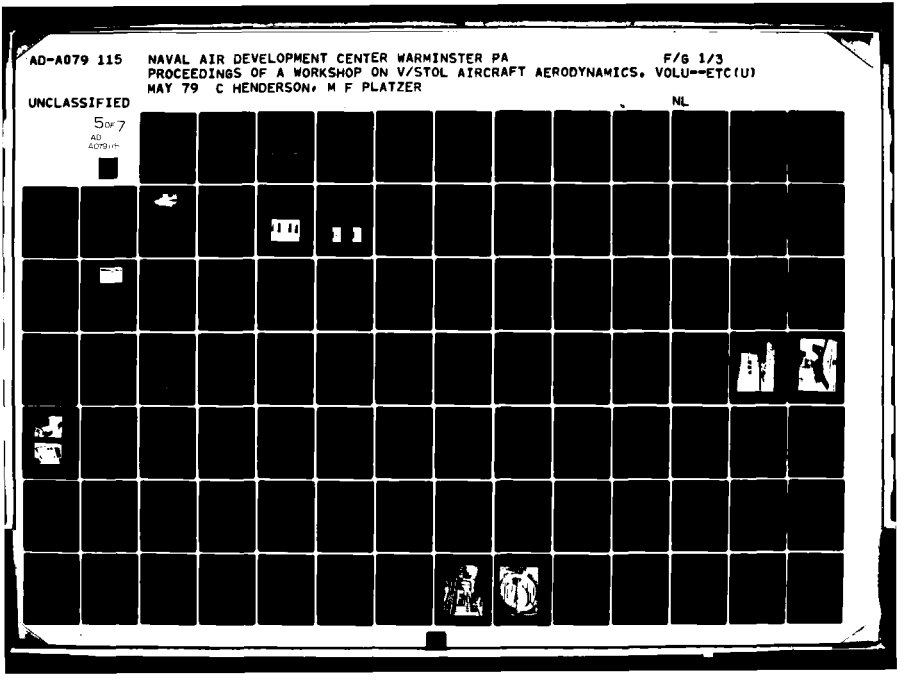

and

$$H(\bar{r}) = \begin{cases} \dfrac{\bar{r}}{\bar{r}_o} & 0 \leqslant \dfrac{\bar{r}}{\bar{r}_o} < 0.75 \\ \dfrac{\bar{r}}{\bar{r}_o} - \left(\dfrac{\bar{r}}{\bar{r}_o} - 0.75 \right)^2 & 0.75 \leqslant \dfrac{\bar{r}}{\bar{r}_o} < 1.25 \\ 1 & 1.25 \leqslant \dfrac{\bar{r}}{\bar{r}_o} < \infty \end{cases} . \tag{48}$$

The constants α, $\bar{r}_o$, C, and λ have the values of 0.2, 110, 3.93, and 0.4, respectively, and the Reynolds number of the turbulence $\bar{r}$ is defined by

$$\bar{r} = \frac{\sqrt{k}\, L}{\nu} . \tag{49}$$

The length-scale distribution L must be specified throughout the flowfield.

The Reynolds number is based on jet centerline properties at the entrance plane to the solution domain.

The Numerical Solution Scheme

In the solution of the flowfield equations for two interacting, initially axisymmetric jets impinging perpendicularly on the ground, a conformal mapping is not required since the computational domain has no irregular boundaries. The governing equations can then be written in either one of the two forms given below.

Poisson equation:

$$\frac{\partial^2 \phi}{\partial x^2} + \frac{\partial^2 \phi}{\partial y^2} + \frac{\partial^2 \phi}{\partial z^2} = \sigma_1 \tag{50}$$

Transport equation:

$$\alpha \left(\frac{\partial^2 \phi}{\partial x^2} + \frac{\partial^2 \phi}{\partial y^2} + \frac{\partial^2 \phi}{\partial z^2} \right) + \mathrm{Re}\, \beta \frac{\partial \phi}{\partial x} + \mathrm{Re}\, \gamma \frac{\partial \phi}{\partial y} + \mathrm{Re}\, \delta \frac{\partial \phi}{\partial z} = \mathrm{Re}\, \sigma_2 + \sigma_3, \tag{51}$$

where ϕ denotes a general flow variable and $\alpha, \beta, \gamma, \delta, \sigma_1, \sigma_2$, and σ_3 denote general coefficients.

The Poisson equations are discretized using the conventional central-difference algorithm, but for the reason discussed in the section on the planar jet, the transport equations are discretized using the augmented-central-difference algorithm due to Hoffman[13].

The coupled system of equations is solved iteratively using Gauss-Seidel line relaxation, where optimum relaxation factors were determined on the basis of numerical experimentation. As in the planar flow analysis, the convergence criterion for each variable ϕ is based on a residual $r_\phi = |\phi_{N+1} - \phi_N| < 10^{-6}$, where N is the iteration counter.

The Computed Flowfields

Incompressible flowfields have been calculated for the three-dimensional jet configuration of Figure 2 using the computational domain shown in Figure 10. The dimensions of the solution domain are normalized by the jet diameter d at the entrance plane to the computational region. The top surface of the latter is taken to be at a distance H - h below the jet exit plane rather than at the exit plane in order to decrease the size of the computational region. Three of the side surfaces are jet symmetry planes; the additional symmetry-plane cut through the fountain (z = 0) is not made so that jets with unequal thrust levels can be treated later by the same computational scheme.

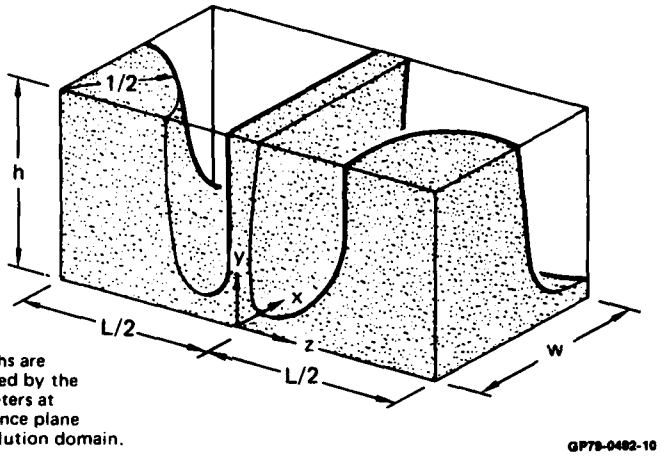

Figure 10. Definition of the computational region for two interacting, initially axisymmetric jets impinging perpendicularly on the ground with fountain formation.

Boundary conditions for this problem are determined from the no-slip, impermeable-wall constraints, symmetry conditions, and experimentally determined inflow/outflow velocity profiles. Turbulent-flow calculations were made with L = 3, h = 1, w = 1, and Re = 100. In setting the finite-difference grid, 9 nodal points were used in the x direction, 9 in the y direction, and 25 in the z direction. Use of the CDC 7600 in future work will permit a greater number of nodes and thereby accurate calculations at higher Reynolds numbers.

Figure 11 shows representative flowfield contours in various planes of the computational region shown in Figure 10. Plots such as these reflect the desired symmetry maintained in the calculations and provide the basic data required to evaluate entrainment rates and fountain properties. However, these planar contour plots, even in large number (which are easily generated using an automated plotting procedure), do not provide a simple visualization of the overall flow patterns.

The physical characteristics of the flowfield are best illustrated through three-dimensional, particle-pathline traces, as shown in Figure 12. These plots are constructed in the following manner: after obtaining a convergent solution of the Navier-Stokes equations, the three components of the velocity vector are stored as a function of position in the computational domain. A point is then selected at a desired position in the flowfield, and a particle is moved along the local velocity vector at that point over a small time increment. When the particle arrives at a new position, it is again directed along the local velocity vector. This procedure is repeated stepwise in time until the particle exits the computational domain. Figure 12 clearly shows the particle movement from the computational domain through the fountain and wall jet. The figure demonstrates the capability of the graphics routine to rotate the flowfield, which can be done about each of the three axes, so that the pathlines are visible from any desired angle.

A fourth year of ONR funding has been proposed by MDRL to extend the flowfield calculations of three-dimensional, turbulent impinging jets. Additional computations would be performed for equal-strength jets with normal impingement in addition to computations for the following cases: unequal strength jets, normal impingement; equal-strength jets, inclined impingement; unequal-strength jets, inclined impingement; and an axisymmetric jet in crossflow. The accuracy of the computed flowfields for interacting jets with normal impingement and fountain formation would be determined in part through comparisons with data which will be obtained in an experimental program funded by ONR and conducted by the Aerodynamics Department of McDonnell Aircraft Company.

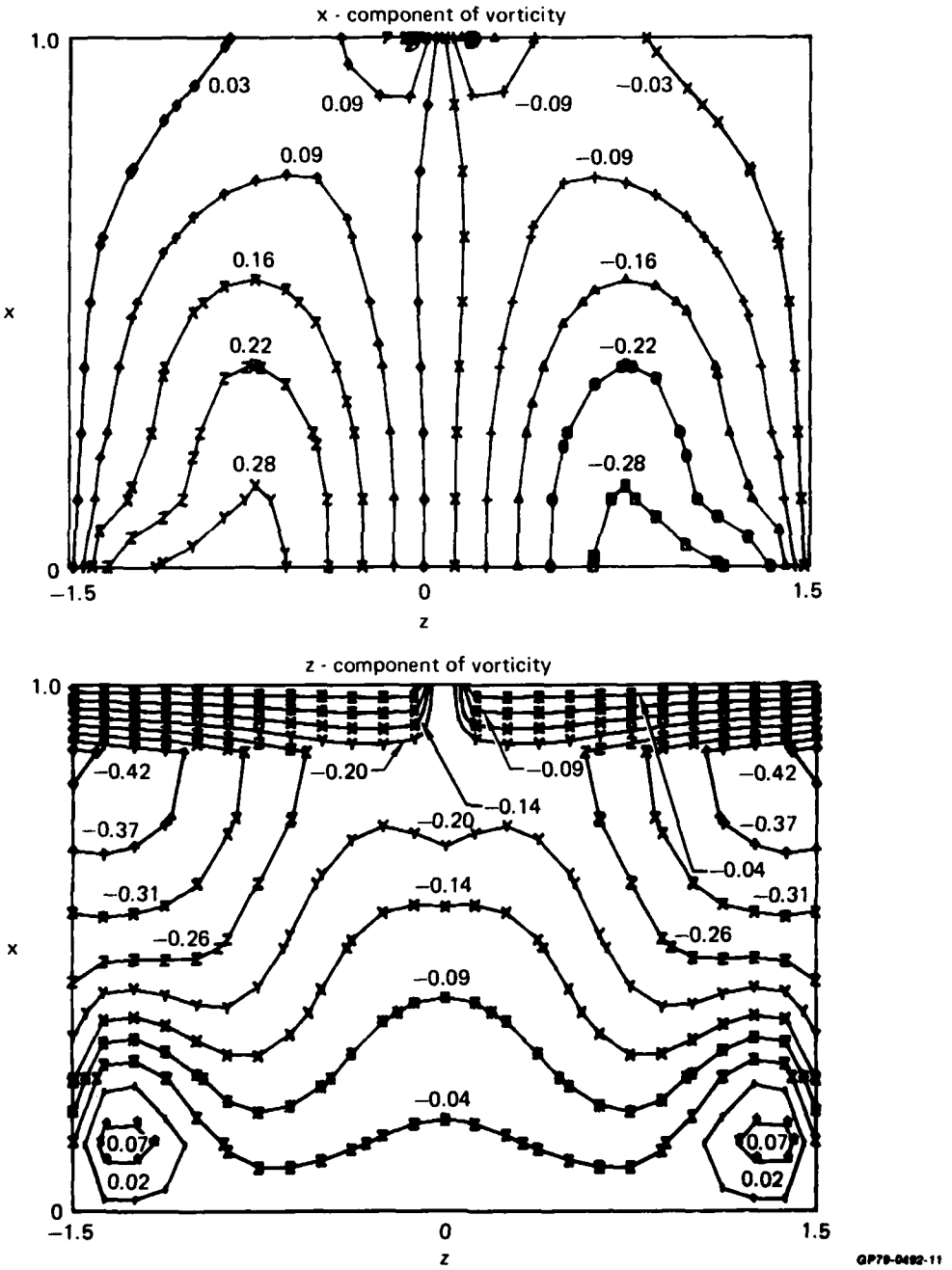

Figure 11. Representative contours on the plane (x, h, z) for the incompressible, *interacting jets in ground effect* (L = 3, h = 1, w = 1, Re = 100).

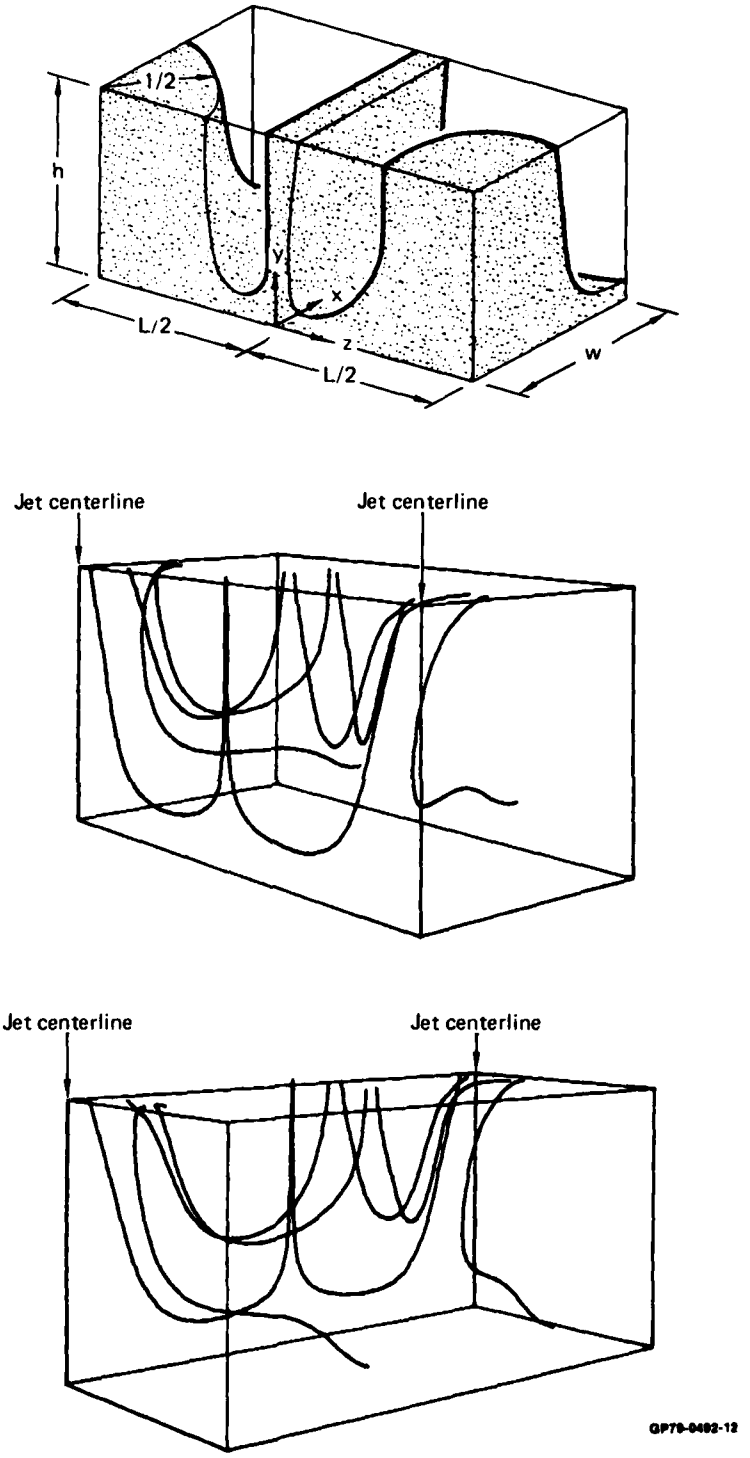

Figure 12. Representative particle pathlines for the incompressible interacting jets in ground effect (L = 3, h = 1, w = 1, Re = 100).

Conclusions

McDonnell Douglas Research Laboratories has developed an approach for predicting two- and three-dimensional turbulent impinging jet flows based on a finite-difference solution of the fully elliptic, time-averaged conservation equations of fluid mechanics in conjunction with a turbulence model.

In the first year of a contracted research program with ONR, MDRL developed a method for the computation of planar, incompressible, turbulent lift jets in the proximity of airframe and ground surfaces. The equations are cast in terms of stream function and vorticity and are solved using an algorithm which provides convergent solutions for a wide range in Reynolds number. In the second year of the program, MDRL generalized the planar jet analysis to include the effects of compressibility. Comparisons between theory and experiment show reasonable agreement, although additional work is necessary to improve the turbulence modeling and a computer with storage capacity greater than the CYBER 175 is required to match test Reynolds numbers. A basic conclusion drawn from the planar-jet studies is that contouring base area away from lift nozzle exits and perhaps the use of nozzle exit extensions will significantly reduce aircraft undersurface suck-down loads.

In the third year of the ONR contract work, MDRL developed a procedure for the calculation of three-dimensional, incompressible, turbulent lift jets in ground effect, with emphasis on a configuration comprised of two interacting jets with fountain formation. The equations are solved using a potential-function/vorticity formulation and an augmented, finite-difference algorithm to ensure convergence at high Reynolds numbers. The computed flowfield, displayed using a computer graphics routine that constructs particle pathlines, demonstrates the expected qualitative behavior. However, additional computations and comparisons with data are required to quantitatively evaluate the procedure.

Further work has been proposed by MDRL under ONR contract to improve the accuracy, efficiency, and generality of the present approach for solution of the Navier-Stokes equations for impinging jets. As Walters and Henderson[2] state in their report "V/STOL Aerodynamics Technology Assessment": "From a heuristic point of view, computerized analysis and prediction techniques for V/STOL aircraft performance, particularly in the hovering mode, must eventually take into account the viscosity and turbulence effects inherent in the Navier-Stokes equations." While the Navier-Stokes analysis developed by MDRL cannot provide the flowfield associated with a complete VTOL aircraft in ground effect, it can provide useful information on the jet entrainment and fountain flow required in potential flow paneling methods that are used to represent complete aircraft configurations. Data of this type cannot always be obtained precisely through experiment. Moreover, the solution scheme described in this paper can be applied to a variety of other problems of interest in incompressible subsonic aerodynamics, such as flow in internal passages.

Acknowledgment

The authors acknowledge Mr. P.W. Bierdeman who wrote the computer graphics routine for constructing the three-dimensional pathlines.

References

1. *A. Rubel, Computations of Jet Impingement on a Flat Surface, AIAA Paper No. 78-207, 1978.*

2. *M. Walters and C. Henderson, V/STOL Aerodynamics Technology Assessment, Naval Air Development Center, Interim Report AIRTASK NO. A03V-320D/001 B/7F41-400-000, 15 May 1978.*

3. *A. Rubel, Computational Techniques for the Calculation of Inviscid Rotational Jet Impingement, AIAA Paper No. 78-1212, 1978.*

4. *M.W. Rubesin and W.C. Rose, The Turbulent Mean-Flow, Reynolds-Stress, and Heat-Flux Equations in Mass-Averaged Dependent Variables, NASA TM X-62, 248, March 1973.*

5. *A. Favre, Equations des Gaz Turbulents Compressibles, J. Mecan. 4, 361 (1965).*

6. *D.R. Kotansky and W.W. Bower, Viscous Flowfields and Airframe Forces Induced by Two-Dimensional Lift Jets in Ground Effect, Office of Naval Research Report ONR-CR215-246-1, March 1977.*

7. *W.W. Bower, Compressible Viscous Flowfields and Airframe Forces Induced by Two-Dimensional Lift Jets in Ground Effect, Office of Naval Research Report ONR-CR215-246-2, March 1978.*

8. *M. Wolfshtein, Convection Processes in Turbulent Impinging Jets, Report SF/R/2, Department of Mechanical Engineering, Imperial College of Science and Technology, November 1967.*

9. *M.W. Rubesin, A One-Equation Model of Turbulence for Use with the Compressible Navier-Stokes Equations, NASA TM X-73, 128, April 1976.*

10. *W.P. Jones and B.E. Launder, The Calculation of Low-Reynolds Number Phenomena with a Two-Equation Model of Turbulence, Int. J. Heat Mass Transfer 16, 1119 (1973).*

11. *K.N. Ghia, W.L.Hankey, Jr., and J.K. Hodge, Study of Incompressible Navier-Stokes Equations in Primitive Variables Using Implicit Numerical Technique, Proceedings of the AIAA 3rd Computational Fluid Dynamics Conference, June 1977, pp. 156-167.*

12. *P.M. Worsøe-Schmidt and G. Leppert, Heat Transfer and Friction for Laminar Flow of Gas in a Circular Tube at High Heating Rate, Int. J. Heat Mass Transfer 8, 1281 (1965).*

13. *G.H. Hoffman, Calculation of Separated Flows in Internal Passages, Proceedings of a Workshop on Prediction Methods for Jet V/STOL Propulsion Aerodynamics 1, 114 (1975).*

14. *D.R. Kotansky and W.W. Bower, A Basic Study of the VTOL Ground Effect Problem for Planar Flow, J. Aircraft 15, 214 (1978).*

15. *Y.A.S. Aregbesola and D.M. Burley, The Vector and Scalar Potential Method for the Numerical Solution of Two- and Three-Dimensional Navier-Stokes Equations, J. Comp. Phys. 24, 398 (1977).*

16. *G.J. Hirasaki and J.D. Hellums, Boundary Conditions on the Vector and Scalar Potentials in Viscous Three-Dimensional Hydrodynamics, Quart. Appl. Math. 28, 293 (1970).*

Appendix:
Definitions of Functions Appearing in the Governing Equations for Planar Compressible Flow

$$\phi_1 = \frac{1}{\bar{\rho}^2}\frac{\partial\psi}{\partial x}\left(\frac{\partial\bar{\rho}}{\partial x}\frac{\partial^2\psi}{\partial x\partial y} - \frac{\partial\bar{\rho}}{\partial y}\frac{\partial^2\psi}{\partial x^2}\right) - \frac{1}{\bar{\rho}^2}\frac{\partial\psi}{\partial y}\left(\frac{\partial\bar{\rho}}{\partial y}\frac{\partial^2\psi}{\partial x\partial y} - \frac{\partial\bar{\rho}}{\partial x}\frac{\partial^2\psi}{\partial y^2}\right) \tag{A-1}$$

$$\phi_2 = \frac{1}{\bar{\rho}}\left(\frac{\partial^2\tilde{\mu}_{eff}}{\partial x^2} - \frac{\partial^2\tilde{\mu}_{eff}}{\partial x\partial y}\right)\left(\frac{\partial^2\psi}{\partial y^2} - \frac{\partial^2\psi}{\partial x^2} - \frac{1}{\bar{\rho}}\frac{\partial\bar{\rho}}{\partial y}\frac{\partial\psi}{\partial y} + \frac{1}{\bar{\rho}}\frac{\partial\bar{\rho}}{\partial x}\frac{\partial\psi}{\partial x}\right) + \frac{2}{\bar{\rho}}\frac{\partial^2\tilde{\mu}_{eff}}{\partial x\partial y}$$

$$\left(\frac{1}{\bar{\rho}}\frac{\partial\bar{\rho}}{\partial y}\frac{\partial\psi}{\partial x} + \frac{1}{\bar{\rho}}\frac{\partial\bar{\rho}}{\partial x}\frac{\partial\psi}{\partial y} - 2\frac{\partial^2\psi}{\partial x\partial y}\right) + \frac{2}{\bar{\rho}^2}\frac{\partial\tilde{\mu}_{eff}}{\partial x}\left\{\left(\frac{2}{\bar{\rho}}\frac{\partial\bar{\rho}}{\partial x}\frac{\partial\bar{\rho}}{\partial y} - \frac{\partial^2\bar{\rho}}{\partial x\partial y}\right)\frac{\partial\psi}{\partial y} + \frac{\partial\bar{\rho}}{\partial y}\frac{\partial^2\psi}{\partial x\partial y} - \frac{\partial\bar{\rho}}{\partial x}\frac{\partial^2\psi}{\partial y^2}\right.$$

$$\left. + \left[\frac{\partial^2\bar{\rho}}{\partial y^2} - \frac{2}{\bar{\rho}}\left(\frac{\partial\bar{\rho}}{\partial y}\right)^2\right]\frac{\partial\psi}{\partial x}\right\} + \frac{2}{\bar{\rho}^2}\frac{\partial\tilde{\mu}_{eff}}{\partial y}\left\{\left(\frac{2}{\bar{\rho}}\frac{\partial\bar{\rho}}{\partial x}\frac{\partial\bar{\rho}}{\partial y} - \frac{\partial^2\bar{\rho}}{\partial x\partial y}\right)\frac{\partial\psi}{\partial x} + \frac{\partial\bar{\rho}}{\partial x}\frac{\partial^2\psi}{\partial x\partial y} - \frac{\partial\bar{\rho}}{\partial y}\frac{\partial^2\psi}{\partial x^2}\right.$$

$$\left. + \left[\frac{\partial^2\bar{\rho}}{\partial x^2} - \frac{2}{\bar{\rho}}\left(\frac{\partial\bar{\rho}}{\partial x}\right)^2\right]\frac{\partial\psi}{\partial y}\right\} \tag{A-2}$$

$$\phi_3 = \frac{2}{3}\left[\frac{3}{\bar{\rho}}\frac{\partial^2\psi}{\partial x\partial y} - \frac{1}{\bar{\rho}^2}\left(2\frac{\partial\bar{\rho}}{\partial x}\frac{\partial\psi}{\partial y} + \frac{\partial\bar{\rho}}{\partial y}\frac{\partial\psi}{\partial x}\right)\right] \tag{A-3}$$

$$\phi_4 = \frac{8}{3\bar{\rho}^2}\left[\frac{2}{\bar{\rho}}\left(\frac{\partial\bar{\rho}}{\partial x}\right)^2 + \frac{2}{\bar{\rho}}\left(\frac{\partial\bar{\rho}}{\partial y}\right)^2 - \frac{\partial^2\bar{\rho}}{\partial x^2} - \frac{\partial^2\bar{\rho}}{\partial y^2}\right]\frac{\partial\psi}{\partial y} + \frac{8}{3\bar{\rho}}\left(\frac{\partial^3\psi}{\partial y^3} + \frac{\partial^3\psi}{\partial x^2\partial y} - \frac{2}{\bar{\rho}}\frac{\partial\bar{\rho}}{\partial x}\frac{\partial^2\psi}{\partial x\partial y}\right.$$

$$\left. - \frac{2}{\bar{\rho}}\frac{\partial\bar{\rho}}{\partial y}\frac{\partial^2\psi}{\partial y^2}\right) + \frac{2}{3}\frac{\partial\omega}{\partial y} \tag{A-4}$$

$$\phi_5 = \frac{1}{\bar{\rho}}\left(\frac{\partial^2\psi}{\partial y^2} - \frac{\partial^2\psi}{\partial x^2} + \frac{1}{\bar{\rho}}\frac{\partial\bar{\rho}}{\partial x}\frac{\partial\psi}{\partial x} - \frac{1}{\bar{\rho}}\frac{\partial\bar{\rho}}{\partial y}\frac{\partial\psi}{\partial y}\right) \tag{A-5}$$

$$\phi_6 = \frac{8}{3\bar{\rho}^2}\left[-\frac{2}{\bar{\rho}}\left(\frac{\partial\bar{\rho}}{\partial x}\right)^2 - \frac{2}{\bar{\rho}}\left(\frac{\partial\bar{\rho}}{\partial y}\right)^2 + \frac{\partial^2\rho}{\partial x^2} + \frac{\partial^2\bar{\rho}}{\partial y^2}\right]\frac{\partial\psi}{\partial x} + \frac{8}{3\bar{\rho}}\left(\frac{2}{\bar{\rho}}\frac{\partial\bar{\rho}}{\partial x}\frac{\partial^2\psi}{\partial x^2} - \frac{\partial^3\psi}{\partial x^3} + \frac{2}{\bar{\rho}}\frac{\partial\bar{\rho}}{\partial y}\frac{\partial^2\psi}{\partial x\partial y}\right.$$

$$\left. - \frac{\partial^3\psi}{\partial x\partial y^2}\right) - \frac{2}{3}\frac{\partial\omega}{\partial x} \tag{A-6}$$

$$\phi_7 = \frac{2}{3}\left[-\frac{3}{\bar{\rho}}\frac{\partial^2\psi}{\partial x\partial y} + \frac{1}{\bar{\rho}^2}\left(2\frac{\partial\bar{\rho}}{\partial y}\frac{\partial\psi}{\partial x} + \frac{\partial\bar{\rho}}{\partial x}\frac{\partial\psi}{\partial y}\right)\right] \tag{A-7}$$

$$\phi_8 = \left\{\left[\frac{3}{\bar\rho}\left(\frac{\partial\bar\rho}{\partial x}\right)^2 \frac{\partial^2\bar\rho}{\partial x^2} + \frac{3}{\bar\rho}\left(\frac{\partial\bar\rho}{\partial y}\right)^2 - 3\frac{\partial^2\bar\rho}{\partial y^2}\right]\frac{2}{\bar\rho^3}\frac{\partial\bar\rho}{\partial y} + \left[\frac{\partial^3\bar\rho}{\partial x^2\partial y}\right.\right.$$
$$\left.\left. + \frac{\partial^3\bar\rho}{\partial y^3} - \frac{4}{\bar\rho}\frac{\partial\bar\rho}{\partial x}\frac{\partial^2\bar\rho}{\partial x\partial y}\right]\frac{1}{\bar\rho^2}\right\}\frac{\partial\psi}{\partial x} + \left[\frac{\partial^2\bar\rho}{\partial x\partial y} - \frac{2}{\bar\rho}\frac{\partial\bar\rho}{\partial x}\frac{\partial\bar\rho}{\partial y}\right]\frac{2}{\bar\rho^2}\left(\frac{\partial^2\psi}{\partial x^2} - \frac{\partial^2\psi}{\partial y^2}\right)$$
$$\left\{\left[\frac{3}{\bar\rho}\left(\frac{\partial\bar\rho}{\partial x}\right)^2 - 3\frac{\partial^2\bar\rho}{\partial x^2} + \frac{3}{\bar\rho}\left(\frac{\partial\bar\rho}{\partial y}\right)^2 - \frac{\partial^2\bar\rho}{\partial y^2}\right]\frac{2}{\bar\rho^3}\frac{\partial\bar\rho}{\partial x} - \left[\frac{\partial^3\bar\rho}{\partial x\partial y^2}\right.\right.$$
$$\left.\left. + \frac{\partial^3\bar\rho}{\partial x^3} - \frac{4}{\bar\rho}\frac{\partial\bar\rho}{\partial y}\frac{\partial^2\bar\rho}{\partial x\partial y}\right]\frac{1}{\bar\rho^2}\right\}\frac{\partial\psi}{\partial y} + \left\{\frac{2}{\bar\rho}\left[\left(\frac{\partial\bar\rho}{\partial x}\right)^2 - \left(\frac{\partial\bar\rho}{\partial y}\right)^2\right] - \frac{\partial^2\bar\rho}{\partial x^2}\right.$$
$$\left. + \frac{\partial^2\bar\rho}{\partial y^2}\right\}\frac{2}{\bar\rho^2}\frac{\partial^2\psi}{\partial x\partial y} + \frac{1}{\bar\rho^2}\frac{\partial\bar\rho}{\partial y}\left(\frac{\partial^3\psi}{\partial x\partial y^2} + \frac{\partial^3\psi}{\partial x^3}\right) - \frac{1}{\bar\rho^2}\frac{\partial\bar\rho}{\partial x}\left(\frac{\partial^3\psi}{\partial x^2\partial y} + \frac{\partial^3\psi}{\partial y^3}\right) \tag{A-8}$$

$$\phi_9 = \frac{1}{\bar\rho^2}\left(\frac{\partial\psi}{\partial x}\right)^2\left[\frac{2}{\bar\rho}\left(\frac{\partial\bar\rho}{\partial y}\right)^2 - \frac{\partial^2\bar\rho}{\partial y^2}\right] + \frac{1}{\bar\rho^2}\left(\frac{\partial\psi}{\partial y}\right)^2\left[\frac{2}{\bar\rho}\left(\frac{\partial\bar\rho}{\partial x}\right)^2 - \frac{\partial^2\bar\rho}{\partial x^2}\right]$$
$$+ \frac{2}{\bar\rho}\frac{\partial^2\psi}{\partial x\partial y}\left(\frac{\partial^2\psi}{\partial x\partial y} - \frac{1}{\bar\rho}\frac{\partial\bar\rho}{\partial x}\frac{\partial\psi}{\partial y} - \frac{1}{\bar\rho}\frac{\partial\bar\rho}{\partial y}\frac{\partial\psi}{\partial x}\right) + \frac{2}{\bar\rho^2}\frac{\partial\psi}{\partial x}\frac{\partial\psi}{\partial y}\left(\frac{\partial^2\bar\rho}{\partial x\partial y} - \frac{2}{\bar\rho}\frac{\partial\bar\rho}{\partial x}\frac{\partial\bar\rho}{\partial y}\right)$$
$$+ \frac{2}{\bar\rho}\left(\frac{1}{\bar\rho}\frac{\partial\bar\rho}{\partial x}\frac{\partial\psi}{\partial x}\frac{\partial^2\psi}{\partial y^2} + \frac{1}{\bar\rho}\frac{\partial\bar\rho}{\partial y}\frac{\partial^2\psi}{\partial x^2}\frac{\partial\psi}{\partial y} - \frac{\partial^2\psi}{\partial x^2}\frac{\partial^2\psi}{\partial y^2}\right) \tag{A-9}$$

$$\phi_{10} = \frac{1}{\bar\rho}\left[\left(\frac{\partial^2\psi}{\partial x\partial y} + \frac{1}{\bar\rho}\frac{\partial\bar\rho}{\partial y}\frac{\partial\psi}{\partial x} - \frac{1}{\bar\rho}\frac{\partial\bar\rho}{\partial x}\frac{\partial\psi}{\partial y}\right)\frac{\partial\psi}{\partial y} - \frac{\partial\psi}{\partial x}\frac{\partial^2\psi}{\partial y^2}\right] \tag{A-10}$$

$$\phi_{11} = \frac{1}{\bar\rho}\left[\left(\frac{\partial^2\psi}{\partial x\partial y} + \frac{1}{\bar\rho}\frac{\partial\bar\rho}{\partial x}\frac{\partial\psi}{\partial y} - \frac{1}{\bar\rho}\frac{\partial\bar\rho}{\partial y}\frac{\partial\psi}{\partial x}\right)\frac{\partial\psi}{\partial x} - \frac{\partial^2\psi}{\partial x^2}\frac{\partial\psi}{\partial y}\right] \tag{A-11}$$

$$\phi_{12} = \tilde\mu_{eff}\left\{\frac{4}{\bar\rho^2}\left(\frac{\partial^2\psi}{\partial x\partial y}\right)\left[\frac{\partial^2\psi}{\partial x\partial y} - \frac{1}{\bar\rho}\frac{\partial\bar\rho}{\partial y}\frac{\partial\psi}{\partial x} - \frac{1}{\bar\rho}\frac{\partial\bar\rho}{\partial x}\frac{\partial\psi}{\partial y}\right]\right.$$
$$+ \frac{4}{3}\frac{1}{\bar\rho^4}\left[\left(\frac{\partial\bar\rho}{\partial y}\right)^2\left(\frac{\partial\psi}{\partial x}\right)^2 + \left(\frac{\partial\bar\rho}{\partial x}\right)^2\left(\frac{\partial\psi}{\partial y}\right)^2 + \frac{\partial\bar\rho}{\partial x}\frac{\partial\bar\rho}{\partial y}\frac{\partial\psi}{\partial x}\frac{\partial\psi}{\partial y}\right]$$
$$\left. + \frac{1}{\bar\rho^4}\left(\frac{\partial\bar\rho}{\partial x}\frac{\partial\psi}{\partial x} - \frac{\partial\bar\rho}{\partial y}\frac{\partial\psi}{\partial y}\right)^2 + \frac{2}{\bar\rho^3}\left(\frac{\partial\bar\rho}{\partial x}\frac{\partial\psi}{\partial x} - \frac{\partial\bar\rho}{\partial y}\frac{\partial\psi}{\partial y}\right)\left(\frac{\partial^2\psi}{\partial y^2} - \frac{\partial^2\psi}{\partial x^2}\right) + \frac{1}{\bar\rho^2}\left(\frac{\partial^2\psi}{\partial x^2} - \frac{\partial^2\psi}{\partial y^2}\right)^2\right\} \tag{A-12}$$

$$\phi_{13} = \tilde{\mu}_{turb}\left\{ \frac{4}{\bar{\rho}^2}\left(\frac{\partial^2\psi}{\partial x\partial y}\right)\left[\frac{\partial^2\psi}{\partial x\partial y} - \frac{1}{\bar{\rho}}\frac{\partial\bar{\rho}}{\partial y}\frac{\partial\psi}{\partial x} - \frac{1}{\bar{\rho}}\frac{\partial\bar{\rho}}{\partial x}\frac{\partial\psi}{\partial y}\right]\right.$$

$$+\frac{4}{3}\frac{1}{\bar{\rho}^4}\left[\left(\frac{\partial\bar{\rho}}{\partial y}\right)^2\left(\frac{\partial\psi}{\partial x}\right)^2 + \left(\frac{\partial\bar{\rho}}{\partial x}\right)^2\left(\frac{\partial\psi}{\partial y}\right)^2 + \frac{\partial\bar{\rho}}{\partial x}\frac{\partial\bar{\rho}}{\partial y}\frac{\partial\psi}{\partial x}\frac{\partial\psi}{\partial y}\right]$$

$$\left.+\frac{1}{\bar{\rho}^4}\left(\frac{\partial\bar{\rho}}{\partial x}\frac{\partial\psi}{\partial x} - \frac{\partial\bar{\rho}}{\partial y}\frac{\partial\psi}{\partial y}\right)^2 + \frac{2}{\bar{\rho}^3}\left(\frac{\partial\bar{\rho}}{\partial x}\frac{\partial\psi}{\partial x} - \frac{\partial\bar{\rho}}{\partial y}\frac{\partial\psi}{\partial y}\right)\left(\frac{\partial^2\psi}{\partial y^2} - \frac{\partial^2\psi}{\partial x^2}\right) + \frac{1}{\bar{\rho}^2}\left(\frac{\partial^2\psi}{\partial x^2} - \frac{\partial^2\psi}{\partial y^2}\right)^2\right\} \quad \text{(A-13)}$$

A STUDY OF UPWASH IMPINGEMENT ON THE VEHICLE FOR A TWO JET TYPE A DESIGN*

William G. Hill Jr. and Richard C. Jenkins

Research Department
Grumman Aerospace Corporation
Bethpage, New York 11714

ABSTRACT

The impingement on the vehicle's lower surface of the upwash resulting from a pair of jets striking the ground was studied experimentally using both cylindrical bodies and aircraft models. Force measurements, flow field total pressure surveys, vehicle surface pressures, and flow field visualization techniques were used. Our primary finding is that the flow field and resulting forces on the vehicle can be very sensitive to the details of the body shape, jet spacing, and other geometric parameters.

* This work was partially supported by NASA Ames Contract NAS 2-10097, Mr. D. Ciffone, Contract monitor.

LIST OF SYMBOLS

D	nozzle exit diameter
F	interference force on vehicle (total force minus thrust)
H	nozzle height above ground
P	ground surface pressure
P_a	ambient pressure
P_j	total pressure at nozzle exit plane
P_s	local static pressure
P_t	local total pressure
q	local dynamic pressure
r	radius of fuselage lower corners
S	nozzle separation distance
T	jet thrust
W	width of fuselage cross section
x	coordinate parallel to ground and to stagnation line
y	coordinate parallel to ground, normal to stagnation line
σ	strake depth from fuselage bottom

INTRODUCTION

The interference forces that occur when a V/STOL aircraft operates in hover or during landing and takeoff form one of the most critical conditions for aircraft design. The fluid mechanics involved in the creation of these forces is quite complex, involving three-dimensional, turbulent flows and both free shear flows and fluid/surface interactions.

We have been engaged in research on the modeling and scaling of these In-Ground-Effect (IGE) flows for several years using a modular subdivision of the flow (Refs 1-9). During our investigation of these flows, we discovered that the IGE interference forces are very sensitive to the details of the fountain/aircraft interaction. Our introduction to this phenomena came from a series of tests involving Grumman's two-jet aircraft, designated design 698, shown in Fig. 1. Interference force tests for this class of vehicle had been conducted in our Research Laboratories. When our V/STOL project conducted similar tests in our Farmingdale V/STOL facility, the results were drastically different, as shown in Fig. 2. Not only the magnitude of the forces, but the entire qualitative behavior was different. An interesting addition to this situation was the fact that single jet force results from the two facilities agreed well (Fig. 3).

We searched through the many variables which appeared likely to cause these differences, such as nozzle pressure ratio, Reynolds number, etc. Surprisingly, we found the reason for the differences to be the sensitivity of the interference forces to the radius at the corners of the flat bottomed fuselage (see Fig. 4, from Ref. 10). This radius was different in the two models tested in the two facilities. When the models were made geometrically similar, the results from these two facilities and those from larger scale facility tests agreed quite well, as shown in Fig 5.

These results led us to undertake a further series of detailed experiments utilizing cylindrical bodies. We chose to utilize these cylindrical bodies (shown in Fig. 6) for detailed fountain/body interaction studies because model construction costs are lower than for aircraft models, and the effect of geometric variables can be more reliably identified. We believe that the general rules of behavior learned from these experiments apply equally to aircraft.

DETAILED EXPERIMENTS WITH CYLINDRICAL BODIES

The results of experiments with the cylindrical bodies showed two series of force curves. As seen in Fig. 7, bodies with corner radii greater than 0.188 W showed a progression of lower force with larger radius and had generally lower forces than the sharper ($r/W \leq 0.188$) corner bodies. The sharper corner bodies also formed a similar progression, but the character of the curves was changed. It was suspected that these differences were connected with separation of the flow around the lower surface corners. At a radius $r/W=0.188$, two force curves were discovered. Initially this appeared to be a hysteresis

phenomenon, but further investigation revealed that the force could be switched from one curve to the other by a temporary disturbance of the flow. Photos of the tuft flow visualization shown in Fig.8 confirmed the postulate that separation of the flow around the corners was the controlling factor in force variation.

Detailed pressure distributions on the body were also measured to aid in understanding and modeling these flows. Figure 9 shows the distrubution of pressure on both the upper and lower body surfaces. Several points should be noted here. First, when the flow around the lower corners is attached, the pressure is higher (more positive) on the bottom surface and lower (more negative) on the top surface than when the flow is attached. Both of these effects contribute towards the differences in forces for the separated vs attached conditions. For a body in an infinite stream we would expect the opposite result, --that is, more drag for a highly separated body.

Another point of interest on these curves is that the circumferential pressure distribution at the center of the body is positive, but it becomes negative as the flow expands around the corner. The total force obtained by integrating pressure on the lower surface is then the small difference between two large forces of opposite sign. This explains the sensitivity of the net force to changes in the corner radius. It also illustrates the importance of the upper surface pressures. Even though the peak magnitude of the upper surface pressure is much smaller than that on the lower surface, its integral forms a substantial portion of the force.

In what could be considered an extension of the corner radius study to sharper corners, we conducted a series of experiments using strakes along the full length of the body. The height of the strakes was varied, producing interference forces which increased with increasing strake depth, as shown in Fig. 10. Large differences in the forces occurred near the ground, but above H/D = 3 the differences were smaller. These experiments were done with a corner radius of r/W = 0.188. With the strakes level with the flat portion of the body (σ = 0 on Fig. 10) the force is somewhat larger than that on the sharp cornered body with no strakes.

EFFECT OF JET SPACING

Experiments on the effect of jet spacing were conducted using a Grumman two-jet aircraft model similar to that shown in Fig. 1 and fitted with strakes. Forces for spacings (S/D) of 3.1, 3.2 and 3.6 are quite close together, except that for a spacing of 3.1 there is a region of height above the ground ($2 < H/D < 2.5$) where large oscillations in the force occur. At a closer spacing (S/D) = 2.7) much lower forces occur, with a different form of variation with height above ground. The oscillations at a spacing of 3.1 are believed to come from an instability in the upwash flow, rather than from the fountain/body interaction. We are conducting further experiments in this area, and more detailed data and discussion will be presented in Ref.11.

REFERENCES

1. Hill, W.G. Jr. and Jenkins, R.C., "Recent Advances in the Study of V/STOL IGE Flow Fields," Eighth U.S. National Congress of Applied Mechanics, June 26-30, 1978, Univ. of California, Los Angeles.

2. Hill, W. G. Jr. and Jenkins. R. C., "Ground Impingement of a Fan Jet Exhaust Plume," Grumman Research Department Memorandum RM-653, May 1978.

3. Jenkins, R.C. and Hill, W.G. Jr., "Investigation of VTOL Upwash Flows Formed by Two Impinging Jets," Grumman Research Department Report RE-548, November 1977.

4. Siclari, M.J., Aidala, P., Hill, W.G., Jr., Jenkins, R.C., Migdal, D., and Wohllebe, F., "Development of a Methodology to Predict the Ground Footprint of V/STOL aircraft," Grumman Aerospace Corporation PDR 698-4, October 18, 1977.

5. Siclari, J.J., Hill, W.G., Jr., and Jenkins, R.C., "Investigation of Stagnation Line and Upwash Formation," AIAA Paper No. 77-615, AIAA/NASA, Ames V/STOL Conference, June 1977.

6. Hill, W.G., Jr., "Propulsion Induced Effects for VTOL Aircraft in Ground Effect," Project Squid Workshop on Engine-Airframe Integration, May 1977, at U.S. Naval Academy, Annapolis, Md. (also available as Grumman Research Department Memorandum, RM-634J, June 1977)

7. Greene, P.R., "Vertical Takeoff Lift Augmentation: the "Sculptured Deck" Concept:," J. Aircraft, Vol. 14, No. 2, pp 111-114, February 1977.

8. Hill, W.C., Jr., and Jenkins, R.C., "Experimental Investigation of Multiple Jet Impingement Flows Applicable to VTOL aircraft in Ground Effect," Grumman Research Department Memorandum RM-605, November 1975.

9. Hill, W.G., Luzzi, T., and Jenkins, R.C., "Experimental Studies of Multi-Jets in Ground Effect," Naval Air Systems Command Jet V/STOL Propulsion Aerodynamics Workshop, Arlington, Virginia, July 1975.

10. Wohllebe, F.A. and Migdal, D., "Some Basic Test Results of V/STOL Jet Induced Lift Effects in Hover," AIAA Paper 79-0339, January 1971.

11. Hill, W.G. Jr. and Jenkins, R.C., "Effect of Nozzle Spacing on Ground Interference Forces for a Two Jet V/STOL Aircraft," to be presented at the AIAA Aircraft Systems and Technology Meeting, August 20-22, 1979.

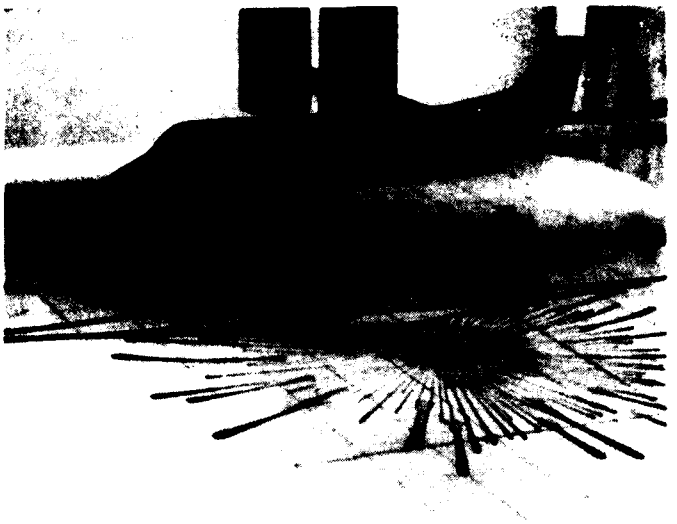

Figure 1 Research Model of Grumman 2 Jet V/STOL Aircraft

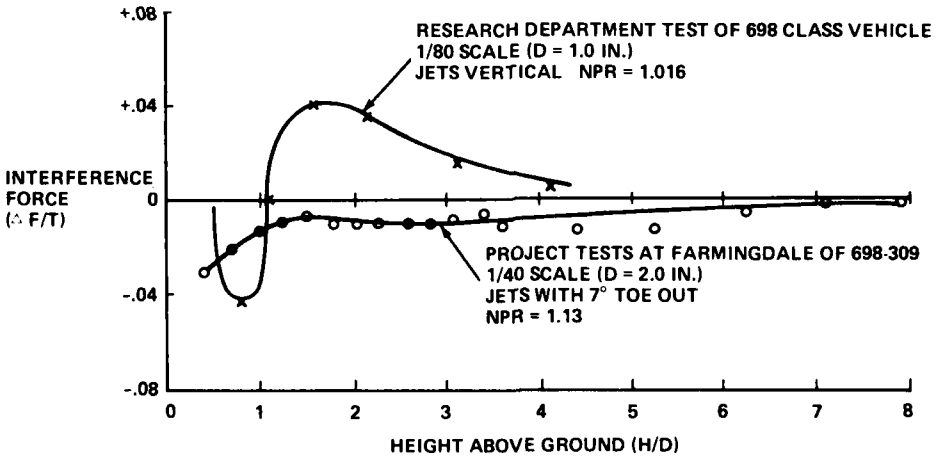

Figure 2 Differences in IGE Forces in Two Facilities

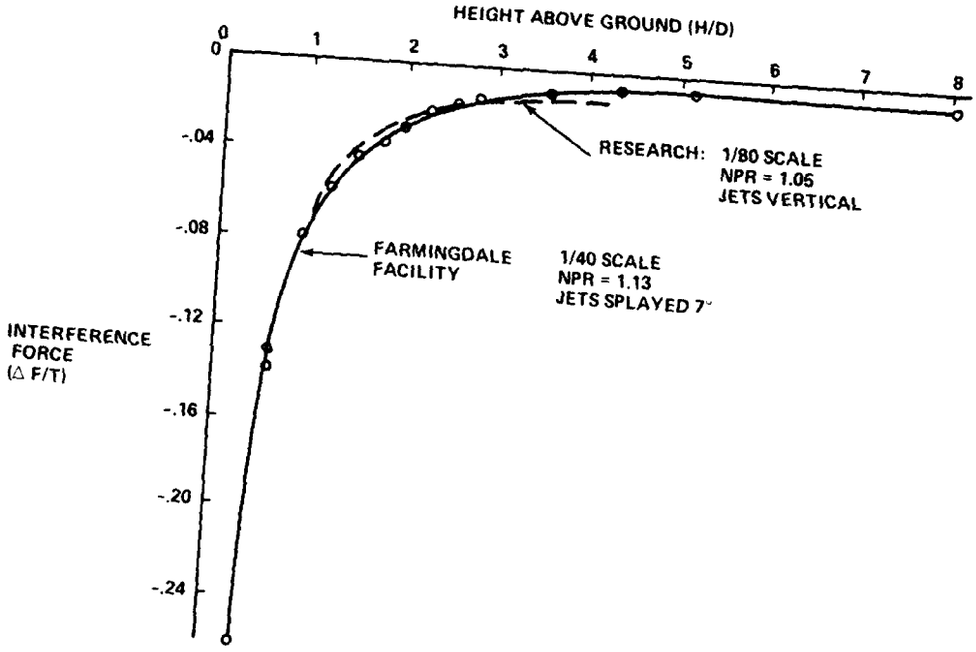

Figure 3 Single Jet Results Agree

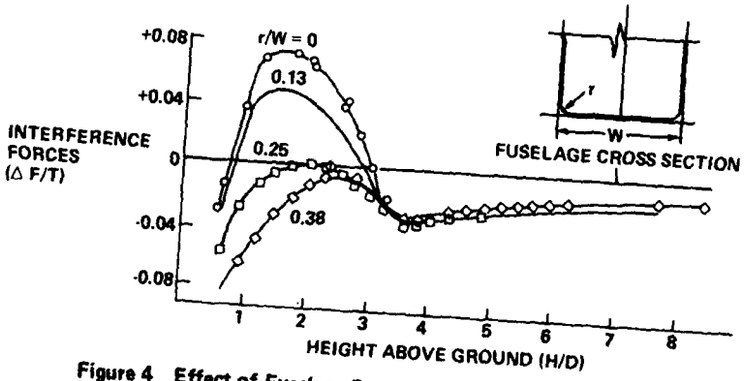

Figure 4 Effect of Fuselage Corner Radius on IGE Forces-698 Aircraft (From Ref. 10)

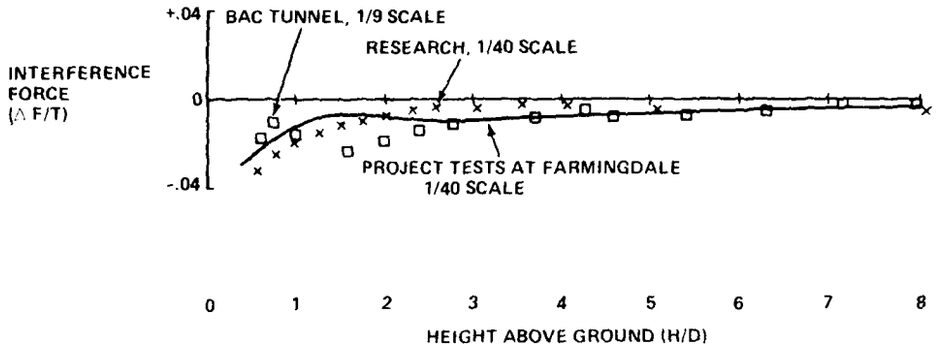

Figure 5 Agreement of Data From Differenct Facilities and Scale

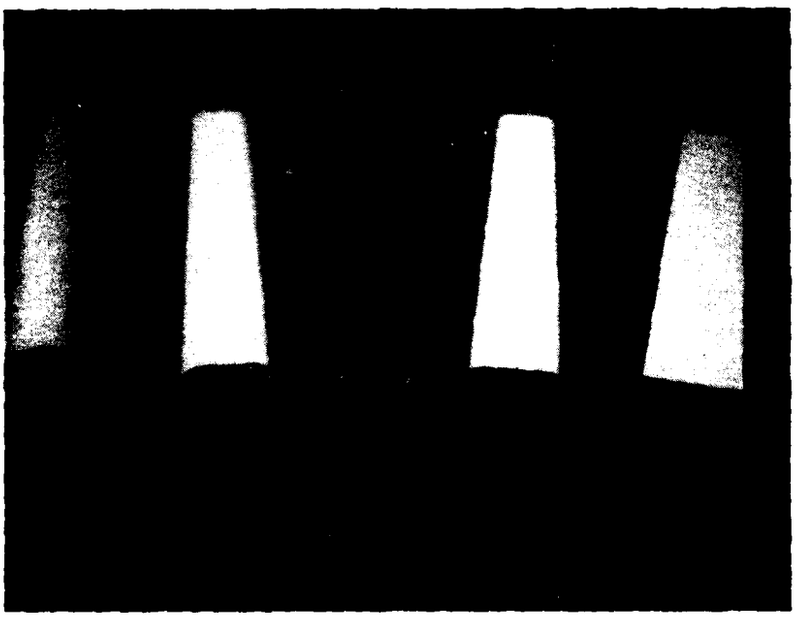

Figure 6 Cylindrical Bodies of Varying Cross Section

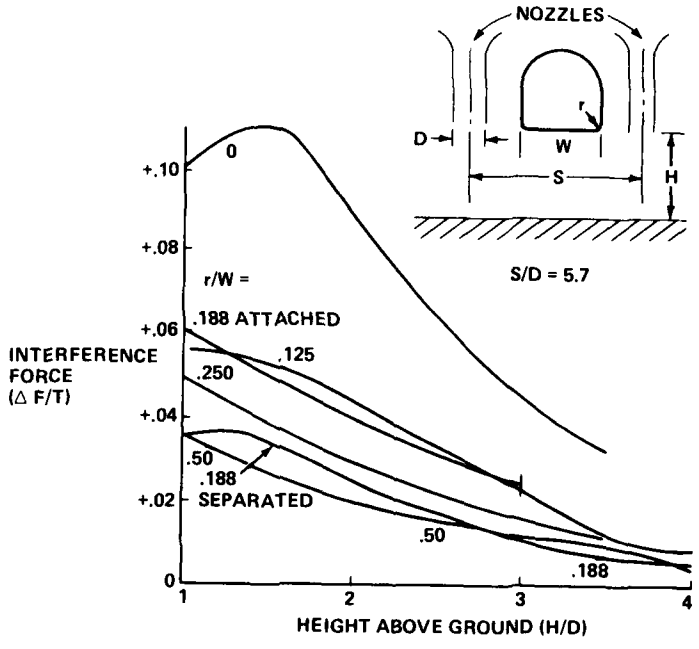

Figure 7 Effect of Corner Radius on IGE Forces – 2D Bodies

a. FLOW SEPARATED

b. FLOW ATTACHED

Figure 8 Flow Visualization of Upwash Impingement on 2-D Body

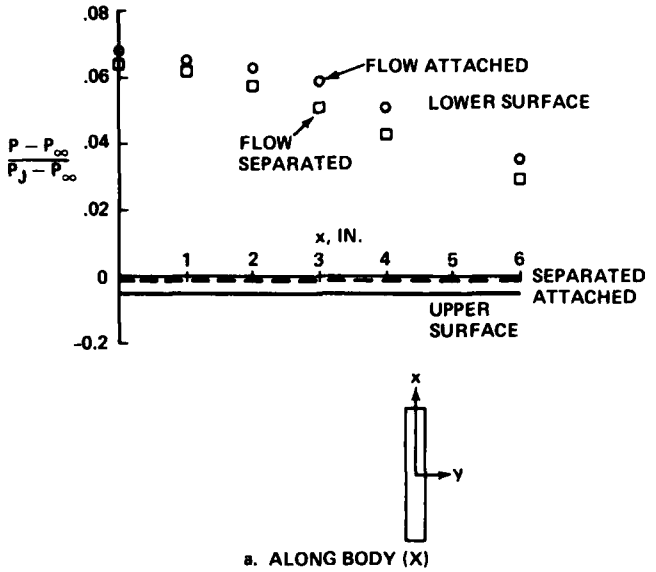

a. ALONG BODY (X)

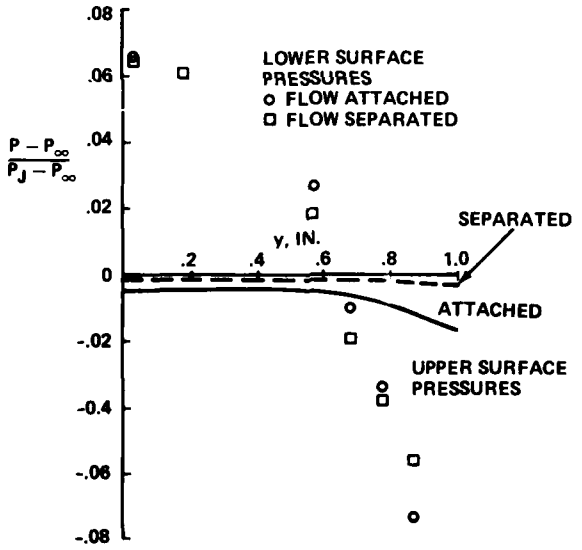

b. ACROSS BODY (Y)

Figure 9 Effect of Flow Spearation on Body Pressure Distribution r/W = .188

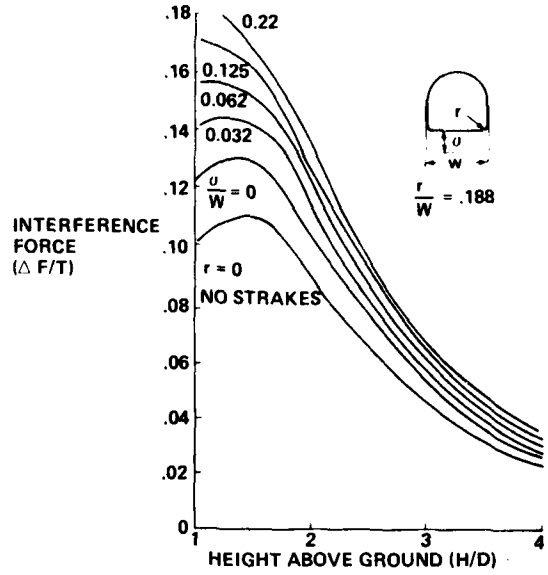

Figure 10 Effect of Strake Depth on IGE Forces – 2D Bodies

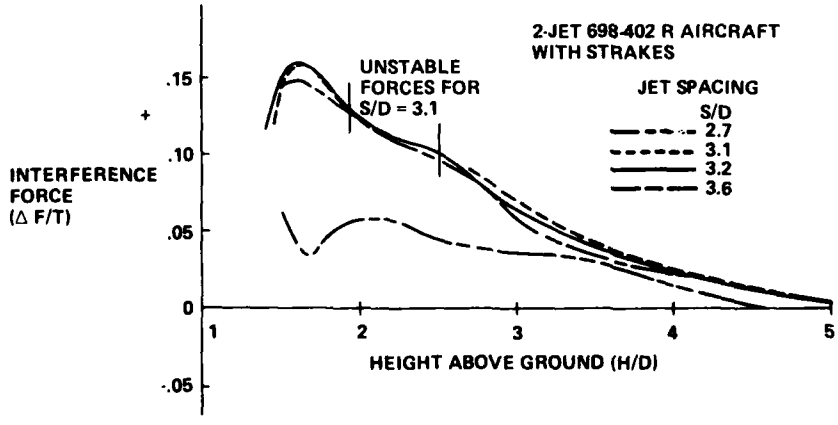

Figure 11 Variation of IGE Forces With Jet Spacing

INVESTIGATION OF THE EFFECTS OF CLOSE NOZZLE SPACING ON UPWASH AND FOUNTAIN FORMATION*

Richard C. Jenkins and William G. Hill, Jr.
Research Department
Grumman Aerospace Corporation
Bethpage, New York 11714

ABSTRACT

A program has been undertaken to extend the modular component modeling of multiple jet in-ground-effect flows to closer jet spacings. Experiments were conducted to determine where the mutual interference between the jets and the upwash caused errors in the modeling techniques and to provide data for making improvements to the modeling. Mechanisms for the upwash/jet interference have also been noted.

---

*A portion of this work was sponsored by NASA Ames under contract NAS 2-10097. The technical monitor is Mr. D. Ciffone.

LIST OF SYMBOLS

D	nozzle exit diameter
H	nozzle height above ground
M_r	flow momentum per radian
P	ground surface pressure
P_a	ambient pressure
P_{CS}	maximum ground pressure on center of stagnation line
P_j	total pressure at nozzle exit plane
P_{ji}	maximum ground pressure in jet impingement region
P_m	maximum ground pressure off center of stagnation line
P_s	local static pressure
P_t	local total pressure
q	local dynamic pressure
q_m	maximum dynamic pressure at given z
S	nozzle separation distance
x	coordinate parallel to ground and to stagnation line
y	coordinate parallel to ground, normal to stagnation line
$y_{.5}$	y-dimension on ground pressure profile for $P = \frac{1}{2}P_m$
$y_{.25}$	y-dimension on upwash dynamic pressure profile for $q = \frac{1}{4}q_m$
z	coordinate normal to ground

INTRODUCTION

Existing VTOL aircraft are severely restricted in performance, sacrificing either payload or range to achieve VTO capability. Performance limitations appear because the aircraft configuration and its propulsion system must be designed to hover close to the ground. Hovering in ground effect produces a strong interaction between the exhaust flow and the vehicle environment, leading to a much greater influence of propulsion-induced effects on VTOL designs than exists with conventional aircraft. Ground impingement of multiple jet exhausts from a VTOL aircraft produces ground effect forces that cannot be predicted by conventional aerodynamic analysis.

Reference 1 describes the development of techniques used by Grumman to predict pressure distributions and aerodynamic characteristics for V/STOL aircraft operating both in and out of ground effect. This method employs a modular approach, dividing the ground interaction flow field into several components that are treated separately in the analysis. Each module (e.g., exhaust-ground impingement, ground flows, fountain formation, and upwash decay) is modeled from existing experimental data and combined into a computer program to predict aircraft performance. The modular nature of the analysis allows improvement of computer predictions as more detailed experimental data becomes available for each module.

This paper describes experiments that were conducted to evaluate and modify

computer predictions of the upwash flow produced by dual jet impingement and presents some of the component modeling techniques that have been developed to describe the ground interaction flow field. The effects of close nozzle spacing are of particular interest for propulsion system design. Close engine spacing reduces the structural support requirements and the weight of internal cross-shafting needed to couple the engines together.

When the nozzles are spaced far apart, the upwash properties can be predicted in terms of wall jet properties, which are available in the literature for single jet impingement in terms of nozzle exhaust conditions. Hence the wall jet properties provide a vital link between nozzle exit conditions and upwash conditions. When the nozzles are close together this may no longer be true. If the upwash formation region occurs without any well developed wall jet region on the ground or if the incoming jets and the upwash collide and interfere with each other, it may not be possible to treat the components of the analysis independently. The work described in this paper represents a first step in modeling the ground impingement flow field produced by closely spaced jets.

DESCRIPTION OF EXPERIMENTAL EQUIPMENT

The ground interaction flow was produced by impingement of two axisymmetric, subsonic air jets from a low turbulence level settling chamber. The air supply was a $7\frac{1}{2}$ hp motor and centrifugal fan that provided 300 ft/sec velocity at the nozzle exits. The nozzles were 2.0 inch I.D. tubes with a constant diameter length of 11 inches, and had an elliptic entrance contour. They were installed eccentric to the center of discs that were mounted on the front face of the settling chamber (Fig. 1) so that separation of the nozzle centerlines could be varied from two to six diameters by disc rotation. All of the work described in this paper was conducted without any simulated fuselage structure near the nozzle exit plane that would deflect the upwash flow and affect nozzle exit conditions.

Ground impingement of the jets produces an upward flow such as shown in Fig. 2. The impinging flows spread radially along the ground, colliding midway between the jet impingement points to form a fan-shaped upwash. The radial flow pattern established on the ground appears to continue into the upwash (Ref. 2), so the flow divergence angle in the upwash is determined by the jet spacing (S). The velocity decay above the surface is determined by the divergence angle of the upwash and by turbulent mixing and entrainment of ambient air. The upwash is also affected by interaction with the shear layers surrounding the incident jets at large heights above ground. Interference between the upwash and the incident jets occurs at lower ground height (H) as the jet separation distance is decreased.

GROUND PLANE PRESSURE

Ground pressure data were obtained from a line of surface pressure taps that were aligned parallel to the stagnation line. Displacement of the ground plane

in a direction perpendicular to the line of taps provided a complete ground pressure survey with constant nozzle height above ground. Figure 3 shows the type of profile obtained from the pressure tap that passed through the two jet impact points and the centerline of the upwash. The maximum pressure in the jet impingement region (P_{j_1}) was always greater than the maximum pressure on the stagnation line (P_{CS}). The dimension $y_{.5}$ represents the half width of the pressure profile at half the maximum stagnation line pressure. Along the stagnation line the maximum ground pressure (P_m) decreases with distance (x) from the centerline.

Figure 4 shows the variation of centerline stagnation pressure with nozzle spacing for a nozzle height of three diameters above ground. The curve shown for comparison was predicted by assuming that the ground pressure on the center of the stagnation line is equal to the maximum pressure that would exist in a wall jet profile at the same radial location from one of the jets if the opposite jet were turned off. The predicted curve is given by the relation

$$\frac{P_{CS} - P_a}{P_j - P_a} = 13.78(S/D)^{-2.4} \tag{1}$$

where P_j is the stagnation pressure at the nozzle exit and P_a is ambient pressure. The constants in this equation were derived from pitot probe measurements taken in the wall jet formed by impingement of a single 4 inch diameter jet. Figure 4 shows that this analysis provides an adequate prediction of the centerline ground pressure for jet spacings of about 4 diameters or greater. At closer nozzle spacings the measured values fall below the predicted curve. This deviation should be expected because at S/D = 4 the stagnation line is two diameters from each jet impingement point, and this radial distance from a single impinging jet represents the beginning of the fully formed wall jet region. Hence the measured and predicted values begin to diverge, because at close jet spacings the ground flow approaching the stagnation line is not a fully formed wall jet.

The variation of maximum ground plane pressure along the stagnation line is shown in Fig. 5 for different nozzle spacings. For each spacing the maximum pressure at a given value of x ($P_m - P_a$) was normalized by the centerline level. When plotted versus x/s the data for each nozzle spacing fall close to the predicted profile

$$\frac{P_m - P_a}{P_{CS} - P_a} = \left[1 + \left(\frac{2x}{s}\right)^2\right]^{-2.2} \tag{2}$$

Eq. (2) was derived by assuming that on the stagnation line only the components of wall jet velocity normal to the stagnation line contribute to the stagnation line pressure. The constants in Eq. (2) were obtained from wall jet measurements with a single impinging jet.

Figure 6 shows the shape of the ground pressure profiles taken across the center of the stagnation line (illustrated in Fig. 3) for three nozzle heights above ground with a nozzle spacing of 4 diameters. For each ground height the pressures were normalized by the maximum value on the centerline and the distance y was normalized by the half-pressure dimension ($y_{.5}$). The data show that the profile shapes are essentially the same and can be represented by a Gaussian profile.

Integration of the ground pressure profile across the stagnation line provides a measure of the force exerted on the ground by the upwash, which can be related to the momentum of the upwash at ground level. Assume that the ground flow approaching the stagnation line from each of the impinging jets is an axisymmetric, radially expanding flow that exhibits constant momentum per radian in the wall jet. If flow momentum is conserved in the upwash formation region, the momentum per radian of the upwash flow normal to the ground at the stagnation line can be found by integrating the stagnation line pressure profile. Using a Gaussian equation to represent this profile, integration yields

$$M_r = S/2 \sqrt{\frac{\pi}{0.6932}} (P_{CS} - P_a) y_{.5} \qquad (3)$$

The momentum is given in lb/radian for pressures in psi and for $y_{.5}$ and S in inches.

Figure 7 shows the variation of maximum stagnation line pressure and half pressure width with nozzle height for S/D = 4. The maximum ground pressure decreases and the width increases as the ground height increases. This general trend appeared for all jet spacings. However, as seen in Fig. 8, the centerline upwash momentum per radian computed from Eq. (3) using the data in Fig. 7 is almost independent of nozzle height above ground. This result is important because it confirms one of the simplifying assumptions that were made for our computer program.

The dashed line in Fig. 8 represents twice the thrust per radian of one of the incident jets. Jet thrust was computed from velocity profiles that were taken at the nozzle exit plane. We conclude that flow momentum is conserved in the upwash formation region, and that the upwash momentum at ground level can be computed from the nozzle exit conditions.

UPWASH CHARACTERISTICS

Pressure probes used to determine flow properties in the upwash consisted of a 0.0625 inch OD Kiel probe and a 0.032 inch OD static probe. These two probes were spaced 0.15 inch apart so that the local dynamic pressure could be determined from the difference in measured pressures. Both probes were also read out separately, referenced to ambient pressure. Data were obtained by

traversing the probes through the upwash in the y-direction at various heights (z) above ground. Figure 9 shows data obtained from a probe traverse across the upwash centerline and the general characteristics exhibited at other values of H, z and S. Note that the static pressure was below ambient throughout the upwash and well beyond its edges. The dynamic pressure profile showed a Gaussian shape except at jet spacings below S/D = 3 where it was distorted by a lack of symmetry.

A series of such profiles were taken across the upwash centerline at the nozzle exit plane for different nozzle spacings and heights above ground. Figure 10 shows values of the maximum dynamic pressure q_m and $y_{.25}$, which represents the distance from the center of the upwash to the value of y for which $q/q_m = 0.25$ (the half-velocity point of the profile). Decreasing nozzle spacing increases the exit plane maximum dynamic pressure, with not much change in upwash width, until a maximum value is reached between 3 and 4 diameters. Further decrease in nozzle spacing brings about a decrease in exit plane dynamic pressure.

At low ground heights we encountered instabilities in the upwash at a nozzle spacing of 3 diameters. Such instabilities appeared as abnormally large fluctuations in probe readings. Kiel probe fluctuations in the upwash were generally found to be in the range of 10 to 20 percent. Unstable upwash conditions increased the magnitude to over 50 percent. Such conditions were encountered for S/D = 3 when H/D was decreased to less than $2\frac{1}{2}$. Corresponding fluctuations in ground plane pressure were noted under the same impingement conditions, indicating that the entire upwash flow was affected. Further decrease in jet spacing provided more stable upwash conditions at low ground heights, but the pressure profiles at the exit plane were somewhat unsymmetric.

Probe measurements were also taken at various heights above ground to define upwash properties for fixed impingement geometry. Figure 11 shows such data obtained from traverses across the center of the upwash with H/D = 2 and S/D = 4. For each height above ground (z) the profile was normalized by q_m and the probe distance relative to the centerline was normalized by $y_{.25}$. This plot shows that data taken at different heights above ground shows the same profile shape, which closely matches the Gaussian profile

$$q/q_m = e^{-1.386(y/y_{.25})^2} \tag{4}$$

Profiles of this shape were found for nozzle separation distances down to S/D = 3 providing the nozzle height above ground was not large enough to provide a significant interaction between the incident jets and the upwash. When the dynamic pressure profile shape is independent of height above ground, at any value of z the upwash properties on the centerline can be specified by the values of q_m/q_j and $y_{.25}$.

Figure 12 shows the dynamic pressure decay along the upwash centerline

for H/D = 4 at different nozzle spacings. For each spacing the values of q_m were normalized by the corresponding maximum ground pressure at the center of the stagnation line. The data are plotted versus $\frac{S/2}{S/2} + z$ to account for changes in the radial flow pattern in the upwash at different values of S. The data for S/D = 5 and 6 fall along a straight line, indicating that the dynamic pressure variation along the upwash centerline can be represented by a power law decay. As the spacing is decreased the data deviates from a straight line because of interference between the upwash and the incident jet flow at this nozzle height above ground.

CONCLUSIONS

For nozzle separation distances of 4 diameters or greater, the upwash produced by normal impingement of 2 parallel jets can be modeled by a modular analysis in which the components of the analysis are treated separately. For closer nozzle spacings this approach must be modified to account for interactions between the upwash and the impinging flow. At a nozzle spacing of 3 diameters, at low ground heights, we encountered instabilities both on the ground and in the upwash. At closer nozzle spacings the upwash was found to be unsymmetric, although the pressure profiles on the ground were almost symmetric. With nozzle spacings between 2 and 3 diameters the upwash appeared to form midway between the impinging jets but then deviate from the vertical flow direction because of interference with the shear layers surrounding the incident jets.

REFERENCES

1. Siclari, M. J., Hill, W. G., Jr., and Jenkins, R. C. "Investigation of Stagnation Line and Upwash Formation," AIAA Paper No. 77-615, AIAA/NASA Ames V/STOL Conference, June 1977.

2. Jenkins, R. C. and Hill, W. G., Jr., "Investigation of VTOL Upwash Flows Formed by Two Impinging Jets," Grumman Research Department Report RE-548, November 1977.

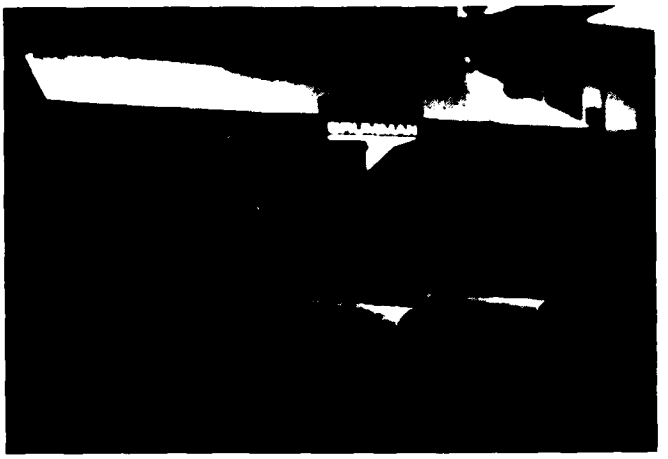

Figure 1 Nozzles and Settling and Chamber

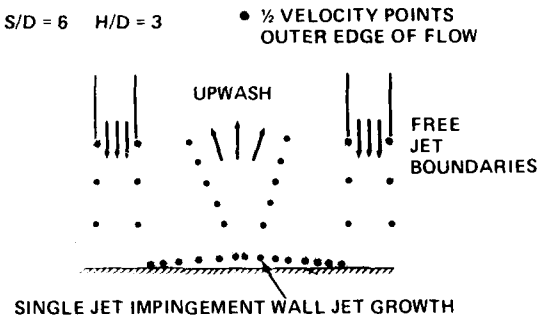

Figure 2 Upwash Dimensions Along Impingement Centerline

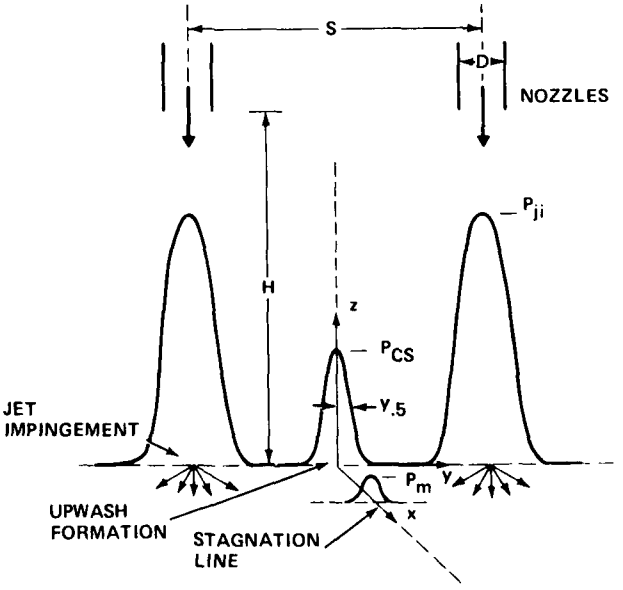

Figure 3 Pressure Profile for Ground Plane Impingement

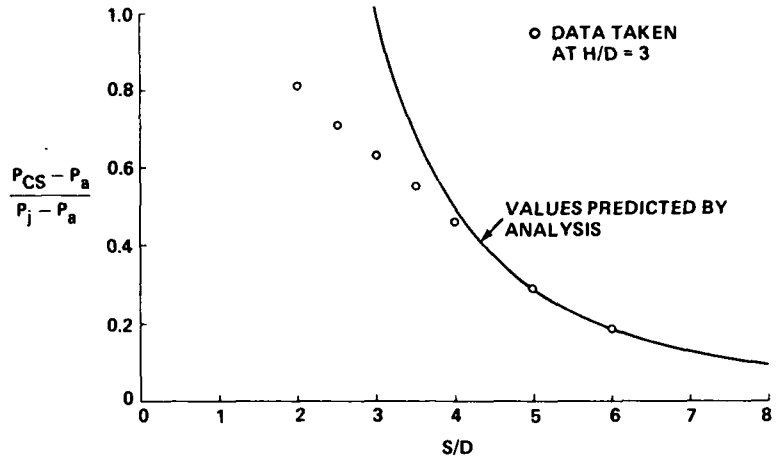

Figure 4 Effect of Jet Spacing on Maximum Stagnation Line Ground Pressure

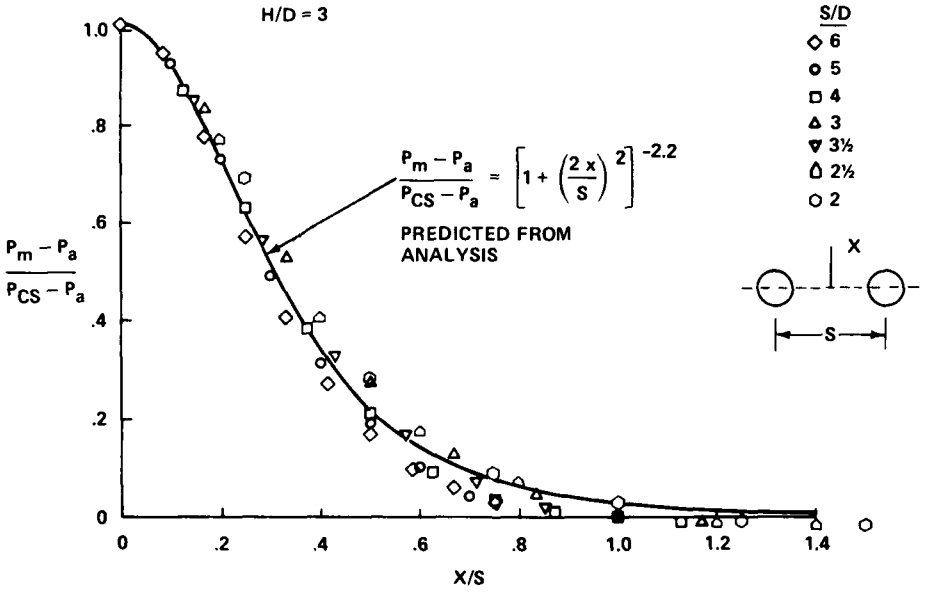

Figure 5 Maximum Ground Pressure Variation Along Stagnation Line

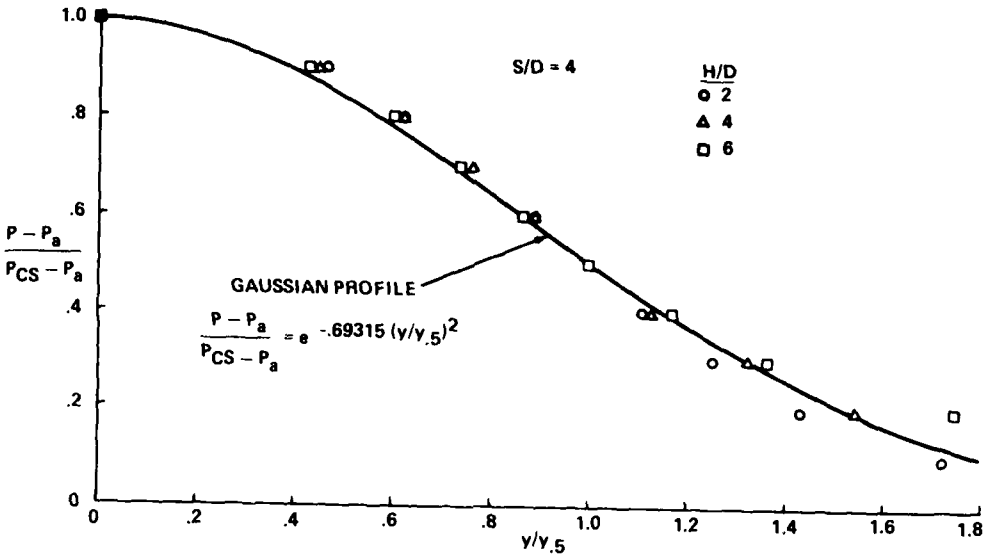

Figure 6 Ground Pressure Variation Across Center of Stagnation Line

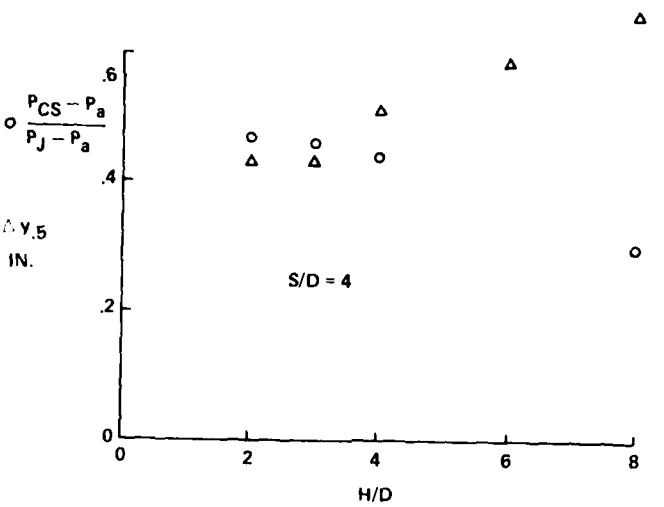

Figure 7 Variation of Ground Stagnation Line Characteristics With Nozzle Height

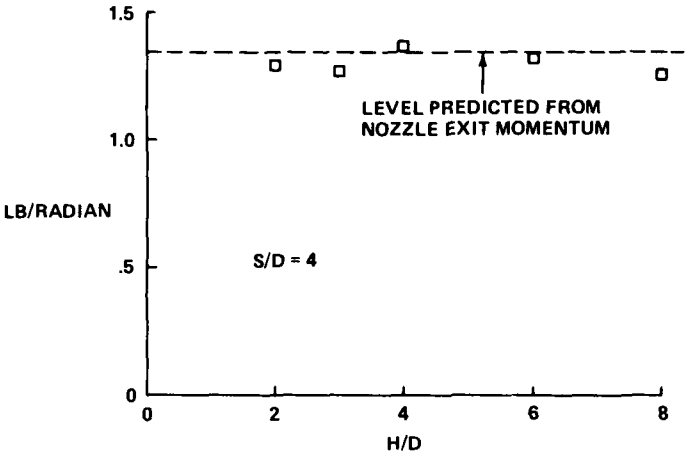

Figure 8 Variation of Integrated Ground Pressure Force With Nozzle Height

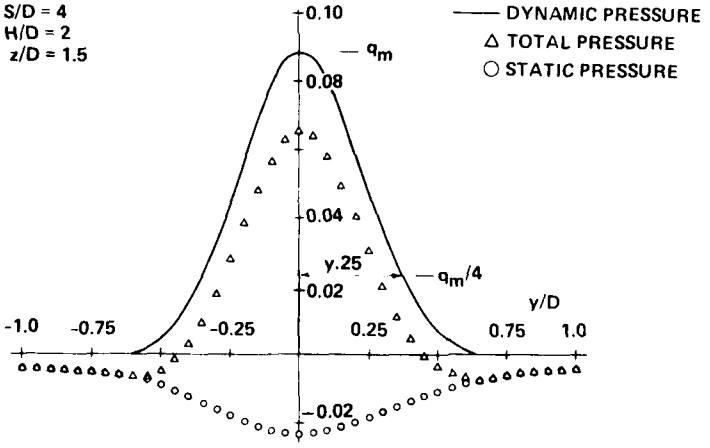

Figure 9 Pressure Profiles Across Upwash Centerline

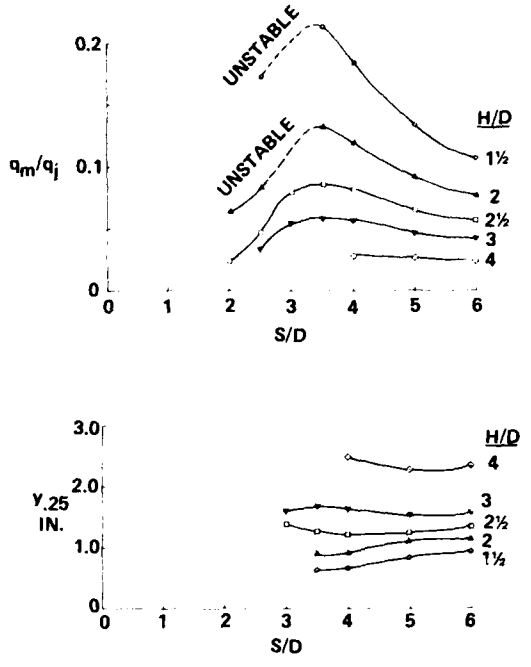

Figure 10 Upwash Properties at Nozzle Exit Plane

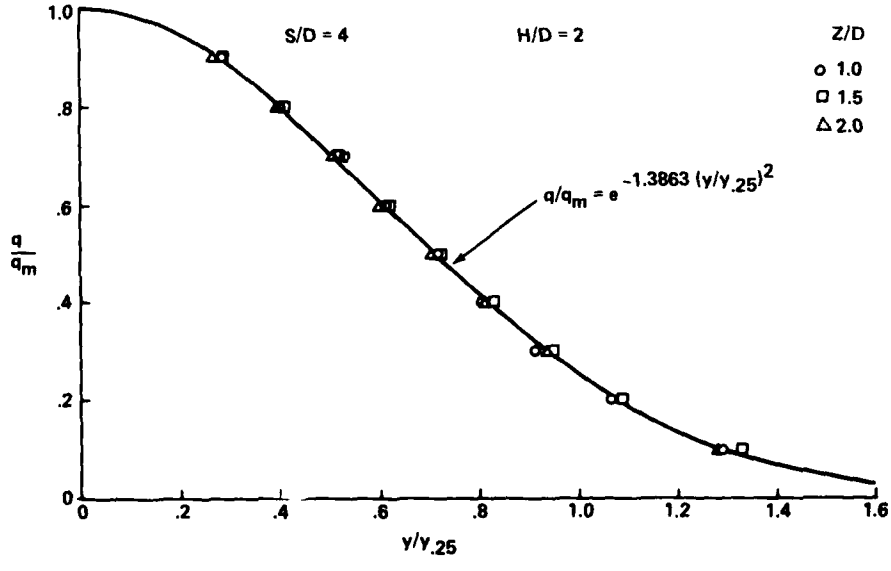

Figure 11 Dynamic Pressure Profiles Across Upwash

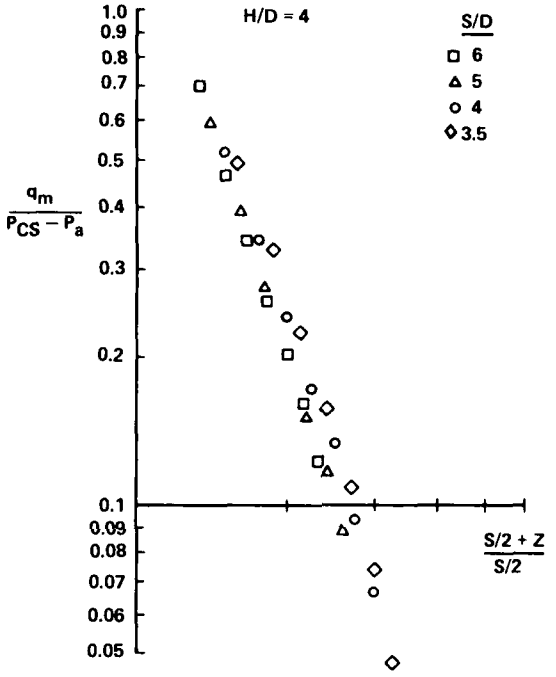

Figure 12 Dynamic Pressure Decay Along Upwash Centerline

COMPUTATION OF INVISCID ROTATIONAL JET IMPINGEMENT REGIONS

by

A. Rubel
Research Department
Grumman Aerospace Corp.
Bethpage, New York

ABSTRACT

A vector potential/vorticity formulation is used to establish the set of partial differential equations governing three-dimensional inviscid rotational jet impingement regions. A finite-difference representation of these equations is solved, within a Cartesian coordinate framework, for the case of normal axisymmetric jet impingement. The results are in excellent agreement with previous frozen vorticity calculations thereby validating the technique for application to truly three-dimensional impingement regions.

Presented at the
Workshop on VSTOL Aerodynamics
Naval Postgraduate School
Monterey, California
May 16–18, 1979

INTRODUCTION

The component approach[1] to the quantitative analysis of VTOL jets in-ground-effect requires that solutions for each constituent regime (i.e., free jet, impingement region, wall jet, collision region, upwash sheet, and secondary flow zone) be coupled to provide the overall flow field. The advantage of this approach is that the individual regimes are, by themselves, amenable to theoretical analysis.

The impingement zone is central to the problem and previous study (e.g., Rubel,[2] Giralt et al.[3]) has shown this region to be determined, in large part, by the balance of pressure and inertia forces as provided by the inviscid rotational flow model. In the case of oblique two-dimensional impingement (normal axisymmetric impingement) the vorticity (vorticity/radius) is "frozen" along streamlines and numerical stream function solutions are easily obtained providing ground plane pressure distributions in excellent agreement with observations.[2]

For fully three-dimensional impingement fields the inviscid rotational flow description no longer implies that vorticity is frozen along streamlines and an alternate solution technique is required. A vector potential/vorticity formulation for this problem has been given[4] and demonstrated to have possibilities for the solution of truly 3-D impingement regions. This approach separates the representation of the flow field into two sets of coupled partial differential equations. The first set, determined by the kinematics of the flow, is elliptic in nature and describes the velocity field in terms of vector and scalar potentials when the vorticity field is specified. The second set, determined by the inviscid rotational flow model, is hyperbolic and describes the behavior of the vorticity for a given velocity field.

In this paper the kinematic formulation is briefly reviewed and a revised technique for the vorticity description is presented. Numerical solutions to the coupled set of equations are given for the case of axisymmetric normal impingement. These solutions are obtained using a rectangular coordinate system which acts to simulate most of the features of a 3-D flow field. The results show that the technique can be used to gain rapid estimates for the nature of 3-D type impingement flow fields.

FORMULATION

A cartesian coordinate system with origin at the intersection of the jet centerline with the ground plane is used to describe the incompressible, inviscid, rotational jet impingement flow field (Fig. 1). Although the jet is considered to have a plane of symmetry ($y = 0$), this involves no loss in generality for the overall formulation of the problem. The boundaries of the impingement regime are such that the influx plane ($z = Z$) is unaffected by the presence of the ground plane ($z = 0$), and the efflux planes ($x = \pm X$, $y = Y$) are sufficiently distant from the stagnation point that the flow has recovered to the ambient pressure of the influx plane. The flow model implies that the impingement zone is a regime where pressure and

inertia forces are balanced so that the velocity-vorticity distribution at the influx plane, along with the assumption of parallel flow at the efflux plane, determines the fluid behavior within the zone.

The formulation is given in terms of dimensionless quantities; velocities are scaled by the maximum jet velocity, distance by the jet half-width (that is, distance measured along the perpendicular from the jet centerline to the point at which velocity is half the maximum), and pressures by the total pressure at the jet centerline. Ambient and jet static pressures are taken to be zero.

The equations governing the kinematic problem are[4]

$$\nabla^2 \bar{A} = - \bar{\omega} \tag{1}$$

$$\nabla^2 \phi = 0 \tag{2}$$

where $\bar{A}$ is the vector potential ϕ, the scalar potential and $\bar{\omega}$ the vorticity. The potentials define the velocity, $\bar{q}$, such that

$$\bar{q} = - \nabla\phi + \nabla \times \bar{A} \tag{3}$$

where the x, y, z components of the vector fields are $\bar{q} = (u, v, w)$, $\bar{A} = (\alpha, \beta, \gamma)$, $\bar{\omega} = (\xi, \eta, \zeta)$. The boundary conditions on the vector potentials are

$$A_{(t)} = \frac{\partial A_{(n)}}{\partial n} = 0 \ , \tag{4}$$

where the subscripts (n), (t), indicate normal and tangential components, respectively. The scalar potential satisfies the conditions

$$\frac{\partial \phi}{\partial n} = - \bar{n} \cdot \bar{q} \quad \text{(symmetry, influx, and ground planes)} \tag{5a}$$

$$\phi_z = \beta_x - \alpha_y \quad \text{(efflux planes)} \tag{5b}$$

where $\bar{n}$ indicates the outward positive normal to the boundary and Eq. (5b) implies parallel flow at the efflux planes. The x, y, z subscripts are used to indicate partial differentiation with respect to that independent variable.

The vorticity forcing functions introduced in Eq. (1) must be evaluated in concert with the scalar and vector potentials. The equation governing the behavior of vorticity is obtained from the curl of the momentum equation. For an inviscid fluid the resulting Helmholtz equation has the incompressible form

$$\bar{q} \cdot \nabla\bar{\omega} - \bar{\omega} \cdot \nabla\bar{q} = 0 \ . \tag{6}$$

Equation (6) is hyperbolic and requires initial conditions

$$\bar{\omega}(x, y, Z) = \bar{\omega}(x, y) \quad \text{(influx plane)} . \tag{7}$$

This direct formulation for the vorticity constitutes a considerable simplification with respect to previous methodology[4] which involved a higher order derivative form of Eq. (6).

APPLICATION TO NORMAL AXISYMMETRIC JET IMPINGEMENT

The normal impingement of an inviscid, rotational axisymmetric jet provides a good case on which to explore the use of the basic three-dimensional technique. The vortex stretching that is readily accounted for by frozen vorticity/radius on stream surfaces must here be resolved via integration of the general Helmholtz equations. Although several simplifications of the governing equations can be effected, the use of a cartesian coordinate system preserves the basic three-dimensionality of the approach.

For this problem, x, y, z scalar components of the vector fields are

$$\bar{q} = (u, v, w), \ \bar{A} = (\alpha, \beta, 0), \ \bar{\omega} = (\xi, \eta, 0)$$

so that the vector potential and vorticity are always parallel to the ground plane. The kinematic equations become

$$\alpha_{xx} + \alpha_{yy} + \alpha_{zz} = -\xi \tag{8}$$

$$\beta_{xx} + \beta_{yy} + \beta_{zz} = -\eta \tag{9}$$

$$\phi_{xx} + \phi_{yy} + \phi_{zz} = 0 \tag{10}$$

with boundary conditions

$$x = \pm X; \ \alpha_x = 0, \ \beta = 0, \ \phi_z = \beta_x - \alpha_y \tag{11a,b}$$

$$y = 0; \ \alpha = 0, \ \beta_y = 0, \ \phi_y = 0 \tag{11c}$$

$$y = Y; \ \alpha = 0, \ \beta_y = 0, \ \phi_z = \beta_x - \alpha_y \tag{11d}$$

$$z = 0; \ \alpha = 0, \ \beta = 0, \ \phi_z = 0 \tag{11e}$$

$$z = Z; \ \alpha = 0, \ \beta = 0, \ \phi_z = -w(x, y) . \tag{11f}$$

The fully developed influx velocity profile is given by

$$w(x, y) = -(1 + c_2 r^2)^{-2}; \ r^2 = x^2 + y^2, \ c_2 = \sqrt{2} - 1 .$$

The scalar vorticity equations are

$$u\xi_x + v\xi_y + w\xi_z = u_x\xi + u_y\eta \tag{12}$$

$$u\eta_x + v\eta_y + w\eta_z = v_x\xi + v_y\eta \tag{13}$$

with initial conditions given by

$$z = Z;\ \xi = 4c_2y(1 + c_2r^2)^{-3},\ \eta = -4c_2x(1 + c_2r^2)^{-3} \tag{14a}$$

consistent with the influx velocity profile, and a symmetry condition given by

$$y = 0;\ \xi = 0,\ \eta_y = 0. \tag{14b}$$

A second-order accurate finite-difference analog of the elliptic Eqs. (8–10) is developed by straightforward central differencing under the constraints imposed by the boundary conditions Eqs. (11a–f).[4] The multi-grid (MG) technique of A. Brandt[5] is employed to converge upon a solution to the difference equations (Fig. 2). The MG approach takes advantage of the relaxation technique's ability to correct short wavelength errors within a few iterations and relies on coarse grid smoothing to correct the larger wavelength errors. The coarse grid computations, here performed on grids with mesh widths in multiples of two, take a minimum of computer time compared with the 3-D fine mesh calculations. Use of this scheme improved convergence times by about a factor of five over standard optimized SLOR techniques when applied to the current set of elliptic equations.

A second-order accurate implicit marching technique is found to be effective for integration of Eqs. (12, 13) when windward differencing is invoked upon horizontal planes (Fig. 3). The difference equations about the point (i, j, k) are

$$u\mathfrak{N}\{\xi_x\} + v\mathfrak{N}\{\xi_y\} + w\xi_z = u_x\mathfrak{N}\{\xi\} + u_y\mathfrak{N}\{\eta\} \tag{15}$$

$$u\mathfrak{N}\{\eta_x\} + v\mathfrak{N}\{\eta_y\} + w\eta_z = v_x\mathfrak{N}\{\xi\} + v_y\mathfrak{N}\{\eta\} \tag{16}$$

where $\mathfrak{N}$ defines the operation

$$\mathfrak{N}\{\xi\} = [\xi(i,j,k) + N\xi(i,j,k+1) + \xi(i,j,k+2)]/(N+2) \tag{17}$$

and N is a weighting parameter, generally chosen to be 1 or 2. The vertical gradient in vorticity, as well as the coefficients in Eqs. (15, 16), are obtained by central differencing about point (i, j, k + 1). Horizontal derivatives are given by

$$\xi_x(i,j,k) = \pm\,[\tfrac{3}{2}\xi(i,j,k) - 2\xi(i \mp 1,j,k) + \tfrac{1}{2}\xi(i \mp 2,j,k)]/\Delta x;\ u \gtrless 0, \tag{18a}$$

$$\xi_y(i,j,k) = [\tfrac{3}{2}\xi(i,j,k) - 2\xi(i,j-1,k) + \tfrac{1}{2}\xi(i,j-2,k)]/\Delta y \tag{18b}$$

with obvious modifications near the symmetry plane.

A marching step consists of utilizing Eqs. (15–18b) to produce two sets of linear equations relating the vorticities at all points in the k plane. These equations are then solved by successive line relaxation sweeping from the line y = 0 at the symmetry plane to the line y = Y at the efflux plane. Details of the overall procedure for convergence of the coupled system of equations are given elsewhere[4] and remain unchanged in substance.

RESULTS

Computations of the normal impingement of a fully developed axisymmetric jet have been carried out within the physical domain

$$-3 \leq x \leq 3,\ 0 \leq y \leq 3,\ 0 \leq z \leq 2.5.$$

The results for a coarse (21 × 11 × 13) grid and fine (41 × 21 × 25) grid calculation are compared with a highly resolved frozen vorticity computation.[2] Execution (CPU) times on the IBM 370/168 are 1–2 minutes for the coarse grid solution and about 30 minutes for the fine grid solution.

The centerline velocity decay predicted by the 3-D technique with fine grid is seen to be in near perfect agreement with the frozen vorticity result (Fig. 4). Moreover, there is little difference between the coarse and fine mesh computation results. For the ground plane pressure distribution (Fig. 5), again the coarse and fine grid solutions are in excellent agreement with the frozen vorticity result even into the tail of the distribution. This is a distinct improvement over previous results[4] and is attributed to the reformulation of the vorticity equation solution technique.

It should be pointed out that the calculations depicted in Fig. 5 include points in the symmetry plane (y = 0) as well as those at 45° from the symmetry plane (y = x). The fact that these points all lie on the frozen vorticity pressure distribution is an indication that the azimuthal independence of the solution is preserved by using the 3-D type formulation upon a cartesian coordinate system. This is further verified by the computed ground plane isobars (Fig. 6) which are circular. The flow structure on the ground plane is of interest for a fully three-dimensional flow case (e.g., oblique axisymmetric jet impingement). A trace of the calculated streamlines and vortex lines for the normal impingement case (Fig. 7) shows the capability of the computation to faithfully reproduce the proper radial and circular behavior, respectively. Thus, it is reasonable to expect that the fully 3-D formulation can predict such flow structures.

CONCLUSIONS

Computations of normal axisymmetric jet impingement, within a Cartesian coordinate framework, have validated the vector potential/vorticity formulation for the calculation of 3-D inviscid rotational impingement regions. In addition,

the results indicate that coarse grid computations have sufficient resolution for the description of such flow fields. The short CPU times for these calculations enhance the feasibility for realizing overall VTOL in-ground-effect flow fields via the component region approach.

ACKNOWLEDGMENT

This investigation was supported by the Office of Naval Research under Contract No. N00014-77-C-0524. The author thanks F. Marconi for a fruitful discourse on the virtues of windward differencing.

REFERENCES

1. Siclari, M. J., Migdal, D., and Palcza, J. L., "The Development of Theoretical Models for Jet-Induced Effects on V/STOL Aircraft," J. Aircraft, Vol. 13, p. 938, 1976.

2. Rubel, A., "Computations of Jet Impingement on a Flat Surface," AIAA Paper No. 78-207, AIAA 16th Aerospace Sciences Meeting, Huntsville, Alabama, Jan. 16–18, 1978.

3. Giralt, F., Chia, C. J., and Trass, O., "Characterization of the Impingement Region in an Axisymmetric Turbulent Jet," Ind. Eng. Chem., Fundam., Vol. 16, 21, 1977.

4. Rubel, A., "Computational Techniques for the Calculation of Inviscid Rotational Jet Impingement," AIAA Paper No. 78-1212, AIAA 11th Fluid and Plasma Dynamics Conference, Seattle, Wash., July 10–12, 1978.

5. Brandt, A., "Multi-Level Adaptive Solutions to Boundary-Value Problems," Math. of Comp., Vol. 31, p. 333, 1977.

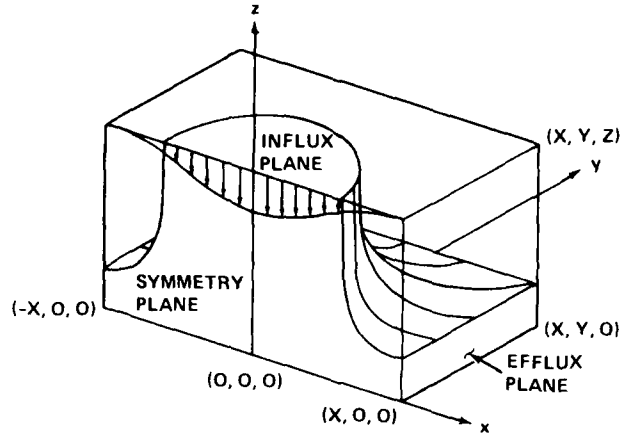

Figure 1 Jet Impingement Zone Geometry and Coordinate System

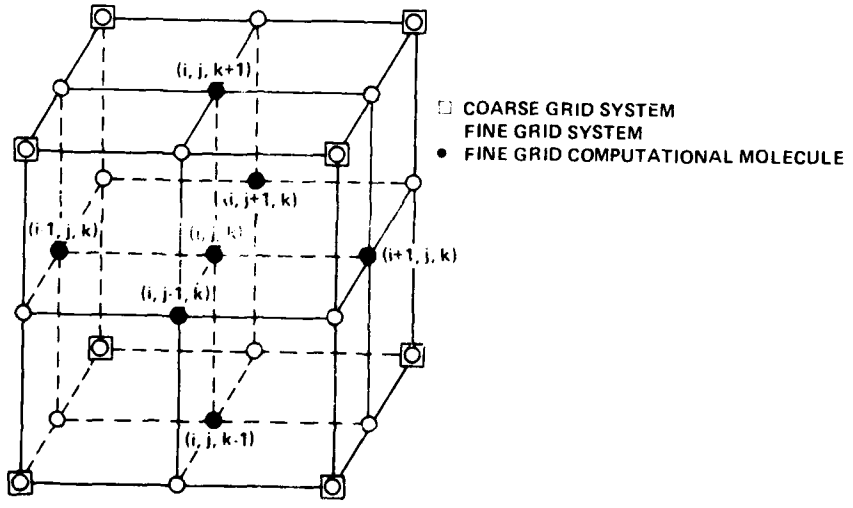

Figure 2 Numerical Method of Solution Potential Equations (Elliptic) Multi-Grid Scheme (A. Brandt) With Line Relaxation

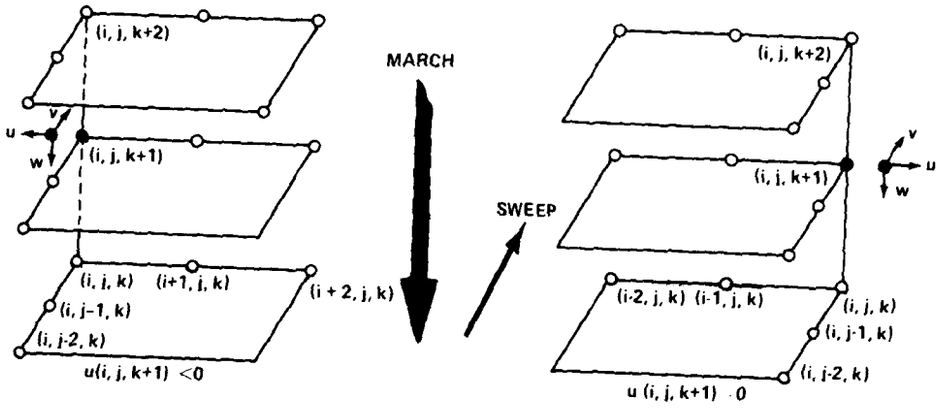

Figure 3 Numerical Method of Solution
Helmholtz Equation (Hyperbolic)
Implicit, Second-Order Accurate,
Windward Difference Scheme

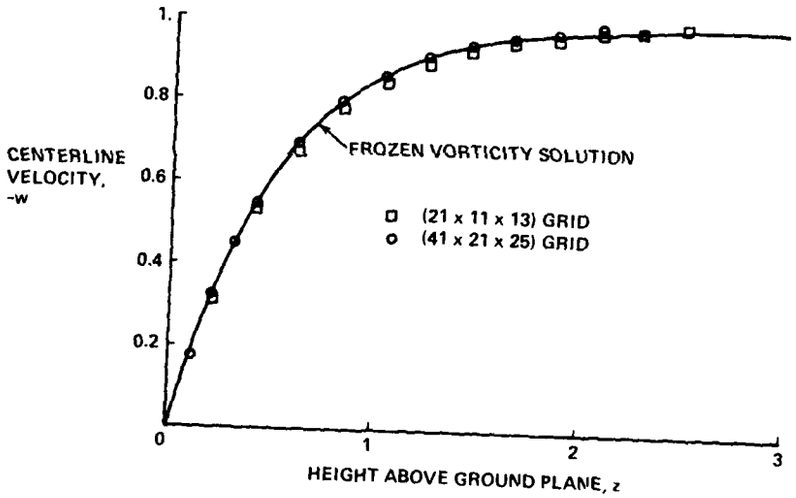

Figure 4 Centerline Velocity Decay
Axisymmetric Fully Developed
Jet Impingement, 3-D Technique;
x = 3, y = 3, z = 2.5

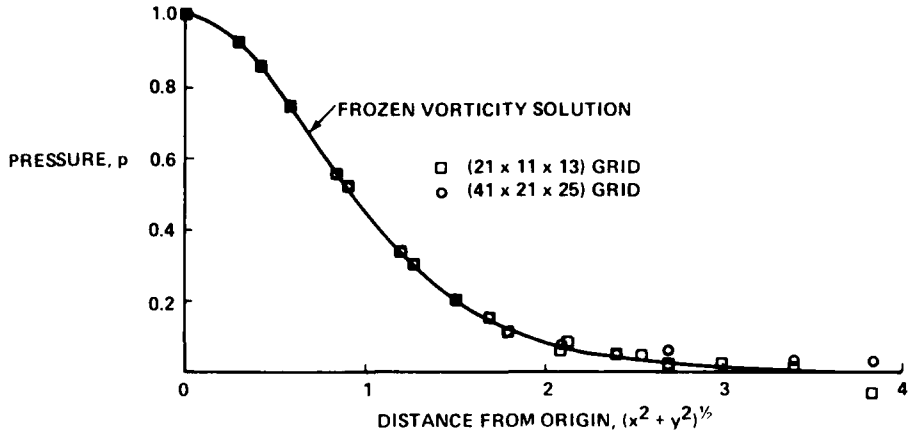

Figure 5 Ground Plane Pressure Distribution
Axisymmetric Fully Developed
Jet Impingement, 3-D Technique;
x = 3, y = 3, z = 2.5

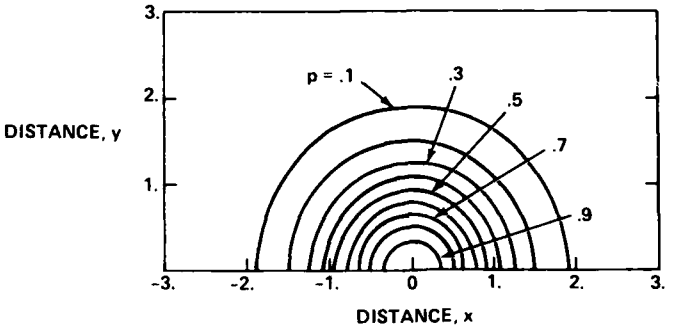

Figure 6 Ground Plane Isobars
Axisymmetric Fully Developed
Jet Impingement, 3-D Technique
x = 3, y = 3, z = 2.5; (41 x 21 x 25) Grid

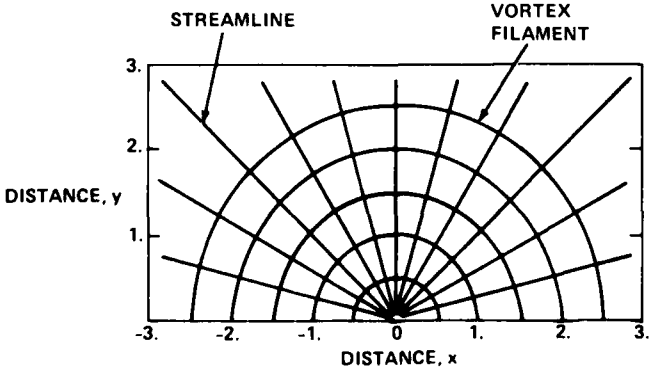

Figure 7 Ground Plane Streamlines and vortex lines
Axisymmetric Fully Developed
Jet Impingement, 3-D Technique;
x = 3, y = 3, z = 2.5; (41 x 21 x 25) Grid

DECK EDGE PROXIMITY EFFECTS ON THE AERODYNAMIC CHARACTERISTICS OF A LIFT-CRUISE-FAN V/STOL CONFIGURATION *

V. R. STEWART
Member of Technical Staff
Rockwell International Corporation
Columbus, Ohio

ABSTRACT

The incremental aerodynamic effects induced on a lift-cruise-fan V/STOL configuration by the presence of a small deck are described. In the operation of a V/STOL airplane near small decks, a portion of the airplane may under some cases overhang the deck edge. A configuration typical of a multimission subsonic V/STOL configuration has been tested, and the results are presented. The configuration was considered with five deck edge locations including full deck, as well as longitudinal and lateral overhangs. Configurations utilizing three and four fan geometries were investigated. The data are presented as an incremental induced force or moment ratioed to engine thrust as a function of height above the deck.

*The study discussed in this paper was performed under NASA Contract NAS2-9882 through cooperation of the U. S. Navy

SYMBOLS

Total Forces

L	lift
D	drag
M	pitching moment
RM	rolling moment
T	thrust

Thrust Induced Aerodynamic Forces (Power ON - Power OFF)

ΔL	lift
ΔD	drag
ΔM	pitching moment
ΔRM	rolling moment

Total Coefficients

CL	lift coefficient L/qS
CD	drag coefficient D/qS
CM	pitching moment coefficient $M/qS\bar{c}$
CRM	rolling moment coefficient RM/qSb
C_T	thrust coefficient T/qS

Thrust Induced Aerodynamic Coefficients (Power ON - Power OFF)

C_{LA}	lift coefficient
C_{DA}	drag coefficient
C_{MA}	pitching moment coefficient
C_{RMA}	rolling moment coefficient

Angles

α	angle of attack
ϕ	bank angle
θ	thrust angle
δ_N	nozzle angle - geometric angle
β	sideslip angle

Dimensions

S	wing area - 0.78 m^2
b	wing span - 2.50 m
$\bar{c}$	wing mean aerodynamic chord - 0.323 m
y	lateral dimension
x	fuselage dimension
z	vertical dimension
H/D h/D	non-dimensional ground height height of fuselage/diameter of one fan
D	equivalent diameter of one fan - 0.13 m

Miscellaneous

V	wind velocity
V_j	nozzle exit velocity
P_R	pressure ratio P_T/P_a
P_T	total pressure behind fan
P_a	ambient pressure
q	dynamic pressure

INTRODUCTION

The operation of V/STOL configurations may involve operation from small elevated landing platforms. Certainly, operation from some of the proposed small ships must utilize small decks. Even in some cases it may prove desirable to perform STOL (free deck) takeoffs and landings from carriers where partial overhang of one wing are encountered. Operation into or out of congested areas with helicopters today involves rooftop landing sites. It is conceivable that operation of fixed wing VTOL configurations into these sites may be desirable in the future.

The particular V/STOL configuration chosen for this study represents the broad class of lift-cruise-fan or deflected thrust configuration which may fulfill these desired operations. The configurations of this study, therefore, represent concentrated generally round jets exhausted from the nacelle or fuselage of the airplane.

Two thrust configurations are discussed. A four fan configuration with nacelle mounted fans, two in the front and two in the rear, was tested at thrust angles representing both the vertical and short field operating conditions. This configuration consists of two front mounted fans, one in each nacelle, exhausting through two swivel nozzles each. Deflections of the thrust from 0^{o} to 120^{o} is possible for these fans. The aft fans are mounted horizontally and thrust vectoring from 45^{o} to 120^{o} is possible through a series of vanes.

The second thrust configuration was a three fan concept and was tested only at deflections representing vertical operation. Here the third fan was mounted similarly to the aft fans in the nose of the fuselage. The nose fan was used in conjunction with the aft fans to simulate a three fan configuration.

DISCUSSION

During the past several years, the subject of V/STOL operation has received considerable attention and study. The aerodynamic characteristics of various configurations were investigated with many engine configurations. Most studies were directed to the free air conditions; and, where the ground effects were considered, it was in all cases with a full deck. Figure 1 presents a comprehensive study in free air of jet effects on a wing-body configuration, reference (1). As can be seen, the induced effects are strongly affected by the relative location of the jet, fuselage, and wing. Locations near the wing leading edge result in suckdown and a lift loss, while jet locations near the wing trailing edge increase the circulation about the wings and produce positive lift increments. The ground effects exert several forces on the airplane configuration. The ground presence may result in a back pressure effect on the engine which has to be considered. In addition, induced forces and moments may be encountered due to increased suckdown by the jets and the fountain from the reflected jets. A study has been made to investigate these latter effects, not only as the

result of the ground presence, but as the induced effects are altered by the edge of a small elevated landing platform.

Model and Test Procedures

The model utilized for the test portions of the study is shown in Figures 2 and 3. The thrust is provided by five tip driven fans. The fans are 1.25 pressure ratio, 5.5 inch fans. Tests were conducted with either three fans, nose and two aft fans; or four fans, nacelle mounted, two vertical and two horizontal. The nozzle arrangements are shown in Figure 4. The front nacelle fans are exhausted through two swivel nozzles located on either side of the nacelle, and the aft fans and the nose fan are exhausted through louvers to direct the flow angle at the desired angle.

The fan thrust and mass flow for each fan were determined by calibrating the variable (thrust or mass flow) against fan exhaust pressure ratio. The calibrations were done with nacelle shielded and were investigated at various ground positions. Figure 5 indicates a typical fan calibration at various heights. Utilizing the fan exhaust pressure as the correlating parameter, eliminates a separate calibration for ground proximity.

The induced effects were determined from tests at static speeds ($V_\infty = 0$) in a ground test rig and at forward speed ($V > 0$) in the Langley Research Center V/STOL Tunnel. Several ground board configurations were tested at both static and forward speed conditions. The various ground board configurations tested in addition to free air are shown in Figure 6. The configurations are full deck, aft edge under center of gravity, forward edge under center of gravity, right edge at wing mid, semi-span, and right edge at model center line.

The model was approximately a 1/8 scale of a subsonic multimission airplane configuration. Figure 7 shows the model and model dimensions. During the static tests, the model was fixed, and the ground board moved to the desired height, pitch angle, and roll angle. During forward speed testing, height and pitch angle variations were obtained by moving the model while roll was obtained by ground board rotation.

Direct thrust effects were accounted for in the data reduction by geometric distances and thrust angles were determined during the isolated nozzle calibrations. The inlet momentum increments to drag and pitching moment were accounted for by use of the secondary mass flow from the fan calibration, and an assumed pitch arm for the inlets. The ram drag reaction point was assumed to be at the center of the vertical inlets. The reaction point for the horizontal inlets was assumed to act 1/4 of an inlet diameter above the inlet face. Figure 7 also presents the geometric arms of the model.

The breakdown of thrust and aerodynamic forces for a representative case is shown in Figures 8, 9, and 10 for lift, drag, and pitching moment coefficients, respectively. It would appear from this breakdown that the ram drag pitching moment arms may have been short. It would appear that, at least in the sample condition, an arm of 1/2 an inlet diameter may have been more appropriate.

Results

Free Air: The model configurations were tested in free air in order to determine the characteristics of the base configuration. Figure 11 shows turning effectiveness of the nozzles at static (zero velocity) for several nozzle angles. The four fan version has approximately a 5% interference at all nozzle angles. This interference is primarily from the swivel nozzles. The study was made with this as the basic configuration since this was not expected to alter the induced ground effects. The swivel nozzles were changed for one series to show the effect. The inboard lip of the nozzles was extended by one nozzle width. The interference was reduced from six to one or two percent by this change. The three fan shows 100% turning for the $80^{o}/90^{o}/90^{o}$ nozzle angles tested.

The effects of height on the model without power and at forward speed are shown in Figures 12 and 13 for the different ground board configurations tested. An increase in lift is demonstrated at all ground board positions except #2, the forward location. A very small loss is shown in this configuration with the largest gain shown with the #3 board position, approximately a 30% increase. A small pitch down is encountered with all deck positions.

Induced ground effects are, in general, characterized by a small lift loss and a pitch down. At static speeds the ground board configuration tested showed an increase in lift loss of about 5% of thrust for the aft ground board position and less for the other positions. The pitch down was relatively small. Figure 14 shows the static condition longitudinal induced forces as a function of height above the deck. Figure 15 presents the induced rolling moments for the zero speed condition. Removal of sections of the ground board from under the right hand wing indicates a left roll as the width of the board is reduced. This reduction is most likely due to the elimination of the suckdown experienced with full deck coupled with a possible fountain change. Induced rolling moments over the varying lateral deck edge position during banked conditions are the result of two factors. The suckdown under the right wing is eliminated, as with zero bank angle, and, in addition, the fountain from the downgoing nozzles is affected. In right roll the fountain is reflected to the left wing creating a large right wing down induced rolling moment. As the ground board is removed, this fountain is eliminated. The left roll or roll away from the removed sections shows no appreciable change due to the removal of the ground board. This is accounted for by the cancelling effect of the fountain and the suckdown.

Wind-on conditions shown in Figures 16 and 17 are similar with one notable exception. A significant lift loss is apparent with the ground board located in the forward position (rear edge under center of gravity). The cause of this lift loss has not been determined, but several possible explanations can be suggested. The entrainment of the forward jet toward and into the rear jet may alter the fountain to a considerable extent. Also, a turbulence may be generated off the leading edge of the ground board causing a steady state lift loss. Another possible reason is a flow around the ground board which induces a downwash at the model. The latter condition was not investigated to any great extent; however, total head probes under the ground board do not indicate this to be a problem.

The three fan was investigated at vertical nozzle angles and wind-over-the-deck conditions. In general, the three fan has similar deck edge effects. The most significant variations occurring with the three fan configuration were approximately 90% thrust lift loss at wheel height for both 1/2 ground board configurations and a large pitch down with full deck at zero speed. The data with three fan were limited and are presented in Figures 18 and 19 for the zero speed case and 20 and 21 at forward speed.

Ground effect at STOL conditions of the four fan configuration are shown in Figures 22 to 25. The model shows almost no ground effects at forward speed. A large induced lift is shown regardless of ground board configuration. A pitch up is encountered at forward speed, and small induced rolling moments are shown.

A positive induced drag has been shown for most all cases tested. There are two variables which are showing up as induced drag. These are: (1) the interference discussed at static test conditions shows up directly in the drag (as well as the lift). Elimination of this interference will reduce the apparent induced drag, and (2) The data are reduced to aerodynamic coefficients utilizing thrust angles obtained during engine calibration tests. The data obtained during testing of the complete configuration (unshielded) show angles more nearly equal to the geometric angle. In other words, the mutual interference of the jets changes the overall thrust angle. For the analysis of deck edge effects this is of no importance; however, it must be considered in utilization of the data.

If one were to consider the results of this study for an airplane, one must look at control requirements. If you establish control power requirements as follows: excess lift = +10%; pitching moment sufficient to give 0.5 radian/sec. acceleration, and rolling moment sufficient for 0.9 radian/sec. acceleration, the greater majority of the data will fall within $\pm$40% of the total requirement. A few exceptions which are apparent are: the four fan with the deck located forward requires about 110% of this lift control; the three fan requires 150% pitch control with the full ground board and approximately 90% of the lift control.

CONCLUSIONS

The partial deck does not present a limiting condition to a V/STOL airplane. For STOL operation with one wing partially overhanging, no change from a full deck is shown.

In a few isolated conditions, larger than expected forces were encountered. The forward board position resulted in a sizable lift loss at forward speed. The three fan configuration tested experienced a sizable pitch down in the presence of a full deck. It is felt that these results could be materially affected with certain configuration changes.

REFERENCES

(1) Carter, A. W., Effects of Jet-Exhaust Location on the Longitudinal Aerodynamics of a Jet V/STOL Model, NASA TND-5333, July 1969

(2) Stewart, V. R., Low Speed Wind Tunnel Tests of Ground Proximity and Deck Edge Effects on a Lift-Cruise-Fan V/STOL Configuration, NASA CR 152247, Apr. 1979

(3) Stewart, V. R., Low Speed Wind Tunnel Tests of Ground Proximity and Deck Edge Effects on a Lift-Cruise-Fan V/STOL Configuration, Data Report CR 152248, Apr. 1979

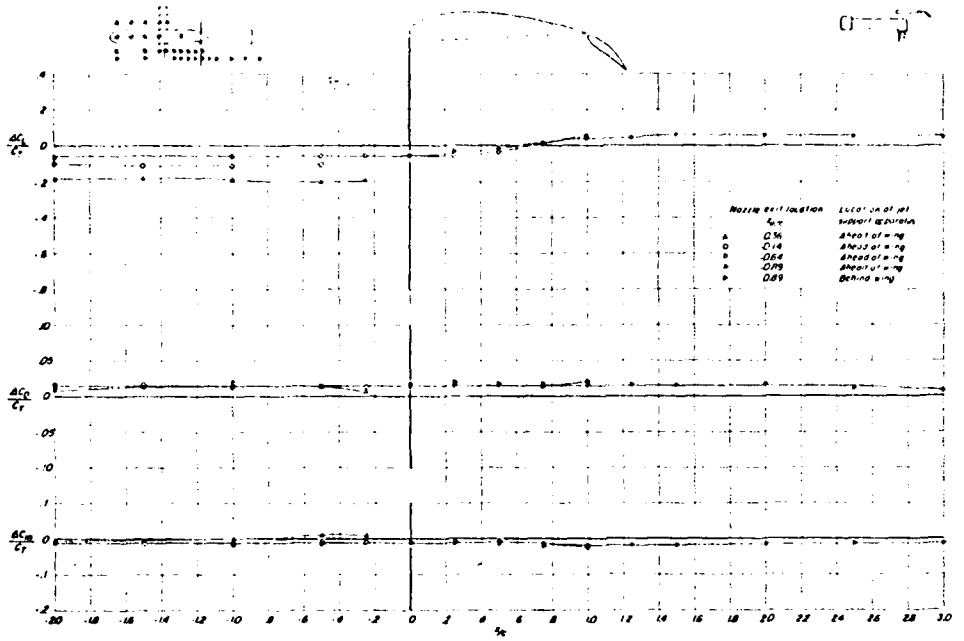

(a) V_e 0.10

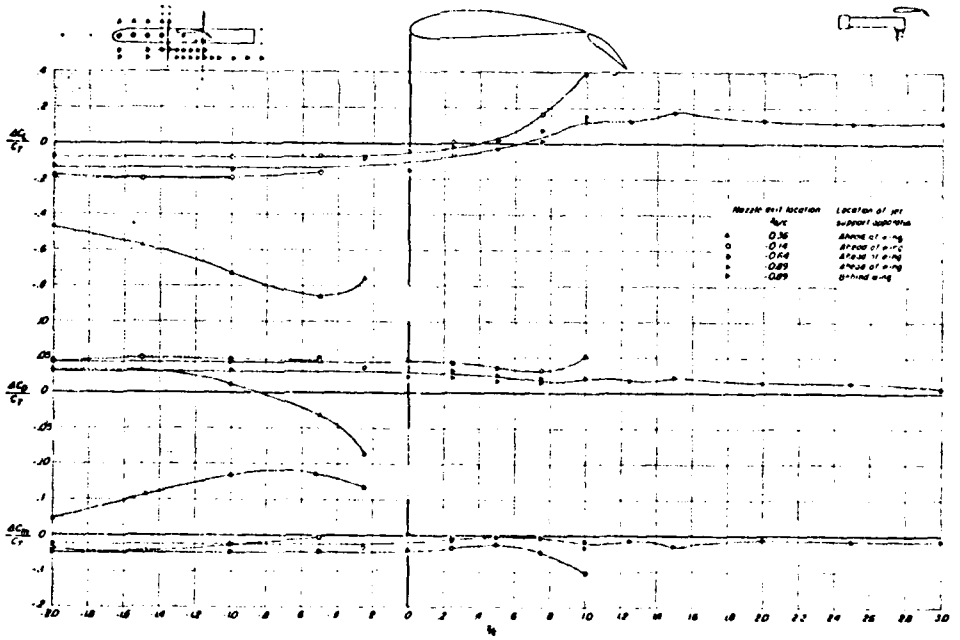

(b) V_e 0.25

Figure 1.- Effect of longitudinal location of the jet exhaust on the incremental lift, drag, and pitching moment due to power. $\delta_f = 40^o$; $\delta_j = 90^o$

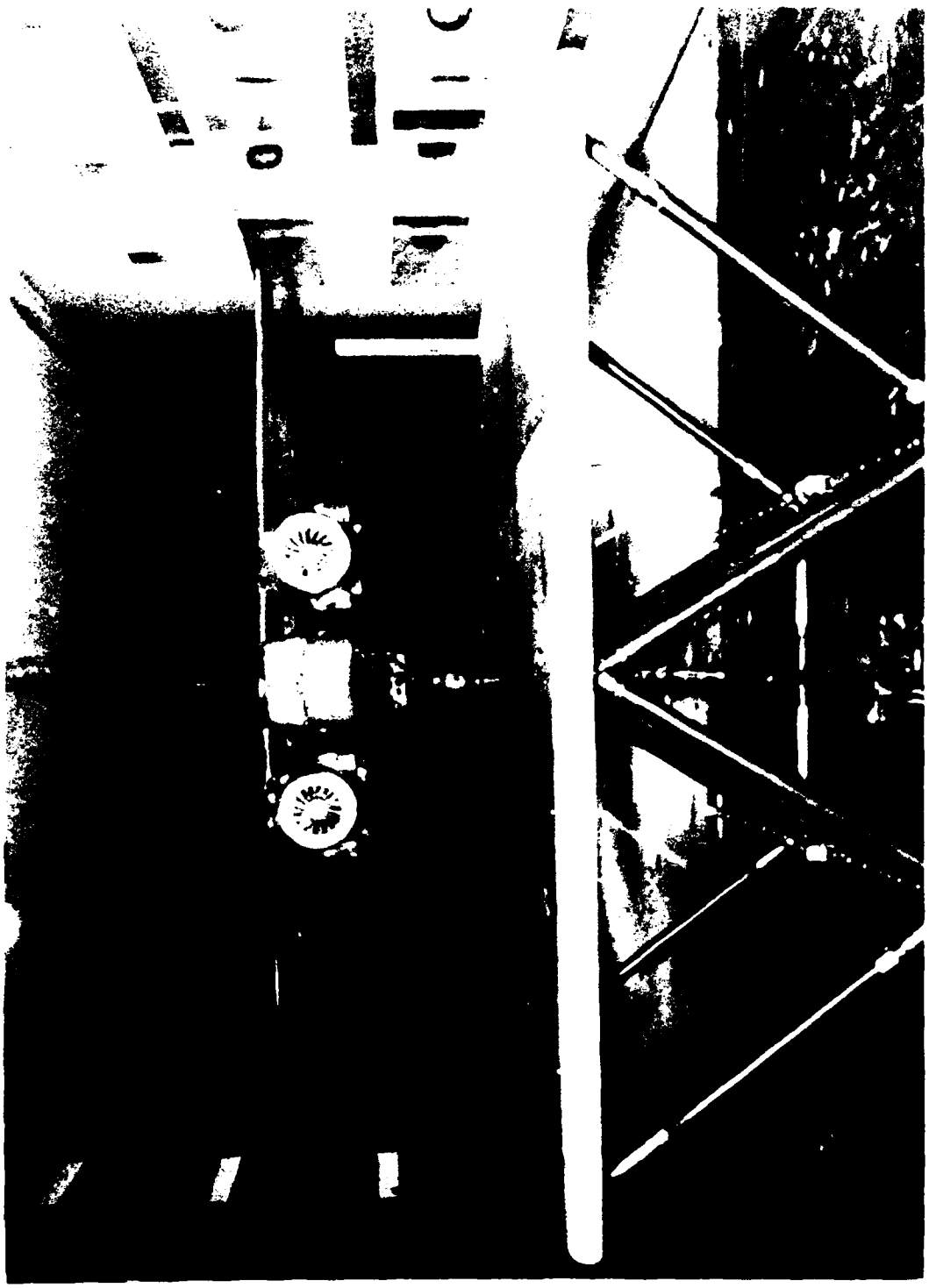

Figure 2. Model front view

Figure 3. Model 1/2 top view

a. (Front Fan)

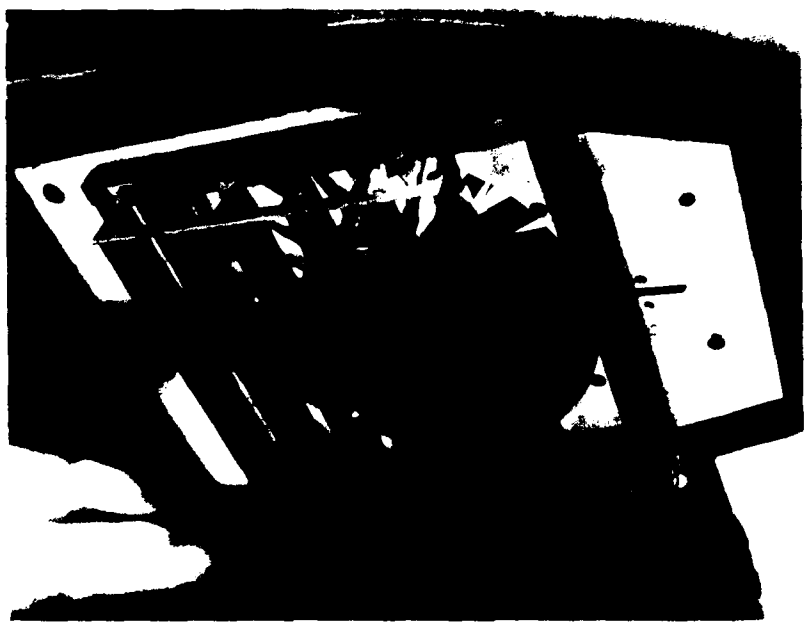

b. (Aft or Nose Fan)

Figure 4. Model Fan Exit

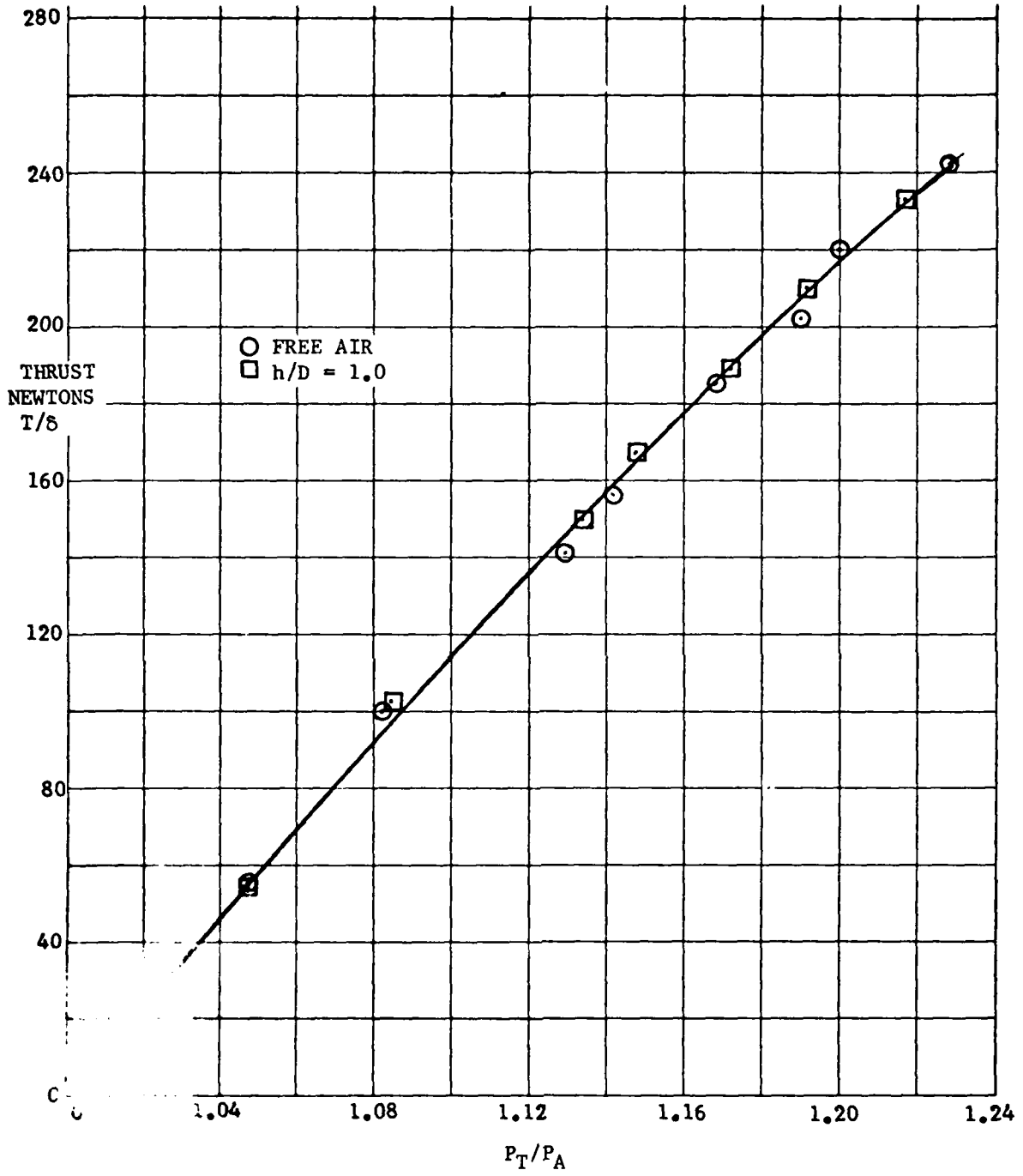

Figure 5. Variation of thrust with pressure ratio at various heights, right hand forward fan, $\delta_N = 90^o$

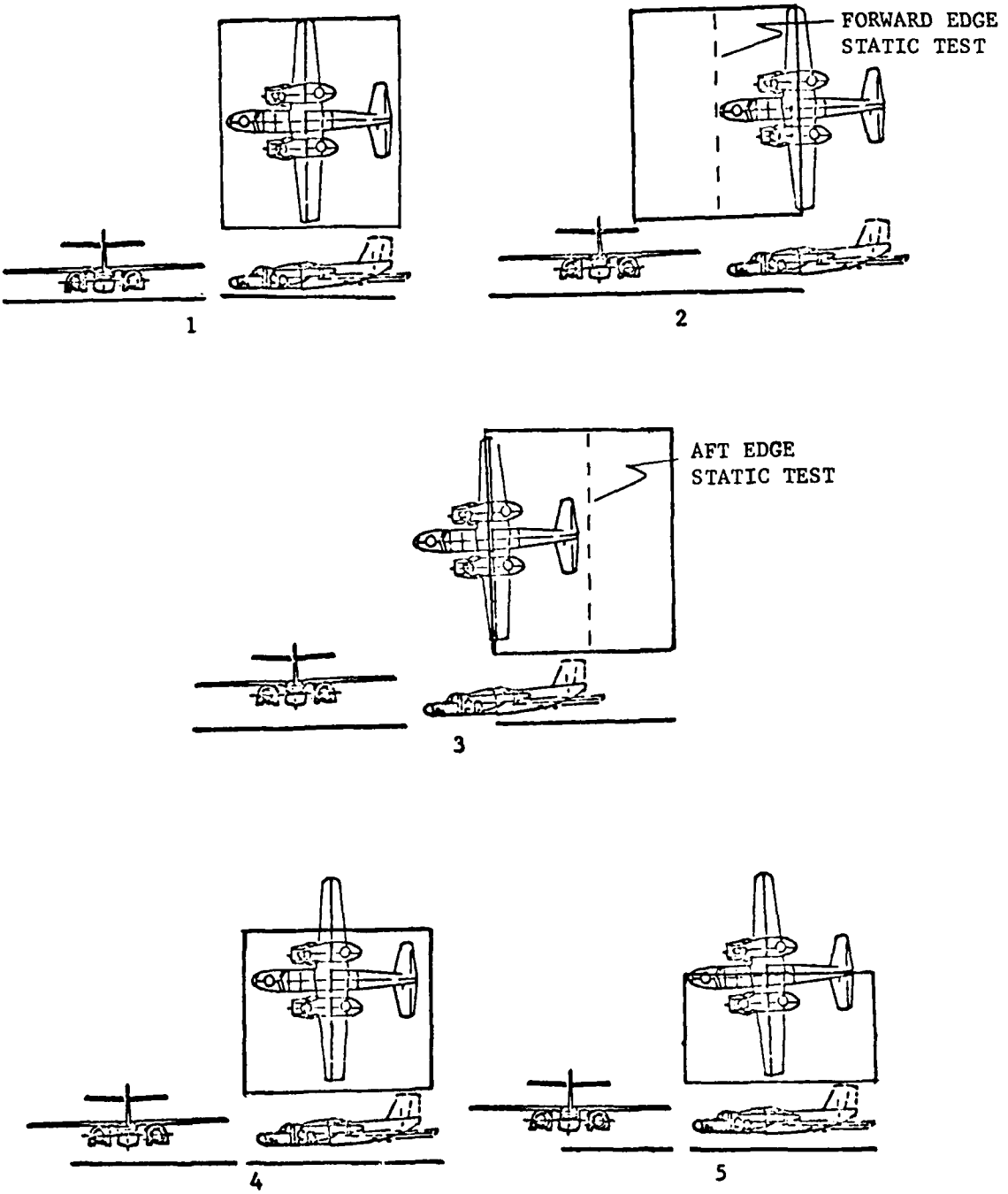

Figure 6. Ground board configurations

WING:		
AREA	0.78 m^2	(8.36 Ft^2)
SPAN	2.50 m	(8.209 Ft.)
CHORD		
ROOT	0.415 m	(16.355 in.)
TIP	0.208 m	(8.178 in.)
MAC	0.323 m	(12.721 in.)
ASPECT RATIO	8.06	
TAPER RATIO	0.50	
F.S. 25 $\bar{c}$	0.861 m	(33.9 in.)
INCIDENCE	5.0°	
WRP AT L.E.	0.152 m	(5.97 in.)
SWEEP		
L.E.	5.717°	
1/4 CHORD	3.334°	
T.E.	-3.817°	
AIRFOIL SECTION - 15% SUPERCRITICAL		
HORIZONTAL TAIL:		
AREA	0.196 m	(2.106 Ft^2)
SPAN	0.866 m	(34.1 in.)
$\bar{c}_H$	0.228 m	(8.98 in.)
ASPECT RATIO	3.83	
TAPER RATIO	0.509	
W.P.	0.376 m	(14.81 in.)
F.S. 0.25 $\bar{c}$	1.79 m	(70.417 in)
VERTICAL TAIL		
AREA	0.107 m^2	(1.158 Ft^2)
SPAN	0.328 m	(12.925 in.)
$\bar{c}_V$	0.234 m	(9.2 in.)

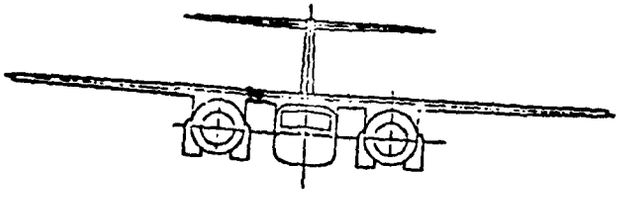

BODY:

DEPTH	0.256 m	(10.1 in.)
WIDTH	0.254 m	(10.0 in.)
LENGTH	2.00 m	(78.685 in.)

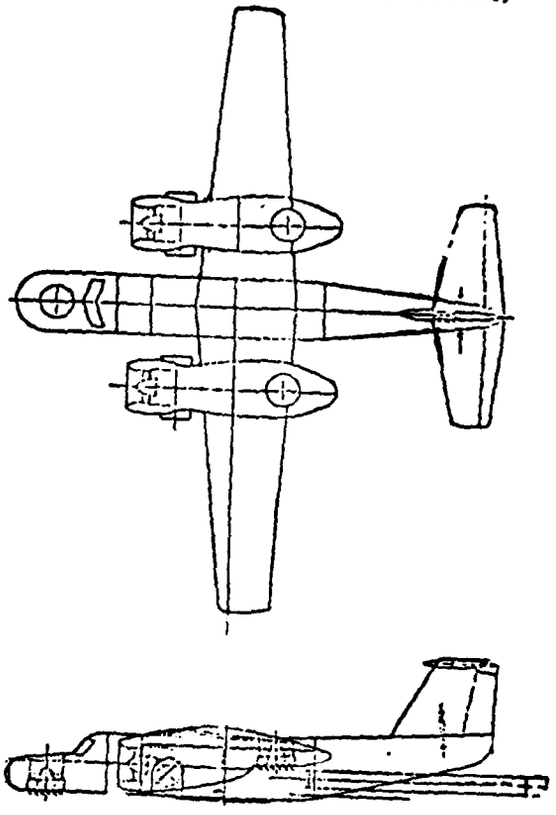

Figure 7. Model dimensions

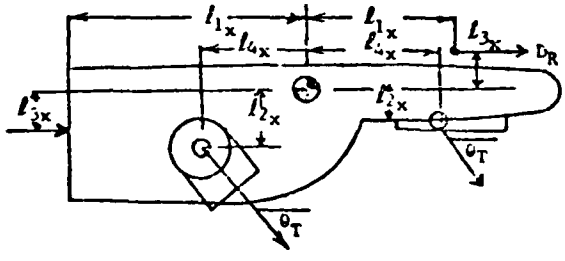

Fan Nomenclature

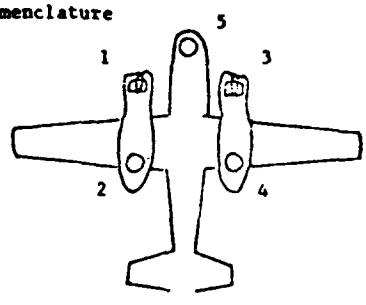

THRUST ARMS ~ Inches

Fan	l_1	l_2	l_3	l_4	l_5
1	16.25	2.40	1.24	8.25	13.98
2	- 9.25	0.50	5.1	- 9.40	13.79
3	16.25	2.40	1.24	8.25	-13.98
4	- 9.25	0.50	5.10	- 9.40	-13.79
5	28.00	6.30	1.00	28.00	0

Figure 7. Model dimensions (Concluded)

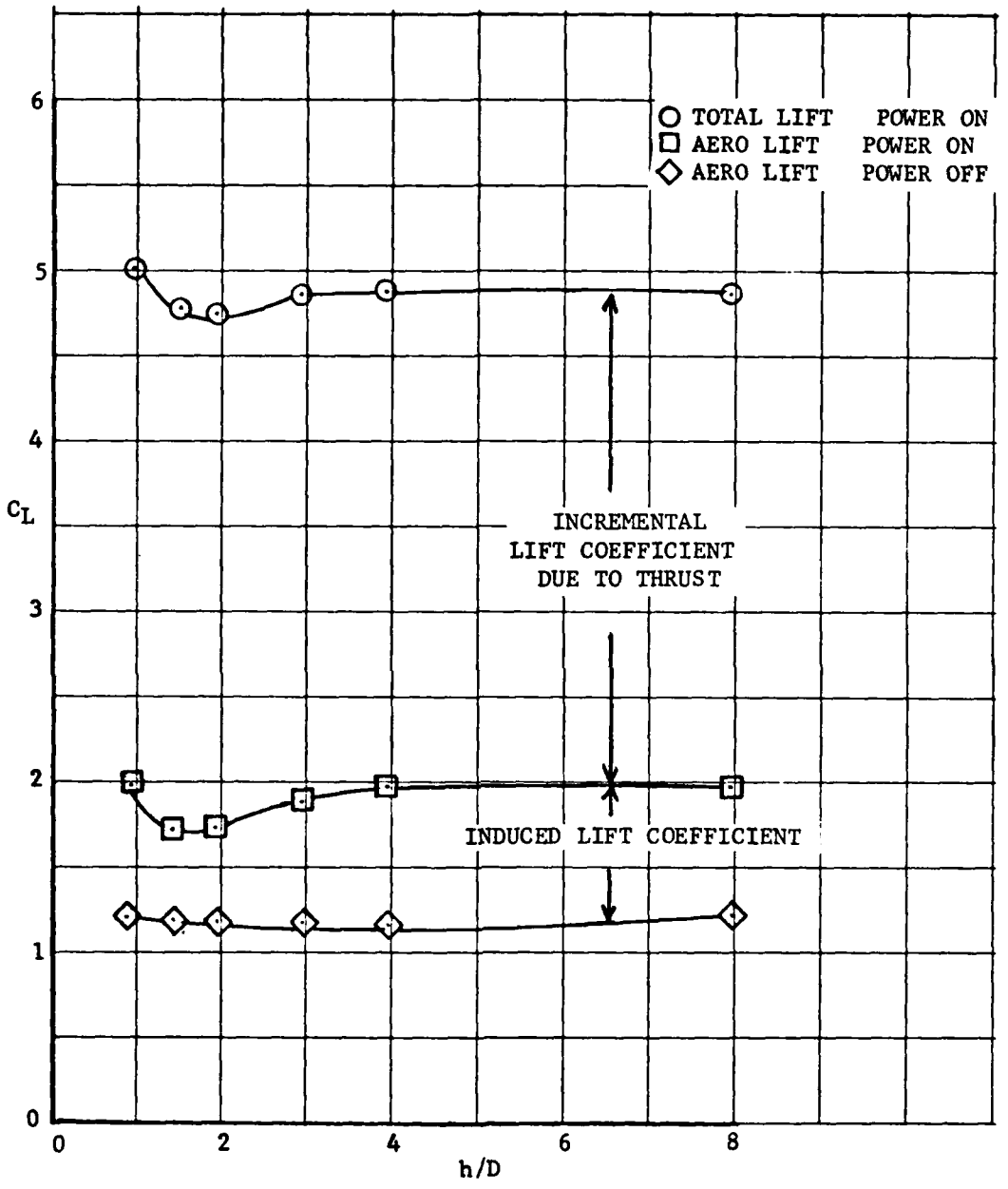

Figure 8. Lift coefficient incremental buildup due to power; $\delta_{N_{Fwd}} = 30^o$; $\delta_{N_{Aft}} = 60^o$; $C_T = 5.1$; $\alpha = 0^o$; $\emptyset = 0^o$

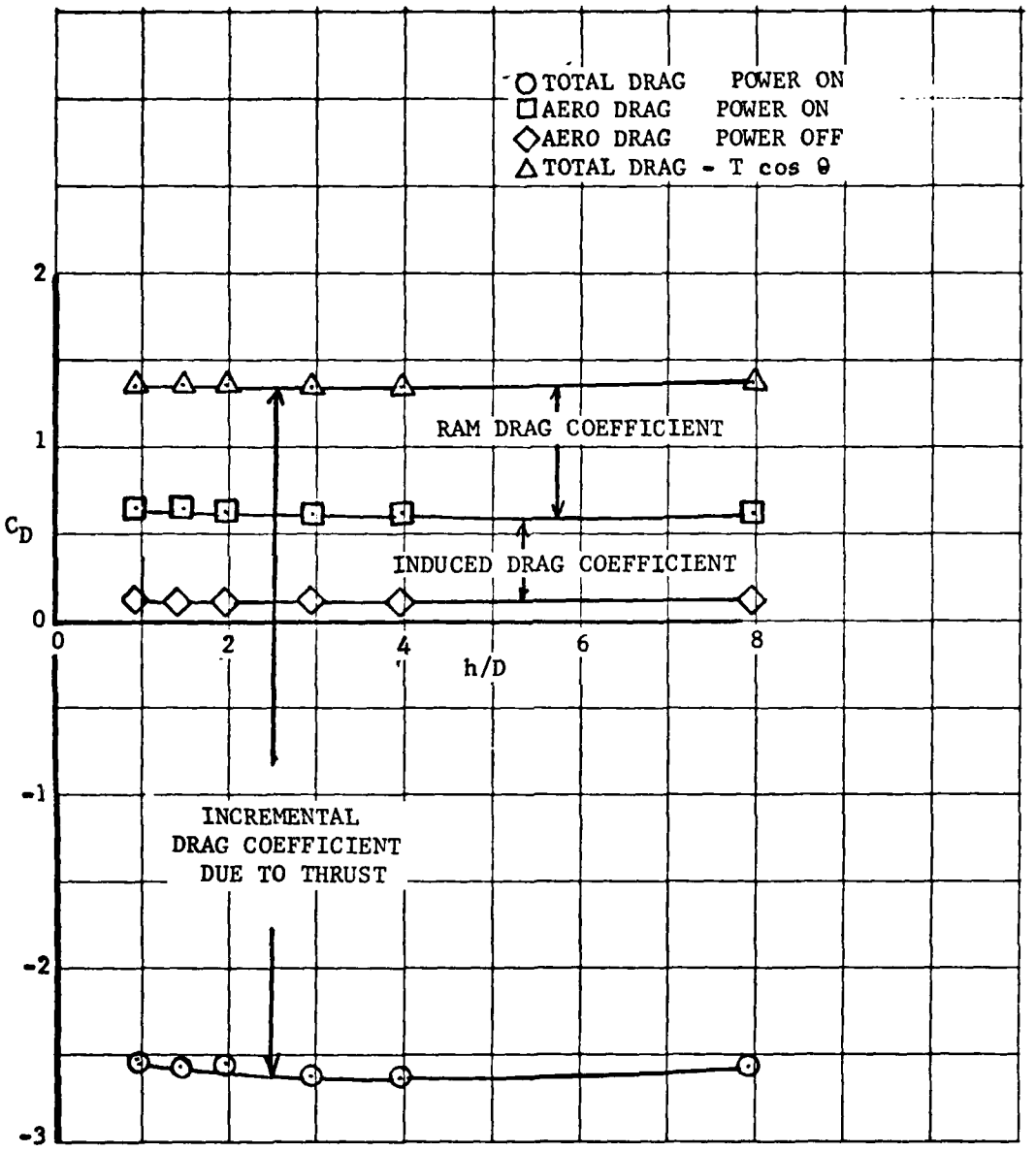

Figure 9. Drag coefficient incremental buildup due to power; $\delta_{N_{Fwd}} = 30^{\circ}$; $\delta_{N_{Aft}} = 60^{\circ}$; $C_T = 5.1$; $\alpha = 0^{\circ}$; $\emptyset = 0^{\circ}$

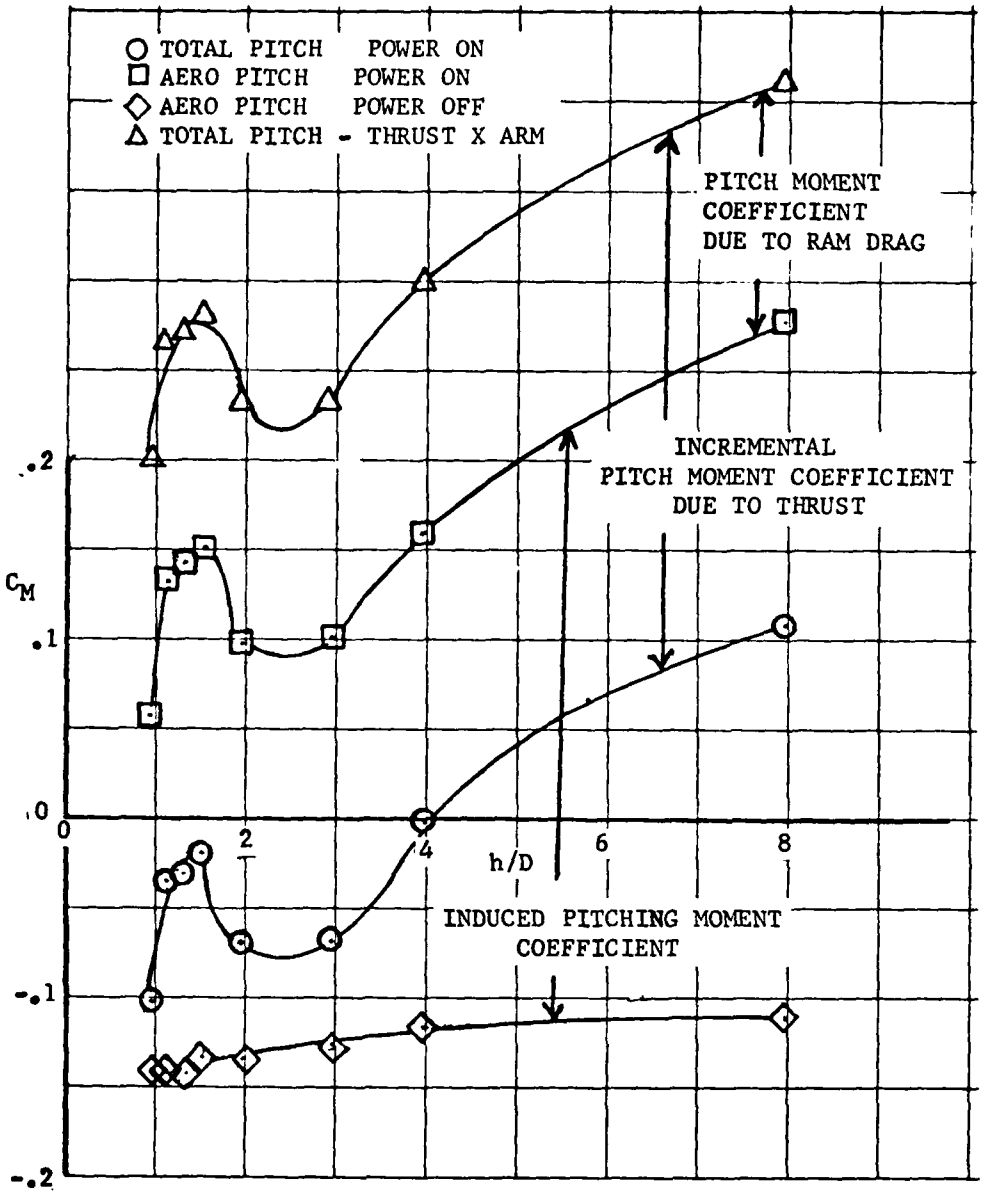

Figure 10. Pitching moment incremental buildup due to power; $\delta_{N_{Fwd}} = 30^{o}$; $\delta_{N_{Aft}} = 60^{o}$; $C_T = 5.1$; $\alpha = 0^{o}$; $\emptyset = 0^{o}$

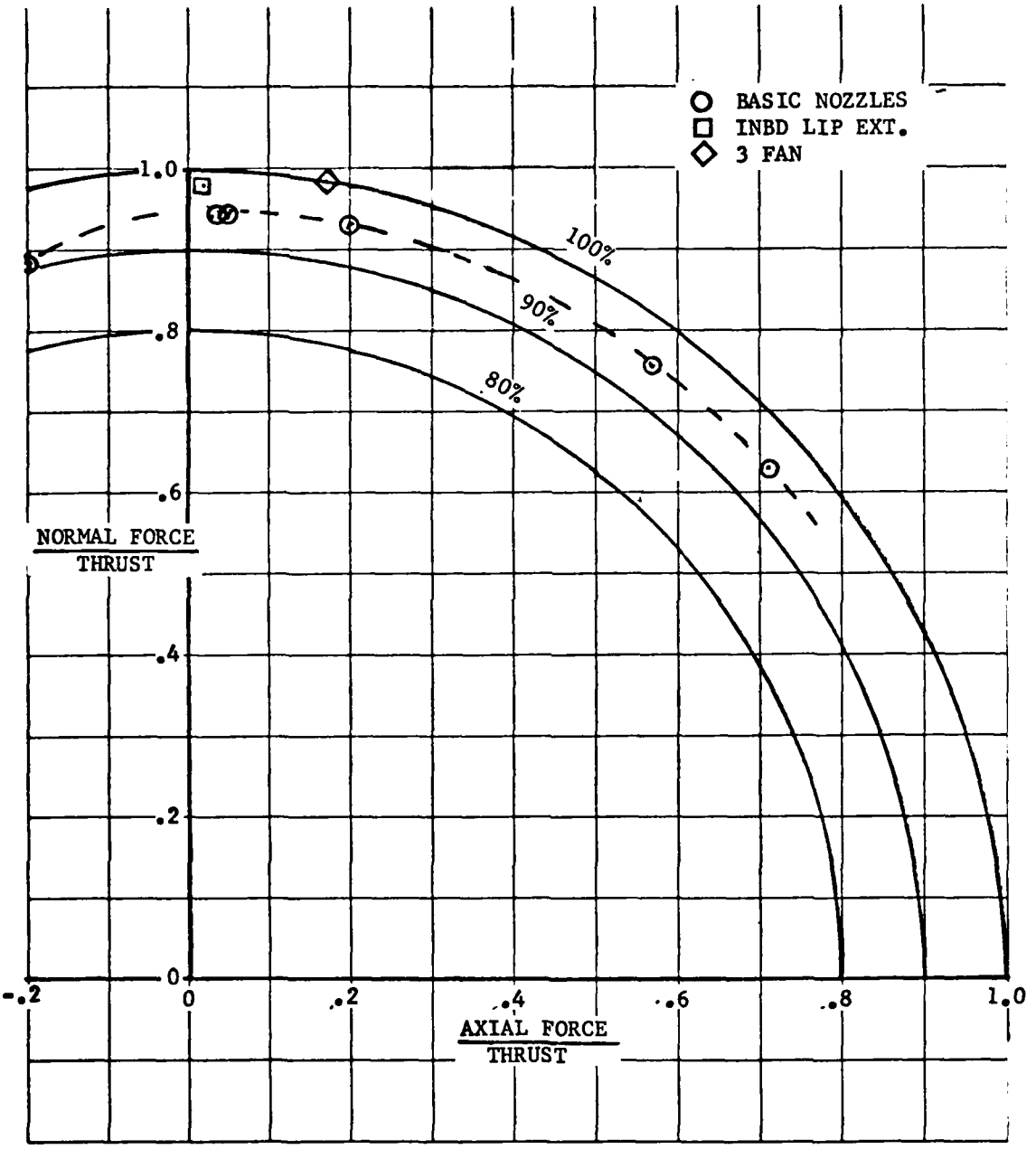

Figure 11. Normal force vs axial force - free air
$V/V_j = 0$, $\alpha = 0^o$, $\phi = 0^o$

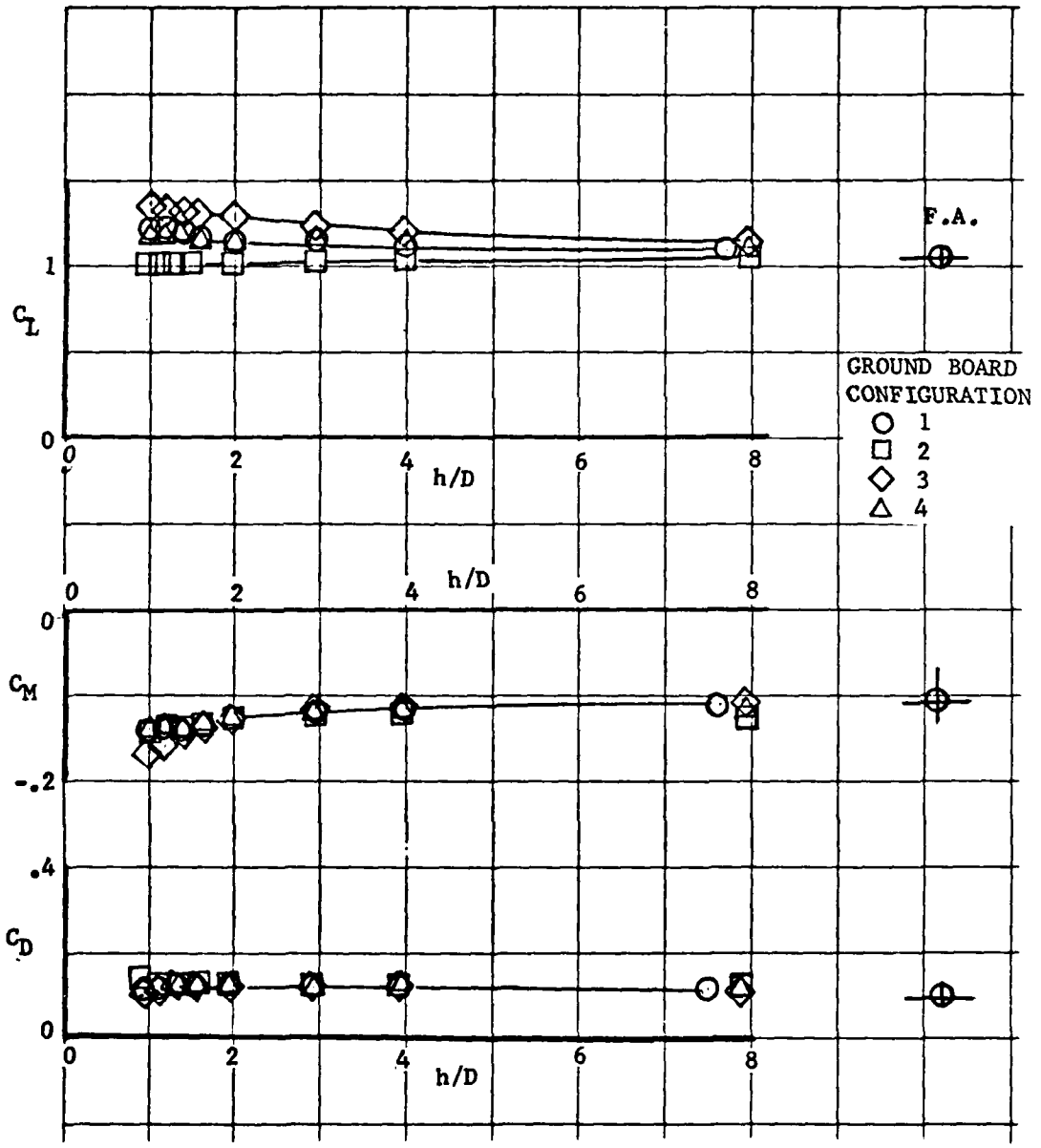

Figure 12. Effect of height on longitudinal characteristics with various ground board configurations - power off, $\alpha = 0^o$, $\phi = 0^o$

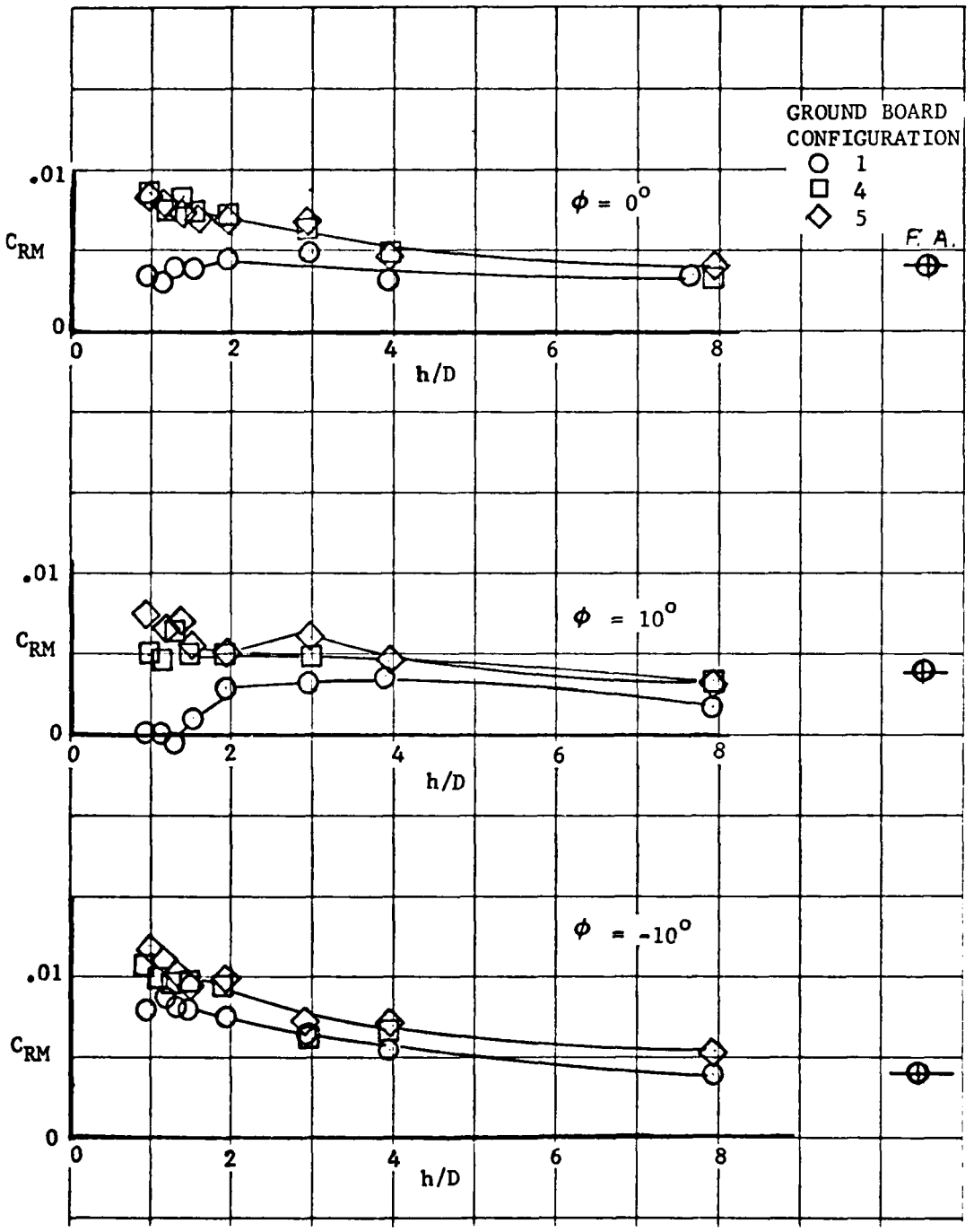

Figure 13. Effect of height on rolling moment coefficient with various ground board configurations - power off, $\alpha = 0^{\circ}$

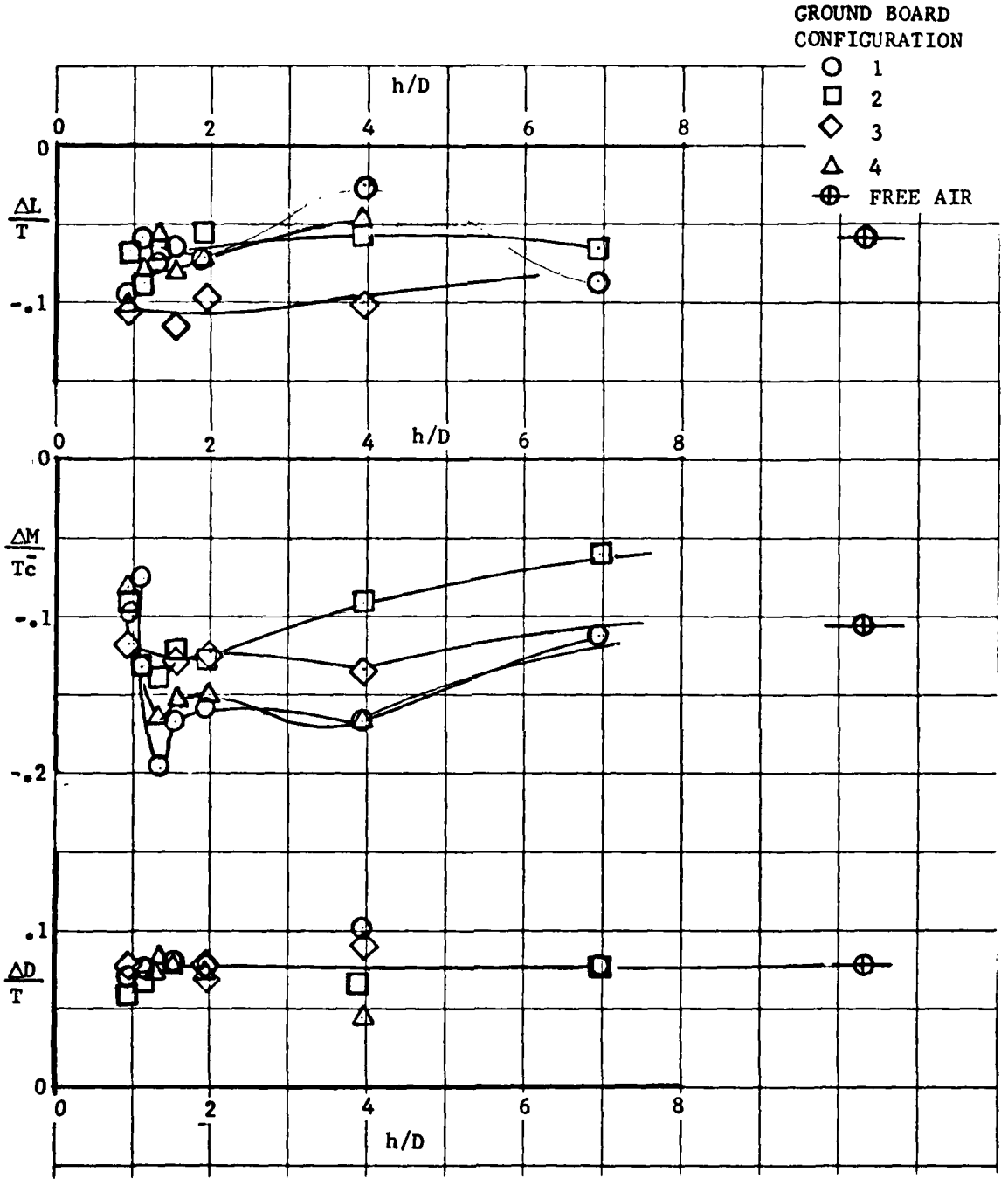

Figure 14. Effect of height on longitudinal thrust effects with various ground board configurations ~ $\delta_N = 90^o$, $V/V_j = 0$, $\alpha = 0^o$, $\phi = 0^o$

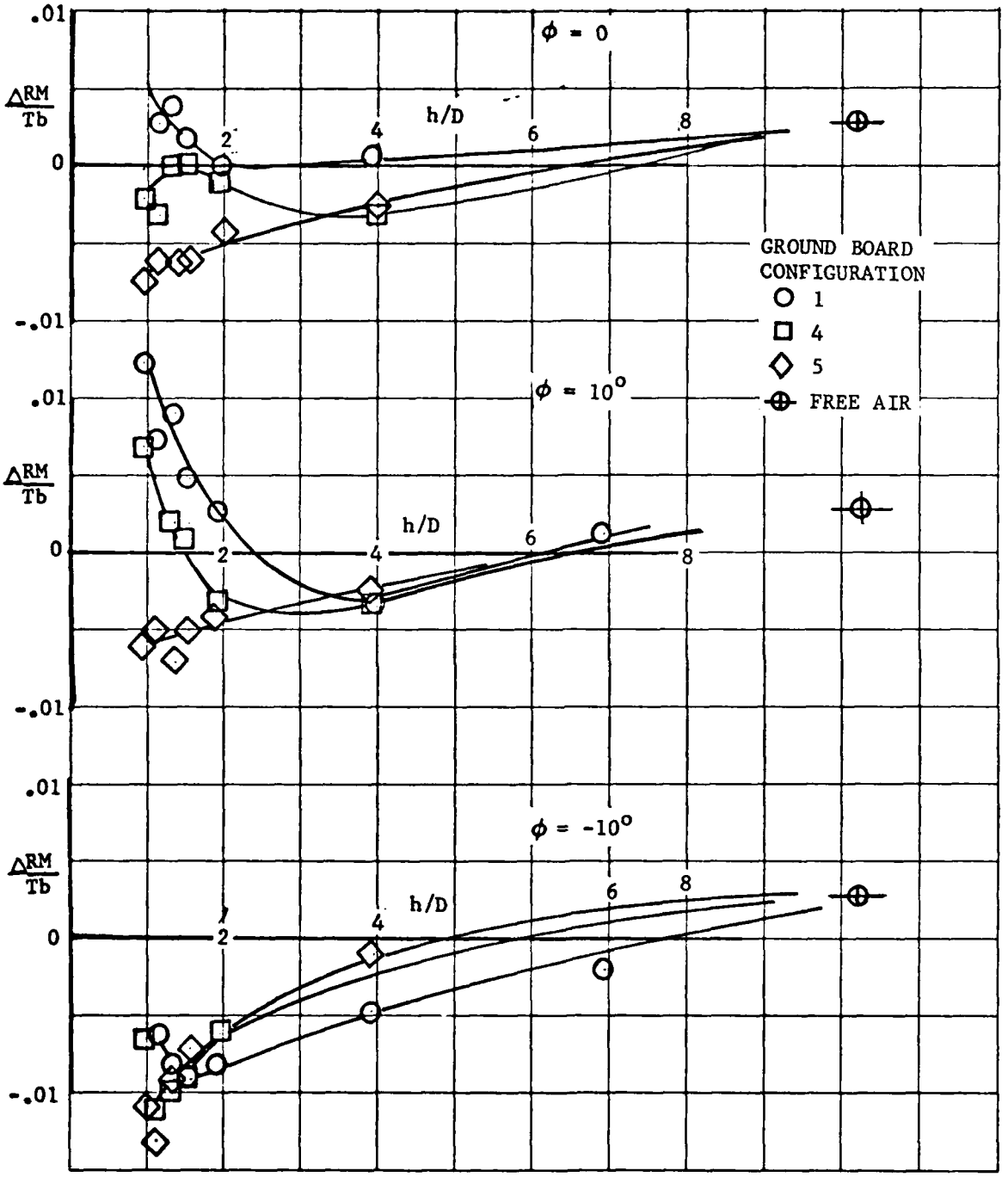

Figure 15. Effect at height on lateral thrust effects with various ground board configurations ~ $\delta_N = 90^\circ$, $V/V_j = 0$, $\alpha = 0^\circ$

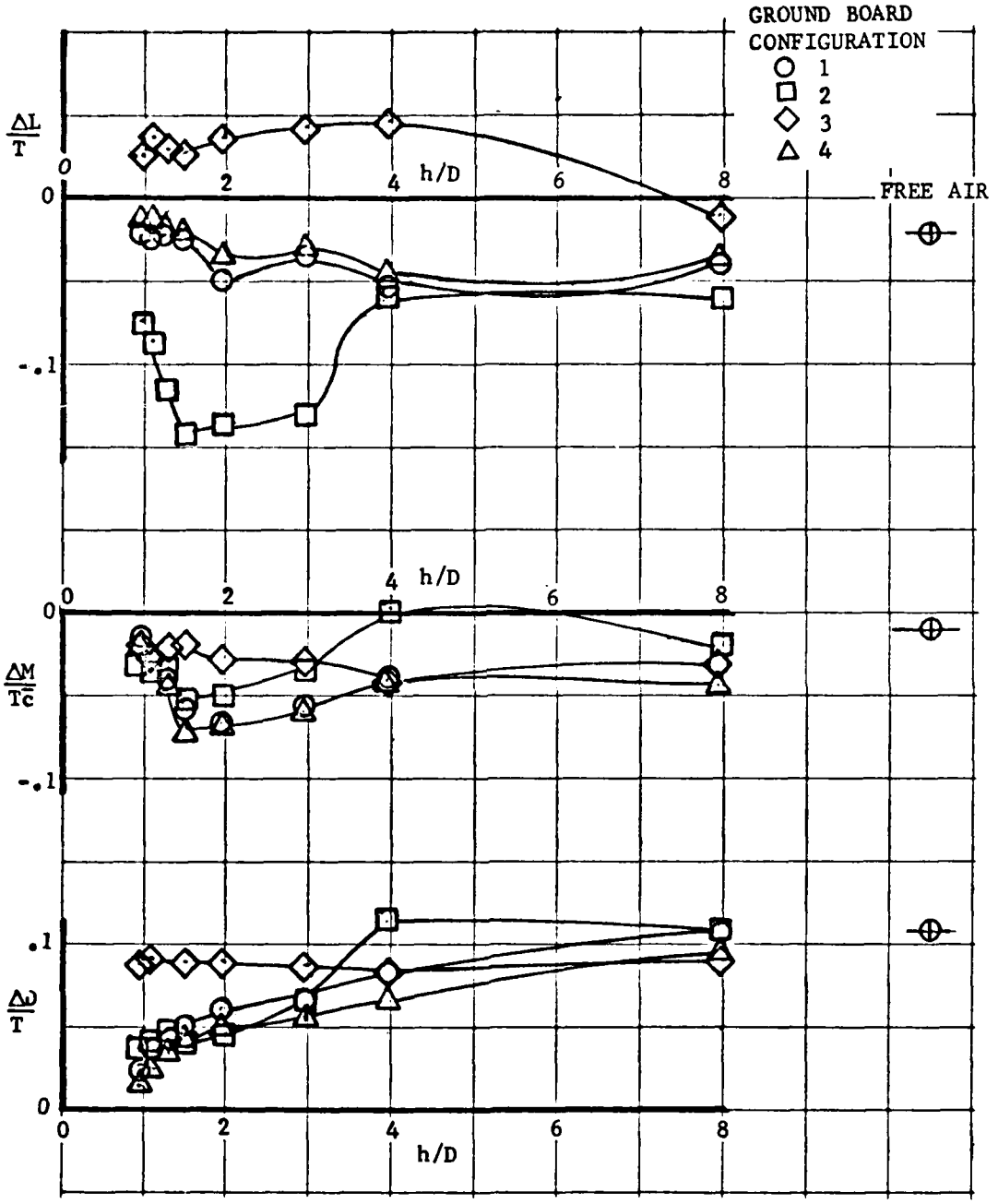

Figure 16. Effect of height on longitudinal thrust effects with various ground board configurations ~ $\delta_N = 90^o$, $V/V_j = .09$, $\alpha = 0^o$, $\phi = 0^o$

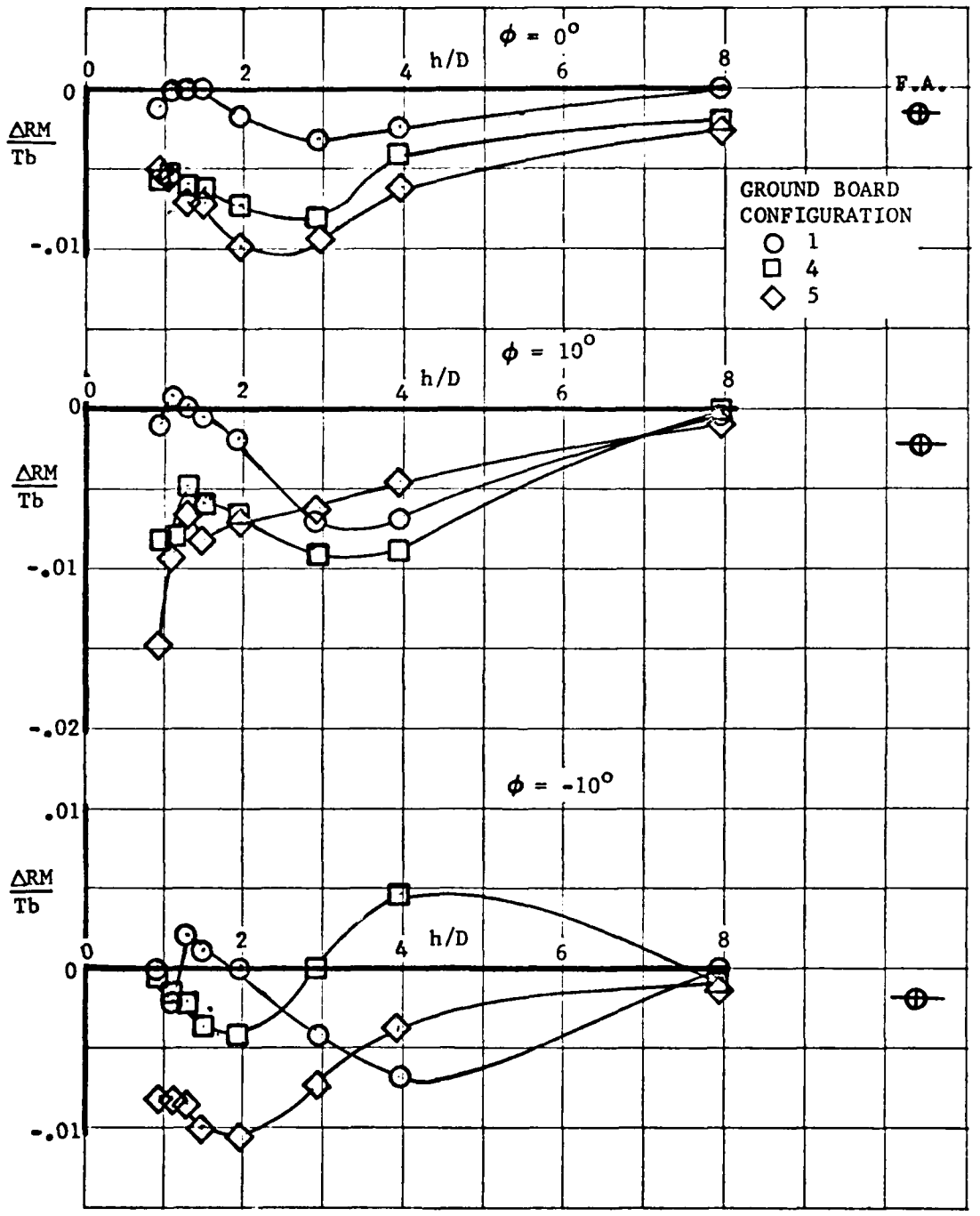

Figure 17. Effect of height on lateral thrust effects with various ground board configurations - $\delta_N = 90^\circ$, $V/V_j = .09$, $\alpha = 0^\circ$

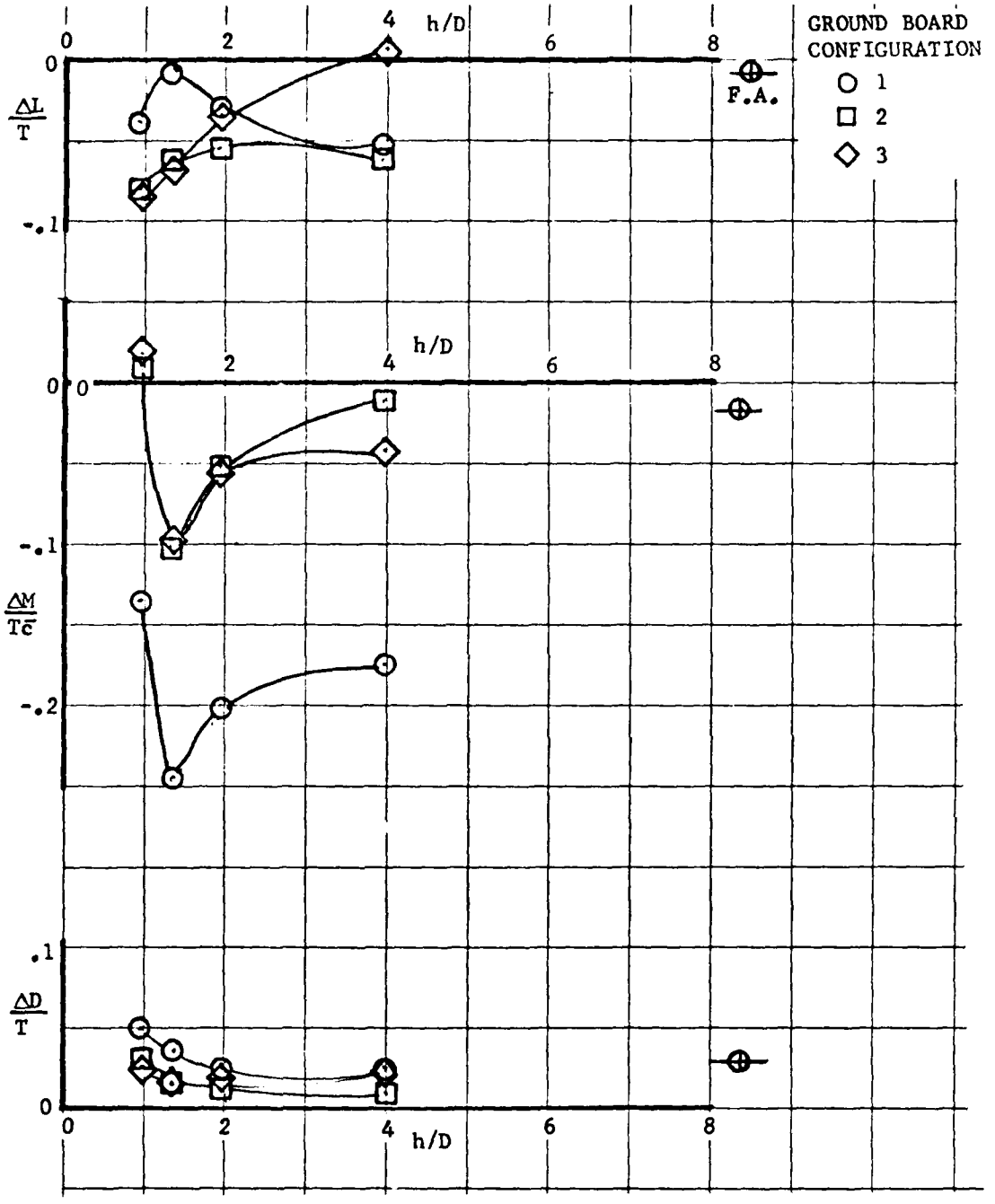

Figure 18. Effect of height on longitudinal thrust effects with various ground board configurations, three fan ~ $\delta_{N_{Nose}} = 80^{o}$, $\delta_{N_{Aft}} = 90^{o}$, $V/V_J = 0$, $\alpha = 0^{o}$, $\phi = 0^{o}$

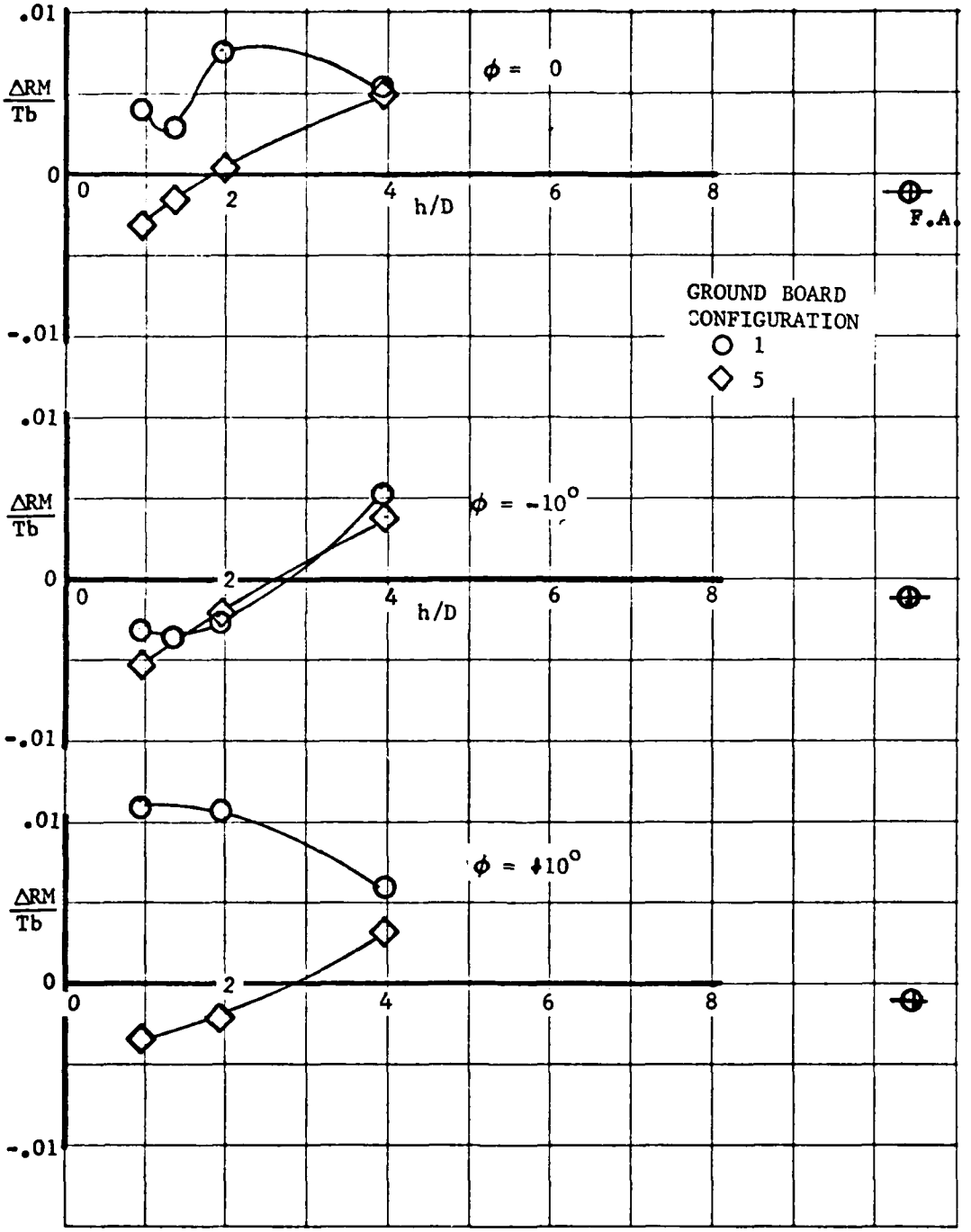

Figure 19. Effect of height on lateral thrust effects with various ground board configurations $\sim\delta_{N_{Nose}} = 80^{o}$, $\delta_{N_{Aft}} = 90^{o}$, $V/V_j = 0$, $\alpha = 0^{o}$

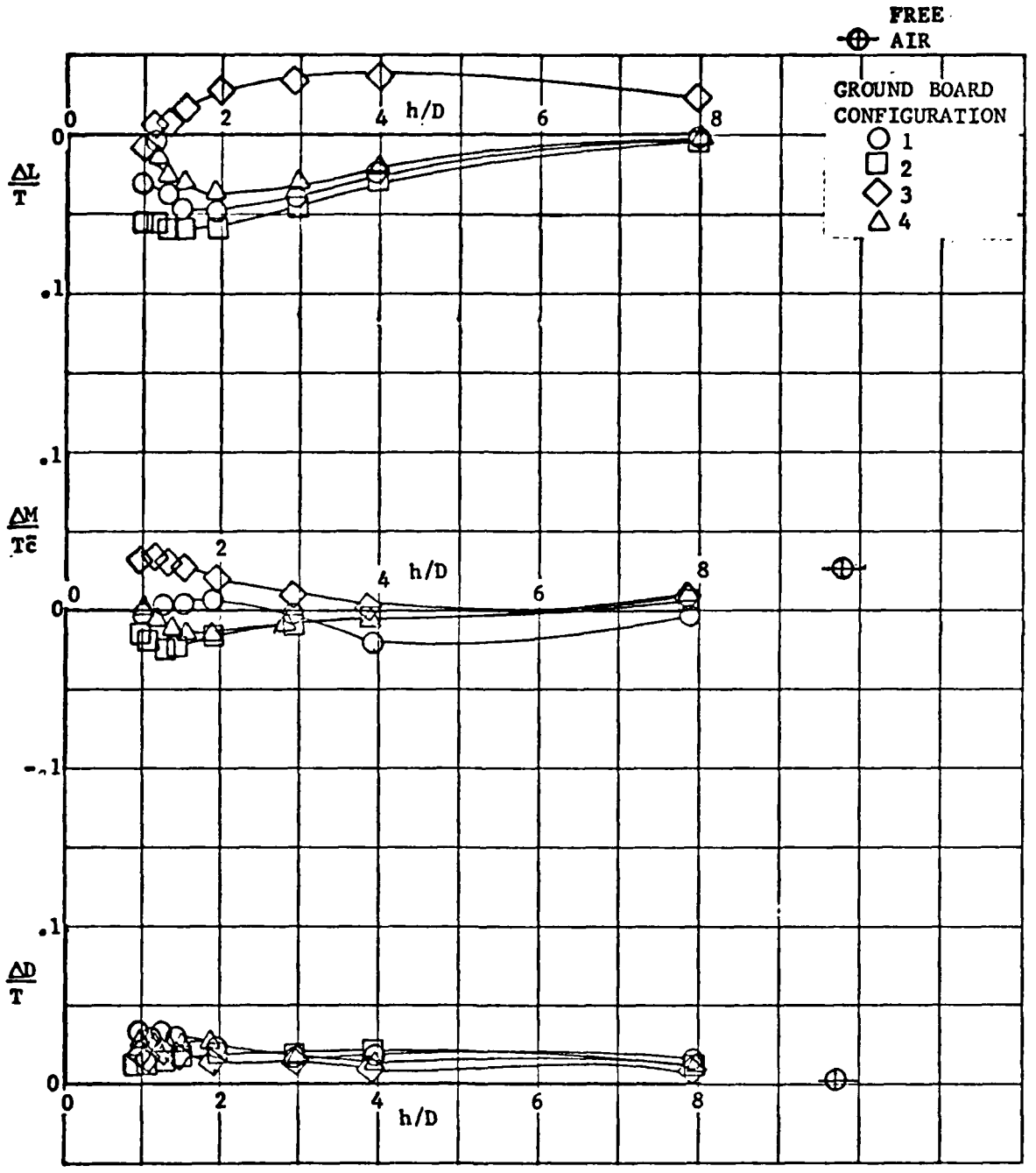

Figure 20. Effect of height on longitudinal thrust effects with various ground board configurations, three fan ~ $\delta_{N_{Nose}} = 80^{\circ}$, $\delta_{N_{Aft}} = 90^{\circ}$, $V/V_j = .068$, $\alpha = 0^{\circ}$, $\emptyset = 0^{\circ}$

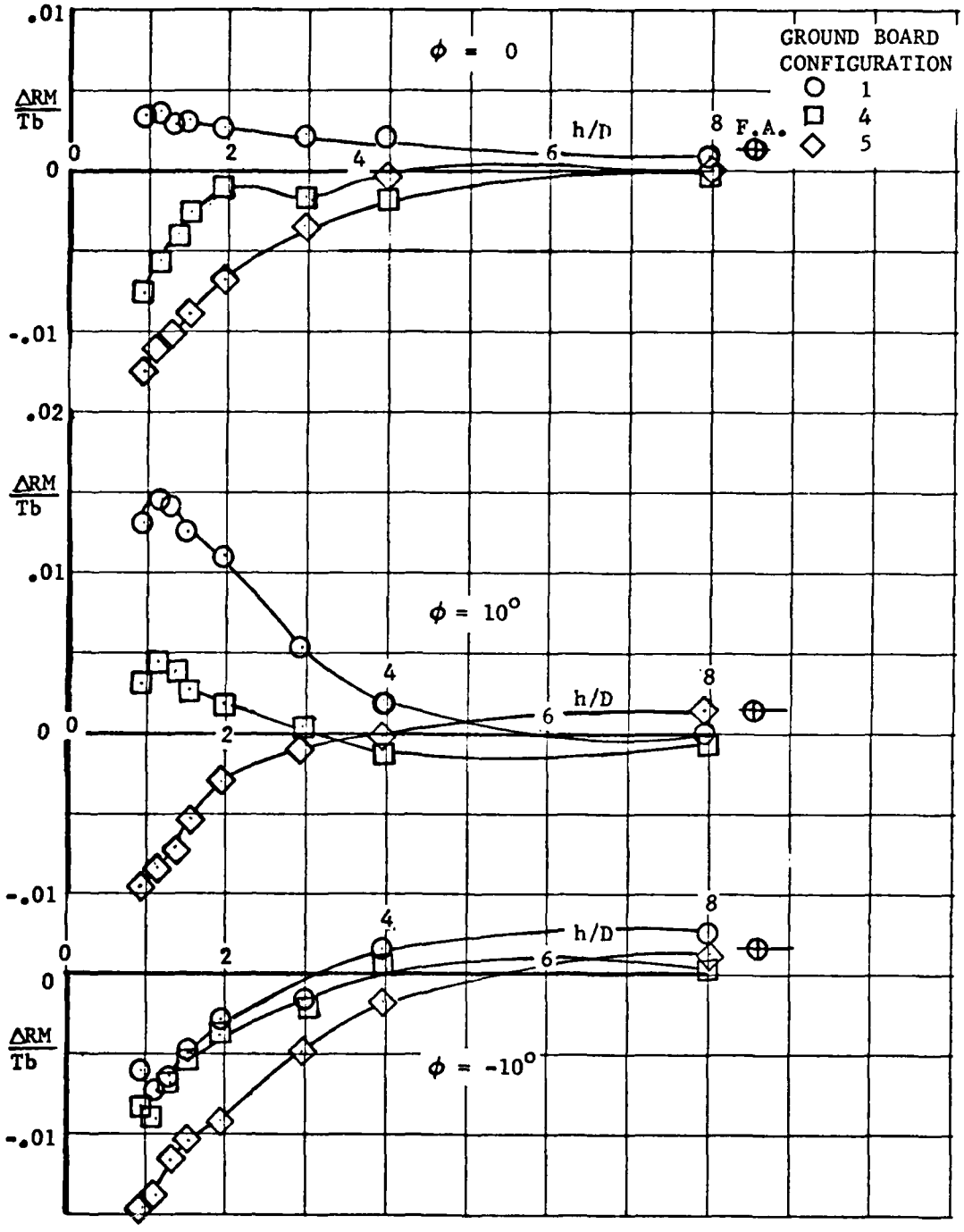

Figure 21. Effect of height on lateral thrust effects with various ground board configurations, three fan ~ $\delta_{N_{Nose}} = 80^{\circ}$, $\delta_{N_{Aft}} = 90^{\circ}$, $V/V_j = .068$, $\alpha = 0^{\circ}$

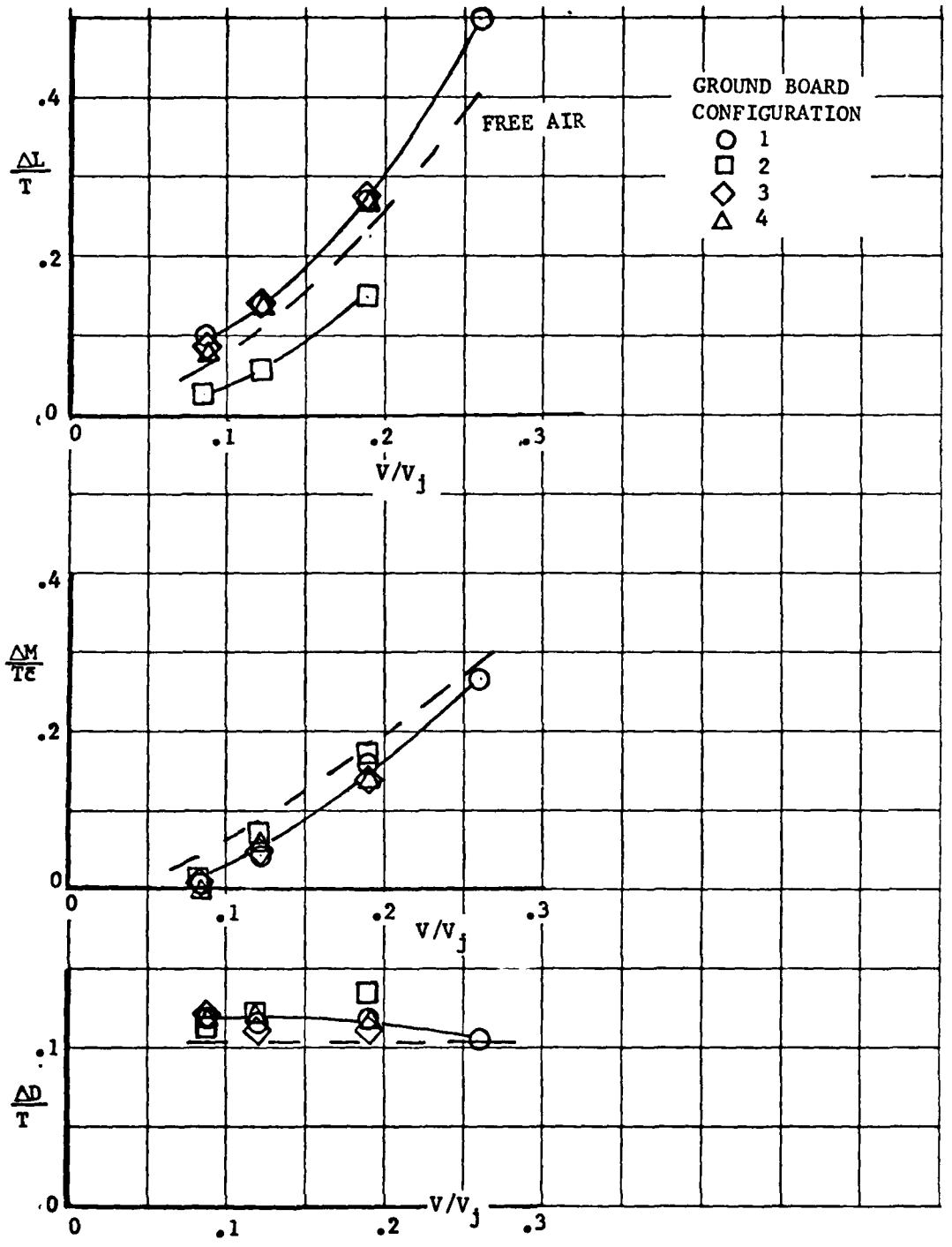

Figure 22. Effect of velocity ratio on longitudinal thrust effects with various ground board configurations ~ $\delta_{N_{Fwd}} = 30^{o}$, $\delta_{N_{Aft}} = 60^{o}$, h/D = 1, $\alpha = 0^{o}$, $\phi = 0^{o}$

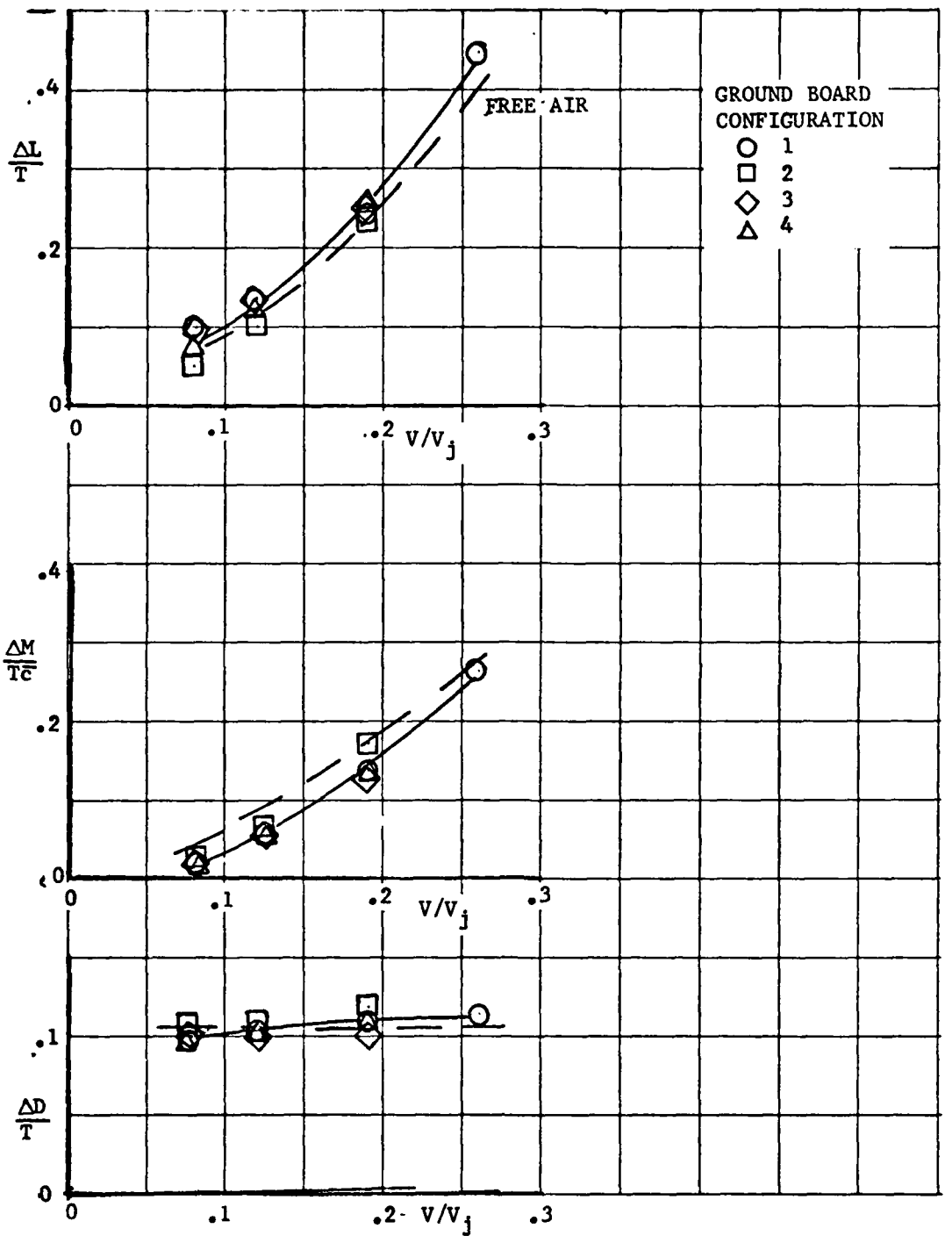

Figure 23. Effect of velocity on longitudinal thrust effects with various ground board configurations - $\delta_{N_{Fwd}} = 30^{o}$, $\delta_{N_{Aft}} = 60^{o}$, h/D = 4, $\alpha = 0^{o}$, $\emptyset = 0^{o}$

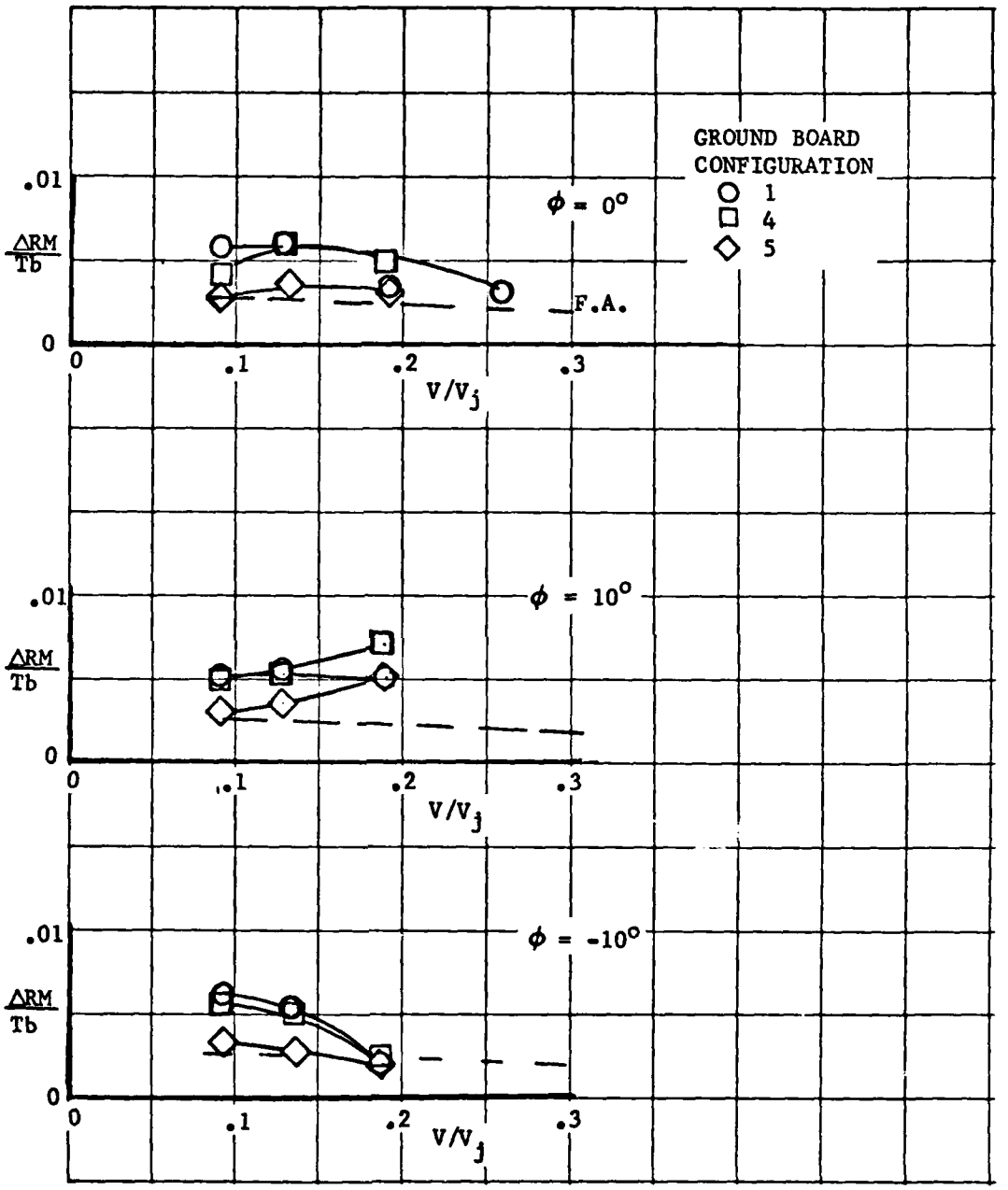

Figure 24. Effect of velocity ratio on lateral thrust effects with various ground board configurations ~ δ_N = 30°/60°, h/D = 1.0, α = 0°

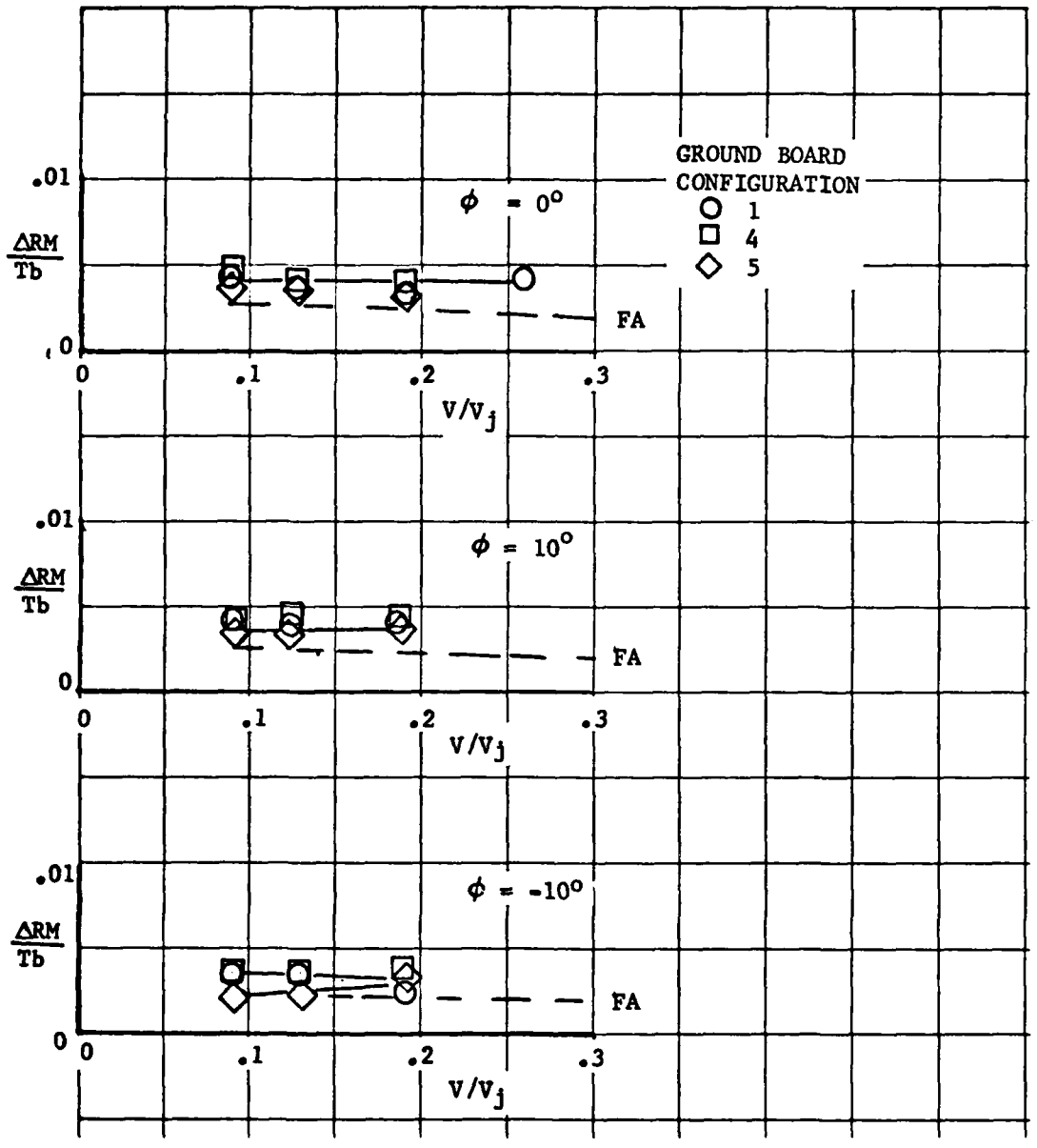

Figure 25. Effect of velocity ratio on lateral thrust effects with various ground board configurations ~ $\delta_N = 30^\circ/60^\circ$, h/D = 4.0, $\alpha = 0^\circ$

SESSION III

EXPERIMENTAL TECHNIQUES

IN

V/STOL AIRCRAFT DEVELOPMENT

Chairman:

David Hickey
NASA-Ames Research Center

ADAPTIVE-WALL TECHNOLOGY FOR V/STOL TESTING *

by

J. C. Erickson, Jr.
Aerodynamic Research Department
Calspan Corporation
Advanced Technology Center
Buffalo, New York 14225

ABSTRACT

The adaptive-wall wind tunnel concept has been proposed for both V/STOL and transonic testing where wall-interference effects are large and corrections cannot be made. The tunnel walls are used actively to control the flow field, and a theoretical calculation is used in conjunction with flow-field measurements to confirm that wall interference has been minimized, if not eliminated. For the transonic case, a two-dimensional adaptive-wall test section is under investigation in the Calspan One-Foot Wind Tunnel. This test section is described and experimental results with a 6%-blockage airfoil model are presented to demonstrate that iterative application of wall control effectively eliminates the wall interference. The V/STOL application is based upon the same principles as the transonic. The principal differences between the transonic and V/STOL cases are discussed, particularly the treatment of ground effect, if present, and the handling of the highly-deflected propulsion-system efflux, when it exists. Certain aspects of the existing adaptive-wall technology could be utilized to provide improved testing capabilities in a timely fashion. In particular, a partial implementation, which does not use active wall control, is described. A passive-wall configuration would be retained, but the flow-field measurements and theoretical calculations would be carried out to assess whether the flow is interference free. Thus, the technique could provide realistic assessments of the validity of a given test, and the basis for corrections if they are meaningful.

* Based, in part, on research sponsored by the Office of Naval Research and the Air Force Office of Scientific Research under Contract No. N00014-72-C-0102, with supplemental support by the NASA/Langley Research Center; by the ONR and AFOSR under Contract No. N00014-77-C-0052; by the Arnold Engineering Development Center under Contract Nos. F40600-76-C-0011 and F40600-78-C-0003; and by NASA/Ames Research Center under Contract No. NAS2-8777.

INTRODUCTION

Research is in progress at several institutions (Refs. 1 to 9, for example) to develop the concept of adaptive-wall wind tunnels, including demonstration that interference-free flows can be achieved by controlling the flow field in the vicinity of the walls. The concept of a self-correcting, or adaptive-wall, wind tunnel has been described in the literature (Refs. 1 and 2). Briefly, it is based on the idea of measuring the components of the disturbance velocity at discrete points along imaginary control surfaces, or interfaces, in the flow field within the tunnel. A theoretical formulation for the flow field external to the control surfaces, including the boundary condition for unconfined flow, i.e., that all disturbances vanish at infinity, is used to determine if those measured velocity components satisfy functional relationships which are consistent with interference-free flow. If they are not, an iteration procedure provides a new approximation for the flow field at the interfaces, and the flow through the tunnel walls is readjusted until the measured quantities are consistent with the boundary condition for unconfined flow. In this way, the best theoretical and experimental features are combined to minimize wall interference. The flow chart for the adaptive-wall tunnel scheme is shown in Figure 1.

The principal activity in adaptive-wall technology has been in the transonic flow regime. Two-dimensional adaptive-wall test sections are under development at several laboratories (Refs. 3 to 5) and attention is now being given as well to the requirements for three-dimensional, adaptive-wall, transonic test sections. The interest in adaptive-wall test sections for transonic flow arose because the applicability of wall-interference corrections is less evident in this regime. There are two main reasons for this. First, transonic tunnels are generally ventilated, with perforated or slotted walls which exhibit complicated flow behavior that cannot be represented adequately by a simple theoretical description. Second, transonic flow is inherently nonlinear and so boundary interference effects are not simply additive as they are in flow fields which are basically linear.

Application of the adaptive-wall concept to V/STOL testing has received very little attention. Nevertheless, many of the same testing limitations exist as in transonic flows, since V/STOL configurations also exhibit nonlinear flows. The aerodynamics of a V/STOL vehicle is profoundly affected by the energized, vortical efflux of its lift/propulsion system. The effects of this efflux are not simply additive, so the applicability of wall-interference corrections is again not so evident. Moreover, passive-wall modifications such as removal of wall segments or their replacement by ventilated segments also contribute to the uncertainty of corrections in V/STOL tests.

In the following sections, we describe the Calspan implementation of the adaptive-wall concept, as well as some representative experimental results which demonstrate how active flow-field control can minimize wall interference. Features unique to the implementation of the concept for the V/STOL application are discussed next. Then a partial implementation of the concept is described for application to existing passive-wall V/STOL tunnels. In this embodiment, the flow disturbance measurements and flow-field calculations are carried out to assess the degree of interference present and, where meaningful, to provide a basis for the quantitative evaluation of wall-interference corrections.

THE CALSPAN ADAPTIVE-WALL WIND TUNNEL

The Calspan One-Foot Adaptive-Wall Wind Tunnel (Figure 2) is a closed-circuit, continuous-flow facility. The test section is two dimensional with perforated top and bottom walls of 22.5% open area. The plenum chambers behind the perforated walls have been divided into 18 segments, 10 on the top and 8 on the bottom, and each segment is connected to a pressure and a suction source through individual control valves. The pressure source is the tunnel stilling chamber, and the suction source is an auxiliary compressor discharging into the tunnel circuit in the diffuser. Six plenum chambers in the immediate vicinity of the model have provisions for a distributed porosity which can be varied linearly in the streamwise direction.

The model and test section are shown in Figure 3. The model is an NACA 0012 airfoil section with a 6-inch chord (6% solid blockage) and is instrumented with a row of pressure orifices and with a three-component force balance supporting a metric section on the tunnel centerline. The test section instrumentation (Figure 3) consists of two static-pressure pipes, each with 52 pressure orifices, and 18 flow-angle probes, with each probe located opposite the center of a plenum segment. These sensors are located outside the wall boundary layers and enable us to infer the normal and streamwise components of the disturbance velocity. Further details of the test section, model and instrumentation are given in Refs. 5 and 6.

EXPERIMENTS

The first experiments were performed with the 6-inch chord model in the Calspan Eight-Foot Tunnel (0.75% solid blockage) to acquire a body of data that could be regarded as essentially free from wall interference. These data are presented and analyzed in Ref. 10.

Initial experiments with the model in the One-Foot Tunnel were made to simulate tests in a conventional perforated-wall facility. This simulation consisted of using wall control to establish a uniform axial pressure distri-

bution in the empty test section. The model was then installed and tested with the same valve settings. The lift, drag and pitching-moment results obtained at $M_\infty = 0.725$ are compared with the Eight-Foot Tunnel data in Figure 4. In general, this comparison shows that there are significant wall-interference effects on the model forces and moment in this simulation. The effects on lift and drag are moderate and on pitching moment are large. The interference includes effects such as changes in the separation point and changes in the shock-wave position at supercritical conditions. This latter effect can be seen in the comparison of airfoil-surface pressure distributions at this Mach number for $\alpha = 2°$ in Figure 5.

Experiments were performed in the self-correcting mode by iterating with the model at $\alpha = 2°$ and $M_\infty = 0.725$. The method we used to begin the iterations was to estimate the streamwise disturbance velocities at the control surfaces by Prandtl-Glauert theory. The free-stream Mach number is established in the test section, and wall control is then applied to obtain the desired distributions of the streamwise disturbance velocities, i.e., local static pressures on the pipes. All data then are recorded and used in evaluating the functional relationships to obtain a second approximation. The pressure distribution after this first iterative step is presented in Figure 6. It can be seen that the shock wave already is located at its interference-free position, as indicated by comparison with the Eight-Foot Tunnel data.

The results of the iteration are shown in Figure 4 by the numbered data points, where each number indicates the iterative step. The solid triangle indicates the equivalent data point in the simulated conventional facility. It can be seen that after three iterations, we have largely eliminated the wall-interference effects in that the lift and drag agree with the Eight-Foot Tunnel data, within the scatter in that data, and the pitching moment agrees to within 5% to 7%. Normally, we would have continued the iterations because the evaluation of the functional relationships did not indicate complete convergence, but we were at the limits of control at one plenum section above the model and could not achieve the next iterative step. Nevertheless, we regard these results, and those obtained at lower Mach numbers and higher angles of attack (Refs. 5 and 6), as a convincing demonstration of the concept. The control limitations were removed subsequently by reducing auxiliary control system losses. Experiments are continuing for cases in which the local supersonic regions extend to the tunnel walls.

V/STOL APPLICATION

The principles for complete implementation of the adaptive-wall concept for V/STOL testing are the same as in the transonic case, but the details necessarily differ. A representative V/STOL configuration is shown in Figure 7 for unconfined flow at a low flight speed. The main differences in this V/STOL case from the transonic are the presence of the highly-deflected efflux of the lift/propulsion system and the absence of locally

supersonic flow and shock waves. In low-speed flight, the efflux will exit through the interface into the external flow in the near vicinity of the model. This is in marked contrast to an aircraft configuration in conventional flight, where the propulsion-system efflux and aircraft wake are only slightly deflected from the flight direction and exit through the interface far downstream of the model where their effect is minimal.

The basic features required in the procedure of Figure 1 will be discussed in turn for the V/STOL application. First, suitable provisions for active control of the flow in the vicinity of the walls is necessary to adjust the desired flow at the interface S within the tunnel. The highly-deflected flow would require different considerations of wall control from the transonic case. In particular, much larger quantities of air would have to be introduced above the model and withdrawn below it. Also, provisions for removing the efflux at the proper location (which is unknown in advance and results from the iterative procedure) must be made.

The second feature is the measurement of the flow disturbance quantities at the interface. It is shown in Ref. 11 that, in the absence of the propulsion-system efflux, it is necessary to measure the distributions of only the streamwise v_{s_m} and normal v_{n_m} components at the interface to provide the redundant measurements for examining whether the flow is unconfined. The tangential component is unnecessary because it can be found directly from the streamwise component and so is not an independent quantity. A discussion of measurement techniques is given in Ref. 6. In addition, we are examining, at present, a technique for using a static pipe to determine the streamwise gradient of v_{n_m} in addition to determination of v_{s_m}. The existence of the propulsion-system efflux, as it exits through the interface near the model, requires additional measurements to complete the boundary conditions for the external flow calculation. We anticipate (Ref. 6) that the distributions of the vorticity and momentum in the energized efflux would have to be measured, but only at its intersection with the interface, as discussed below.

The third feature of the adaptive-wall procedure is the calculation of the unconfined flow exterior to the interface; i.e., the evaluation of the functional relationships which must be satisfied by v_{s_m} and v_{n_m}. If the presence of the efflux in the exterior flow region is neglected, the distribution of v_{n_m} along the interface can be used as the boundary condition for the exterior flow calculation, just as in transonic flow. This enables the corresponding unconfined-flow distribution v_{s_c} to be calculated from the outer flow and compare with v_{s_m}, as shown in Figure 1. Alternatively, the roles of v_{n_m} and v_{s_m} can be reversed with v_{s_m} used as the boundary condition. For these cases, well-established contemporary inviscid calculation methods for subsonic flows; e.g., source-panel or vortex-lattice methods, can be used for the exterior-flow calculation (Refs. 6 and 11). These procedures are accurate for calculation of the inviscid flow exterior

The presence of the propulsion-system efflux in the exterior flow (Figure 8) presents a fundamentally different problem. In this case, the efflux must be modeled theoretically with the initial conditions on its vorticity and momentum distributions at the interface specified as determined by the flow measurements there. The key problem is to establish the accuracy necessary in modeling the efflux. Fortunately, when the efflux enters the exterior flow, it should be sufficiently deformed, in most cases, so that the trailing vorticity is the dominant feature and the efflux should make a relatively small angle with respect to the free stream. In this situation, it might be feasible to model the efflux realistically by relatively simple means, say, by an adaptation of three-dimensional jet-flap theory. In any case, the extensive literature on jets in cross flow should provide a suitable model. Thus, the complete exterior-flow calculation procedure would involve a combination of either a source-panel or vortex-lattice representation of the interface, together with a model of the efflux in the exterior flow with the vorticity and momentum of the efflux determined from the measurements at the interface. It should be emphasized that in a complete implementation of the adaptive-wall concept, no calculations of the flow within the interface, i.e., about the wind tunnel model, are required. All information concerning the flow about the model is communicated by means of the measurements at the interface.

The final feature of the adaptive-wall concept is the control logic, i.e., how to proceed toward unconfined flow if the exterior-flow calculation indicates that the flow remains confined by the walls. It is assumed that sufficient flow control is provided at the walls to set any streamwise or normal flow velocity distributions that are desired at the interface. Then, if the v_{n_m} distribution is set in each step as in Figure 1, the difference between v_{n_c} and v_{n_m} is used in an iterative relaxation procedure to prescribe a new v_{n_m}. This process continues until convergence is achieved. A full discussion is given in Reference 6.

Attention has been focused here on the use of the adaptive-wall concept for achieving flows that are unconfined; i.e., as if the wind-tunnel model were located in a flow that extends indefinitely in all directions from the model and its propulsion-system efflux and wake. Another important flow regime in V/STOL testing occurs when the model is in ground effect. With the ground present, the disturbances vanish far away from the model, efflux and wake in all directions, except below the model. At the ground plane, the velocity component normal to the ground must be zero. The adaptive-wall principles are applicable in ground effect, too. The interface S must be located entirely above the ground-plane location. Then, the calculation of the exterior flow in ground effect can be carried out in a similar fashion to that for fully unconfined flow, except that the boundary condition of zero normal velocity would be imposed at the ground plane location. When the propulsion-system efflux extends into the exterior flow, its modeling must account properly for its interaction with the ground.

PARTIAL IMPLEMENTATION OF ADAPTIVE-WALL CONCEPT

Complete implementation of the adaptive-wall concept in V/STOL tunnels holds considerable promise in the long term. However, such implementation will not be achieved for several years, as there is a great deal of hardware and software development required. Some of the development tasks involved have been touched upon in the previous section.

On the other hand, there are many currently operational V/STOL tunnels with passive walls. These tunnels will remain in operation for many years. In addition, there have been several proposals recently for passive-wall modifications which would extend the operating envelope of existing V/STOL tunnels. These modifications generally involve some ventilation of the tunnel walls, say by removing wall segments or replacing them with perforated or slotted sections. When such changes are made to solid-wall tunnels, the boundary condition that there be no flow through the walls no longer holds everywhere, and ventilated-wall boundary conditions must be used to estimate the amount of wall interference on the model. Unfortunately, these boundary conditions are not well established because of the complex flow processes in and out through the walls. It is in this situation that the adaptive-wall tunnel ideas can be applied to verify that there are, in fact, reductions in the level of interference present. This could be accomplished by carrying out measurements of the flow disturbance quantities, including those characterizing the efflux, and the subsequent evaluation of the external-flow functional relationships. The differences between the measured and calculated velocity components at the interface would indicate the amount of interference present.

Up to this point, the steps are the same as for full adaptive-wall implementation. However, in marked contrast with complete implementation, theoretical consideration of the flow within the interface, i.e., about the model, is necessary in order to correlate the differences in the measured and computed velocity components at the interface with the interference present at the model. If a theoretical representation for the interior flow is introduced in this way, it can be used in conjunction with the flow measurements and exterior-flow calculations to examine the wall interference. In the most direct application, the procedure can be used to ascertain whether significant wall interference exists. Significant interference implies here that the flow is not even qualitatively similar to unconfined flow, so that the test data would be of little value. If the procedure indicates that the flow is qualitatively similar to unconfined flow, but that there is residual wall interference which can be represented by simple stream speed and angle of attack corrections, the technique can be extended to carry out the corrections to the data. The advantage of calculating corrections in this way, when they are appropriate, is that they rely upon measured disturbance velocities at the interface and not on idealized boundary conditions for the flow through ventilated walls of arbitrary geometry. This distinction between flows that can be corrected and those that cannot, has been drawn by Kemp (Ref. 12) in his work on correctable-interference transonic wind tunnels.

There is, at the present time, a great deal of activity in the use of flow-field measurements as a basis for wall-interference corrections. In two-dimensional flow, work has been carried out by Kemp (Refs. 12 and 13), Capelier, et. al. (Ref. 14), Lo (Ref. 15) and Sawada (Ref. 16), while Stahara and Spreiter (Refs. 17 and 18) have considered transonic flow around axisymmetric and non-axisymmetric slender shapes. In three-dimensional flow, procedures using the measured disturbance velocities have been described by Hackett and Wilsden (Ref. 19), Erickson (Ref. 11) and Capelier, et al. (Ref. 14). Most important, in as yet unpublished research at the University of Arizona, Sears and Moses are using a complete adaptive-wall interior- and exterior-flow iteration technique to determine corrections for a wing tested in a wind tunnel.

We believe that extension of these principles to three-dimensional V/STOL flows, including suitable treatment of the propulsion-system efflux, could provide a timely and significant improvement in V/STOL testing capability. This could be achieved in existing tunnels and those with future passive-wall modifications.

CONCLUDING REMARKS

A two-dimensional transonic adaptive-wall wind tunnel has been built and tested at Calspan to demonstrate that wall-interference effects can be minimized by actively controlling the flow in the vicinity of the tunnel walls. Experiments were made with a 6%-blockage airfoil model, using the facility to simulate a conventional wind tunnel, to show that the wall-interference effects can be large in such tunnels. Several cases have been iterated successfully in the adaptive-wall mode and the interference has been essentially eliminated in several cases and reduced significantly in others.

The same adaptive-wall principles can be applied to V/STOL tunnels. The elements necessary for a complete adaptive-wall implementation are believed to be within current analytical and experimental capabilities. However, construction of an adaptive-wall V/STOL test section would require a major development effort over an extended time period. On the other hand, related procedures which use flow-field measurements as a basis for assessing wall interference and for establishing corrections, when they are meaningful, are under development for transonic tunnels. These procedures hold promise for timely application to existing passive-wall V/STOL tunnel testing.

REFERENCES

1. Sears, W.R.: Self-Correcting Wind Tunnels (The Sixteenth Lanchester Memorial Lecture). The Aeronautical Journal, Vol. 78, No. 758/759, February/March 1974, pp. 80-89.

2. Ferri, A. and Baronti, P.: A Method for Transonic Wind Tunnel Corrections. AIAA Journal, Vol. 11, No. 1, January 1973, pp. 63-66.

3. Chevallier, J.P.: Soufflerie Transsonique a Parois-Adaptables, AGARD-CP-174, Wind Tunnel Design and Testing Techniques, pp. 12-1 thru 12-8, October 1975; also translated into English as European-Space Agency Report ESA-TT-326, October 1976, available as NASA Accession No. N77-13085.

4. Goodyer, M.J.: A Low-Speed Self Streamlining Wind Tunnel, AGARD-CP-174, Wind Tunnel Design and Testing Techniques, pp. 13-1 thru 13-8, October 1975.

5. Vidal, R.J., Erickson, J.C., Jr. and Catlin, P.A.: Experiments with a Self-Correcting Wind Tunnel. AGARD-CP-174, Wind Tunnel Design and Testing Techniques, pp. 11-1 thru 11-13, October 1975.

6. Sears, W.R., Vidal, R.J., Erickson, J.C., Jr. and Ritter, A.: Interference-Free Wind-Tunnel Flows by Adaptive-Wall Technology. Journal of Aircraft, Vol. 14, No. 11, November 1977, pp. 1042-1050.

7. Vidal, R.J. and Erickson, J.C., Jr.: Experiments on Supercritical Flows in a Self-Correcting Wind Tunnel. AIAA Paper No. 78-788, AIAA 10th Aerodynamic Testing Conference, San Diego, April 19-21, 1978.

8. Vidal, R.J. and Erickson, J.C., Jr.: Research on Adaptive-Wall Wind Tunnels, AEDC Report No. AEDC-TR-78-36, November 1978.

9. Lo, C.F. and Kraft, E.M.: Convergence of the Adaptive-Wall Wind Tunnel, AIAA Journal, Vol. 16, No. 1, January 1978, pp. 67-72.

10. Vidal, R.J., Catlin, P.A. and Chudyk, D.W.: Two-Dimensional Subsonic Experiments with an NACA 0012 Airfoil. Calspan Report No. RK-5070-A-3, December 1973.

11. Erickson, J.C., Jr.: Application of the Adaptive-Wall Concept to Three-Dimensional Low-Speed Wind Tunnels, NASA CR-137917, 1976.

12. Kemp, W.B., Jr.: Toward the Correctable-Interference Transonic Wind Tunnel, AIAA Paper No.76-1794, AIAA Ninth Aerodynamic Testing Conference, Arlington, Texas, 7-9 June 1976.

13. Kemp, W.B., Jr.: Transonic Assessment of Two-Dimensional Wind Tunnel Wall Interference Using Measured Wall Pressures, in Advanced Technology Airfoil Research, Vol. 1, NASA CP-2045, Part 2, March 1979.

14. Capelier, C., Chevallier, J.P. and Bouniol, F.: A New Method for Correcting Wall Interference, La Recherche Aerospatiale, 1978, No. 1, January-February 1978, pp. 1-11; also translated into English as European Space Agency Report ESA-TT-491, August 1978, available as NASA Accession No. N79-11997.

15. Lo, C.F.: Tunnel Interference Assessment by Boundary Measurements, AIAA Journal, Vol. 16, No. 4, April 1978, pp. 411-413.

16. Sawada, H.: A General Correction Method of the Interference in 2-Dimensional Wind Tunnels with Ventilated Walls. Transactions of the Japan Society for Aeronautical and Space Sciences, Vol. 21, No. 52, August 1978, pp. 57-68.

17. Stahara, S.S. and Spreiter, J.R.: Transonic Flows Past Nonaxisymmetric Slender Shapes - Classical Equivalence Rule Analysis. AIAA Journal, Vol. 17, No. 3, March 1979, pp. 245-252.

18. Stahara, S.S. and Spreiter, J.R.: A Transonic Wind Tunnel Interference Assessment - Axisymmetric Flows. AIAA Paper No. 79-0203, January 1979.

19. Hackett, J.E. and Wilsden, D.J.: Determination of Low-Speed Wake Blockage Corrections via Tunnel Wall Static Pressure Measurements. AGARD-CP-174, Wind Tunnel Design and Testing Techniques, pp. 22-1 thru 22-9, October 1975.

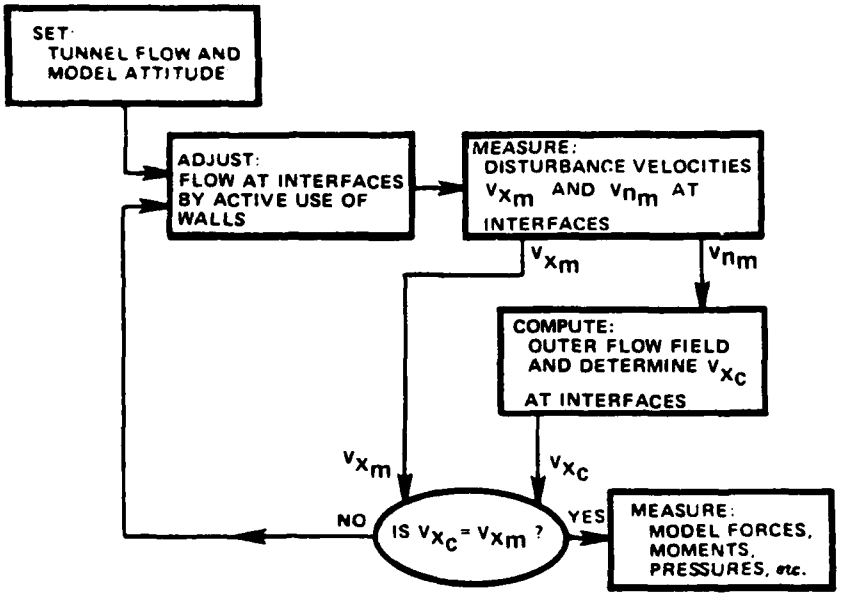

Figure 1 ADAPTIVE-WALL WIND TUNNEL SCHEME

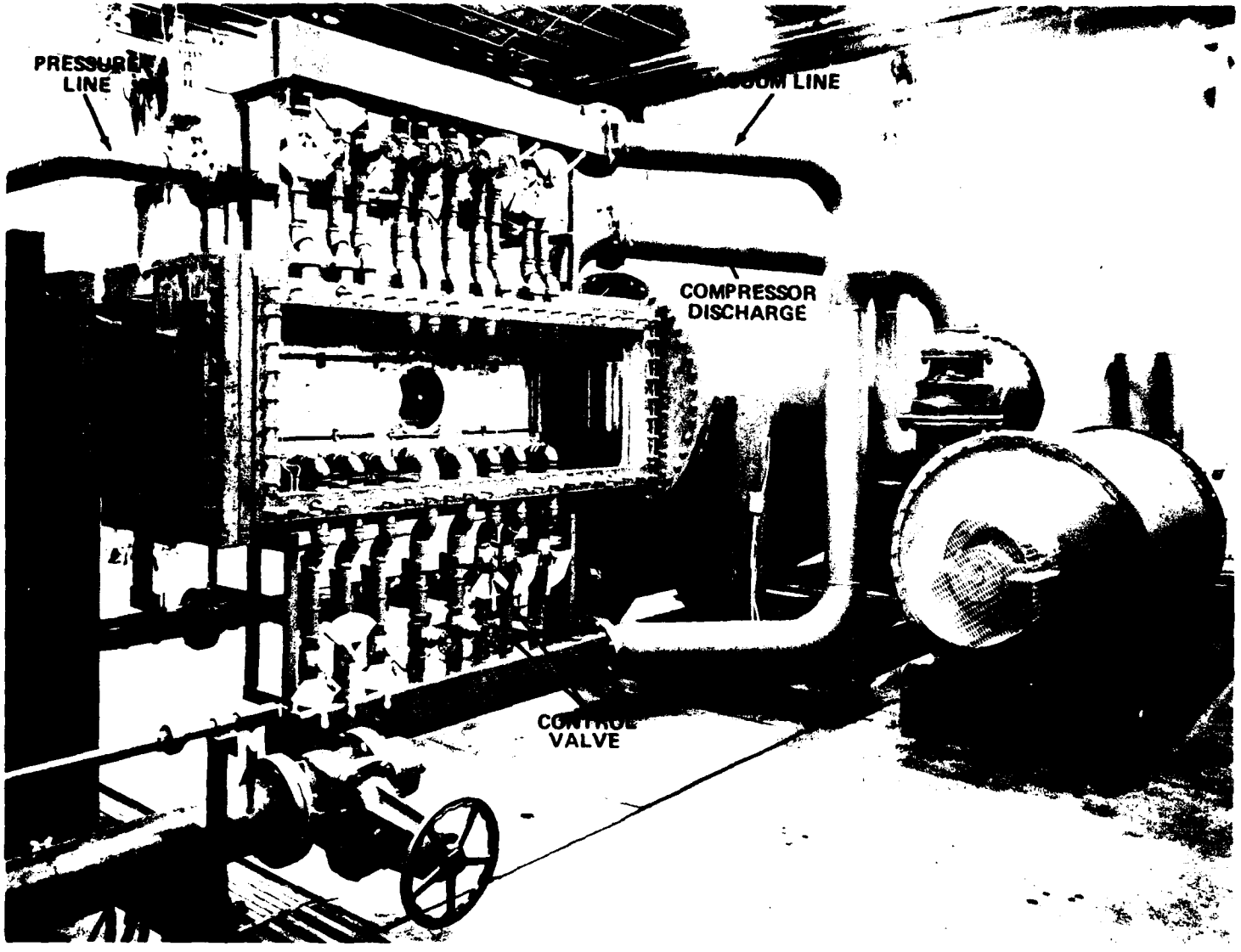

Figure 2 THE CALSPAN ADAPTIVE-WALL WIND TUNNEL

Figure 3 TEST SECTION OF THE ADAPTIVE-WALL WIND TUNNEL

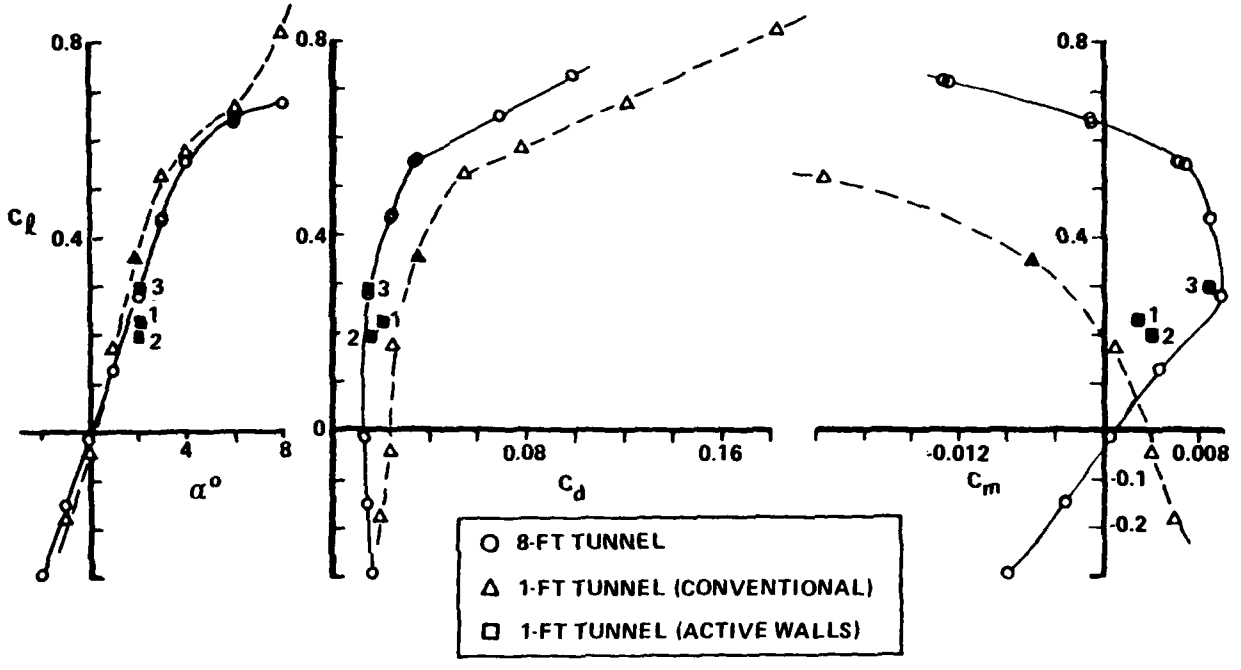

Figure 4 THE EFFECTS OF WALL CONTROL AT $M_\infty = 0.725, \alpha = 2$ DEG. ON NACA 0012 AIRFOIL LIFT, DRAG AND PITCHING MOMENT

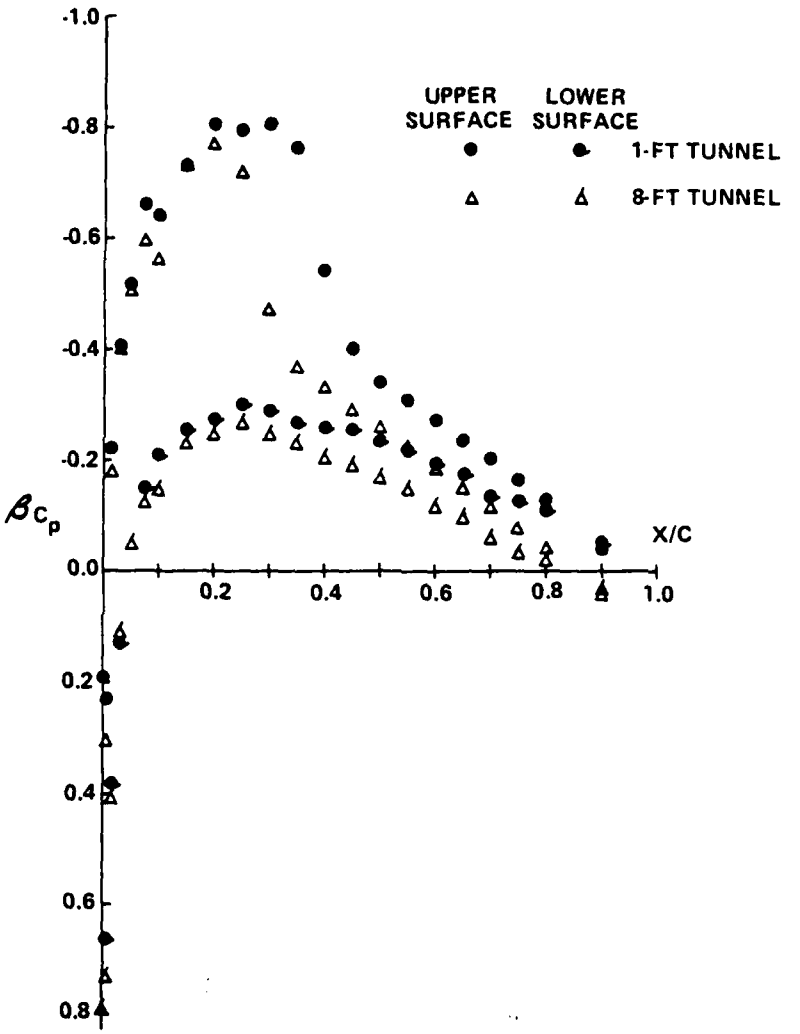

Figure 5 PRESSURE DISTRIBUTION ON NACA 0012 AIRFOIL AT $M_\infty = 0.725$, $\alpha = 2$ DEG - SIMULATED CONVENTIONAL PERFORATED-WALL TUNNEL

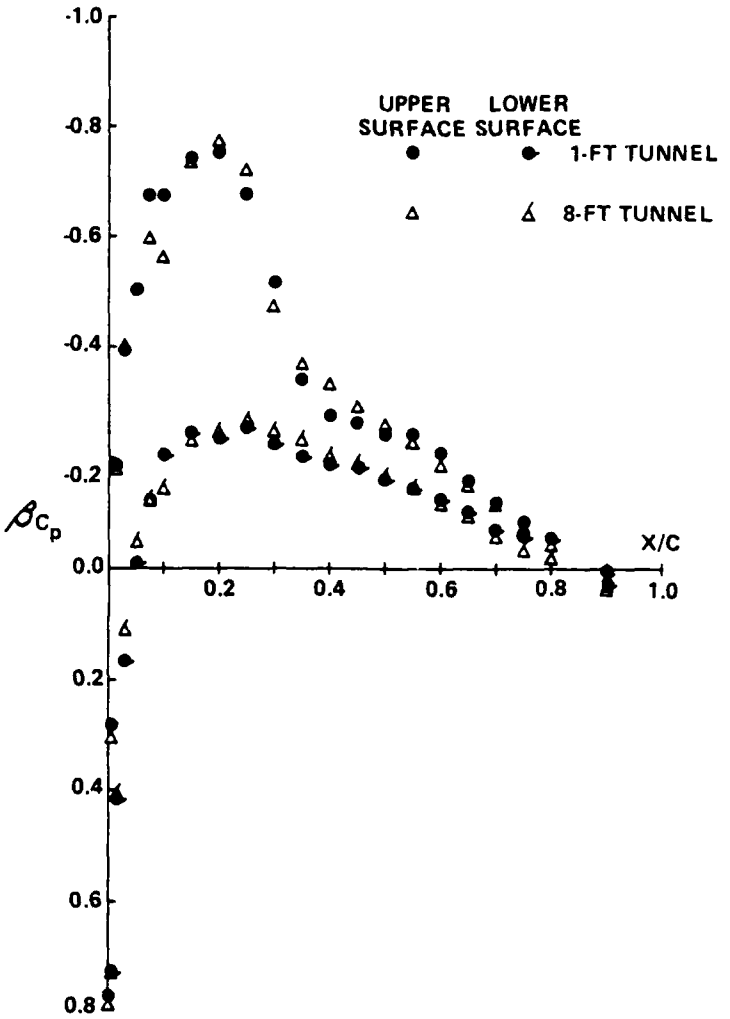

Figure 6 PRESSURE DISTRIBUTION ON NACA 0012 AIRFOIL AT $M_\infty = 0.725$, $\alpha = 2$ DEG - ADAPTIVE-WALL TUNNEL AFTER FIRST ITERATIVE STEP

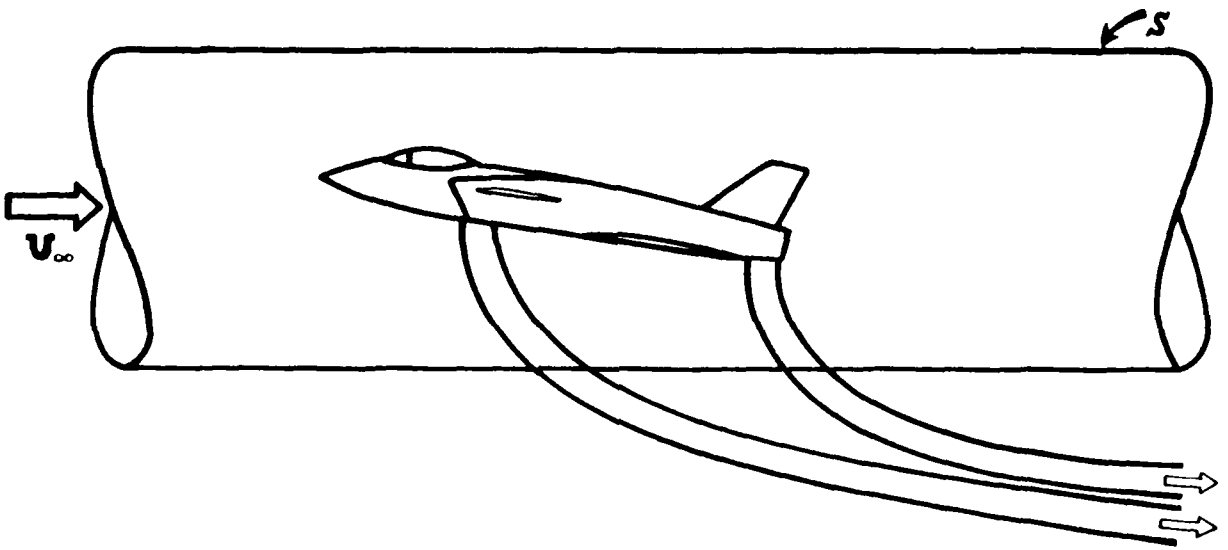

Figure 7 INTERFACE S BETWEEN INTERIOR AND EXTERIOR REGIONS IN UNCONFINED FLOW ABOUT A V/STOL AIRCRAFT

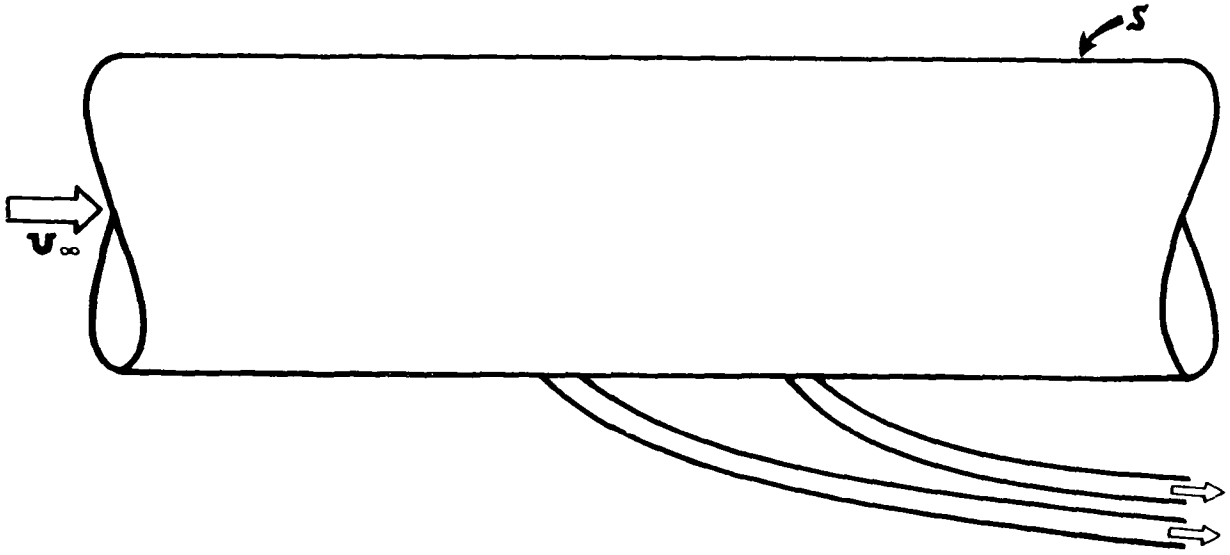

Figure 8 FLOW EXTERIOR TO INTERFACE S WITH PROPULSION SYSTEM EFFLUX PRESENT

AD-A079 115 NAVAL AIR DEVELOPMENT CENTER WARMINSTER PA F/G 1/3
PROCEEDINGS OF A WORKSHOP ON V/STOL AIRCRAFT AERODYNAMICS. VOLU--ETC(U)
MAY 79 C HENDERSON, M F PLATZER

UNCLASSIFIED NL

6 OF 7
AD
A079115

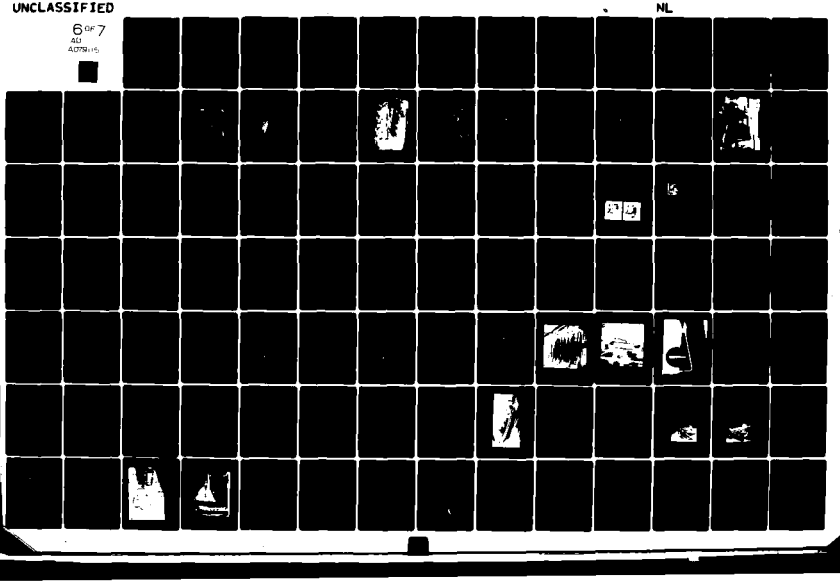

A UNIQUE FACILITY FOR V/STOL AIRCRAFT HOVER TESTING

by

Richard G. Culpepper
NASA Langley Research Center
Hampton, VA

and

Ronald D. Murphy
Naval Air Systems Command
Washington, DC

Presented at the Second Annual Dynamic Performance Workshop
at the Arnold Engineering Development Center
Arnold Air Force Station, Tennessee
May 8-9, 1979

A UNIQUE FACILITY FOR V/STOL AIRCRAFT HOVER TESTING

by

Richard G. Culpepper
NASA Langley Research Center
Hampton, VA

and

Ronald D. Murphy
Naval Air Systems Command
Washington, DC

ABSTRACT

From the beginning of the Navy's XFV-12A V/STOL Technology Demonstrator Aircraft Program, there was considerable discussion as to the most appropriate method to investigate the hover capabilities of the total aircraft in a realistic, and yet safe, environment. The consensus of those who had previously tested V/STOL aircraft was that tether rigs or pedestals provided unrealistic inputs to the aircraft handling qualities; and in some cases, created erroneous impressions as to the aircraft control responses. Testing devices, such as grids, constructed to remove ground effect provided no safety for investigation of aircraft response to large control inputs during hover flight.

It was desired that the test facility for the XFV-12A have the capability to obtain static force and moment data and to allow assessment of aircraft handling qualities during dynamic tethered hover "flight."

It was determined that NASA Langley Research Center's Impact Dynamics Research Facility (IDRF) could be modified to achieve these objectives and minimize the objections to previous hover test facilities.

Static lift and control measurements were obtained and limited dynamic tethered hover "flight" was conducted during the first half of 1978 in the IDRF.

SUMMARY

The NASA and the Naval Air Systems Command entered into an agreement to conduct tethered hover testing of the Navy's XFV-12A Thrust Augmented Wing V/STOL Technology Demonstrator aircraft in the Langley Research Center's Impact Dynamics Research Facility (IDRF). The IDRF was modified for the testing and a joint test team conducted the testing during the first half of 1978.

Tethered hover testing of the XFV-12A in the IDRF has indicated that valid force and moment data can be obtained from static testing and that dynamic tethered hover flying qualities can be evaluated.

INTRODUCTION

From the beginning of the Navy's XFV-12A V/STOL Technology Demonstrator Aircraft Program, there was considerable discussion as to the most appropriate method to investigate the hover capabilities of the total aircraft in a realistic, and yet safe, environment. The consensus of those who had previously tested V/STOL aircraft was that tether rigs or pedestals provided unrealistic inputs to the aircraft handling qualities; and in some cases, created erroneous impressions as to the aircraft control responses. Testing devices, such as grids, constructed to remove ground effect provided no safety for investigations of aircraft response to large control inputs during hover flight.

It was desired that the test facility for the XFV-12A have the capability to address the following capabilities in the hover mode:

1. The ability to statically test the aircraft by rigidly positioning the aircraft at a desired altitude and attitude to obtain:

   - force and moment data both in and out-of-ground effect
   - aircraft lift and balance characteristics both in and out-of-ground effect
   - final VTOL system adjustments

2. The ability to dynamically test the aircraft in a limited hover envelope to obtain:

   - correlation with static test results
   - aircraft control response data both in and out-of-ground effect, including large control inputs
   - effects of stability augmentation system both in and out-of-ground effect
   - effects of ambient wind and gusts

3. The ability to provide a realistic environment for pilot training and proficiency in VTOL flight.

It was determined that NASA Langley Research Center's Impact Dynamics Research Facility (IDRF) could be modified to achieve these objectives and minimize the objections to previous hover test facilities.

An agreement was entered into by NASA and the Naval Air Systems Command in late 1976 to conduct tethered hover testing of the XFV-12A in the IDRF. The facility was modified as required for the program in 1977 and during the first half of 1978, tethered hover testing of the XFV-12A was carried out by a joint test team composed of NASA, Navy and Rockwell International/Columbus Division personnel. Static force and moment data were obtained and limited dynamic tethered hover testing was accomplished.

SYMBOLS

Measurements and calculations were made in U. S. Customary Units. They are presented herein in the International System of Units (SI) and U. S. Customary Units.

"flight"	powered portion of static and dynamic testing
IWRC	independent wire rope center
SLST	sea level static thrust, N (lb)
STOL	short takeoff and landing
V/STOL	vertical/short takeoff and landing
VTOL	vertical takeoff and landing
"Z" system	overhead suspension system for the aircraft
δ_D	diffuser half angle, deg
$\delta_{D,c}$	canard diffuser half angle, deg
$\delta_{D,w}$	wing diffuser half angle, deg
δ_{LL}	lift lever position, cm (in.)
δ_{Lat}	lateral stick position, cm (in.) (aircraft right wing down positive)
δ_{Long}	longitudinal stick position, cm (in.) (aircraft nose-up positive)
δ_R	rudder position, cm (in.) (aircraft nose right positive)
ϕ	augmentation ratio, $\frac{\text{measured lift}}{\text{isentropic thrust}}$

$\phi_{free\ air}$	augmentation ratio in free air
$\phi_{ground\ effect}$	augmentation ratio in ground effect

DESCRIPTION OF TEST AIRCRAFT

The XFV-12A, shown in figure 1, is a unique V/STOL aircraft being developed by the Navy. This technology demonstrator aircraft program is intended to explore the suitability of applying a thrust augmented wing/canard ejector concept to an operational air superiority fighter-type aircraft with V/STOL capability. It is not intended that the XFV-12A program produce an operational production aircraft, but rather serve as a research tool to explore ejector thrust augmentation technology. It is anticipated that the aircraft will eventually develop into a flight-worthy vehicle to investigate and develop aircraft characteristics in vertical and conversion flight modes at typical fighter takeoff and landing weights. A list of the physical characteristics of the aircraft is given in Table I.

TABLE I.- PHYSICAL CHARACTERISTICS OF THE XFV-12A

Takeoff gross weight (STOL mode)	107.9 kN (24 250 lb)
Takeoff gross weight (VTOL mode)	85.1 kN (19 130 lb)
Length	13.4 m (43.9 ft)
Span	8.7 m (28.5 ft)
Height	2.8 m (9.1 ft)
Engine: one YF-401	73.4 kN (16 500 lb) (SLST)
Maximum fuel capacity:	
Wing	9.1 kN (2 040 lb)
Fuselage	12.3 kN (2 774 lb)
Moment of inertia:	
Pitch	69 397 kg-m^2 (51 200 slug-ft^2)
Roll	18 298 kg-m^2 (13 500 slug-ft^2)
Yaw	85 120 kg-m^2 (62 800 slug-ft^2)

CONFIGURATION FEATURES

The XFV-12A is a V/STOL fighter design which features a high wing and low canard arrangement and is powered by a single YF-401 engine. An aircraft cutaway is shown in figure 2. The air induction system for the YF-401 engine is comprised of two external compression inlets located along the sides of the fuselage and an auxiliary inlet located on top of the fuselage. Flow from the engine exits into the diverter which directs the engine exhaust flow aft through the plug nozzle for conventional flight or forward to the wing and canard ducting/augmenter systems for V/STOL operation.

For V/STOL operation the engine exhaust is directed between the diffuser flaps by means of a centerbody nozzle and coanda nozzles located on the diffuser flaps. This arrangement causes ambient air to be entrained in quantities several times the mass flow of the engine exhaust. Thrust from the augmenter is increased above the basic nozzle thrust because of the transfer of kinetic energy of the engine exhaust to the entrained secondary air.

During conversion from hover to conventional flight, this secondary air is accelerated over the aerodynamic surfaces by the pumping action of the augmenters, thus creating a rapid buildup of aerodynamic circulation lift on the wing and canard. As the flaps are retracted to mean augmenter flap angles less than 30^{o}, the engine flow transitions to normal tailpipe operation and the flaps and ejector centerbody fold into a high performance wing, with the trailing-edge flap on both the wing and canard used for aerodynamic control.

Hover Control System

Hover height and attitude control are also achieved through the augmenter flap system (figure 3). Variation of the diffuser half angle modulates the amount of secondary air flow, and thereby the lift created on each augmenter surface. With no change of engine thrust, height control is obtained by variation of the diffuser half angles on all four of the augmenters simultaneously. This collective change of diffuser half angles is accomplished by the pilot modulating the aircraft lift lever which is located beside the throttle in the throttle quadrant. At the designed augmenter performance level the "neutral" position of the lift lever would produce zero rate of climb. A forward or positive movement of the lift lever from "neutral" would produce a positive rate of climb and an aft or negative movement would produce a negative rate of climb. Attitude control is achieved by differential movement of the diffuser half angles on the wing and canard for pitch, the differential movement of the diffuser half angles on the right and left wings for roll, and the differential movement of the left and right wing mean augmenter flap angles of yaw.

DESCRIPTION OF TEST FACILITY

The IDRF gantry was built in the early 1960's as the Lunar Landing Research Facility (LLRF) in support of the Apollo Program. The gantry is approximately 73 m (240 ft) high, 122 m (400 ft) long and 61 m (200 ft) across at ground level. The LLRF provided the capability for pilots and astronauts to maneuver the Lunar Landing Research Vehicle through the final 46 m (150 ft) altitude before landing while under the influence of a simulated lunar gravitational field. After completion of the Apollo Program, the LLRF was converted into the IDRF to conduct research on aircraft crash safety.

Development of Tethered Facility

The IDRF as developed for the tethered hover testing of the XFV-12A, as shown in figure 4, provides a facility which allows both static and dynamic tethered hover test operations to be undertaken with utmost safety. This development consisted of the following:

1. Installing the "Z" system which is used as the overhead suspension system for the aircraft.
2. Installing an enlarged winch platform under the center of the gantry bridge to house the "Z" system winch and IDRF pull-back winch.
3. Installing an umbilical cable for data transmission.
4. Installing a mechanical restraint system to limit lateral and longitudinal translations of the aircraft.
5. Installing static tie down anchors to secure the aircraft in desired position for static tests.
6. Increasing test pad area.
7. Installing pilot cues.
8. Building hangar to house aircraft and adding office trailers for test personnel.
9. Modifying control room.
10. Modifying communication system.
11. Installing video cameras and recorders to monitor testing.

"Z" System.- The tether or "Z" system includes all components from the winch to the structural attach unit on the aircraft, namely the winch, "Z" cable, shock absorber, position sensor, slack sensor, load cell and structural attach unit. The "Z" system is illustrated in figure 5. The initial dynamic test operating restrictions are given in Table II.

TABLE II.- INITIAL DYNAMIC TEST OPERATING RESTRICTIONS

Horizontal displacement	±7.6 m (±25 ft)
Height	0 - 15.2 m (0 to 50 ft)
Horizontal velocity	±0.9 m/s (±3 ft/s)
Vertical velocity	±0.9 m/s (±3 ft/s)
Horizontal acceleration	±0.9 m/s^2 (±3 ft/s^2)
Vertical acceleration	±0.6 m/s^2 (±2 ft/s^2)
Pitch and roll	±5 deg
Heading	0 - 360 deg

There are two modes of "Z" system operation, manual and automatic. In manual, the "Z" system serves as a hoist to raise or lower the aircraft. In the automatic mode the "Z" system operates through a feedback system to track the aircraft's vertical motion using signals from the position sensor. This allows the aircraft to hover essentially free of the tether. In addition, the system is designed to "catch" the aircraft if trouble develops.

Winch: A modified Navy highline shipboard underway replenish winch was installed in a new winch platform under the gantry bridge structure approximately 61 m (200 ft) above the ground.

"Z" cable: The upper portion of the "Z" cable is a wire rope of 2.5 cm (1 in.) diameter 6- by 37-IWRC extra improved plow steel wire rope with a breaking strength of 459.9 kN (103 400 lb). The lower 32 m (105 ft) of the "Z" cable is a 2.9 cm (1 1/8 in.) diameter 18- by 7-nonrotating wire rope constructed from extra improved plow steel with a breaking strength of 472.4 kN (106 200 lb).

Shock absorber: The pneumatic-hydraulic shock absorber was included in the "Z" system to limit shock loads to the aircraft to less than 177.9 kN (40 000 lb). The outer cylinder is filled with hydraulic fluid while the inner cyliner is pressurized with nitrogen to a nominal 22.8 MN/m^2 (3 300 psi).

Position sensor: The position sensor is an electro-mechanical device that provides the feedback signal which enables the "Z" system to automatically track the vertical aircraft motion during dynamic tether "flight." The feedback signal is furnished by the wiper of a linear potentiometer (pot) that is mechanically linked to the position sensor piston. The pot is mechanized so that when the piston is centered within its range of travel, the pot has zero output. As the aircraft ascends or descends, the piston translates from the center or neutral position and the resulting pot output commands the winch to

reel in or pay out cable to recenter the piston. At the neutral position the unit is maintaining approximately 890 N (200 lb) of tension in the "Z" cable. This level of tension was chosen to minimize the "Z" system effects on aircraft dynamic hover characteristics. When the aircraft vertical velocity exceeds the winch's maximum vertical rate of approximately ±1.5 m/s (±5 ft/s), the piston will activate either the up or down warning switch. These switches activate warning lights for the Pilot in the cockpit and the Console Operator in the control room which indicate that the aircraft's vertical velocity is exceeding the winch's capability. If the aircraft is ascending faster than the winch's capability, the upper switch will also activate an aural warning on the test intercommunications (ICOM) network.

Slack sensor: During dynamic operations with lift-to-weight ratios greater than one, a slack sensing device is included in the "Z" system to detect any slack in the linkages between the load cell and the structural attach unit. The output from this sensor triggers an additional aural warning on the ICOM network.

Load cell: A dual bridge load cell serves as a continuous monitor of the load in the "Z" system. The output of one bridge is transmitted via the aircraft's telemetry system and recorded on the data tape, the other bridge is hardwired to the control console for visual monitoring by the Test Director and Console Operator.

Structural attach unit: The structural attach unit for the XFV-12A provides the interface between the "Z" system and the aircraft load pickup points. In addition, it provides freedom for the aircraft to roll and pitch.

Qualification of the system: To qualify the "Z" system for operation all components were designed to a minimum yield strength and static proof loaded to a minimum of 177.9 kN (40 000 lb). In addition, several dynamic proof loadings were conducted.

Restraint System.- The restraint system is a mechanical cable/ring arrangement suspended from the gantry around the "Z" cable, as shown in figure 6. This system limits the lateral and longitudinal translations of the "Z" cable and hence the translation of the aircraft. Two limits were provided in the system by inclusion of a small ring within the larger cable restraint as shown in figure 7. The elastic characteristics of the wire rope suspension holding the restraint in the gantry reduce the harshness of the "Z" system impacting the restraint during over-travel excursions. The 30.5 m (100 ft) height of the restraint system results in a dynamic test envelope, shown in figure 8, of 15.2 m by 15.2 m (50 ft by 50 ft) at ground level decreasing to 11.6 m by 11.6 m (38 ft by 38 ft) at 15.2 m (50 ft).

Static Tie-downs.- For static testing, the aircraft is suspended at the desired altitude and attitude by the "Z" system cable and seven ground tie-down cables as shown in figure 9. Each of the seven cables have a single component load cell attached and are restrained by ground tie-down anchors placed in the concrete pad.

Control Room and Control Console.- The control room is equipped with an ICOM system to all parts of the facility, a public address system, walkie-talkie sets, and the control console for the tether tests. During test operation, the control room is manned by the Test Director, Console Operator, NASA Safety Observer, NASA Facility Coordinator, and Test Coordinator as shown in figure 10. Other personnel are kept to a minimum during tests to prevent distraction of the control room personnel.

The control console, located in the control room, is equipped to enable both normal and emergency control of the tethered tests. The equipment includes controls and indication for:

1. Winch operation
2. Aircraft emergency fuel shutoff valve
3. Aircraft fire warning
4. Voice communication

QUALIFICATION OF THE FACILITY FOR MANNED TESTING

The modification of the facility as described in the previous sections and the operation of the modified facility had to be approved in accordance with Langley Research Center Management Manual Instruction (LMI) 7000.2 entitled "Review of Major Construction or Facility Modification Projects." In addition, since the XFV-12A is a manned aircraft, the modified facility had to be man-rated in accordance with LMI 1710.1 entitled "Human Factors Research, Man-Rating Requirements, and Committee Review Procedures."

In order to comply with these management instructions, the following review was held: Critical Design Review (CDR), Man-Rating Committee (MRC), and Integrated Systems Review (ISR)/Operational Readiness Review (ORR).

Critical Design Review

The CDR is a review of the project by an independent NASA committee with primary emphasis on modifications being made to the test facility. If this committee identifies problem areas that have been overlooked in the design or need additional work, it charges the project management to address the problem and present a solution to the Chairman of the CDR.

Man-Rating Committee

The MRC is appointed by the Chairman of the Langley Research Center Executive Safety Board. The MRC is responsible for reviewing the entire program and recommending to the Chairman of the Executive Safety Board whether the program meets the safety requirements for manned operation or not.

The MRC requires in-depth documentation of the safety aspects of the program. This documentation for the XFV-12A Tethered Hover Test Program included a Safety Analysis Report, Sneak Circuit Analysis, Failure Mode and Effects Analysis, Dynamic Analysis of the Aircraft/"Z" System, and Development of Operational Test Procedures.

Safety Analysis Report (SAR).- The SAR identifies and classifies potential system and operational hazards or undesired events. This enables corrective actions to be taken so as not to expose personnel or equipment to unacceptable risks. The classification include an evaluation of the consequence of the undesired event if it happens (hazard category) and an evaluation of the risk with the selected hazard control implemented (risk classification). The hazard categories and risk classifications are listed below:

I. Possible serious or fatal injury to public or test subject

II. Possible serious or fatal injury to test facility personnel

III. Possible damage to major equipment

IV. Terminated or delayed operation

V. Nuisance failure

VI. Acceptable risk due to adequate controls, procedures, and/or safety factors

Undesired events with hazard categories of I, II, or III have to have design or procedure controls to reduce their risk classification to a IV, V, or VI. The hazard control priority is as follows:

1. Eliminate the hazard through design.

2. Minimize the probability of the hazard occurring through design safety factors.

3. Provide safety devices to control the hazard.

4. Provide warning device to alert crew members to the hazard.

5. Develop procedures to minimize the hazard.

Sneak Circuit Analysis.- A sneak circuit analysis for the XFV-12A Tethered Hover Test Program was performed on the "Z" system electronic control circuitry to confirm that no sneak circuits existed in the system that could cause undemanded electrical inputs to the "Z" system electronics.

Failure Mode and Effect Analysis.- A failure mode and effects analysis for the XFV-12A Tethered Hover Test Program was performed on the "Z" system winch and control electronics to identify possible failure modes and their effects on the system. This analysis was used to identify undesired events in the winch and its electronics for the SAR. This analysis was useful in identifying possible failures that could have caused severe hazard or time delays.

Dynamic Analysis.- A dynamic analysis of the aircraft/"Z" system was performed by using a man-in-the-loop computer simulation. This analysis was to determine that with the Pilot and Console Operator in-the-loop a recovery from an undesired condition could be performed without exceeding the "Z" system's capability. The most severe undesired conditions defined by the analysis were verified by dropping dead weights attached to the "Z" system with various amounts of slack in the system between the aircraft attach unit and the shock absorber.

Operational Test Procedures.- Operational test procedures for the XFV-12A Tethered Hover Test Program were established for all test conditions. These include pre-"flight" checkouts, "flight", post-"flight", and abort procedures. The procedures were developed by the test team and approved by the MRC. After the testing was underway, the procedures were modified to reflect the experience gained during testing. To modify the procedures, the operation's staff (Test Director, Pilot, Console Operator and NASA Safety Observer) would propose the modification to the Program Managers of the three test agencies and if they concurred with the proposed modification, the procedures were changed and issued to the test team.

Integrated Systems Review/Operational Readiness Review

The ISR and ORR are senior level reviews of a project that grant final approval for testing to begin. For this project, the ISR and ORR were combined. All open items from the CDR and MRC must be closed in order to obtain an ISR/ORR approval for testing. The ISR/ORR reviews the project as a whole, but with emphasis on operation and safety considerations. In the case of this interagency program, plans to cover such things as public information, visitor control, and accident investigation procedures were addressed. This committee assures that all open action items are resolved before testing commences.

AIRCRAFT TEST RESULTS

Typical aircraft test results for both the static and dynamic operational modes are presented in this section. These results illustrate the type of data that can be acquired through utilization of the IDRF as a tethered hover test facility for V/STOL aircraft.

For XFV-12A static testing, the tie-down cables were constructed to give test altitudes of 0, 0.9, 3.0, and 9.1 m (0, 3, 10, and 30 ft). These altitudes are adequate to generate aircraft force and moment data both in and out of ground effect. During the static testing, considerable attention was given to developing the augmenter performance.

Initially, only single-axis control inputs were evaluated. A typical result is given in figure 11. This plot shows the primary moment variation and the cross-coupling effects with pitch control input.

At the conclusion of static testing, dynamic testing to assess aircraft controllability with lift-to-weight ratios less than one was initiated. Most of the XFV-12A dynamic tests were conducted at a lift-to-weight ratio of approximately 0.75 for a trimmed configuration with adequate controllability. Since significant tension load still remained in the "Z" cable, which was attached above the aircraft center of gravity, the aircraft control was not totally representative of a free-air hover. However, a good qualitative evaluation of the aircraft's handling qualities was possible when the "Z" cable was near the vertical and the pitch and roll angles were small.

Typical examples of data gathered during dynamic testing are shown in figures 12 and 13. Figure 12 shows the effect of the stability augmentation system on the pilot control inputs required to maintain constant attitude. Figure 13 shows the variation of normalized augmentation ratio at various aircraft altitudes.

Since most of the dynamic test results are either qualitative or dynamic parameters that do not exist from static testing, only the total aircraft lift is available for comparing static and dynamic tests. Nine data points were compared at various conditions, as shown in Table III. These points represent a "slice of time" from stabilized dynamic runs. The ratio of lift (dynamic) to lift (static) varied between 0.99 and 1.01 which indicates an extremely good correlation between the static and dynamic tests.

TABLE III.- DYNAMIC/STATIC LIFT COMPARISON FOR XFV-12A

Data Point	$\delta_{D,w}$	$\delta_{D,c}$	$\frac{\text{Lift (Dynamic)}}{\text{Lift (Static)}}$
1	-3^{o}	6^{o}	1.00
2	0^{o}	1.0^{o}	1.00
3	1.5^{o}	0^{o}	1.00
4	5.5^{o}	3^{o}	1.00
5	4.0^{o}	4^{o}	0.99
6	-1.0^{o}	2.0^{o}	1.00
7	-0.4^{o}	1.4^{o}	1.01
8	0.2^{o}	0.3^{o}	0.99
9	0.2^{o}	1.1^{o}	1.00

CONCLUSIONS

Modifications of the IDRF to support the XFV-12A Tethered Hover Test Program were accomplished and procedures to utilize the facility for tethered hover testing were established. During the 6 months of static and dynamic testing the following conclusions were drawn.

1. Several unique capabilities for hover testing of V/STOL aircraft were demonstrated. These include the following:

   a. The ability to "catch"/recover the aircraft any time during a test.

   b. The ability to rapidly and safely define control limits and investigate operation in regions of reduced control margins.

   c. The capability to rapidly define ground-effect boundaries and variations of aircraft characteristics within these boundaries, and to safely demonstrate dynamic hover flight in a realistic ground-effect environment.

   d. The ability to quickly convert from dynamic to static test modes allows for rapid definition and resolution of any anomolies incurred.

   e. The capability to define the external environment (flow field velocity, pressure and temperature, and noise) around the aircraft for various aircraft attitudes and altitudes and wind conditions.

   f. The ability to provide a realistic environment for pilot training and proficiency in VTOL flight.

2. XFV-12A tethered hover testing within the IDRF has indicated that valid force and moment data can be obtained from static testing and dynamic tethered hover flying qualities can be evaluated.

RECOMMENDATIONS

Based on experience gained during the tethered hover testing of the XFV-12A at the IDRF, the following recommendations are made:

1. Validate the facility for dynamic tethered hover testing at lift-to-weight ratios greater than one, by performing dynamic tethered hovers with an aircraft having known hover characteristics such as the AV-8A Harrier aircraft using several experienced AV-8A pilots.

2. Modify the IDRF so that the facility can be used for both the aircraft crash safety program and tethered hover testing with minimum interference.

3. Upgrade the IDRF for tethered hover testing based on experience from XFV-12A testing, that is, improve control room, ICOM system, video system, pilot cues, aircraft maintenance work areas, etc.

4. Incorporate tethered hover testing as an integral part of the developmental process for future V/STOL aircraft, that is, wind tunnel-simulation-tether test-flight.

REFERENCES

1. Culpepper, Richard G.; Murphy, Ronald D.; Gillespie, Edward A.; and Lane, Archie G.: A Unique Facility for V/STOL Aircraft Hover Testing. NASA TP 1473, 1979.

XFV-12A

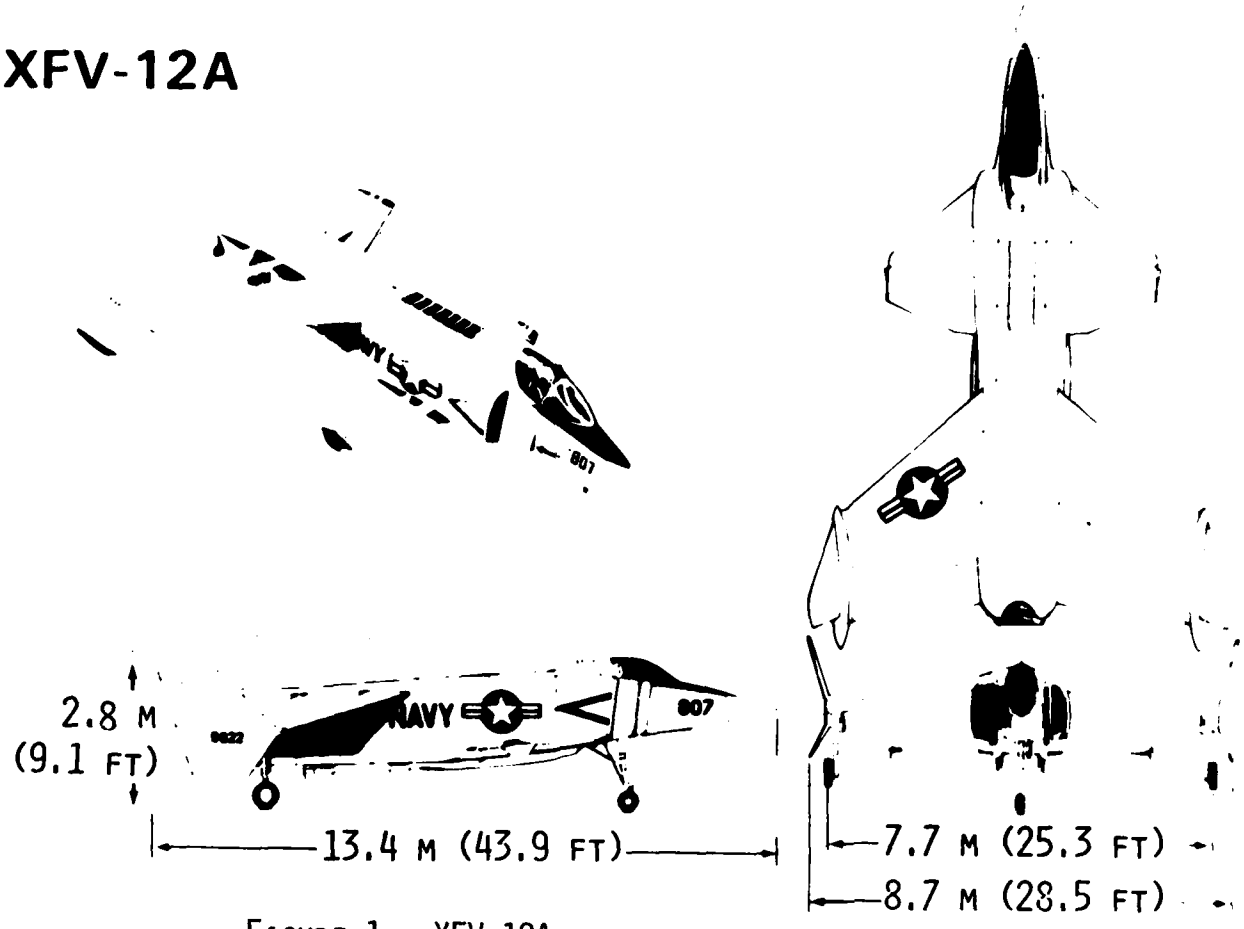

FIGURE 1.- XFV-12A GENERAL ARRANGEMENT.

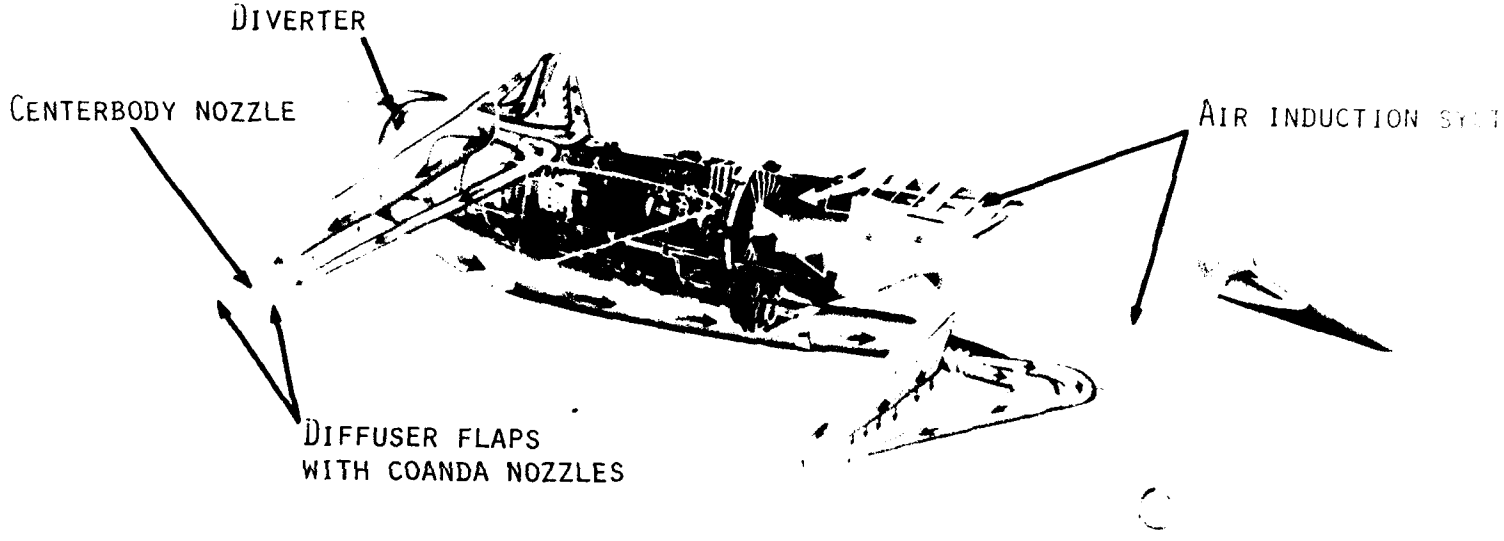

FIGURE 2.- CUTAWAY OF XFV-12A ILLUSTRATING AIRFLOW FOR V/STOL MODE.

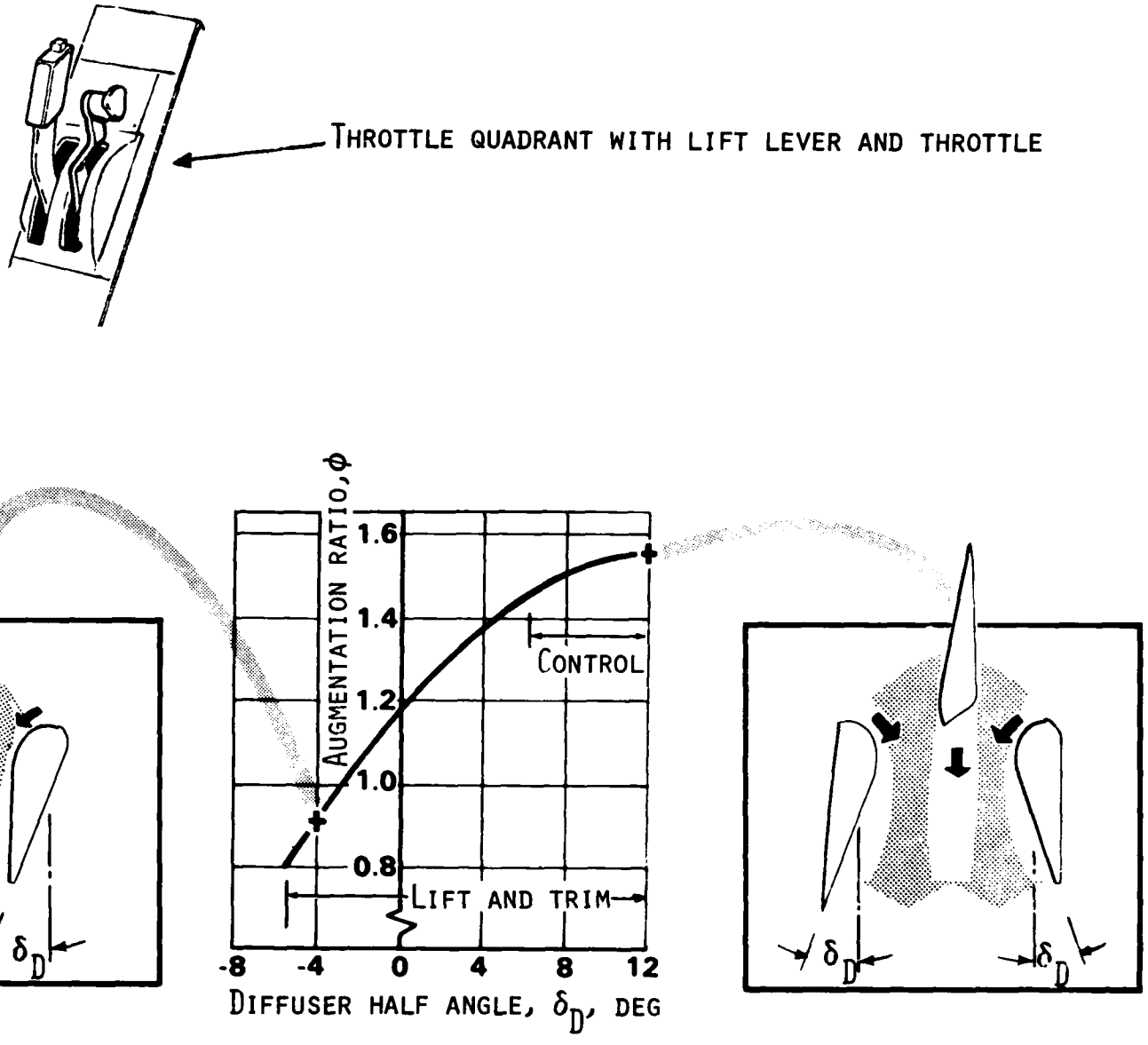

FIGURE 3.- HOVER CONTROL CONCEPT OF XFV-12A.

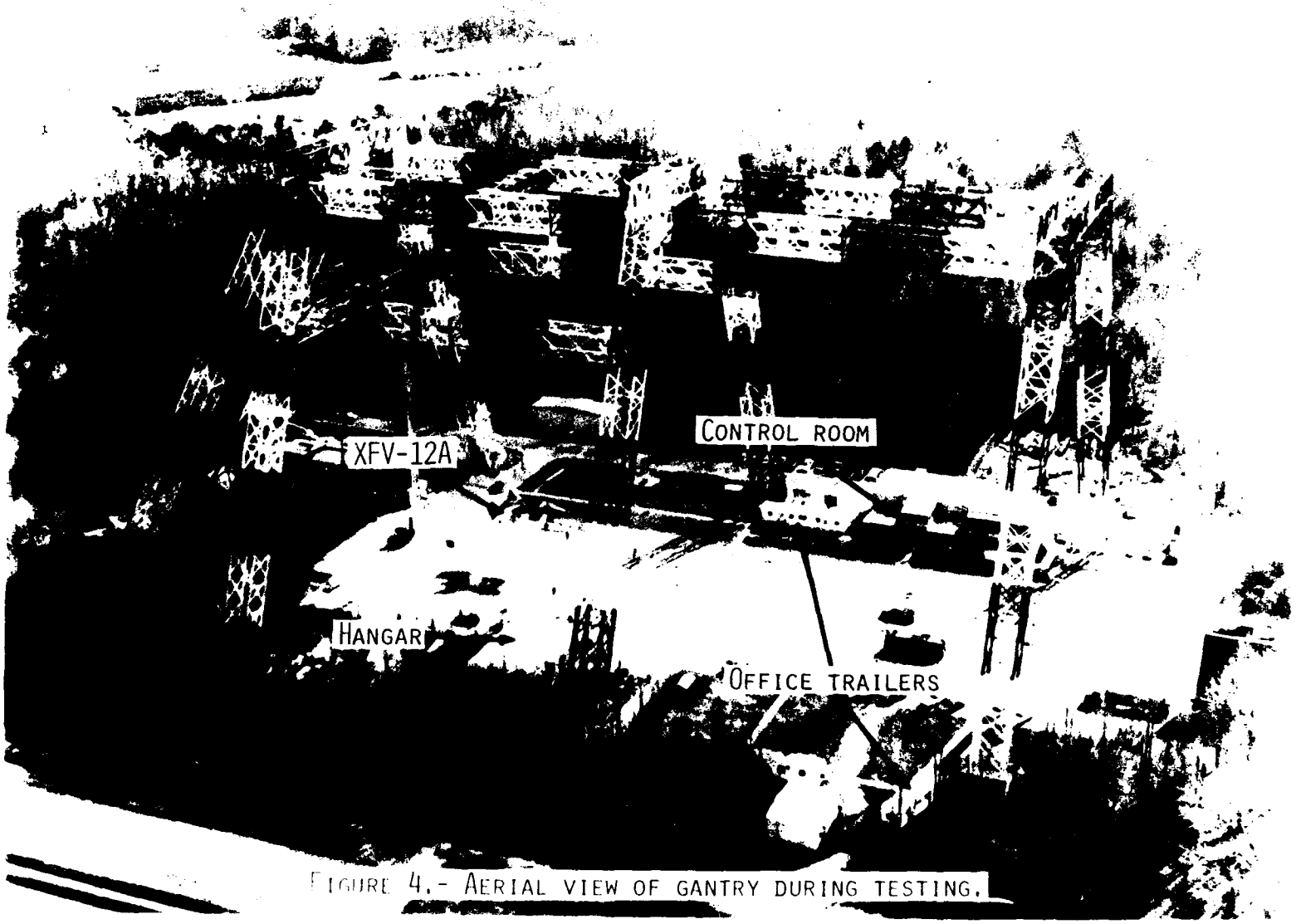

FIGURE 4.- AERIAL VIEW OF GANTRY DURING TESTING.

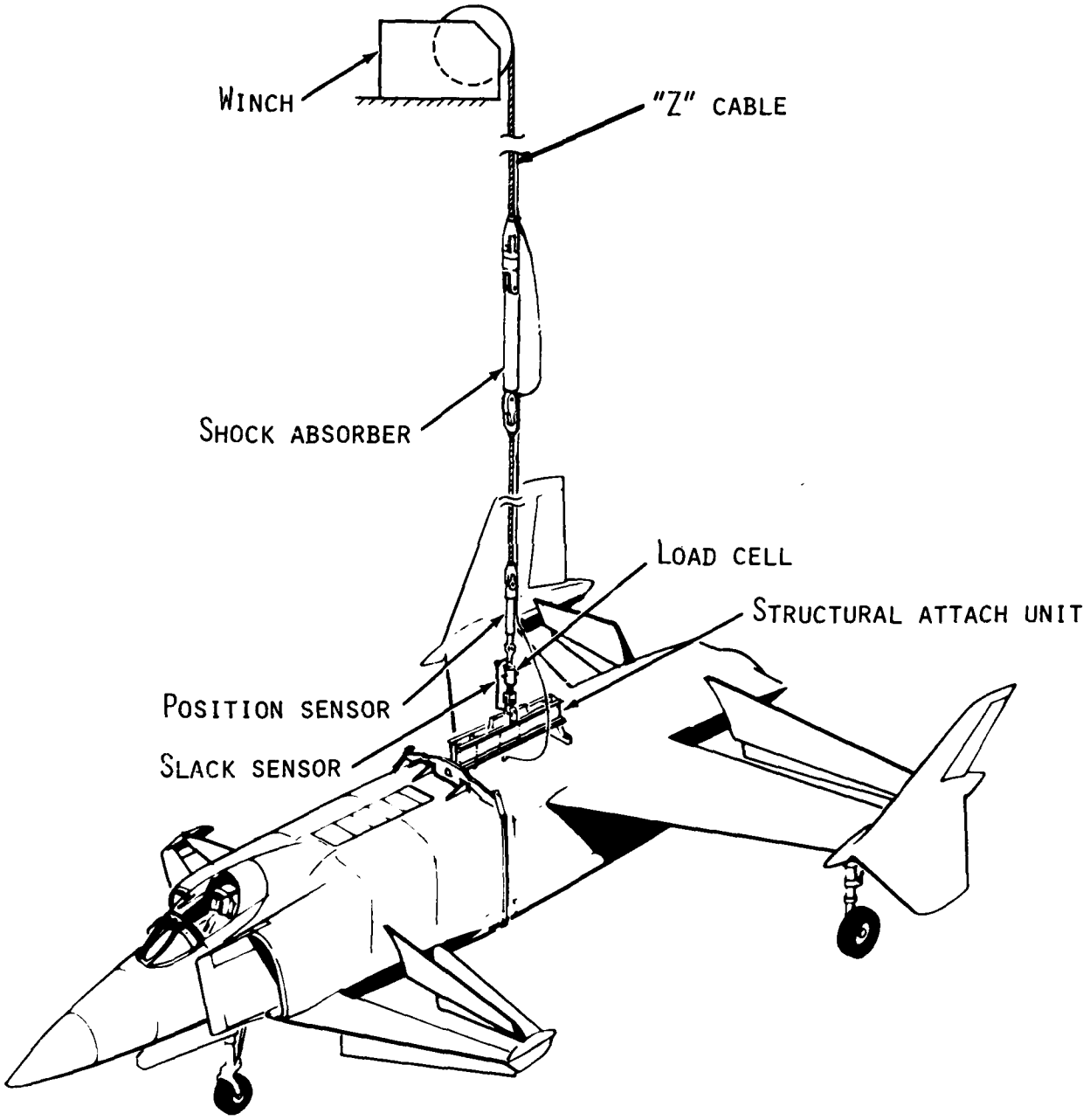

FIGURE 5.- "Z" SYSTEM.

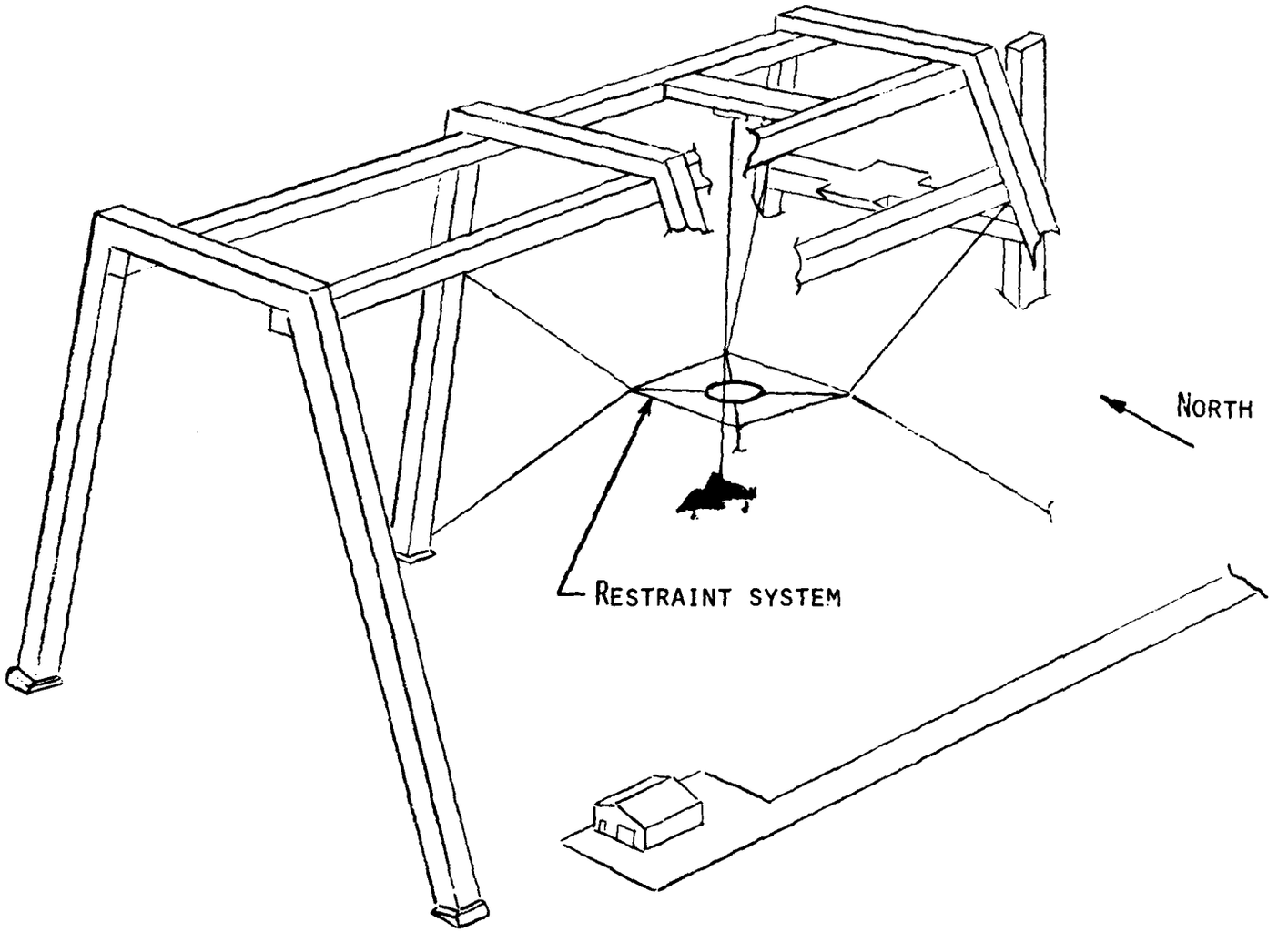

FIGURE 6.- RESTRAINT SYSTEM.

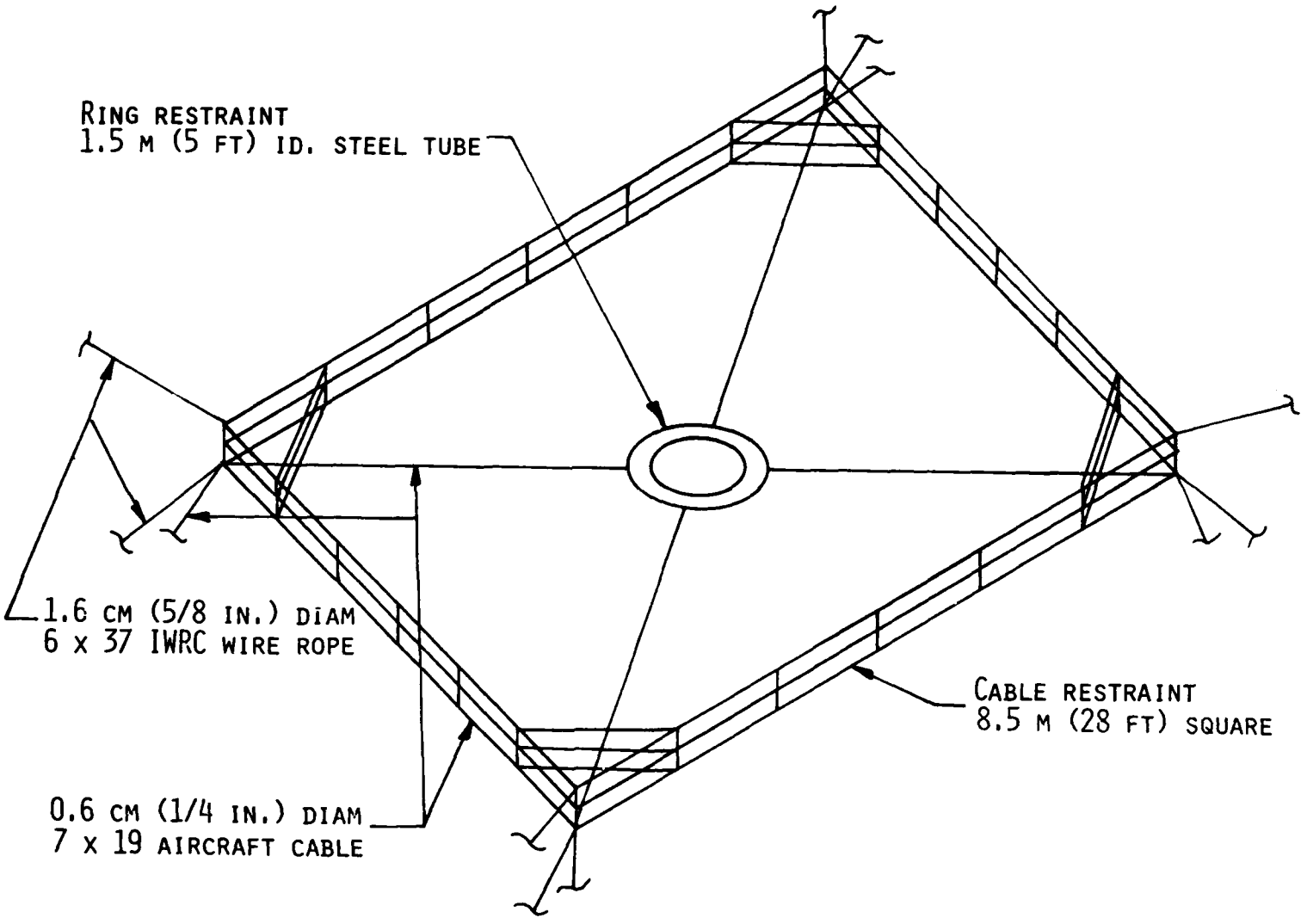

FIGURE 7.- RESTRAINT SYSTEM DETAILS.

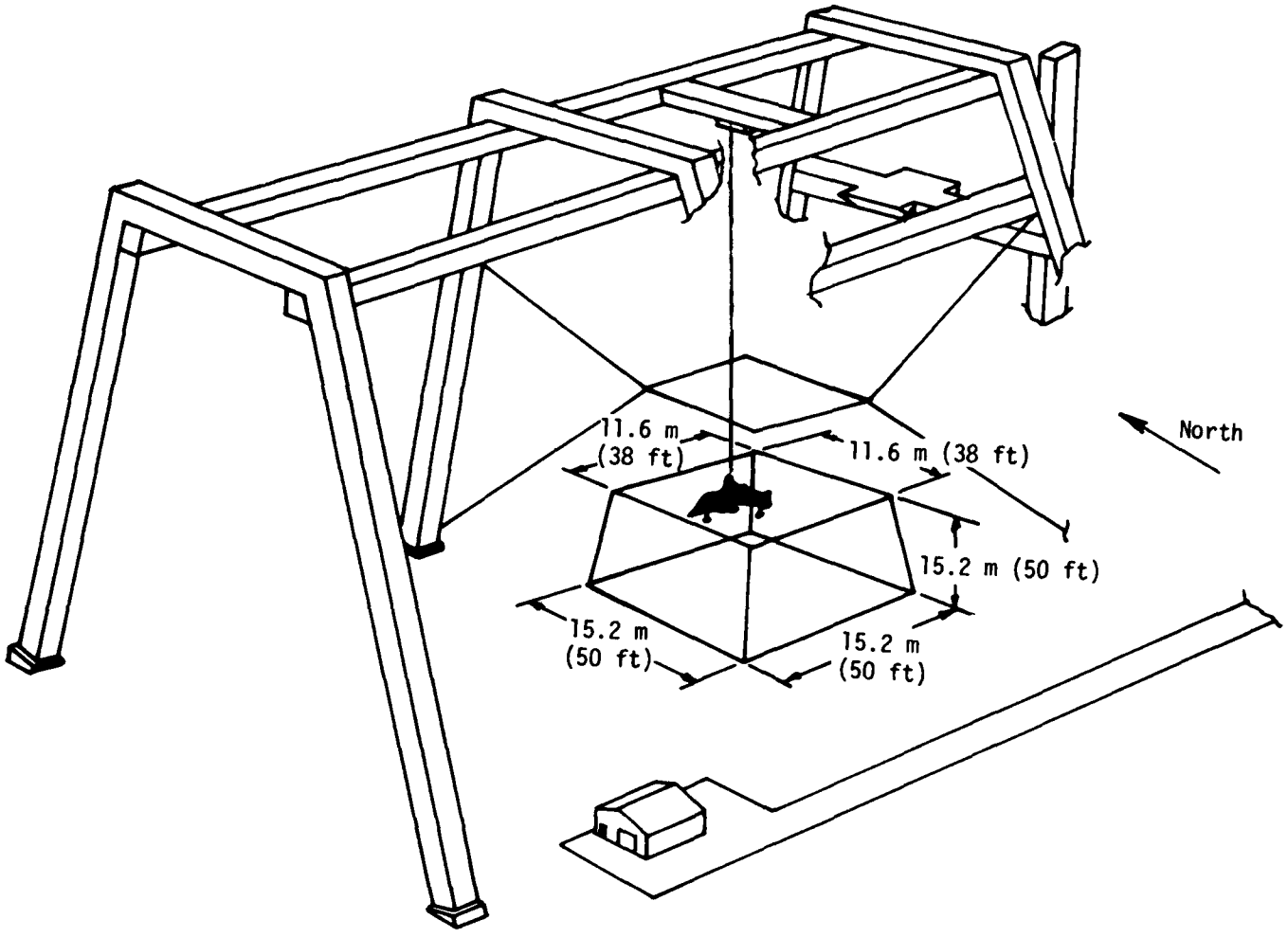

FIGURE 8.- DYNAMIC TEST ENVELOPE.

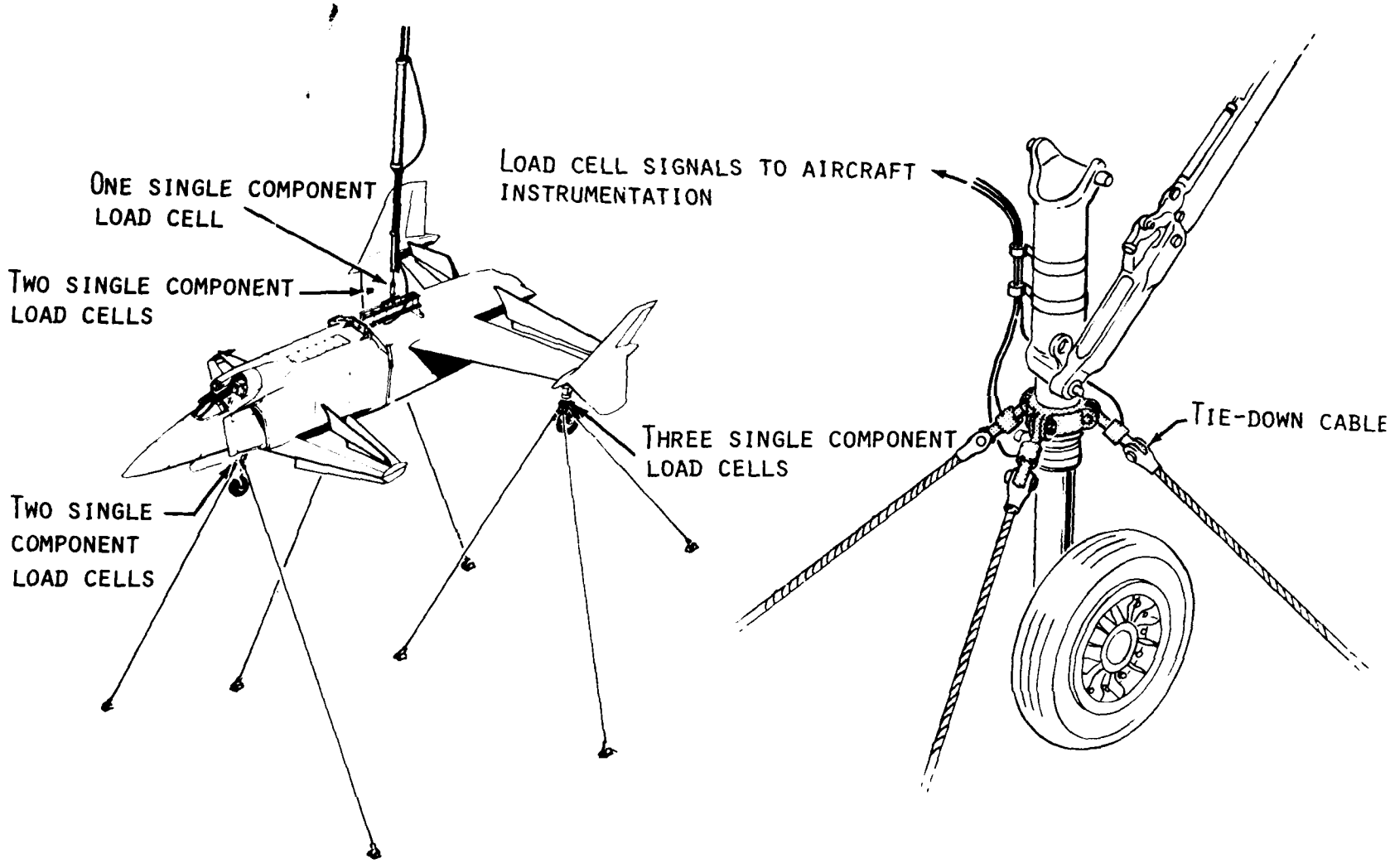

FIGURE 9.- STATIC TEST TIEDOWN ARRANGEMENT FOR XFV-12A.

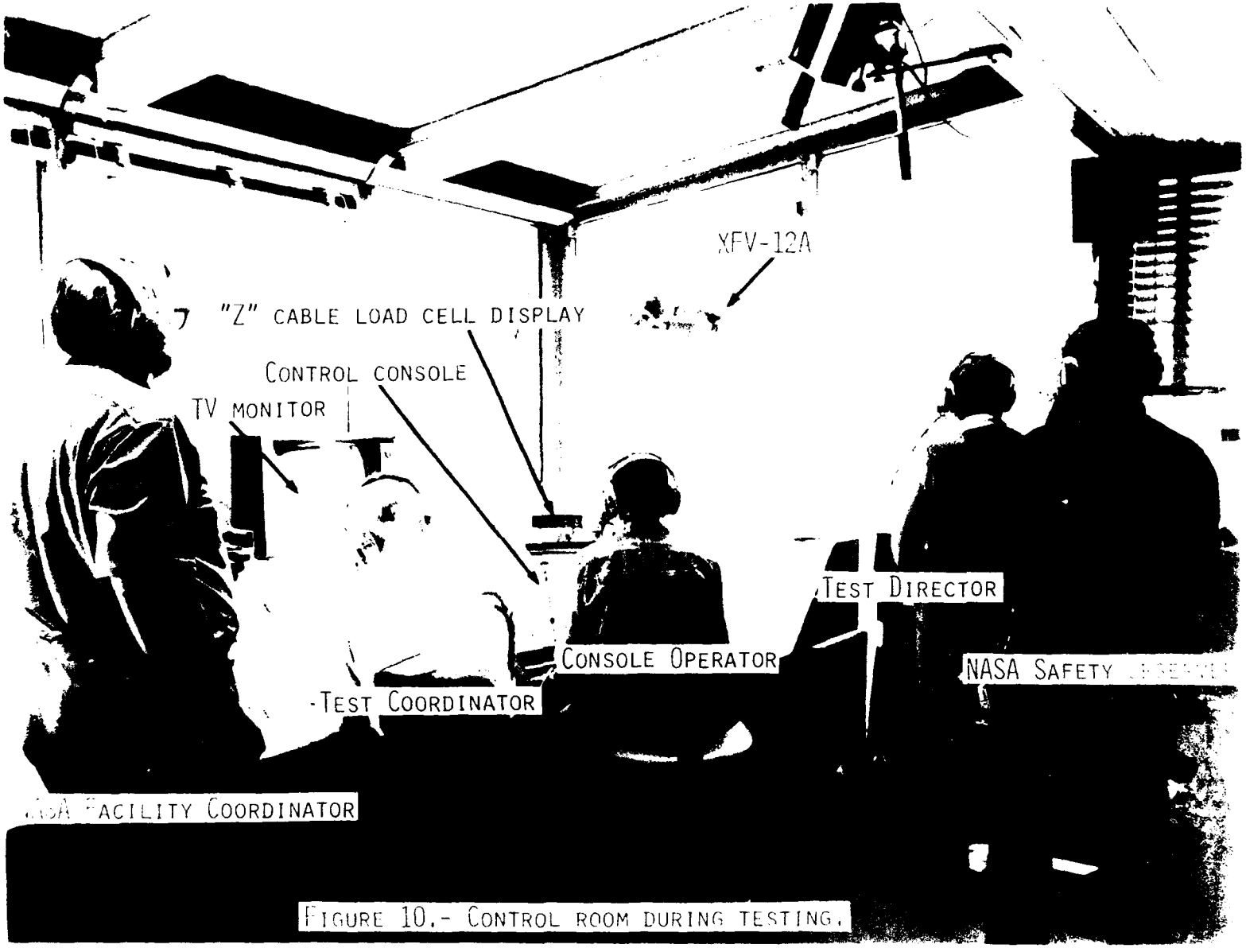

FIGURE 10.- CONTROL ROOM DURING TESTING.

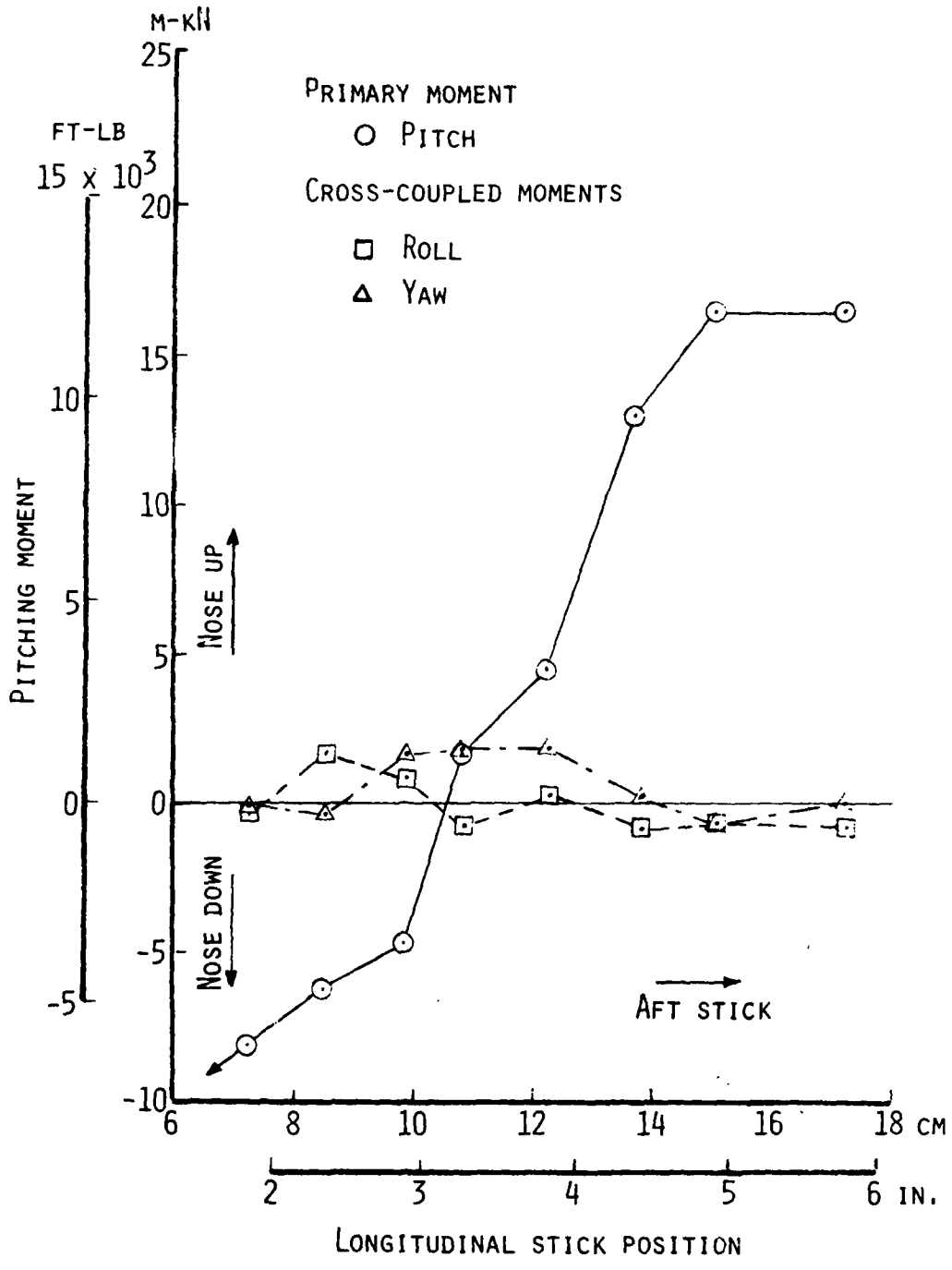

FIGURE 11.- CONTROL MOMENT VARIATIONS WITH SINGLE-AXIS PITCH INPUT FOR XFV-12A.

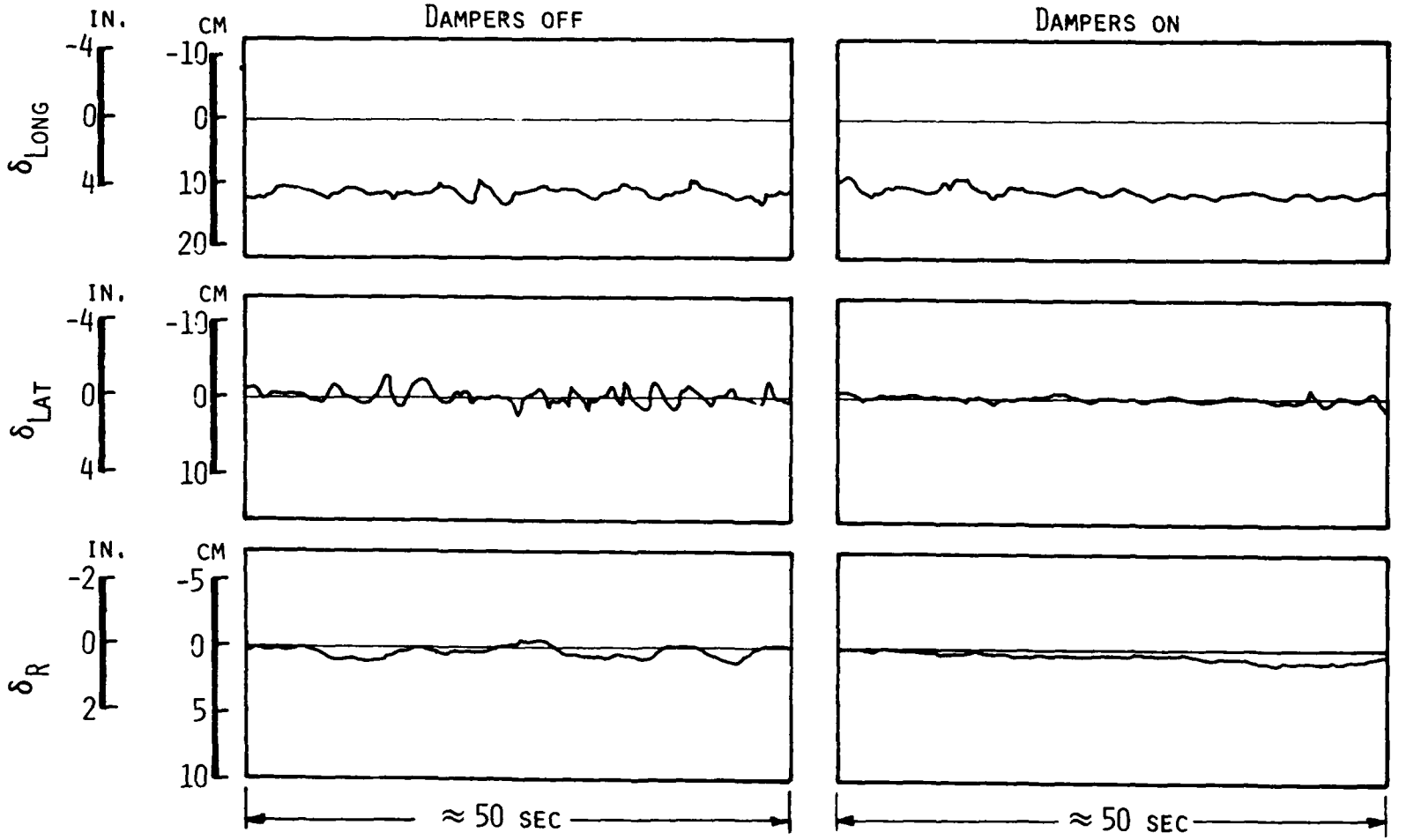

FIGURE 12.- COMPARISON OF PILOT CONTROL INPUTS REQUIRED TO MAINTAIN CONSTANT ATTITUDE DURING DYNAMIC TETHERED HOVER WITH DAMPERS OFF AND ON FOR XFV-12A.

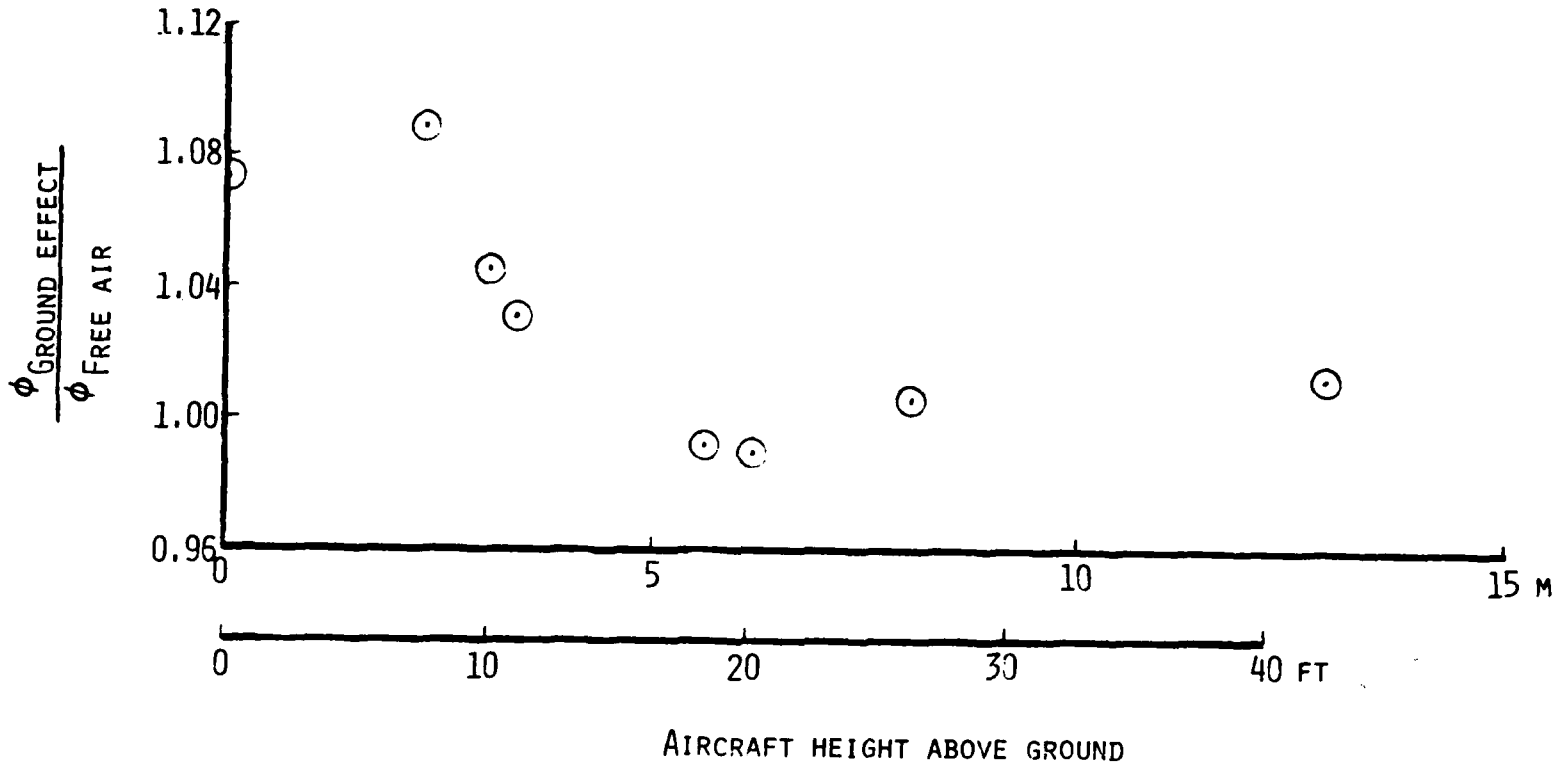

FIGURE 13.- VARIATION OF NORMALIZED AUGMENTATION RATIO WITH ALTITUDE FOR XFV-12A.

V/STOL JET-INDUCED INTERACTIONS

E. David Spong
James H. Kamman
Joseph D. Flood

McDonnell Aircraft Company
St. Louis, Missouri

ABSTRACT

Several experimental investigations have been conducted by McDonnell Aircraft Company (MCAIR) to assess the propulsive lift system induced forces and moments on V/STOL aircraft. Results of these tests indicate the high sensitivity of the induced aerodynamics in ground effect to various configuration variables and show the degree of geometric simulation required for representative data. Included in these investigations have been comprehensive evaluations of the isolated fountain forces as well as the total induced forces on both supersonic and supersonic V/STOL aircraft configurations. Further tests have been performed to determine the effects of ship deck motion on the jet-induced aerodynamics.

NOMENCLATURE

D	Nozzle diameter
f	Frequency
F	Fountain force
F_g	Nozzle gross thrust
H	Model height
h	Deck heave amplitude
L	Induced lift
L	Plate length
LID	Lift Improvement Device
NPR	Nozzle pressure ratio
r	Radius
S_A	Lateral nozzle spacing
SF_A	Longitudinal nozzle spacing
W	Plate width
α	Angle of attack
β	Apex angle
Δ	Increment
γ	Roll angle
θ_{ji}	Jet impingement angle
ϕ	Phase angle

Subscripts

ej	Equivalent jet
h	Heave
γ	Roll

Superscripts

$\hat{}$	Peak
-	Average

INTRODUCTION

V/STOL aircraft operating near the ground or above a seaborne platform are subject to potential performance losses and control problems due to the propulsive lift system induced aerodynamics. In ground effect, the development of practical V/STOL aircraft is complicated by the complex nature of the ground effects flowfield and the high degree of configuration dependence. Therefore, over the past several years MCAIR has conducted numerous in-house and contracted experimental studies, portions of which are documented in References 1 through 4, to investigate propulsion system related effects critical to V/STOL aircraft development. To accomplish these studies, test techniques were developed to allow economical evaluation of a wide range of potential V/STOL configurations. Propulsion system arrangement, nozzle operating conditions, and model simulation requirements have been extensively investigated.

The investigations were conducted in the MCAIR Propulsion Subsystem Test Facility using models representative of both subsonic and supersonic V/STOL configurations. Inner region models representing the fuselage undersurface bounded by the nozzles were used to isolate the fountain impingement forces. The tests were conducted with the models centered over a ground plane or simulated ship landing platform with no crosswind. The jet-induced forces and moments acting on the models were measured with a six-component force balance. For simulations of the heaving, pitching, and rolling motions of a seaborne platform, a three degree of freedom Deck Motion Simulator was used having a scaled size comparable to the landing area on a DD 963 class destroyer.

TEST FACILITY

The V/STOL jet-induced aerodynamics test programs, described in this paper were performed in the Jet Interaction Test Apparatus of the MCAIR Propulsion Subsystem Test Facility. The test apparatus, shown in Figure 1, has two independent nozzle plenum chambers from which as many as six nozzle pipes can be mounted over the complete range of practical V/STOL aircraft nozzle arrangements.

A six-component force balance is attached to a support beam which is centrally mounted off the settling chamber. The test models are attached to the force balance in the vertical plane approximately one wing span from the plenums. The balance is installed with the axial force gage in the lift direction for improved accuracy. The nozzles are non-metric to further maximize the accuracy of the jet-induced force measurements. The thrust characteristics of each nozzle were calibrated in the MCAIR Nozzle Thrust Stand.

For some tests, the static ground plane is supported from a second force balance, which measures the forces acting on the ground plane at ground level. These data have been found to be useful for assessing nozzle spacing effects with isolated nozzles.

The Deck Motion Simulator consists of a scaled landing platform, a hydraulic actuation system, a movable support cart, and an electronic control

system. The deck is lightweight and rigid for the fast movements required to simulate full scale deck motions with small scale models. The hydraulic actuation system consists of a rotary actuator for the heaving motion and two linear actuators, located at right angles to one another, for pitch and roll.

MODEL DESCRIPTIONS

Models representative of subsonic and supersonic V/STOL aircraft designs were used in the tests to investigate the induced aerodynamics of complete aircraft configurations. In addition, models representing the aircraft surface bounded by the nozzles, referred to as "inner region models", were used to investigate the fountain strength for a variety of nozzle arrangements. The fountain strength was also evaluated using the metric ground plane with isolated nozzles.

The degree of aircraft simulation required for accurate jet-induced aerodynamic measurements was investigated with the three-jet subsonic V/STOL configurations shown in Figure 2: one a fully-contoured model and the other a flat plate planform model. The use of flat planform models allows for inexpensive fabrication and simple configuration changes to investigate various aircraft and propulsion system variables. These models, approximately five percent scale, have identical planforms simulating the same vehicle. The configuration represented an aircraft having a lift fan in the forward fuselage and two lift-cruise fans mounted above the wings.

The supersonic V/STOL model used is a flat plate planform model, shown in Figure 3. This model can be configured to represent a wide variety of propulsion concepts including twin or single forward lift systems. Tandem or side-by-side front twin nozzle arrangements can be simulated as well as various fore to aft spacings. In addition, rectangular and circular lift/cruise nozzles are available.

Lift Improvement Devices (LID's) consisting of lower fuselage fences can be incorporated on each of these models. Other ancillary hardware is also available, including nozzle vectoring vanes, landing gear and stores.

PARAMETRIC FOUNTAIN FORCE DATA

While recognizing that many factors enter the selection of the propulsion system arrangement for V/STOL aircraft, an induced lift data base as a function of nozzle spacing is useful in the early design stages and for preliminary evaluations. However, due to the configuration dependency, establishing a data base for all potential V/STOL aircraft configurations is an insurmountable task. Thus, the need exists to establish basic data trends of a generic nature. To this end, two test techniques were developed to study the fountain forces for a wide range of nozzle arrangements. These two techniques termed the "upwash" and the "inner region" test techniques are illustrated in Figure 4.

In the upwash technique, isolated nozzles are tested to determine the strength of the fountain at ground level by measuring the ground plane reaction force and subtracting from it the known nozzle thrust characteristics. A small back pressure correction is also applied to account for pressure changes on the backside of the ground plane.

In the inner region technique, the induced lift force is measured directly by the force balance mounted on the inner region plate. Since the fountain forces predominant in the inner region, this technique provides an excellent means of studying fountain force characteristics. These two techniques allow the basic trends in the jet-induced aerodynamic characteristics related to nozzle spacing to be established essentially independently of the aircraft configuration.

The upwash technique was developed specifically to investigate the effects of jet spacing completely independent of the fuselage planform and to do so at low cost. Although the presence of thefuselage modifies the ground effects flowfield and thus the magnitude of the fountain forces, results from the upwash technique do identify useful fountain force data trends. To illustrate this, fountain forces measured by the ground plane balance with no model present (upwash technique) are compared in Figure 5 with the forces on inner region plates and the forces on the same inner region plates with side fences simulating Lift Improvement Devices (LID's). The fountain force levels are substantially different, but the data trends as a function of nozzle spacing and height are similar. For example, comparing the upwash results to those with the clean inner region model, the height range of the fountain and the increase in fountain strength with spacing is similar. In addition, due to the conservation of momentum, the ground plane force balance indicates nearly the same forces as the inner region balance with the model present, as also shown in Figure 5.

The upwash and inner region data trends as a function of nozzle spacing also apply to complete aircraft configurations, as shown by the planform data in Figure 6. The peak fountain strength variation as a function of nozzle spacing is predicted accurately with the inner region and upwash techniques.

Since the stagnation regions formed between pairs of jets also contain upwash flow outside of the inner region, tests were conducted to determine the magnitude of the potential error in measuring the fountain forces only on the inner region. To investigate this, "tabs" of variable length and width were attached to the inner region plate for a three-nozzle arrangement, as shown in Figure 7. The induced lift data presented in Figure 7 show that, for the narrowest tabs tested, the inner region "captures" approximately 84% of the upwash force. The decrease in lift with increasing tab length for the wider tabs is attributed to the development of suckdown forces on the tabs. These results illustrate that the fountain forces do predominate in the inner region.

For a two-nozzle configuration, the fountain forces result from a stagnation upwash without a central core. The inner region for this case is somewhat arbitrary and therefore, tests were performed to study the effects of plate length and width on the upwash force. As seen in Figure 8, the fountain forces can be substantial for a two nozzle arrangement, reaching 12% at an H/D_{ej} of about 2 for the narrowest and longest plate representing the center fuselage between the two nozzles. The results are also consistent with the isolated nozzle data, since the curves appear to originate from the level acquired with the upwash method.

An additional configuration effect investigated was the lower surface curvature with the two nozzle arrangement. As shown in Figure 9, the corner curvature effect on the fountain impingement force is very strong. For example, with a corner radius of only 1/8 of the plate width, the fountain strength is totally eliminated. These results, of course, would be substantially changed by the addition of longitudinal fences or the presence of adjacent wing surfaces.

Using the upwash technique, fountain strength data were obtained for three- and four-nozzle arrangements to determine in parametric fashion, the effect of nozzle spacing. Typical results are shown for the three-nozzle arrangement in Figure 10. A definite peak is evident close to the expected equilateral triangle arrangement and fountain strength is seen to increase for a given apex angle as the nozzles are brought closer together. This latter effect is seen to be linear in terms of the nozzle spacing to nozzle diameter ratio (S_A/Dj) since the data collapses when the fountain force values (F/Fg) are multiplied by S_A/Dj, Figure 11. Excellent correlation of data for a four-nozzle arrangement was also obtained, as shown in Figure 11. As expected, the fountain strength for the four-nozzle arrangement is greater than for the three-nozzle arrangement. Nearly linear dependence on S_A/Dj is also evident in the complete planform data shown in Figure 12. This data was acquired for a typical subsonic V/STOL planform model, Reference 4.

MODEL SIMULATION REQUIREMENTS

To determine the degree of configuration simulation required for accurate jet-induced aerodynamic data, tests have been conducted on the effect of model contouring and nozzle geometry.

The effect of model contouring was evaluated in tests of a subsonic V/STOL configuration as: (1) a fully contoured model, (2) a semi-contoured model with contoured lower fuselage and raised tail and (2) a simple flat plate planform model with a raised tail. The results, shown in Figure 13 indicate that the planform model has a significantly higher induced lift in ground effect although the peak induced lift occurs at nearly the same height and the data trends are similar. The lower induced lift with the contoured model is attributed to the extreme sensitivity of the fountain impingement force to lower surface curvature, as shown in Figure 9. The data for the semi-contoured model agrees well with the fully contoured model above a height of 1.5 nozzle diameters. Below 1.5 diameters, the higher lift of the semi-contoured model is attributed to a higher fountain upwash impingement force on the flat plate planform extension, which was added to simulate the aft-end.

The effects on the induced lift of adding pitch and yaw vanes and a hub centerbody to the front nozzle and yaw vanes to the rear nozzles are presented in Figure 14. The addition of these nozzle components is seen to reduce the lift near the ground by about two percent. This results from modification of the jet decay rates and thus, the flowfield stagnation areas, as verified in other tests by lower surface pressure instrumentation.

The effect of nozzle shape on the induced lift characteristics is seen to be very strong for a typical supersonic V/STOL configuration in Figure 15. This data, which was acquired on a planform model with three-sided LID's

shows that both the in ground and out of ground effect lift are influenced. These results are attributed to the difference in flow entrainment characteristics of the nozzles and the different mass flux distributions in the ground jets.

NOZZLE OPERATION CONDITIONS

Induced lift characteristics can be modified by changing the ratio of forward nozzle thrust to total thrust as shown in Figure 16. Data for both subsonic and supersonic configurations indicate that peak induced lift in ground effect occurs above 40% thrust split for the subsonic configuration and between 40 and 60 percent thrust split for the supersonic configuration. While this is also true at greater heights, the penalties associated with operating at various thrust splits are less severe.

LIFT IMPROVEMENT DEVICES

Much data has been generated and published on the magnitude of induced lift obtainable with fuselage fences (LID's), References 4 through 6. However, one area of concern is the effect of LID's on aircraft lift and stability with respect to roll. The concern is that LID's may not be effective at roll due to the inability to capture the fountain. However, if properly spaced, LID's are effective in increasing the lift over a rather large range of roll angles, as seen in Figures 17 and 18 for both subsonic and supersonic configurations. Due to the change in location of the fountain impingement, some effect on rolling moment can occur, as shown for the subsonic configuration in Figure 17. Adequate hover control power would be able to compensate for such rolling moment changes since the rolling moment variation with LID's is essentially linear. The supersonic configuration shows no effects on rolling moment due to the installation of the LID's, Figure 18.

DECK MOTION EFFECTS

In Navy sponsored and additional MCAIR funded efforts, the jet-induced aerodynamics of representative V/STOL aircraft were assessed over a three degree of freedom ship deck motion simulator. The primary objective of this study was to determine the effects of a variety of deck motions on the jet-induced aerodynamics of V/STOL aircraft during landing and take-off operations from small seaborne platforms. The complete results of the Navy sponsored program are reported in Reference 7. Probably the most critical finding impacting V/STOL aircraft development was that landing and take-off operations cannot generally be considered as quasi steady-state. This finding is illustrated in Figures 19 and 20 where dynamic data are compared to predictions based on data obtained with static fixed deck positions. It can be seen that the dynamic data can differ from the steady state predictions, the largest differences being for combined motions, Figure 20. To account for these changes in the induced aerodynamics, sufficient thrust margin and control power are required in V/STOL aircraft designed to operate from smaller ships in rough seas. Further efforts are necessary to develop useful empirical prediction tools for correcting steady state data for these deck motion effects.

CONCLUSIONS

A survey of MCAIR conducted jet-induced aerodynamic tests indicates that:

- o Data trends established with isolated nozzles and with inner region models are sufficiently similar to complete aircraft data for representative evaluations of fountain forces.
- o Lower surface curvature effects on fountain forces and induced lift are very strong.
- o The induced lift can be significantly influenced by nozzle geometry and complexity.
- o Selection of the thrust split between forward and aft nozzles is critical to obtaining acceptable in ground-effect performance.
- o Lift improvement devices are effective at roll and do not appear to compromise aircraft stability.
- o V/STOL aircraft landing and take-off operations from a moving deck cannot generally be considered as quasi steady-state.

REFERENCES

1. Weber, W.B. and Williams, R.W., "Experimental Determination of Propulsion Induced Ground Effects of Typical Three Fan Type A V/STOL Configurations", AIAA Paper 78-1507, presented at AIAA Aircraft Systems and Technology Conference, 21-23 August 1978.

2. Kamman, J.H., Hall, C.L., and Walters, M.M., "Jet-Induced Aerodynamics of V/STOL Aircraft Over a Moving Deck", AIAA Paper 79-0337, presented at 17th Aerospace Sciences Meeting, 15-17 January 1979.

3. Kotansky, D.R., "The Influence of V/STOL Vehicle Configuration Variables on Vectored Jet Induced Flow Fields in Ground Effect", AIAA Paper 78-1021, presented at AIAA/SAE 14th Joint Propulsion Conference, 25-27 July 1978.

4. Schuster, E.P., and Flood, J.D., "Important Simulation Parameters for the Experimental Testing of Propulsion Induced Lift Effects", AIAA Paper 78-1078, presented at AIAA/SAE 14th Joint Propulsion Conference, 25-27 July 1978.

5. Wohllebe, F.A., and Migdal, D., "Some Basic Test Results of V/STOL Jet-Induced Lift Effects in Hover", AIAA Paper 79-0339, presented at the 17th Aerospace Sciences Meeting, 15-17 January 1979.

6. Sherrieb, H.E., "Ground Effects Testing of Two, Three, and Four Jet Configurations", AIAA Paper 78-1510, presented at AIAA Aircraft Systems and Technology Conference, 21-23 August 1978.

7. Kamman, J.H., and Hall, C.L., "Lift System Induced Aerodynamics of V/STOL Aircraft in a Moving Deck Environment", NADC-77-107-30, 29 September 1978.

FIGURE 1
V/STOL JET INTERACTION TEST APPARATUS

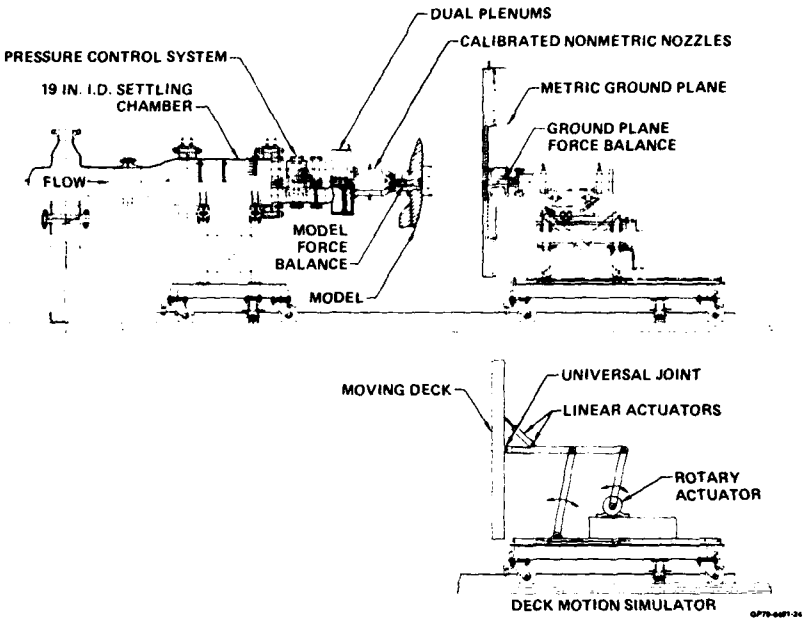

FIGURE 2
SUBSONIC V/STOL MODELS

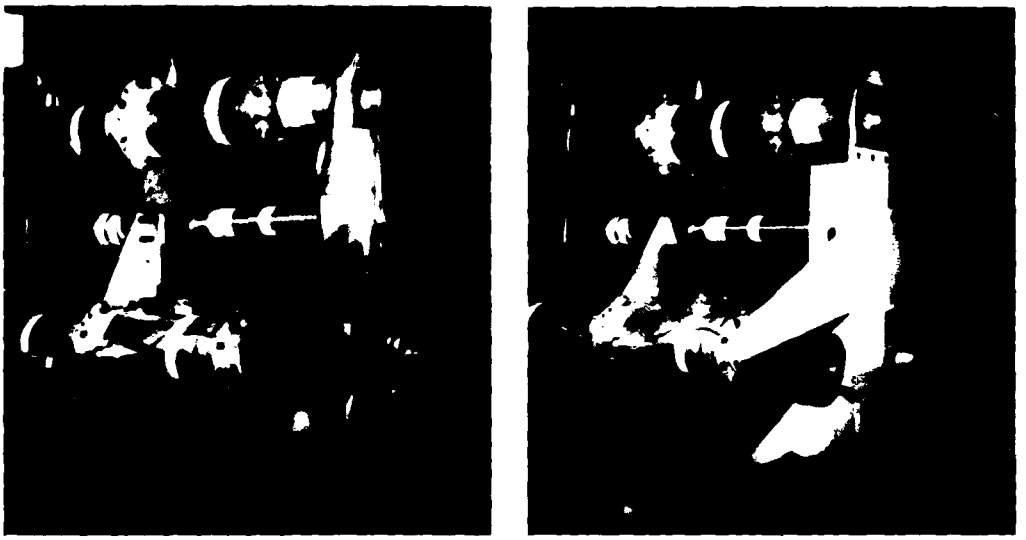

SUBSONIC V/STOL
FULLY CONTOURED MODEL

SUBSONIC V/STOL
2-D PLANFORM MODEL

FIGURE 3
SUPERSONIC V/STOL MODELS

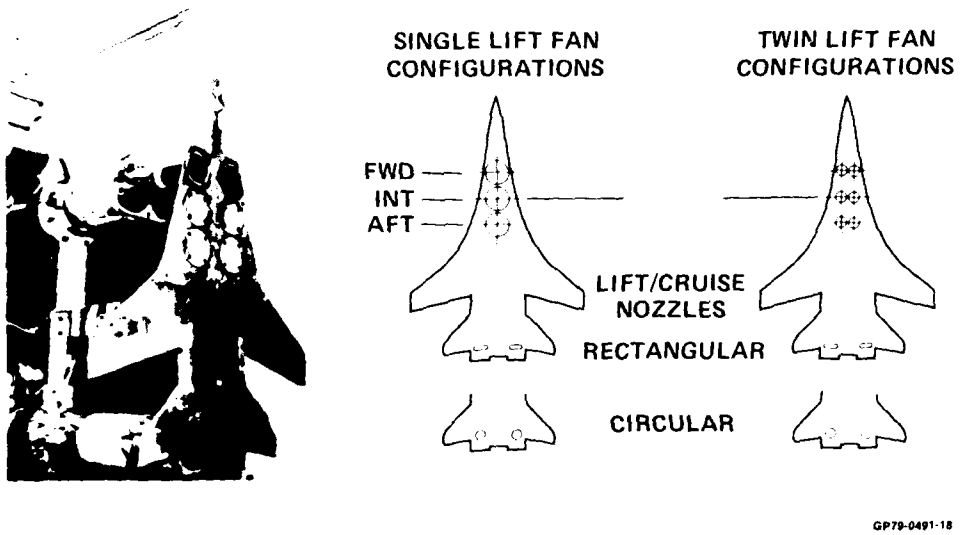

FIGURE 4
JET FOUNTAIN PERFORMANCE TEST TECHNIQUES

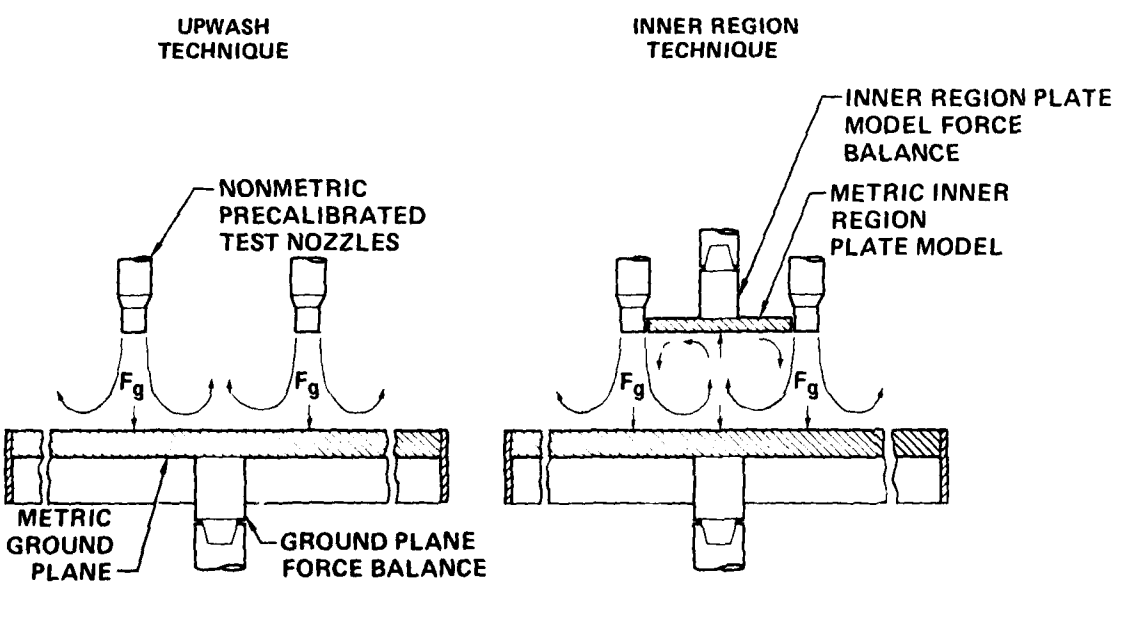

FIGURE 5
JET SPACING EFFECT ON FOUNTAIN FORCES
3-Jet NPR = 1.89

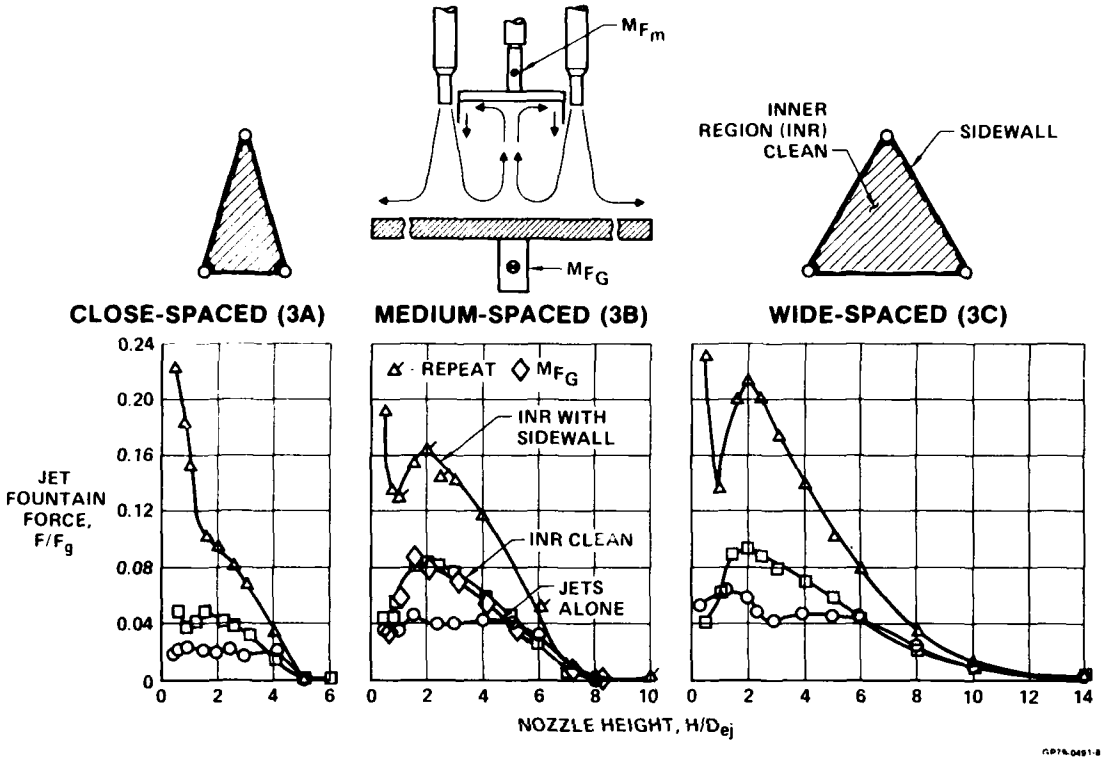

FIGURE 6
JET SPACING EFFECT ON TOTAL LIFT FORCES
3-Jet Planform Models NPR = 1.89

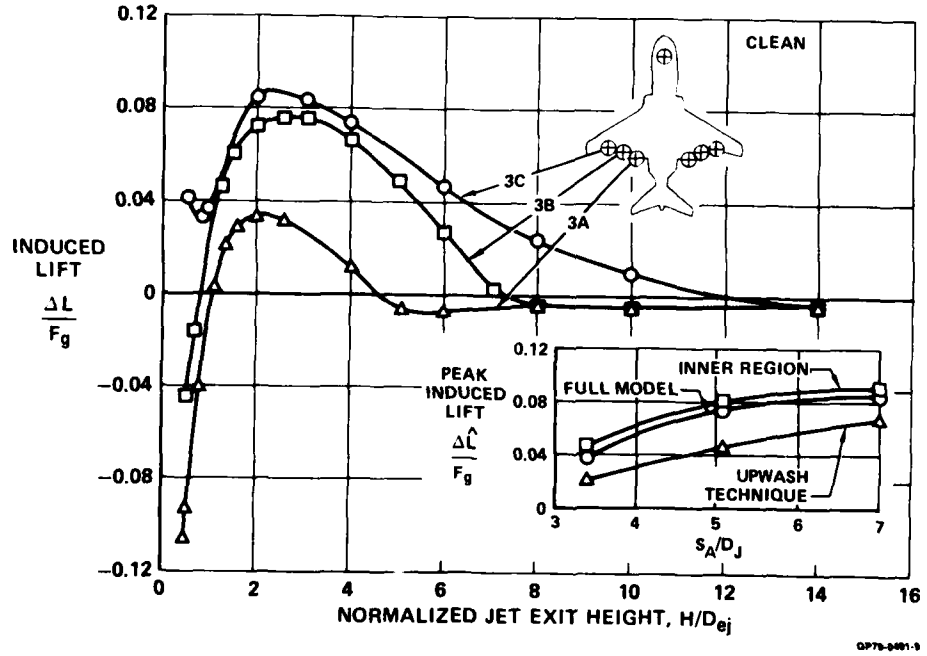

FIGURE 7
EFFECT OF OUTER REGION PLATE WIDTH AND LENGTH ON PEAK JET FOUNTAIN STRENGTH
3-Jet Triangle

NPR = 1.89 θ_{ji} = +90° SIMPLE CIRCULAR NOZZLES β = 60°

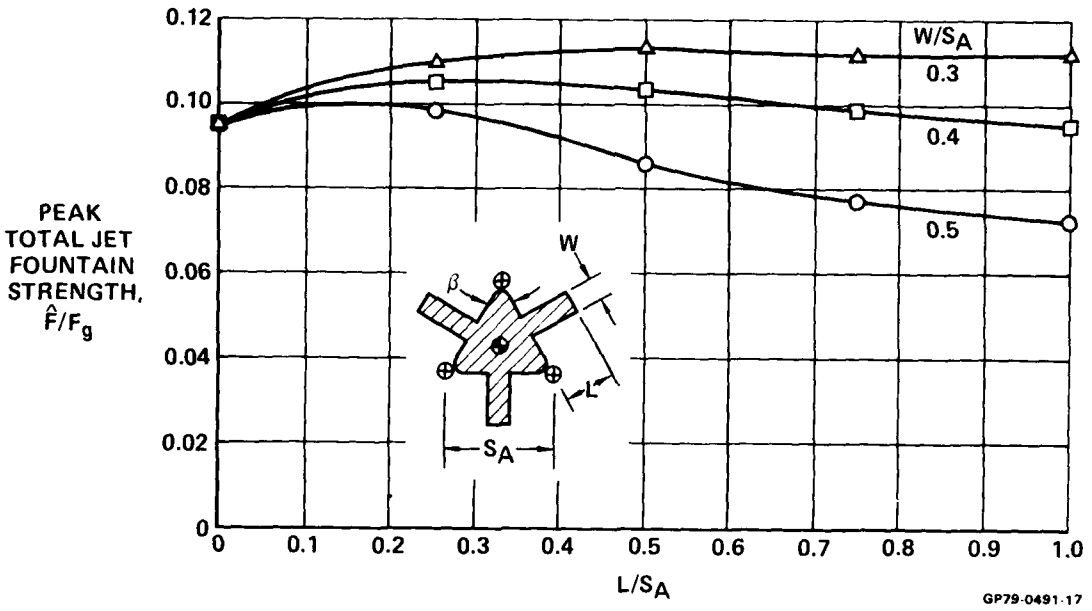

FIGURE 8
EFFECT OF PLATE GEOMETRY ON FOUNTAIN IMPINGEMENT FORCE
2 Jets NPR =1.89

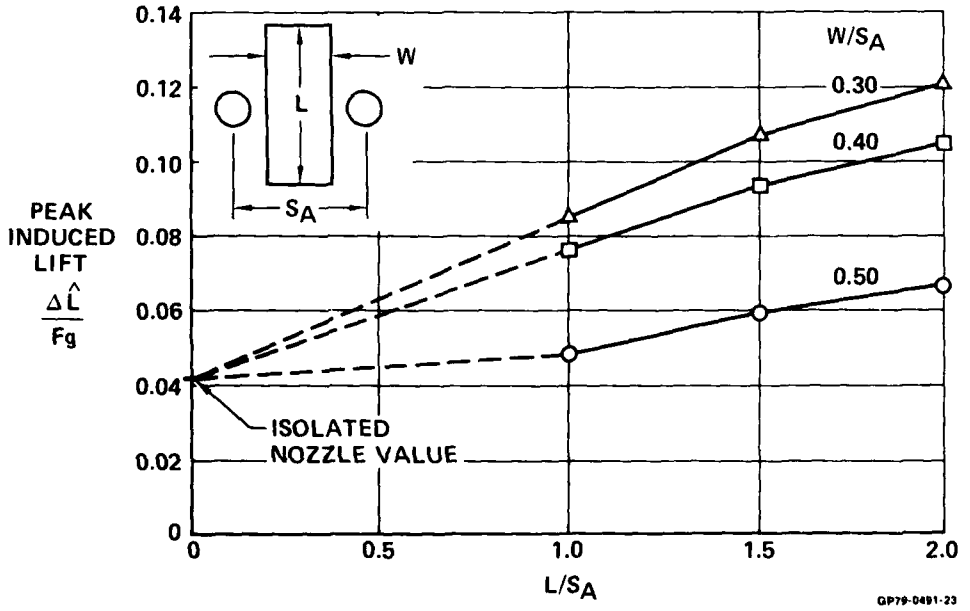

FIGURE 9
EFFECT OF CURVATURE ON FOUNTAIN IMPINGEMENT FORCE

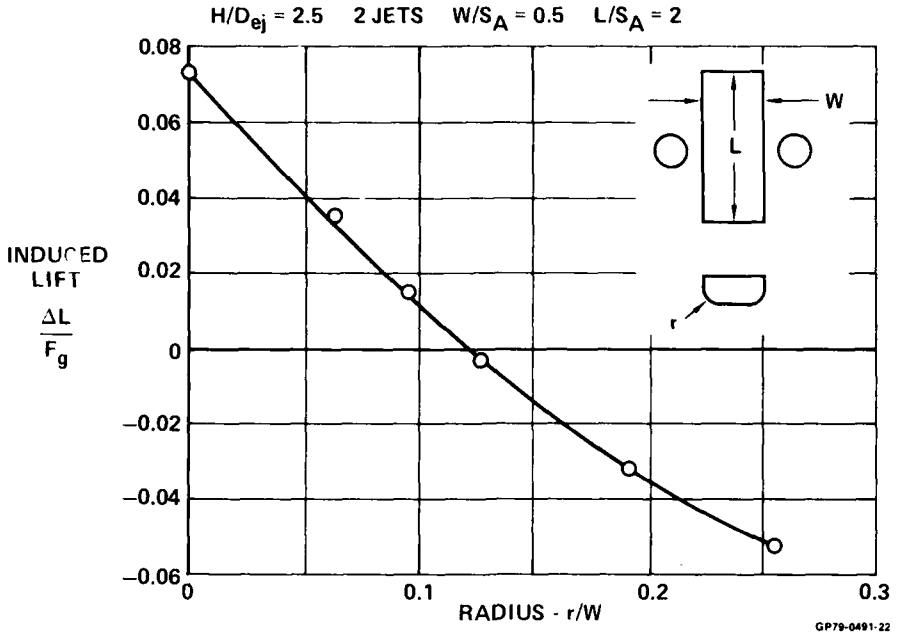

FIGURE 10
AVERAGE PEAK JET FOUNTAIN STRENGTH
3-Jet Triangle

NPR = 1.89 θ_{Ji} = +90° SIMPLE CIRCULAR NOZZLES

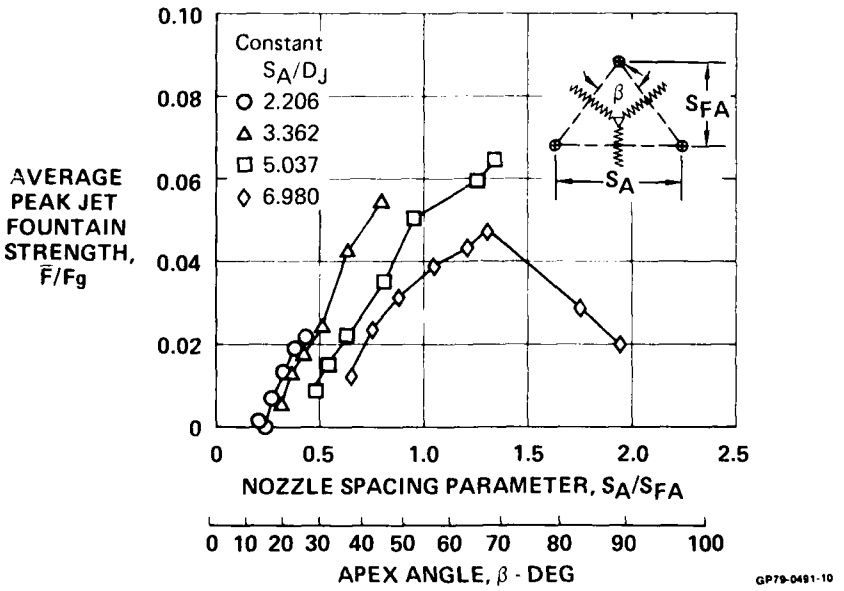

FIGURE 11
CORRELATION OF AVERAGE PEAK JET FOUNTAIN STRENGTH PERFORMANCE TEST DATA

NPR = 1.89 θ_{Ji} = +90° SIMPLE CIRCULAR NOZZLES

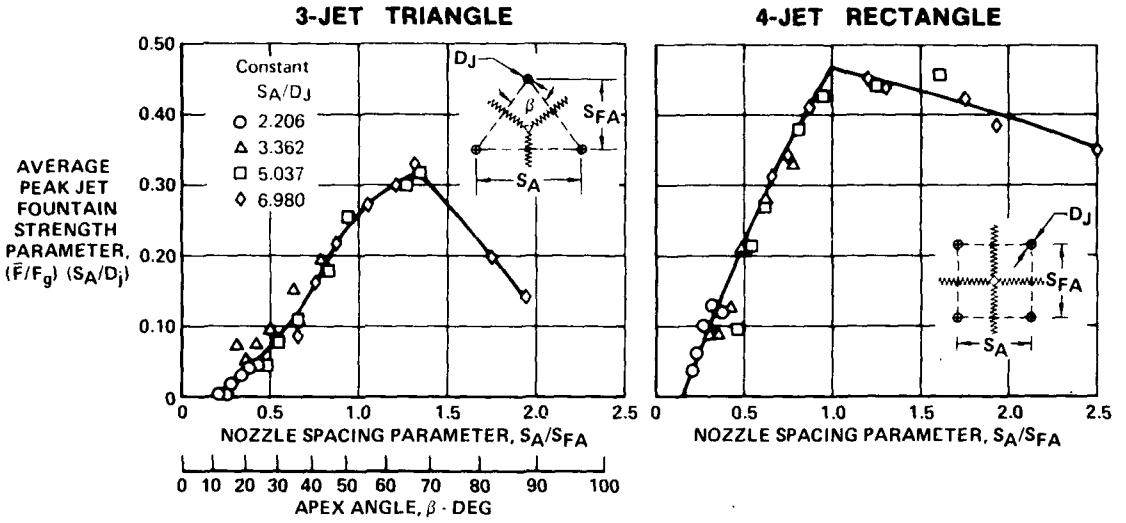

GP79-0491-11

FIGURE 12
EFFECT OF NOZZLE SPACING TO DIAMETER RATIO

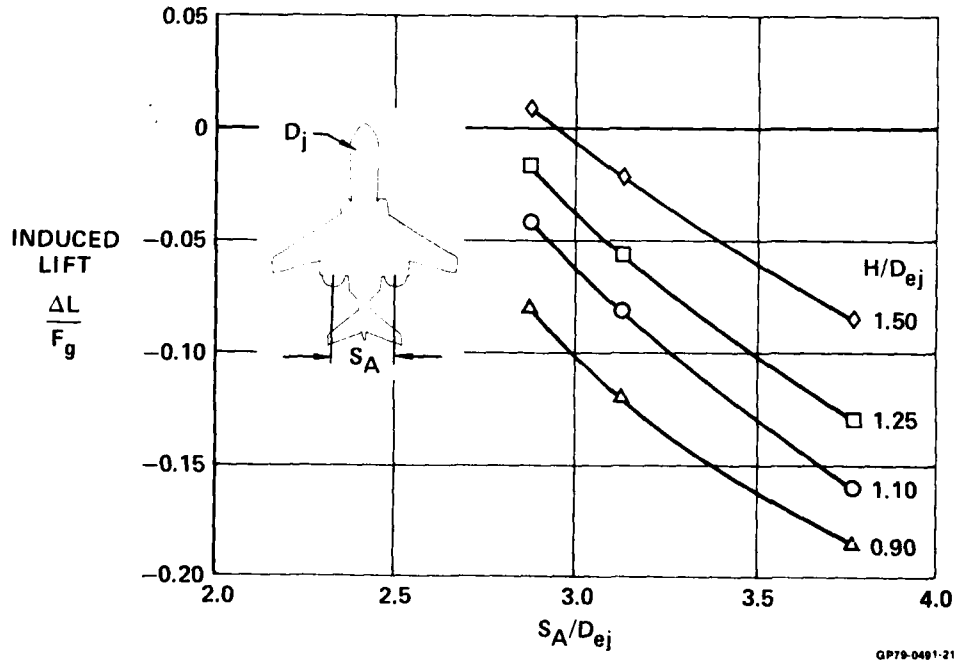

GP79-0491-21

FIGURE 13
FUSELAGE CONTOURING EFFECTS

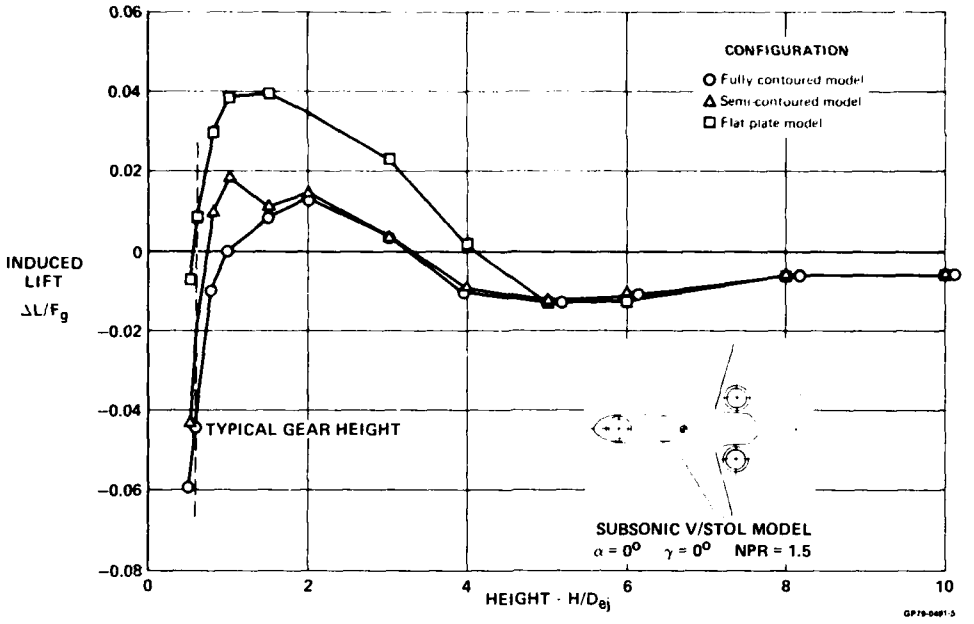

FIGURE 14
SUBSONIC V/STOL COMPLEX NOZZLE EFFECTS

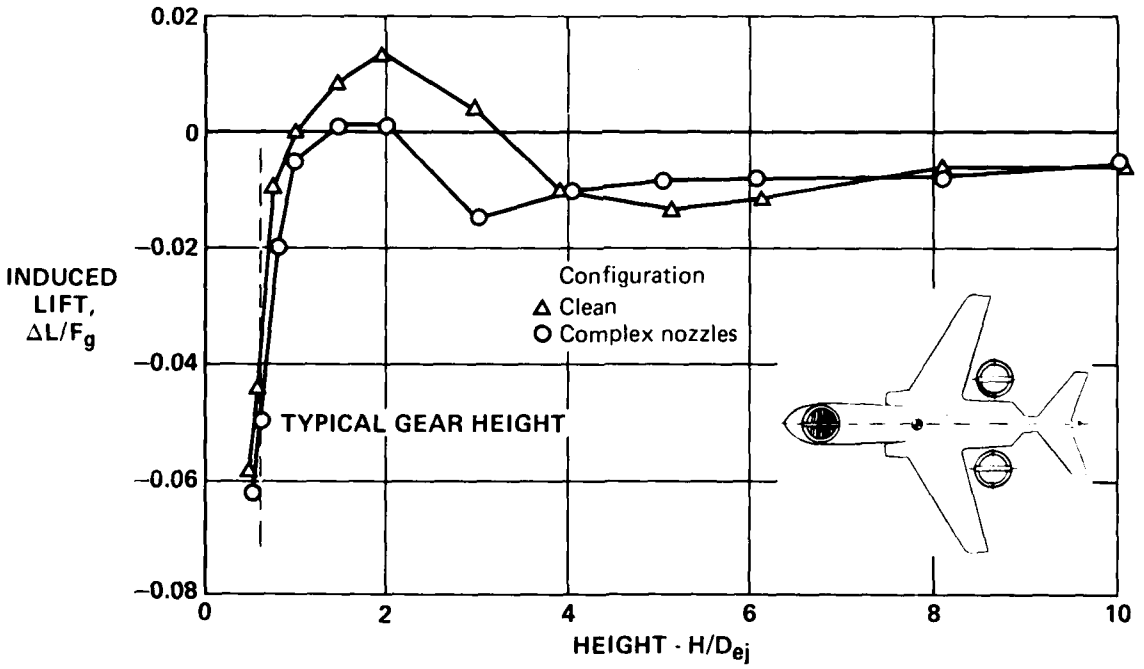

GP-0491-4

FIGURE 15
EFFECT OF AFT NOZZLE GEOMETRY
Twin Fan Configuration

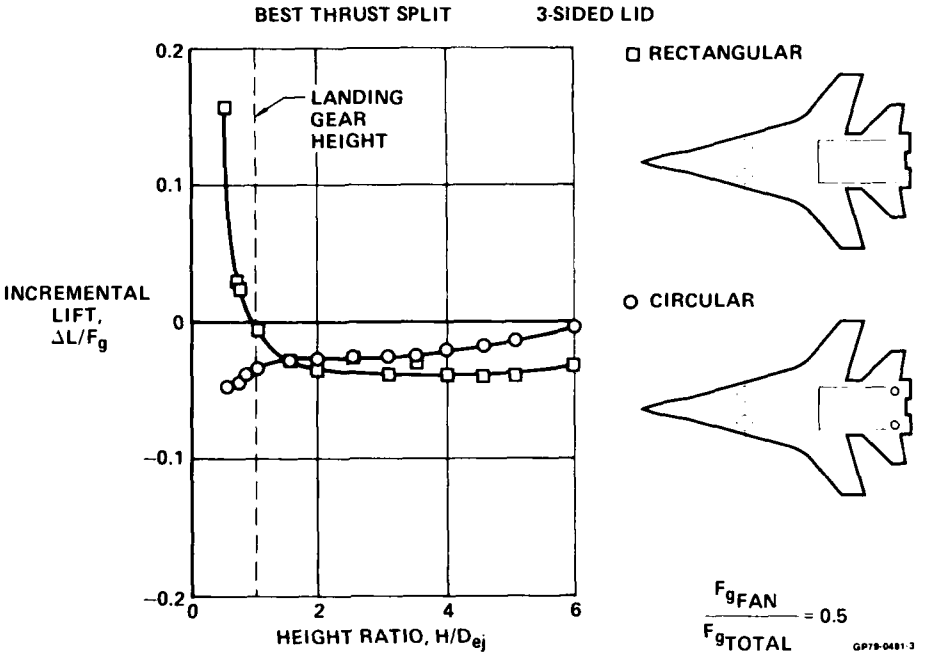

FIGURE 16
THRUST BIAS EFFECT ON INDUCED LIFT

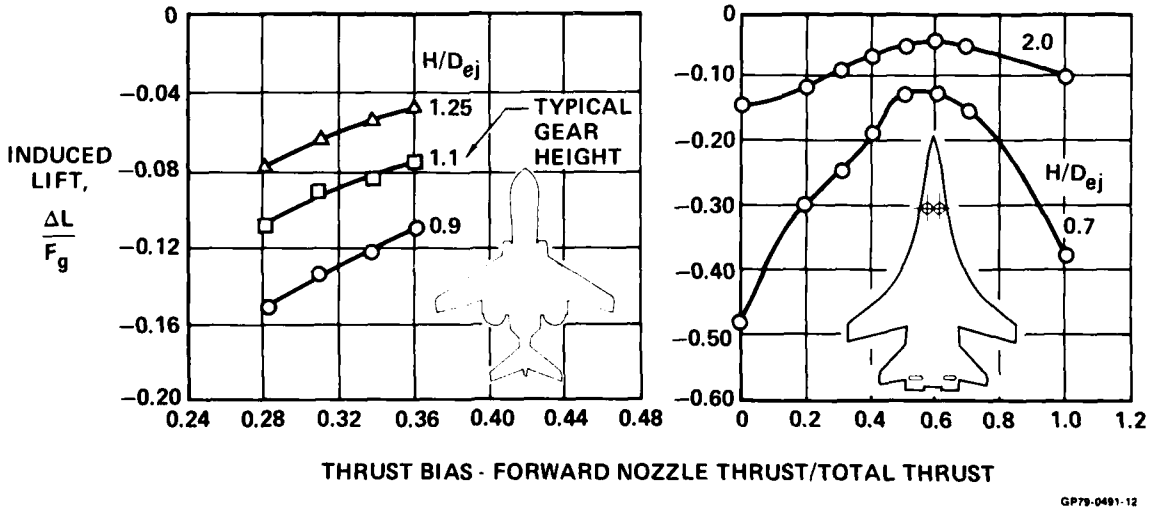

FIGURE 17
SUBSONIC V/STOL - EFFECT OF LID
H/Dje = 0.8 = 0°

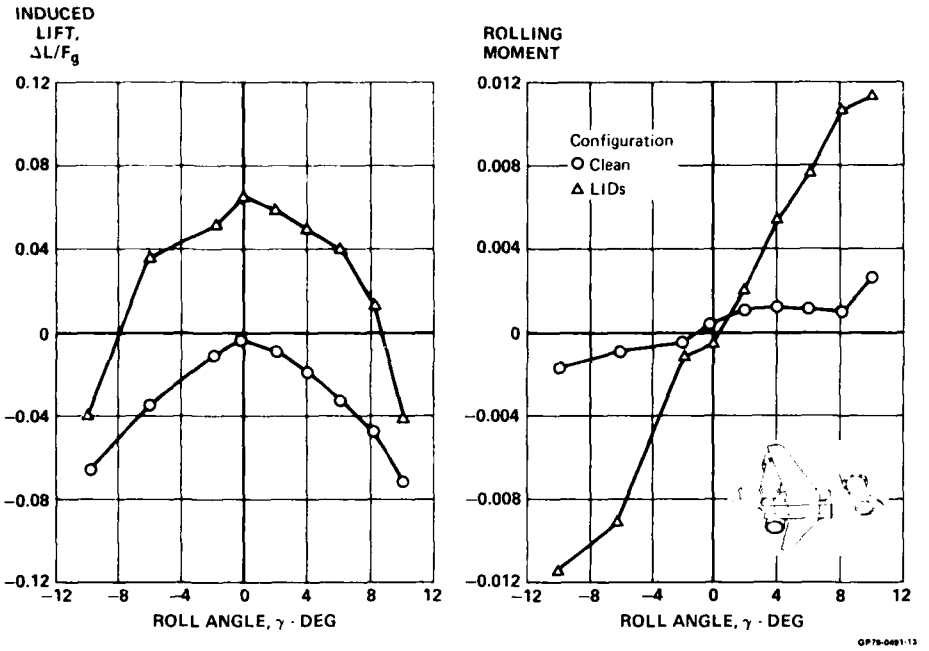

FIGURE 18
SUPERSONIC V/STOL - EFFECT OF LID
3-Jet = 0°

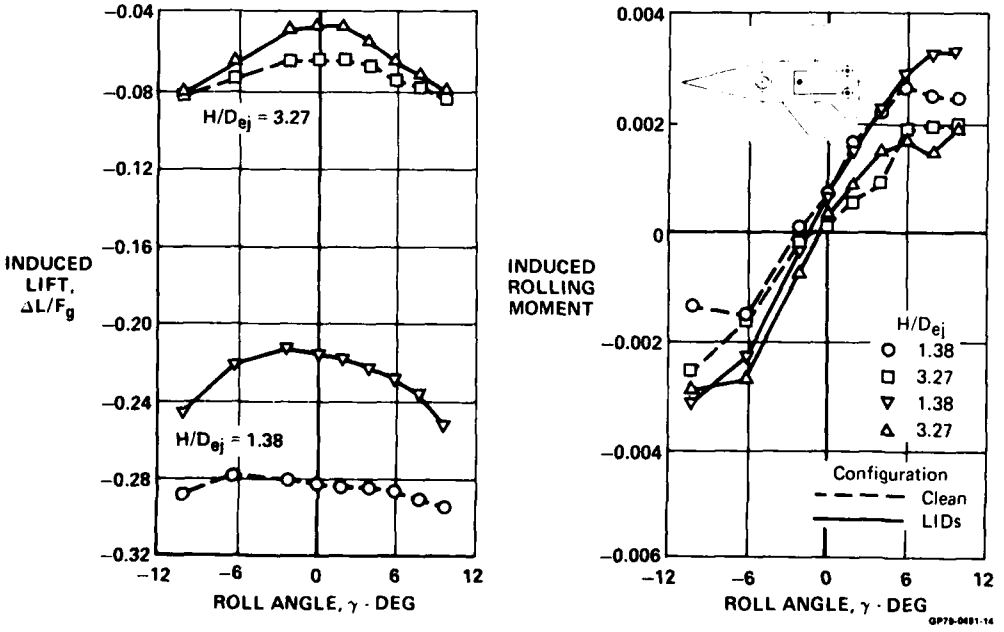

FIGURE 19
COMPARISON OF DYNAMIC DATA TO PREDICTION BASED ON STEADY STATE DATA FOR HEAVING DECK

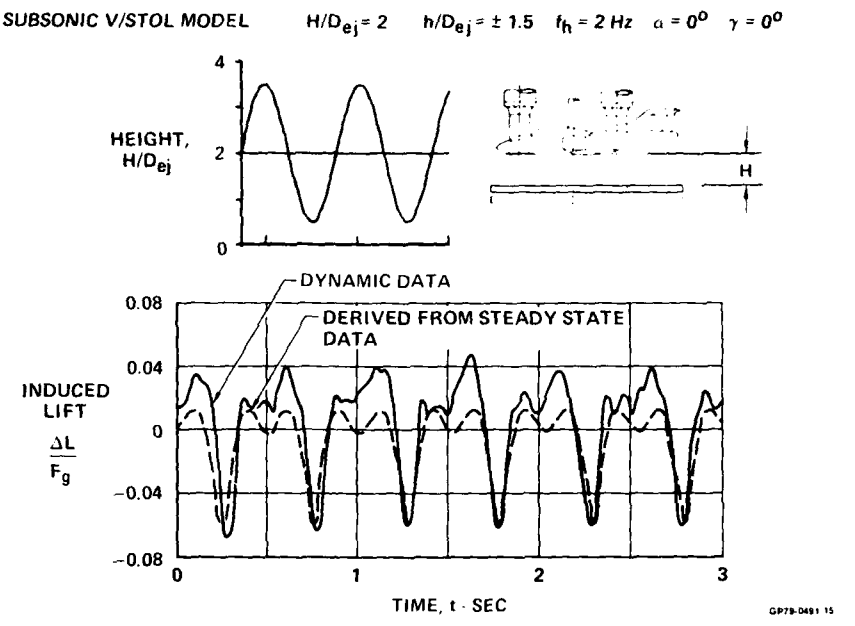

FIGURE 20
COMPARISON OF DYNAMIC DATA TO PREDICTIONS FOR HEAVING AND ROLLING DECK

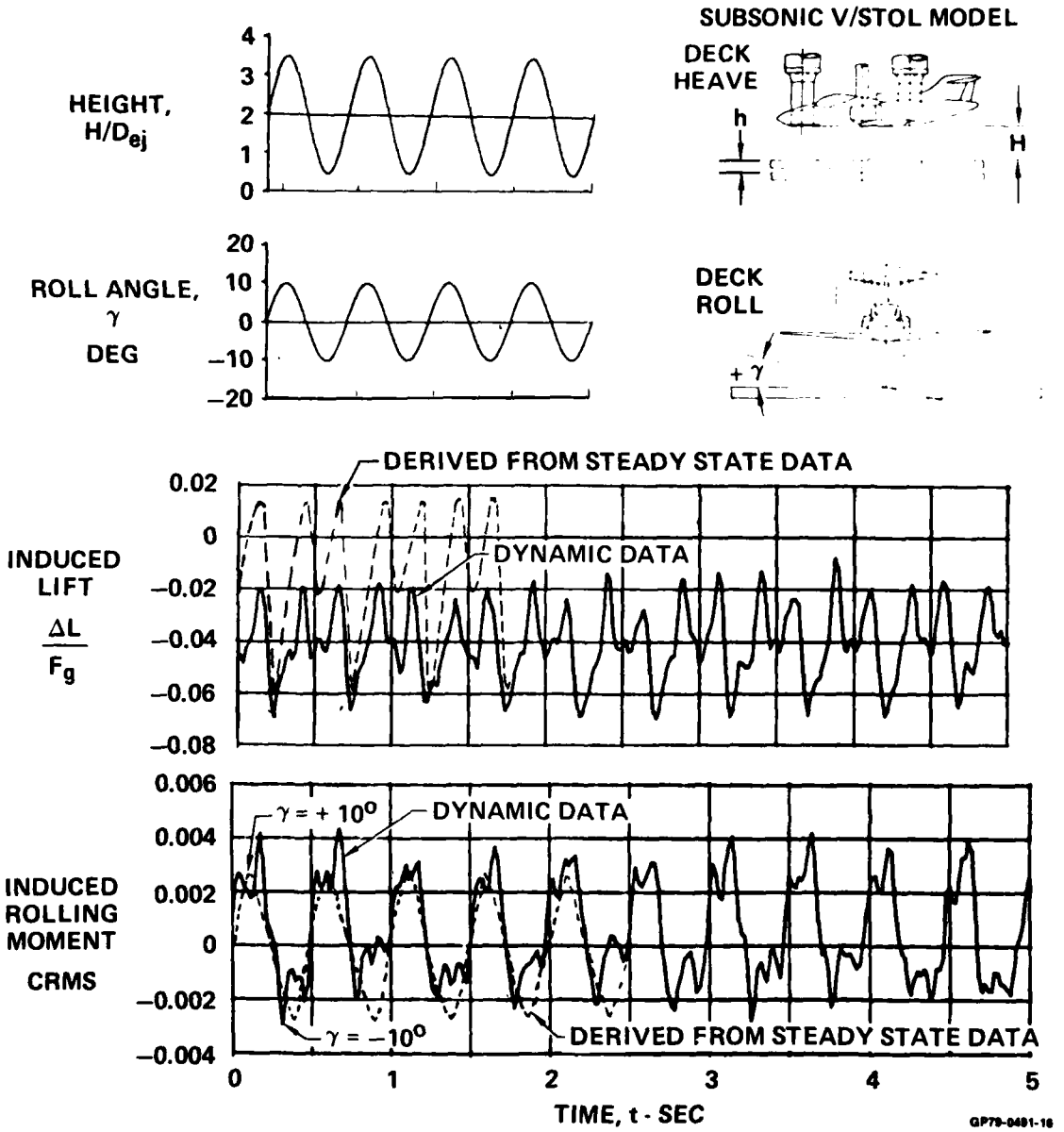

PROGRESS TOWARDS A THEORY OF THRUST RECOVERY

Paul M. Bevilaqua

Paul E. Cole

ROCKWELL INTERNATIONAL

Military Aircraft Division

Columbus, Ohio

ABSTRACT

The hypothesis that mixing with the main stream reduces the thrust of a jet flap will be tested by comparing the predictions of a mathematical model based on the hypothesis with experimental data. The equal but opposite forces on the airfoil and jet will be calculated by matching a finite difference solution for the turbulent jet to a vortex panel solution for the airfoil and jet flap. The aerodynamic forces and moments predicted by this analysis will be compared to the results of classical jet flap theories and existing data. In addition, tests will be performed at the large thrust coefficients and deflection angles typical of V/STOL systems, and the analytic results will be compared to these data.

INTRODUCTION

The jet flap is an aerodynamic device for increasing wing lift, especially at low speeds, by blowing a jet sheet downward from the trailing edge of a wing, as shown in Figure 1. This generates both direct lift, as a reaction to the jet thrust, and an increment in the aerodynamic lift, as a result of changes in the airfoil pressure distribution caused by the deflection of the mainstream. The phenomenon is called the jet flap effect by analogy to the action of a mechanical flap.

Because the duct losses associated with a jet flap system are typically large, the pure jet flap is no longer considered practical. However, the jet flap effect makes some contribution to the forces induced by all powered lift systems. For example, in both the YC-14 and YC-15 propulsion systems the engine exhaust is deflected down over the flaps at the trailing edge of the wing, so that the aerodynamic lift is increased by the jet flap effect. Similarly, the wing lift of the various ejector wing and vectored thrust propulsion systems are increased by the trailing jet sheet.

In addition to producing an increment in the aerodynamic lift, the jet flap also generates a thrust on the airfoil greater than the horizontal component of the jet thrust. This phenomenon was discovered during testing of jet flap airfoils at the British National Gas Turbine Establishment. As a result of this discovery, Stratford (1956) suggested the hypothesis that, in ideal flow, the total jet thrust is always recovered as a horizontal force, regardless of the initial deflection angle, because the jet is ultimately turned in the direction of the free stream. He did not attempt a formal proof of this hypothesis, but reasoned from the control volume in Figure 1, that the force on the airfoil and momentum of the jet must be equal but opposite.

This hypothesis was received with a great deal of skepticism, but the existence of the phenomenon was established by experiments performed at Stanford University, when Foley(1962) measured almost complete thrust recovery over a range of jet deflection angles up to 60°. However, in subsequent tests in the same apparatus,Tsongas (1962) found that the thrust recovery decreased rapidly at jet deflection angles greater than 70°. These results are shown in Figure 2.

Various analytic methods have been developed to predict the increments of lift and moment induced by the jet flap. These methods are based on Spence's (1956) now classical jet flap theory, in which the inertia of the jet sheet is related to the strength of an equivalent vortex sheet. However, none of these methods predict the reduction in thrust recovery. In current practice, complete recovery is assumed for calculating lift, while an empirical function derived from the Stanford data is used to specify the actual decrease in thrust recovery.

This loss of recovery has been attributed to various three-dimensional and real fluid effects: Maskell and Spence (1959) showed that deflection of the jet wake by the downwash behind a finite wing reduces the recovery, while Williams, et.al (1961) pointed out that leading edge separation on the airfoil would also cause a loss of thrust, and Tsongas (1962) concluded that separation of the main stream from the jet flap at large deflection angles reduced the recovery in his experiments. Earlier, Stratford (1956) had argued that entrainment by the jet itself decreased the thrust recovery, because it induced a form drag on the airfoil, and Wygnanski (1966) suggested that the entrainment and, consequently, the form drag increase with the jet deflection angle. More recently, Wilson (1974) used an empirical entrainment function to show that the jet drag is on the order of the observed loss in thrust recovery. This analysis was extended by Chandra (1975), who used integral methods to improve the entrainment function.

Although such entrainment functions have been useful for determining the importance of mixing in reducing the thrust recovery, this approach only treats half of the jet/airfoil interaction - the jet drag induced on the airfoil. Because complete thrust recovery is assumed in calculating the position of the jet, the other half of the interaction - the equal and opposite reduction of the jet thrust by the action of the airfoil - is neglected. The actual reduction in the jet thrust affects the position of the jet sheet, which in turn affects the magnitude of the force on the airfoil.

The purpose of this paper is to describe progress in developing a quantitative theory of thrust recovery which includes the interaction between the force on the airfoil and the jet thrust. A combination of analysis and experiment has been utilized to develop this theory. In the next section of this paper, the mechanism of thrust recovery is discussed. The way mixing changes the thrust of the jet flap is outlined in the following section. The last section describes the planned test program.

THRUST RECOVERY MECHANISM

The thrust recovery is induced by an interaction between the circulation of the airfoil and inertial forces in the jet sheet. According to Spence's (1956) theory, inertia forces due to curvature of the jet sheet are balanced by a pressure difference between the upper and lower surfaces of the jet. This pressure difference is related to the strength of an equivalent vortex sheet located along the axis of the jet. A vortex segment bound in the wing induces a downwash velocity of magnitude, $\Gamma_w/2\pi r$, on a vortex in the jet. A horizontal force, $\rho\Gamma_j\ (\Gamma_w/2\pi r)$ is therefore induced on the jet in the downstream direction. Similarly, the jet vortex induces an upwash, $\Gamma_j/2\pi r$, on the wing vortex, which then experiences an equal force, $\rho\Gamma_w\ (\Gamma_j/2\pi r)$ directed upstream.

It is the integrated effect of all such vortex pairs that results in an effective "thrust recovery". Figure 3 is a sketch of the forces on the airfoil, jet, and surrounding control volume. The jet thrust is not strictly turned and recovered. Rather, the force of the main stream on the jet increases the horizontal component of the jet thrust, and reduces the vertical component. The reaction to this force on the jet transmits the vertical component of the jet to the free stream and produces a horizontal thrust on the airfoil, as shown in the figure.

If the entrainment of the jet is neglected, classical jet flap theory predicts complete thrust recovery. This can be shown from the equilibrium of the forces which then act on the jet. Consider the segment of the jet shown in Figure 4. The forces due to the main stream and the wing vortex system deflect the jet through an angle, θ, as shown. The final thrust of the jet, T_2, is not assumed to be the same as the initial thrust, T_1. Since entrainment has been neglected, the jet will be a streamline of the flow and the pressure force, P, must therefore act normal to the segment.

The summation of forces in the direction of T_2 yields

$$T_2 = T_1 \cos \theta + P \sin \frac{\theta}{2} \tag{1}$$

which says that the thrust of the jet leaving the segment equals the sum of the initial thrust component plus the force on the jet in this direction. The summation of forces normal to the direction of T_2 gives

$$P \cos \frac{\theta}{2} = T_1 \sin \theta \tag{2}$$

Solving this equation for P and substituting in Equation (1) gives

$$T_2 = T_1 \left(\cos \theta + \sin \theta \tan \frac{\theta}{2}\right) \tag{3}$$

Using the half angle formula, $\tan \frac{\theta}{2} = (1 - \cos \theta)/\sin \theta$, yields

$$T_2 = T_1 \tag{3}$$

Therefore, the thrust of the jet is conserved. Because the jet can be considered to consist of a series of these segments, its total thrust is ultimately recovered in the far wake as a horizontal force.

Since the horizontal component of the jet at the nozzle was $T\cos \delta$, the total horizontal force exerted on the jet is $T (1 - \cos \delta)$. The equal but opposite reaction to this force must be induced on the wing, because the net horizontal force on the wing plus jet is zero in uniform flow. Therefore, the horizontal force on the wing due to the jet is the sum of the horizontal reaction force on the nozzle, $T \cos \delta$, and the thrust induced on the wing, $T (1 - \cos \delta)$. This sum is equal to the initial thrust of the jet.

THRUST LOSS MECHANISM

The mixing loss hypothesis is that the thrust recovery is reduced by the mutually induced forces on the vortex sheet bound in the wing and a sink distribution which represents the entrainment of the jet. The origin of the force on the wing is relatively easy to understand; the sinks on the jet change the surface pressure distribution so as to increase the wing drag. There are two contributions to this force, as shown in Figure 5. The jet drag due to thickness originates in the interaction between the jet sinks and the source distribution which defines the airfoil thickness. The jet drag due to lift originates in the interaction between the jet sinks and vortex distribution which determines the wing lift.

The origin of the reaction force on the jet may not be as apparent. This force is conceptually similar to the drag experienced by a sink in an external stream. However, the sink/vortex interaction is only an irrotational simulation of the jet mechanism. The fluid entrained into the jet becomes rotational, so that an understanding of how the reaction force actually develops requires consideration of the jet mixing process.

This process is basically an inelastic collision between the jet and surrounding fluid. As such, jet mixing is governed by the same laws of momentum and energy conservation as simple collisions between discrete particles. If the mixing occurs in a region of constant static pressure, the thrust of the jet is conserved. But if the jet passes through a region where the static pressure, P*, is different from the undisturbed pressure at infinity, P_∞, the mixing changes the momentum flux. The following simple analysis illustrates this phenomenon.

Inside the region where the pressure is P*, the velocities in the jet and coflowing stream, before mixing, are

$$U_j^* = \left[\frac{2(P_o - P_*)}{\rho}\right]^{1/2}$$

and

$$U_s^* = \left[U_\infty^2 + \frac{2(P_\infty - P_*)}{\rho}\right]^{1/2}$$

in which P_o is the stagnation pressure of the jet and U_∞ is the velocity of the coflowing stream at infinity. Momentum is conserved during the mixing process itself, so that

$$\dot{m}_j U_j^* + \dot{m}_s U_s^* = (\dot{m}_j + \dot{m}_s)\, U_m^*$$

in which $\dot{m}_j$ is the initial mass flux of the jet, $\dot{m}_s$ is the quantity of mass entrained in the region, and U_m^* is the average velocity of the mixed flow.

The velocity of the mixed stream changes as it passes into the region of undisturbed pressure; the velocity becomes

$$U_m = \left[U_m^{*2} - \frac{2\,(P_\infty - P_*)}{\rho} \right]^{1/2}$$

The ratio of the final thrust of the mixed stream, $(\dot{m}_p + \dot{m}_s)\,U_m$, to the thrust, $\dot{m}_p U_j$, obtained by an isentropic expansion of the jet, without mixing, to the final pressure may be evaluated by substituting in turn for U_m, then U_m^*, and finally for U_j^* and U_s^*. Performing these substitutions yields for this ratio

$$\phi = \left[1+2M \left\langle (1+S)^{1/2}\,(U^2+S)^{1/2} - S \right\rangle + M^2U^2 \right]^{1/2} - MU$$

in which $M = \dot{m}_s/\dot{m}_p$, is the entrainment ratio, $U = U_\infty/U_j$ is the velocity ratio, and $S = 2(P_\infty - P^*)\rho U_j^2$ is the normalized pressure change.

If there is no mixing between the jet and the coflowing stream, then $M = 0$ and the thrust of the jet is conserved; that is, $\phi = 1$. similarly, if there is no pressure change, then $S = 0$ and the solution reduces to that for free jet mixing; the thrust is conserved in this case, also. However, if the pressure in the mixing region is less than the pressure at infinity, then $S<0$ and the thrust of the jet increases. For the case in which $U_s = 0$, the thrust ratio has the simple form,

$$\phi = (1+M)^{1/2}$$

and the jet thrust increases with increasing entrainment. This is the basic mechanism of ejector thrust augmentation, which has been discussed in greater detail by Bevilaqua (1978).

If the pressure in the mixing region is above ambient, the thrust of the jet is reduced. For the case in which $U_s^* = 0$, the thrust ratio also has a simple form

$$\phi = 1 - MU$$

and in this case the jet thrust decreases with increasing entrainment. Because the effect of the airfoil circulation is to increase the static pressure in a region behind the trailing edge of the wing, this mixing loss mechanism will reduce the jet thrust. According to Newton's law of action and reaction, the net loss of thrust must be equal to the jet drag on the wing.

The equal but opposite forces on the airfoil and jet will be calculated by matching a potential flow solution for the airfoil and jet flap to a viscous solution for the turbulent mixing. A jet flap panel method, in which the thrust of the jet is not assumed to be constant, will be used for the inviscid solution. For the viscous jet solution, a finite difference analysis utilizing a two-equation turbulence model will be developed. The basic scheme will be that devised by Patankar and Spalding (1970) for thin shear layers: the full Navier-Stokes equations are reduced to a simpler set by the assumption that there is a primary direction of flow (along the jet), and that the diffusion of fluid properties is negligible in that direction. The effects of curvature on the development of the jet will be treated as a perturbation of this basic scheme.

EXPERIMENTAL PROGRAM

A two-dimensional wind tunnel was chosen for the test program, in order to minimize the induced drag and thus isolate the thrust force. This facility,shown in Figure 6, is an open return design, powered by an ejector at the end of the test section. The test section is nominally 50 cm wide, 365 cm high, and 370 cm long. Smooth flow into the tunnel is achieved with an elliptical bellmouth section. The sidewalls diverge at approximately 0.2° on each side to allow for boundary layer growth in the test section. The maximum velocity of the main stream is approximately 30 meters/sec.

The model is mounted 150 cm from the inlet section and 210 cm above the tunnel floor. It is mounted in aluminum plates installed flush with the tunnel sidewalls. A pair of plexiglass windows are installed in each plate to permit flow visualization. A set of boundary layer control nozzles are also provided, one located just upstream of the model, and the other over the model at the midchord. The speed of the main flow will be measured with calibrated static pressure taps in the tunnel walls just downstream of the bellmouth. Aspects of this installation, the model, and the data acquisition system were influenced by Englar's (1973) work on two dimensional, high lift testing.

The jet flap airfoil to be tested is a 20% thick uncambered elliptical section, modified near the trailing edge to include a short chord flap. A photo of this model, mounted on a thrust stand for calibration, is shown in Figure 7. The thick elliptical section has an equivalent leading edge radius of approximately 5.5% which was designed to alleviate leading edge separation. The jet nozzle is located on the upper surface blowing parallel to the model chord. The jet is turned to the proper deflection by the coanda effect on the short flap. The series of jet flap tests at Stanford showed that this arrangement alleviated aft separation problems. The flap is attached to internal brackets to vary the jet deflection and may be shimmed to change the nozzle gap from the design gap of 1.4 mm. Seventy-four pressure taps are located at the midspan of the model. An additional eight taps are located in two spanwise rows on the upper surface to monitor two-dimensionality. One model plenum pressure will be calibrated versus the nozzle integrated average total pressure. The model is constructed of aluminum with steel end fittings which also serve as supply air inlets.

During the test, model lift will be calculated by integration of the midspan model pressures. Model drag will be calculated from wake surveys taken with a traversing three-dimensional flow probe. This probe, shown in Figure 8 will measure total and static pressure and flow direction for flows inclined $\pm$50 degrees from the probe axis. The wake will be surveyed to determine the model drag. The airfoil surface pressures will also be integrated to give a drag measurement, but due to experimental inaccuracy involved in this method, these data will be more qualitative in nature.

While force balance measurements might seem simpler from a data reduction point of view they present difficult problems in eliminating three-dimensional effects from the data. Every effort is being made to minimize sidewall separation effects, but it is unrealistic to expect these effects to be nonexistent. By proper treatment of the sidewall boundary layer and proper positioning of the wake probe, endwall separation effects can be essentially eliminated from the measured wake drag data. Corrections to the geometric angle-of-attack caused by three-dimensional effects can be estimated by comparing leading edge stagnation point location with theoretical predictions.

Model data will be acquired and reduced on an IBM 1800 computer. All data will be plotted to allow "bad" data points to be eliminated, and an intelligent choice of wake integration limits to be chosen. Model surface pressures will be integrated to give the lift coefficient. (Drag coefficient will also be calculated from the surface pressures, but will be used only qualitatively). The wake survey data will be integrated using the method of Jones (Schlichting 1962). An additional term to account for the momentum introduced into the control volume by the jet will be included in the calculation of drag.

Analysis of the data to quantify thrust recovery will be accomplished in a manner similar to that used in the Stanford University studies. In this method, recovered thrust is calculated as the change in drag, at a fixed lift coefficient, which results from jet discharge. Thrust recovery, r, is then defined as the ratio of recovered thrust to the jet momentum coefficient. The unblown wing drag is obtained by linear extrapolation of the experimental data for $C_\mu = 0.0$. This extrapolation to large lift coefficients is justified by the fact the C_D vs C_L^2 curve is linear in the unseparated flow regime, and the jet flap is an effective boundary layer control up to large lift coefficients. The validity of this extrapolation can be substantiated by plotting constant C_L contours of C_D versus C_μ for the blown wing data. When extrapolated to $C_\mu = 0$, the C_D value should equal that obtained by extrapolation of the unblown wing data.

It is probable that some finite aspect ratio effects will be experienced during portions of the test. It is extremely difficult, if not impossible , to completely eliminate side wall effects at very large lift

coefficients. The magnitude of these induced effects can be determined, and corrections made to the data, using a leading edge stagnation point matching technique described by Englar (1973). Because the jet acts as strong boundary layer control, potential flow pressure distributions correlate well with experimental data except in the vicinity of the jet. Theoretical pressure distributions, for the same C_L, can be calculated for several angles of attack below the experimental geometric angle-of-attack. Comparisons of the position of the leading edge stagnation point will then give the effective angle-of-attack of the experimental data point. Corrections can then be made to the experimental drag values before the thrust recovery factor is calculated.

With the jet flap thrust recovery quantified for the complete range of test variables, the pressure distributions and wake surveys will be reviewed. Evidence will be summarized to validate the hypotheses that leading edge suction, "jet drag", and/or large increases in viscous drag are the primary phenomena affecting thrust recovery at large flap angles and high C_μ's.

Jet/wake surveys taken at several downstream locations will be used to infer the entrainment characteristics of a jet sheet deflected by a cross flow. The jet path, spreading rate and peak velocity decay will be quantified from these data. Comparisons will be made with an undeflected plain jet in a co-flowing stream.

The actual model testing for this study is scheduled to begin the last week in June, 1979. An angle-of-attack sweep will be made using the basic airfoil with no flap deflection and the jet nozzle faired. These data will be used to determine the small induced drag coefficient as discussed above. A second series of runs will be made for the static ($V_\infty = 0$) blowing airfoil data. These data will be measured for a matrix of flap angles and nozzle pressure ratios. The primary data to be acquired in this test will be a complete matrix of jet deflections (30°, 50°, 70°, 90°) and momentum coefficients (.5, 1, 2, 4, 10, 20, 30). All data will be taken at zero angle-of-attack. Several repeat data runs will be made throughout the test in keeping with good wind tunnel test techniques.

Additional surveys are planned to acquire wake surveys at five downstream locations to allow measurement of jet path and entrainment characteristics. These data will be acquired at a momentum coefficient of 1.0 for jet deflections of 30°, 50°, 70°, and 90° and at momentum coefficients of 2, 4, 8, 16, and 32 for jet deflections of 30° and 90°. These data will be used to correlate and improve the viscid/inviscid matching procedure discussed in an earlier section.

REFERENCES

1. Bevilaqua, P. M., "Lifting Surface Theory for Thrust Augmenting Ejectors," AIAA Journal, Vol. 16, No. 4, April 1978

2. Chambers, T. L. and Wilcox, D. C., "Critical Examination of Two Equation Turbulence Closure Models," AIAA Paper 76-352, 1976

3. Chandra, S., "Asymmetric Entrainment of Two-Dimensional Curved Jets," PhD Thesis, West Virginia University, 1975

4. Englar, R. J., "Test Techniques for High Lift Two-Dimensional Airfoils with Boundary Layer and Circulation Control for Application to Rotary Wing Aircraft", Canadian Aeronautics and Space Journal, Vol. 19, No. 3, March 1973, pp. 93-105

5. Foley, W. M., "An Experimental Study of Jet Flap Thrust Recovery," Stanford University, SUDAER No. 136, Sept. 1962

6. Launder, B. E. and Spalding, D. B., "The Numerical Computation of Turbulent Flows," Computer Methods in Applied Mechanics and Engineering," Vol. 3, No. 2, March 1974

7. Maskell, E. C. and Spence, D. A., "Theory of the Jet Flap in Three-Dimensions," Proceedings of the Royal Society of London, Vol. A251, 1959, pp. 407-425

8. Patankar, S. V. and Spalding, D. B., "Heat and Mass Transfer in Boundary Layers," International Textbook Co., Ltd., London, 1970

9. Schlichting, H., "Boundary Layer Theory," 4th ed. N.Y., McGraw Hill, 1962

10. Spence, D. A., "Lift Coefficient of a Thin, Jet-Flapped Wing," Proceedings of the Royal Society of London, Vol. A238, 1956, pp. 46-68

11. Stratford, B. S., "Mixing and the Jet Flap," Aeronautical Quarterly, May 1956

12. Stratford, B.S., "A Further Discussion on Mixing and the Jet Flap," Aeronautical Quarterly, August 1956

13. Tsongas, G. A., "Verification and Explanation of the Controllability of Jet Flap Thrust," SUDAER No. 138, October 1962

14. Williams, J., Butler, S. F., and Wood, M. N., "The Aerodynamics of Jet Flaps," ARC R&M 3304, January 1961

15. Wilson, J. D., Loth, J. L., Chandra, S., "Thrust Augmented Wing Sections in Potential Flow," West Virginia University, AE TR-25, August 1974

16. Wygnanski, I., "Effect of Jet Entrainment on Loss of Thrust for a Two-Dimensional Jet Flap Airfoil," Aeronautical Quarterly, Feb. 1966

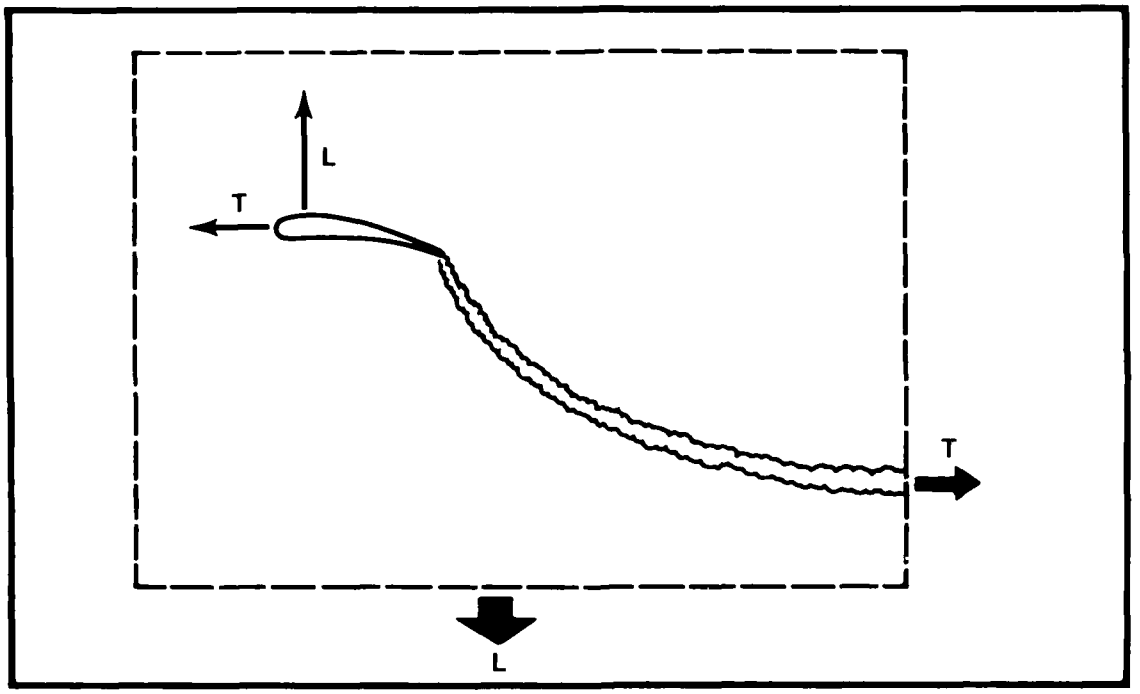

Figure 1. Jet Flap Thrust Recovery Hypothesis

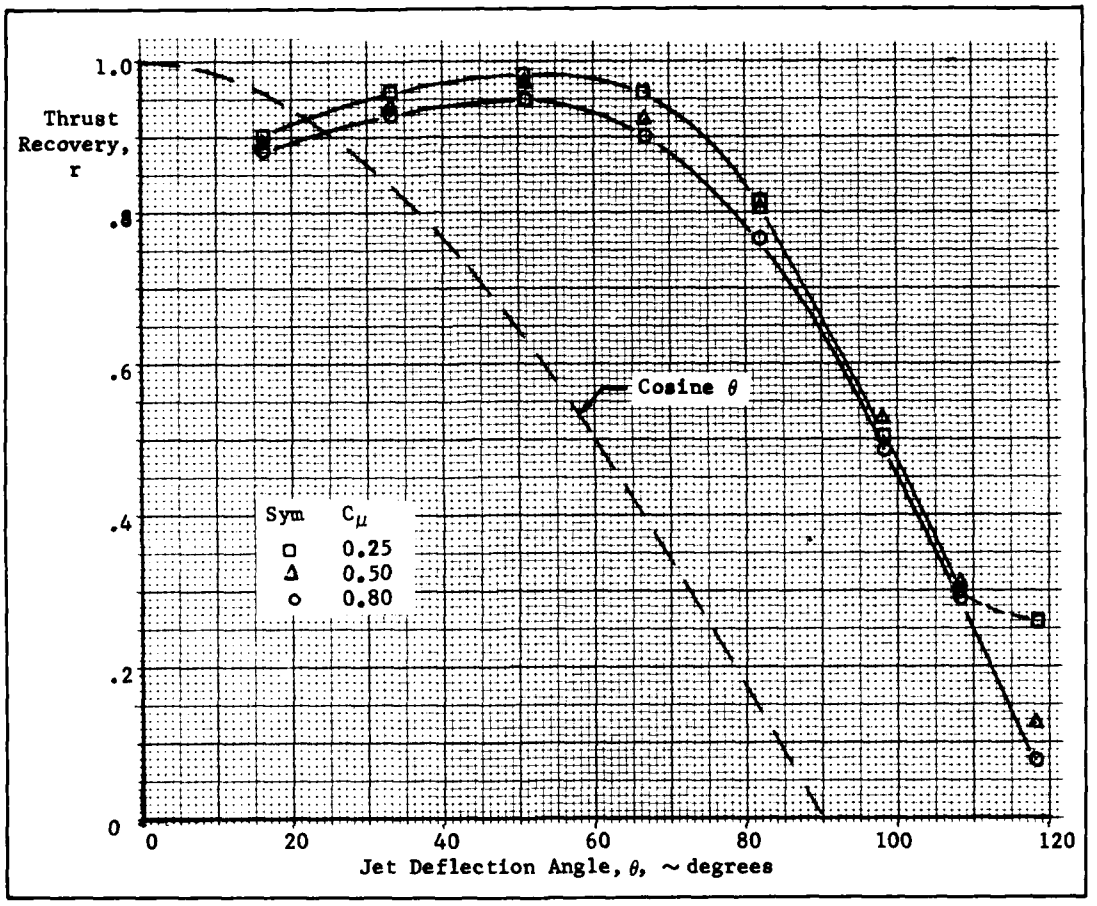

Figure 2. Measured Thrust Recovery vs Jet Deflection

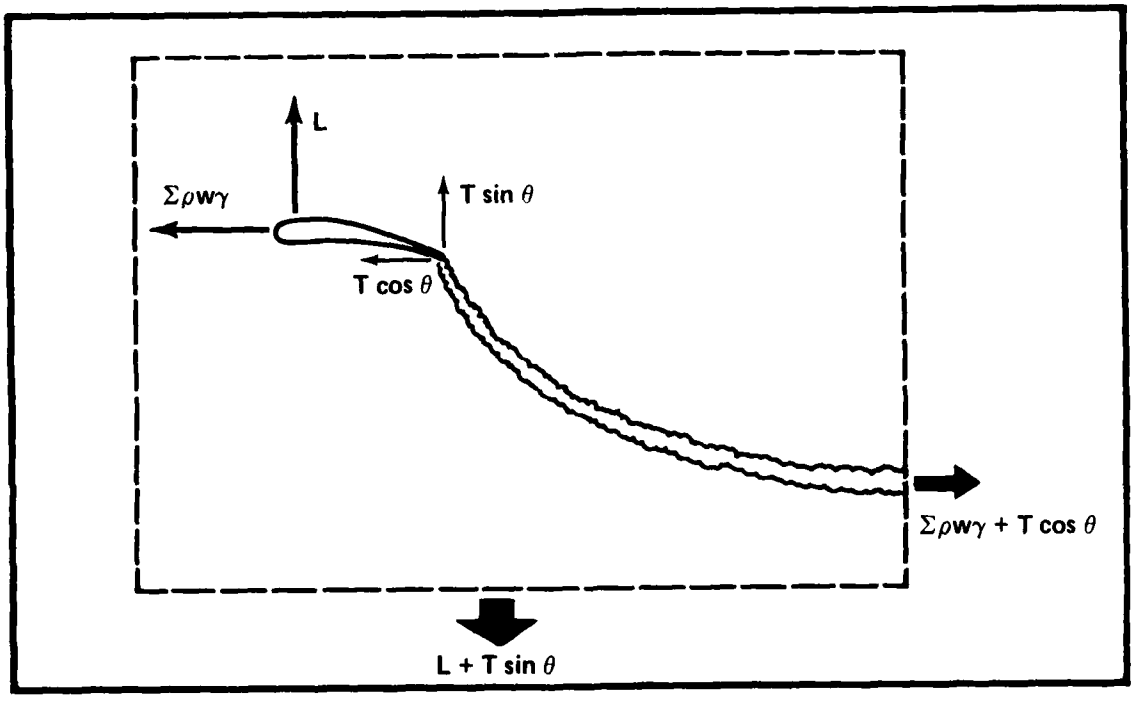

Figure 3. Vortex Sheet Model Predicts Complete Thrust Recovery

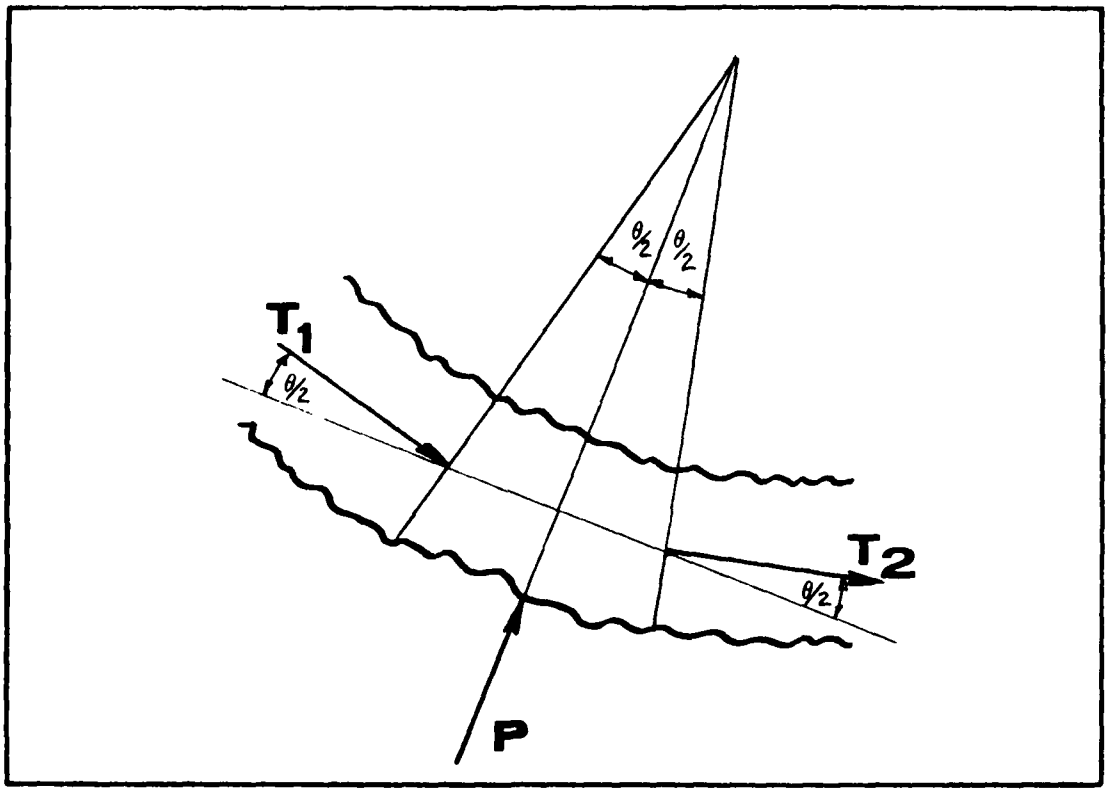

Figure 4. Forces on a Section of the Jet Sheet

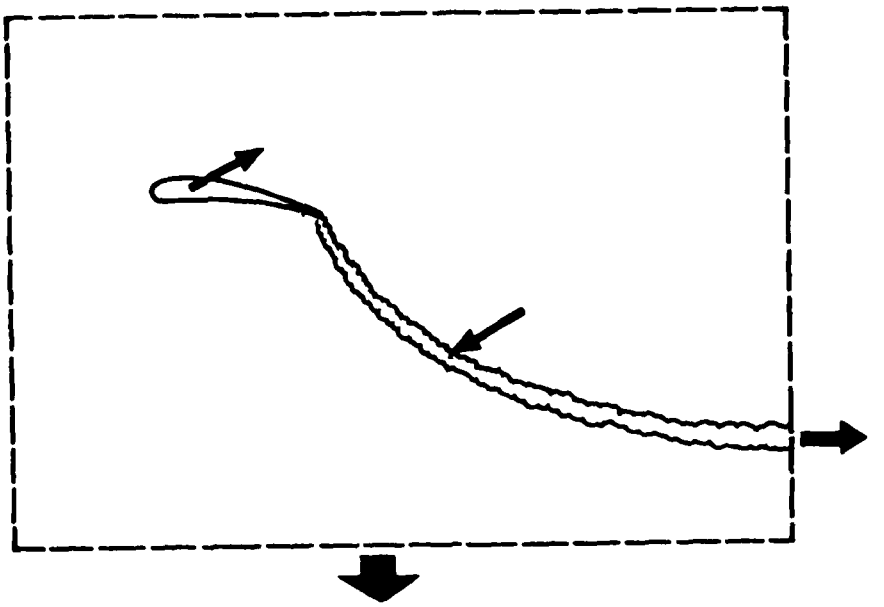

SINK-SINK DRAG DUE TO MIXING

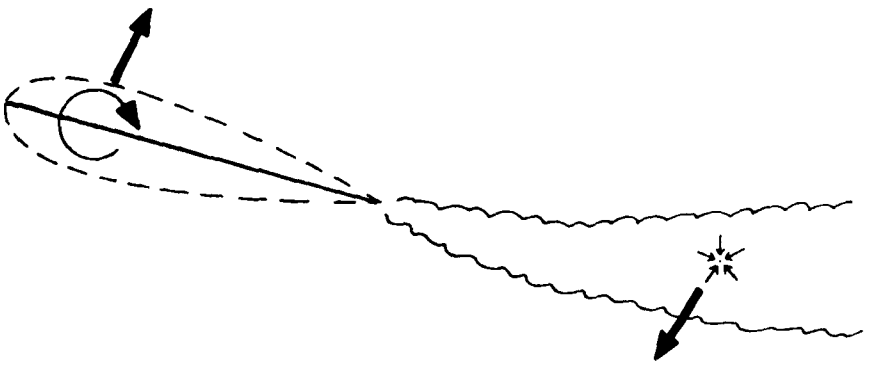

VORTEX-SINK DRAG DUE TO MIXING

Figure 5. Origin of the Mixing Loss

Figure 6. 2-D Wind Tunnel

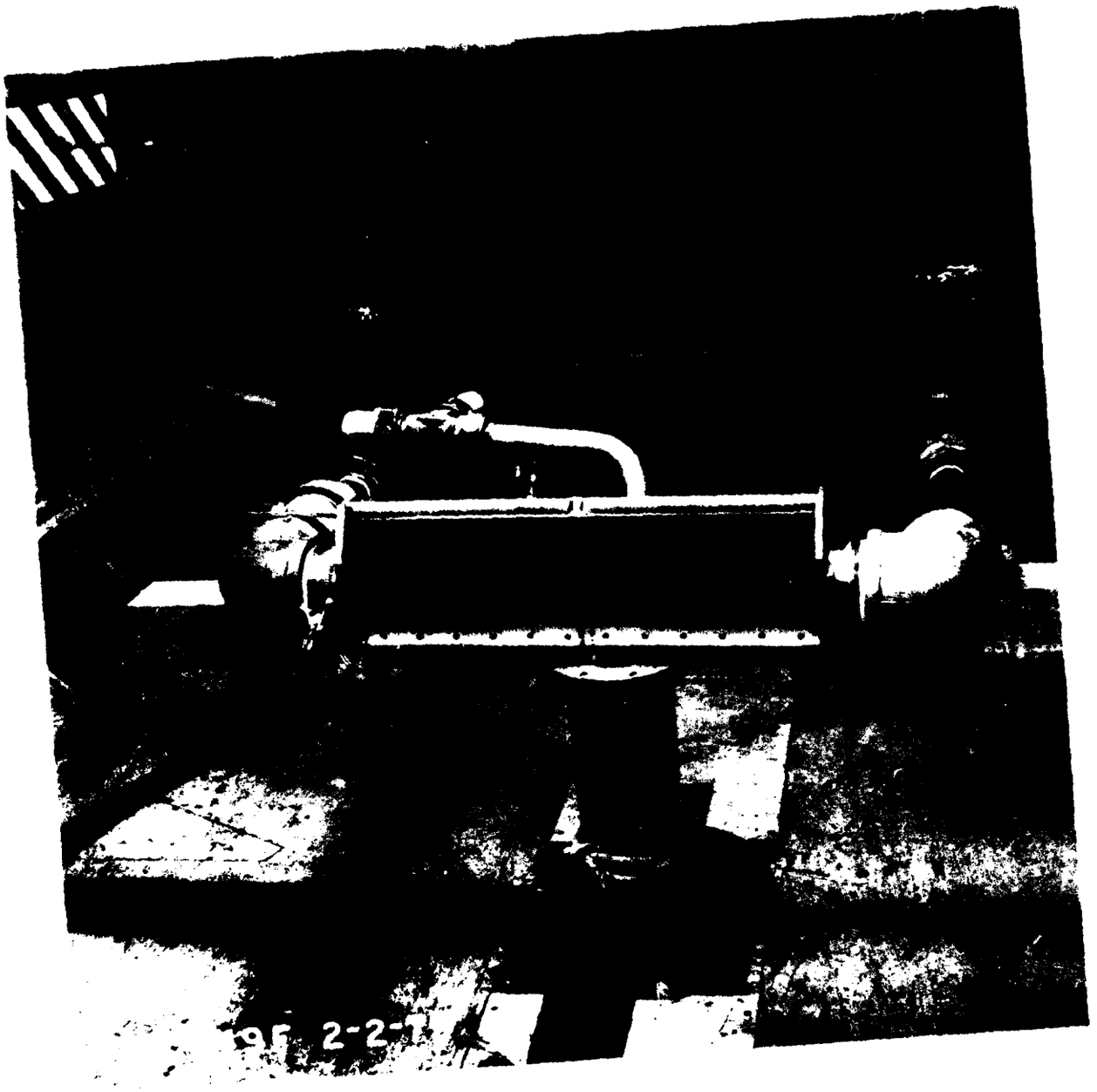

Figure [illegible] 2-D Jet Flap Model

Figure 8. 3-D Wake Survey Probe

A CASE FOR
VATOL FLIGHT DEMONSTRATION

by

C. Joseph Martin

David W. Taylor Naval Ship Research and Development Center

ABSTRACT

This paper reviews the ongoing work on the Vertical Attitude Takeoff and Landing (VATOL) technology development. Studies of vertical and short takeoff and landing aircraft have shown a significant advantage in payload or performance for the vertical attitude concept. The additional payoff from the incorporation of Post-Stall Combat Maneuvering is identified. The VATOL post-stall control system that requires control at high angle-of-attack, provides a decisive combat advantage over a conventional fighter. The planning for post-stall aerodynamic studies at DTNSRDC and NASA Ames is presented. This includes a large powered model to be tested in the NASA 40- x 80-foot wind tunnel. Progress toward a moving base simulation of the vertical attitude landing is reviewed. Results of design studies indicating the feasibility of a VATOL research aircraft, using an existing propulsion system are outlined along with a possible configuration for an advanced VATOL fighter that incorporates a novel control system.

INTRODUCTION

Vertical and short takeoff and landing (V/STOL) aircraft have existed for years. The air museums of the world have many examples of the different concepts but very few of these vehicles have actually been in use in the armed forces. However, there is now a resurgence of V/STOL interest and this, coupled with advances in propulsion and avionics technology, are providing the impetus to further development of operational V/STOL aircraft.

Navy interest in V/STOL for use at sea is accelerating as more nations introduce V/STOL capable ships to their naval fleets. The U.S. Marines adapted the AV-8A Harrier to helicopter-capable carriers; the first AV-8A was delivered to the U.S. in 1971. Three USMC combat squadrons are currently equipped with the AV-8. The Spanish Navy also flies Harriers. These aircraft, delivered in 1976, compose one squadron of the Spanish Navy and are now deployed on the DEDALO. The British are modifying the basic Harrier for fleet use. Known as the Sea Harrier, this aircraft will begin deployment on the INVINCIBLE Class through-deck cruisers in 1979 (Reference 2).

The Soviets have deployed a V/STOL air-capable ship, the KIEV, equipped with the YAK-36 Forger, the first non-Harrier vertical takeoff aircraft to become operational. Russia's second KIEV Class aircraft carrier, the MINSK, has deployed from the Black Sea and is in the Mediterranean. MINSK has been seen operating with her sister ship in what has been described as the largest collection of Soviet naval fire power ever. A third KIEV Class carrier, the KHARKOV, is undergoing sea trials in the Baltic. This V/STOL combination is a formidable opponent for it has demonstrated a capability to harass and interdict the reconnaissance and patrol capability of NATO Air Forces and to attack and, thereby, eliminate NATO surface shipping.

The U.S. Navy has plans to convert its air arm to V/STOL aircraft by the year 2000. The vertical approach will allow for an effective dispersal of air assets over a broad geographic range. This dispersal will reduce the present reliance on a few large ships. In doing this, the survivability of the dispersed elements may be enhanced. The Navy's commitment to V/STOL will have a major impact on virtually every facet of naval operations. In fulfilling the major military needs of the Navy, V/STOL must present itself as not only effective but also economical.

Today, the high thrust required during air combat maneuvering has resulted in some fighter aircraft with thrust-to-weight ratios greater than one at takeoff (Figure 1). This would seem to make vertical takeoff and landing easy to achieve, having only to direct the thrust down and lift off. However, there are many compromises to make and losses to overcome in configuring a supersonic fighter aircraft to provide adequate control and thrust margin for horizontal attitude hovering and vertical takeoff and landing. Most of these compromises disappear if the vertical attitude approach is considered. Studies indicate that vertical attitude provides, by far, the most efficient aircraft in terms of payload for a given size aircraft.

Vertical attitude takeoff and landing (VATOL) aircraft (Figure 2) have many potential advantages over horizontal attitude aircraft. The advantages include much simpler and cheaper design, development, and maintenance; lighter weight; higher performance; reduction of hot gas

reingestion and other in-ground-effect problems; and improved stability in hover. On the other hand, vertical attitude takeoff and landing requires ship modifications and an unusual pilot attitude during landing. This unusual pilot attitude, coupled with the lack of conventional visual cues on landing must be reviewed.

In the past, there has always been a penalty associated with vertical flight operations. While vertical attitude minimizes this penalty, it is nonetheless still there. Now, a new German concept called Post-Stall Combat Maneuvering appears to offer highly synergistic advantages in combination with VATOL. This is very significant since the VATOL's requirement for a high angle control system, formerly regarded as its only design "penalty" relative to conventional fighters, now becomes an asset rather than a penalty. The David W. Taylor Naval Ship Research and Development Center (DTNSRDC) has undertaken a technology study to evaluate and demonstrate successful VATOL as a means of reducing the risk for vertical attitude to provide the Navy with a very cost effective overall system option.

VATOL THE BEST V/STOL

The VATOL concept is a superior approach to V/STOL. The VATOL aircraft concept consistently shows the highest payload to empty weight fraction of all the various supersonic V/STOL concepts. A study of five jet vertical takeoff and landing fighter concepts was made considering height and attitude control, ground effect, ingestion losses, control bleed effects, installation losses, component weights, and short takeoff performance (Reference 1). A fixed gross weight of 35,000 pounds (15,750 kilograms) was assumed for each of the following concepts studied:

Lift plus Lift/Cruise – L + L/C
Lift/Cruise plus Remote Burner – L/C + Burner
Lift/Cruise (bleed air for control) – L/C
Vertical Attitude Takeoff and Landing – VATOL
Tilt Wing – TW

Assuming a baseline aerodynamic design of the so-called "supercruiser," the baseline was perturbated to establish a family of V/STOL concepts. The results of the study indicate the VATOL has a greater payload to empty weight fraction than the others (Figure 3); a 25 percent greater payload weight fraction than the L + L/C, and twice the payload to weight fraction of the L/C (Harrier type) aircraft. Similar studies have been conducted by many of the major airframe manufacturers. VATOL consistently comes out as the smallest airplane or highest payload per empty weight. Since cost is always a function of operating weight, this translates into greater performance aircraft for the least cost. VATOL is the best concept for V/STOL when one considers the aircraft system. This has been confirmed by both in-house studies and industry studies. The following is a conclusion quoted from a Vought Corporation paper, "Sensitivity Studies for Several High Performance V/STOL Concepts," presented at the Society of Automotive Engineers Aerospace Meeting in 1977: "The highest performance in every category was achieved by the vertical attitude takeoff and landing (VATOL) concepts." (Reference 3).

A PENALTY IS AN ASSET

There has always been a penalty associated with vertical flight. The gross weight of an aircraft is increased to accommodate the extra systems for lift and control. It must still be accounted for, although the vertical attitude concept minimizes this increase in weight. It has been postulated that there are portions of the flight regime where the additional weight and equipment installed for vertical attitude flight would provide a significant advantage in combat over conventional aircraft.

A new German concept called Post-Stall Combat Maneuvering appears to offer highly synergistic advantages in combination with VATOL (Reference 2). It postulates that a fighter with thrust vectoring and a reaction control system capable of maintaining precise attitude control at very high angles of attack would enjoy a decisive combat advantage over a conventional fighter. Air-to-air combat simulations in Germany have shown the exchange ratio to be as high as 4 for a post-stall aircraft over an advanced conventional stall-limited aircraft. Joint American/German combat simulations have provided dramatic confirmation of this hypothesis. McDonnell-Douglas and Messerschmidt-Bolkow Blohm have conducted manned air combat simulations, further demonstrating an enhancement in air combat kills for aircraft capable of post-stall flight.

Earlier studies by the Vought Corporation have shown that there is an advantage to thrust vectoring in air combat (Reference 4). The advantage of thrust vectoring in air combat was evaluated in a manned simulator - a baseline conventional fighter was flown against a vectored thrust version of the baseline. The engagements were scored by relative time in advantageous position. Figure 4 shows results in terms of time advantage ration (the conventional baseline at 1). With the forward hemisphere the vectored thrust time advantage ratio is near 5. Similar trends are noted for 10,000-feet (3,050-meters) and 3,000-feet (915-meters) range cases.

In March of this year actual air-to-air combat simulations were conducted in the NASA Langley Differential Maneuvering Simulator under the sponsorship of the Office of Naval Research. The simulations flown by fleet naval aviators from the Oceana Naval Air Station and the Pax River Naval Air Test Station demonstrated a significant advantage for an aircraft equipped with the post-stall capability. The study consisted of each pilot flying a total of twenty-four neutral flights. Twelve engagements were flown with an aircraft simulating the flight characteristics of a conventional high performance aircraft. Twelve engagements were flown with an aircraft simulating the flight characteristics of the conventional aircraft with additonal post-stall control forces provided by reaction control.

The initial conditions for these engagements were neutral, that is, a head-to-head pass with an initial separation of 15,000 feet (4,575 meters) at an altitude of 25,000 feet (7,625 meters) and Mach number of 0.7. In addition to the above neutral flights, 12 disadvantageous engagements were also conducted. Eight of these engagements gave the conventional aircraft an advantage and four flights gave the reaction control aircraft the advantage. These flights were conducted at altitudes from 15,000 to 30,000 feet (4,575 to 9,150 meters) and initial Mach numbers of 0.6. These simulations were initiated with the advantage aircraft in trail formation with a 5,000-foot (1,525-meter) separation.

The scoring criteria presented in a preliminary summary is time on advantage (TOA). Time on advantage is defined as having the opposition in your forward hemisphere while you are in his aft hemisphere.

The post-stall fighter experienced a 4-to-1 time advantage ratio over a conventional stall-limited aircraft in neutral engagements. When at a disadvantege, it has a TOA ratio of 1.66 -to-1 and when at an advantage the post-stall airplane TOA ratio jumped to 28-to-1. This is very significant since the VATOL's requirement for thrust vectoring and reaction control were formerly regarded as its only design "penalty" relative to conventional fighters. This has now become an asset rather than a penalty. On a VATOL, two separate control systems may not be needed as on the V/STOL. The facts that VATOL aerodynamic requirements are congruent with those for good post-stall maneuvering and that the VATOL approach makes all installed thrust available for combat maneuvering are further evidence of synergism.

POST-STALL AERODYNAMICS

This is an area of emerging importance for highly maneuvering aircraft as well as for VATOL aircraft and, while little systematic research has been done, much has been learned in exploring and improving the characteristics of aircraft developed in recent years. Maximum lift can be increased and stall delayed by the use of leading edge extensions and canards to control vortex lift. Lateral and directional characteristics can be improved by proper shaping of the fuselage forebody and by proper sizing and positioning of vertical tails with respect to the flow field. The general flow phenomena are beginning to be understood, but good characteristics can only be obtained as the end result of an extensive wind tunnel program, guided by concurrent aircraft design studies.

In an attempt to gain maximum benefits from the post-stall combat and realize a smooth vertical attitude transition, high angle of attack aerodynamic programs have been initiated at both DTNSRDC and NASA Ames Research Center.

The DTNSRDC program will look at many different variations of proven and "far-out" aerodynamic components to determine the effects on post-stall aerodynamics. The goal is to identify those components suitable for an aircraft that exhibit minimum trim requirements in the high angle of attack regime (30 to 75 degrees). Figure 5 is one example of the configurations under study. Initial experiments are scheduled to begin in August 1979.

A joint Navy and NASA project was initiated at NASA Ames in 1977 to study the aerodynamics of advanced high performance fighter attack aircraft. During Phase I of this program two VATOL aircraft were designed and analytically evaluated (References 6 and 7) by Vought and Northrop. These aircraft are depicted in Figures 6 and 7. An extensive high speed experimental program is ongoing at NASA utilizing the Northrop design (see Reference 5 for details).

NASA Ames has also undertaken to generate low speed aerodynamics for both configurations. The experiments will be conducted in the 40 x 80-foot wind tunnel using one-third scale powered models. The models will be capable of going to an angle of attack of 110 degrees (Figure 8). Each of the two configurations will be equipped for a systematic configuration evaluation. The models will be equipped with various leading edge and trailing edge devices and canard or lex planforms. The top or side inlets will be installed and 12-inch fans will simulate the engines. The experiments are scheduled to take place in February and April of 1980.

OPERATING CONCEPT

The operating concept envisioned for fleet operations is shown in Figure 2. After a constant altitude transition from wingborne horizontal flight to jetborne vertical attitude, the aircraft would then approach the landing platform which has been raised to the vertical position (Figure 9). A harpoon like hook on the nose wheel would engage a grid or wire on the landing platform to secure the aircraft (Figure 10). Takeoff could be either a reverse of the landing sequence or, at higher gross weights, a short horizontal takeoff using a ski-jump ramp. Although Figure 2 shows a stern mounting on a small waterplane area, twin-hull (SWATH) ship, there is nothing to restrict the VATOL to this position or ship type. Both stern and side mounting of the platforms on conventional monohulls is acceptable. On land bases, the aircraft could land conventionally or, in restricted space, a landing platform might be mounted on a truck so that it can be moved and dispersed easily.

MANNED SIMULATIONS

Demonstrating an acceptable level of flight control during transition and landing and quantifying pilot performance during this task are being accomplished using a full-scale, moving base simulation at NASA Ames. In this way the total representation of the landing can be duplicated and analyzed. One of the primary problems facing the VATOL concept is the combined physiological and psychological problem of "the pilot laying on his back." One reason for the manned simulation is to dispose of these problems by developing techniques and demonstrating that the VATOL concept is operationally functional.

Another purpose of the manned simulation is to investigate flying qualities and control. The flying qualities requirements for vertical takeoff and landing (VTOL) aircraft have been derived largely from experience with horizontal attitude types. The moments of inertia and the pilot are oriented differently in a VATOL and there may be significant difference in the control power requirements; particularly for roll and yaw. Also ship motions should be included as they may make a sizable difference in the requirements. The NASA Ames six degree of freedom manned simulator will be used for piloted simulations of VATOL in hover and transition to landing (Figure 11). The aerodynamic characteristics for the aircraft described in Reference 6 will be used initially. Aerodynamic and propulsion computer models along with the control laws are being established under contract with Vought Corporation. Ship motions will eventually be included in the simulation. The first phase to be conducted in the Spring of 1980 will be moving based with a fixed cockpit. The second phase, in the Fall of 1980, will include provisions for pilot tilting and incorporate some advanced displays.

RESEARCH AIRCRAFT

It has been recommended that the best approach to assuring proper development of the VATOL technique is to build a research aircraft (Reference 8.)

The vertical attitude takeoff and landing (VATOL) concept is not a new approach to V/STOL. This concept was explored in the late 1950's with turboprop and turbojet demonstrators having been flight tested (Convair/Navy XFY-1, Lockheed/Navy XFV-1, and Ryan/USAF X-13). These tests showed that, in a demonstration flight test environment, the pilots could adapt to this somewhat unorthodox mode of operation. The X-13 jet VATOL has already demonstrated numerous vertical attitude takeoff's and landings (Figure 12) and transitions to and from conventional flight; including a demonstration from the parking lot in front of the Pentagon. This testing, however, has not resolved the questions of feasibility of VATOL for day-to-day operations in a fleet operating environment. Fleet operations are often performed in adverse weather with a minimum of ground handling personnel and a demand for rapid launch and recovery of many aircraft.

Although these earlier flight programs were completed (over 20 years ago) without serious incident, they were not followed up because of the weight and performance penalties due to the then available technology. Modern engine, structures and avionics technology has largely eliminated these penalties. There remains, however, concern about the operational feasibility of the concept in the hands of service pilots operating in field conditions in all kinds of weather.

A flight research program is needed to explore the operational problems, to develop and demonstrate solutions and operating techniques, and to determine the operational feasibility and limitations of the VATOL concept. Because the areas of concern relate only to the low speed region of performance, it should not be necessary that the research aircraft demonstrate the full supersonic fighter envelope. It should be possible to build such a research aircraft using available engines.

Conceptual designs of suitable research aircraft have been identified in Reference 8 and are presented in Figures 13 and 14. A research aircraft to study the VATOL operations would not need an afterburning engine and considerable development cost and time can be saved by using an available engine. The aircraft in Figure 13 is based on a Pratt and Whitney YF-401 engine and in Figure 14 on a General Electric TF-34 engine.

In hovering and transition flight, a VTOL aircraft must derive its control from the engine either from bleed air reaction control and/or by thrust vectoring. Bleed air is very expensive in terms of thrust penalty resulting either in significant oversizing the engine to provide the bleed air or limited overheating the engine during the brief intervals when bleed air is being used. In Reference 9, a small scale remotely piloted VATOL vehicle was flown in hovering using only jet vane thrust vectoring for control about all three axes. A direct scale up of the concept to fighter size aircraft showed that vanes in the exhaust of a conventional round nozzle could not provide enough moment for roll control. A modification of the concept was adopted.

The new control system ducts the fan air to two two-dimensional (or 2-D) nozzles, one on either side of the core nozzle. These 2-D nozzles are deflected differentially for roll control and together for pitch control.

With the YF-401 engine operating dry (afterburner removed), the fan air could be taken off at the beginning of the burner section and ducted to 2-D nozzles. These nozzles would provide pitch and roll control with a maximum deflection of +31 degrees.

The TF-34 powered research aircraft would duct fan air to the 2-D nozzles and uses only a 10-degree deflection for pitch and roll control, since 80 percent of the thrust is from the fan.

The YF-401 powered research aircraft would be close to an actual fighter. A conceptual fighter is shown in Figure 15. This airplane would require an engine development program. The fan flow would be taken off downstream of the fan section, through two duct burners, to the 2-D nozzles. These nozzles would have to be convergent-divergent nozzles as well as provide thrust deflection. This is shown in a cutaway drawing in Figure 16. The engine characteristics are based on a Pratt and Whitney STF 527-529 class with a BPR of 1.0. With the engine bypass ratio of about 1.0, each nozzle would provide about 1/4 of the thrust and only about ±20 degrees deflection is needed for control. The remainder of the deflection would be available for high lift (along with the all-moving canard) in STO operation. Yaw control would be provided by lateral deflection of the core nozzle.

The conceptual designs were sized by standard methods to ensure that performance, weights, stability, and control were realistic. They are not the result of detailed design and should be considered only as a conceptual arrangement intended to illustrate potential VATOL concepts.

CONCLUDING REMARKS

A VATOL flight demonstration is aimed at developing the technology to introduce a superior fighter aircraft with VTOL capability into the fleet. Numerous studies have shown that, of the various approaches to VTOL capability, the vertical attitude requires the least change from a good fighter configuration and has the least weight penalty. Coupled with the post-stall capability and common control in all flight modes, the VATOL penalty is reduced further and the air combat capability is enhanced significantly.

The VATOL concept involves an unusual operating mode resulting in a transition from wingborne to jetborne flight that may present a unique operation for the pilot. The previous VATOL test beds have demonstrated, on numerous research flights, that it can be done. The VATOL manned simulation and research aircraft are needed to explore, develop, and demonstrate the full operational feasibility of the VATOL concept for routine fleet use.

Vertical attitude may well prove to be, by far, the most efficient and cost effective solution to the problem of equipping the Navy's air arm with a V/STOL capable fighter. A course of technology development which will make this option fully available and viable is being pursued.

REFERENCES

1. Kuhn, R.E., "An Examination of the Factors Affecting the Thrust Requirements and the Hover and Short Takeoff Performance of Several Jet V/STOL Fighter Concepts," David W. Taylor Naval Ship Research and Development Center/ASED-78/08 (May 1978).

2. Martin, C.J., "An Assessment of the Technology and Potential for V/STOL in Europe," Office of Naval Research, London, R-3-78 (Jul 1978).

3. Driggers, H., "Sensitivity Studies for Several High Performance V/STOL Concepts," Society of Automotive Engineers Aerospace Meeting, Los Angeles, Report 770982 (14-17 Nov 1977).

4. James, C.R., "Vectored Thrust in Air Combat," Vought Aeronautics Company. Presented at AGARD Conference on Inlets and Nozzles for Aerospace Engines; Sandeford, Norway, AGARD Conference Preprint 91 (Sep 1971).

5. Nelms, W.P., "Studies of Aerodynamic Technology for V/STOL Fighter/Attack Aircraft," presented at The AIAA Aircraft Systems and Technology Conference, Los Angeles, California (21-23 Aug 1978).

6. Driggers, H.H., "Study of Aerodynamic Technology for V/STOL Fighter/Attack Aircraft, Phase I, Final Report," National Air and Space Administration CR-152132 (May 1978)

7. Gerhardt, H.A. and W.S. Chen, "Study of Aerodynamic Technology for V/STOL Fighter/Attack Aircraft: Vertical Attitude Concept," National Air and Space Administration CR-152131 (May 1978).

8. Kuhn, R.E., "Research and Development Needs of Vertical Attitude Takeoff and Landing (VATOL) Aircraft," David W. Taylor Naval Ship Research and Development Center/ASED-79/05 (May 1979).

9. Martin, C.J. and W. Eilertson, "Tethered Hover Flight Tests of a Vertical Attitude Takeoff and Landing Remotely Piloted Vehicle," presented at the Military Electronics Defense Exposition, Weisbaden, Germany (27-29 Sep 1977).

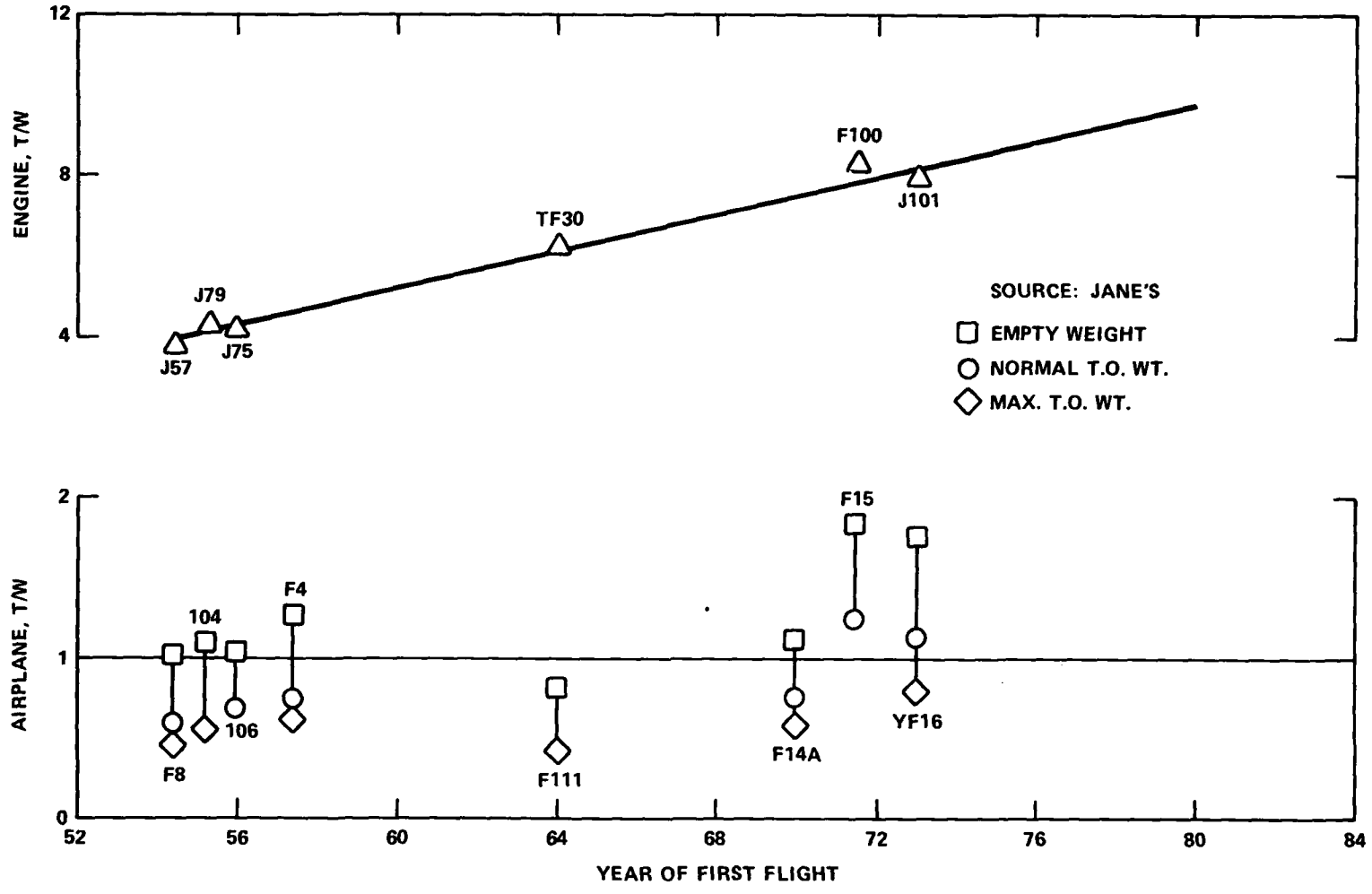

Figure 1 – Thrust to Weight Trends of Fighter Aircraft

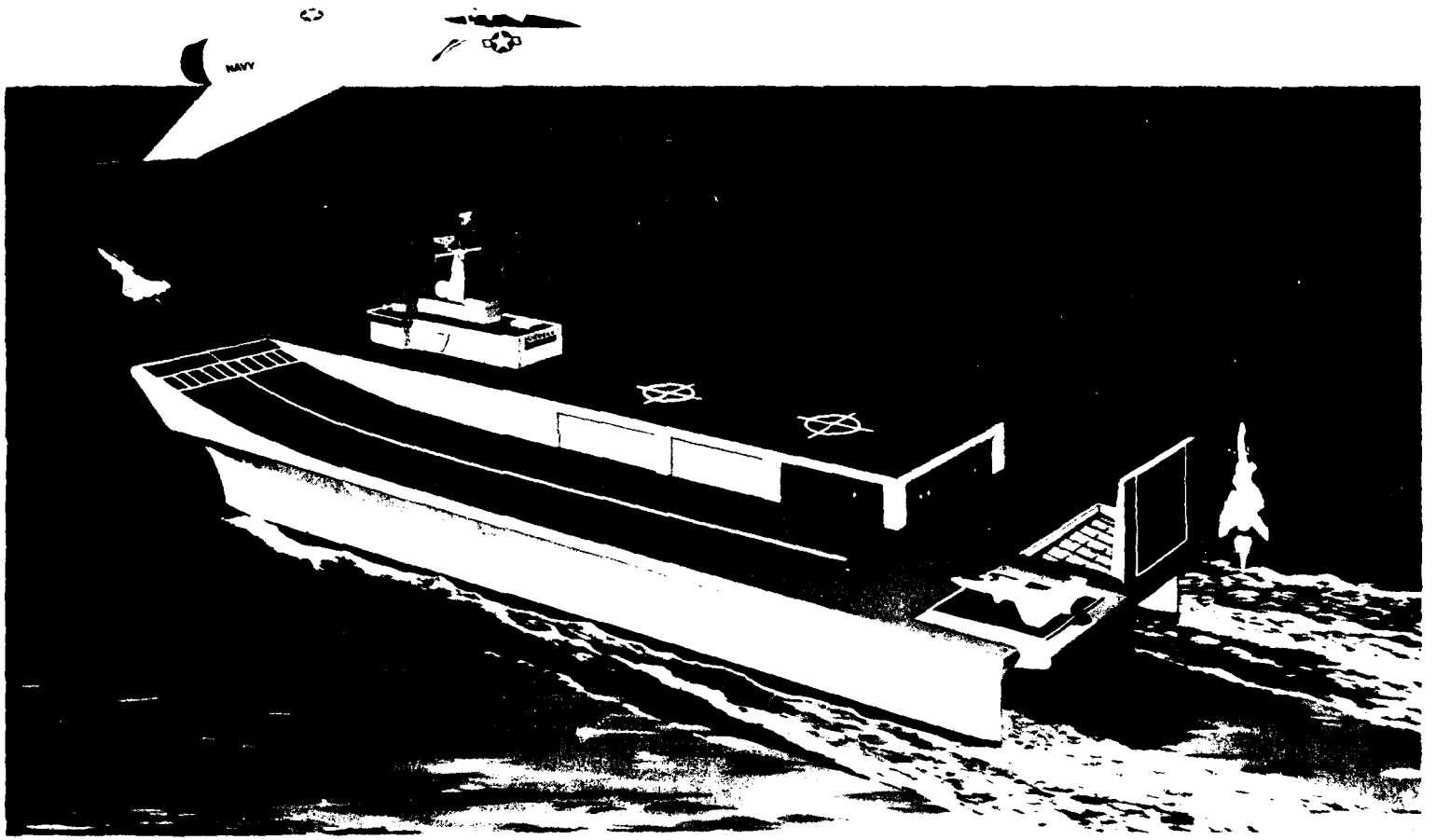

Figure 2 VATOL Aircraft on SWATH Ship.

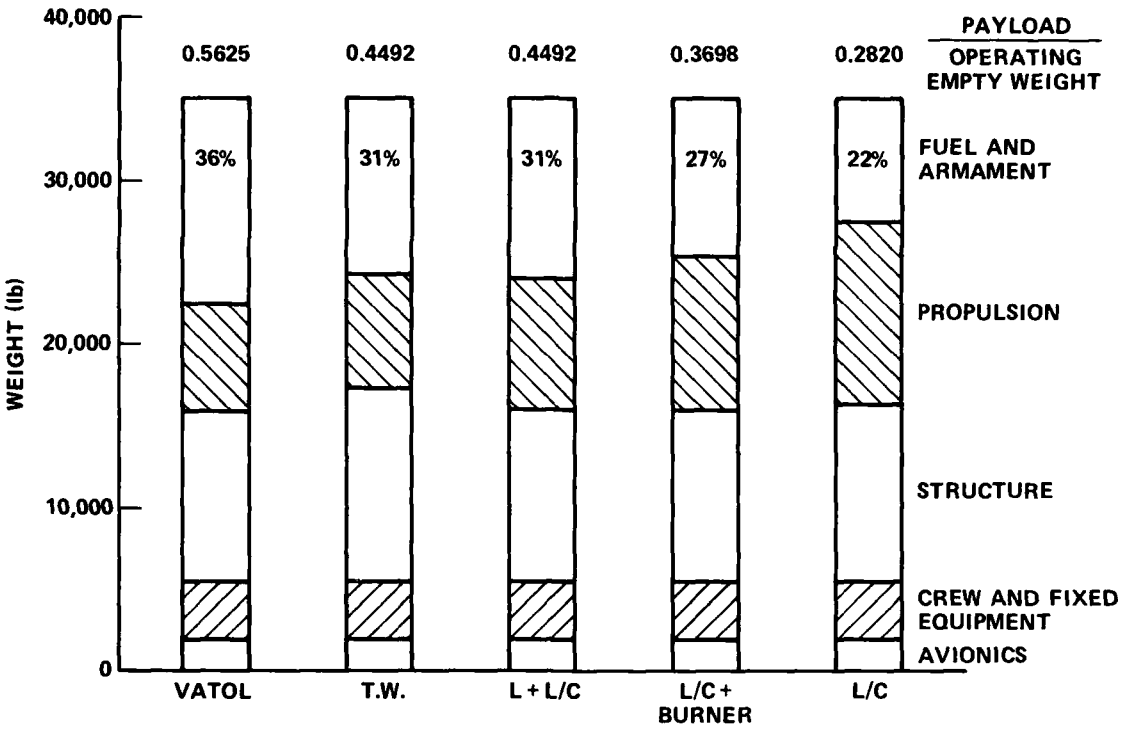

Figure 3 – Weight Breakdown of VTOL Configurations
(Figure from Reference 1)

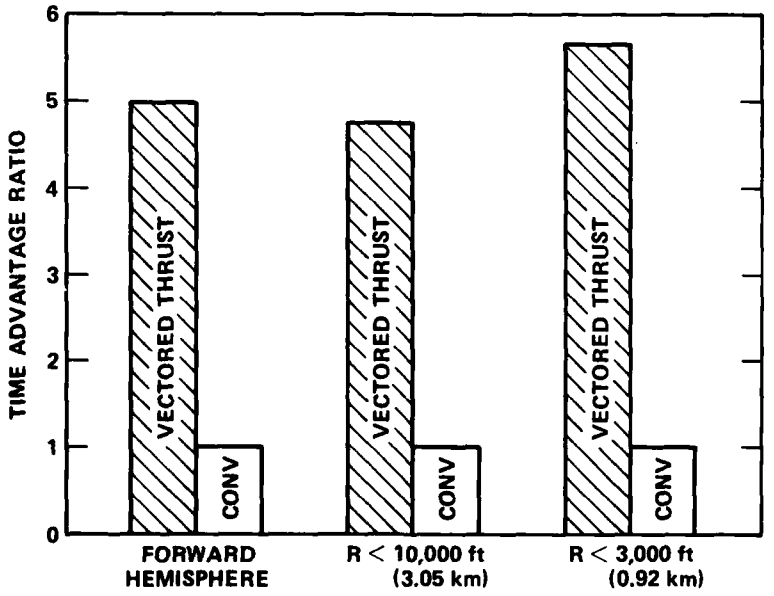

Figure 4 – Time Advantage Ratio for Vectored Thrust Fighters
(Figure from Reference 4)

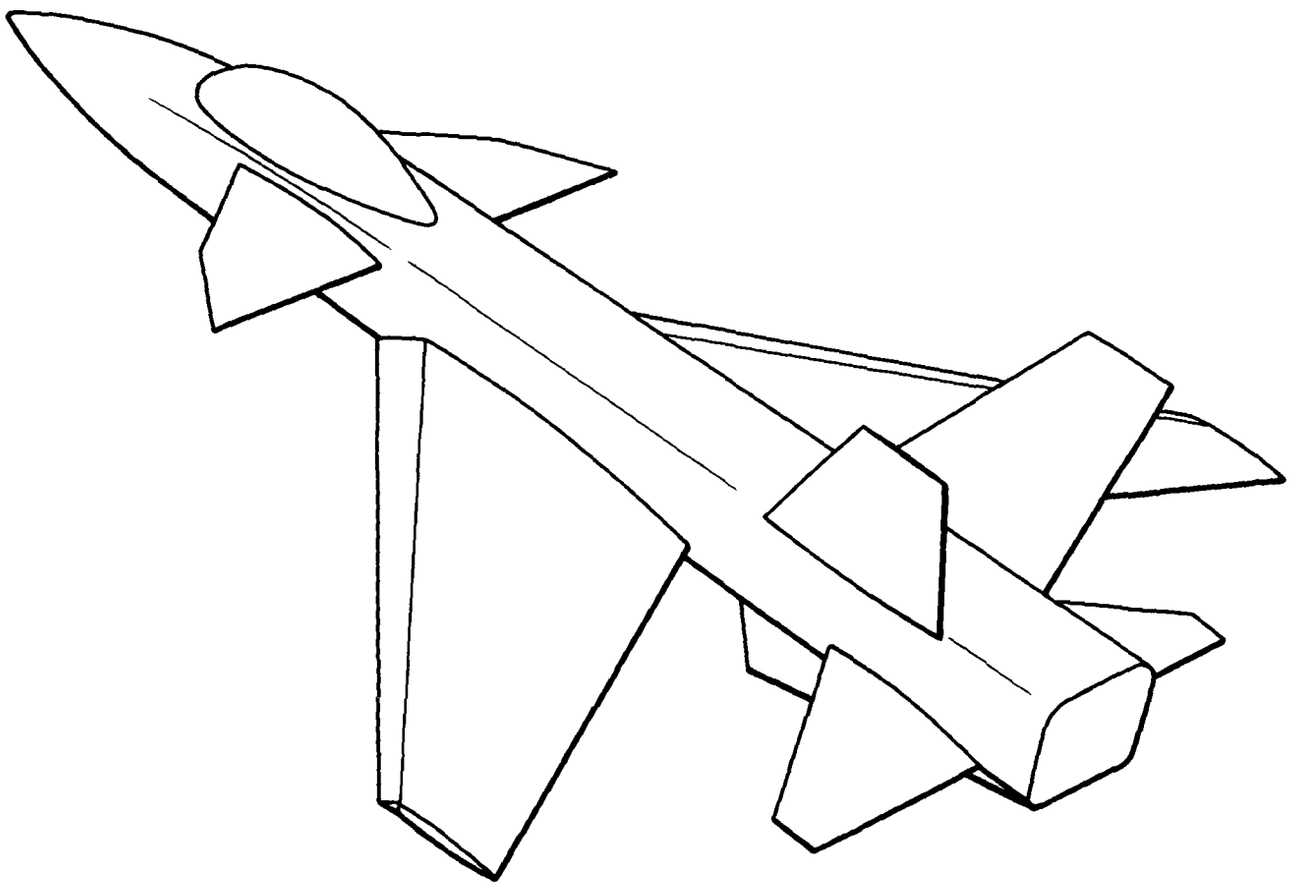

Figure 5 – DTNSRDC Post-Stall Aerodynamics Wind Tunnel Model

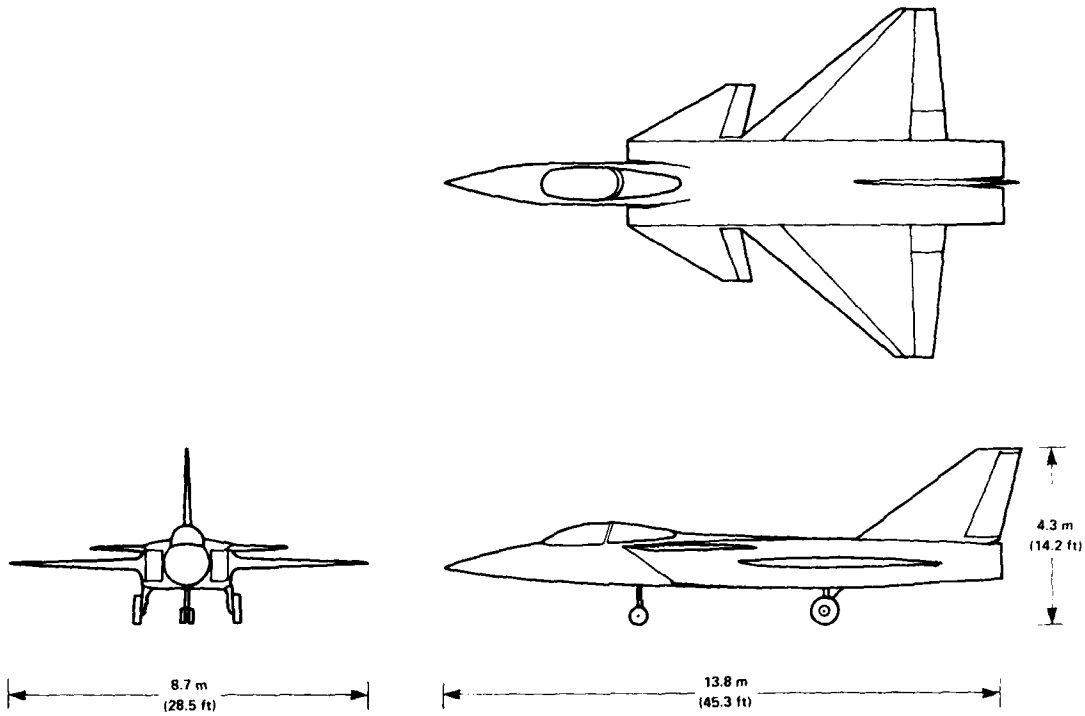

Figure 6a – Three View.

Figure 6b – Artist Rendering of the Vought VATOL Concept in a STOVL Configuration.

Figure 6 – Vought VATOL Concept Reference 5.

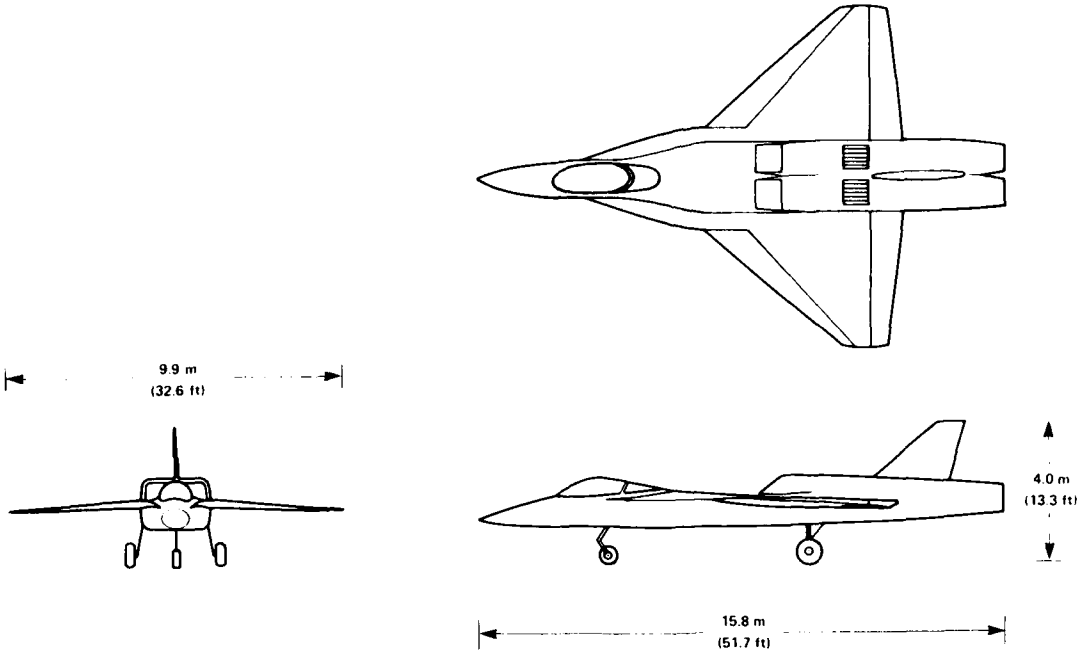

Figure 7a – Three View.

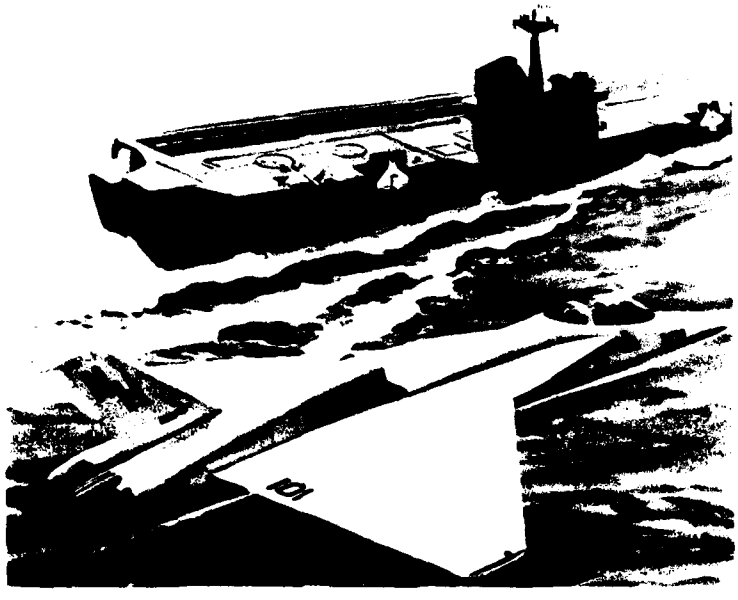

Figure 7b – Artist Rendering of the Northrop VATOL Concept.

Figure 7 – Northrop VATOL Concept Reference 5.

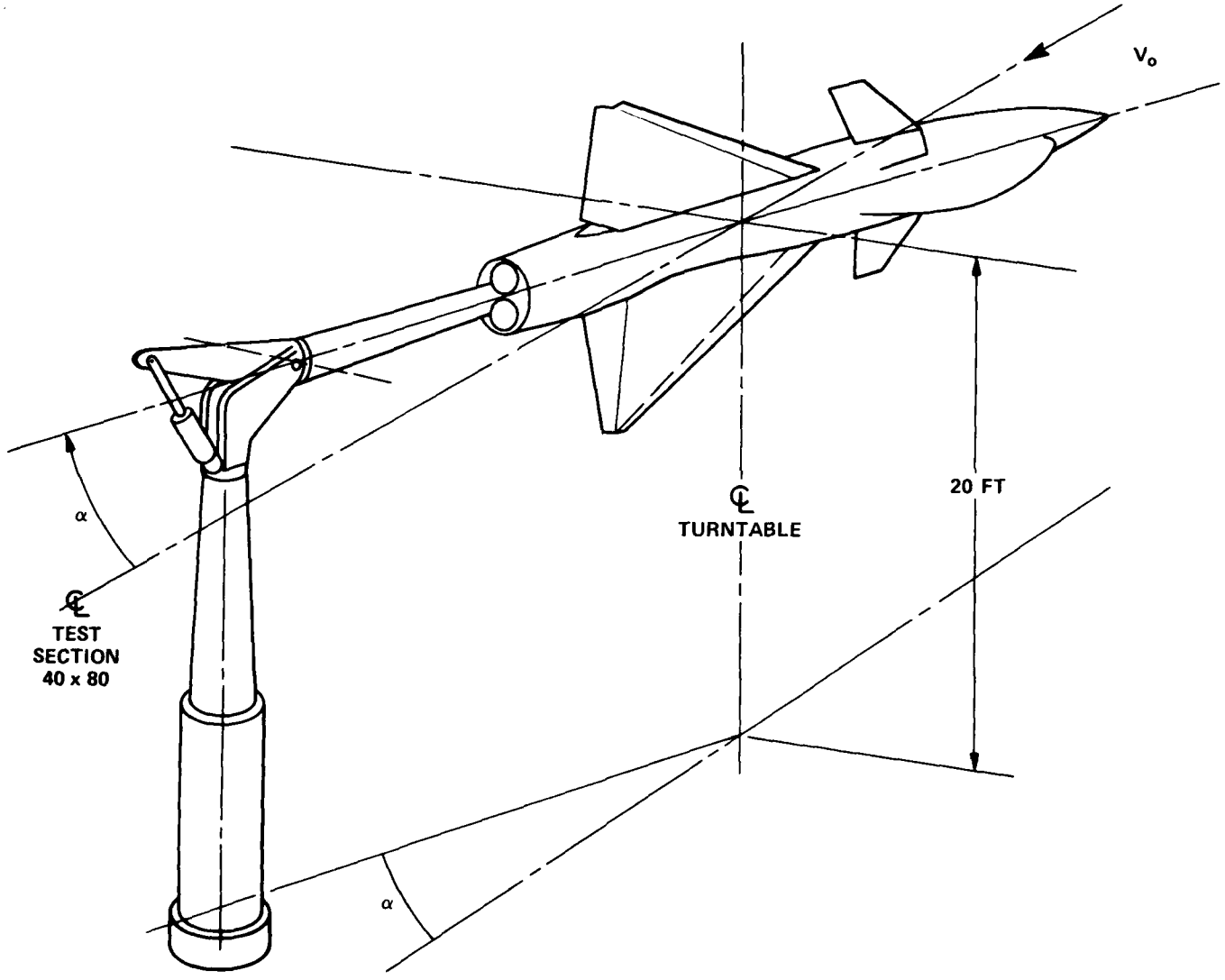

Figure 8 – Installation Sketch of VATOL 0.38 Scale Model in NASA Ames 40 x 80 Foot Wind Tunnel

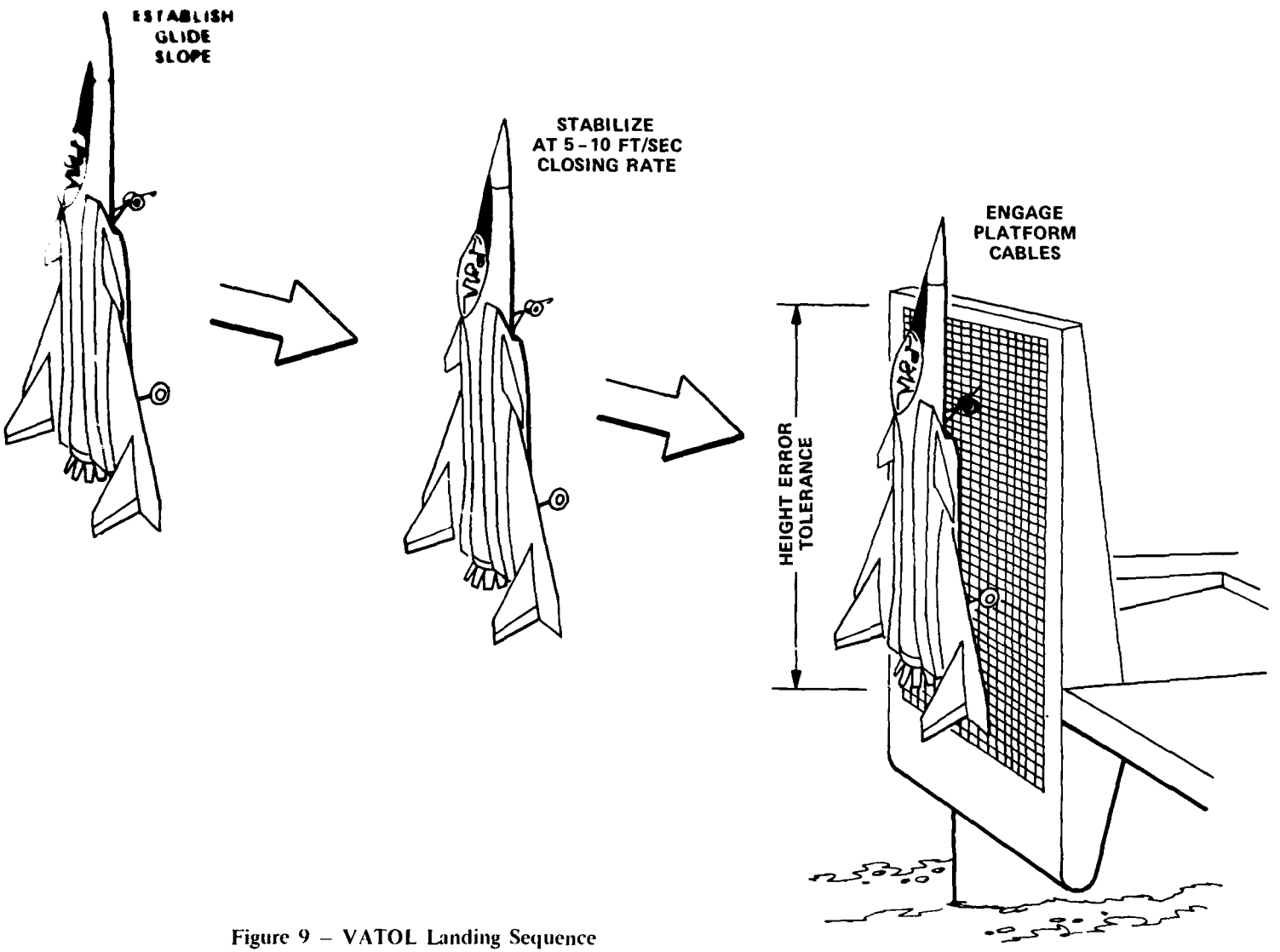

Figure 9 – VATOL Landing Sequence

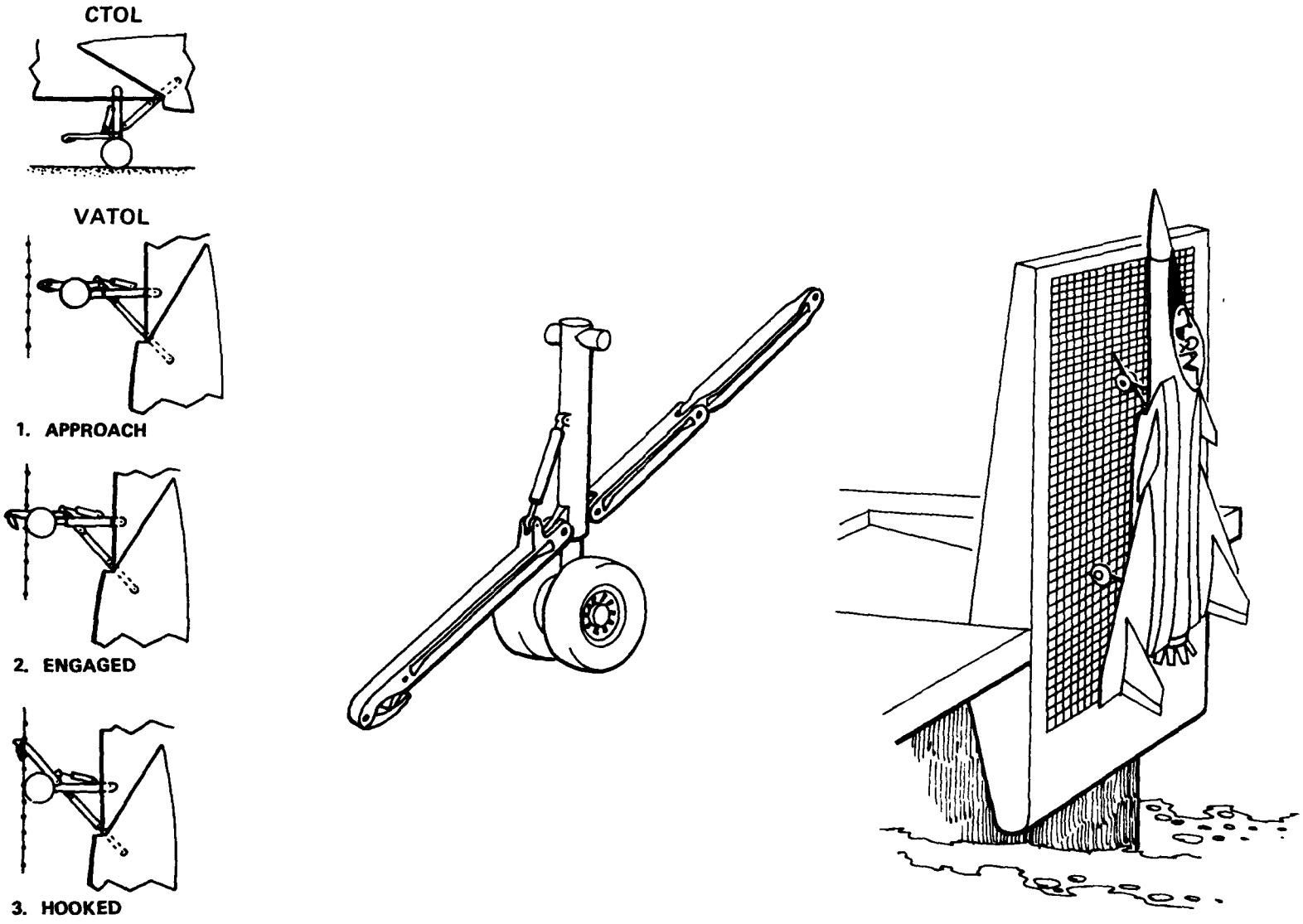

Figure 10 – VATOL Vertical Launch and Recovery System

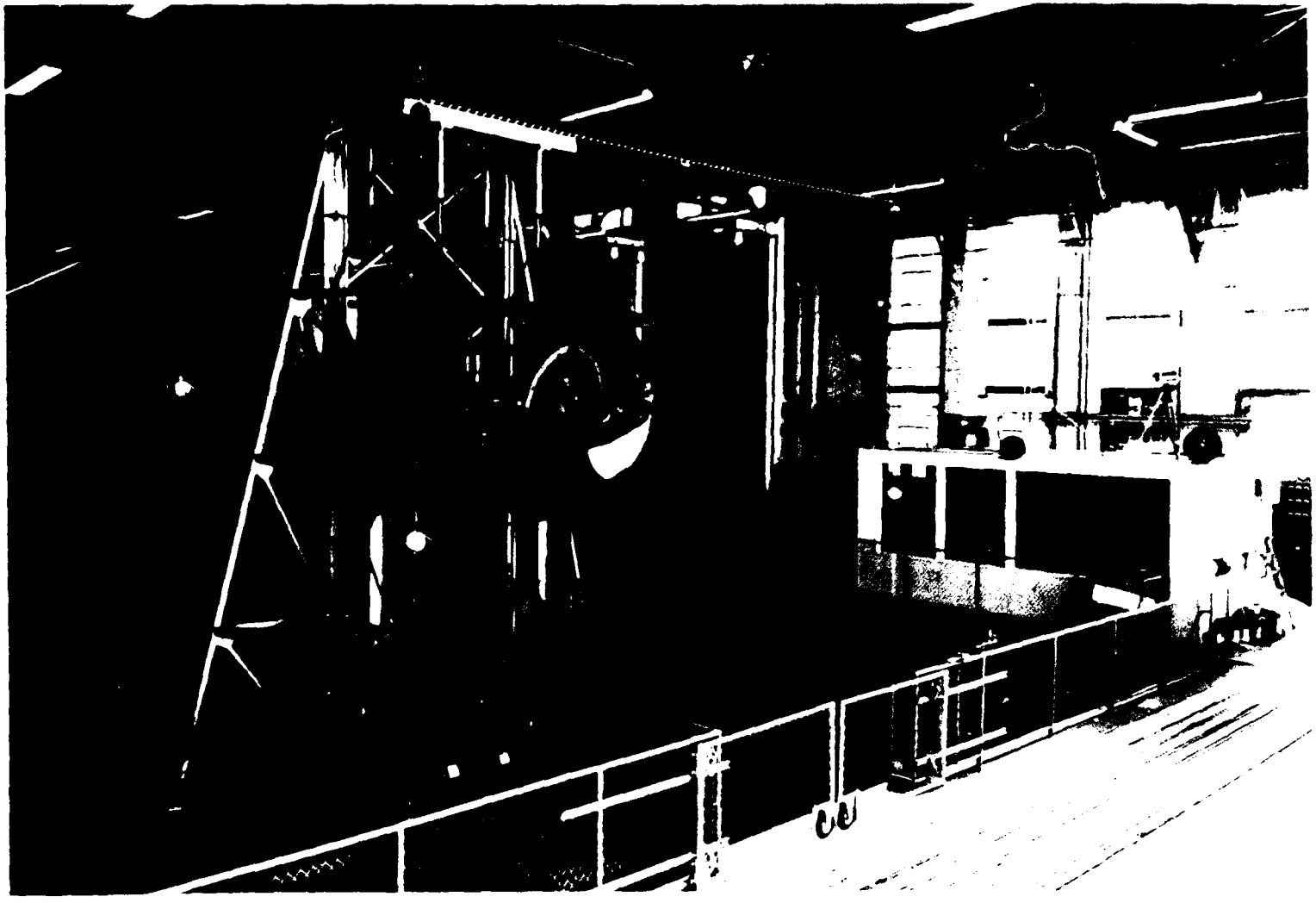

Figure 11 NASA Six Degree of Freedom Simulator.

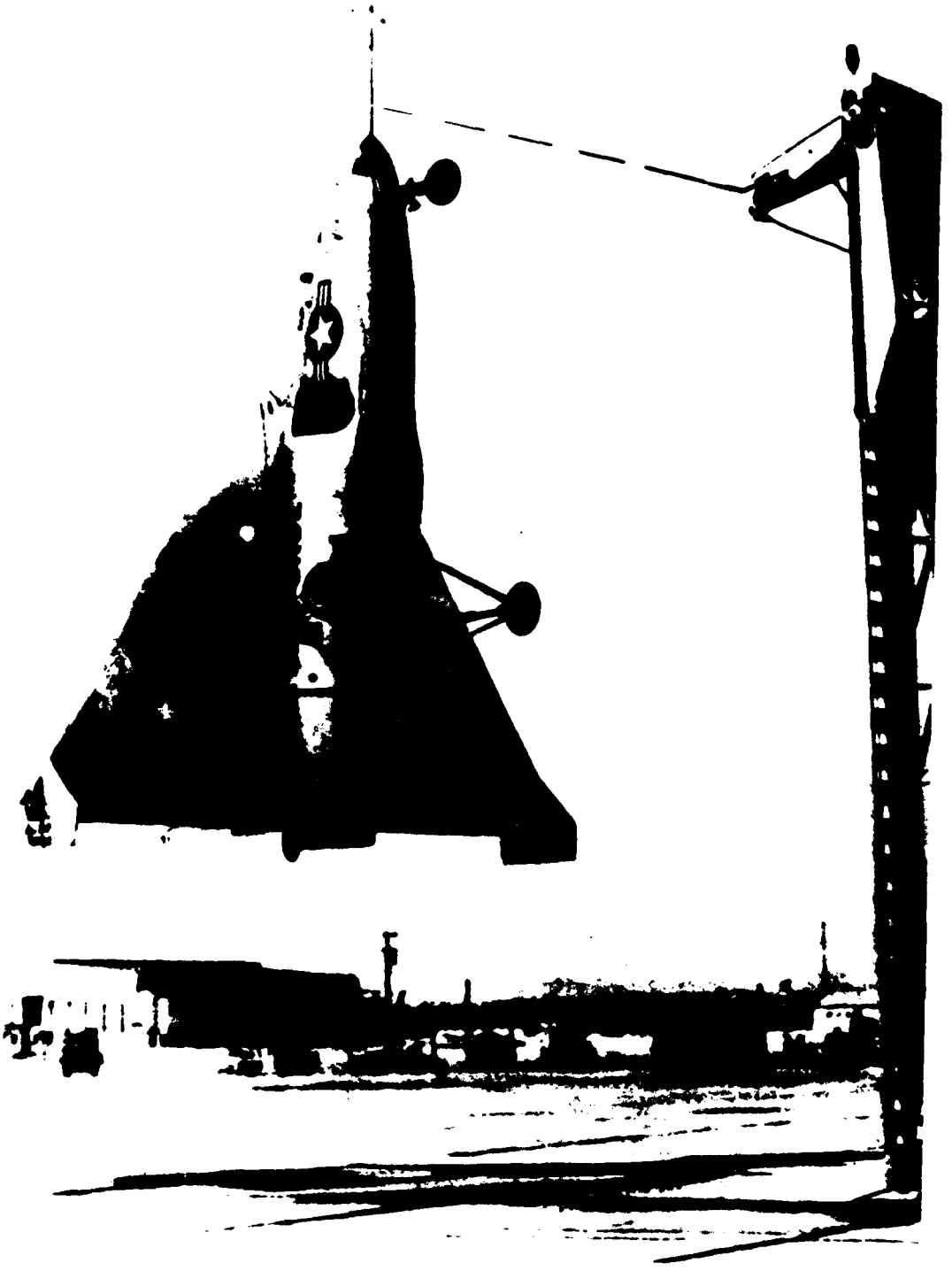

Figure 12 – Ryan X-13 VATOL in Hover.

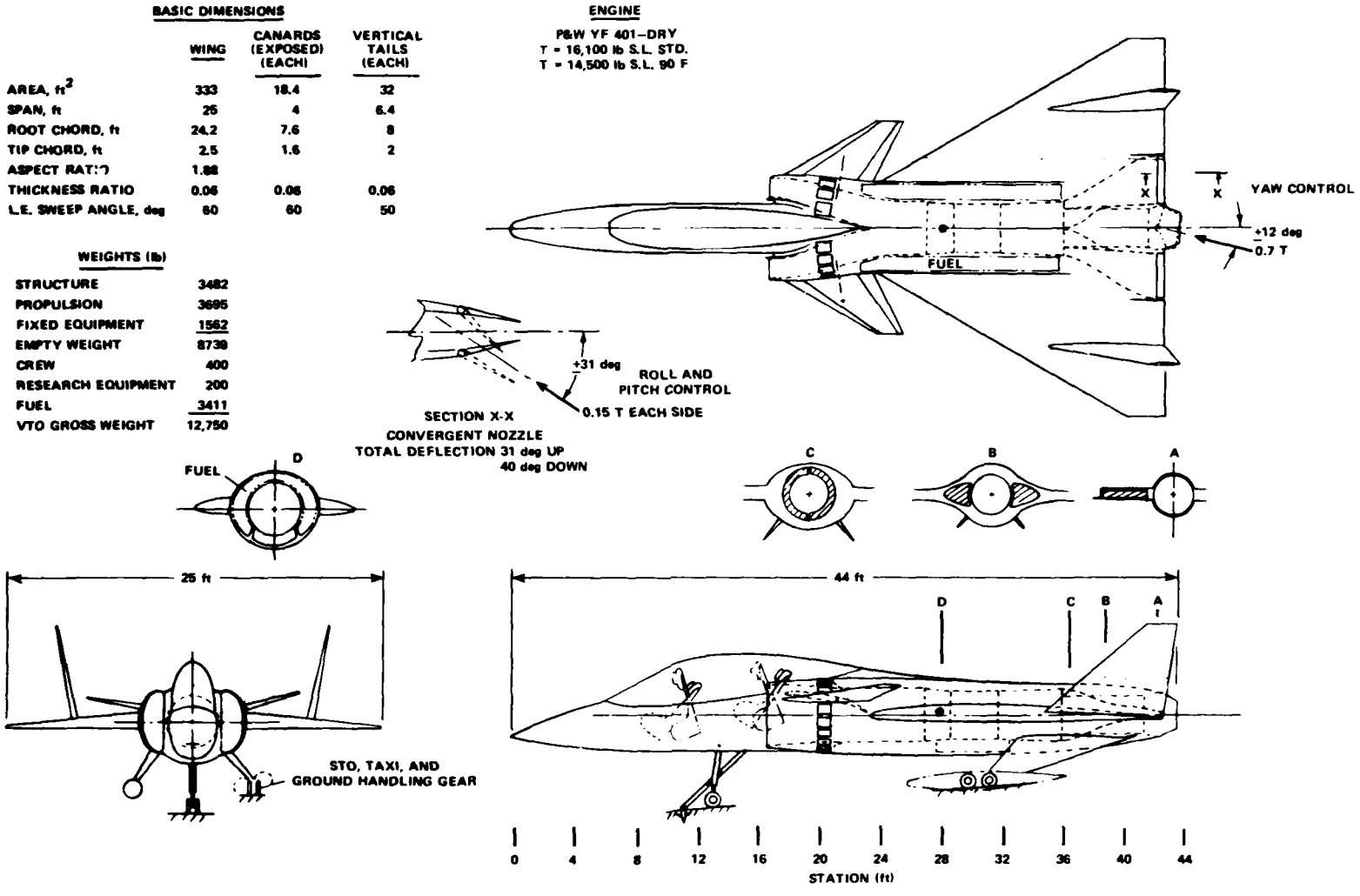

Figure 13 – VATOL Research Aircraft Conceptual Arrangement P&W 401 Engine.

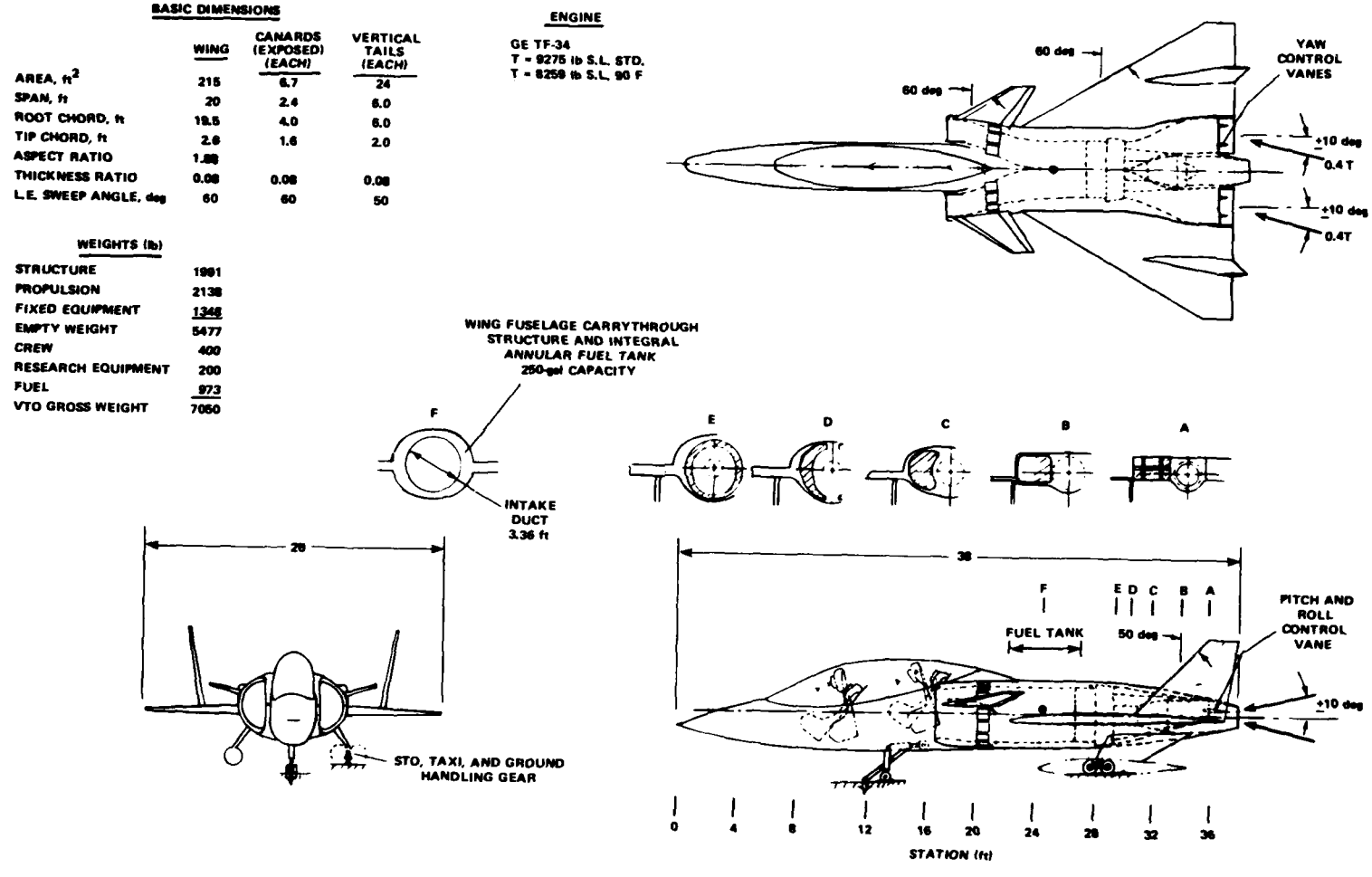

Figure 14 – VATOL Research Aircraft Conceptual Arrangement GE-TF-34.

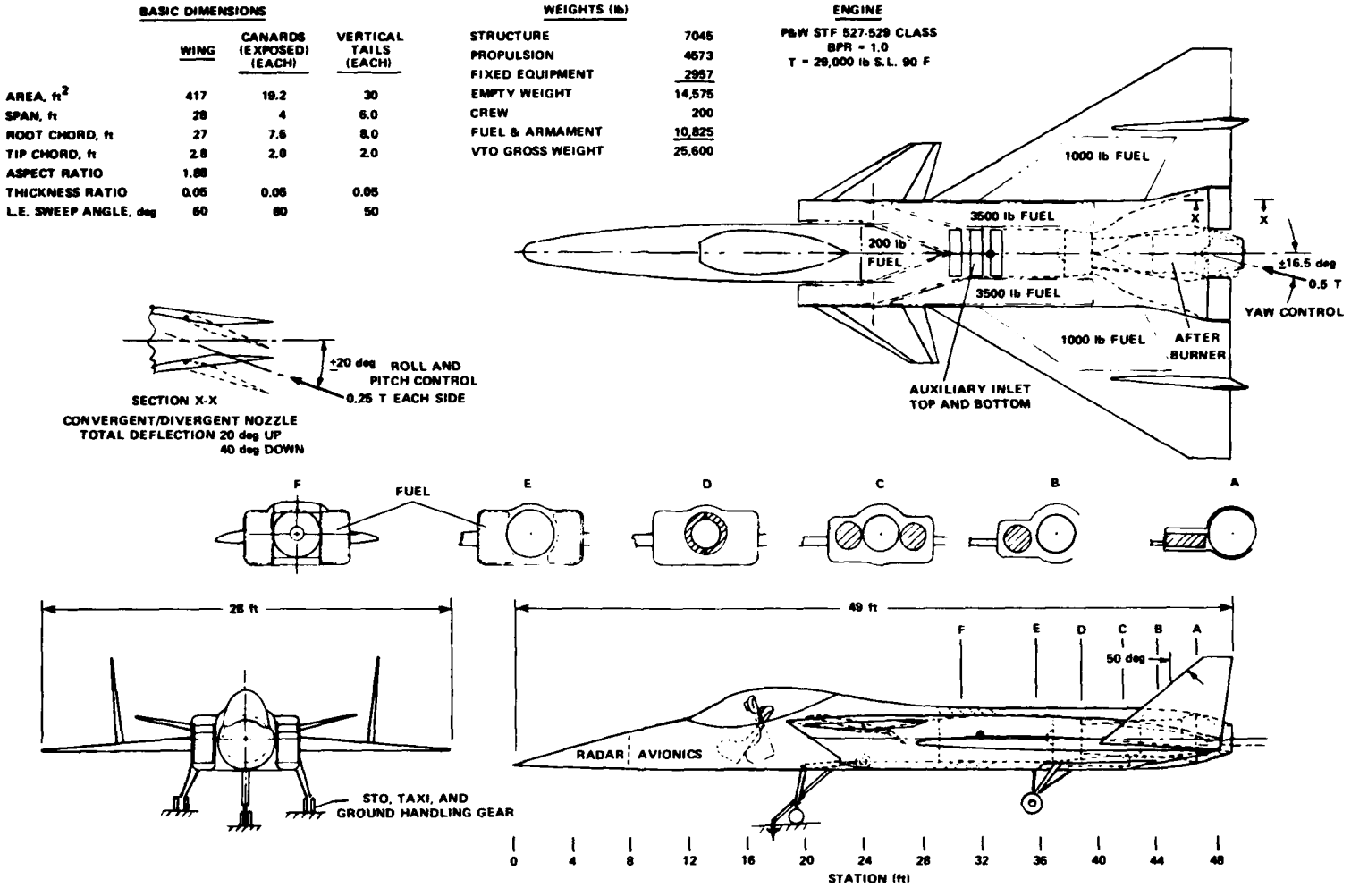

Figure 15 – VATOL Fighter – New Engine.

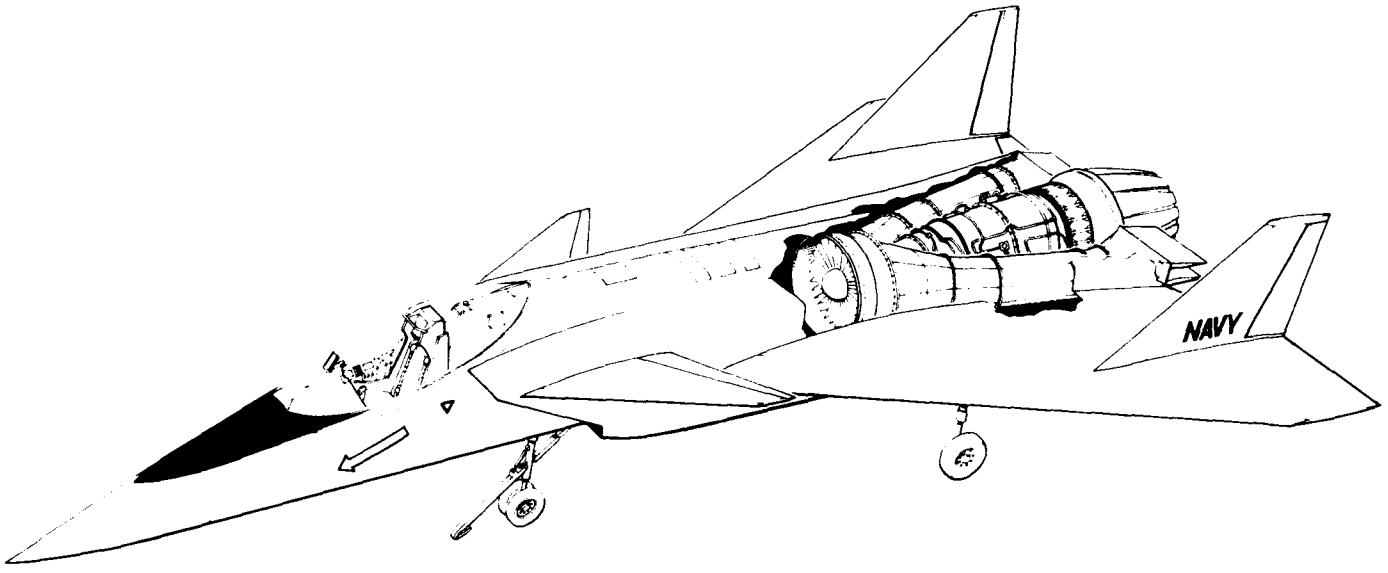

Figure 16 – VATOL Fighter Cutaway of Engine Installation

PREDICTION OF A THREE DIMENSIONAL CIRCULAR TURBULENT JET IN CROSSFLOW

by

D. Adler* and A. Baron+

Faculty of Mechanical Engineering
Technion, Israel Institute of Technology
Haifa, Israel

September 1978

Jets, Wakes, and Viscid-Inviscid Flow Interactions
*Associate Professor
+Research Student

Abstract

A quasi three dimensional integral method is used to solve the problem of the isothermal incompressible turbulent jet. The jet is submerged and is circular at its origin. The mathematical model is based on two integral momentum equations. One is written for a direction parallel to the jet centerline and the other is written for a direction perpendicular to the centerline. For their solution, the entrainment rate into the jet is determined as the linear combination of a modified straight jet entrainment and the entrainment into a vortex pair. The family of velocity profiles, required for the integration of the momentum equations is three dimensional. The profiles are determined along the jet centerline on the basis of the distorted jet cross-sections, thus being non similar. The mathematical model is numerically solved yielding the internal jet flow-field. Results are compared to experiments with different injection velocity to cross flow velocity ratios and with different injection angles. Agreement between theory and experiment is found to be satisfactory in some cases and good in others.

Nomenclature

A - Cross section area

A_0 - Initial cross section area

A_1 - A constant in equation 8

b - Jet width in the ξ direction

C_D - Drag coefficient

D_o - Initial jet diameter

E - Entrainment function (defined in equation A2)

F_c - Centrifugal force

G - Rate of increase of a straight jet radius (defined in equation 6)

h - Maximum jet velocity excess (defined in figure 1)

$I_1 \equiv \int_A U dA$

$I_2 \equiv \int_A U^2 dA$

K_1 - A constant in equation 8

K_2 - A constant in equation 8

L_p - Length of potential core

$M \equiv U_o/W$

$\dot{m}$ - Mass flux through A

$\dot{m}_o$ - Initial mass flux through A_o

N - Number of vortices (equations 10 to 12)

n - Current number of a vortex (equations 10 to 12)

P - A constant in equation 13

p_{st} - Static pressure

Q - A constant in equation 13

R - Equivalent radius of the jet

Nomenclature

(continued)

R_o - Initial radius of a jet

R_p - Radius of the potential core (defined in figure 3)

$\overline{R} \equiv R/R_o$

T - Auxiliary function

T_{max} - Maximum value of the auxiliary function

U - Normalized velocity in the jet in the Z direction

u - Actual velocity in the jet in the Z direction ($u = W\cos\Theta + Uh$, see figure 1)

u_o - Initial jet velocity

V_ξ - Induced velocity of a vortex in the ξ direction

V_η - Induced velocity of a vortex in the η direction

X - Coordinate in figure 1

Y - Coordinate in figure 1

W - Velocity of the cross flow

Z - Coordinate in the direction of the center line (defined in figure 1)

Z_s - Coordinate in the direction of the center line in a straight jet

$\overline{Z}_p$ - Dimensionless distance along the center line of a developing vortex pair ($\overline{Z}_p \equiv \frac{Z}{R_o}$)

α - A constant in equation 8

Γ_o - A constant defined in equation 12

η - Coordinate defined in figure 1

Θ - Angle defined in figure 1

ν_t - Turbulent dynamic viscosity

ξ - Coordinate perpendicular to η in figure 1

ρ - Density

Introduction

The turbulent mixing of a circular jet in crossflow is of significant importance in combustion engineering, VTOL or STOL aircraft design, heat transfer calculation of injection cooled gas turbine blades, missile control system development and environmental engineering. Due to its practical importance, this mixing problem received much attention, and many attempts, theoretical as well as experimental, were made to throw some light on this extremely complex flow problem.

A number of approximate predictive methods were developed by Abramovich (1), McAllister (2), Keffer and Baines (3), Snel (4), Stoy and Ben Haim (5), Sucec and Bowley (6), Wooler (7) and Clamp (8). All these are basically integral methods based on simplifying assumptions, introduced for mathematical simplicity. Thus, simple similarity profiles (approximately true only for a straight jet) are used, or the complex jet cross section geometry, perpendicular to the center line, is represented by rectangles, circles or ellipses. These approximate approaches are well justified because a solution of the Reynolds equation in this turbulent mixing field seems to be an enormous task if only the prediction of the "turbulent viscosity" is considered (not to mention entrainment or numerical problems). Simple mixing length or kinetic energy-dissipation rate concepts cannot represent reality because of strong and not negligible curvature effects,

Bradshaw (9, 10), So and Mellor (11, 12), and Ramaprian and Shivaprasad (13), and coriolis like, centripetal acceleration field effects, Johnston (14, 15) and Kayams and Masuda et al (16).

One of the unknowns in integral mixing field prediction methods is usually the shape of jet cross section. Braun and McAllister (17), Margason (18) and Hackett and Miller (19) mention in this connection Chen's idea (20) of vortices distributed along the edge of the orifice in potential flow. This idea was later further improved by Strauber (21). Resulting cross section shapes were close to reality; however, the idea was not extended to full jet mixing calculation, but concentrated merely on cross section prediction.

The second unknown in integral methods is a velocity profile parameter (or parameters). Such a parameter is usually connected to an appropriate similarity assumption, which actually does not exist in a curved jet. Therefore, Keffer and Baines (3) divided the jet into three similarity regions: Potential core, developed turbulent flow and far downstream region. They assumed that the main cross section distortion happens in the potential core region but Kamotani and Greber's measurements (23) show that this is not accurate. Kamotani and Greber further conclude that similarity cannot exist in a curved jet. This conclusion is obvious from theoretical considerations.

The problems of similarity and cross section shape in the curved jet are closely associated with entrainment. An entrainment sub model coupled to velocity decay and cross section shape and growth is required for a solution. In

AD-A079 115 NAVAL AIR DEVELOPMENT CENTER WARMINSTER PA F/G 1/3
PROCEEDINGS OF A WORKSHOP ON V/STOL AIRCRAFT AERODYNAMICS. VOLU--ETC(U)
MAY 79 C HENDERSON, M F PLATZER

UNCLASSIFIED NL

7 OF 7
AD
A079115

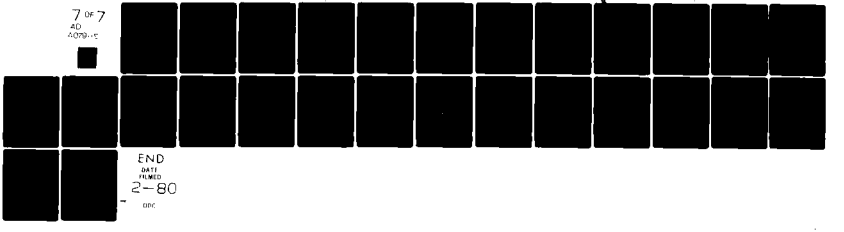

END
DATE FILMED
2-80
DDC

references (4, 5, 7, 23) the entrainment is calculated on the basis of the velocity difference between the jet and its surroundings. In the models reported in (1, 2, 6) the entrainment is represented in a similar way by the cross section growth and is determined with the continuity equation. Baines and Keffer (3, 25) go a step further and assume that entrainment is composed of two components: Straight jet entrainment and helical entrainment. Schwartz and Tulin (26, 27) suggest that the local jet growth can be represented by a vortex pair. Their idea is used here.

The present method was developed with the aim to improve the integral method and extend its ability to predict the inner structure of the deflected jet more accurately, or in other words, to include non similar three-dimensional effects. Modifications included in the method are: I) Improved jet growth function based on straight jet growth and vortex pair concept II) Cross section shape is not of an assumed simple geometry, but is approximately calculated resulting in a more realistic horseshoe shape III) Velocity profiles are non similar quasi-three-dimensional. They are not similarity profiles because their definition is based on the distorted shape of the jet cross section.

Mathematical Model

The model is developed on the basis of some simplifying assumption, namely:

1) External flow field is irrotational

2) The mixing field is isothermal and of uniform composition (no heat transfer of diffusion)

3) The flow is turbulent

4) The flow is incompressible and steady

5) The jet centerline is defined as the locus of the momentum centers of cross sections

6) Velocities are parallel to the centerline

7) Cross section boundary of the jet is the locus of points at which the velocity excess in the direction of the centerline vanishes (or is smaller than a prescribed small value)

8) Pressure on cross sections is uniform and proportional to $W\cos\Theta$

9) Most of the entrainment takes place in the vortex pair tail

A control volume in the jet is defined in figure 1. It is used to derive the governing two momentum equations of the integral model.

These two integral momentum equations, together with four additional equations, namely: the expansion rate equation, the shape equations and the normalized velocity profile equation describe the jet mixing field completely.

1) Momentum equation in centerline direction

For steady flow, surface forces are equated to momentum flux. Gravity is neglected. The result is

$$A\frac{dp_{st}}{dZ} + \frac{d}{dZ}\int_A \rho u^2 dA = \rho E W \cos\Theta \qquad (1)$$

In view of assumptions 8) and 1) using Euler's equation for the

external flow we can write

$$\frac{A}{\rho}\frac{dp_{st}}{dZ} = \frac{1}{2} AW^2 \sin\theta\cos\theta \frac{d\theta}{dZ} \qquad (2$$

furthermore, E, the volumetric entrainment rate, is given in equation A3 of appendix 1.

With equation 2 and A3, the rearranged form of equation 1 will be

$$\frac{dh}{dZ} = \frac{W^2 A \frac{d\theta}{dZ} \sin 2\theta - \frac{dI_2}{dZ} h^2 - wh \left(\frac{dI_1}{dZ}\cos\theta - \frac{d\theta}{dZ} 2I_1 \sin\theta\right)}{2I_2 h + I_1 W\cos\theta} \qquad (3$$

2) Momentum equation in direction normal to the centerline.

Here surface forces and centrifugal body forces are equated to the momentum flux due to entrainment. Surface forces are calculated as a "drag force" acting on the jet considered to be "rigid". A drag coefficient C_D (having values similar to C_D of a circular cylinder) is utilized for this purpose and the force can be expressed as $C_D \frac{b}{2} \rho W^2 \sin^2\theta dZ$. The centrifugal force is

$$F_C = \rho \left[I_2 h^2 + 2I_1 hW\cos\theta + AW^2\cos^2\theta\right] \frac{dA}{dZ} dZ \qquad (4$$

The η momentum flux is $\rho EW\sin\theta dZ$. (E given in equation A3). Using these expressions the η momentum equation is given the following form:

$$\frac{d\theta}{dZ} = \frac{\frac{1}{2} C_D bW^2 \sin^2\theta + W\sin\theta \left(h\frac{dI_1}{dZ} + I_1 \frac{dh}{dZ}\right) + W^2 \sin\theta\cos\theta \frac{dA}{dZ}}{AW^2\sin^2\theta - h^2 I_2 - 2hI_1 W\cos\theta - AW^2\cos^2\theta} \qquad (5$$

To complete the formulation the rate of the jet growth, the shape of the cross sections and the velocity profiles have to be determined.

3) Expansion rate of the jet cross section area

It is assumed here that the jet cross section area growth is a linear superposition of two growing mechanisms: I) Growth of a straight turbulent jet in a quiescent environment, II) Growth of a vortex pair (in accordance with assumption number 9). Although this model of jet growth seems to be an oversimplification, it yields acceptable results as will be seen later in comparison to experiments.

For the straight jet growth in quiescent environment we assume

$$\frac{dR}{d\bar{Z}_S} = G \qquad (6$$

Abramovich (1) suggests that G = 0.22 for turbulent jets and we will use this value in the present study. Equation 6, written for a straight jet, is modified for a curved jet to give

$$\frac{dR}{d\bar{Z}} = \frac{Gh}{h+W\cos\theta} \qquad (7$$

The growth of a vortex pair was studied by Tulin and Schwartz (26, 27). They suggested a growth rate of

$$\frac{1}{\alpha}\frac{d\bar{R}}{d\bar{Z}_p} = (K_1 - \frac{K_2}{\alpha}\frac{d\bar{R}}{d\bar{Z}_p})\,\bar{R}^{(1-A_1)} \qquad (8$$

Tulin and Schwartz achieved good agreement with experiments using

$$\alpha K_1 = 0.38 \quad \text{and} \quad K_2 = 0.5$$

A_1 is a measure to the cancellation of vorticity in the vortex pair tail. For $A_1 = 0$ cancellation is complete. In the present case, due to the sweeping effect of the cross flow, cancellation is not complete and, therefore, $A_1 > 0$. A value of $A_1 = e^{-\left(\frac{2ZW\sin\Theta_o}{\pi D_o u_o}\right)} \frac{M}{6.2}$ gave good results though the generality of this expression is not completely verified.

Equation 8, modified for curved jet conditions, is added to equation 7 to yield the jet growth written in terms of cross section area A, rather than in terms of equivalent normalized radius $\bar{R}$.

$$\frac{dA}{dZ} = \frac{2\sqrt{\pi A}}{h+W\cos\Theta}\left[Gh + \frac{\alpha K_1 W\sin\Theta}{(A_o/A)^{(1-A_1)/2} + K_2}\right] \qquad (9$$

This equation with $W = 0$ reduces to $dR/dZ_S = G$. Indeed, for $W = 0$ the expression for a straight jet in quiescent environment is expected.

4) Cross sections shape

The aim of the cross section shape calculation is to predict approximately the development of the geometry of these shapes (but not the areas) from a circle into the developed horseshoe configuration. This shape development contains much of the non similarity of the mixing process so that its prediction is essential for a representative model. Chang-Lu Hsiu-Chen (20) and Strauber (21) studied the deformation of a potential circular jet deflected by crosswind. The cross section distortion is determined by evenly seeding a finite number, N, of vortices on the instantaneous boundary of the jet and calculating their displacement over a small

time period, dt, due to their induced velocity. The induced velocities of the vortices including viscous damping are given by the following three equations. The detailed derivation of these equations is described in references [20] and [21].

$$V_\eta = \frac{2\Gamma_o}{\pi} \sum_{n=1}^{N} \left\{ \sin\left[\frac{2\pi}{N}(n-1)\right] \frac{(\xi-\xi_n)\left[1-e^{-\frac{(\eta-\eta_n)^2+(\xi-\xi_n)^2}{4\nu_t}}\right]}{(\eta-\eta_n)^2+(\xi-\xi_n)} \right\} \quad (10$$

$$V_\xi = -\frac{2\Gamma_o}{\pi} \sum_{n=1}^{N} \left\{ \sin\left[\frac{2}{N}(n-1)\right] \frac{(\eta-\eta_n)\left[1-e^{-\frac{(\eta-\eta_n)^2+(\xi-\xi_n)^2}{4\nu_t}}\right]}{(\eta-\eta_n)^2+(\xi-\xi_n)^2} \right\} \quad (11$$

where

$$\Gamma_o = W\sin\Theta\, R_o \sin\Theta\,(\tfrac{\pi}{N}) = \text{const.} \quad (12$$

For a known instantaneous cross section, the induced velocity components V_x and V_y of each vortex is calculated. The vortex is then displaced by $V_x dt$ and $V_y dt$. All the new positions of the vortices describe the new cross section shape. The viscosity ν_t for the turbulent jet can be calculated with Owen's formula (22). Figure 2 gives an example of computer plotted results of such a computation.

5) Normalized velocity distribution

As the curved jet is not a similarity phenomenon, similarity profiles cannot be used in the present integral method if it is to be realistic. Further, the profiles should be three-dimensional to represent the flow correctly. However, in an integral method, only parameters of a profile family but not exact profiles are determined. Therefore, a special, downstream varying, calculated

familty of velocity profiles is used. In the non normalized form they include the familiar parameter, h, but they are not similarity profiles because they are calculated on the basis of the varying cross section shape as determined by equations 10 and 11. This family of velocity profiles, in analogy to similarity profiles in classical integral methods, has to contain qualitatively correct velocity profiles which also satisfy the physical boundary conditions. Therefore, to satisfy these two simple conditions, and these two conditions only, the familty of velocity profiles, U, is computed using the previously determined cross section shapes, and an auxiliary function, T, which is numerically computed. T satisfies $V^2T=q$ inside the domain of the cross section (q being a constant in the domain) and T=0 on the boundary. With T known, U is given by

$$U = \left(\frac{T}{T_{max}}\right)^{\frac{T}{T_{max}}(P-Q)} + Q + 1 \qquad (13$$

where Q and P are distortion parameters used to adjust the profiles as to correspond to measured turbulent velocity profiles. Q distorts the function in the neighborhood of the boundaries of the domain while P affects the profile inside the domain as shown in Figure 3. These parameters were evaluated using

$$P = 0.15 + \frac{0.126(Z-L_p)}{15\ D_o - L_p} \quad \text{and} \quad Q = 0.945$$

which gave good results in the present examples though their generality is not confirmed. The value of the constant q is immaterial because the normalized function T/T_{max} is used to determine U. q=1 was used in the present work. Physically the curved jet can be divided into three major regions: 1) The potential core region where the excess center line velocity is constant, 2) The deflection region where the flow is highly non similar, and 3) The similarity region

far downstream where the jet is almost parallel to the deflecting main flow. Expression 13 can also be used to describe the profile in the potential core region by cutting U at $r = R_p$ and renormalizing the profile so that U = 1 on the center line. Such a potential core profile is given in Figure 3 in broken line. Figure 4 gives an example of a computer plotted velocity distribution in the deflection region.

The curved jet is described by equations 3, 5 and 9 together with cross section shapes according to equations 10 and 11 and velocity distributions given by equation 13. Equations 3, 5, and 9 are ordinary coupled differential equations. They are numerically solved with a combined four point Runge-Kutta procedure for the unknown functions h, A, and Θ in terms of the independent variable Z. The functions I_1, I_2 and b required for this solution are obtained in each Runge-Kutta step with the results of equation 13 numerically integrated over the appropriate cross section area. The shapes of these cross sections are determined by equations 10 and 11 and are subsequently corrected (maintaining geometric similarity) to include the area as predicted by equation 9. The time intervals Δt required for vortices displacement calculation are calculated with $\Delta t = \Delta Z/\bar{u}$ where $\bar{u}$ is the average jet velocity and ΔZ is the Runge-Kutta step.

In the potential core region and in the similarity region the equations can be simplified. The centerline velocity in the potential core region is simply given by

$$h = u_o - W\cos\Theta \qquad (14$$

which is used instead of equation 3. The length of the potential core is derived using the empirical correlations of Kamotani and Greber(23).

$$L_P = \frac{D_o}{0.154 + 0.72M} \qquad (15$$

Once L_p, the length of the conical core, is known the values, R_p, required for the velocity profiles, are easily determined. In the similarity region the cross section shape and profile calculations are not necessary. Instead, similarity of shapes and profiles is used to determine the values of I_1, I_2 and their derivatives to be used in the solution of equations 3, 5 and 9.

Comparison Between Calculated Results and Experiments

The present mathematical model was solved numerically for a number of jets for which experimental data is available in literature. The experiments chosen ranged from M values of about 4 to 12, from Z/D_o values of about 0 to 25 (in some cases well into the similarity region) and from injection angles of 90^o to 20^o, so that the present method is tested over a reasonably wide field of jet parameters.

Figure 5 compares velocity contours measured by Kamotani and Greber (23) at $\Theta_o=90^o$ to results of the present method for a case where the velocity maximum is located on the centerline. Figure 6 shows velocity profiles along the axes of Figure 5. Figure 7 describes another experiment of Kamotani and Greber (23) with $\Theta_o=90^o$ at larger M values and further downstream, where the velocity maximum is not located on the centerline but in the centers of the horseshoe branches. Figure 8 shows velocity profiles along the axes of Figure 7. Here agreement is not as good as in the previous case, but the general character of the jet (i.e., the two velocity peaks) is well predicted by the present method.

In Figure 9 calculated centerlines all for $\Theta_o=90^o$ are compared for three M values with experiments of Kamotani and Greber (23) and Jordinson (28). In Figure 10 calculated centerlines for three Θ_o values and a constant higher M value are compared to Zandbergen and Joosen's experiments (29). Agreement between prediction and experiment is good over the whole range of jet injection angles and M values.

The calculated relative mass flux $\dot{m}/\dot{m}_o$ which is a measure to entrainment as represented by the jet growth model and the velocity profiles is compared to experiments of Kamotani and Greber (23) for $\Theta_o=90^o$ injections in Figure 11 and to Zandbergen and Joosen (26) for a higher M value and lower injection angles in Figure 12. Here scatter is bigger because of the difficulty in the jet boundary definition. The ratio $\dot{m}/\dot{m}_o$ for constant density is calculated with

$$\frac{\dot{m}}{\dot{m}_o} = \frac{\int_A (hU+W\cos\Theta)\,dA}{u_o A_o} \qquad (16$$

$u_o A_o$ is well defined while definition of A, the integration boundary of the nominator, is not exact at the jet edge, the region where u gradients are small. The end result of the integration depends on A because external velocity is not zero.

Conclusions

An integral method using a new family of not similar quasi three-dimensional velocity profiles (based on a realistic jet cross section shape), and a new jet growth model (based on a

a linear combination of straight jet and vortex pair entrainments), is developed to describe the curved jet. It is demonstrated that this technique can predict in principle the non similar three-dimensional mixing region of a jet in cross flow including its internal velocity field. The constant q and the parameters P and Q as determined in the present work gave satisfactory agreement for $4 < M < 12$ and $20° < \theta < 90°$ The accuracy of their use outside this range is not known and should be the subject of future investigations. More experiments are necessary to derive reliable correlations for these coefficients in order to increase the accuracy, and much more important, the generality of the method. In the meantime, however, the technique can be used in the range of jet parameters tested for incompressible isothermal submerged jets in cross flows. Another problem is the applicability of the present method in cases where $\theta > 90°$ (injection against the cross flow). In this case some of the present assumptions concerning rate of entrainment and cross section shape might not be acceptable. Extension of the technique to compressible non isothermal deflected jets is possible and will be carried out in the near future.

APPENDIX I

Derivation of the entrainment rate equation for incompressible jet

The control volume of Figure 1 is used for this derivation. The mass flux through a jet cross section, A, is

$$\rho\int_A u dA = \rho\int_A (U_h + W\cos\theta)\, dA = \rho I_1 h + \rho A W\cos\theta \qquad \text{(A1}$$

The volumetric entrainment rate is defined as

$$E \equiv \frac{1}{\rho}\frac{d}{dZ}(\rho I_1 h + \rho A W\cos\theta) \qquad \text{(A2}$$

differentiation gives

$$E = \frac{d}{dZ}(hI_1) + W\frac{d}{dZ}(A\cos\theta) \qquad \text{(A3}$$

REFERENCES

1. Abramovich, G. N., The Theory of Turbulent Jets, Massachusetts Institute of Technology Press, 1963.
2. McAllister, J. D., A Momentum Theory for the Effects of Cross Flow on Incompressible Turbulent Jets: The University of Tennessee Ph.D. Thesis, 1968.
3. Keffer, J. F. and Baines, W. D., The Round Turbulent Jet in a Cross-Wind, Journal of Fluid Mechanics, Vol. 15, 1963, pp. 481-496.
4. Snel, H., A Model for the Calculation of the Properties of a Jet in a Cross Flow, NLR TR 74080 U., 1974.
5. Stoy, R. L. and Ben Haim, Y., Turbulent Jets in a Confined Cross Flow, ASME Paper No. 73-FE-15, 1973.
6. Sucec, J. and Bowley, W. W., Prediction of the Tranjectory of a Turbulent Jet Injection into a Cross Flowing Stream, Journal of Fluids Engineering ASME Series I, Vol. 98, 1976, pp. 667-673.
7. Clamp, Brian G., Smoke Abatement in Coal Field Metallurgical Furnaces, University of Sheffield, Ph.D. Thesis, 1959.
8. Wooler, P. T., Development of Analytical Model for the Flow of a Jet into a Subsonic Cross-Wind, NASA SP-218, 1969.
9. Bradshaw, P., The Analogy Between Streamline Curvature and Buoyancy in Turbulent Shear Flow, Journal of Fluid Mechanics, Vol. 36, 1969, pp. 177-191.
10. Bradshaw, P., Complex Turbulent Flows, Journal of Fluids Engineering, Vol. 96, 1975, pp. 146-154.

11. So, R.M.C. and Mellor, G. L., Experiments on Convex Curvature Effects in Turbulent Boundary Layers, Journal of Fluid Mechanics, Vol. 60, 1973, pp. 43-62.

12. So, R.M.C. and Mellor, G. L., Experiment on Turbulent Boundary Layers in a Concave Wall, Aeronautical Quarterly, Vol. 26, 1975, pp. 35-40.

13. Ramaprian, B. R. and Shivaprasad, B. G., The Structure of Turbulent Boundary Layers along Mildly Curved Surfaces, Journal of Fluid Mechanics, Vol. 85, 1978, pp. 273-303.

14. Johnston, J. P., The Suppression of Shear Layer Turbulence in Rotating Systems, Journal of Fluids Engineering, Vol. 95, 1973, pp. 229-236.

15. Johnston, J. P., Eide, S. A., Turbulent Boundary Layers on Centrifugal Blades: Prediction of the Effects of Surface Curvature and Rotation, Journal of Fluids Engineering, Vol. 98, 1976, pp. 374-381.

16. Koyama, H., Masuda, S. et al, Stabilizing and Destabilizing Effects of Criolis Force on Two Dimensional Laminar and Turbulent Boundary Layers, ASME Paper 78-Gt-1, 1978.

17. Braun, G. W. and McAllister, J. D., Cross Wind Effects on Trajectory and Cross Sections of Turbulent Jets, NASA SP-218, 1969.

18. Margason, Richard J., Analytic Description of Jet-Wake Cross Sections for a Jet Normal to a Subsonic Free Stream, NASA SP-218, 1969.

19. Hackett, J. E. and Miller, H. R., The Aerodynamics of the Lifting Jet in a Cross Flowing Stream, NASA SP-218, 1969.

20. Chang-Lu Hsiu-Chen, Aufrollung Eines Zylindrischen Strahles Durch Querwind, University of Gottingen, Doctoral Dissertation, 1942.

21. Strauber, M., Berechnung von Strahlkonturen mit Hilfe eines Wirbelringmodells, Zeitschrift fur Fluguissenschaften, Vol. 23, 1975, pp. 394-400.

22. Owen, P. R., The Decay of a Turbulent Trailing Vortex, Aeronautical Quarterly, Vol. 21, 1970, pp. 69-78.

23. Kamotani, Y. and Greber, Isaac, Experiments on a Turbulent Jet in a Cross Flow, NASA CR-72893 FTAS/TR-71-62, 1971.

24. Wooler, P.T., Burghart, G.H. and Gallagher, J.T., Pressure Distribution on a Rectangular Wing with a Jet Exhausting Normally into an Airstream, Journal of Aircraft, Vol. 4, 1967, pp. 537-543.

25. Keffer, F. J., The Physical Nature of the Subsonic Jet in Cross Stream, NASA SP-218, 1969.

26. Tulin, M.P. and Shwartz, J., The Motion of Turbulent Vortex Pairs in Homogeneous and Density Stratified Media, Tec. Rep. 231-15, Hydronautics, Inc., 1971.

27. Shwartz, J. and Tulin, M.P., Chimney Plumes in Natural and Stable Surrounding, Atmospheric Environment, Vol. 6, 1972, pp. 19-35.

28. Jordinson, R., Flow in a Jet Directed Normal to the Wind, R&M No. 3074, British A.R.C., 1956.

29. Zandbergen, T. and Joosen, C.J.J., Experimental Investigation of Round Turbulent Jet in a Cross Flow, NLR TR 74013, 1973.

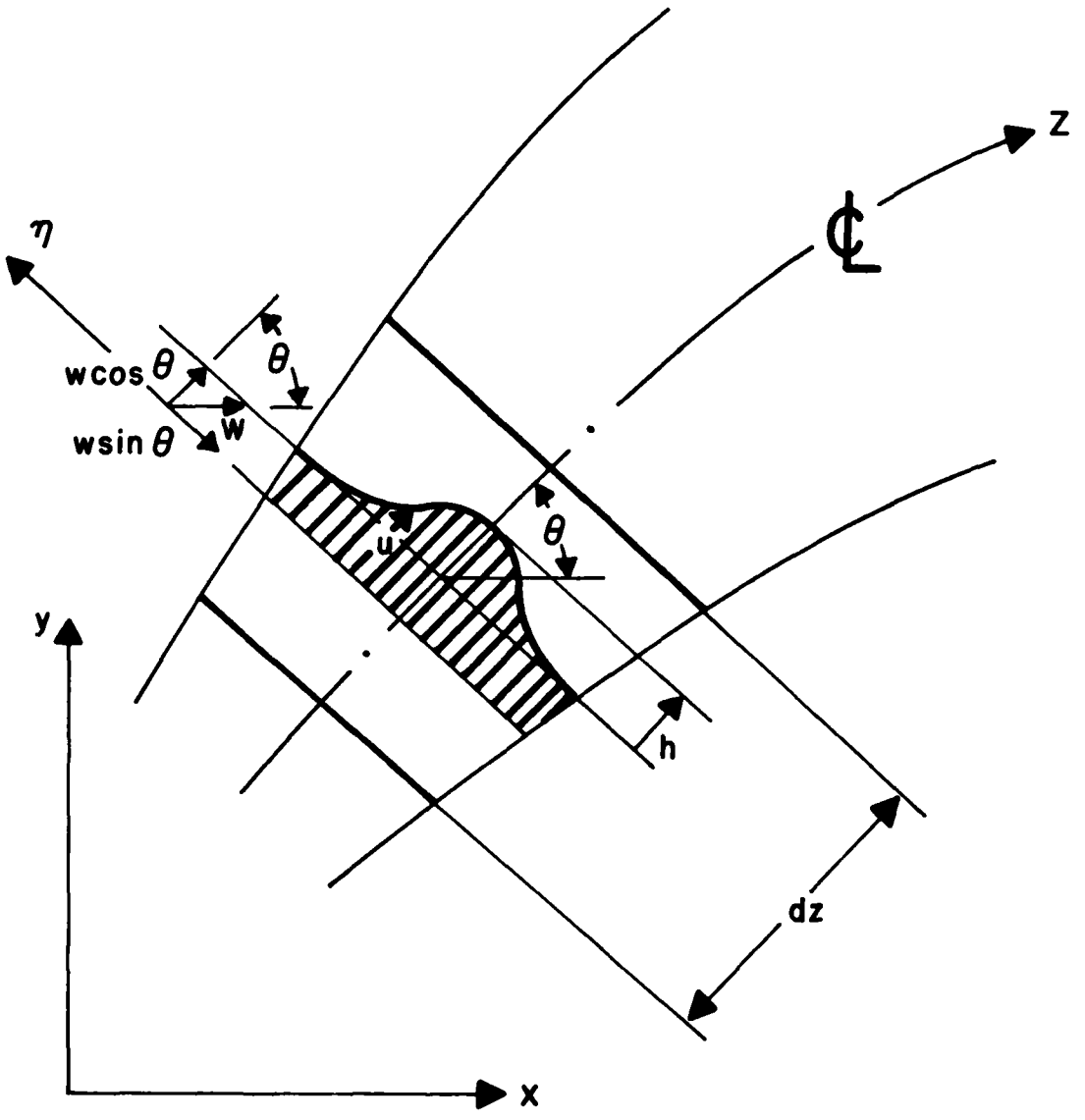

Fig. 1: Definition of a control volume some dimensions and the coordinate systems used to analyze the deflected jet.

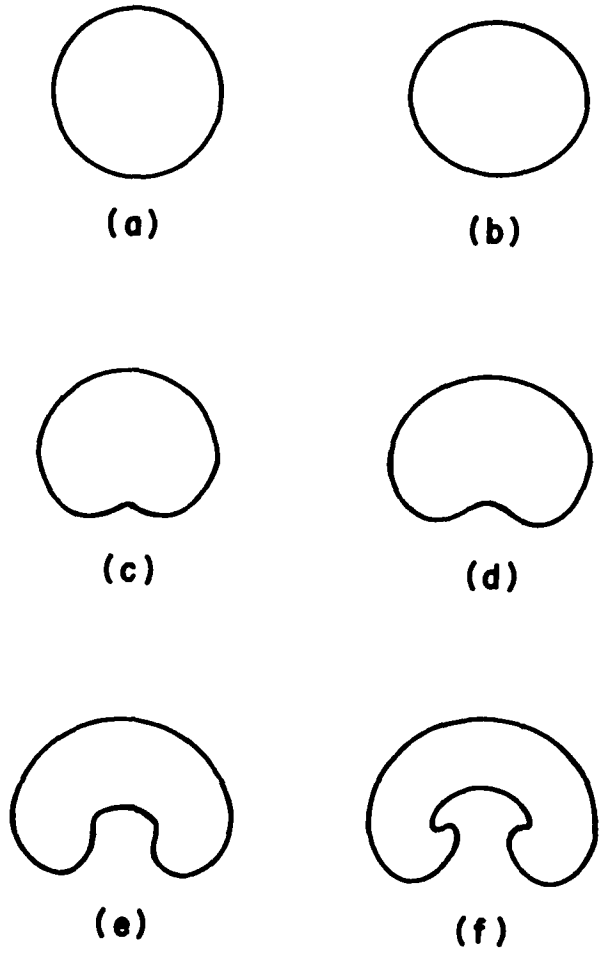

Fig. 2: Development of jet cross sections downstream along its centerline.

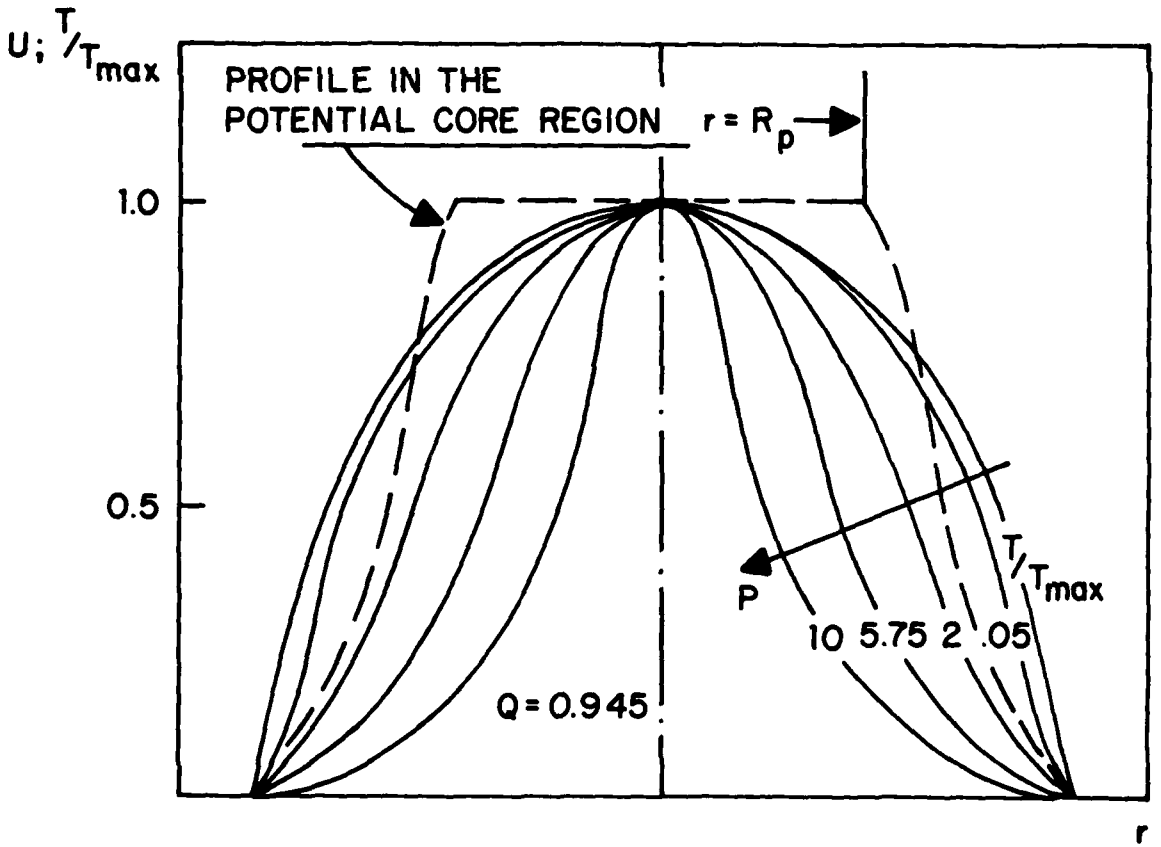

Fig. 3: An example of normalized velocity profiles as used in the integral solution (in this case for a circular cross section).

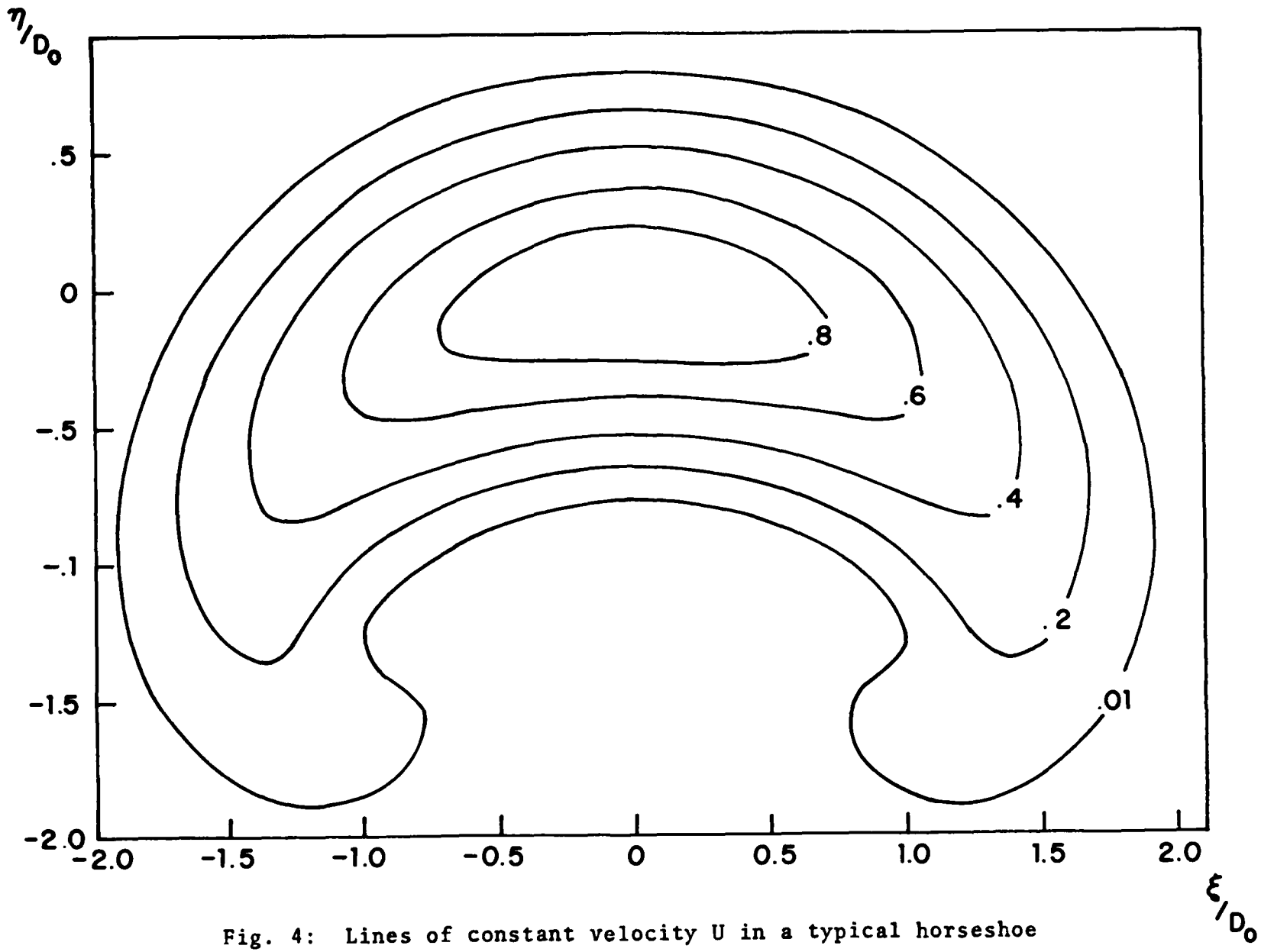

Fig. 4: Lines of constant velocity U in a typical horseshoe cross section.

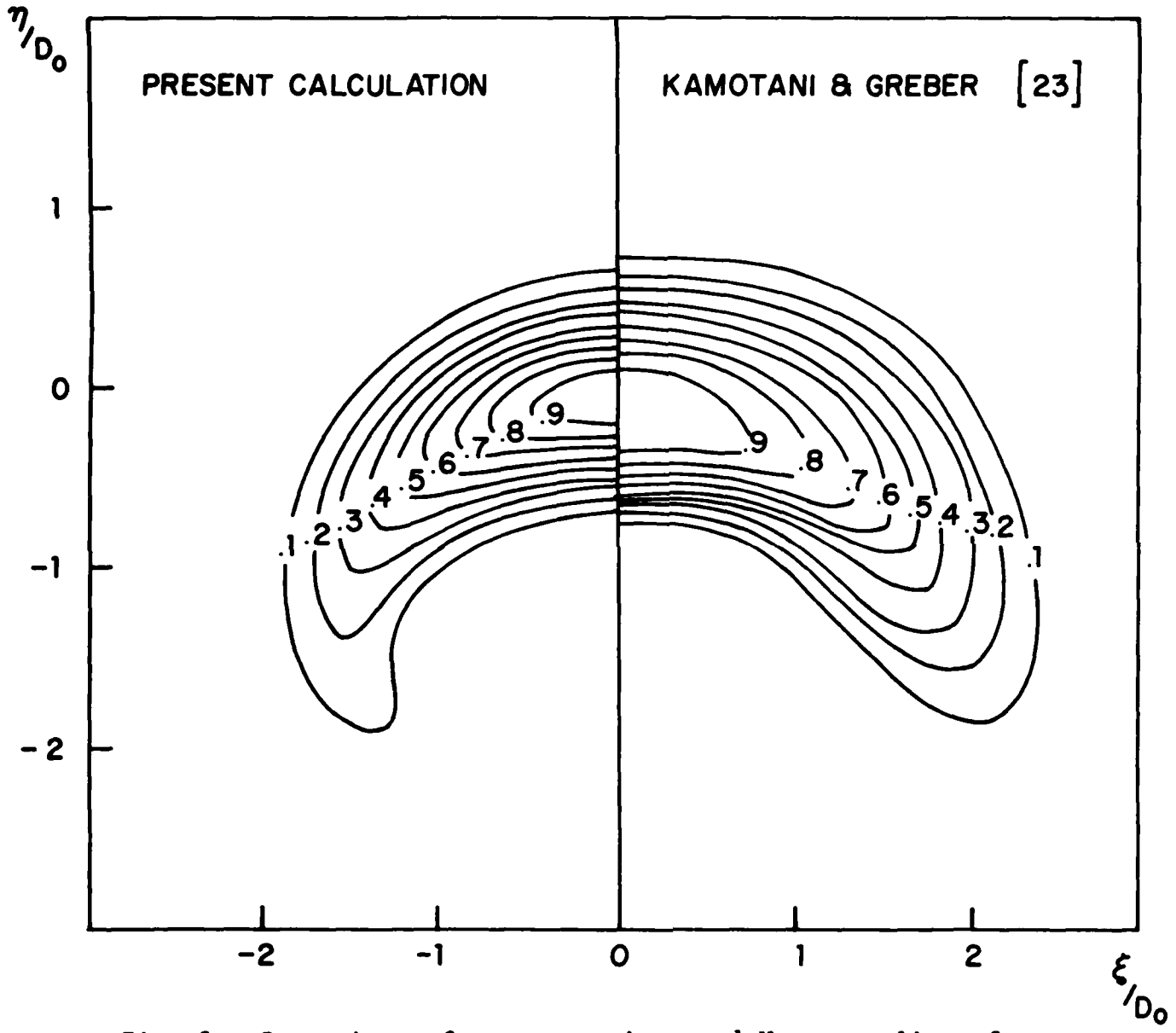

Fig. 5: Comparison of cross sections and U=const. lines for M=3.91 and at $Z/D_o=7$ ($\theta_o=90^o$).

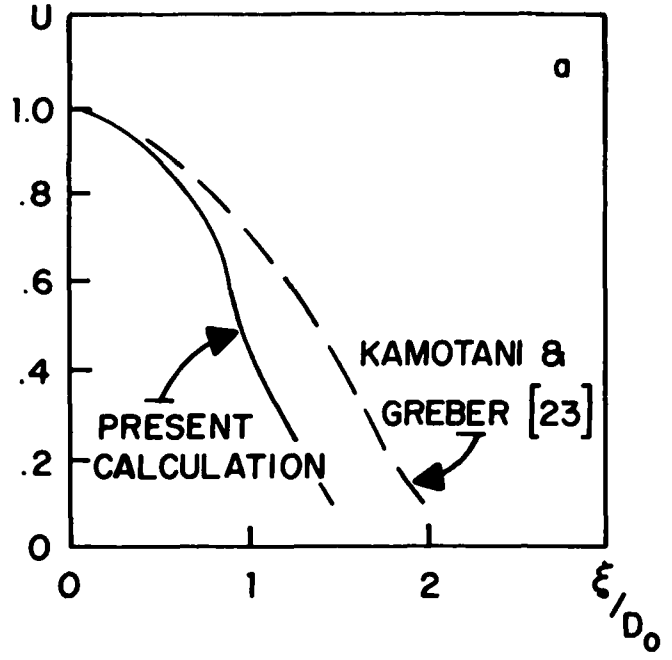

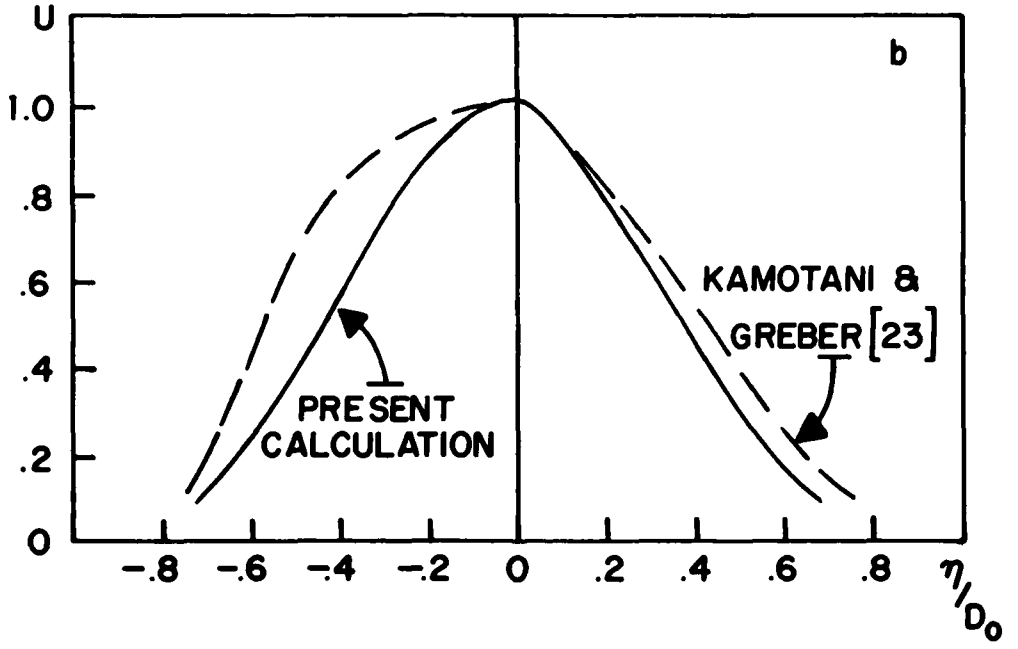

Fig. 6: Comparison of velocity profiles in fig. 6: a) along $\eta/D_o=0$ b) along $\xi/D_o=0$.

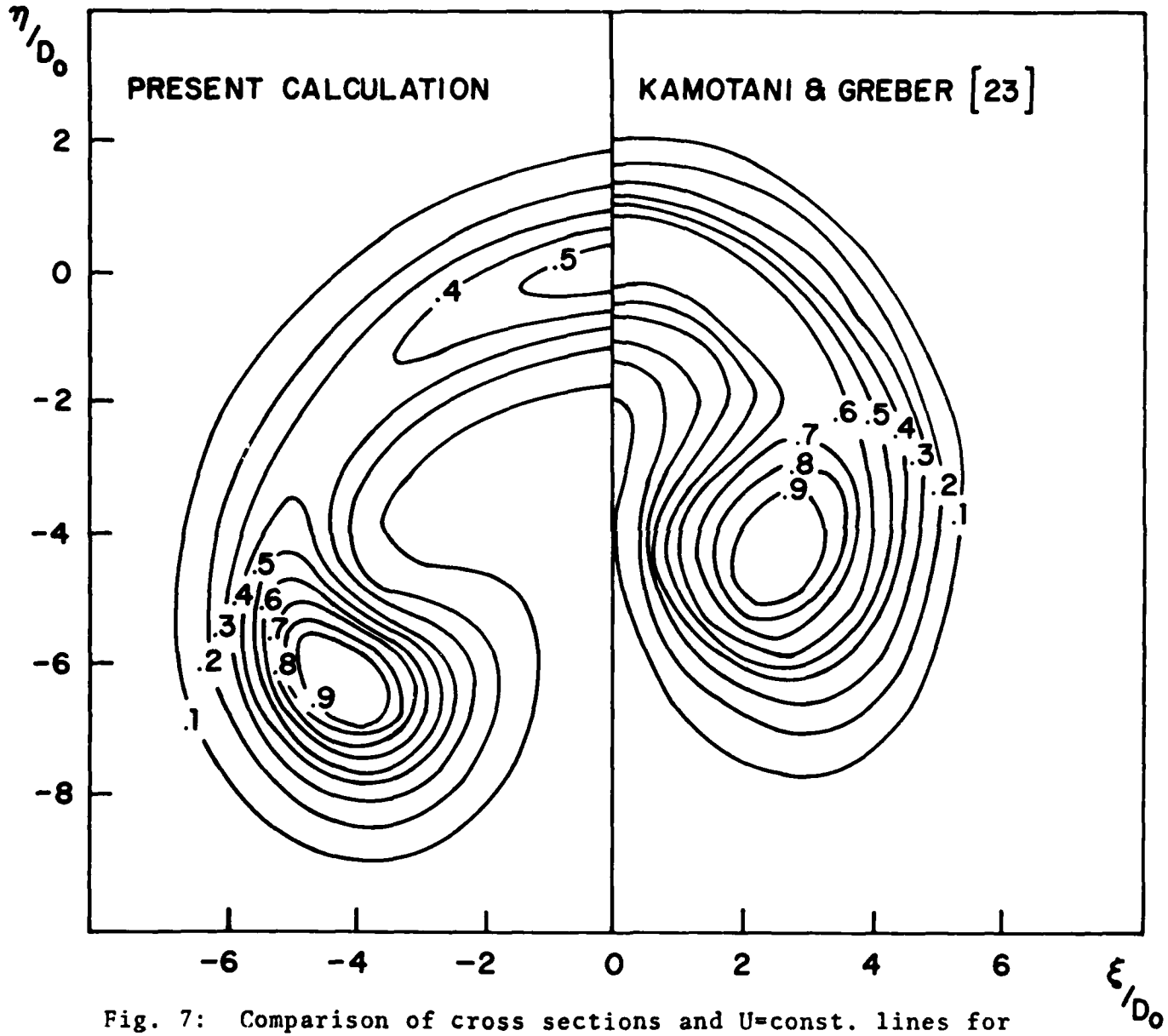

Fig. 7: Comparison of cross sections and U=const. lines for M=7.73 and at $Z/D_0=23$ ($\theta_0=90^0$).

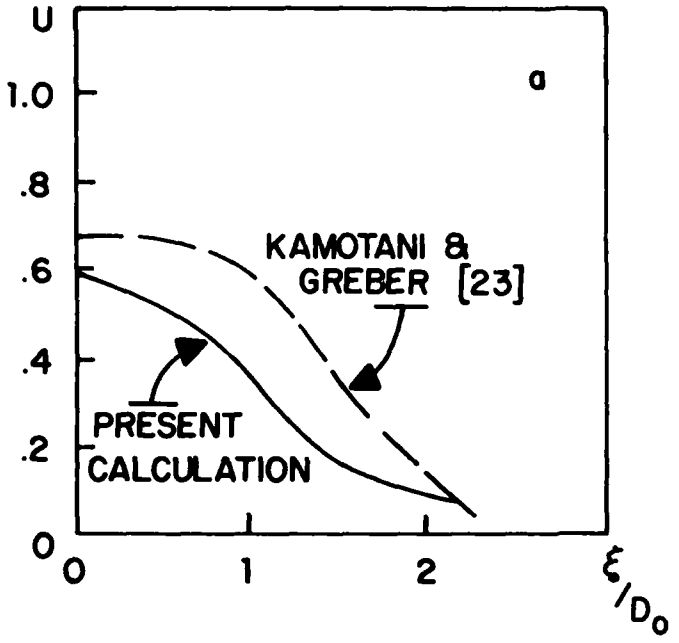

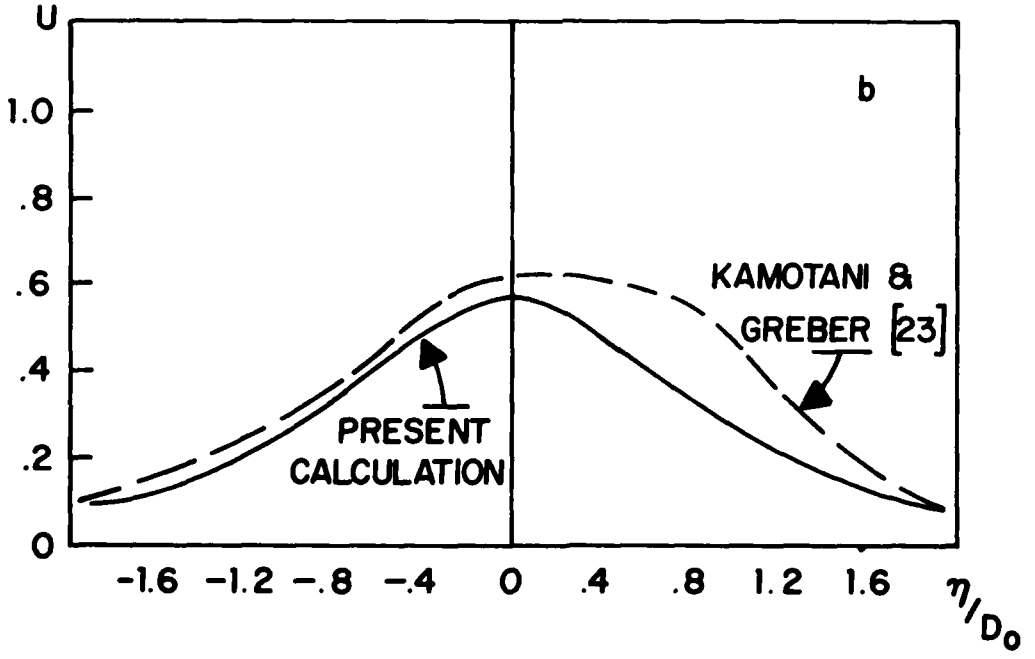

Fig. 8: Comparison of velocity profiles in fig. 7:
a) along $\eta/D_o=0$ b) along $\xi/D_o=0$.

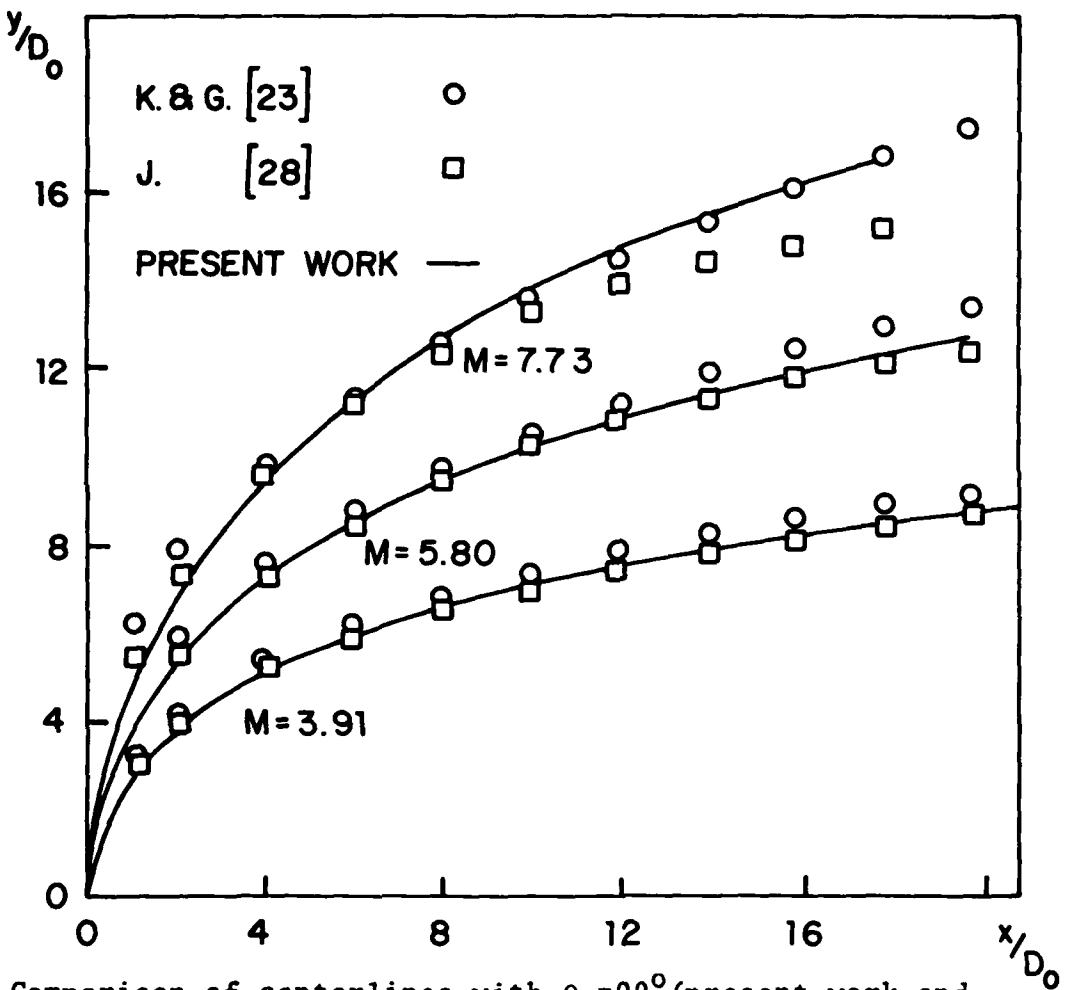

Fig. 9: Comparison of centerlines with $\theta_o=90^o$ (present work and K & G are centerlines of maximum velocity. Jordinson's are centerlines of maximum total pressure for M values of 8.1, 6.2 and 4.7)

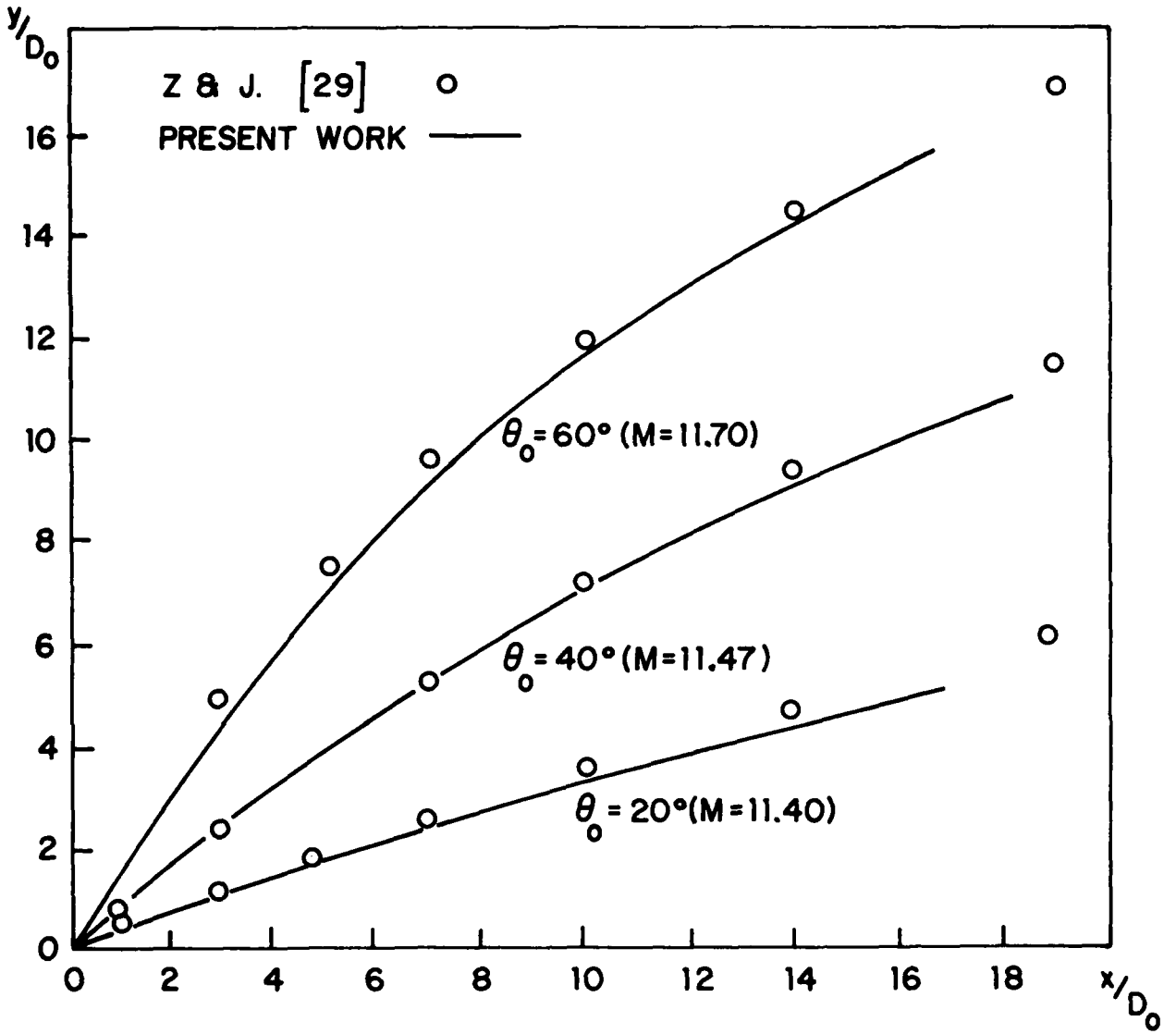

Fig. 10: Comparison of maximum velocity centerlines of jets injected in the direction of the cross flow. ($\theta_o > 90^o$)

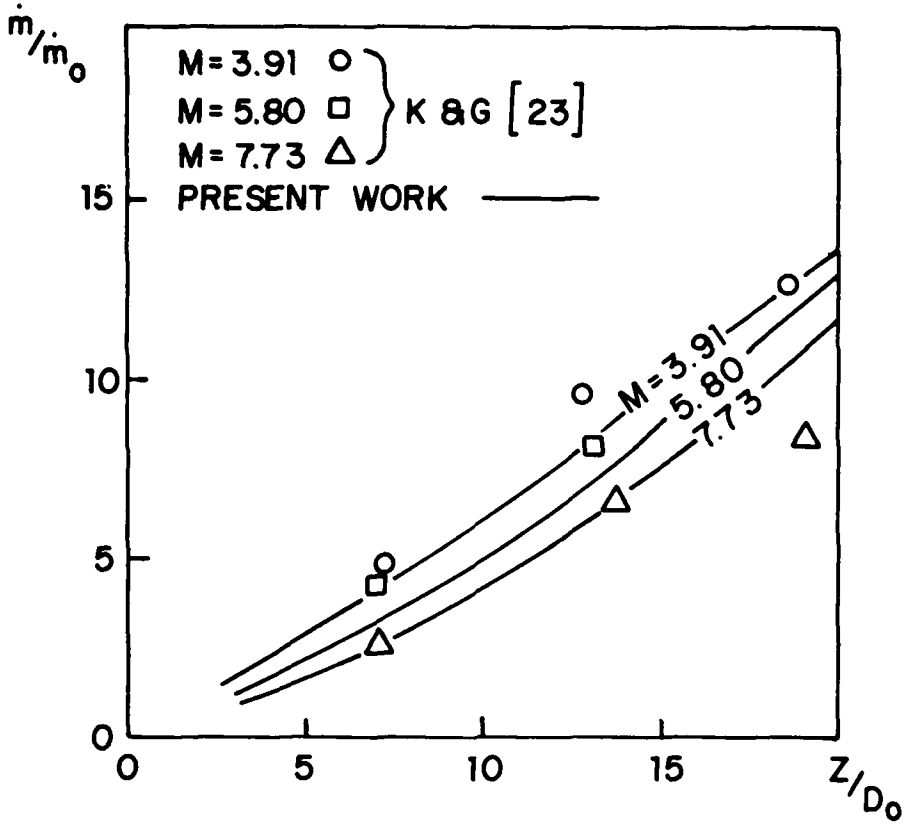

Fig. 11: Comparison of the relative mass flux for jets with $\Theta_o=90^0$.

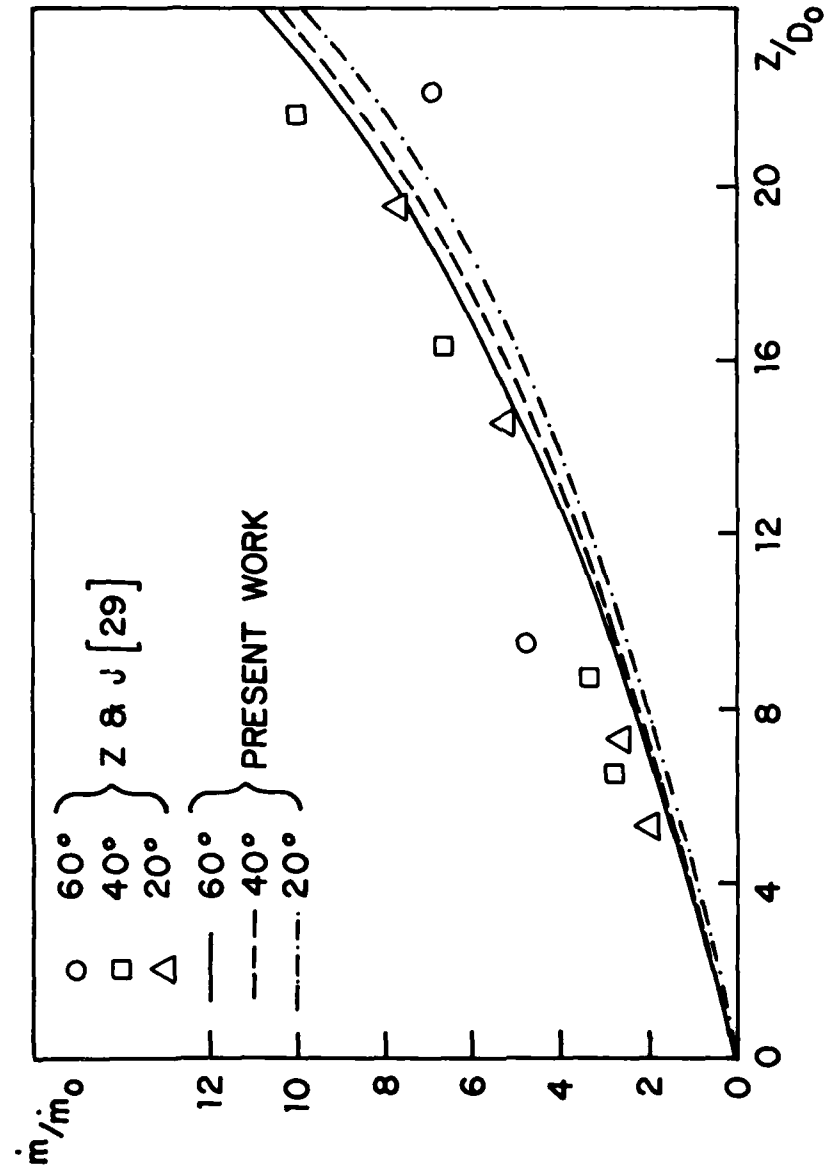

Fig. 12: Comparison of the relative mass flux for jets with $\Theta_o < 90^o$ (M values as in fig. 10).

UNCLASSIFIED

SECURITY CLASSIFICATION OF THIS PAGE (When Data Entered)

REPORT DOCUMENTATION PAGE		READ INSTRUCTIONS BEFORE COMPLETING FORM
1. REPORT NUMBER	2. GOVT ACCESSION NO.	3. RECIPIENT'S CATALOG NUMBER
4. TITLE (and Subtitle) V/STOL AIRCRAFT AERODYNAMICS, PROCEEDINGS OF A WORKSHOP VOLUME I		5. TYPE OF REPORT & PERIOD COVERED Workshop Proceedings 6. PERFORMING ORG. REPORT NUMBER
7. AUTHOR(s) C. Henderson and M. Platzer (Editors)		8. CONTRACT OR GRANT NUMBER(s)
9. PERFORMING ORGANIZATION NAME AND ADDRESS Naval Postgraduate School Monterey, CA		10. PROGRAM ELEMENT, PROJECT, TASK AREA & WORK UNIT NUMBERS
11. CONTROLLING OFFICE NAME AND ADDRESS Naval Air Development Center Warminster, PA		12. REPORT DATE May 16 - 18, 1979 13. NUMBER OF PAGES 604
14. MONITORING AGENCY NAME & ADDRESS(if different from Controlling Office)		15. SECURITY CLASS. (of this report) UNCLASSIFIED 15a. DECLASSIFICATION/DOWNGRADING SCHEDULE
16. DISTRIBUTION STATEMENT (of this Report) Unlimited		DISTRIBUTION STATEMENT A Approved for public release; Distribution Unlimited
17. DISTRIBUTION STATEMENT (of the abstract entered in Block 20, if different from Report)		
18. SUPPLEMENTARY NOTES		
19. KEY WORDS (Continue on reverse side if necessary and identify by block number) V/STOL Aircraft, Low Speed Aerodynamics, V/STOL Testing, Powered Lift Systems, Jet Flap, Transition Aerodynamics, Propulsion System/Airframe Interactions, Ground Interference Effects		
20. ABSTRACT (Continue on reverse side if necessary and identify by block number) This report contains the proceedings of the Workshop on V/STOL Aircraft Aerodynamics held at the Naval Postgraduate School on May 16 to 18, 1979. This workshop was sponsored by the Naval Air Development Center. The workshop participants included representatives from industry, government, universities and abroad.		

DD FORM 1 JAN 73 1473 EDITION OF 1 NOV 65 IS OBSOLETE
S/N 0102-014-6601

SECURITY CLASSIFICATION OF THIS PAGE (When Data Entered)

GPO 693-486/47